3rd International EuroConference on

High-Performance Marine Vehicles

HIPER'02

Bergen, 14-17 September 2002

Volker Bertram (Ed.)

A WEGEMT event supported by the European Commission,
Human Potential Programme, Contract HPCFCT-1999-???

Contents

Wind Tunnel Measurement of 6-Component Forces and Moments Acting on a Model of New Wing-In-Surface-Effect Craft of All-Wing Type for 8 Passengers

Hiromichi Akimoto, Yasuhisa Matsuzaki, Yoshinori Ogawa, Takahiro Taketsume, Syozo Kubo
Dept. of Applied Mathematics and Physics, Faculty of Engineering, Tottori University, Japan
akimoto@damp.tottori-u.ac.jp

Abstract

The present authors are developing a new Wing-In-Surface-Effect craft of all-wing type for 8 passengers (6th Int. Conf. FAST2001, Southampton, Papers, Vol.3, pp.1-6.). They report their result of wind tunnel measurements of 6-componennt forces and moments. The tests were conducted for a full ship model of scale of 1/50 to the real ship at wind speed 30 m/s. The Reynolds number was 5.2×10^5. *A solid plane with boundary layer suction simulated the water surface. The main result is as follows. First, the surface effect is significant at an altitude less than 12.5% chord. Second, the ratio of lift by drag is over 9 at an altitude of 10% chord in spite of the low aspect ratio of the wing, 0.71. Third, the horizontal stabilizer and the elevator work well to control the ship. Fourth, the maximum available value of lift coefficient is 1.2. From the fact we will be able to estimate the performance of the ship. The take-off/ alighting speed is 94 km/h. The best cruising speed is 150 km/h, in which the engine power is 58% of its maximum rating. The cruising speed at 75% power is 165 km/h. The maximum speed is 210 km/h. These cruising and maximum speeds are the same order of speed of cars on a highway. At any speed the craft can be controlled.*

1. Introduction

Wing-In-Surface-Effect craft is a kind of ship flying in the vicinity of ground/ water surfaces. The craft is considered a hopeful candidate of high-speed marine craft of the next generation[1)]. For modern countries and areas high-speed transportation is a necessary factor for human activities. High-speed trains and highways are typical examples to support modern life. However, only ships and aircraft are means of transportation over seas. Ships can carry huge amount of passengers and goods in a very low cost. But they are too slow to meet the above-mentioned modern needs. On the other hand aircraft is very fast but very expensive. There is a big gap between the speeds of ships and aircraft. We are going to use Wing-In-Surface-Effect craft in the gap region[2)].

Many craft with wing-in-surface-effect have been developed[3)]. They are famous Russian big craft for military use, civilian craft including Bolga-2 and Amphistar, German Airfishes and Joerg's craft and Chinese craft. All of them are unsuitable for civilian use in Japan. In Japan the primary route of the craft is on an open sea with relatively high waves instead of closed water surface of lake, river and gulf. Therefore our craft should have a high operational wave height. This is the reason that we must develop our own craft for operations in Japan.

We are now developing a craft for 8 passengers in cooperated with Fukusima Shipbuildings[4)], Fig.1, Table 1.

Wind tunnel test is one of important items for development of an essentially new type of craft. We carried out the wind tunnel testing. This is the report of the test. Such a kind result of wind tunnel test is seldom reported. If we hope for international development of Wing-In-Surface-Effect craft, we must compile these data as far as possible.

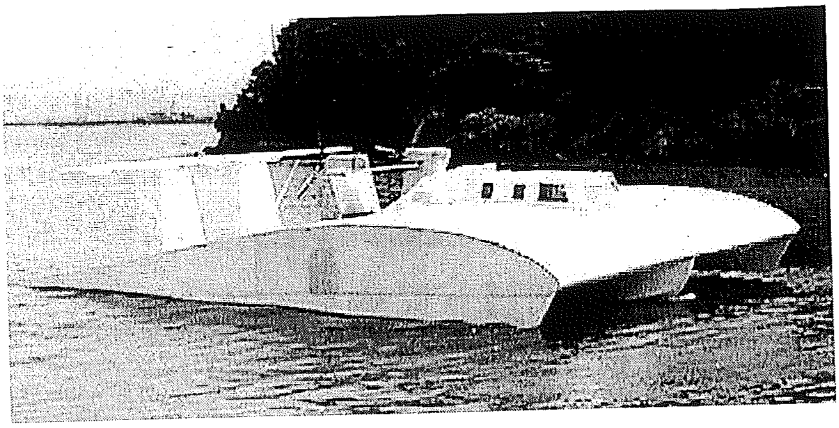

Figure 1. Wing-In-Surface-Effect craft for 8 passengers

Table 1. Main data of a Wing-In-Surface-Effect craft for 8 passengers.

Length	12.00 m
Breadth	8.50 m
Width of the center part	2.80 m
Draught	0.25 m
Power Plants	250 HP $\times$2
Passenger/ Crew	8/1
Total Weight	2.8 ton
Gross Tonnage	8.5 ton

2. Model and Apparatus

The arrangement of our experiment is shown in Fig.2.

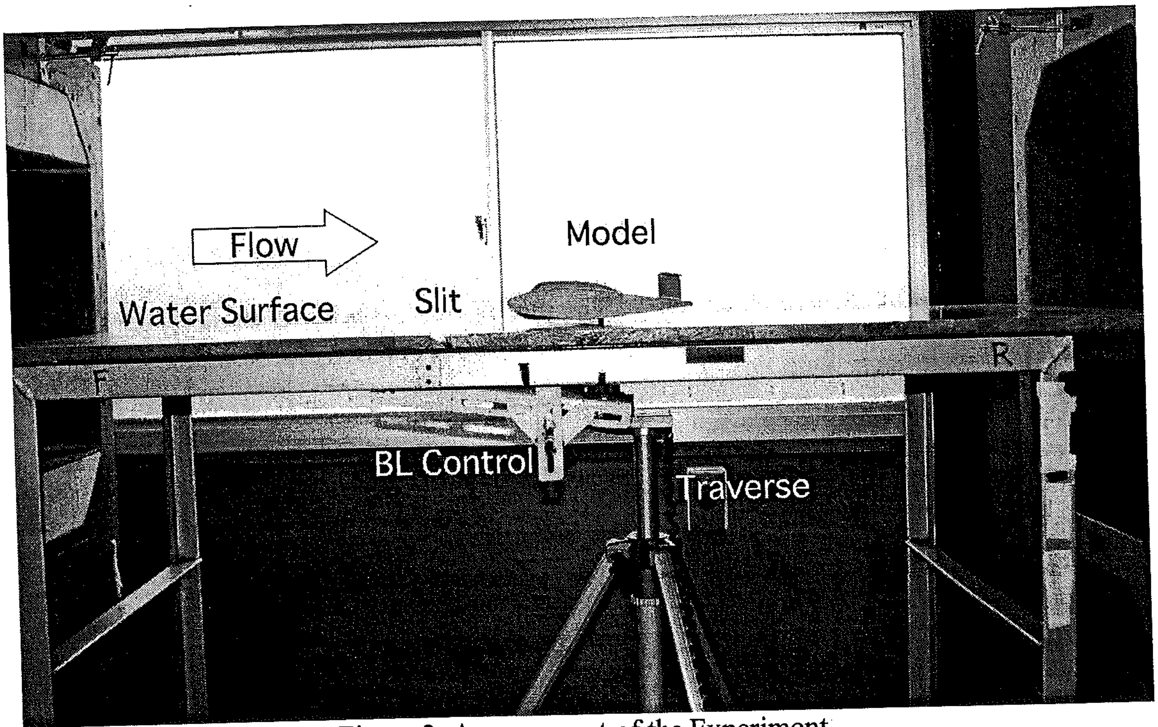

Figure 2. Arrangement of the Experiment.

We show the model and apparatus used in the wind tunnel test as follows.

Our model is a full ship model of 1/50 scale of the real craft with main wing, hull and tail unit, Fig.3, Table 2. We omitted detailed structures e.g. engines, propellers and struts. The model is made of wood. Angles of its horizontal stabilizer and elevator are adjustable. The model is supported from its bottom through a coupling just after the step by a stem connecting to a sensor of forces and moments.

Table 2. Main model parameters

Length	240 mm
Width	170 mm
Aspect Ratio	0.71
Wing Area	$3.43 \times 10^{-2}\ m^2$
Plan Form	Rectangle
Thickness of the End Plate	1 mm
Weight	417 g (4.09 N)

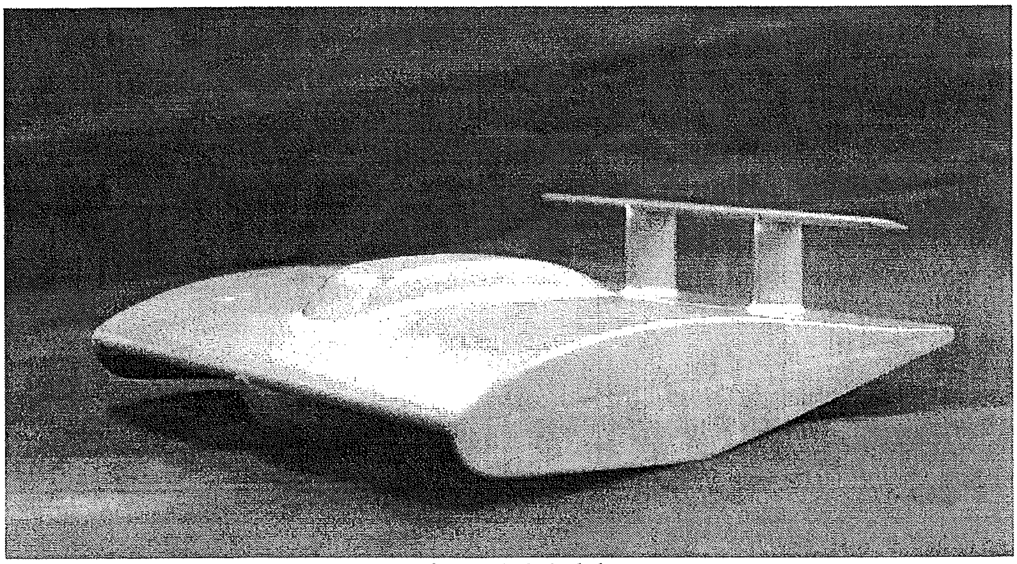

Figure 3. Model

We simulate the water surface by a solid plate as shown in Fig.4. The plate has a hole through which the stem is connected to the sensor under the plate. In this configuration the boundary layer developing on the plate has a considerable thickness in comparison to the height of the model. The boundary layer is sucked out through a slit of the plate just before the position of the leading edge of the model by a guide wing under the plate. We used a sensor to measure components of air forces and moments acting on the model, Table 3. The system of the model, the stem and the sensor are mounted on a vertical traverse devise to change the height of the model.

Table 3. Main parameters of sensor

Name		50M31A-I25-25LB
Size	Diameter	50 mm
	Height	31.5 mm
Reference Point		The middle of the sensor
Capacity	F_x	130 N
	F_y	122 N
	F_z	206 N
	M_x	84 dNm
	M_y	79 dNm
	M_z	103 dNm
Accuracy		1% of the capacity

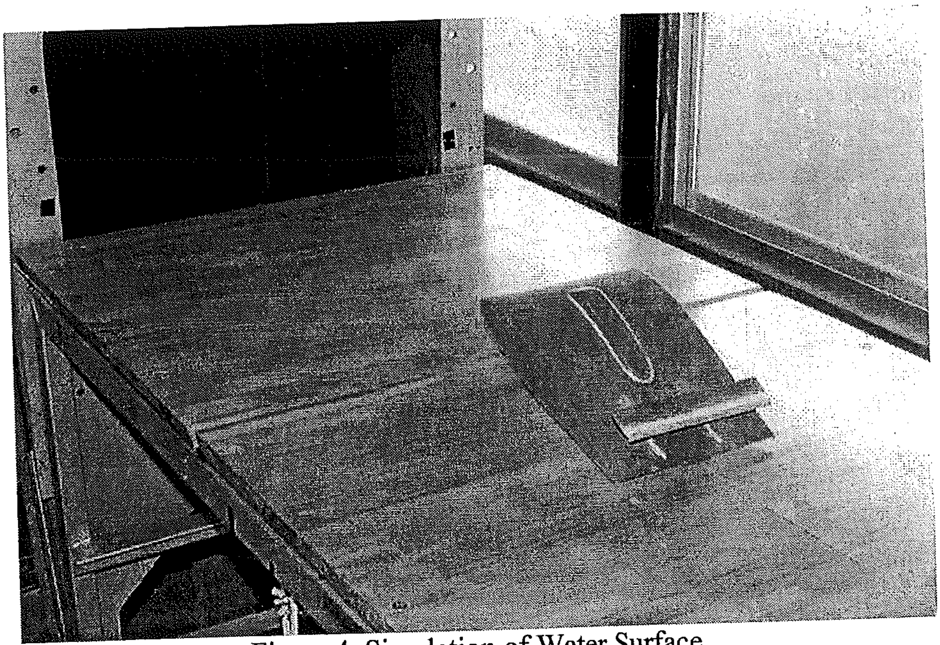

Figure 4. Simulation of Water Surface.

Changing the stem changes the angle of attack of the model. A stem can be leaned in the range of –2~+2 degree. We use a set of stems of different angles of the coupling, Fig.5, to change the angle of attack of the model.

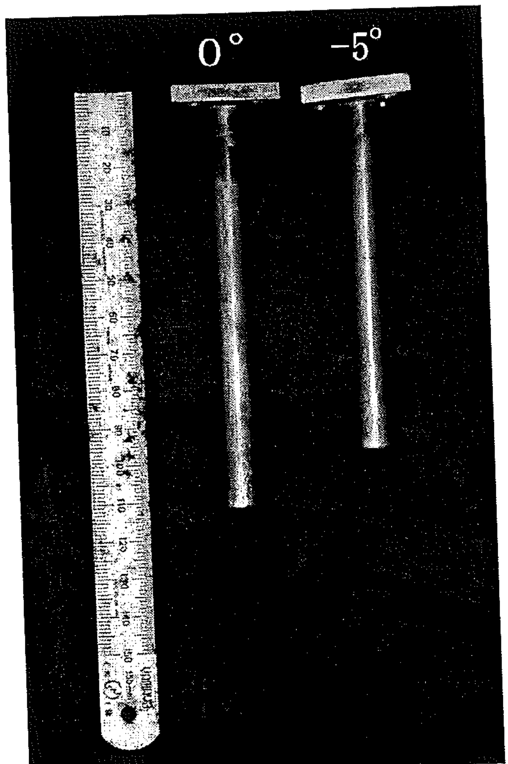

Figure 5. Stems

We used a wind tunnel of slow speed circular type with maximum wind speed 38 m/s. We used a speed of 30 m/s throughout the tests. The Reynolds number was 5.2×10^5. The expected Reynolds number of the real craft is 5.3×10^7. The test section of the wind tunnel is the open type, Fig.6.

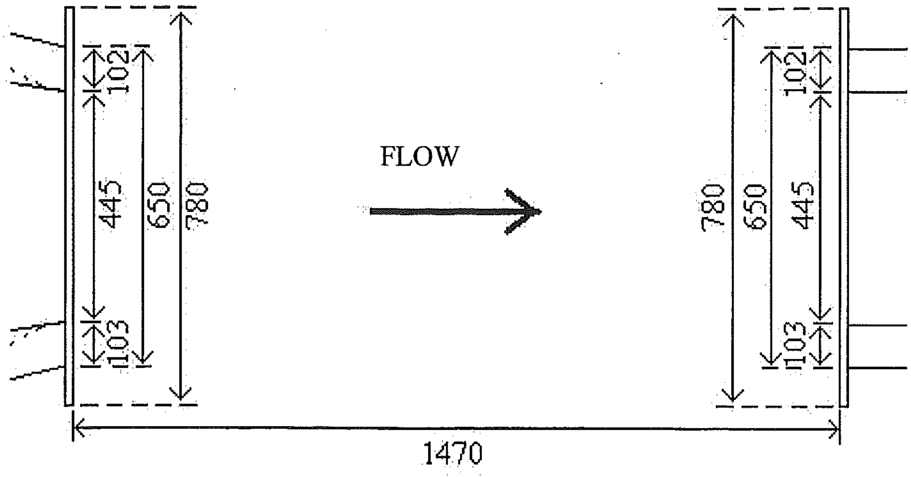

Figure 6. Dimensions of wind tunnel test section

3. Preparation of Measurement

We need preparation to measure the force and moment acting on the model as follows.

- Calibration of the Sensor
  The sensor used needs calibration of the internal cross coupling of components of force and moment. We calibrated it by applying 6 independent forces and moments to obtain the calibration matrix. The maximum expected error is less than 2 % of the reading values.
- Adjustment of Suction of the Boundary Layer
  The amount of suction of the boundary layer was adjusted by changing the position and the angle of attack of the guide wing to minimize the boundary layer thickness at the position of the trailing edge of the model. The velocity profile of the main flow just above the plate is shown in Fig.7.
- Measurement of Force and Moment Acting on the Support System of the Model
  The force and moment are including not only those acting on the model but also those acting on the support system. We must subtract those on the support system. Therefore we measured force and moment acting only on the support system without the model. Possible interference between the model and the support system was neglected.

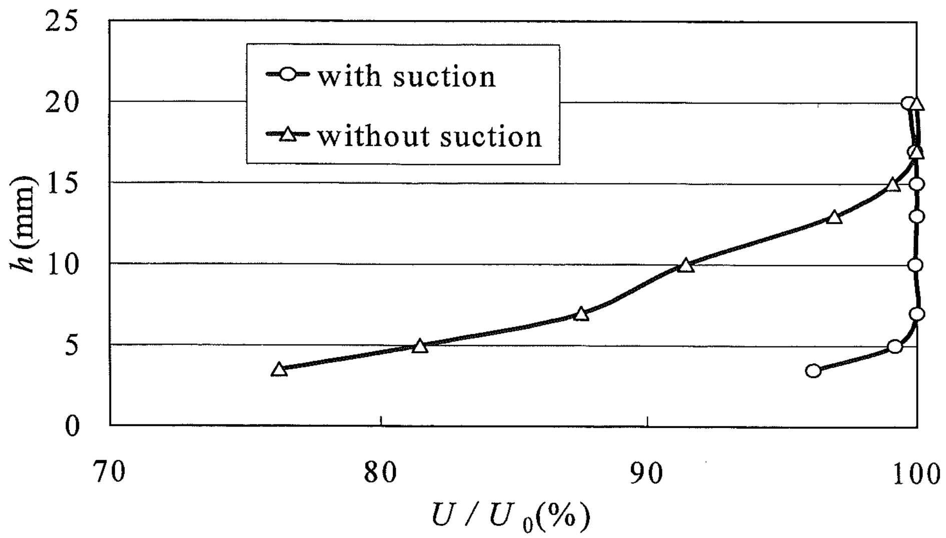

Figure 7. The velocity Profile in the Boundary Layer at the Position of the Trailing Edge.

4. Results

Table 3 gives conditions of the measurements. The vacant parts in the table showed conditions that we could not conduct as part of the model touched to the plate or the clearance between them was too small to measure.

Table 3. Conditions of measurements

Angle of attack α (degree)	1.91	3.81	5.74	8.14
Relative height *h/c*	-	-	0.2	0.2
	0.15	0.15	0.15	0.15
	0.125	0.125	0.125	0.125
	0.1	0.1	0.1	0.1
	-	0.075	0.075	0.075
	-	-	0.058	0.058
Angle of attack of the horizontal tail	4.18 degree			

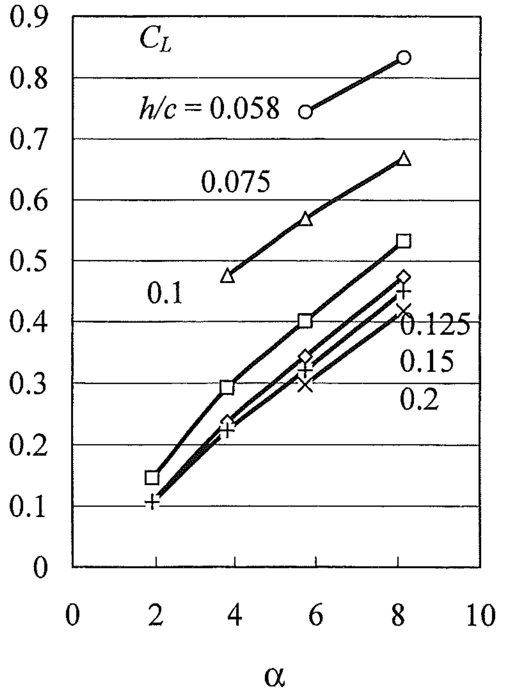

Figure 8. Lift Coefficient.

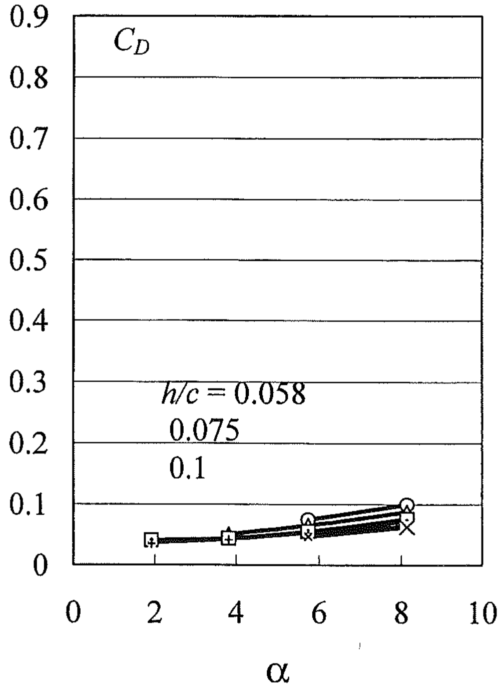

Figure 9. Drag Coefficient.

Measured lift coefficient and drag coefficient are shown in Figs.8 and 9 versus the angle of attack. A typical characteristic of the lift coefficient is its small rate of increase to the angle of attack. It is caused by the fact that the aspect ratio of the main wing is very small value of 0.71. In spite of the small aspect ratio the maximum value of the lift coefficient has a high value in the surface effect e.g. $h/c < 0.1$, where h is the height of the trailing edge from the plate and c the wing chord length. This shows surface effect of the wing.

Significant characteristics of the drag coefficients are small change in the angle of attack and slight increase according to decrease of flight altitude. The drag reduction by the surface effect is not apparent. This is explained as follows. The lift increases according to the increase of the angle of attack. The drag induced by the lift increases proportional to the square of the angle of attack. The present result of drag does not show such increase, because the surface effect suppresses the increase of drag. A slight increase of drag at a lower altitude will be caused by the drag of hull. The drag of the model due to viscosity will be different a little bit from that of the real craft because the Reynolds number is different. The above results are rearranged against *h/c* in Figs.10 and 11. The surface effect is shown clearly at a high angle of attack. At a low angle of attack we could not conducted our experiment by the reason that a part of the model touched the surface plate. Therefore the surface effect is less significant at a low angle of attack. When *h/c* is small, the lift coefficient depends less on the angle of attack, or the slope of $C_L - \alpha$ curve is small.

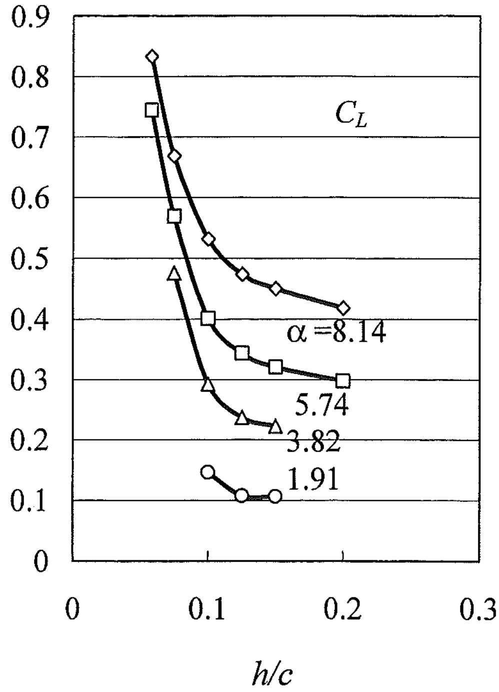

Figure 10. Lift Coefficient.

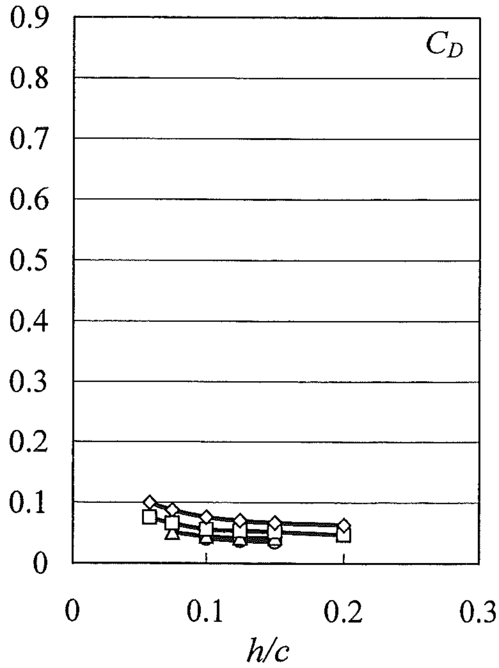

Figure 11. Drag Coefficient.

The drag coefficient increases according to the decrease of *h/c*. This does not contradict to the surface effect as explained above. This is shown again in the polar curve, or $C_L - C_D$ curve, Fig.12. When *h/c* > 0.125, $C_L - C_D$ curves show similar characteristics for different values of *h/c*. The values of C_L are small for a value of C_D. This is easy to be expected for a wing of small aspect ratio as shown by Wieselsberger and Betz[5]. Usually wings of low aspect ratio like this cannot be used by their bad efficiency caused by tip vortices outside the surface effect. However *h/c* decreases, C_L increases drastically. In other words, C_D decreases drastically for a value of C_L. This shows suppression of the effect of tip vortices by the surface effect and tip plates. The tendency is shown again clearly in $C_L / C_D - h/c$ curve in Fig.13. The values of C_L / C_D increase rapidly for decrease of h/c at any angle of attack when *h/c* < 0.125. The tendency is the clearest at angle of attack of 4 degree. This fact is corresponding to the fact that the most favorable lift to drag ratio is realized at $\alpha = 4$ degree. A slight change of angle of the horizontal tail and/or elevator has a considerable effect on C_L / C_D near its maximum point. This fact is remarkable to determine the state of cruising of the craft.

One of the important problems of the wing-in-surface-effect craft is the considerable change of longitudinal moment according to its flying altitude. To overcome the difficult problem we designed and used a special wing section of *S*-figured profile[1]. Coefficient of pitching moment about a point located 40 % of the wing chord is shown against the angle of attack in Fig.14. The positive value of C_{m40} denotes pitch up of the bow. All values in the figure show positive values. This does not mean that our craft is statically unstable. The real craft has its propulsion system above its main wing to avoid water spray. The thrust causes considerable pitch down moment. The value C_{m40} shows complicated dependence on α and *h/c*.

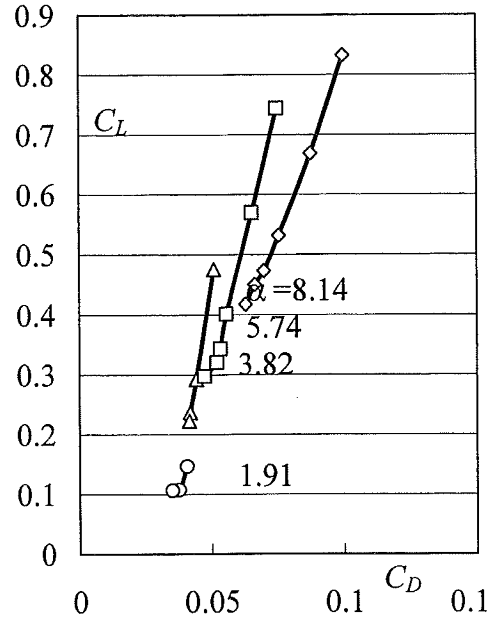

Figure 12. Polar Curve.

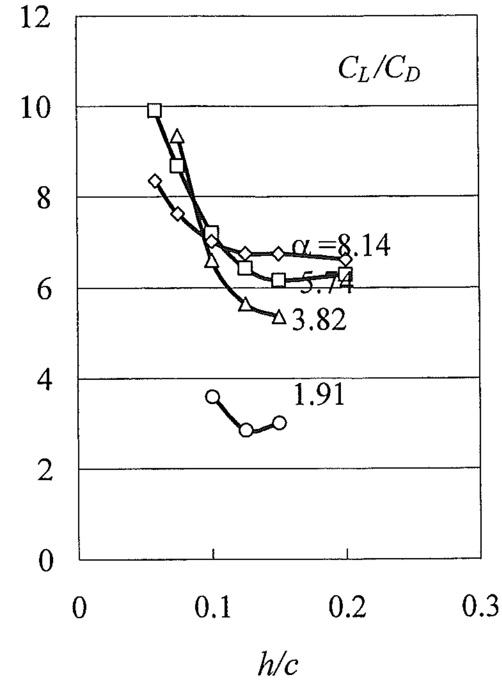

Figure 13. C_L/C_D.

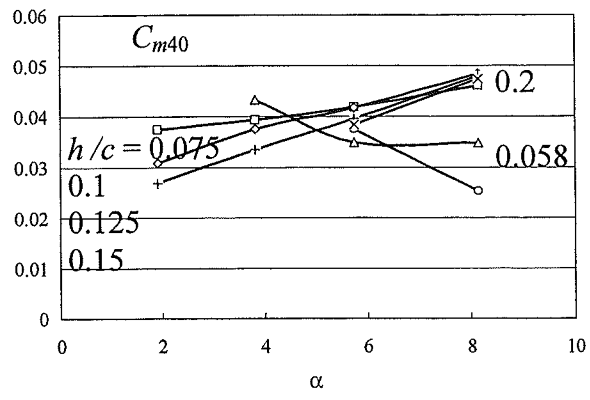

Figure 14. Coefficient of pitching moment with respect to 40 % chord

Table 4 : The value of x_{CG}/c

h/c	α	α_S	δ	x_{CG}/c
0.058	8.14	4.18	18.18	0.400
0.058	8.14	6.68	---	0.397
0.075	5.74	4.18	18.18	0.373
0.075	5.74	9.46	---	0.373

α: angle of attack of the main wing (degree),
α_S: angle of attack of the horizontal stabilizer (degree),
δ: angle of the elevator (degree).

We can estimate the thrust required by the data of C_L, C_D and the weight of the craft. The moment arm of the thrust is determined by the geometrical configuration of the craft. Thus we can calculate the pitch down moment by the thrust. By the data and C_{m40} we can estimate the trim position of the center of gravity of the craft in various states of flight. The position is x_{CG} measuring from the leading edge of the main wing. The value of x_{CG}/c is shown in Table 4 for various values of α and *h/c*. We find a possibility to control the position of center of gravity by the change of the angle of the elevator, i.e. by piloting the craft, in a suitable choice of the angle of the horizontal stabilizer.

5. Estimation of the performance of the real craft

The present wind tunnel test is related to the development of a real craft. We estimate the performance of the real craft from the result obtained.

5.1. Cruising

The important factor for cruising is the maximum value of the lift-to-drag ratio. It is about 10 at *h/c* = 0.058 and α = 5.74°. The value is comparable to the lift-to-drag ratio of aircraft commonly used. Therefore the wing-in-surface-effect craft now considered has comparable cruising performance to common aircraft. This is achieved by the surface effect even to the wing of aspect ratio 0.71. The real flying height is only 0.7 m. The seaworthiness of the cruising state is 1.5 m of wave height, which is suitable for a normal sea state. When *h/c* is 0.075-0.10, the altitude is 0.9-1.2 m for possible wave height 1.8-2.4. The seaworthiness is acceptable in a wide range of operation of the craft. The lift-to-drag ratio corresponding to the height is 9.5-7.2, which is not enough high but acceptable for practical use. Generally speaking a high seaworthiness reduces efficiency by the reason of its high flight altitude. However this does not mean that a craft of high seaworthiness is less efficient in commercial use. When sea is calm, the craft cruises at a low altitude with high efficiency. Its high seaworthiness guarantees operation on a rough sea to keep a schedule. The efficiency of commercial operation is an average efficiency through one year on a specific route. The fact suggests us the importance of precise measurement of flying altitude and application of automatic control to achieve and to maintain the best flying altitude in cruise. From this point of view the highest seaworthiness of the present craft is realized 5 m of wave height at 8.14 degree of angle of attack. The lift-to-drag ratio is 7 in this case. Consequently the efficiency and seaworthiness of the present craft is high enough for practical use.

5.2. Take-Off and Alighting

Take-off and alighting is ruled by the maximum value of the lift coefficient at an extreme low altitude. The maximum lift coefficient is 0.85 at *h/c* = 0.058 and α = 8.14° in the data of the present measurement. An extrapolation shows a higher lift coefficient at a lower altitude. We expect 1.2 as the maximum lift coefficient at take-off and alighting. The value is 3-4 times of that in cruising 0.3-0.4. From this we find that the speed ratio of the cruising speed to the take-off or alighting speed is 1.7-2.0. The estimated take-off and alighting speed is 94 km/h, and cruising speed 164 km/h.

Seaworthiness at take-off and alighting is determined by the wave height at the condition. This is very difficult question to answer by data of wind tunnel. We consider as follows. We can estimate the height of the bow from the angle of attack at take-off and alighting. The height is 1.5 m. The seaworthiness of the craft will be the order of magnitude of the height.

5.3. Pitching Trim

The position of the center of gravity for trim of the craft is located in a narrow region near 35 % of the chord as already shown in the last of Section 4. Therefore the craft does not need a huge horizontal tail or elevator.

We consider here about the effect of propellers, which we cannot measure by the wind tunnel test. A large part of the horizontal stabilizer and elevator locates in the slipstream of propellers. At first this means that the control surfaces experience higher stream of air than the speed of the craft. Second, the slipstream decreases the effect of down wash of the main wing. By these effects the control surfaces of the real craft work more efficiently with the propulsion system. It will be significant at a low speed of the craft. We will be able to expect well controllability of the craft. Third, the slipstream suppresses local separation on the main wing at a high angle of attack. We will be able to realize higher angle of attack with a higher lift coefficient at take-off and alighting than expected from the data of the present wind tunnel test. These will be proved through test run of the real craft.

Acknowledgements

The authors express their cordial thanks to Mr. Kunimitsu Fukushima, who constructed the real craft for 8 passengers.

References

1. G. H. Fuller, *Near Surface Vehicles – The Next Breakthrough or the Niche Cul-de-Sac?*, Intl. Conf. Wing-In-Ground-Effect Craft (WIGs), 1997, London, pp.1-3.

2. S. Kubo, *A Concept of Wing-In-Surface-Effect Craft as a Future Passenger Transport in Japan*, 2nd Intl. Conf. FAST 1993, Vol. 2, pp.1573-1584.

3. *"Wing-In-Ground-Effect Craft"* in Jane's High-Speed Marine Transportation 2001-2002, ed. S. J. Phillips, 2001, Jane's Information Group, Coulsdon, pp.279-291.

4. H. Akimoto, S. Kubo, K. Fukushima & N. Fukushima, 6th Intl. Conf. FAST2001, Southampton, Vol. 3, pp.1-6.

5. C. Wieselsberger and A. Betz, in H. Schlichting and E. Truckenbrodt: *Aerodynamics of the Airplanes*, McGraw-Hill International, 1979, New York, pp.121-123.

Control Automation of Passenger Ekranoplans

G.V. Alexandrov, V.Ye. Gryazin, VladimirV. Strelkov

Central Aerohydrodynamic Institute (TsAGI), Zhukovsky, Russia, flight15@tsagi.ru

Abstract

Some features of the flight near water surface are considered; principles for manual control automation of a sea-going passenger-carrying ekranoplan are proposed. The present work is a part of the comprehensive applied investigations conducted at TsAGI for improving cost-effectiveness and operational safety of future passenger ekranoplans.

Introduction

In the historical perspective, it has been that first Russian ekranoplans were created by shipbuilding specialists and are currently assigned to the maritime administration. The same kind of situation seems to take place in other countries. To-day, it is IMO that raises questions on establishing worthiness regulations for this type of vehicles; the IMO classifies ekranoplans as vehicles with dynamic support principles, see [1]. WIG effect vehicles are traditionally a topic of international scientific and technical conferences dealing with high-speed vessels -- whereas ICAO conferences consider WIG craft much more seldom. But within the IMO-adopted classification the type B and C ekranoplans are the air-supported vehicles because their main movement conditions are certainly described by aerodynamics and flight dynamics laws; as well, the craft has the airplane-typical aerodynamic configuration (Fig. 1), control surfaces and control levers, see [2-4]. It is not by coincidence that the R.E. Alexeev Central Hydrofoil Design Bureau (Nizhny Novgorod, Russia) - the definite leader in ekranoplans development – uses widely the experience gained by aviation science and engineering. For many years the ekranoplans are the subject of joint studies carried out by the Central Hydrofoil Design Bureau and TsAGI - the major research institute of Russian aircraft industry. However, the WIG effect vehicle is totally different from usual airplanes in its specific operational envelope. This is a new type of the air-supported vehicles using advantages of flight-in-ground-effect which is not covered by airplane airworthiness regulations. The ekranoplan as a new transportation means is interesting due to its combination of high speeds and high sea-going ability. Prospects for it are in sea/ocean regions with underdeveloped aviation infrastructures, see [5].

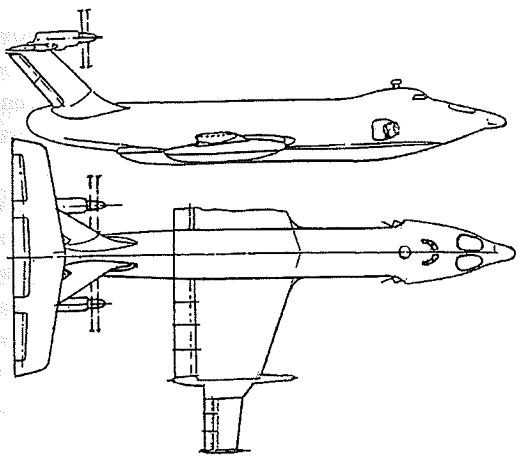

Fig. 1. Configuration of the second-generation WIG effect vehicle

The ground effect increases values of lift and lift-to-drag ratio when the distance from the wing trailing edge to the water surface is less than the wing chord length. The ekranoplan flying at the relative altitude $\overline{h} \approx 0.2$ may ensure the lift-to-drag ratio as high as that of the best state-of-the-art passenger airplanes - $L/D \approx 18 \div 20$; and these results are attained at a wing aspect ratio notably lower than that of airplanes. Figure 2 shows lift-to-drag ratios of some airplanes and future ekranoplans vs. the parameter $A = \sqrt{\frac{AR}{S_W / S}} c^{1/6}$ defined by the wing aspect ratio *AR*, wing surface area *S*, wetted airframe area S_w. and mean aerodynamic chord *c,* see [6]. In addition, the ground effect makes it possible to ensure a naturally stable flight at some altitude in the direct proximity to the water surface.

In the issues of flight-in-ground-effect, TsAGI investigates aerodynamics, hydrodynamics, structural static and fatigue strength, aeroelasticity, flight dynamics, control and operational performance. The present article deals only with a particular issue: the concept of an automatic system for controlling a sea-going passenger ekranoplan having the potential for leaving the ground effect zone (i.e., type B and C vehicles). Type A WIG-ships with air-cushion (such as Volga-2 and Amphistar, see [7]) are principally "attached" to the water surface, so these vehicles are not considered in the present work.

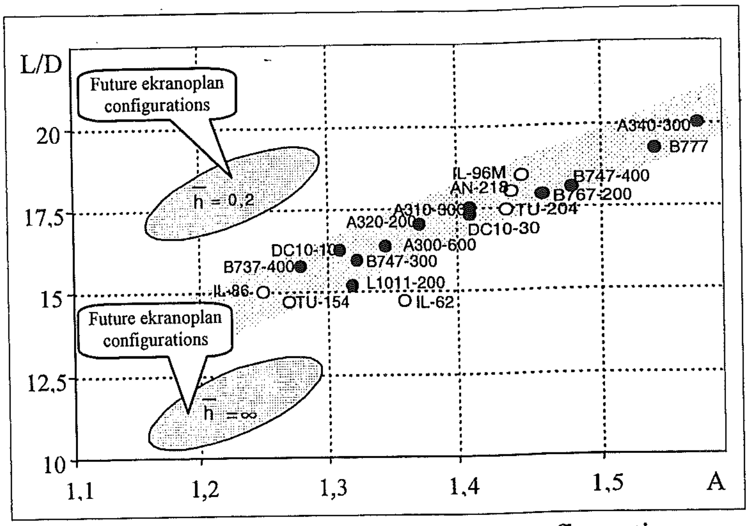

Fig. 2. Lift-to-drag ratio of airplane configurations

The flight in an extremely narrow range of altitude (of tenths of the wing chord length) greatly limits the allowable maneuvers of the vehicle and makes us take a different view on requirements for stability/controllability characteristics and of ekranoplan control concepts. An experience in development and operation of sea-going ekranoplans revealed the necessity of a control automation to improve stability/controllability characteristics, ensure flight safety and reduce the pilot's workload. In their complexity the control systems for first-generation ekranoplans are not inferior to the airplane ones as shown in [8]. The high-level crew training is required for ekranoplan guidance and control. The automatic control systems become more important, and their functions get extended, in the case of future passenger ekranoplans. The reason is the change in requirements for the WIG effect vehicles as the facility for passenger-and-freight transportation. Major criteria for assessing a commercial transportation means include cost efficiency, operation within sea areas with intense traffic, and transportation safety. These requirements may be met by highly automated control systems only.

1. Features of flight dynamics in ground effect zone

Sustained flight conditions were analyzed to show that the trimming characteristics in the domain of notable influence of ground effect (where $\bar{h}<0.5$) are totally different from those typical of airplanes. In the longitudinal control channel a prescribed angle of attack and a certain engine setting define certain values of flight speed and altitude (Fig. 3). As for the roll control channel, the presence of a roll controlling moment during ground-effect flight establishes a certain roll angle.

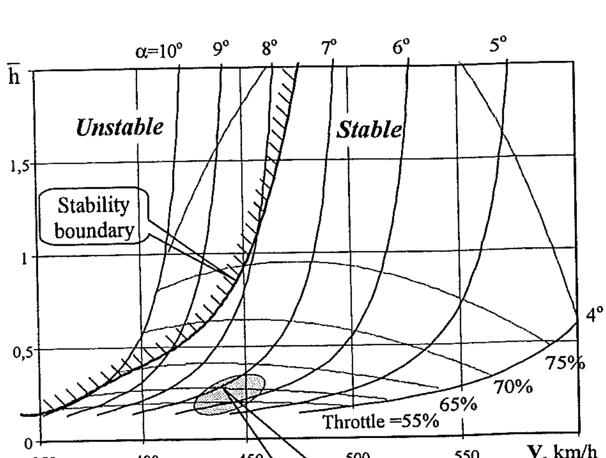

Fig. 3. Ekranoplan sustained flight envelope

Natural stability characteristics (and stability criteria, see [9-11]) get notably changed when flying in the narrow altitude range (immediately near the water surface). Ensuring stability becomes more important in the case of future passenger-and-freight ekranoplans: the desire to improve weight efficiency leads designers to decreasing the stabilizer surface area, and this reduces longitudinal stability margins. Natural stability characteristics (in the case with no stability augmentation system) of new-generation ekranoplans may turn out to be poor due to the stability boundary being close to the cruise flight area (Fig. 3).

Note that stability/control characteristics of both longitudinal and lateral motion within the altitude range vary with altitude, and the dependence is clearly nonlinear. For example, the response to the control input of the ekranoplan in the vertical plane principally depends on the initial altitude and the input magnitude and sign (Fig. 4). The natural "attachment" of the vehicle to the ground implies altitude sensitivity to the flight speed and angle of attack (Fig. 3) and drastically relaxes as the vehicle moves to the ground effect zone boundary. Note that in even the case of insignificant inputs the vehicle runs out of the ground effect zone (Fig. 4). The diagram in Fig. 3 makes it easy to evaluate the inputs and disturbances which do not force the ekranoplan to leave the ground effect zone at various initial cruise flight conditions.

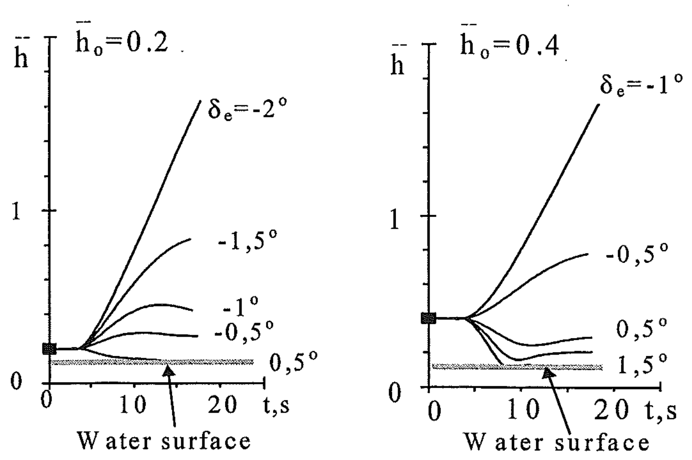

Fig. 4. WIG effect vehicle response to stepwise elevator deflection

As the ekranoplan moves from the underlying surface and the ground effect relaxes, the controllability gets close to that of airplanes, and at $\bar{h} \geq 1.0 \div 2.0$ (as referred to the wing mean aerodynamic chord) the control characteristics become almost airplane-typical.

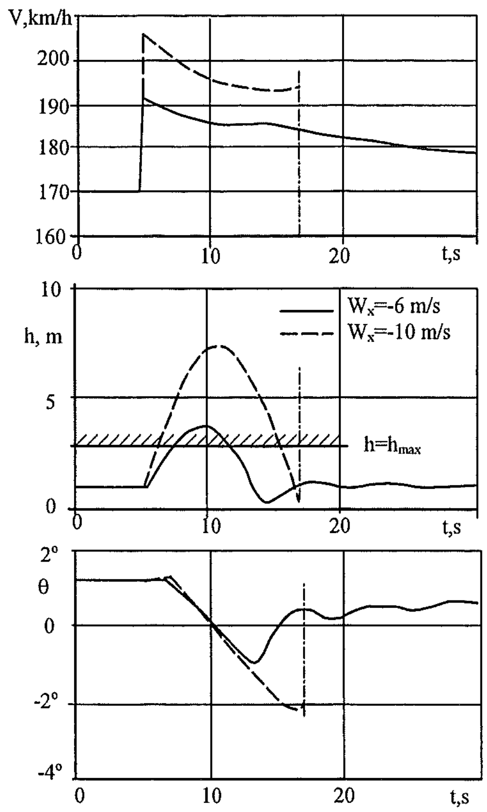

Fig. 5. WIG effect vehicle response to headwind gust

One of the most important problems in ekranoplan control is to keep the vehicle within the narrow allowable altitude range upon various disturbances such as wind gusts, equipment failures and pilot's inputs.

Atmospheric perturbation is the most dangerous to ekranoplans with their low specific wing load (and low cruise flight speed). A tailwind gust can make the vehicle touch the water surface; whereas the headwind gust can push the ekranoplan out of the ground effect zone, and the vehicle will unfavourably develop its natural motion unless there is a powerful automatic control system (Fig. 5). No ekranoplan is allowed, in both the longitudinal and lateral control channels, to undertake intense maneuvers that could push the vehicle out of the operational domain and/or result in collision with the water surface (Fig. 4). The flight altitude may be allowed to be changed, while not incurring the risk of leaving the operational domain, at the vertical load factor n_z of around 1 only; and turns are permitted at low roll angles only. These limitations imply the relatively low maneuverability of WIG craft. Therefore, one should address operability of high-speed ekranoplans on busy defined water areas and meandering rivers. For keeping to a prescribed route and avoiding an obstacle, pilots can bear in mind maneuvers in both horizontal and vertical planes, see [12].

Let us consider in detail the horizontal maneuver. During the maneuver the ekranoplan remains within the ground effect zone. Figure 6 depicts two situations: the avoidance of a single obstacle (such as a ship) and the avoidance of collision with a group of ships or the coast. The latter situation definitely requires the shortest turn radius.

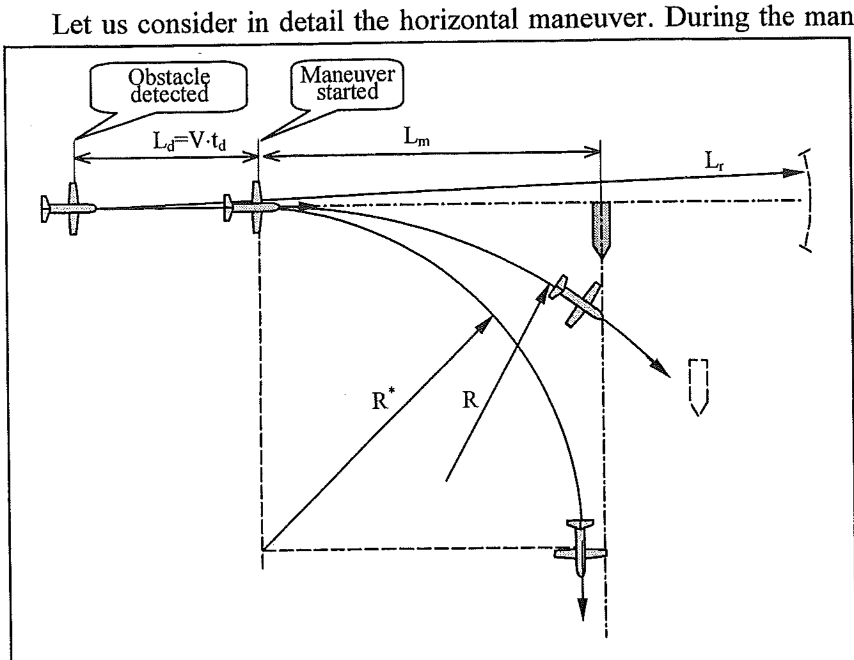

Fig. 6. Horizontal maneuver for avoiding an obstacle

The radius can be estimated as

$$R \approx \frac{V^2}{\left|g(n_y + \text{tg}\phi)\right|}$$

where n_y is the lateral load factor (in the body axes) and ϕ is the roll angle.

The simplest and safest is the "flat" turn with roll angle close to zero ($\phi \approx 0^\circ$). The centripetal force is created by sidesleep angle β only. In the case of flat turn we see the maximum turn radius (Fig. 7) -- and, respectively, the maximum necessary distance L_m. The latter is governed not only by the radius but also by the obstacle dimension and the minimum allowable distance between the ekranoplan and the obstacle. In the case of the coast, the required distance is close to the turn radius: $L_m \approx R$. For instance, at the flight speed V ~ 400 km/h both the radius and the required distance would be as large as 12 to 13 km. Reference [13] evaluates the obstacle-by-radar detection distance with approximately the same value: $L_r \approx 12 \div 13$ km. It should be noticed that a pilot must have a certain time interval t_d from the obstacle detection instant to initiation of the maneuver in order to identify the obstacle, assess the situation and take the decision on the maneuver. Sometimes the interval is as long as tens of seconds, and the ekranoplan becomes nearer to the obstacle by the distance $L_d = Vt_d$.

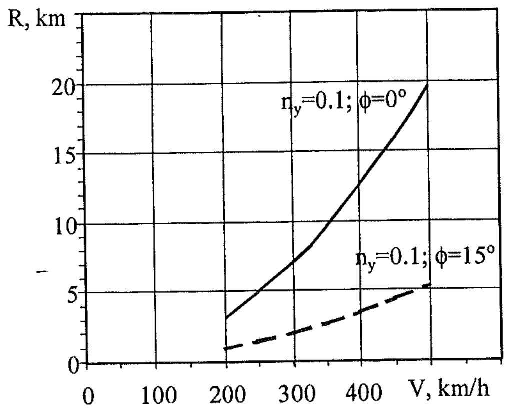

Fig. 7. WIG effect vehicle turn radius

The other disadvantage of the flat turn is appearance of the lateral load factor n_y (in body axes). A human organism is very sensitive to the lateral acceleration. So the latter should be restricted to offer passengers and crew members comfortable conditions.

The roll control improves ekranoplan maneuverability. For example, the theoretical minimum turn radius at the roll angle $\phi_{max} = 15^\circ$ and the allowable g-factor $n_y = 0.1$ is one-third or even one-fourth of the flat-turn radius, Fig. 7. Here, one should take into account that the allowable roll angle depends on the distance h_p between the water surface and the planing step. The relative contribution of the sideslip angle to reducing the turn radius gets less significant when roll angle is used. So the unfavourable lateral acceleration may be decreased while attaining almost the same radius.

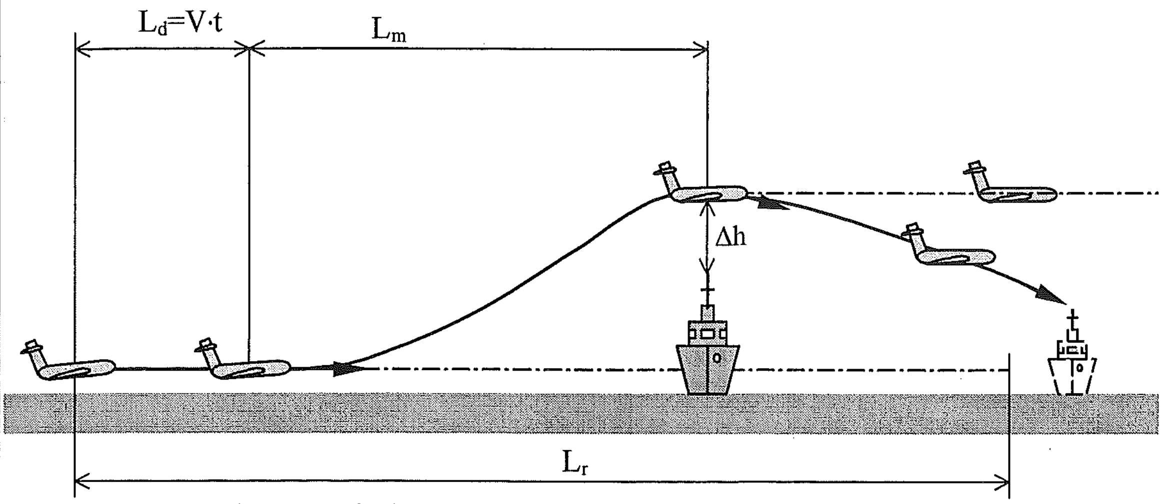

Fig. 8. Vertical maneuver (jump-up) for avoiding an obstacle.

The turn with roll and sideslip is of special interest as it may be effected by controlling the pedals only -- due to the correct natural response of ekranoplan roll motion to the rudder deflection. To perform turn at a minimum radius (for the specified flight altitude) we shall take into account sideslip-dependence of the roll moment -- and either restrict or enhance natural sensitivity of the vehicle to the roll angle. To carry out turn at the maximum allowable roll angle, the flight altitude may be required to be increased in comparison with the initial value. When turning the WIG effect vehicle, all aerodynamic surfaces and the engine must be controlled. Studies in the TsAGI flight-simulator have revealed that it is only the flat turn that the pilots may perform successfully during manual piloting. A spatial turn with the maximum roll angle and the necessity to increase the flight altitude requires automating the control.

There exists the potential to avoid an obstacle by maneuvering in the vertical plane, thus leaving the ground effect zone (Fig. 8). However, safety of maneuvers of this kind in mass transportation operations requires suitable stability/control characteristics and respective piloting techniques for a wider altitude range. Moreover, the necessity of such maneuvers for passenger ekranoplans is insufficiently justified as of to-day.

Thus, the WIG effect vehicle is a complex control object, which requires a rather high level of control automation. As for new-generation sea-going ekranoplans, there is every reason to redistribute control functions between the pilot and the automatic system in order to reduce the human factor role in control activities. This is primarily dictated by the fact that a pilot is short of time when making decisions during flight in the close vicinity of the water surface.

The automatic control systems have no "psychophysiological" time delay, do not suffer from stresses and feature a high reliability. Therefore, in even the case of manual control a notable proportion of controlling all devices is advisable to assign to the automatic system which operates in parallel with the pilot -- that is, to stability and control augmentation system (SCAS). The pilot is given the possibility to permanently vary main phase coordinates only by using a few principal cockpit levers. In addition, the pilot can act on ekranoplan motion via the autopilot. The pilot's role is specifying flight mode and monitoring the flight.

Below is the list of major functions that would be carried out by the automatic control system including both SCAS and the autopilot blocks:

- ensuring necessary stability/controllability characteristics for the operational envelope;
- improving maneuverability (and decreasing the turn radius) during cruise flight to enable operations on busy water areas;
- simplifying the manual piloting techniques to reduce the pilot's workload and improve operational safety during all modes including take-off and landing;

- preventing the ekranoplan from reaching dangerous flight conditions and
- accurately maintaining the specified parameters in the course of sustained flight with the autopilot.

2. Concepts for ekranoplan control automation

Ekranoplans look much like airplanes and have airplane-typical control devices. However, ekranoplans should be controlled in a totally different manner. In the vertical plane, the airplane motion is controlled by changing the angular attitude and applying the vertical force due to deflection of the longitudinal control stick (and the elevator). In horizontal maneuvers, pilots usually use the roll angle (and deflect ailerons); in this case both the lateral acceleration in body axes and the sideslip angle are almost zero. The rudder is mainly operated to trim the airplane in cases of engine failure, sidewind landing, etc. The trailing edge flaps are only involved as high-lift device components and have a few fixed setting angles.

Obviously, the airplane piloting techniques are not applicable to WIG effect vehicles. It has been shown above that ekranoplan cruise flight parameters should be varied at the vertical load factor $n_z \sim 1$; and turns at low roll angles. Therefore, the major control device for the longitudinal control channel during cruise flight is the engine. This implies the altitude varying simultaneously with the flight speed variation. Pilots have tried this feature by using flight simulators and regard it as a negative circumstance (Fig. 9). To decrease the altitude variation duration, the automatic system might in addition control trailing edge flaps as the means for immediate variation of lift.

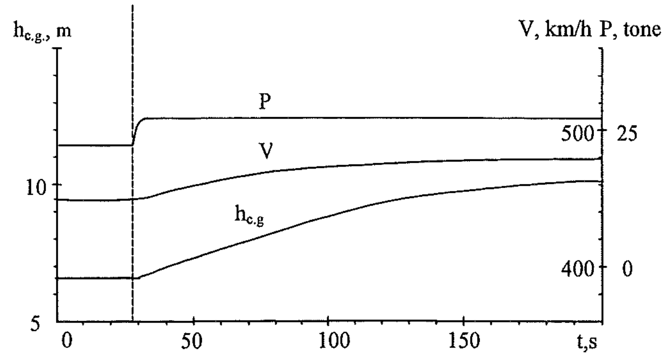

Fig. 9. WIG effect vehicle response to stepwise throttle input at constant pitch angle (θ = const)

The elevator may only be utilized to smoothly trim the ekranoplan when varying altitude and/or speed, except for

- take-off when the elevator may be required to be deflected quickly due to features of change in the disturbing pitch moment during acceleration and lift-off;
- transients when the disturbing pitch moment caused by extension and retraction of high-lift device should be compensated for;
- failures (e.g., of engines), and some other situations.

The pitch angle control channel is the most critical in what concerns flight safety. It is due to vehicle angular attitude variation that the flight path changes most quickly and might result in either collision with water or going from the water surface (and the subsequent dangerous 3D motion or the pilot's induced oscillations (PIO) in attempts to return it to the initial flight altitude). Let us note that the pitching motion restriction does not almost degrade operational performance of the WIG effect vehicle as the passenger-and-freight transport, but definitely simplifies control and improves operational safety. Therefore, the use of the pitch control stick during cruise flight should be limited (as stated in [14-17]); otherwise, the automatic control system algorithms must ensure proper altitude response to stick deflection throughout the operational altitude range. The pitch angle should be stabilized, and pitch disturbance compensated for, by the automatic control system.

Algorithms for angular attitude damping and stabilization are favourable for stability and dynamic characteristics of longitudinal disturbed movement of the vehicle when in the ground effect zone. The root locus at various pitch damper is shown on fig. 10. This means that pitch angle stabilization (for ensuring a constant pitch angle $\theta = const$) is the basis for elevator control algorithm covering all ekranoplan movement modes:

$$\delta_{e_{SCAS}} = k_q q + k_\theta(\theta - \theta_0) + k_\int \int(\theta - \theta_0)dt$$

It would also be noticed that effective methods for enhancing longitudinal motion stability include automation of control of trailing edge flaps (or flaperons). Roots of the characteristic equation

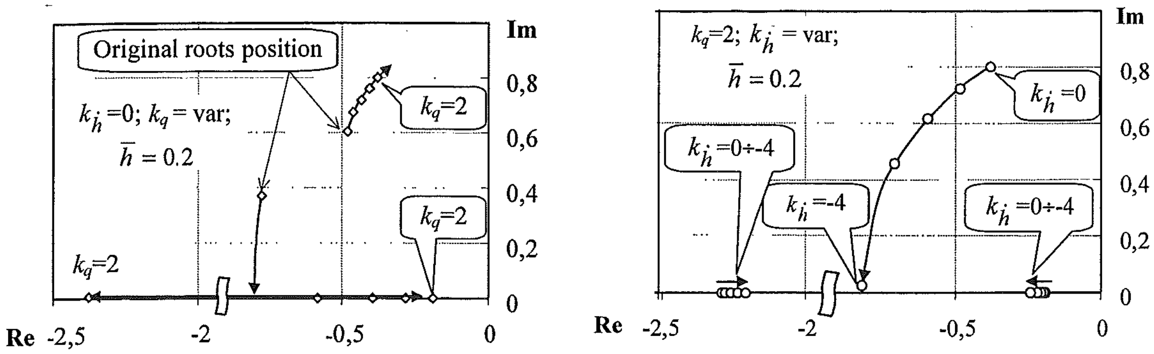

Fig. 10. Changes in longitudinal motion root locus upon introducing a stability and control augmentation system (SCAS)

for longitudinal disturbed movement were computed (see Fig. 10) to demonstrate the notable improvement in altitude oscillation damping if trailing edge flaps are included in the stability enhancement system:

$$\delta_{f_{SCAS}} = k_{\dot h}\dot h$$

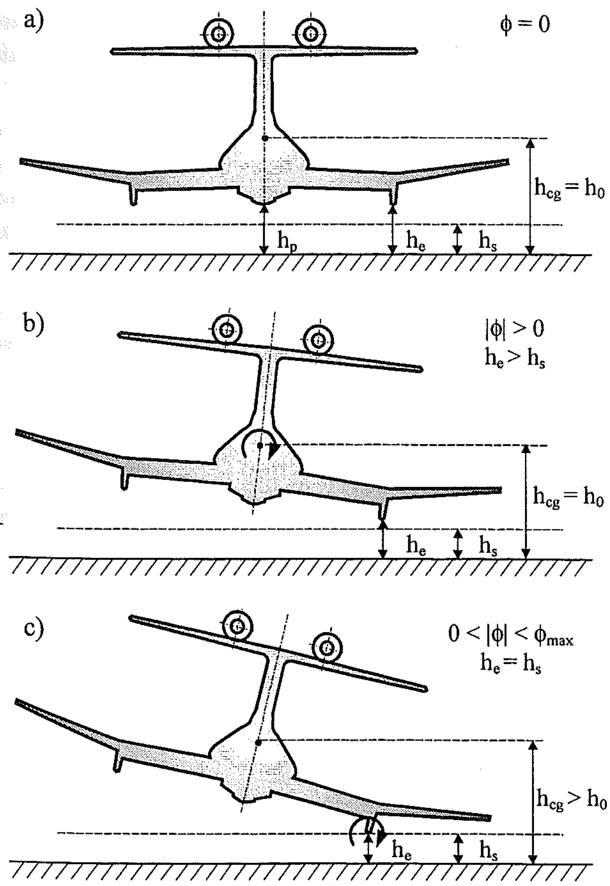

Fig. 11. The ekranoplan performs turn

The latter is the feature in ekranoplan control automation: in airplanes trailing edge flaps are usually involved only to increase lift during take-offs and landings. The idea to use the trailing edge flaps as the means for vertical movement damping and immediate lift control (when varying the flight altitude) poses corresponding requirements for trailing edge flap actuators.

In lateral and directional movement the ekranoplans usually show natural stability. Of the greatest interest is automating the directional control (for turn) to make the maximum use of the vehicle potentiality at a rather simple piloting technique -- so that the directional control be mainly carried out by deflecting pedals; at the maximum pedal deflection the turn should have the minimum radius. Inputs to ailerons, elevator and engine thrust, necessary for the turn, are provided by the control automation system. The pilot is enabled to influence a maneuver by acting on any control device. Several versions of automated turn may be proposed. Below we detail one of them.

Depending on the prior altitude and the pedal deflection, the control automation devices implement the following motion modes.

1. "Flat turn at $h_{c.g.} = const$" if $\left|X_p\right| \le \left|X_p^*\right|$ and $h_e > h_s$ (Fig. 11a):

$$\beta = \beta(X_p), \quad \phi = 0^\circ; \quad h_{c.g.} = const,$$

where X^*_p, the pedal deflection value which outlines the range of "low" control inputs;

$h_{c.g.}$, the centre-of-gravity height;

h_e, the wingtip float height;

h_s, lowest safe height.

2. "Turn with roll and sideslip angles at $h_{c.g.} = const$" if $|X_p| > |X^*_p|$ and $h_e > h_s$ (Fig. 11b):

$$\beta = \beta(X_p), \quad \phi = \phi(X_p); \quad h_{c.g.} = const.$$

3. "Spatial turn" if $|X_p| > |X^*_p|$ and $h_e = h_s$ (Fig. 11c):

$$\beta = \beta(X_p), \quad \phi = \phi(X_p), \quad h_{c.g.} > h_0.$$

Thus, the latter, most complex movement (with variation in all phase coordinates – sideslip angle, roll angle, altitude) is only implemented when the course must be changed for a very short time at minimum initial ground-effect altitudes. The second mode is close to the natural ekranoplan response to pedal deflection during stabilization of altitude and speed. And the flat turn is the simplest maneuver for a pilot of the existing WIG effect vehicles when the flight path would be changed insignificantly. Probably, the conventional operations will be mainly based on the first two modes.

Algorithms developed for automatically controlling ailerons, elevator, trailing edge flaps and engine thrust implement the aforementioned turn and utilize the ekranoplan potentiality while assuming the pedal deflection only.

To conclude with, note that in the case of commercial (passenger-carrying) ekranoplans many of the most important control functions are dealt with by the automatic system. Automation is required for almost all control channels and loops. The automation algorithms taken together will be rather complex. Therefore, a digital fly-by-wire system seems to be the most appropriate version for the future ekranoplan.

The experience gained developing and operating the first-generation WIG effect vehicles, as well as the airplane automation level, form the state-of-the-art basis to implement the principles above and create ekranoplans meeting flight safety requirements.

References

1. Bogdanov A.I. Discussions on the Operational Aspects of WIG Craft at the IMD Sub-Committee on Safety of Navigation. – Workshop Proceeding of Ekranoplans & Very Fast Craft, pp 213-229, University of New South Wales, Sydney, Australia, 5-6 December, 1996.
2. D.Sinitsyn, A.Maskalik, L.Litinsky. The present day state and prospect for the development of commercial ecranoplans. Workshop Proceeding of Ekranoplan and Very Fast Craft. Sydney, Australia, 1996.
3. Cui E. Design Characteristics of Ekranoplane DXF-100 and Some Considerations for Further Development. Proceeding of V International Symposium "New Aviation Technologies of the XXI Century", Russia, Zhukovsky, August, 17-22, 1999.
4. Maskalik A.I., Kolyzayev B.A., Zhukov V.I., Radovitsky G.L., Sinitsyn D.N., Zagorul'ko L.K. Ekranoplans. Features of theory and design. -- Sudostroyeniye, Saint Petersburg, 2000.
5. Bulanov V.V., Kirillovykh V.N., Sokolov V.V. Scientific and practical issues in operating ekranoplans. -- Proceedings of Gelenjik '96 seaplane science conference, Russia, 1996.
6. "Scientific&Technical basis of unification concept of civil aviation and forming of the programs and schedules of its development". Review in Russian journal "Aerokosmicheskie novosty", p.26(74), 1998.

7. Sinitsyn D.N., Maskalik A.I. Amphistar, the first civil ekranoplan. -- Sudostroyeniye, Saint Petersburg, 1999.
8. Diomidov V.B. Automatic control of ekranoplan motion. -- Central Research Institute "Elektropribor", Saint Petersburg, 1996.
9. Irodov R.D. Criteria of ekranoplan longitudinal stability. -Uchenyye Zapiski TsAGI, 1970, v. 1, no. 4.
10. Zhukov V.I. Features of aerodynamics, stability and controllability of dynamic ground effect vehicle. - TsAGI publishing office, 1997.
11. Sinitsyn D.N. Peculiarities of the longitudinal disturbed motion of a WIG craft. Proceeding of the International Conference on Ground Effect Machines, S-Petersburg, Russia, 21-23 June, 2000.
12. Colon A.E.. Formulation of correct collision avoidance safety regulations: Radar detection vs. Ekranoplan climb dynamics. – Workshop Proceeding of Ekranoplans & Very Fast Craft, University of New South Wales, Sydney, Australia, 5-6 December, 1996.
13. Bragazin V.F., Strelkov V.V. Automating the flying vehicle turn during flight in ground effect. -- Proceedings of the 4th Gelenjik international seaplane science and technology conference, Russia, 4-8 September 2002.
14. Gryazin V.E., Strelkov V.V., Shelyukhin Yu.F., Alexeev V.V., Kirillovikh V.N. Concepts for Manual Control Systems of Light-Weight WIG Effect Vehicles. Proceeding of V International Symposium "New Aviation Technologies of the XXI Century", Russia, Zhukovsky, August, 17-22, 1999.
15. Strelkov V.V. Control tasks and manual control system for the wing-in-ground effect vehicle. Proceeding of the International Conference on Ground Effect Machines, S-Petersburg, Russia, 21-23 June, 2000.
16. Strelkov V.V. Functions and concepts of ekranoplan control system. -- Proceedings of the 3rd Gelenjik international seaplane science and technology conference, Russia, 6-8 September 2000.
17. Aleksandrov G.V., Gryazin V.Ye., Strelkov V.V. Features of dynamics and control of a flying vehicle during flight in ground effect. -- Trudy TsAGI, no. 2649, 2001.

High-Performance Marine Vehicles as Naval Platforms - An Overview

Rodrigo Azcueta, MTG Marinetechnik GmbH, Hamburg, azcueta@MTG-Marinetechnik.de
Volker Bertram, ENSIETA, Brest, bertram@waves.insean.it

Abstract

An overview of advanced naval platforms includes air-cushioned vehicles, surface-effect ships, wing-in-ground, foil-assisted craft and assorted multi-hull forms including trimarans. The survey describes the main features of these craft and gives references and figures for recently built or projected ships. Main features and advantages/disadvantages are listed.

1. Introduction

The design of hull types for naval combatants has long been dominated by fast displacement monohulls. However, as the marine environment imposes limits on the vessel's characteristics, such as speed, maneuverability and seaworthiness, which the conventional hull type is unable to overcome, novel concepts for unconventional hull types have evolved.

These are the so-called advanced marine craft or high-performance craft, which is any type of marine vehicle not of simple monohull form and weight supported either by hydrostatic buoyancy, hydrodynamic lift, powered lift, or aerodynamic lift. Advance marine craft should be able to achieve high speeds, have good seakeeping characteristics, enhanced maneuverability and/or reduced signatures. *Müller-Graf (1991)* has reviewed various concepts up to the 1990 with focus on civilian applications. We will here focus on naval applications of fast and unconventional ships.

MTG Marinetechnik has been long time involved in the development of novel concepts for future combatants for the German Navy. These studies were run under the name SYTKA, System Technology for Future Combatants, *MTG (1995)*. Besides the fast displacement monohull, which has traditionally dominated the design of naval combatants in Germany, this study showed that other candidates such as SWATH, high-speed SWATH, surface effect ships, and trimaran could be a suitable alternative depending on the requirements imposed by the navy.

Advantages and disadvantages of the different advanced and hybrid vehicles can generally be looked at with regard to their characteristics:

1. Design: platform stability, general arrangement (deck area and volume space), maximum draft.
2. Hydrodynamic: range of operating speed, propulsion configuration, speed loss in waves, seakeeping, maneuverability, weight and trim sensitivity.
3. Structural: global strength, local strength, dynamic loads (slamming), use of advanced materials, complex structures.
4. Others: acquisition and operating costs, state of development of the technology, survivability (detectability or stealth characteristics and vulnerability).

2. Classification

The classification of advanced vehicles and their hybrid derivations usually follows the classical sustention triangle, *Jewell (1973,1976*). The corners of this triangle represent the vessels supported by hydrostatic buoyancy, hydrodynamic lift and powered lift. The edges and the inside of the triangle represent the hybrids, Fig.1.

Hybrid vehicles combine more than one source of sustention or lift simultaneously and may combine the advantages of the different types of advanced craft from which they derive. To address all the various hybrids – of which more than 100 different concepts exist – would go far beyond the scope of this paper. Therefore we will focus only on the most promising types, which are in different stages of development: preliminary concept, prototypes and demonstrators or in operation.

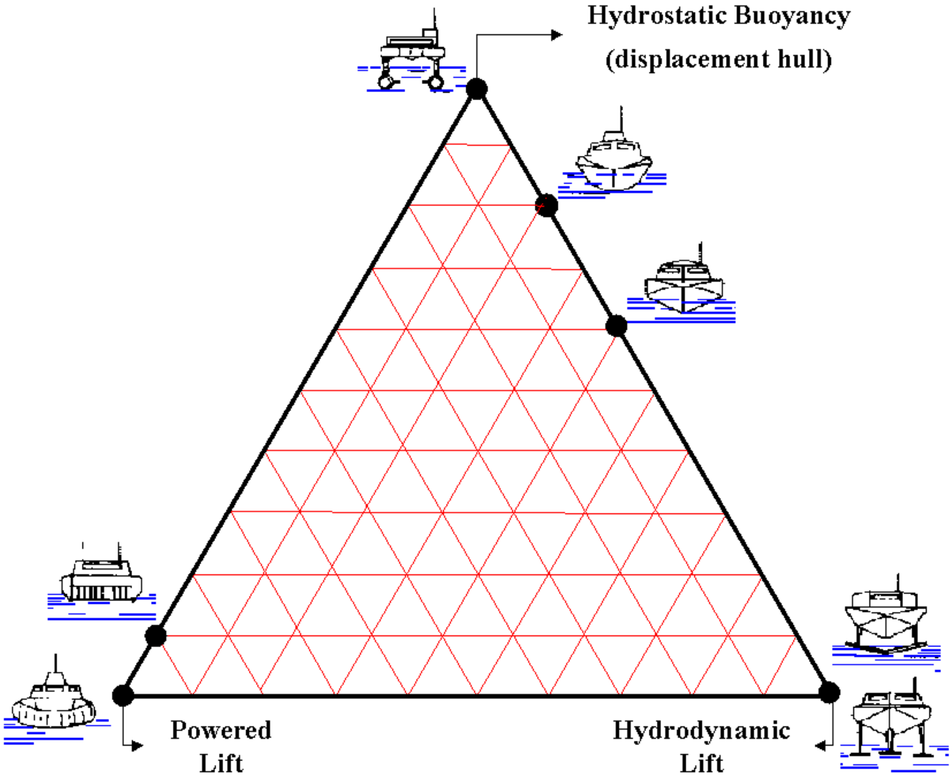

Fig.1: Classical sustention triangle

3. Displacement ships

In the hydrostatic buoyancy corner we find apart from conventional fast displacement monohulls, conventional displacement catamarans, SWATH ships and displacement trimarans, *Jansson and Lamb (1992), www.swath.com.*

SWATH (Small Waterplane Area Twin Hull) ships are semi-submerged catamarans, *Gore (1985), Lang and Slogett (1985), Papanikolaou (1996).* SWATH advantages are seakeeping superior to similar-sized conventional and unconventional craft and a large deck area for helicopter operation. Disadvantages are its higher resistance and installed power requirements due to greater wetted surface, its sensitivity to displacement changes and to trim, large draft, increased acquisition and operating costs compared to monohulls. Early SWATH prototypes have been built as technology demonstrators for the US navy (T-AGOS) and the Japanese navy. One of the Japanese SWATH built by Mitsui is the surveillance vessel "Hibiki" for the Japanese defense forces, Fig.2, *Hynds (2001).* Fig.3 is a 3-D rendering of the design currently under construction at TNSW in Emden, the “Wehrforschungsschiff”. In Germany, Abeking+Rasmussen has recently built various SWATH ships and proposed naval SWATH based on that experience, *Spethmann (2000,2001).*Fig.4 shows a photo of the "Sea Shadow" experimental ship, a stealth technology demonstrator, also based on SWATH technology. Most SWATH ships were designed for speeds lower than 25 knots. Almaz Shipbuilding Company in Russia has built a 32 m vessel in 1998 with a service speed of 28 knots. Other research in Russia has led to the development of a semi-planing SWATH concept designed for higher speeds with patrol craft applications, *Dubrovskiy (2000).* A recent addition to the family of SWATH designs is the SLICE design of Lockheed Martin, Fig.5, *Schmidt (2001).* This design has four surface-piercing struts.

A variant of a SWATH is the HSS (High Speed SWATH), which combines a SWATH bow section with a planing catamaran astern section, combining the good seakeeping of a SWATH and the high performance of a catamaran, Fig.6. A commercial application for a car/passenger ferry, built for STENA Lines, is shown in Fig.7. This ferry achieves speeds in excess of 40 knots.

Conventional displacement catamarans operate at Froude numbers larger than 0.4. They are well proven in commercial applications, usually as fast ferries. Their main advantage compared to monohulls are: larger deck area, higher speeds at same cost, reduced roll motions, higher initial stability, better maneuverability and better survivability. The main disadvantages are greater heave and pitch motions and structural problems in the transversal box connection.

Displacement trimarans are a recent development. Their overall advantages compared to monohulls are expected to be: lower resistance at high speed, better damage stability, good seakeeping, efficient layout of payload, good survivability, reduced operating costs. Fig.8 shows the trimaran demonstrator research vessel "Triton", *Smith and Jones (2001)*. A typical hull form designed by MTG is shown in Fig.9.

Wave piercers are most famous as catamarans like the Incat wave-piercing catamarans. Examples for navy applications are the "Jervis Bay" chartered by the Royal Australian Navy, *Moss (2001),* and the "Joint Venture" HSV-X1 chartered by the US army, Fig.10. The “Jervis Bay” was the first vessel of its type to be operated by any navy worldwide. In its role as fast- sea-lift ship, it can transport up to 500 fully equipped troops, together with vehicles and equipment, to ranges of up to 1000 nautical miles at speeds of more than 40 knots. The wave-piercing principle can also be applied to displacement monohulls like the US navy project DD21 "Zumwalt" class destroyer, Fig.11, the MTG project of a 7000 t frigate, Fig.12, or the British project for a stealth frigate "Sea Wraith". A wave-piercing navy patrol boat offered on the market is the VSV (very slender vessel) patrol boat from Paragon Mann Ltd., Fig.13.

4. Hydrofoils and Air-Cushion Vehicles

On the hydrodynamic corner of the sustention triangle we find the hydrofoil craft, *Johnston (1985), Meyer and Wilkins (1992), www.foils.org.* Hydrofoils can be either surface-piercing hydrofoils (SPH) or fully submerged hydrofoils (FSH). Their overall advantages compared to other types of fast vessels of the same size are the higher cruising speed and the higher level of comfort up to the wave heights which prevent foil-borne mode. Even in hull-borne operation in very rough seas, the presence of the immersed foils reduce vertical, roll and pitch motions. The principal disadvantage of the hydrofoil craft is the limited payload capability and large draft. Fig.14 shows the Italian patrol boat "Falcone" of Sparviero class (FSH), Fig.15 the Canadian "Bras d'Or" (SPH). While hydrofoils were largely abandoned by NATO navies in the 1980's, Russia continued operation, e.g. with the Russian fast attack patrol hydrofoil of Mukha class.

At the powered lift corner of the sustention triangle we find Air Cushion Vehicles (ACV), *Lavis (1985,1992).* The outstanding features of ACV’s are their ability to operate at very high speeds, their low vulnerability to underwater explosions, their small draft and underwater signatures and foremost their amphibious capability. Their disadvantages are that they are affected by wind, are sensitive to trim changes and have high acquisition and maintenance costs due to the seals and lift fan systems and specific electronic equipment for ride-control devices. Fig.16 shows the Russian landing craft (LCAC) of Pomornik class (Zubr class), currently the world’s largest ship of this class with 150 t payload and a maximum operating speed of 63 kts. The Greek Navy operates 4 of such boats as well. Fig.17 shows the Russian landing craft (LCAC) of Aist class (Dzheyran class). Its operating speed is 70 knots. Fig.18 shows the USN LCAC I, *Bobeck (1992).* Beyond its basic mission of transporting personnel and equipment from ship to shore, LCAC I has become a multimission craft. LCAC I is an effective mine-hunter-sweeper or a troop carrier.

5. Hybrid designs: SES and hybrid hydrofoils

At the edges and inside our sustention pyramid the hybrid craft are located. The most popular hybrid type is represented by the air cushion catamarans, *Butler (1985), Lavis and Spaulding (1991), Wessel (1995).* They are commonly known as SES (surface effect ships), but this is a wrong definition since there is no surface effect involved here. SES are a crossover between a displacement catamaran and an ACV. The outstanding features of SES are the ability to operate at high speeds in excess of 40 knots (F_n>1.0), reduced underwater signature levels and improved shock resistance to underwater explosions, good platform stability, shallow draft, and large deck area. Disadvantages are speed loss in head seas, the loss of amphibious capability compared to the ACV, higher production and maintenance costs. Examples of this type of craft are: The French AGNES-200, in 1992 the largest SES in the world with 250 t displacement, Fig.19, the German MEKAT class "Corsair" Blohm+Voss, Fig.20, *N.N. (1989), Bohlayer (1999),* the Norwegian Oksøy class mine-hunter, Fig.21, and the Norwegian Skjold class fast patrol boat, *Kilhus (2001),* Fig.22, and the Russian missile corvette "Bora", which combines SES technology with hydrofoil technology and attains a speed of 53 knots, Fig.23, and the Swedish stealth SES “Smyge”,
www.canit.se/~griffon/diverse/miltech/stealthships.html.

More recently, air-cavity ships have been investigated in Western Europe, *www.dkgroup.dk*, although it is believed that the Soviet Union performed extensive development long before. Air cavity ships supply gas through nozzles under a profiled bottom generating an air cavity under the ship. Around the cavity are rigid bottom sections which are in stationary contact with water, however the layer is much thinner and smaller than for an SES. The side hulls are planing. The ACS uses 1.5-2.5% of the engine power for the air cavity compared to typical 20-30% for an SES. Air is constantly escaping at the back end of the cavity, thus requiring a constant new supply of air and the concept is only attractive at higher speeds.

Several hybrid designs combine buoyancy and hydrodynamic lift, *Meyer (1991).* The HYSWAS (hybrid small waterplane area single hull) is a monohull version with a deeply submerged torpedo-like buoyancy body and hydrofoils giving 30%-70% of the required lift force, *Meyer (1992), Bertram (1994).* HYSWAS have been projected up to frigate size, but so far only the TSL-F (Techno-Superliner) demonstrator (ferry, Japan) and the US navy "Quest", Fig.24, *Meyer et al. (1995),* have been built. "Quest" is a 9 m 35-knot demonstrator for an unmanned, high-speed, rough-water capable craft that is deployable from another vessel, e.g. for reconnaissance or mine-hunting. Hydrofoil-assisted catamarans have been more widely accepted. A typical representative is the South African HYSUCAT, *www.unistel.com/technologies/hysucat/, www.hydrospeed.co.za, Migeotte and Hoppe (1999), Hoppe (2001),* Fig.25. Several types have been built as patrol boats reaching speeds up to 50 knots. The design features good seakeeping and relatively low resistance, but the foil design is sensitive and requires tailoring towards specific design conditions.

6. Wing-in-ground

Since the exponents for aerodynamic lift are not included in the classical sustention triangle, the triangle should be extended to a pyramid, with a corner representing the aerodynamic lift, Fig.26. At this corner we find the wing-in-ground vehicles (WIG), *Butler (1985), Hooker and Terry (1992), www.airforce.ru/english/aircraft/ekranoplans/index.htm, jpcolliat.free.fr/ekra/ekraA.html, www.se-technology.com.*

A WIG craft can be seen as a crossover between an ACV and an aircraft. WIGs operate in a speed range of 100 to 500 km/h. WIGs could be an efficient replacement of conventional transport systems (ships, aircraft) on existing routes and also where there is no infrastructure such as airports. It has a very high transport efficiency compared to airplanes expressed as the amount of fuel used per passenger per km. A main problem with WIG technology is the power requirement for take-off, which is several times larger than that required for cruising. Moreover, there are safety concerns for craft operating in densely populated areas at such speed and low altitude. The technology is not really mature yet and there is limited experience outside Russia, Fig.27. WIGs were known as Ekranoplan in the former Soviet Union. Fig.28 shows the "Caspian Sea Monster" of the former Soviet Union. It weighs 550 t and operates at 500 km/h. It was built 1966. Fig.29 shows the 400 t Soviet "Lun", built in 1987 as a missile launcher operating at 450 km/h, Fig.30 the 110 t Soviet "Orlyonoks", built in 1973 as troop transport and assault vehicle operating at 400 km/h (payload of 15 t).

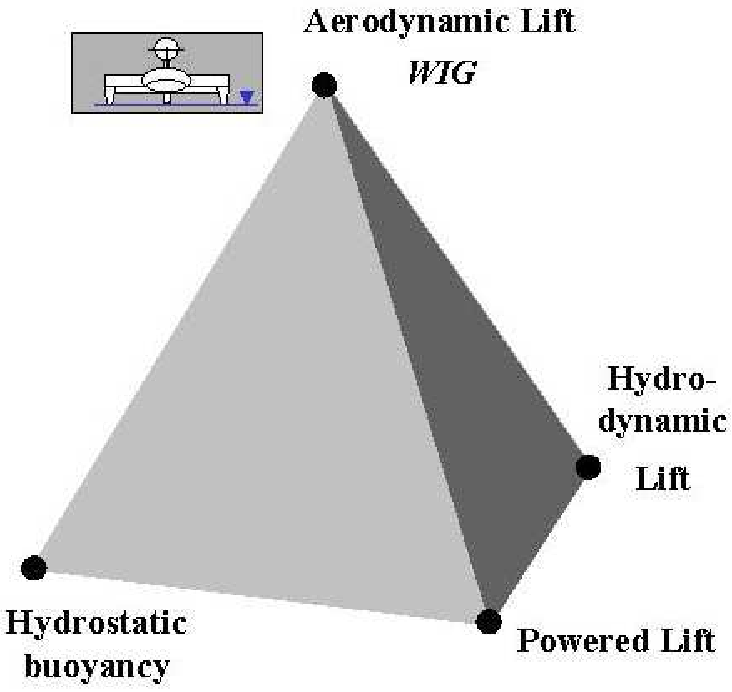

Fig.26: Sustention Pyramid

The German military developments of WIGs were stopped some years ago. However, under the sponsorship of the German Ministry of R&D a program was started in the commercial field for the development of a 80 passenger WIG ferry, *Hynds (2000),* based on the Hoverwing family, *Fischer and Matjasic (1998,1999).*

7. Other concepts

Among the many other types of hybrid craft and unconventional hull forms, *ANEP (1996),* not discussed in this short overview due to time and space limitations, are:

– Fast monohull by Blohm+Voss, *Langenberg (1995),* a displacement hull with the hull volume as deep submerged as possible, Fig.31. The ship type has been proposed for naval applications, but so far only fast cruise vessels of this type have been built, *Engelskirchen and Marzi (2001).*
– Deep-V monohull with excellent calm water performance and payload, acceptable seakeeping.
– Planing hulls, *Savitsky (1985)*
– Fast catamarans, usually planing or almost-planing hulls.
– Weinblume, *Söding (1997),* are catamarans with staggered hulls excellent wave resistance at moderate speeds, acceptable seakeeping, and low wash. However, disadvantages in deck arrangement and structural problems have prevented so far any demonstrator to be built.

References

ANEP (1996), *The application of costing and operational effectiveness methods for the selection of hull types*, ANEP 52, NATO

BERTRAM, V. (1994), *Tragflügelgestützte Hybridschiffe*, Jahrbuch Schiffbautechnische Gesellschaft, pp.355-362

BOBECK, D.F. (1992), *LCAC: A system evolution*, High-Performance Marine Vehicles Conf., Arlington, ACV113-122

BOHLAYER, W. (1999), *High speed craft for governmental maritime services*, 1st High-Performance Marine Vehicles Conf., Zevenwacht, pp.20-27

BUTLER, E.A. (1985), *The surface effect ship*, Naval Engineers Journal, pp.200-258

DUBROVSKIY, V. (2000b), *SWATH seakeeping allows growth in speed*, Speed at Sea, February, pp.27-28

ENGELSKIRCHEN, J.; MARZI, J. (2001), *Development of a fast displacement hull form for a RoPax day ferry*, 2nd High-Performance Marine Vehicles Conf., Hamburg, pp.139-148

FISCHER, H.; MATJASTIC, K. (1998), *Die Nutzung des Bodeneffektes zur Verbesserung der Wirtschaftlichkeit beim Transport über Wasser*, Schiff&Hafen 6, pp.61-65

FISCHER, H.; MATJASTIC, K. (1999), *The hoverwing technology - Bridge between WIG and ACV*, 1st High-Performance Marine Vehicles Conf., Zevenwacht, pp.72-78

GORE, J.L. (1985), *SWATH ships*, Naval Engineers Journal 97/2, pp.83-112

HOOKER, S.F.; TERRY, M.R. (1992), *Hydroaviation*, High-Performance Marine Vehicles Conf., Arlington, WS1-8

HOPPE, K.G.W. (2001), *Recent applications of hydrofoil supported catamarans*, Fast Ferry International, September, pp.30-36

HYNDS, P. (2000), *Commercial interest revived in WIG technology*, Speed at Sea, February, pp.45-48

HYNDS, P. (2001), *SWATH designs continue to make steady headway*, Speed at Sea, August, pp.28-29

JANSSON, B.O.; LAMB, G.R. (1992), *Buoyantly supported multihull vessels*, High-Performance Marine Vehicles Conf., Arlington, MH1-17

JEWELL, D.A. (1973), *Hybrid fluid-borne vehicles*, The Senior Engineer 23/9, pp.7-11

JEWELL, D.A. (1976), *Possible naval vehicles*, Naval Research Reviews, Office of Naval Research, October

JOHNSTON, R.J. (1985), *Hydrofoils*, Naval Engineers Journal 97/2, pp.142-199

KILHUS, G. (2001), *Operational experience with the Skjöld-class SES-FPD's*, Jahrbuch Schiffbautechnische Gesellschaft, Springer

LANG, T.G.; SLOGETT, J.E. (1985), *SWATH developments and performance comparisons with other craft*, Int. Conf. SWATH Ships and Advanced Multi-Hulled Vessels, RINA, pp.7-23

LANGENBERG, H. (1995), *Fast displacement ships - An economical option for high speed transport*, FAST'95, Travemünde, pp.283-294

LAVIS, D.R. (1985), *Air cushion craft*, Naval Engineers Journal 97/2, pp.259-316

LAVIS, D.R. (1992), *Hovercraft development*, High-Performance Marine Vehicles Conf., Arlington, ACV1-38

LAVIS, D.R.; SPAULDING, K.B. (1991), *Surface effect ship (SES) developments worldwide*, Naval Engineers Journal, September, pp.39-83

MEYER, J.R. (1991), *Hybrid hydrofoil technology - An overview*, FAST'91, Trondheim, pp.623-640

MEYER, J.R. (1992), *Hybrid hydrofoil technology applications*, High-Performance Marine Vehicles Conf., Arlington, HF25-36

MEYER, J.R.; DeVENY, J.A.; JORDAN, P.D. (1995), *HYSWAS concept demonstrator*, Int. Hydrofoil Society 25th Anniversary Conf., Arlington, pp.203-213

MEYER, J.R.; WILKINS, J.R. (1992), *Hydrofoil development and applications*, High-Performance Marine Vehicles Conf., Arlington, HF1-24

MIGEOTTE, G.; HOPPE, K.G.W. (1999), *Developments in hydrofoil assistance for semi-displacement catamarans*, FAST'99, Seattle, pp.631-642

MOSS, S. (2001), *A wave-piercing catamaran as fast troop transport vessel*, Jahrbuch Schiffbautechnische Gesellschaft, Springer

MTG (1995), *SYTKA: Systemtechnologie moderner Kampfschiffe/-boote*, MTG Report 286/00/0010-001

MÜLLER-GRAF, B. (1991), *Schnelle unkonventionelle Schiffe, ihre Technologien und ihre Entwicklung*, Hansa 128/12, pp.659-667, 128/13-14, pp.744-748

N.N. (1989), *Luftkissen-Katamaran SES "Corsair", ein neuartiges Hochgeschwindigkeitsfahrzeug*, Hansa 126/11,12, pp.800-801

PAPANIKOLAOU, A. (1996), *Developments and potential in open sea SWATH concepts*, WEGEMT workshop Conceptual Designs of Fast Sea Transportation, Glasgow

SAVITSKY, D. (1985), *Planing craft*, Naval Engineers Journal 97/2, pp.113-141

SCHMIDT, T.W. (2001), *Technology for the 21st century: SLICE - A revolutionary new ship*, Jahrbuch Schffbautechnische Gesellschaft, Springer

SMITH, R.P.; JONES, J.B. (2001), *Design, construction and trials of the trident trimaran test craft*, Jahrbuch Schiffbautechnische Gesellschaft, Springer

SÖDING, H. (1997), *Drastic resistance reduction in catamarans by staggered hulls*, FAST'97, Sydney, pp.225-230

SPETHMANN, K. (2000), *Nach Ablieferung des Stationsschiffes "Elbe" ist das neue*

Lotsenversetzsystem komplett, Schiff&Hafen 10, pp.121-130

SPETHMANN, K. (2001), *A realised SWATH-application as an example for naval purposes,* Jahrbuch Schiffbau-Technische Gesellschaft, Springer

WESSEL, J. (1995*), Review on German SES developments and government funded R+D programme SUS C,* FAST'95, Travemünde, pp.917-930

Fig.2: SWATH "Hibiki" by Mitsui

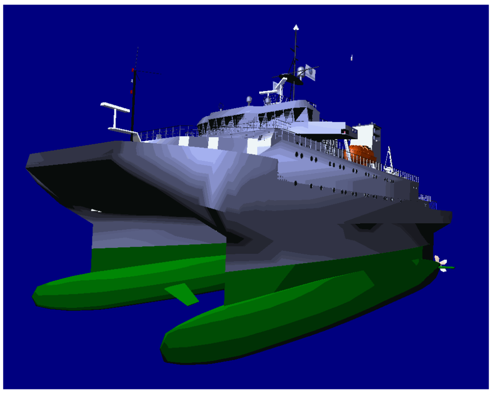

Fig.3: TNSW "Wehrforschungsschiff"

Fig.4: "Sea Shadow" (www.fas.org)

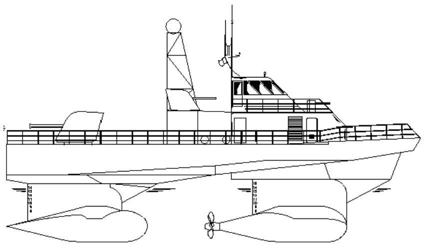

Fig.5: SLICE by Lockheed Martin

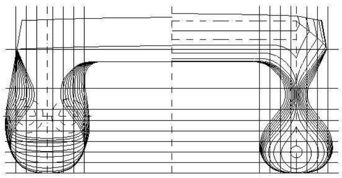

Fig.6: HSS designed by MTG

Fig.7: GTS Stena Explorer (HSS)

Fig.8: Trimaran "Triton"
(www.trimaran.dera.gov.uk)

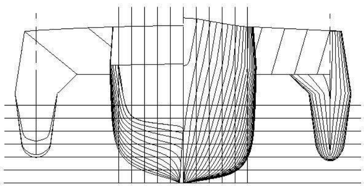

Fig.9: Trimaran designed by MTG

Fig.10: "Joint Venture" Incat conversion

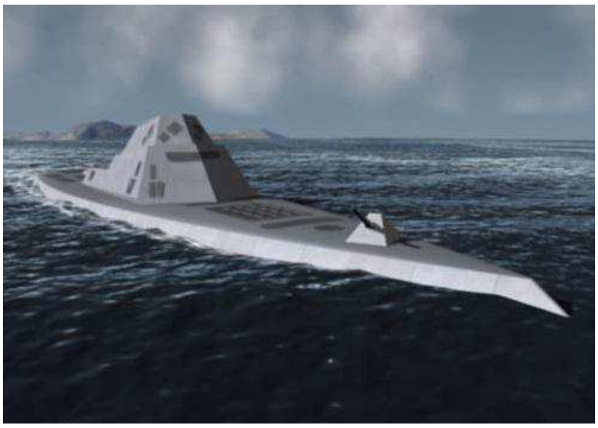

Fig.11: DD21 "Zumwalt" class destroyer
(www.dd21.goldteam.com)

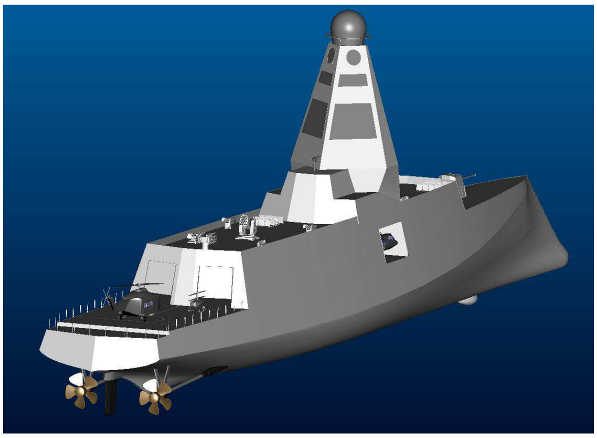

Fig.12: Wave piercer frigate study MTG

Fig.13: VSV Paragon Mann
(www.halmatic.co.uk)

Fig.14: Italian Sparviro class "Falcone"

Fig.15: Canadian "Bras d'Or"

Fig.16: Russian landing craft Pomornik class

Fig.17: Russian landing craft Aist class

Fig.18: USN LCAC I (www.tmls.textron.com)

Fig.19: French AGNES 200

Fig.20: German "Corsair" (www.blohmvoss.com)

Fig.21: Norwegian Oksøy class SES

Fig.22: Norwegian Skjøld class SES

Fig.23: Russian missile corvette "Bora"

Fig.24: "Quest" HYSWAS

Fig.25: HYSUCAT for Thai navy

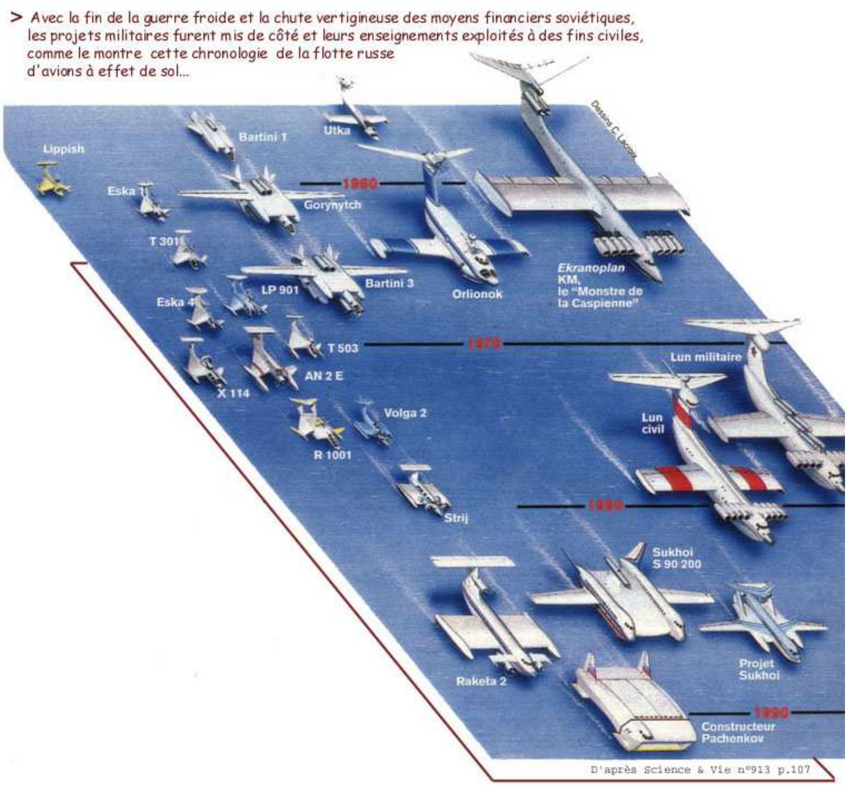

Fig.27: Overview of WIG developments, *jpcolliat.free.fr/ekra/ekraA.html*

Fig.28: "Caspian Sea Monster"

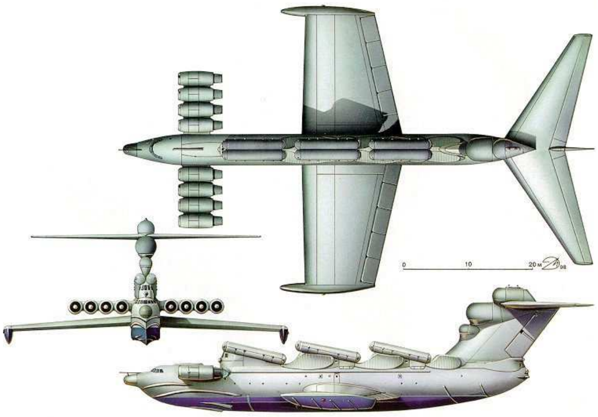

Fig.29: Russian missile launcher "Lun" WIG

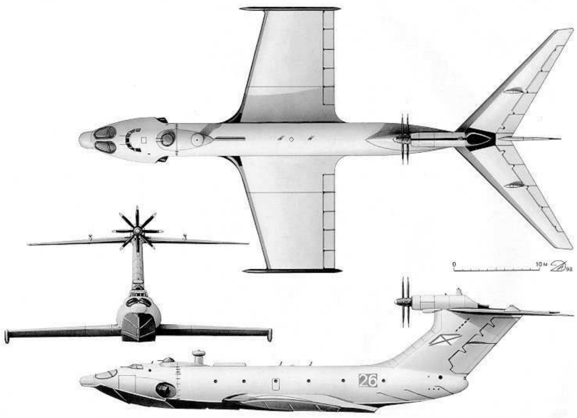

Fig.30: Russian "Orlyonoks" WIG

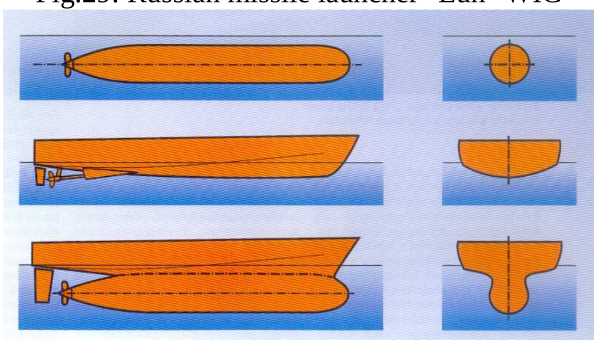

Fig.31: Fast monohull of Blohm+Voss

Resistance and Structural Modulus for Multiattribute Trimaran Hull Design

Marcello Barone, Carlo Bertorello

Department of Naval Architecture, University of Naples “Federico II”, mabarone@unina.it

Abstract

In a research program jointly carried out by Naples, Genoa and Trieste Universities, the resistance characteristics of different hull configurations suitable for small size fast ferries have been extensively investigated; a trimaran hull design for a 350 passengers 40 knots fast ferry has been developed as a very promising alternative to more conventional hull forms. Towing tank tests have identified the best outrigger transversal and longitudinal position for the operative Fn range.In the paper the global and local loads relative to three longitudinal and two transversal outrigger positions of the afore mentioned trimaran hull have been evaluated. From this data hull scantlings and hull structural weights have been assessed. The differences in the structural weights have allowed a more complete consideration of the achieved results about optimal outrigger position based only on hydrodynamic performances. The strong reciprocal influence of hydrodynamic and structural characteristics suggests a multiattribute approach for the performance optimisation of such craft. The best hull configuration has been selected applying the principle of non dominance to the normalised attribute. This work is one of the steps in the development of a multiattribute design model for small size multihull fast ferries.

1. Introduction

The request for high speed vessels, especially for coastal passenger ferries has led to the search for unconventional hull-forms with superior performances.

Although many experimental and theoretical investigations have been carried out till now, fast ships are still presenting some problematic questions due to inadequate information on the splitting of the total resistance into different components, on the interference phenomenon for the multi-hulls, on the model ship correlation and on the performance comparison of different craft. This last aspect is very important at early design stage; it needs the simultaneous consideration of several parameters and reliable tools to consider their effects.

While the mono-hull and the catamaran are the leading commercial types, recent researches have been focused also on the trimaran, which for large deck area, easy machinery arrangement and good powering performances could be preferred to the above mentioned high speed craft.

One of the most interesting aspects of the trimaran hull design is the powering optimisation through the identification of optimum outrigger longitudinal and transversal position. In fact, due to the interference phenomenon, the outrigger position has been shown to be one of the most significant parameter affecting hydrodynamic resistance and, as a consequence, power requirements.

In previous works the results of tank tests of models relative to a small trimaran fast passenger ship have been reported. Several staggers and clearances have been investigated. The results have pointed out that, in the operative Froude number range for small size fast ferries ($0.6 < Fn < 1.0$), the lowest resistance has been achieved shifting the outriggers forward and outwards, i.e. for the highest values of clearance and the lowest values of stagger.

Further studies, reported in this paper, were conducted at Naval Architecture Department of Naples University with the aim to assess the influence of the outrigger position on hull scantlings and structure weight. To this purpose, three staggers (y/L_{wl} = 0.25, 0, -0.1) and two clearances (x/L_{wl} = 0.10, x/L_{wl} = 0.113 = maximum allowed clearance) have been considered. Global loads acting on the hull have been evaluated referring to RINa (Registro Navale Italiano) formulas. Local loads have been assessed also; the scantlings and the consequent hull weights have been calculated. The structural design has been carried out considering a GRP structure which seems a suitable material for small size fast ferries. Composite materials, that are very promising for hull weight reduction, have limits due to their poor fire resistance. This results in a limited operative range imposed by Classification Societies that handicaps only larger vessels, while small size fast ferries used on coastal routes do not suffer this constrain. The evaluation of the different structural weights has been performed for the hull bottom and side plating and for the cross deck with the relative stiffeners as those are the elements influenced by stagger. The effect of clearance on structural weight has been quantified for stagger -0.1.

Published data about hydrodynamic performances and displacement values achieved through different structural weights have allowed to assess effective power requirements and to identify the best hull configuration.

1.1 - Hull form

The design of the trimaran hull has been developed on the basis of the requested lay-out, of the limits due to service considerations and on available data from existing studies.

Main hull has been selected as a slender round bilge hull form from Series 64. The outriggers have been chosen from Series 64 and stretched by geometrical affinity so as to increase the value of the L/B ratio according to their higher Froude number (Fig. 1).

Table 1 details the principal main hull and outrigger characteristics of the considered trimaran ship.
Three different outrigger longitudinal positions (stagger) and two different outrigger transversal positions (clearance) have been considered. Stagger has been assessed as the ratio between main hull and side hull midship longitudinal distance y, and main hull waterline length L_{wl}. Clearance has been assessed as the ratio between main hull and sidehull centerplanes distance x, and main hull waterline length L_{wl}.

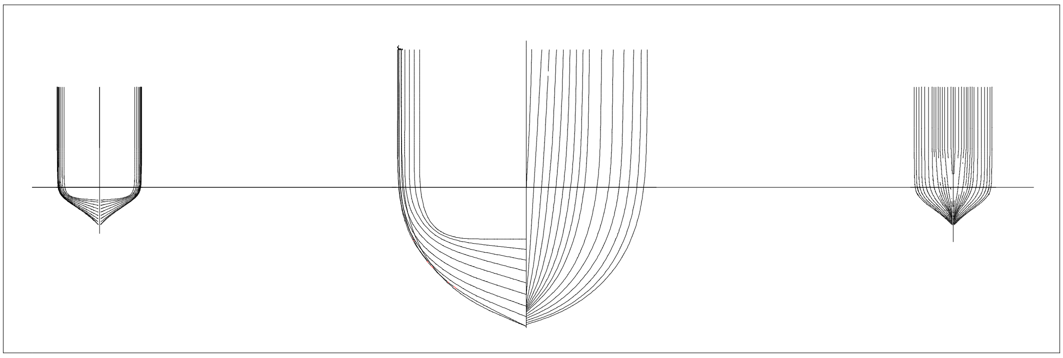

Fig. 1: Trimaran hull body plan.

Fig. 2-4 show the considered stagger that are:

1) +0.25: main hull and side hull transom aligned
2) 0: main hull and side hull midships aligned
3) - 0.1: side hull midship shifted 4.694 m (0.1 Lwl) forward of the main hull midship.

For stagger – 0.1 two different clearances have been examined:

1) 0.100 $\Rightarrow$ x = 4.70m
2) 0.113 $\Rightarrow$ x = 5.30m, corresponding to the maximum allowed breadth of the trimaran.

In the following figures the considered staggers are reported as well as the hull subdivision.

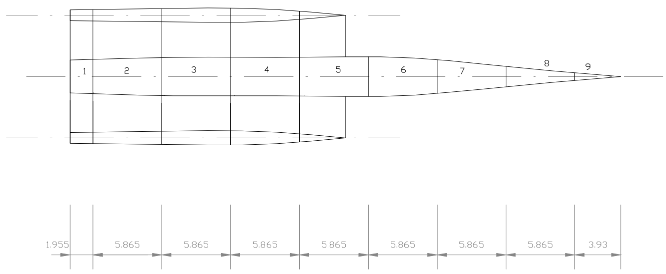

Fig.2: Trimaran hull; stagger +0.25.

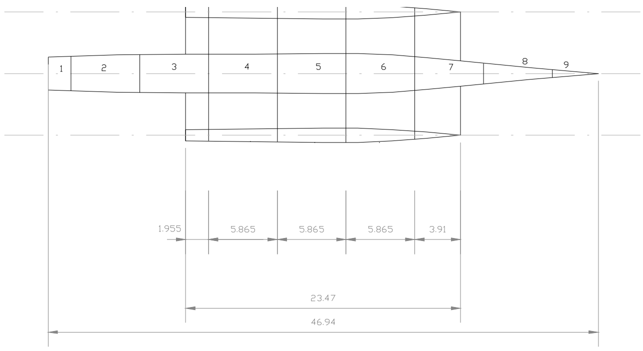

Fig.3: Trimaran hull; stagger 0.

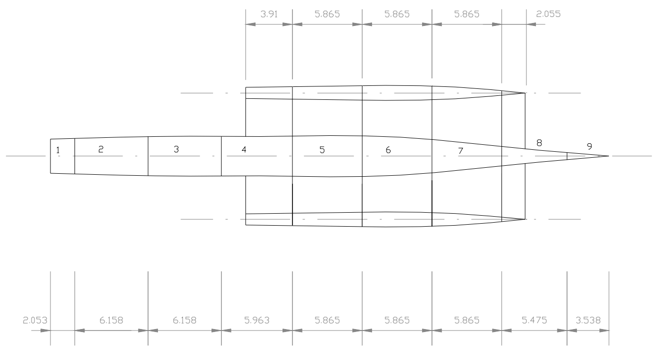

Fig.4: Trimaran hull; stagger –0.1.

Table 1: Principal characteristics of the trimaran in full scale.

	MAIN HULL	SIDE HULL	TRIMARAN
Length over all (m)	47.700	23.850	47.700
Length waterline (m)	46.940	23.470	46.940
Beam waterline (m)	3.336	1.092	
Draught (m)	1.668	0.463	1.668
Wetted surface (m^2)	194.8	25.2	245.2
Displacement (t)	120.489	4.259	129.007
Max speed (kn)			40

CB	0.45	0.35
L/B	14.070	21.500
B/T	2.000	2.356
Fn	0.958	1.356

2. Hull structures

The hull scantlings and the structural weights have been assessed through the following steps:

a) Ship structural lay-out definition
b) Acting loads evaluation and safety factors assessment
c) Material characteristics evaluation
d) Scantlings evaluation
e) Structural weight assessment

Three different staggers have been considered for clearance 0.10; the stagger with the lowest value of hull weight has been then selected amongst these hull configurations and the hull weight evaluation has been repeated with respect to a different clearance (the maximum allowed one) in order to quantify the influence of this parameter.

2.1 Structural lay-out

Scantling Rules influence structural lay-out through the usual practice of designing according to their prescriptions. As regards GRP structures Classification Societies generally refer to single skin and sandwich plating with longitudinal and transversal reinforcements.

A structural lay-out representative of the usual practice in the field has been chosen and it has been developed with the aim to provide the hull with enough resistance to support local and global loads and to meet subdivision requirements. Its main characteristics can be summarised as follows:

- single skin plating
- trimaran hull is divided into nine compartments by 8 watertight bulkheads extended for the entire local breath of the ship. (Figg. 2-4).
- 15 transversal web frames are extended for the entire local breath of the ship (Fig. 5)
- longitudinal stiffeners spacing is s = 0.6 m
- bulkheads stiffeners spacing is s = 0.6 m
- bottom longitudinal girders are 1.20 m spaced.

In Fig. 5 the trimaran main section for stagger 0 and maximum clearance is reported.

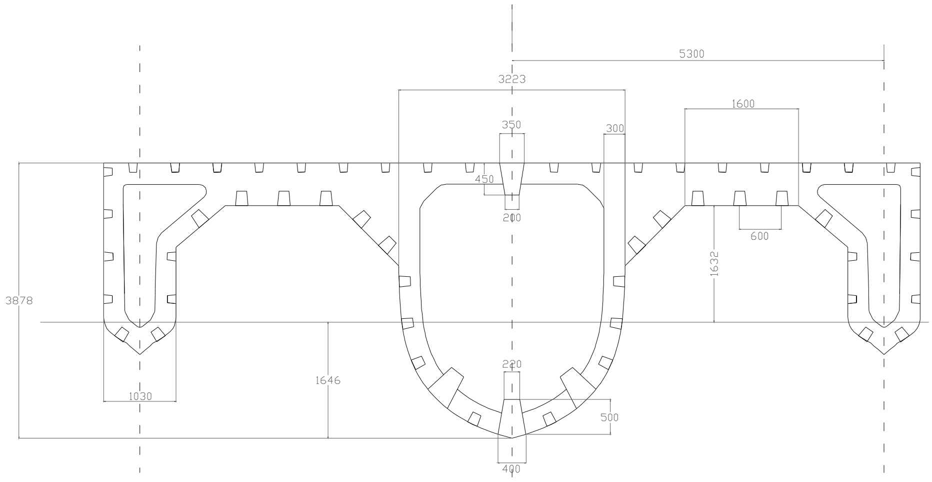

Fig.5: Trimaran main section (stagger 0, clearance max).

2.2 Global loads

First step of the global loads evaluation is the assessment of weight distribution. Weight components have been estimated from the data analysis of small passenger ferries presently in service. In Table 2 the formulas for weight assessment and the resulting values are reported.

Table 2: Weight preliminary evaluation

Item	formula for preliminary evaluation	preliminary values (t)
Hull	$np*15 + Lwl^{2.63}$	30.965
Engine and propulsion	$P_B*6.5$	26.000
Fitting out and equipments	20% lightship	18.600
Passengers and crew	80*np + nc*75	28.750
Fuel	$0.212*P_B*12/1000$	10.176
Water and consumable	np*14.5/1000	5.075
Safety equipments	np*20/1000	7.000
Margin	2.5% of the total (126.566)	3.160
total displacement Δ		129.720

np = number of passengers; P_B = brake horsepower; nc = number of crew members

A simplified weight distribution has been assumed to calculate longitudinal shear and bending moment with respect to three different conditions: still water, hogging and sagging.

Loads evaluation has been carried out referring to quasi-static conditions, i.e. as difference between weights and buoyancy distribution curves. In the sagging condition, an approximate estimation of dynamic loads has been realised as well, following the RINa procedure for HSC: an additional weight distribution curve has been calculated to take in account slamming and inertia loads effects.

Longitudinal shear and bending moment distribution curves do not depend on clearance but are heavily influenced by stagger as the diagrams, reported in Figs. 6-11, relative to each hull configuration, show.

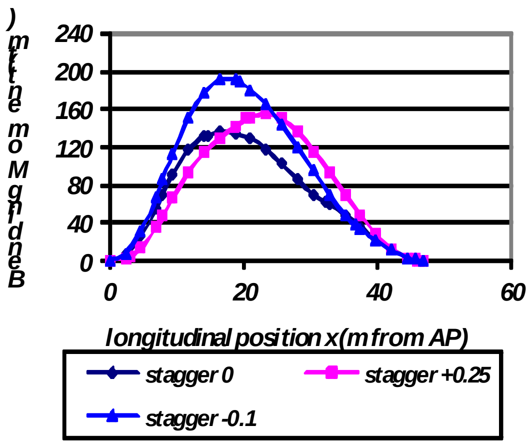

Fig.6: Bending moment – Still water.

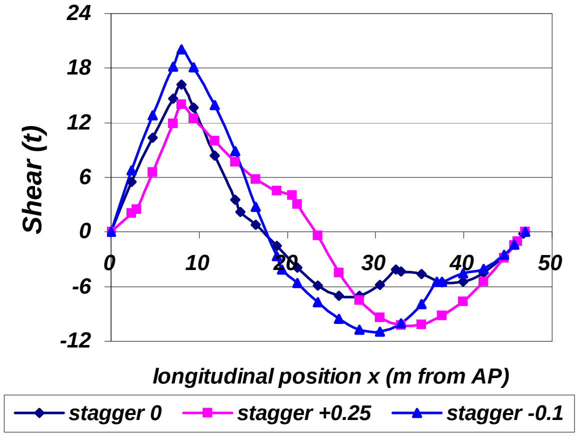

Fig.7: Shear – Still water.

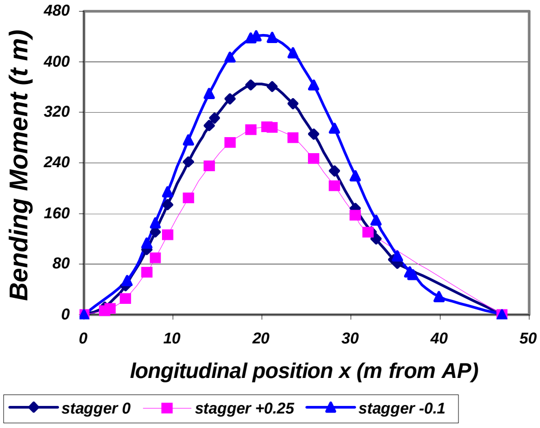

Fig.8: Bending moment – Hogging.

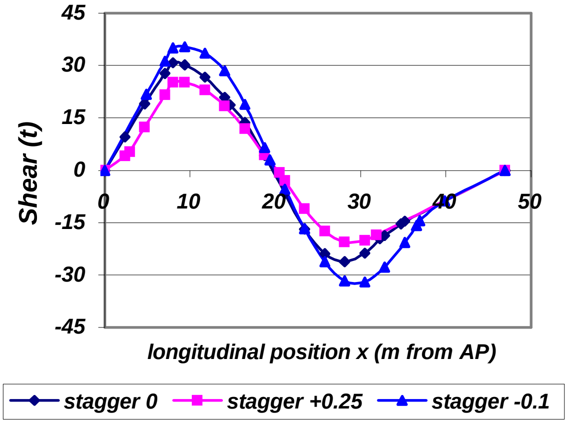

Fig.9: Shear – Hogging.

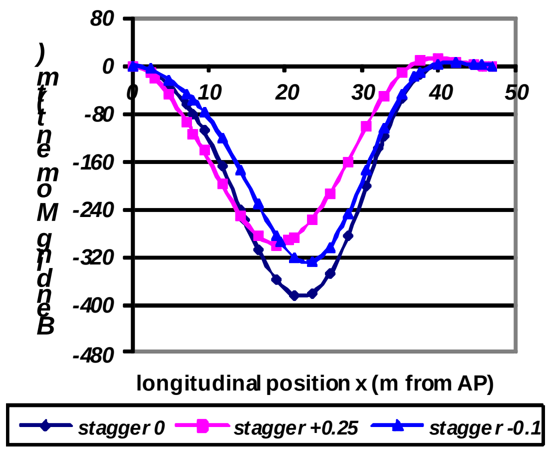

Fig.10: Bending moment – Sagging.

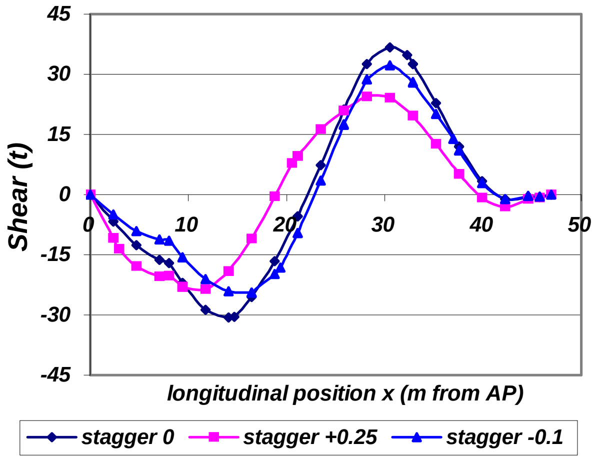

Fig.11: Shear – Sagging.

Maximum values of shear and of bending moment are reported in Table 3.

Table 3: Maximum shear and bending moment values.

	stagger +0.25	stagger 0	stagger -0.1	Max diff. (%)
	max value (t m)			
Bending Moment still water =	155	136	191	29
Bending Moment hogging =	297	363	441	33
Bending Moment sagging =	-300	-384	-329	09
	max value (t)			
Shear still water =	13.99	16.18	20.09	19
Shear hogging =	25.17	30.83	35.38	29
Shear sagging =	24.41	36.72	32.17	24

From the analysis of reported data it is possible to draw the following conclusions:

- in still water as well as in hogging conditions, the highest values of both shear and bending moment are achieved for the stagger –0.1, i.e. with outriggers shifted in the most advanced position;
- in the sagging condition, highest loads are obtained for stagger 0, i.e. with main hull and outriggers midship sections aligned;
- the gap amongst the maximum values in the three different hull configurations is considerable: it reaches values of 29 % for the shear and of 33 % for the bending moment;
- these results will not influence very much the hull weight of the different hull configuration for the considered ship, due to its reduced Lwl that makes longitudinal global loads very low in comparison with local loads at high speed; otherwise the differences in bending moments and shear values would be most important for the design choices in the case of larger ships and, in any case, they cannot be neglected.

2.3 Local loads

Local loads have been evaluated referring to RINa (Italian Register) formulas for twin-hull ships reported in HSC Rules. The stagger influences pressure values on outrigger bottom and sides and on cross deck panels. Pressures calculation has been carried out dividing the main hull into four longitudinal parts from FP with lengths equals to 0.25 Lwl. Impact loads acting on both cross-deck and side hull bottom show high sensitivity to the outrigger longitudinal position. Table 4 summarises the reference values of impact pressure acting on these hull portions for the three staggers:

Table 4: Impact pressures along side hulls and cross-deck.

	stagger +0.25		stagger 0		stagger -0.1	
location	Pshb (*) (kN/m^2)	Pcd (**) (kN/m^2)	Pshb (*) (kN/m^2)	Pcd (**) (kN/m^2)	Pshb (*) (kN/m^2)	Pcd (**) (kN/m^2)
0 < x/Lwl < 0.25	57	61	-	-	-	-
0.25 < x/Lwl < 0.5	69	49	76	49	85	49
0.5 < x/Lwl < 0.75	-	-	69	86	69	86
0.75 < x/Lwl < 1	-	-	-	-	69	123

(*) Pshb = pressure acting on side hull bottom panels; (**) Pcd = pressure acting on cross-deck panels;

2.4 Material characterization and Laminate characteristics definition

Scantling Rules refer to the most widely used matrixes and reinforcements and to the hand lay-up as the production process. The influences given by the curing process and by the shape of the piece to material characteristics are only qualitatively considered. The resulting values predicted according to formulas proposed by R.I.Na. in HSC Rules, are relative to a fibre weight fraction of 0.35 and concern a typical glass/vinylester laminate.

The following materials have been considered as a reference for the ship scantlings evaluation:

- Matrix : Vinylester resin
- Reinforcement fibres: E glass

Combined layers of chopped strand mat (CSM) and woven roving (WR) have been used for plating; unidirectional laminate (UDR) have been used for longitudinal stiffeners and transversal web frames with the aim to increase their longitudinal stiffness. Table 5 summarises the materials properties.

Table 5: Materials and laminate properties.

	ρ_r (Kg/m^3)	E (N/mm^2)	ν_r	
MATRIX	1.12	3400	0.3	
FIBRES	2.55	72000	0.2	
	Ψ	P (g/m^2)	E_L (N/mm^2)	E_T (N/mm^2)
CSM	0.35	300/450	9295	9295
WR	0.45	450	13615	13615
UDR	0.45	800	21535	5695

Ψ = fibre weight fraction; ρ_r = specific gravity; P = fibre weight per square meter; ν_r = Poisson's ratio; E_L = longitudinal elastic modulus; E_T = transversal elastic modulus

2.5 Safety Factors Assessment

The High Speed Craft Rules in the scantling evaluation procedure consider explicitly the comparison between the laminate stresses and the material ultimate strengths on the basis of given safety factors. The values given by the principal Classification Societies differ significantly among them and the comparison relative to the main structural elements is shown in Table 5 where values proposed by American Bureau of Shipping (ABS), Lloyd's Register (L.R.) and Det Norske Veritas (DNV) are reported. In this work the safety factor proposed by R.I.Na. (4.5) has been used.

Table 6: Safety Factors.

	R.I.Na.	ABS	L.R.	DNV
in general	6			
el. subj. to imp. press.	4.5	3	5-4	3.3
bottom shell	4.5	3	5-4	3.3
side shell	4	3	4-3	3.3
deck shell	4	3	4	3.3
wt bulkheads	5	2	3	3.3

2.6 Hull scantlings

The scantlings for each structural element of the hull have been verified according to the formulas proposed by R.I.Na. in HSC Rules. Plating thickness has been assessed taking into account the local loads; starting from the minimum value, provided by RINa formulas, thickness have been increased until induced local stresses resulted below the maximum allowable values. The same procedure has been applied to evaluate longitudinal stiffeners and transversal web frames scantlings. Then the obtained structure has been verified to global loads. To give an example the thickness of the plating for the different hull regions is reported in Table 7.

Table 7: Outriggers and cross-deck plating thickness in mm.

	stagger +0.25	stagger 0	stagger -0.1
bottom x/Lwl < 0.25	14.2	-	-
bottom 0.25 < x/Lwl < 0.5	16.3	16.3	18.4
bottom 0.5 < x/Lwl < 0.75	-	16.3	16.3
bottom x/Lwl > 0.75	-	-	16.3
side hull x/Lwl < 0.25	10.0	-	-
side hull 0.25 < x/Lwl <0.5	10.0	10.0	10.0
side hull 0.5 < x/Lwl < 0.75	-	10.0	10.0
side hull x/Lwl > 0.75	-	-	10.0
cross-deck x/Lwl < 0.25	16.3	-	-
cross-deck 0.25 < x/Lwl <0.5	14.2	14.2	14.2
cross-deck 0.5 < x/Lwl < 0.75	-	20.5	20.5
cross-deck x/Lwl > 0.75	-	-	22.6

Table 8: Flexural stress due to local and global loads acting on the cross-deck structure.

σ (N/mm²)	stagger +0.25		stagger 0		stagger -0.1		
	0.25<x/L<0.5	0.5<x/l <0.75	x/L <0.25	0.25 < x/L < 0.5	0.25 < x/L < 0.5	0.5 < x/l < 0.75	x/l > 0.75
	CLEARANCE MAX						
σd'	8	7	6	14	6	13	27
σd"	11	7	11	7	11	12	6
σtot	19	14	17	21	17	25	33
σr / SF	43						
CLEARANCE A							
σd'	5	5	4	10	4	9	20
σd"	9	6	9	6	9	10	5
σtot	14	11	13	16	13	19	25
σr / SF	43						

SF = safety factor = 4.5

σd' = flexural stress due to local loads (impact pressure) acting on the cross-deck bottom panel

σd'' = flexural stress due to global loads (maximum transversal bending moment) acting on the cross-deck/main hull connection structure

σt= σd' + σd''

σr = ultimate tensile stress of the considered laminate

In Table 8 flexural stress values relative to reference local and global loads acting on the cross-deck for the considered hull configurations are reported.

Obtained results point out that hull scantlings are significantly affected by local loads; transversal bending moment is very important for cross deck scantlings and significantly influenced by clearance.

2.7 Hull weight assessment

The bare hull weight calculation has been carried out for the four examined hull configurations.
Reported values show a sensible variation of the total trimaran hull weight depending on outriggers longitudinal and transversal position (Table 9). For a given clearance (0.10), maximum weight difference is achieved when side hulls are shifted from after (stagger +0.25) to forward position (stagger –0.1) due to the strong increase of local impact loads acting on both outriggers and cross deck bottom; the difference reaches about 7.5%. Outrigger transversal position also seems to affect the total hull weight: for stagger –0.1, shifting the outriggers from the lower to the higher clearance, a total weight difference of about 1.8 t (5.4% of the lowest hull weight value) is reached.

Table 9: Trimaran hull weight components and total weight for different values of stagger and clearance.

	clearance 0.10			clearance max
	stagger +0.25	stagger 0	stagger -0.1	stagger -0.1
Hull plating weight (t)	19.27	20.1	21.03	22.26
Bulkheads plating weight (t)	1.22	1.22	1.19	1.19
Hull stiffeners weight (t)	10.04	10.25	10.64	11.22
Bulkheads stiffeners weight (t)	0.55	0.55	0.55	0.55
Total plating weight(t)	20.49	21.32	22.22	23.45
Total stiffeners weight (t)	10.59	10.8	11.19	11.77
Total weight (t)	31.08	32.12	33.41	35.22

3. Hull configuration comparison

3.1 Performances evaluation

Trimaran ship power requirements can be evaluated from calculated hull weights and from available hydrodynamic data. It must be noticed that for a given value of clearance, tank tests showed that the best trimaran performances can be achieved for stagger –0.1 due to the very low interference factor. On the other hand the scantlings evaluation procedure points out the stagger +0.25 as the best configuration leading to the lowest hull weight value.

Power requirements evaluation procedure has been realized through the following steps:

a) for each hull configuration the total displacement has been calculated as a sum of bare hull weight and of other weight components (considered independent from stagger and clearance); the results are reported in the following Table 10;
b) the relative wetted surfaces have been evaluated;
c) residual resistance coefficient as well as frictional resistance coefficient for a 129 t ship displacement have been obtained from tank tests results;
d) from these values, residual and frictional resistances as well as effective power requirements have been assessed for each hull configuration using interference factors given by tank tests.

From the analysis of the obtained results, reported in Table 11, it is possible to notice that the best power performance is achieved for stagger –0.1 and maximum allowed clearance, i.e. for the heaviest hull configuration. This result allows to conclude that interference phenomenon seems to have a primary influence on trimaran power requirements, overcoming weight increases consequent to the different outrigger longitudinal and transversal positions.

Table 10: Ship displacement for different hull configurations.

	clearance 0.10			clearance max
	stagger +0.25	stagger 0	stagger -0.1	stagger -0.1
Δ (t)	129.85	130.87	132.17	133.98

Table 11: Effective power requirements for the operative Fn.

	clearance 0.10			clearance max
Fn = 0.81	stagger +0.25	stagger 0	stagger -0.1	stagger -0.1
Total non-interference resistance Rt* (N)	105351	106496	107333	108319
Interference factor (*)	8.9	3.0	2.0	-1.85
Total resistance Rt (N)	114727	109691	109480	106315
Effective power values (kW)	1998	1911	1907	1852

(*) Interference factor I given as (Rt - Rt)/ Rt* x 100*

3.2 - Ranking hull configurations

The best hull configuration can be identified and the different staggers and clearances can be ranked considering Effective power P(kW) and Displacement Δ(t) as design attributes. No attribute preference is considered, that means effective power and displacement are equally important.

The values of the attributes have been normalised to make them commensurate. Here, normalisation is done as:

$$\Delta' = (\Delta - \Delta_{min})/\Delta_{min}$$

$$P' = (P - P_{min})/P_{min}$$

where (‘) indicates the normalised values.

Designs are ranked according to minimum Euclid distance from the ideal point of the considered attributes, defined as

$$(\Delta'^2 + P'^2)^{0.5}$$

Table 12: Attribute values

	clearance 0.10			clearance max
	stagger +0.25	stagger 0	stagger -0.1	stagger -0.1
Δ (t)	129.85	130.87	132.17	133.98
P (kW)	1998	1911	1907	1852

	normalized values			
$\Delta' = (\Delta - \Delta_{min})/\Delta_{min}$	0.000	0.008	0.018	0.032
$P' = (P - P_{min})/P_{min}$	0.079	0.032	0.030	0.000
	distance from ideal point			
$(\Delta'^2 + P'^2)/^{0.5}$	0.079	0.033	0.035	0.032

In Fig. 12 the attribute values of the considered hull configurations are shown. In Table 12 the attribute values, the normalised attribute values and the minimum distance values are reported.

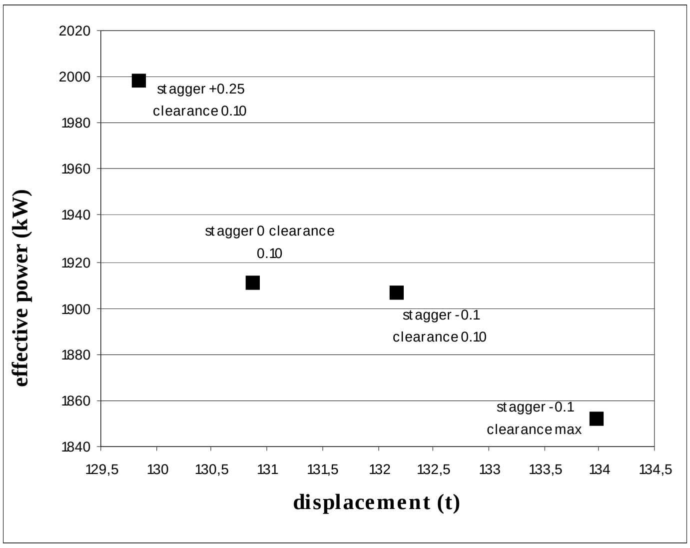

Fig. 12: Effective power versus Displacement for the considered hull configurations.

4 Conclusions

From the reported results it is possible to appreciate the influence of outrigger longitudinal positions on the global and local loads applied to a small size trimaran hull. The effects of this factor on the structure weight and on the ship displacement seems not negligible although less important than stagger influence on hydrodynamic characteristics. The effect of clearance has been identified; also in this case hydrodynamic benefits of larger clearance clearly overcome the consequent small increase in the structure weight.

Multiattribute procedure is apt to consider these factors. Although in this case it has been used only to rank existing hull configurations, it can be effectively used to develop optimal design proposal. To this aim and to get the whole picture about trimaran hull performances further researches to take into account also stability and seakeeping attributes seems necessary.

Acknowledgments

This work has been financially supported by University of Naples “Federico II” within the frame of 2000-2001 research program.

References

BERTORELLO, C.; BRUZZONE, D.; CASSELLA, P.; ZOTTI, I. (2001), Experimental Performance Investigation on different High Speed Crafts: Monohull Catamaran and Trimaran, HIPER 2001, Hamburg, Germany, pp.107-114

BERTORELLO, C.(2001), Design Trends of a Small Size Fast Passenger Ferries, Hiper 2001, Hamburg, Germany, pp.79-91

BRIZZOLARA, S.; RIZZUTO, E. (2001), Global Wave Loads for a Trimaran Ship, FAST 2001, Southampton,UK, pp.191-202

BEGOVIC, E.; BERTORELLO, C.; BUZZONE, D.; CASSELLA, P.; ZOTTI, I. (2001), High Speed Trimarans Validation of Numerical Results by Geosim Tests, FAST 2001, Southampton, UK, pp.191-202

GRUBISIC, I.; BEGOVIC, E. (2001), Multi-attribute Concept Design Model of the Adriatic Type of Fishing Vessel, BRODOGRADNJA, Vol 49, 2001, No 1, pp.39-54

MIGALI, A.; MIRANDA, S.; PENSA, C. (2001), Experimental Study on the Efficiency of Trimaran Configuration for High-Speed Very Large Ships, FAST 2001 Southampton, UK, pp.109-113

BERTORELLO, C. (2000), Trimaran Hull Performances for Fast Passengers Ferries, Proc. of NAV 2000, Venezia, p.2.4.1

BEGOVIC, E.; MIGALI, A.; PENSA, C. (2000), Experimental Study on The Resistance of a Trimaran Hull Configuration, NAV 2000, Venezia, Italy

MIZINE, I.; THORPE, R. (2000), High Speed Slender Monohull-Trimaran: Optimised Chain of Efficiency, IMAM 2000, Vol 2, p.H26

BEGOVIC, E. (1999), Trimaran Ships – General Review, Dipartimento di Ingegneria Navale, Internal Report, Napoli, Italy, 1999

ACKERS, B.B.; MICHAEL, T.J.; TREDENNICK, O.W; LANDEN, H.C. (1997), An Investigation of the Resistance Characteristics of Powered Trimaran Side-Hull Configurations, Conf. SNAME TRANSACTION, Vol 5, 1997, pp.349-373

GRUBISIC, I.; ZANIC, V.; BEGOVIC, E. (1997), Concept Design Model of an Outrigger Trimaran Ferry, IMAM 1997, Istanbul, Turkey, pp. 5.1-17-5.1-26

On The Effect of Viscous Forces on the Motions of High Speed Hulls

Ermina Begovic[1], G. Boccadamo[1], I. Zotti[2]

1 Univ. of Naples Federico II, begovic@unina.it, boccadam@unina.it
2 Univ. of Trieste, zotti@univ.trieste.it

Abstract

For fast slender hullforms, the damping forces due to generated waves are so small that the damping forces relative to viscosity cannot be neglected in evaluating the vertical motions.
In this paper the numerical and experimental assessments of the vertical motions in head sea for three monohulls are presented. The considered hulls are fast slender displacement type with transom stern and L/B ratios 14, 12, 8. The most slender hull is a trimaran main hull, the second one is a catamaran demihull and the last one is the Model 5 (Blok and Beukelman, 1984). The calculations were performed using 2 ½ D high speed theory by Faltinsen and Zhao (1991). To obtained potential flow theory results the viscosity correction from the cross flow was added. The effect of the viscosity from cross flow was considered as reported by Lee (1977), Chan (1992), Centeno (2000). At the Trieste towing tank experimental program was conducted for the catamaran demihull and the trimaran main hull for four different speeds while for the Model 5 experimental data were collected from the literature.
The effect of cross flow coefficients is evaluated and discussed, and empirical coefficients are set. Furthermore, the influence of slenderness ratio and ship speed is discussed and finally some conclusions are given.

1. Introduction

The assessment of seakeeping characteristics of fast marine vehicles is important for several aspects of the design. Structure, plants, and layout of the vessel in general and in particular of the passenger accommodation areas are strongly influenced by the results of calculation performed on seakeeping characteristics. Optimisation of the vessel for motion response is done at the design stage and usually by means of prediction software and model tests. Model tests are neither simple or cheap and at an early stage designers depend mostly on computer software. Most of the software used are based on 2-D strip theory with some corrections, to take into account the forward speed. Although they have proved to be useful when dealing with ship operating at low speed and high frequency, as speed increases, the classic strip theory is stretched beyond its limits and gives unreliable predictions of motions. In the 3-D theories interaction along the hull is taken into account while the speed could be taken or as a correction factor or could be implemented in the mathematical model (i.e. translating pulsating source method) depending how the free surface and body boundary conditions are satisfied. The former leads to a better prediction especially for the loads prediction but is very time consuming.
One of the hybrid methods developed for the taking into account the interaction along the hull is the 2½ D high speed theory by Faltinsen and Zhao (1991) which has been used in this work.
When dealing with high speed vessels, for both monohulls and multihulls, the slenderness of hull is becoming significant in order to obtain better resistance characteristics. From the seakeeping point of view, the damping forces of slender or very slender hull due to generated waves are so small that the damping forces relative to viscosity cannot be neglected, either in evaluating the vertical motions. To overcome this problem, Lee (1977), Chan (1992, 1993, 1995), Schellin (1995), Centeno (2000) used the cross flow approach as Thwaites (1960) described for the aeroprofiles.
In this work, the hydrodynamic coefficients from potential flow were determined by 2 ½ D high speed theory as implemented in VERES software. The numerical code TRIM was developed for calculating viscous lift and viscous drag coefficients and adding them to the coefficients calculated by potential

theory. Then the motions were recalculated in iterative way until reasonable convergence was obtained.

2. Theory Overview

We consider the ship as a rigid body travelling at the constant forward speed *U*. Furthermore, we assume that the rigid body will oscillate harmonically in time with six degrees of freedom with the complex amplitudes: η_j (j=1, 2..., 6), where j=1, 2..., 6 refer to surge, sway, heave, roll, pitch and yaw respectively, as shown in the *Fig.1*. We can write the motion equations as:

$$\sum_{k=1}^{6}\left(\left(M_{jk}+A_{jk}\right)\cdot\ddot{\eta}_k+B_{jk}\cdot\dot{\eta}_k+C_{jk}\cdot\eta_k\right)= F_j^W+F_j^V \qquad (1)$$

where $\ddot{\eta}_k$ and $\dot{\eta}_k$ are motion acceleration and velocity respectively. M_{jk} is the mass matrix; A_{jk} is the added mass; B_{jk} is the damping; C_{jk} is the restoring coefficients; F_j^W is the wave-exciting force (moment is understood hereafter) and F_j^V is the viscous excitation force. The indexes *j* and *k* indicate the direction of the fluid force and the mode of motion respectively.

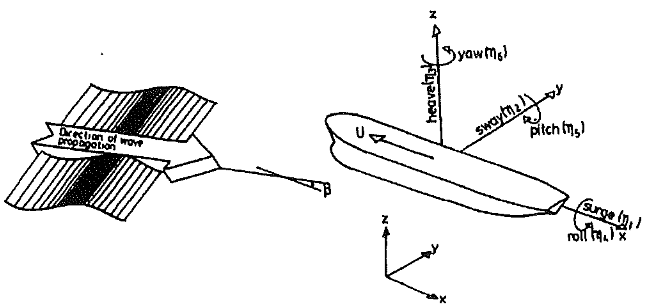

Figure 1.Motions, VERES User's Manual

Considering regular seaway, i.e. sinusoidal waves of small amplitude, wavelength λ and frequency ω, we can write:

$$\xi = \xi_0\, e^{i\varpi_E t}$$

$$\xi_0 = \xi_a\, e^{-ik(x\cos\beta + y\sin\beta)} \qquad (2)$$

where:
ξ_0 – complex wave amplitude
ξ_a – incident wave amplitude
k – wave number = ω^2/g
ω_E – wave encounter frequency = $\omega + kU\cos\beta$
β – angle of incidence with x-axis (0^0 at head seas)

In mathematical model used for the hydrodynamic problem of a ship advancing with constant forward speed a very important simplification has been done using linearisation. This means that the small amplitude incident waves will produce small amplitude ship motions. It also means that every linear operator could be considered as the linear combination of linear terms and gives us the possibility to consider hydrodynamic problem of body moving in the regular waves as two separate sub-problems:

- Diffraction problem - the body subjected to incident waves is restrained to oscillate and experiences wave excitation loads F_j^W, which consist of Froude-Krylov forces and diffraction forces.

- Radiation problem - when the body is oscillating in any of rigid body motion mode but without presence of incident waves, the hydrodynamic loads on the body are called reactive hydrodynamic forces and are composed from added mass A_{jk} and damping B_{jk}.

Formulation of fluid flow caused by the presence of the body is simplified by means of velocity potential. We assume incompressible, inviscous fluid (i.e. ideal fluid assumption) and irrotational flow and mathematically from these two assumptions follows that velocity potential has to satisfy Laplace's equation given by

$$\frac{\partial^2\phi}{\partial x^2}+\frac{\partial^2\phi}{\partial y^2}+\frac{\partial^2\phi}{\partial z^2}= 0 \tag{3}$$

At this point, the problem of finding velocity potential of irrotational and ideal fluid motions consists of the solution of the Laplace's equation with the relevant boundary conditions on the fluid which are:

- linearised free surface condition:

$$\left(i\omega_e+U\frac{\partial}{\partial x}\right)^2\phi+g\frac{\partial\phi}{\partial z}=0 \quad \text{on } z=0 \tag{4}$$

- linearised body boundary condition:

$$\frac{\partial\phi}{\partial n}=\vec{V}\bullet\vec{n} \qquad \text{on mean body surface} \tag{5}$$

- sea bed condition:

$$\frac{\partial\phi}{\partial n}=0 \qquad \text{at } z\rightarrow-\infty \tag{6}$$

and a suitable radiation condition at far field.

Again using the principles of linear theory, the total velocity potential ϕ can be separate into steady potential $\overline{\phi}$ and unsteady potential $\widetilde{\phi}$. Unsteady potential can be further separated into components due to the incident waves, diffraction waves and radiation waves.

$$\phi(x,y,z,t)=\left[Ux+\overline{\phi}(x,y,z)+\widetilde{\phi}(x,y,z,t)\right]e^{i\varpi_e t} \tag{7}$$

$$\widetilde{\phi}(x,y,z,t)=\phi_I+\phi_D+\sum_{j=1}^{6}\eta_j\phi_j \tag{8}$$

where:

ϕ_I – incident wave potential defined as $\phi_I=\frac{ig\zeta_a}{\varpi}e^{kz}e^{-ik(x\cos\beta+y\sin\beta)}$

ϕ_D – diffraction wave potential

η_j – complex amplitude of j-th mode of body motion

ω_e – encounter frequency

Of these components the most difficult to evaluate are the radiation and diffraction potentials and in fact different methods are treating this problem in different manner, while beginning is the same for all of them. It could be solved just for 2D case, making assumption of no interaction between ship sections, as in the strip theory, using conformal mapping or Frank close fit methods for the determination of unknown potential. It could be treated in 3D using panel methods or as 2½ D using high speed theory as here will be shortly described.

2.1. 2 ½ D high speed theory

The high speed formulation, Faltinsen and Zhao (1991) is based on a strip theory approach, Salvesen et al (1970), where the free surface condition is used to step the solution in the downstream direction. The solution is started assuming that both the velocity potential and its x derivate are zero at the first step, counted from the bow. In the solution procedure, the radiation and diffraction potentials are rewritten as:

$$\phi = e^{-i(\varpi_e/U)x}\,\Psi(x,y,z) \tag{9}$$

The following boundary conditions have to be satisfied at each cross section for Ψ where the conditions holds for both radiation and diffraction:

- Laplace'e equation:

$$\frac{\partial^2\Psi}{\partial y^2}+\frac{\partial^2\Psi}{\partial z^2} = 0 \tag{10}$$

- Free surface condition:

$$U^2\frac{\partial^2\Psi}{\partial x^2}+g\frac{\partial\Psi}{\partial z}=0 \quad \text{on } z=0 \tag{11}$$

This free surface condition differs from the ordinary strip theory formulation because the terms proportional to U^2 are retained, while they are neglected in the ordinary strip theory. Therefore in the strip theory if the velocity of advance is not zero or small enough, or if the frequency of encounter is very small as in the case of following sea, the results are strongly influenced by neglecting this member in the free surface condition.

- Body boundary condition:

$$\frac{\partial\Psi}{\partial n}=i\omega_e n_j - Um_j \qquad j=2,...6 \tag{12}$$

$$\frac{\partial\Psi_D}{\partial n}=(in_x-n_z)\omega\zeta_a e^{kz+i(\omega/U)x-iky\sin\beta} \tag{13}$$

- the potentials and their x derivates are set to zero at the foremost part of the vessel:

$$\Psi=0$$

$$\frac{\partial\Psi}{\partial x}=0 \qquad \text{on } x=x_B \tag{14}$$

where x_B denotes the first strip. This solution procedure assumes that are no upstream waves. When the radiation potentials Ψ_j and the diffraction potential Ψ_D are solved for each strip, the total solution can be found by applying (9) and integrating over the wetted surface.

3. Viscous Effects From Cross Flow

For the vertical motion prediction of conventional ship types (vertical walls, slow speed hulls) where the wave damping is the predominant damping mechanism, hydrodynamic coefficients obtained by potential theory have been found satisfactory. When the slenderness is increasing, the ship does not produce large surface waves in vertical oscillations, so wave-damping is not predominant in overall damping and viscous effects of fluid have to be taken into account for all modes of motion. The first attempt to include effects from viscous damping in prediction of ship motions has been done by Lee and Curphey (1977) for the SWATH vessels. Within the frame of linear theory, they formulated hydrodynamic coefficients in the motion equations as the sum of 3 parts calculated independently as:

- the first part is obtained under potential flow assumption using strip theory approach
- the second part is associated with viscous damping - obtained by the empirical method derived from cross-flow approach to a slender body at a moderate angle of incidence in uniform flow
- the third part is associated with the stabilizing fins

This approach was applied by Chan (1992, 1993), Fang et al (1995), Centeno et al (2000) considering only coefficients from the cross flow, while Schellin and Rathje (1995) have taken into account also the influence of stabilizing fins.

3.1. Mathematical model of cross flow forces

According to Thwaites (1960) for a harmonically oscillating body at the constant forward speed U in regular waves, the fluid force due to the viscous effects, viscous lift and cross-flow drag, could be written as:

$$F_J = \frac{1}{2}\rho A_J \left(U^2 \alpha\alpha_J(x) + C_D v_J(x)\left|v_J(x)\right|\right) \text{ for J = 1,2,3} \tag{15}$$

where
A_J - projected plane area of the body in the j-th direction
α - viscous lift coefficient
α_J - angle of attack to uniform flow
C_D - viscous drag coefficient
v_J - relative fluid velocity with respect to the body in the j-th direction

The coefficients α and C_D depend on the geometrical characteristics of the body, the mode of motion and the frequency of oscillation. They should be determined experimentally and the values we are using derive from the experiments on airship models with circular or polygonal sections. According to Lee and Curphey (1977) α is about 0.07 and C_D from 0.4 to 0.7.

Relative fluid velocity with respect to a slender body can be expressed as:

$$v_2 = -\left(\dot{\eta}_2 + x\dot{\eta}_6 - z\dot{\eta}_4 + U\eta_6\right) + w_y$$

$$v_3 = -\left(\dot{\eta}_3 - x\dot{\eta}_5 + y\dot{\eta}_4 - U\eta_5\right) + w_z \tag{16}$$

where:
x, y, z - coordinates of the considered point P(x, 0, $-T^*$)
T^* - mean immersion of cross section = A_{IMM} / b(x)
w_y –horizontal fluid velocity induced by the incoming wave, $w_y = \dfrac{\partial\Phi}{\partial y}$
w_z – vertical fluid velocity induced by the incoming wave, $w_z = \dfrac{\partial\Phi}{\partial z}$
Φ – incoming wave potential
$\dot{\eta}_j$ - velocity of the ship in the j-th mode of motion

From the (16) the angle of incidence could be written as:

$$\alpha_1 = 0,\ \alpha_2 = \frac{v_2}{U},\ \alpha_3 = \frac{v_3}{U} \tag{17}$$

The term $v_J(x)|v_J(x)|$ in the (15) is nonlinear and cannot be introduced directly in the linear equations of motions. It can be shown by Fourier analysis that for any harmonic motion given by $x = x_a \cos \omega t$ could be introduced an approximation (equilinearization method):

$$\dot{x}\,|\dot{x}| \approx \frac{8}{3\pi}\omega x_a \dot{x} \tag{18}$$

Finally, using the (18), the strip theory and the assumption that no viscous interaction between sections is taken into account, the complex amplitude fluid force for one hull can be expressed as:

$$F_{O2} = \frac{1}{2}\rho \int_L U^2 \alpha \alpha_2(x) d(x) dx + \frac{1}{2}\rho \int_L \frac{8}{3\pi} C_D v_{O2}(x)|v_{O2}(x)| d(x) dx \tag{19}$$

$$F_{O3} = \frac{1}{2}\rho \int_L U^2 \alpha \alpha_3(x) b(x) dx + \frac{1}{2}\rho \int_L \frac{8}{3\pi} C_D v_{O3}(x)|v_{O3}(x)| b(x) dx \tag{20}$$

Moments contributed by the fluid forces for one hull can be written as:

$F_4 = -F_2 z + F_3 y$ in the P (x, 0, -T*) - i.e. remains only F_2 contribution

$$F_{O4} = \frac{1}{2}\rho \int_L U^2 \alpha \alpha_2(x) d(x) T^*(x) dx + \frac{1}{2}\rho \int_L \frac{8}{3\pi} C_D v_{O2}(x)|v_{O2}(x)| d(x) T^*(x) dx \tag{21}$$

$F_5 = -F_3 x + F_1 z$ - i.e. remains only F_3 contribution

$$F_{O5} = -\frac{1}{2}\rho \int_L U^2 \alpha \alpha_3(x) x b(x) dx - \frac{1}{2}\rho \int_L \frac{8}{3\pi} C_D v_{O3}(x)|v_{O3}(x)| x b(x)\, dx \tag{22}$$

$F_6 = -F_1 y + F_2 x$ - - i.e. remains only F_2 contribution

$$F_{O6} = \frac{1}{2}\rho \int_L U^2 \alpha \alpha_2(x) d(x) x\, dx + \frac{1}{2}\rho \int_L \frac{8}{3\pi} C_D v_{O2}(x)|v_{O2}(x)| d(x) x\, dx \tag{23}$$

where:
d(x) - draft at section x
b(x) - beam at section x
$v_{O2}(x)$, $v_{O3}(x)$ - complex amplitudes of relative fluid velocities
Substituing (16) into (19) to (23), the forces due to the viscous effects can be separated into viscous damping forces, viscous restoring forces and viscous excitation forces in the form:

$$F_j = \sum_{k=1}^{6}\left(b_{jk}\dot{\eta}_k + c_{jk}\eta_k\right) - F_j^V \tag{24}$$

where
$b_{jk}^{\;V}$ - sectional damping coefficient
$c_{jk}^{\;V}$ - sectional restoring coefficient
F_j^V - excitation force due to the viscous effects

In the case of multihull ships the forces are calculated for each hull and then summed up assuming that the interference between hulls is negligible because of high speed.
It should be noted that the coefficients α and C_D are assumed to be constant over the length of the ship. It is possible to consider separately influence of viscous lift and of viscous drag because the

viscous lift forces are linear, damping and restoring coefficients are not frequency dependent, while the drag ones are quadratic, and frequency and amplitude dependent.
In this manner the method for solving motion equations is an iterative procedure, which in the first step calculates the ship motions only due to the potential flow and viscous lift from the cross flow. In the second step the viscous forces are calculated for the viscous drag. The procedure for viscous drag is repeated until reasonable difference between two consecutive iterations is obtained.

4. Experimental Results

Even if our numerical program TRIM is done both for multihulls and monohulls, in this stage of research we prefered to consider only monohulls. We wanted to have very slender, displacement type hulls, but with significant L/B variation. Therefore we choose the trimaran main hull designed as the 4797 model of 64 Systematic Series (Bertorello et al. 2001) and the demihull of a catamaran operating in Bay of Naples (Bertorello et al. 2001). The third considered model is very well known Model 5 by Blok and Beukelman (1984), tested later also by Keuning (1990) and used by Faltinsen (1991, 1993) as the test case. Data elaboration is from Begovic and Chan (2001). The L/B values are: 14,12 and 8 respectively. The body plans are shown in the Fig. 2,3,4, while in the Table 1 the main dimensions are summarized.
The seakeeping tests were performed at towing tank of University of Trieste. The tank dimensions are: 50 x 3.1 x 1.7 meters. The wave generator is plunger type, producing regular waves ranging from 0.7 to 5.5m of wavelength, and up to 0.22m of waveheight. The models were built in GRP, were towed at the point at the deck, free to heave and pitch and constrained to other motions. The turbulence was not stimulated. The tests were performed for five frequencies and four speeds.

Table 1: Models Main Dimensions

	MH 64 - 4797	CAT 915 - VM	MODEL 5
L_{WL}	1.805	1.38	5.0
B	0.128	0.103	0.625
T	0.064	0.059	0.1562
C_B	0.45	0.451	0.396
R_{55}	0.28 L_{WL}	0.30 L_{WL}	0.25 L_{WL}
$X_{TOW.\ POINT}$	0.419	0.345	CG
$Z_{TOW.\ POINT}$	deck	deck	0.169m ab. BL
h / λ	1/100	1/80	2/100

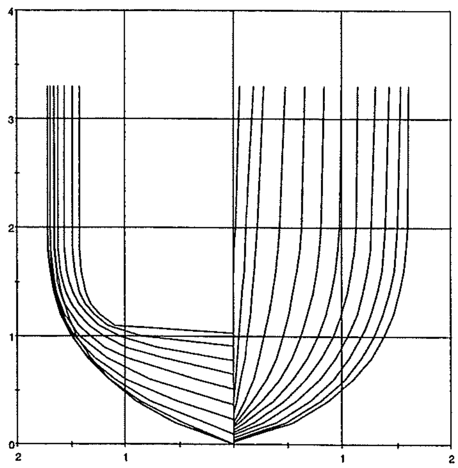

Fig.2: Body Plan of Model 4797

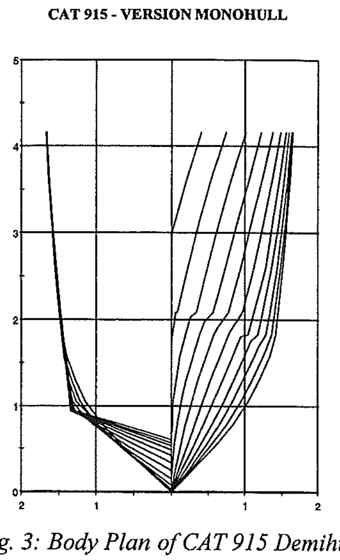

Fig. 3: Body Plan of CAT 915 Demihull

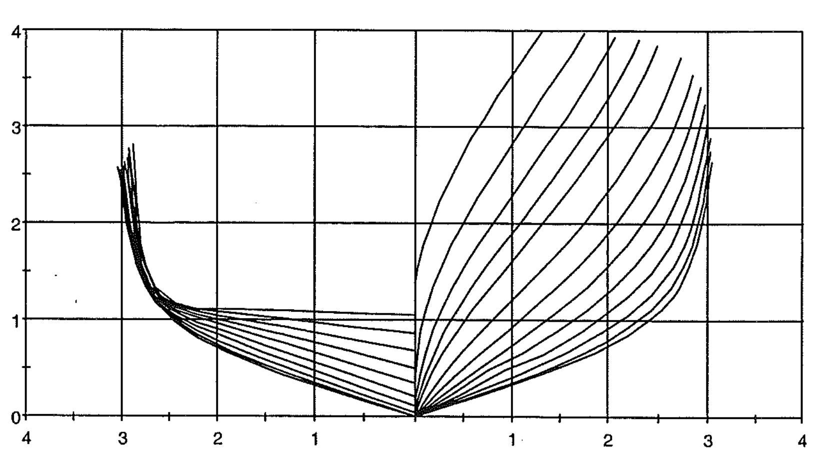

Fig. 4: Body Plan of Blok and Beukelman Model 5

5. Comparison of Numerical and Theoretical Results

5.1 Main hull S64 - 4797

The calculations were performed with: α=0.0, C_D=0.0 (i.e. VERES prediction)- POT, α=0.07, C_D=0.0 - LIFT, α=0.07, C_D=0.5 - DRAG, α=0.0, C_D=0.5 and α=0.035, C_D=0.25 as marked in the diagrams. For the heave prediction at F_N=0.496, we used the 2 ½ D high speed theory even if it is a lower limit of applicability of the theory. All the results are quite close to those obtained from the experiments in the higher frequency range, but the POT gives 2nd peak which is avoided using the cross flow correction. It should be noted that the experimental results seem to have a peak at very low frequency, what neither of theory predicts. Pitch prediction at the same F_N is somewhat better. With only lift the results are overpredicted, while with the proposed values of α and C_D (0.07 and 0.5)- DRAG, the results are underestimated. In this case other authors like Fang et al (1995), Ceteno (2000) modified only the viscous drag coefficient to value 0.01, but we tried with the intermediate values for both coefficients: α=0.035, C_D=0.25 and limit case α=0.0, C_D=0.5.
Heave prediction at F_N=0.704 could be considered very satisfying in the cases: only lift, only drag and α=0.035, C_D=0.25, while POT overestimates and DRAG underestimates the experiments. It is the same behaviour for the F_N=0.882 and F_N=0.942 but having more pronounced differences for the POT and DRAG predictions. Pitch prediction at F_N=0.704 is the best matched only with the lift coefficient

α=0.07. From the trend of experimental results we can assume that the peak in η_5 is between ω_e = 1.8 and 2.4 and seems that all the calculations underestimate experimental data. At the F_N=0.882 and 0.942, the first experimental point is close to the VERES prediction and the peak seem to be higher than predicted by TRIM in all cases.

5.2. CAT 915 - VM

The calculations were performed with: α=0.0, C_D=0.0 (i.e. VERES prediction)- POT, α=0.07, C_D=0.0 - LIFT, α=0.0, C_D=0.5 and α=0.035, C_D=0.25 as marked in the diagrams. As it has been seen that the performed calculations fit well the experiments, the calculation with α=0.07, C_D=0.5 - DRAG, has been avoided.
For the heave motions, the prediction for the F_N=0.498 is overpredicted in the afterpeak region by all calculations, while the beggining is very well matched by all of them. For the higher F_N (0.693, 0.902, 1.005) is possible to notice the same trend of the different calculations. The experimental results are between the POT and LIFT. As the F_N increases, the results are moving closer to LIFT. When considering the pitch motion at F_N = 0.498 and 0.693, the experimental results are perfectly fitted by LIFT. At the two higher speeds, calculation with LIFT prediction is always the best one, but the first experimental point is underestimated. Motion predictions by two others calculations are fair, but not as good as LIFT.

5.3. Blok and Beukelman MODEL 5

The calculations were performed with: α=0.0, C_D=0.0 (i.e. VERES prediction)- POT, α=0.07, C_D=0.0 - LIFT, α=0.07, C_D=0.5 - DRAG, α=0.0, C_D=0.5 and α=0.035, C_D=0.25
Heave at F_N=0.57 is perfectly matched with the LIFT and α=0.035, C_D=0.25 in the higher frequency range, while the first part is a little bit overpredicted and shifted by all calculations. At the F_N=1.14 the prediction with DRAG is perfect. Regarding the pitch, at F_N=0.57, again the DRAG is the best in the first part, while higher frequency range is overpredicted by all calculations. At the F_N=1.14 there do not exist large differences between various calculations, but the results obtained by the calculation with α=0.035, C_D=0.25 can be considered the best one.

5.4. Sensibility Analysis of Cross Flow Coefficients

The sensibility analysis of the cross flow coefficients was done by performing the calculations for the cases: α = 0.0 and C_D = 0.0 (coincide with the potential flow), α = 0.07 and C_D = 0.0 (only linear correction to potential flow), α = 0.07 and C_D = 0.5 (linear and quadratic correction to potential flow), α=0.035, C_D=0.25 (linear and quadratic correction to potential flow), α=0.0, C_D=0.5 (only quadratic correction to potential flow) at the speeds: F_N=0.5, 0.7, 0.9 and 0.95 for the S64 - 4797 model.
There is no large difference in motion prediction using the only lift, only drag or α=0.035, C_D=0.25. This conclusion is consistent for all the considered velocities and in the other words, it could means that the proposed values for α and C_D are too high. It could also means that for the so slender hull there is no influence of C_D as it was supposed by the Fang (1995) and Centeno (2000) putting the C_D values to 0.01.
At the lower speed the difference between all calculations is rather small, but as speed increasing the nonlinear and speed dependent C_D is starting to be important so differences are significant.
The calculation for the other two hulls repeated the trends of S64.

5.5. Effect of Ship Slenderness on Cross Flow Coefficients

In our test cases, DRAG prediction underestimates an experimental results in the cases of L/B=14 and 12. For the Model 5 (L/B=8) at F_N=1.14, DRAG prediction perfectly fitts the experimental data. It seems that as the slenderness decreases, the drag is becoming more important, i.e the value of C_D is increasing.

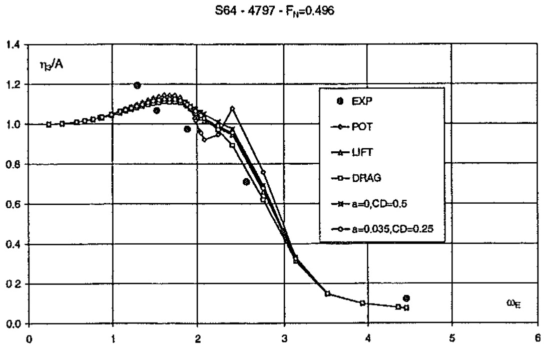

Fig. 5: Heave prediction at F_N=0.498

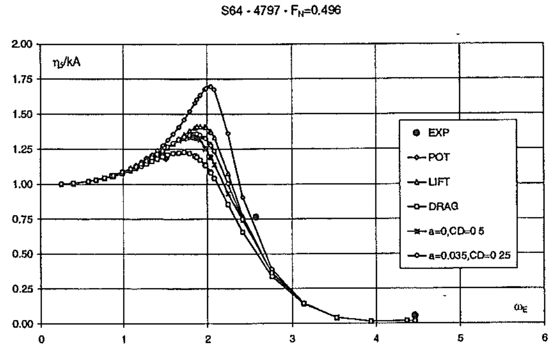

Fig. 6: Pitch prediction at F_N=0.498

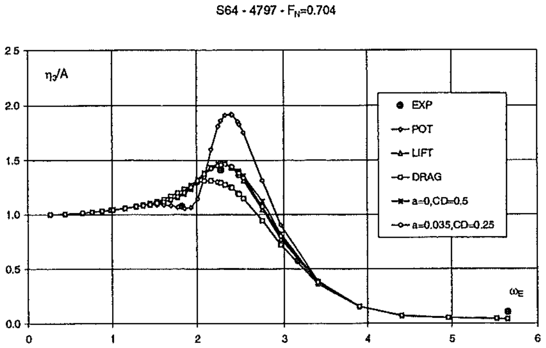

Fig. 7: Heave prediction at F_N=0.704

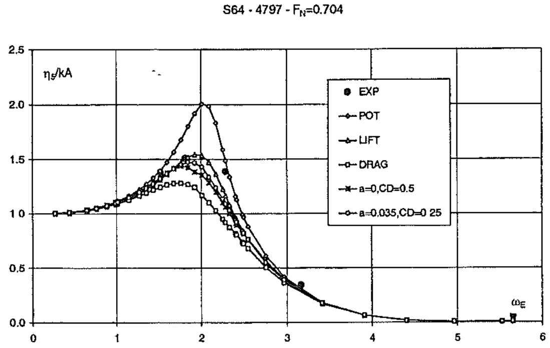

Fig. 8: Pitch prediction at F_N=0.704

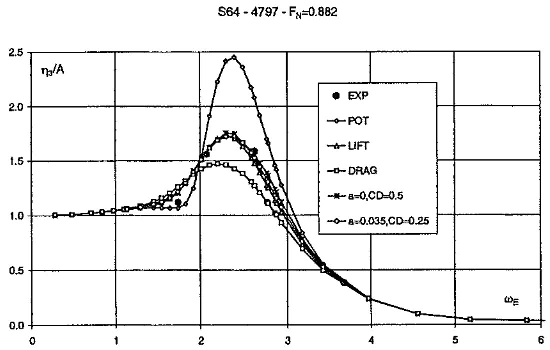

Fig. 9: Heave prediction at F_N=0.882

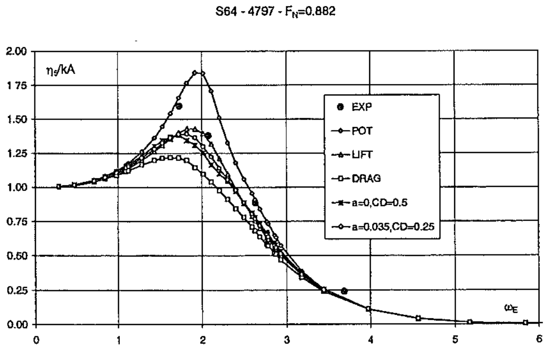

Fig. 10: Pitch prediction at F_N=0.882

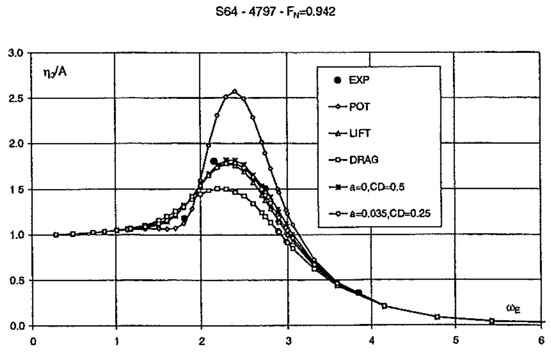

Fig. 11: Heave prediction at F_N=0.942

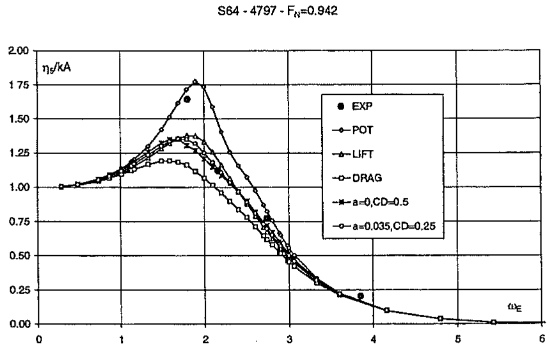

Fig. 12: Pitch prediction at F_N=0.942

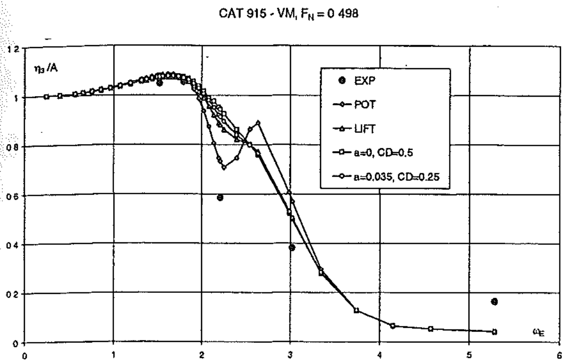

Fig. 13: Heave prediction at F_N=0.498

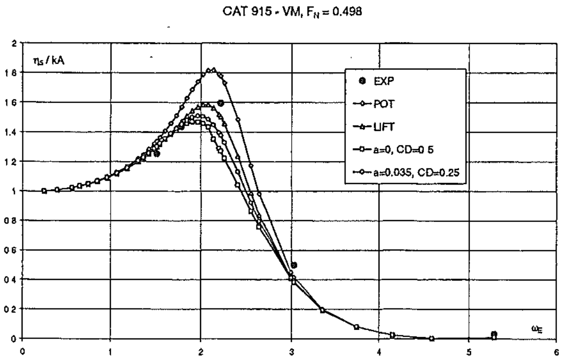

Fig. 14: Pitch prediction at F_N=0.498

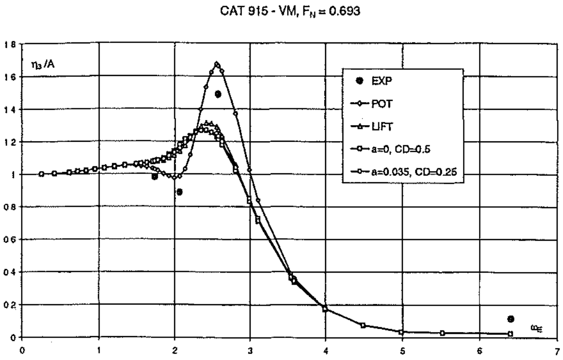

Fig. 15: Heave prediction at F_N=0.693

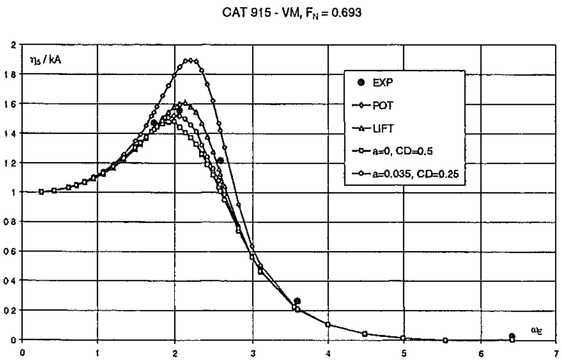

Fig. 16: Pitch prediction at F_N=0.693

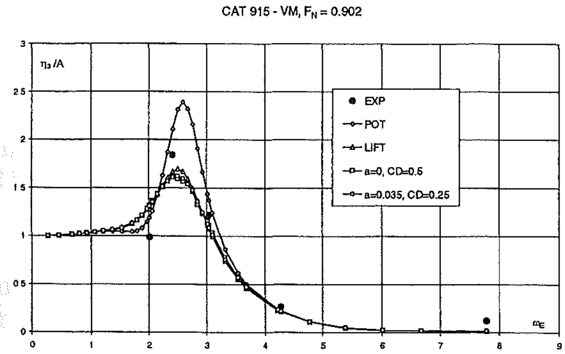

Fig. 17: Heave prediction at F_N=0.902

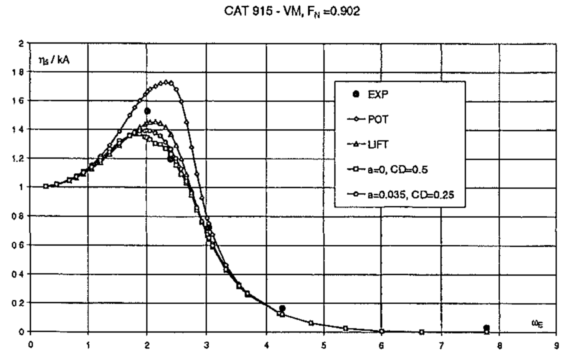

Fig. 18: Pitch prediction at F_N=0.902

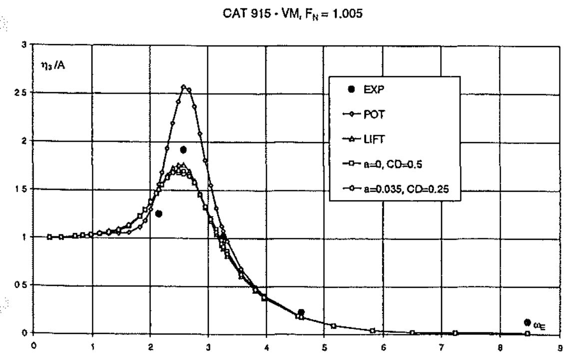

Fig. 19: Heave prediction at F_N=1.005

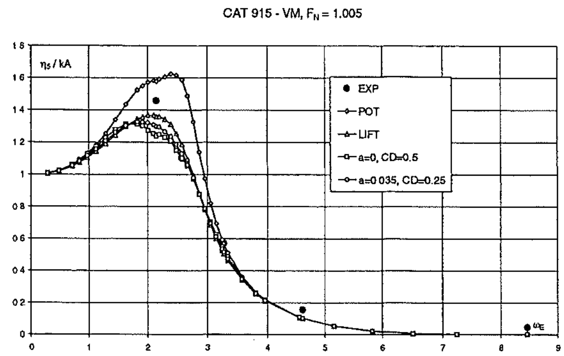

Fig. 20: Pitch prediction at F_N=1.005

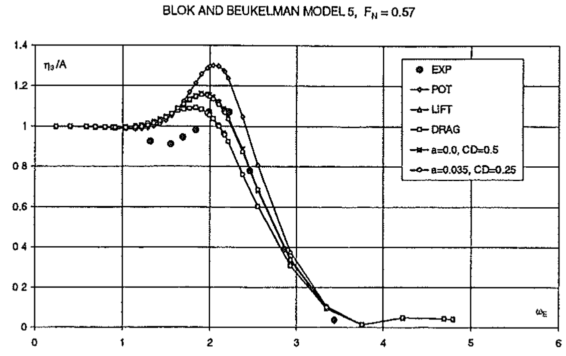

Fig. 21: Heave prediction at F_N=0.57

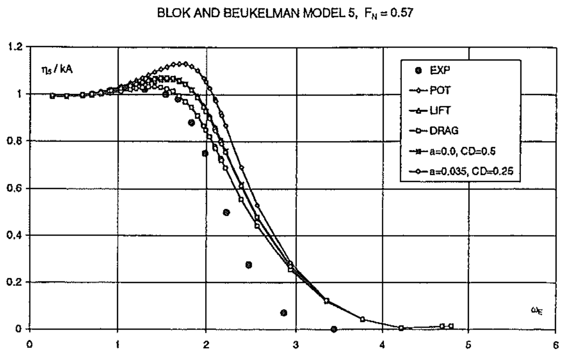

Fig. 22: Pitch prediction at F_N=0.57

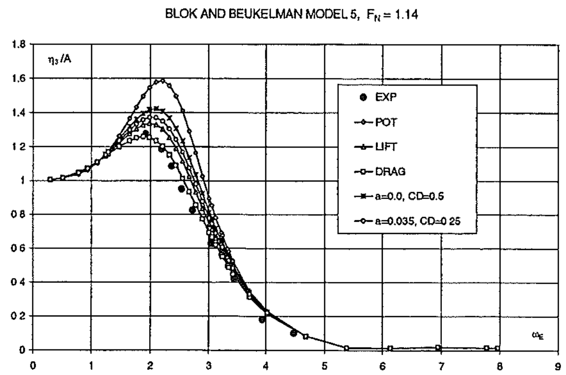

Fig. 23: Heave prediction at F_N=1.14

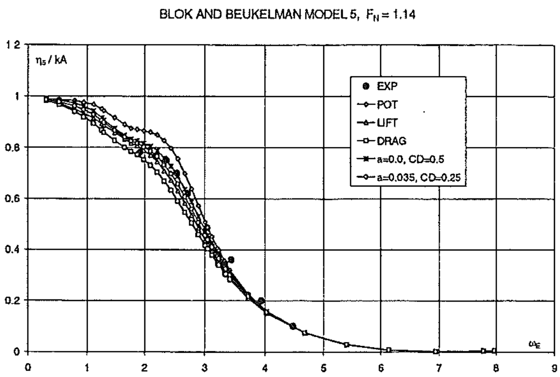

Fig. 24: Pitch prediction at F_N=1.14

6.Conclusions

- From all the calculations performed for three high speed monohulls, the prediction of vertical motions in head sea by the potential theory is overestimated. As the slenderness ratio of the considered hull increases, the motion prediction becomes more unrealistic.
- The value for the viscous lift coefficient α proposed by Thwaites and used also by other authors, seems to be too high. This could be explained considering that in this case the hull experiences non uniform flow, while the empirical coefficients were derived by Thwaites in uniform flow experiments.
- The results obtained from our calculations and experiments performed on the forementioned hulls suggest for α and C_D the values of: 0.035 and 0.25 respectively.
- From the results obtained, the trend of decreasing the viscous drag coefficient as the slenderness ratio increases was noticed.
- Velocity does not seem to influence the values of α and C_D.
- It should be noted that even with very different viscous coefficient values, the prediction obtained considering cross flow are always closer to experimental data than that one by the potential theory.

Acknowledgements

The work was financed by University of Naples "Federico II", research funds 2000 and MURST [Ministry of Scientific and Technological Research (PRIN 1999 funds)]

References

1. Begovic E., Chan H.S. (2001), *"Comparative Study on the Motion Prediction of high Speed Crafts Using Two Different Methods"*, Report No. MT-2001-028, Department of Marine Technology, University of Newcastle, UK, 2001.
2. Bertorello C., Bruzzone D., Cassella P., Zotti I. (2001), *"Experimental Performance Investigation on Different High Speed Craft: Monohull, Catamaran and Trimaran"*, 2nd International Conference on High-Performance Vehicles HYPER'01, Hamburg, 2001, pp.92-106
3. Blok J.J., Buekelman W. (1984), *"The High-Speed Displacement Ship Systematic Series Hull Forms - Seakeeping Characteristics"*, Trans. SNAME, Vol. 99, 1984, pp. 125-150
4. Centeno R., Fonseca N., Guedes Soares C. (2000), *"Prediction of Motions of Catamarans Accounting for Viscous Effects"*, Int. Shipbuilding Progress, Vol. 47, No.451, 2000, pp. 303-323
5. Chan H.S. (1993), *"Prediction of Motions and Wave Loads of Twin-Hull Ships"*, Marine Structures, Vol. 6, No.1, 1993
6. Chan H.S. (1993), *"Dynamic Structural Responses of a Monohull Vessels to Regular Waves"*, Int. Shipbuilding Progress, Vol. 39, No.419, 1992, pp.287-315
7. Couser P., Hudson D., Price W.G., Temarel P. (1995), *"Prediction of Hydrodynamic Loads and Motions of a High Speed Catamaran in Regular Waves"*, Proceeding of the 3rd International Symposium High Speed Marine Vehicles, Naples, 1995
8. Faltinsen O. (1993), *"On Seakeeping of Conventional and High Speed Vessels"* Journal of Ship Research, Vol 37, No.2, 1993, pp. 87-101
9. Faltinsen O., Zhao R. (1991), *"Numerical predictions of ship motions at high forward speed"* Phil. Trans. R. Soc. London, No. 334, 1991, pp.241-252
10. Keuning J.A. (1990), *"Distribution of Added Mass and Damping Along the Length of a Ship Model Moving at High Forward Speed"*, Int. Shipbuilding Progress, Vol. 37, pp. 123-150, 1990
11. Lee C.M., Curphey M.R. (1977), *"Prediction of Motion, Stability and Wave Load of Small-Waterplane-Area Twin-Hull-Ships"*, SNAME Transactions, Vol. 85, 1977, pp. 94-130
12. Lee C.M., Jones H.D., Curphey R.M. (1973), *"Prediction of Motion and Hydrodynamic Loads of Catamarans"*, Marine Technology, October, 1973, pp. 392-405
13. Salvesen N., Tuck E.O., Faltinsen O. (1970), *"Ship Motions and Sea Loads"*, Trans. of SNAME, Vol. 78, 1970, pp. 250-287
14. Schelin T.E., Rathje H. (1995), *"A Panel Method Applied to Hydrodynamic Analysis of Twin-Hull Ships"*, Proceedings of 3rd International Conference-FAST'95, Lübeck–Travemünde, Germany, 1995, pp.1017-1030
15. Thwaites B. (1960), *"Incompressible Aerodynamics"*, Oxford University Press, UK, 1960
16. MARINTEK - Sintef Group: *VERES Version 3.1 - User's Manual*, January 1998

High Speed Craft - Investigation on the Resistance Towing Test Procedure

Carlo Bertorello*, D. Bruzzone, P. Cassella*, I. Zotti*****

*Dept. of Naval Architecture and Marine Eng., Univ. of Naples Federico II, bertorel@unina.it
** Department of Naval Architecture and Marine Technology, University of Genoa
*** Department of Naval Architecture, Ocean and Environmental Engineering, Univ. of Trieste

Abstract

The paper deals with the resistance model test procedure for high speed displacement craft in the Froude number range 0.60-1.00. An experimental research was conducted on three geosim models of a monohull with the goal to examine the effects of the towing test procedure on the model-ship correlation. Within this work two key factors have been pointed out, that is the effect of the turbulence stimulation and of the towing force position on the model resistance.
As regards turbulence stimulation the present work concerns investigation on the use of different devices fitted to geosim models.
Resistance results relative to different size of geosims, with several types of turbulence stimulators have been analysed and compared according to Fn values.
The effect of the towing force adjustment, often strictly connected with the model dimensions, is the second considered factor. The direction of the towing force and its point of application can significantly influence the dynamic trim that is, for the considered hull forms, closely connected to the resistance values.
Resistance test results obtained with towing force different directions and application points have been also compared to evaluate the effect of these factors.
The results of this work are proposed as a reference for the test procedure and for model-ship correlation of high speed slender hull forms.

1. Introduction

As far as the power prediction of fast ships by model tests is concerned, some uncertainties still exist, which are due both to the towing tank procedure and to the model-ship correlation.
As it is well known, the flow on the ship in full scale is entirely turbulent. Therefore, for a correct frictional resistance comparison between model and ship, the laminar flow around the model must be avoided by the use of turbulence stimulators fitted at the forward region of the hull surface to assure turbulent flow on the whole surface that is abaft the used device. At the present time does not exist a definitive rule about the selection of the proper type and size of turbulence stimulator devices.
The problems involved have been considered by several researchers and different devices to perturb the flow have been proposed. The most commonly used are pins, trip wires and sand strips. Empirical standardized rules for dimension and position of the stimulators in the resistance model tests of the conventional ships have been established by practice in the towing tanks.
However, for a correct comparison among the resistance results of different geosim model sizes, the turbulent flow must be stimulated as near the bow profile as possible. The stimulator must be placed also in a region of model where it is effective. Moreover, the added resistance of the stimulator should be negligible or exactly known. Otherwise, the drag loss due to the laminar flow at the bow should be compensated by the parasitic drag of the stimulators.
The techniques generally applied by the towing tanks for the turbulence stimulation of model tested in low Froude number ranges could be ineffective, if adopted to high speed tests of slender hull forms, because of the bow up condition and/or the spray resistance due the stimulator.
Another important factor is the effect on the model resistance results of the position and direction of the towing force.

In order to give an indication on the best procedure for the high speed tests with different model sizes, an experimental research was jointly carried out on three geosims of a slender hull form at the Universities of Naples and Trieste.
The results of the resistance tests were analysed and verified according to the different model scale.
Form factors were determined by iso-Froude lines from geosim model tests. The mean value of the form factors 1+k(Fn) so obtained in the range Fn= 0,70-1,00 has been compared with those derived by Prohaska and Hughes methods through low speeds model tests carried out with transom emerged.

2. Experimental program

2.1 Hull form and experimental model tests

The investigated round bilge hull form (Fig. 1) was derived from series 64 with L/B = 14.070 and B/T = 2. This hull form is suitable for fast multihulls both catamaran and trimaran and it is representative of slender monohulls.

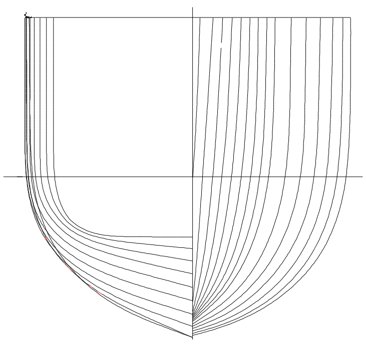

Fig. 1 Hullform body plan.

Length over all (m)	47.700
Length waterline	46.940
Beam waterline (m)	3.336
Draught (m)	1.668
Wetted surface (m^2)	194.8
Displacement (t)	120.489
Max speed (kn)	40
CB	0.45
L/B	14.070
B/T	2.000
Fn	0.958

Table 1. Main characteristics of the full scale ship

The main dimensions in full scale are given in Table1. They are relative to the main hull of a small trimaran fast ferry that has been already considered in previous works.
The experiments on three geosims (model scales 10, 20 and 26) were carried out at the towing tank of the University of Naples (m.140 x m. 9,00 x m.4,20) where all the models were tested and at the towing tank of University of Trieste (m.50 x m. 3,10 x m.1,60) where the smallest model was tested also.
The largest model was built in wood, while the smaller ones are in fibreglass to get adequately low weights and to avoid the use of counterweights in the resistance tests.
Model dimensions were chosen according to the considered ship cruising speed of 40 kn and by taking inTO account the maximum carriage speed and the blockage effect at the towing tanks.
In the standard procedure of the resistance model tests adopted by the towing tanks it is common practice that turbulence stimulators are applied for all the models of the conventional ships. For large models studs or trip wires are generally used, for small models sand strips or wires are frequently used.
The additional resistance due to the turbulence stimulators should be calculated and subtracted from the measured resistance.
However, generally no correction is made in model-ship correlation. This correction could be necessary for high speed craft, for which the projection of the turbulence devices could also cause a further additional resistance due to the spray effect.
Therefore, in order to verify the effect of turbulence stimulators in model-ship correlation of high speed craft, the geosim model tests were carried out in the Froude number range 0,60- 1,00 both with bare hull and with sand strips or trip wires as stimulators .A large number of experiments

was carried out, adopting one, two or three sand strips and changing diameter and longitudinal position of trip wires.
The position of the wires was chosen both to reduce as most possible the forward region of laminar flow and to have wire diameters comparable with the boundary LAMINARlayer thickness

$$\delta = 5.5x/R_{nx}^{0.5} \qquad (1)$$

at the position x from the leading edge, being $R_{nx} = xV/\nu$, the local Reynolds number at point x for model speed V.
The arrangements of the different stimulators relating to the three geosims are given in Table 2.

Table 2. Type and position of the different used stimulators.

Model scale	Stimulator	Position abaft FP
10	0.5 diam. trip wire	60 mm
	0.8 diam. trip wire	60 mm
	0.8 diam. trip wire	180 mm
	Sand single strip 6 mm wide	60 mm
	Sand double strip 6 mm wide	60 mm – 90 mm
20	0.5 diam. trip wire	30 mm
	0.8 diam. trip wire	30 mm
	0.8 diam. trip wire	90 mm
	Sand single strip 6 mm wide	30 mm
	Sand triple strip 6 mm wide	30 mm – 45 mm – 60 mm
26	0.3 diam. trip wire	23 mm
	0.4 diam. trip wire	23 mm
	0.5 diam. trip wire	23 mm

Fig. 2 shows for each model the projection of the used wire diameters outside (positive values) and inside (negative values) the boundary layer thickness. In any case this projection should avoid additional spray resistance.
For the model scale 10 the tests of the bare hull were also conducted considering three different towing positions: on the base line, on the main deck and on a intermediate height as the point of application of the towing force could have effect on the running trim and consequently on the resistance results.
Generally the model is towed by a point at a given height defined to the facilities and to the model testing techniques of the towing tanks, as it is no practical to exactly simulate the direction and the point of application of the thrust.
Moreover, it is not always possible to arrange the towing force at a given direction. The choice of this direction that should simulate the thrust direction is allowed only by some experimental set-up, while generally the direction of the towing force is horizontal.
On the other hand the facilities of some tanks impose the use of inclined direction for the towing force of slender small models, as the towing equipment cannot be contained inside the model.
Therefore, tests were also carried out with the smallest model towed by horizontal and inclined towing force, in order to ascertain the influence of the towing direction on the running trim and on the resistance.

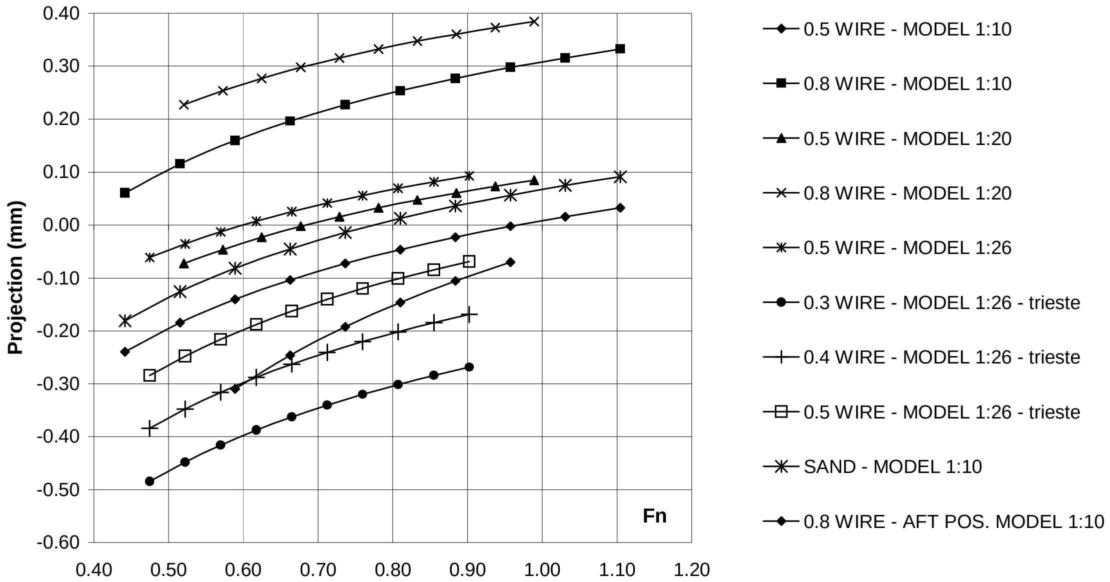

Fig. 2. Projection of the used wire diameters outside (positive values) and inside (negative values) the boundary layer thickness.

3. Analysis of Experiments

3.1 Towing force position

The effects of the towing force position on resistance and trim have been analysed by the results obtained with the bare hull tests relating to model scale 10, considering the three different above mentioned heights . In all cases the direction of the towing force was horizontal.
From the analysis of the results (Fig.3) we can deduce that this effect on the trim and consequently on the resistance, can be considered negligible, being the differences of the resistance due to the different positions in the order of 1 per cent in the considered Froude range Fn 0,60- 1,00.

3.2 Towing force direction

The usual practice in Naples and Trieste towing tanks is to tow models by an horizontal force. The 1:26 model when towed in Trieste University could not be arranged in this way due to towing equipment size. So that a force inclined 1° to the horizontal was used and the resulting force acting on the model was divided into vertical and horizontal components. The horizontal component values are very similar to the resistance values assessed at Naples towing tank where the same model was towed by an horizontal force, as reported in Fig. 4. This means that very small trim differences, also reported in the same Fig. 4, and due to the longitudinal moment given by the vertical component have no significant influence for the resistance evaluation of this hullform.

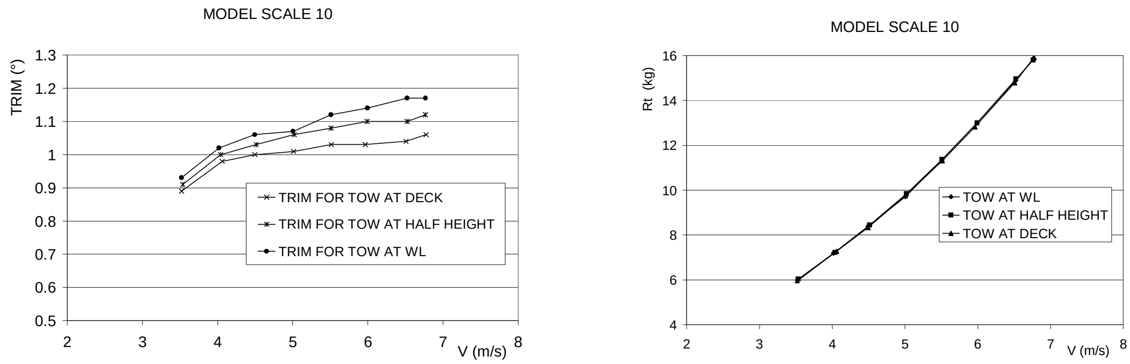

Fig.3. Trim and Resistance values for towing different positions.

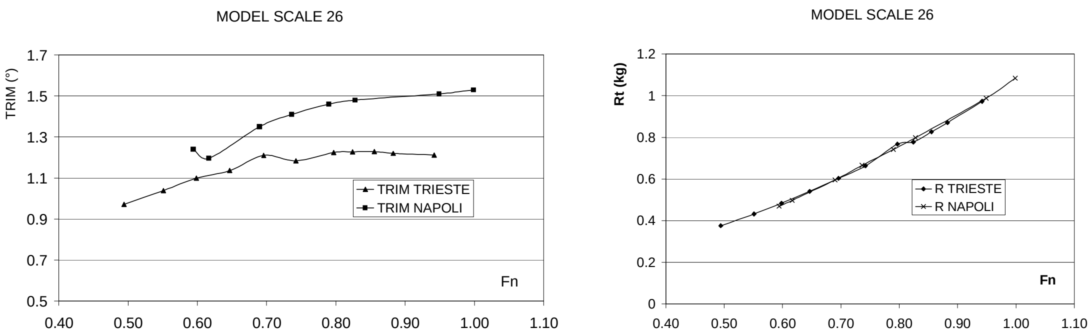

Fig.4. Trim and Resistance values for towing different directions.

3.3. Turbulence stimulation

3.3.1. Resistance results

The cooperative tests between Naples and Trieste Universities were conducted at load condition of ship in full scale both with bare hull and stimulators devices, whose dimensions should be great enough to promote the turbulence abaft their position without an appreciable parasitic resistance, but small enough to avoid the spray phenomenon. As the critical dimension depends on the thickness of the laminar layer, the position and the dimension of the stimulators where chosen taking into account the model dimensions and the Froude number range of the resistance tests.
Great care was also taken to obtain the maximum possible accuracy of the resistance results.
For this aim:
-the geosim model offsets were carefully checked;
-the resistance dynamometer was precisely and repeately calibrated;
-the tests were repeated several times and in different times;
-the tests on all the three geosims were carried out in the Naples University towing tank and the smallest model was also tested in the Trieste University towing tank in order to compare data obtained from the two different tanks.

In order to estimate the parasitic drag due to stimulators the tests on geosim model scales 10 and 20 were conducted at first without any stimulator and successively, with sand strips 6 mm wide fitted near bow profile. Specifically the 1:10 model was fitted with one, then with two identical but separated strips, with the first strip 60 mm abaft the FP and the two strips 30 mm distant one from the other. The 1:20 model was fitted with one strip, then with three identical but separated strips with first strip 30 mm abaft the FP and the three strips 15 mm offset one from the other.

From the measured differences of the resistances an evaluation of the additional resistance due to turbulence strip has been obtained. So the difference between the turbulent and the laminar flow resistance on the forward model surface has been determined also.

The results obtained are reported in the Tables 4 and 5, being:
-R_1 the resistance without stimulator;
-R_2 with one sand strip;
-R_3 with two (model scale 1:10) or three (model scale 1:20) identical strips;
-$Rp = R_3 - R_2$ for model scale 1:10 and $Rp = 1/2\ (R_3 - R_2)$ for model scale 1:20, the evaluated parasitic resistance;
$\Delta R = R_2 - (R_1 + Rp)$, the measured difference of the resistance between the turbulent and the laminar flow.

Table 4.(Model scale 10)

Fn	V(m/s)	R_1 (kg)	R_2 (kg)	R_3 (kg)	Rp (g)	ΔR_1 (kg)	$\Delta R_1 / R_1$)100
0.60	4.070	7.305	7.397	7.421	24	68	0.93
0.70	4.750	9.001	9.112	9.138	26	85	0.97
0.80	5.430	11.055	11.190	11.220	30	105	0.91
0.90	6.100	13.335	13.488	13.523	35	118	0.85
1.00	6.780	15.791	15.969	16.014	45	133	0.80

Table 5.(Model scale 20)

Fn	V(m/s)	R_1 (kg)	R_2 (kg)	R_3 (kg)	Rp (g)	ΔR_1 (kg)	($\Delta R_1 / R_1$)100
0.60	2.870	1.034	1.055	1.075	10	11	1.06
0.70	3.360	1.290	1.315	1.340	13	13	0.97
0.80	3.838	1.576	1.607	1.641	17	14	0.89
0.90	4.318	1.909	1.945	1.985	20	16	0.84
1.00	4.798	2.292	2.335	2.380	23	21	0.89

The analysis of the model data highlights that the laminar region on the naked model, in all the examined Froude number range (Fn =0, 60- 1,00), is very small for the two tested geosims, being only 1 per cent the increase ΔR on the resistance of the naked model due to the sand strip.
Briefly it can be concluded that the influence of the turbulence stimulation device applied near the leading edge of the high speed craft models is very small, as the transition point from laminar to turbulent flow takes place for the low local Reynolds number generally $2.5\text{-}3.0 \times 10^5$ and consequently very near to bow profile.
Such result could be consequence of a turbulence stimulation due to the very small but inevitable thickness of the model bow and to the round form of the bow profile of the examined hullform.
A large number of geosim tests was also carried out with trip wires of different diameters d, fitted in different longitudinal positions and with different projection ($d-\delta$) on the boundary layer thickness δ.
The tests results were evaluated both by flow observation and by resistance assessment.
The resistance values measured testing the geosim models were reducted to coefficient form by the usual relation

$$C_T = R_T / (0.5\ \rho\ S\ V^2) \qquad (2)$$

and the results are reported in Figg. 5,6,7 for the model scale 1:10, 1:20, 1:26 respectively.

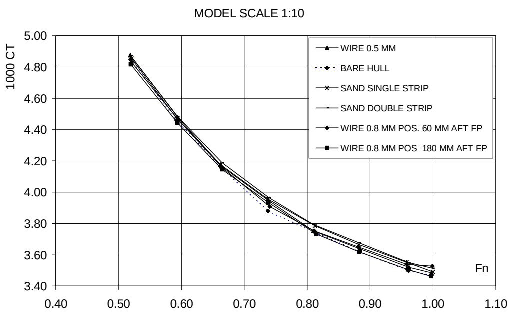

Fig. 5. C_T values for model scale 10

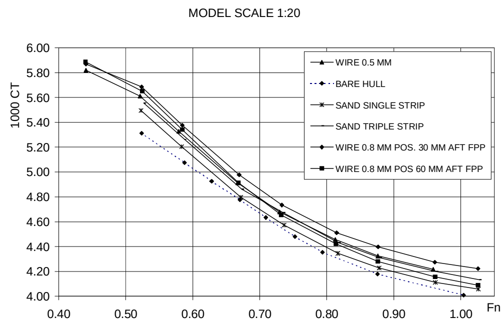

Fig. 6. C_T values for model scale 20

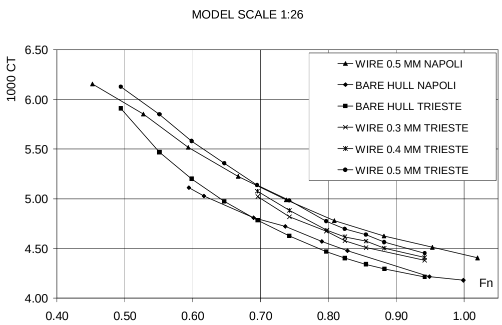

Fig. 7. C_T values for model scale 26

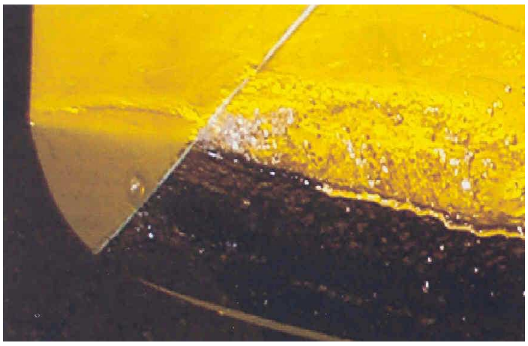

Fig. 8. Spray phenomenon at Fn 0.83 with 0.8 mm diameter trip wire on model scale 10.

Fig. 8 shows an evident spray phenomenon on the model forward surface. The photograph refers to model scale 20 tested at Fn 0.83 with a 0.8 mm diameter trip wire placed 30 mm abaft FP. In this position the boundary layer thickness δ is 0.49 mm and the projection (d-δ) is 0.31 mm.
In a further test the same stimulator has been shifted to 120 mm abaft FP where it is inside the boundary layer thickness in the whole considered Fn range as shown by Table 6.

Table 6 Projection of 0.8 mm trip wire on the boundary layer thickness

Model speed (m/s)	2.5	3.0	3.5	4.0	4.5	5.0
Fn	0.521	0.625	0.733	0.833	0.938	1.042
Rn	$2.42\ 10^5$	$2.99\ 10^5$	$3.39\ 10^5$	$3.87\ 10^5$	$4.36\ 10^5$	$4.85\ 10^5$
δ (mm)	1.294	1.181	1.093	1.023	0.964	0.915
(d-δ)	-0.494	-0.381	-0.293	-0.223	-0.164	-0.115

In this position the spray phenomenon is absent and the parasitic additional resistance due to stimulator is comparable with that other determined with the sand strip.

3.3.2 Residuary resistance

The values of the residuary resistance coefficient

$$C_R=C_T-C_F \qquad (3)$$

were calculated based on the ITTC line. Fig. 9 and Fig. 10 show the curves of C_R relating to the three geosims obtained by the tests carried out with bare models (Fig.9) and with the same trip wire diameter of 0.5 mm fitted near the bow profile inside the boundary layer thickness (Fig. 10)
The C_R values concerning the three geosims tested without stimulators are pratically constant in the region of Fn>0.8. The differences are less than 3 per cent. For Fn<0.70, the C_R values of the model 1:26, in consequence of a higher proportional effect of the laminar flow on the forward surface, are smaller than that of the two other models.
Due to the different proportional parasitic resistance of the stimulators, the C_R values concerning the tests carried out with trip wire show differences increasing according to Froude number and model scale. The C_R values of 1:10 scale model are 8 per cent smaller than that ones relative to 1:20 scale model and these last values are are about 4 per cent smaller than those relative to1:26 scale model.

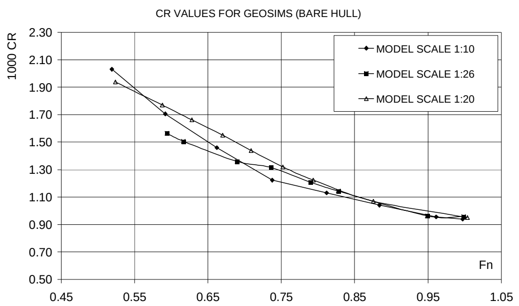

Fig. 9 C_R values for bare hull of geosims 10,20,26.

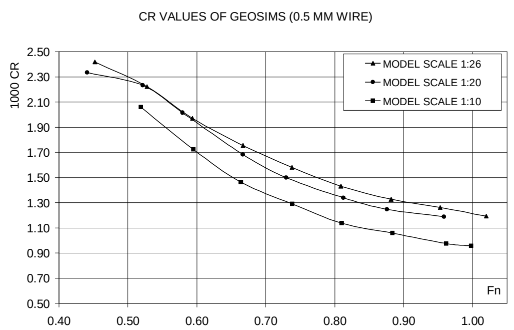

Fig. 10 C_R values geosim 10,20,26 hulls fitted with 0.5 mm trip wire.

3.3.3 Form factors
Form factor values (1+k) were determined for each Fn in the range of Froude number 0.60-1.00 by the slope of the total resistance coefficient C_T of the three geosim models versus the frictional resistance coefficients C_F (iso-Froude method) based on ITTC line.
The results are given in Fig. 11 for the tests carried out without stimulators and in Fig. 12 for the tests performed using 0.5 mm diameter trip wire stimulator.
The form factors so obtained for the bare hull show a higher proportional effect of the laminar flow on the forward surface of the smallest model, mostly at the lower Froude number 0.60 and 0.70, being the value of C_T for the model scale 26 much lower than those aligned by the other two models.
The values of C_T relating to models fitted with trip wire stimulators fit roughly the straight lines and no significant difference can be seen among the values of the form factors so obtained.
However the values 1.38-1.44 for (1+k) seem very high for this slender hullform.
This result is undoubtedly due to wrong values of C_T consequent to the stimulator additional resistance in the examined Fn range.

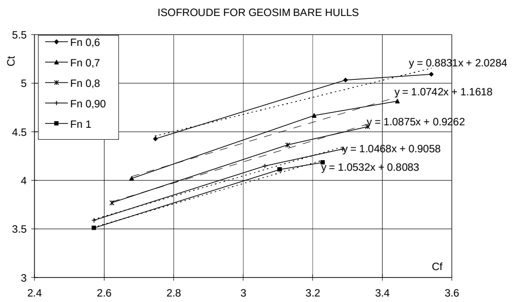

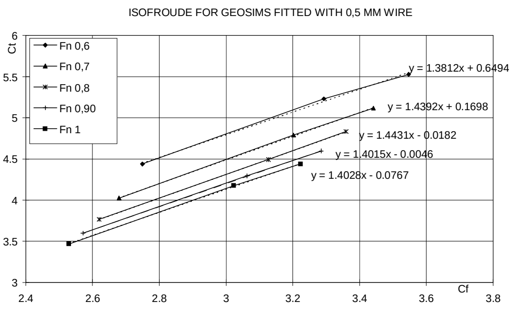

Fig. 11 Form factors by iso-Froude (bare hull) Fig. 12 Form factors by iso-Froude (0.5 wire)

The form factor values have been also determined for each Fn by means of the following formula:

$$1+k' = (C_{T(20)} - C_{T(10)}) / (C_{F(20)} - C_{F(10)}) \qquad (4)$$

where C_T and C_F are referred to the two larger models with scale ratios 1:10 and 1:20.
The 1+k' values so determined for the models without stimulators in the range 0.70-1.00 of Fn are roughly constant and the mean value shows a good agreement (Fig. 13) with that one derived from the low speed model tests conducted with transom emerged, by enveloping the curves of the total resistance coefficient C_T versus Reynolds number Rn (Hughes method).
In table 7 the 1+k' values so obtained both without stimulators and with trip wire are compared with those determined by iso-Froude.

Table 7. (1+k') values compared with (1+k) determined by iso-Froude.

Fn	(1+k') bare hull	(1+k) bare hull	(1+k') 0.5 mm wire	(1+k) 0.5 mm wire
0.70	1.206	1.074	1.307	1.439
0.80	1.158	1.085	1.316	1.443
0.90	1.112	1.046	1.294	1.401
1.00	1.123	1.053	1.340	1.402

3.3.4 Wave resistance
The values of the wave coefficient resistance can be calculated by the following relation

$$C_W = C_{Tm} – (1+k)\, C_{Fm} \qquad (5)$$

Where the form factors (1+k) for the conventional ship is considered as constant determined by the resistance tests at low Froude number. For high speed craft the flow regime around the hull is very sensible to the speed of the ship. The presence of hydrodynamic lift and consequently the variation of the trim , of the wetted surface area and the possible spray formation could preclude a satisfactory determination of a constant value of the form factor for model-ship correlation.
However for the present analysis of the geosim model tests, the wave resistance coefficients have been calculated using form factors (1+k') derived by the formula (4).
Fig. 14 shows, for the two model scales 1:10 and 1:20, the curves of $C_W = C_{Tm} – (1+k') C_{Fm}$ determined for the model tested without stimulators and with trip wires.
The results highlight that the value of C_W relating to the two considered geosims without stimulators are almost the same in the whole Fn range, but there is discrepancy among the C_W values relating to the models tested with stimulators. Moreover these Cw values in the Fn range 0.80-1.00 are 19% - 15.3% of C_{Tm} for the models without stimulators and only 8.2% - 2.8% of C_{Tm} for the models fitted with trip wires.

As the last values of the wave resistance C_W are not realistic, being very small, the results seem to indicate that the model tests for displacement slender hullforms should be carried out without stimulators.

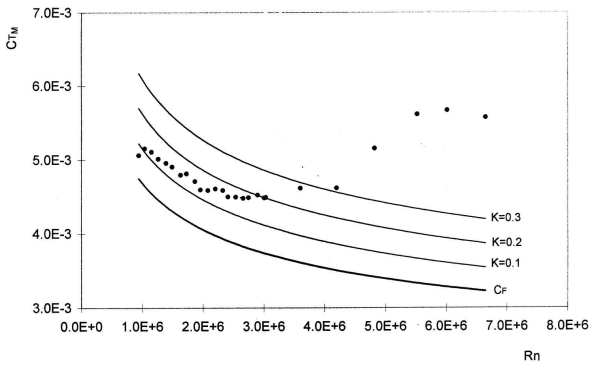

Fig. 13 Form factors by Hughes method.

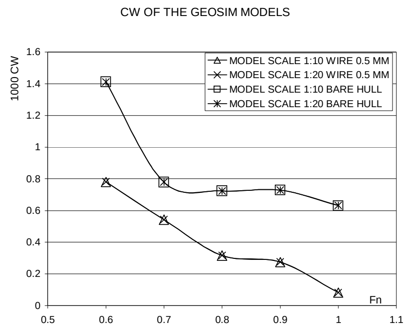

Fig. 14 Wave Coefficient C_W for the geosims with scale ratio 10 and 20.

4 Conclusions

An investigation has been made on the resistance model test procedure for displacement high speed craft using three geosim models of a very slender hullform.
The following conclusion can be drawn from this research:

1. The effect of the towing position on the running trim and on the resistance, if the direction of the towing force is horizontal, can be considered negligible on the results.
2. Due to smaller drag values measured with bare models, because of the influence of the laminar flow, and to higher values in the tests carried out with trip wire stimulation, because of the influence of the additional parasitic resistance, the dimension of the smallest model (L = 1.805 m) could be problematic for the resistance model tests of a high speed displacement hullform.
3. The resistance data obtained from the medium and the large models in the range of Fn 0.60-1.00 show that the influence of the turbulence stimulation devices applied near the leading edge ,is very small. However the stimulator should be inside the boundary layer thickness, in order to avoid the spray phenomenon.
4. The high form factors determined as a function of Froude number with trip wire stimulator are not realistic for a slender hullform, as shown also by the very small derived values of the wave resistance coefficients. On the contrary, the form factors values determined with the bare models are roughly constant and the mean value agrees with that obtained from low speed model tests (with transom emerged). Therefore no stimulator is recommended in the high speed resistance model tests in order to avoid wrong C_T values due to additional parasitic resistance.
5. Different, but both reliable results seem derived from the two different model ship correlations; ITTC 57 and ITTC 78 with k derived from low speed model tests. Further geosim tests data and reliable full scale data will allow to ascertain the validity of the most correct model ship correlation.

Acknowledgments
This work was supported by University of Naples "Federico II" in the frame of the 2001-2002 research plan.

References

BERTORELLO C., BRUZZONE D., CASSELLA P., ZOTTI I., (2002) Investigation on model-ship correlation and on power prediction for high speed multi-hulled vessels, IMAM 2002

BERTORELLO C., BRUZZONE D., CASSELLA P., ZOTTI I. (2001) Experimental Performance Investigation on Different High Speed Craft: Monohull, Catamaran and Trimaran, 2nd International Conference on High-Performance Vehicles HYPER'01, Hamburg, May 2001, pp.92-106.

BEGOVIC E. BERTORELLO C., CASSELLA P. (2001)
Calm Water Experimental Research in Geosims of High Speed Trimaran. Hydrodynamic Characteristics and Model Ship Correlation PRADS 2001 pp 143-150.

BEGOVIC E. BERTORELLO C., BRUZZONE D., CASSELLA P., ZOTTI I. (2001) High Speed Trimarans Validation of Numerical Results by Geosim Tests Proc. of the 6th International Conference on Fast Sea Transportation FAST 2001, Southampton, Sept. 2001, vol. II, pp.285-294

BERTORELLO C. (2000) Trimaran Hull Performances for Fast Passenger Ferries. Proc. of NAV 2000, Vol.1, pp. 2.4.1 –2.4.10, Venice, Italy.

BRUZZONE D., CASSELLA P., COPPOLA C., RUSSO KRAUSS G., ZOTTI I. (1999) Power prediction for High- Speed Catamaran from Analysis of Geosim Tests and from Numerical Results FAST 99 pp 789-801 , Sept. 1999 Washington D.C. (USA)

MOLLAND A.F.; WELLICOME J.F.; COUSER P.R. (1994) Resistance Experiments on a Systematic Series of High Speed Displacement Catamaran Form: Variation of Length- Displacement Ratio and Breadth-Draught Ratio. Ship Science Report No. 71, University of Southampton.

CORDIER S.; DUMEZ F. X. (1993) Scale Effects on the Resistance Components of a High Speed Semi-Displacement Craft. Proceedings of FAST '93 Conference, Yokohama, Vol. I, pp. 409-419.

UEDA T.; TSUKADA Y., SUGAI N. (1992) Some Considerations on Tank Test and Power Estimation of Semi-Displacement Type Mono-Hull Ship. SRI, Vol.29,pp 1-31.

INSEL M.; MOLLAND A.F. (1992) An Investigation into the Resistance Components of High Speed , Trans. RINA, vol. 134, pp. 1-22, 1992.

NEWMAN N. (1977) Test of Marine Hydrodynamic. Printed by Massachusetts Institute of Technology.

JONES D. P. (1976) Turbulence Study Effect on Model Resistance. Beng. Report No. 39, Department of Ship Science, University of Southampton.

YEH H. Y. H. (1956) Series 64 ResistanceExperiments on High-Speed Displacement Forms. Marine Technology, July 1965.

HAMA F. R.; LONG J. D.; HEGART J. C. (1956) On Transition from Laminar to Turbulent Flow. University of Maryland, Technical Note.

HUGHES G.; ALLAN J. F. (1951) Turbulence Stimulation on Ship Models. Trans. SNAME, Vol.59.

ALLAN J. F.; CONN J. F. C. Effect of Laminar Flow on Ship Models (1950) Trans. I.N.A., pp. 107-137, Vol. 92.

Construction of the world largest solar powered catamaran

C. Bolinger
BEng (Hons) Yacht and Powercraft Design

Stadelmann Bolinger
Naval Architecture Yacht Design
bolinger@yachtdesign.ch

Abstract

The construction of the solar powered catamaran, MobiCat, can be regarded as a start to a new era of solar powered water vehicles. This 33m passenger ship, licensed for a passenger capacity of 150 persons and for the largest of the Swiss lakes, sets an example for the use of solar energy in professional shipping.

The paper presents the design and construction processes of the catamaran MobiCat. Starting with the first technical ideas, followed by the preliminary design and the actual project. The co-ordination between naval architects, electronic engineers, government officials and the later shipping company is described. Hull forms, structural elements and materials are analysed and the electronic systems are explained. The construction methods will be discussed in depth, showing the peculiarity of building a craft of these dimensions without an actual shipyard, but rather many specialised firms. The paper will be concluded with the results of the performance tests on the water. In the light of these results, suggestions are also made as to possible developments that might be made in further projects.

1 Introduction

The aim of the project was to build a professionally-run, solar powered, passenger ship on which a passage should not only be a cruise on three Swiss lakes, (connected by canals) but also a new experience given by the fascination of modern technology and environment friendly mobility. A further aim was to illustrate the possibilities of renewable energy in public transport to a large public. Until the beginning of the project, all existing solar powered ships have been on a rather experimental level or of much smaller scale. Solar ships with an autonomy of more than several hours and professional gastro, sanitary and heating installations did not exist. All these mentioned elements were crucial criteria for the later shipping company. Initial researches has shown that by using modern solar and naval technology, it is possible to design a solar powered ship comparable to common ships of its size regarding cost, safety, operations and passenger capacity. However, this first work has also shown that the cruising speed of over 22 km/h, which would have been necessary for a ferry operation, could only be sustained for a short period of time. It was therefore decided to optimise the ship as a charter and party vehicle, running at an average speed of 12 km/h, and having an autonomy of over seven hours in the dark, maintained by the stored energy in its batteries.

As the project could only be realised with the financial support of sponsors, building just a reliable solar powered passenger ship was not enough, it had to be the world's largest. With the satisfied sponsors on board, their needs had to be as well as those of the shipping company. The most difficult condition set by the sponsors was the fixed launch date, some 15 months after the beginning of the actual project. Due to this short design and building phase and a very small budget, it was not possible to undertake any academic research or testing. Thus the design was in many ways done by interpolating empirical data and for most of the solar and naval systems, standard or semi custom components were chosen.

The above mentioned timing and financial constraints were one of several reasons for not commissioning a conventional shipyard. By choosing a project set-up as shown in Figure 1 and Figure 2, it was possible to involve many different companies specialised in their own field. In this way it was possible to build the ship within the given budget and timeframe. A further advantage of this set-up was the early involvement of the shipping company, which acted both, as general constructor and owner in one. Since its launch, 5th July 2001, the company has been successfully running *MobiCat*, covering over 2,000 kilometres and transporting more than 5,000 passengers.

Legal and financial organisation

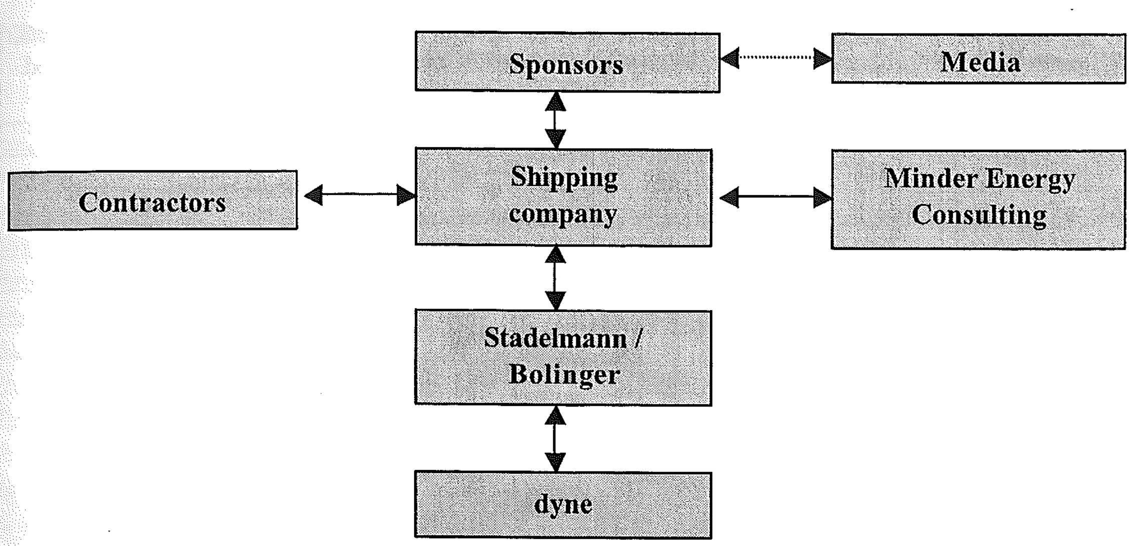

Figure 1 Organisational structure for legal and financial issues

Operational organisation

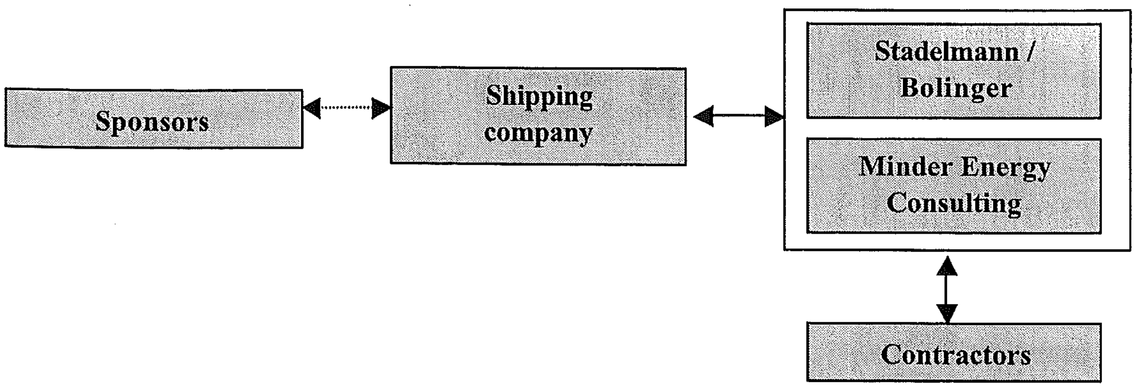

Figure 2 Organisational structure for operational issues

2 Preliminary Design

In a first design phase, investigations into the energy balances of a possible concept for a solar powered passenger ship were made. This preliminary design was financed by a national fund for renewable energy and had not only to serve as a basis for the subsequent design processes, but also as a record for finding an interested shipping company and sponsors. At this stage, it was assumed that the project could only be realised by applying a lightweight composite construction method. Since the financial situation and the building costs were unknown at the time, it seemed reasonable to plan the craft in composite materials. Figure 3 shows the preliminary catamaran design, with its global structure based on two hulls connected by three large beams. The voids between the beams and hulls are closed by sandwich plates which can be regarded as independent of the global structure. This configuration met the structural requirements of the ship as well as the logistical needs of the builders, as all parts could be produced in the workshop, transported to the launching site, and then assembled.

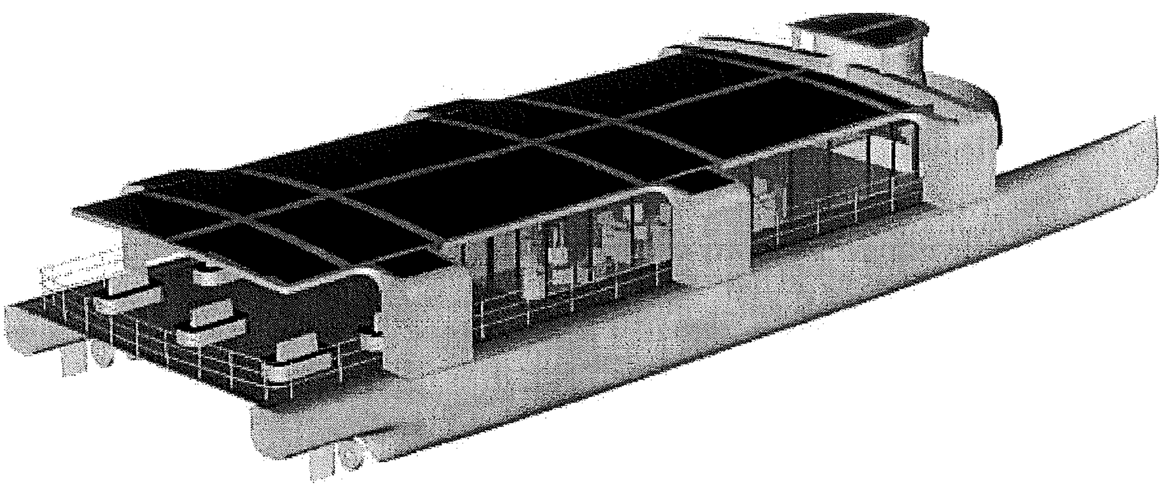

Figure 3 3D Rendering of the preliminary design.

In the time between the preliminary design phase and the beginning of the actual project, the work undertaken has showed that the ship could not be built in composite for the following reasons:

- the construction cost of the composite structure itself would have been approximately 70 % of the available budget
- the Swiss authorities were not able to approve a composite construction; a classification society would have been needed, resulting in additional costs
- there was no local shipyard able to build a craft of this size within the given time frame
- the shipping company was not confident in composite as building material
- fire insulation for such kind of construction is very expensive

Weight and resistance calculations showed that the ship structure could also be built in steel. Table 1 shows the weight-difference for the two construction methods for a ship of 33 meters in length and 11 meters in width. Due to the fact that they are based on the same construction concept, these figures are somewhat approximate, but accurate enough to illustrate the point. (For an actual composite design the structural concept would be further refined and reduced in weight by few tonnes).
Figure 4 shows the power requirements for the two construction types. The upper curve is the required power input per shaft for a ship of a steel structure, the lower that for a ship of a composite structure. The graphs are based on the same hull shape, only varying in length of the waterline, displacement, draft and wetted surface area. It is inevitable that by increasing the size of the craft, the proportion of structural to overall weight decreases. It was therefore decided to increase the size of the ship to a maximum and accept the relatively small disadvantage of a heavier steel structure.

Table 1: Comparison of steel and composite structure	Steel structure Weights in kg	Steel structure % of light ship		Composite structure Weight in kg	Composite structure % of light ship
Structure	81000	70.4%		45000	55.6%
Insolation	0	0.0%		2000	2.5%
Prop. System incl. Solar gen. + Batteries	12200	10.6%		12200	15.1%
Backup	2000	1.7%		2000	2.5%
Steering	500	0.4%		500	0.6%
Domestic Systems	7500	6.5%		7500	9.3%
Safety Systems	1600	1.4%		1600	2.0%
Navigation Systems	1300	1.1%		1300	1.6%
Interior	4000	3.5%		4000	4.9%
Bar	1300	1.1%		1300	1.6%
Kitchen	3000	2.6%		3000	3.7%
Toilets	600	0.5%		600	0.7%
total light ship	**115000**	100.0%		**81000**	100.0%
Variable weight	14000			14000	
Fully loaded	129000			95000	
Wetted surface area per hull	110 m2			89 m2	
LWL	32.5 m			29.5 m	

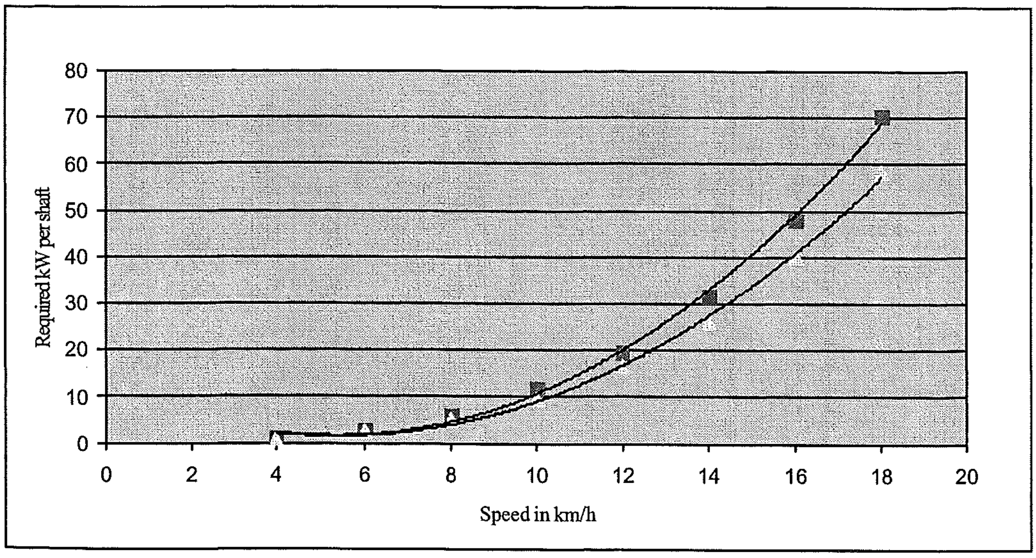

Figure 4 Power requirement per shaft for a steel and composite structure, regression line with a least square fit (R^2). Upper line representing the steel structure. Lower line representing the Composite structure.

3 Design

3.1 General design concept

The general design of the craft was driven by the needs of a large free area for the solar panels, the characteristics of a catamaran itself, and the requirements of the shipping company. Furthermore the design group wanted to combine modern aesthetics with the optical characteristics of classic inland water ships. This was done by creating a large open area covered by a superstructure of a filigree look and guard rails made of stainless steel tubes and cables. In contrast to the fine aft superstructure, the exterior of the cockpit was designed in a classical solid look. The two items share several details such as the shape of their roofs and the corner roundings. They are separated by the gangway to the outdoor steering consoles, which themselves are designed in stainless steel to match the light look of the guard rails. The philosophy of combining in- and outdoor as much as possible was realised by the fully glassed sides and the bar which is positioned in two halves between the aft façade which can be totally opened. The design was emphasised with high quality materials such as teak for the deck and a light weight interior. However, as finances were limited, several ideas had to be renounced to at a late stage, such as the teak deck .

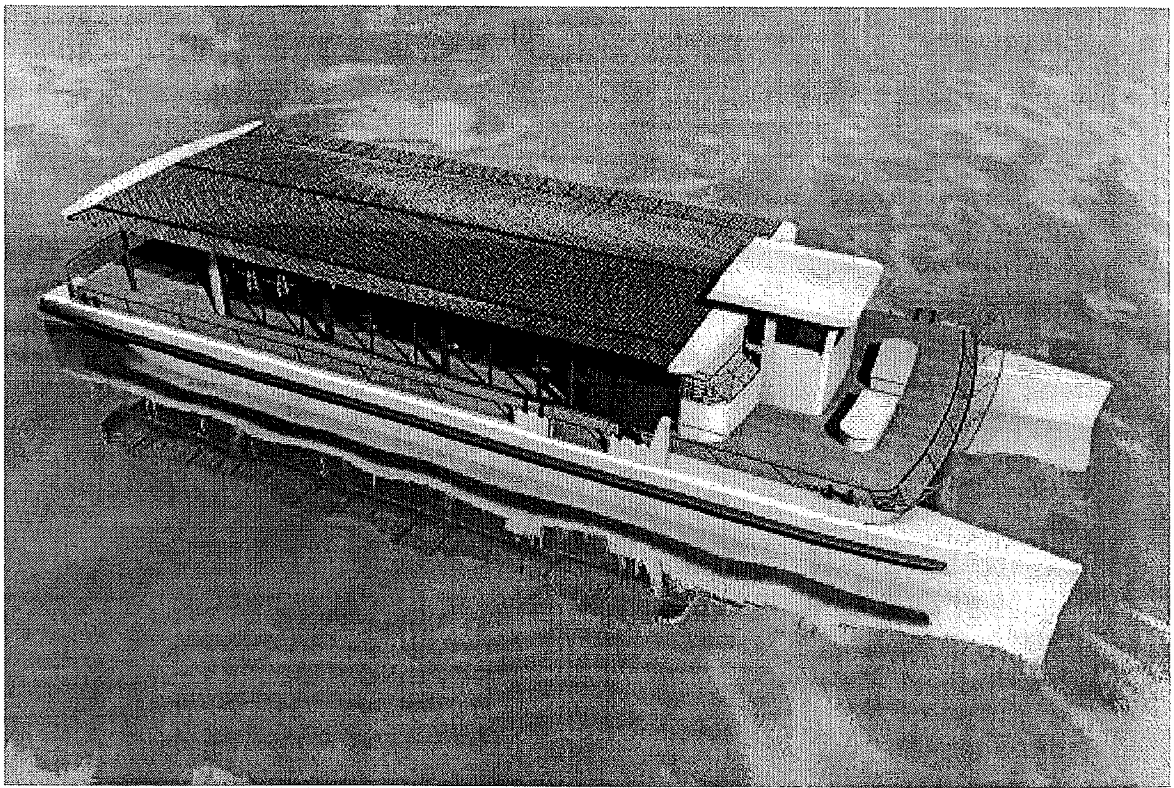

Figure 5 3D Rendering of the final design, figure was created in collaboration with C. Dransfeld of dyne

3.2 Interior design

The philosophy for the interior design was to create one spacious room in which the passenger has the feeling of sitting outdoors but protected by a large roof. The fully glassed façade gives a panoramic view of the lake and its nearby shore. Except for the bar, all the domestic installations are in the front part of the superstructure and therefore unobtrusive for the passenger. The design also allowed all the sanitary, heating and electric items to be installed in one area. The room underneath the gangway, between the cockpit and the superstructure serves as a connection path for all the tubes and wiring between the two hulls, the crew room, the kitchen and the toilets. While pressure pumps, waste- and freshwater tanks are all installed in the hulls, the gas tank and heating for safety reasons is installed underneath the cockpit. Figure 6 shows the general arrangement of *MobiCat*.

Figure 6 Plan View of the general arrangement

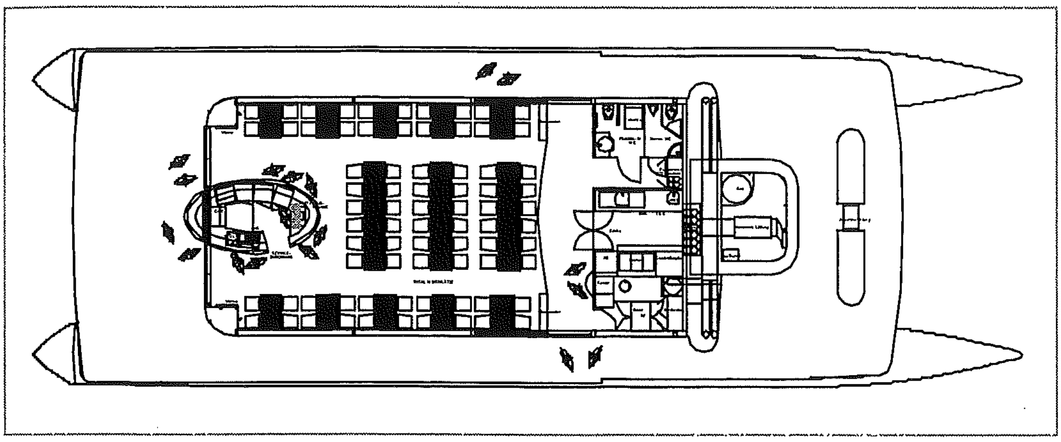

3.3 Structural design

As the shipping company had only a launching site but no shipyard, the logistics of transporting and assembling the ship had to be respected from the beginning of the early design phase. In particular the structural concept was strongly influence by these circumstances. The structure was designed in a way that allowed the ship to be built in the following parts: two hulls, seven cross beams, reinforced plates for the deck between hulls and beams, superstructure and cockpit. All these parts had to be small enough for a relatively easy transport, but large enough for rapid construction at the launching site.

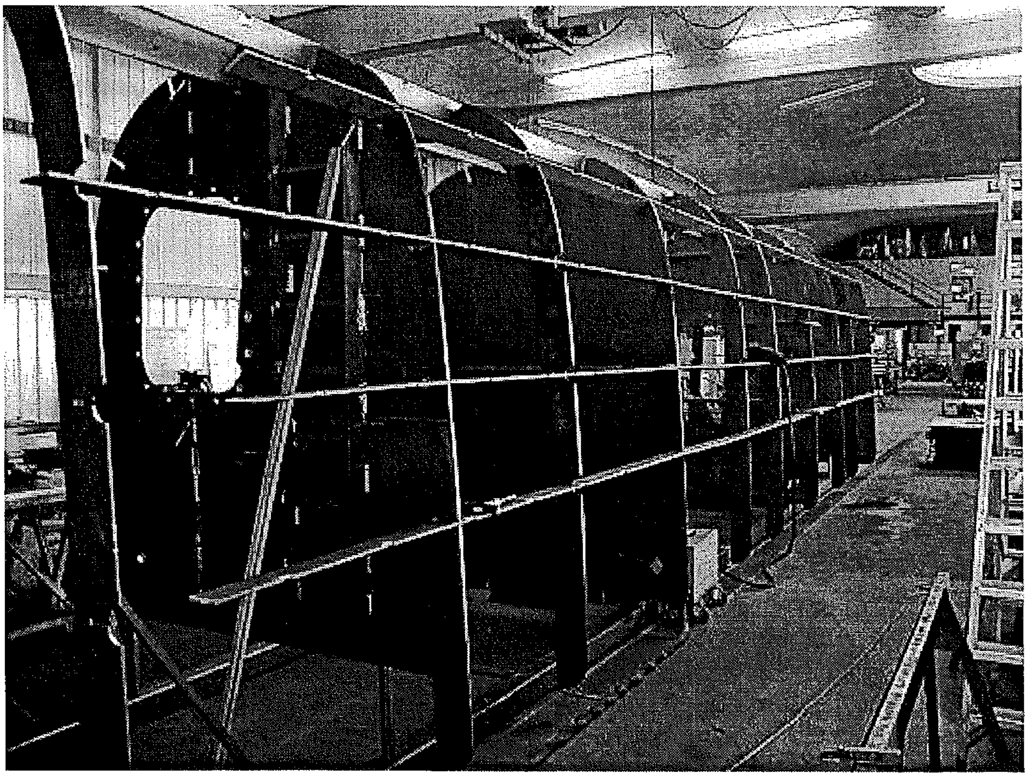

Figure 7 The interior structure of the up-side-down parallel midship body for the port hull.

Swiss passenger ships have to conform to rules which are only applicable in Switzerland. As these rules are somewhat superficial, they had to be combined with the more stringent and specific rules of a classification society. It was decided to use "Rules for High Speed and Light Craft " by Det Norske Vertitas as they take special ship types, such catamarans into consideration. All the structural calculations have been done in collaboration with C. Dransfeld of dyne and the author. The loads were calculated according to service restriction class notation R4 and subdivided into: loads due to wave acceleration, local loads, global loads on hull and global loads on cross structure. Dimensioning the structure was first done in a conventional manner according to the rules and then verified by the use of finite element analysis (FEM).

Figure 8 shows the bending analysis of the seven beams which connect the two hulls with each other and are the basis of the platform. For the bending analysis, the beams have been fully fixed at one end and on the other end connected to each other by coupling equations. The earlier established moments were simulated by equivalent loads applied at the free end. The change in colour and intensity show the difference of stress within each beam. The reason for the stress difference of each beam is due to the fact that the first two beams (from the left) are 400mm higher than the others. This was done to lift the fore deck area and so prevent an encounter of waves in rough sea. The shown configuration had not only been analysed to bending, but also to pitching and torsion moments. Apart from detail work, FEM was further used for the superstructure but not for the hulls.

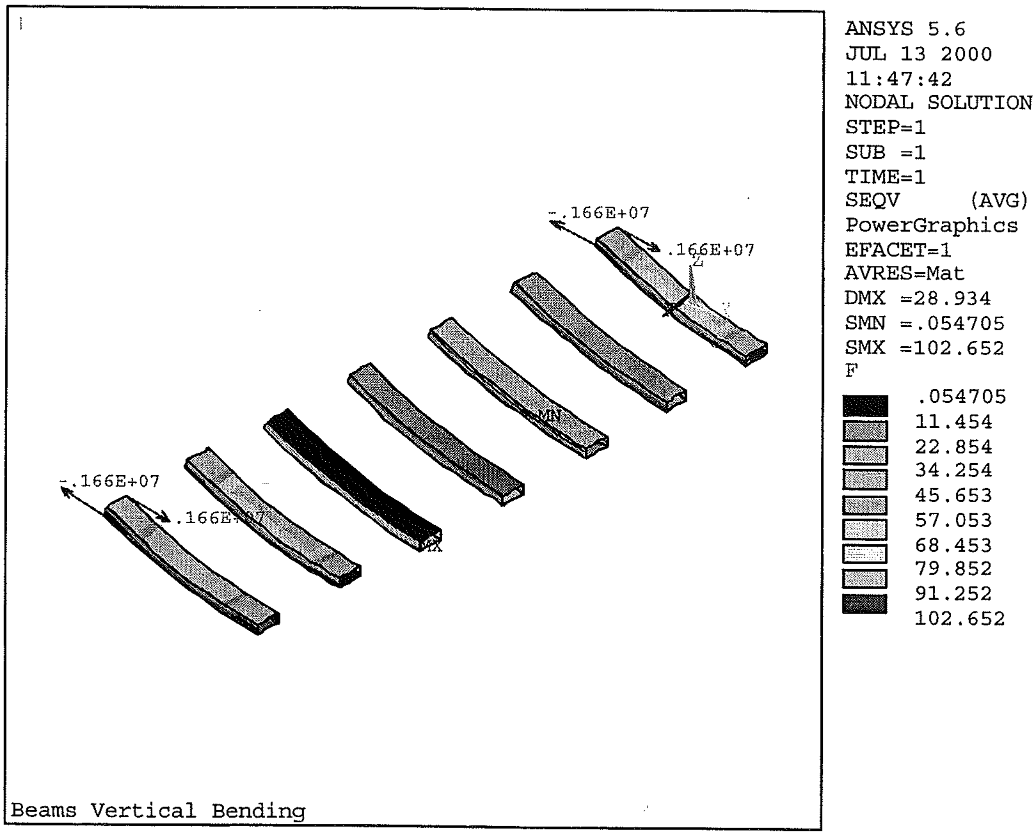

Figure 8 FEM plot for the vertical bending analysis of the seven cross beams, courtesy of C. Dransfeld, dyne.

3.4 Hull design

The design of the two symmetrical hulls was guided by the following three main criteria:

- Hydrodynamic characteristics

  As there was no suitable resistance prediction programmes for slow catamaran hull shapes available on the market and due to financial restrictions tank testing could not be undertaken. The resistance had to be predicted by a combination of calculations and comparative data analysis. The frictional drag was calculated by the ITTC 1957 formula. To estimate the residual drag, known resistance curves of slender crafts such as IACC sailing yachts were analysed to obtain an average percentage of residual drag to total resistance at a each specific Froude number. These percentages were then used to predict the residual hull resistance of the ship. Since the applied slender hull form has a lower percentage of wave making drag compared to conventional forms such as sailing yachts, the predicted results were assumed to be slightly larger than the actual resistance. Therefore this method was accepted as a very simple but secure resistance prediction method. As discussed in section 7, future projects could be further refined by the application of more sophisticated resistance prediction methods such as CFD and tank testing.

  The hull was optimised for a cruising speed of 12 km/h, which corresponds to a Froude number of 1.9. To minimise wave drag, the largest possible slenderness ratio within the given draft limitation of 1.5 m was chosen. It was estimated that the slight increase in wetted surface area accompanied by the maximum slenderness ratio has a smaller influence on the total hull resistance than increasing breath to optimise wetted surface area. To further minimise wave making drag und ensure low wash, much attention was paid to creating a low pressure distribution along the hull. This however, stood in contrast to the constructional and ultimately financial considerations. A compromise between optimum pressure distribution and economies on building costs was necessary, as further discussed below. To reduce energy losses (and once again costs) of the propulsion system, it was decided to install a stern gear as short as possible and at 0° inclination. This has further influenced the deign of the aft section, resulting in a rather blunt stern with a somewhat large change in pressure. Since the ship is run at low cruising speeds, this pressure change seemed acceptable. However, it is clear that this stern would create waves and large drag at higher speeds. For future projects, requiring higher speeds over a short period of time, a different stern arrangement would be necessary.

- Hydrostatic characteristics

  As the ship is of a catamaran type, its transverse intact stability is naturally sufficient. Therefore transverse stability aspects did not influence the hull design. In contrast the longitudinal stability was more carefully analysed, since the extreme slenderness ratio of a catamaran results inevitably in a small longitudinal stability. This is not much of a problem for the intact stability, but it showed that the ship had to be equipped with a relative large number of subdivisions to correspond to the criteria's of the Swiss authority for the damaged stability.

  The large slenderness ratio also increases the proneness of the catamaran to the dynamic problem of pitching. But the ship cruising at low speeds has a low centre of gravity and is only running on inland water lakes with a short fetch, thus it encounters waves of relatively small amplitude and length. Due to this and the fact that the prediction of small ship motion in waves is a highly non-linear hydrodynamic phenomena which cannot be solved by a simple approach of the strip theory O. Khattab[1] (1998), it was decided to neglect the prediction of motions. To ensure that the bottom of the centre platform does not hit coming ahead waves, it was designed to maximum height, given by the desired height of the gangway entrance. As discussed later, trials have shown that the platform stays clear of waves and the motions in rough seas are not a problem.

- Constructional considerations
  Since the construction material was steel and production costs had to be as low as possible, the hull design was subdivided into three parts: a stern of 6 m, a parallel midship body of 18 m and a bow of 8 m. Keeping the pressure distribution in mind, the parallel mid ship section was chosen as long as possible to reduce costs. The bow was designed in a way that allowed the side and bottom plating to be built by conventional plate bending. Due to the above mentioned stern criteria, the stern section had to be produced by performing several smallish steel plates. This was done by a Dutch company to a 3D iges file which was transmitted by the author via email.

Final hull dimensions:

Length over all:	33 m
Length between perpendiculars:	32.5 m
Waterline beam:	1.7 m
Draft:	1.4 m
Volume of displacement:	57.5 m^3
Wetted surface area:	110 m^2
Prismatic coefficient:	0.79
Block coefficient:	0.67

4 Electronic system

As the author is not an electronic engineer, this section is mainly a translation of a publication on the electronic system of the solar powered passenger ship *MobiCat* by Dr. R. Minder[2] (2001). It was decided to use proofed standard components available on the market, accepting some compromises regarding their efficiency but with a reliable solid and economic system of low maintenance. Figure 9 shows a schematic overview of the electro technical system.

4.1 Solar generator

The solar generator is divided into two fields of approximately 10 kW each, both charging a battery of 480V and 240 Ah. The largest area of the roof is covered by standard BP 580 cells, mounted on aluminium profiles, which itself are glued to the GRP sandwich roof. The roofing of the side gangways consists of custom made see-through cells. In this area the photovoltaic installation is visible to the passenger. The solar generator transfers the gained energy directly into the batteries. The voltage of the batteries defines the characteristics for each cord of in-series connected cells.

4.2 Batteries

Due to technical and financial aspects, no other type than lead batteries were applicable. Their minimal voltage was defined by the drive inverter. The batteries are in plastic housing and installed as groups in a compartment in each hull. To increase their efficiency and reduce the development of gas they are equipped with an electrolyte pump.

4.3 Battery voltage switches and distribution

Each battery compartment is equipped with a battery switch and distribution system consisting of:

- Main switch with magnetic- and thermal actuator, as well as a low voltage actuator
- 480 VDC distributor
- DC/DC conservator for the 24 V systems

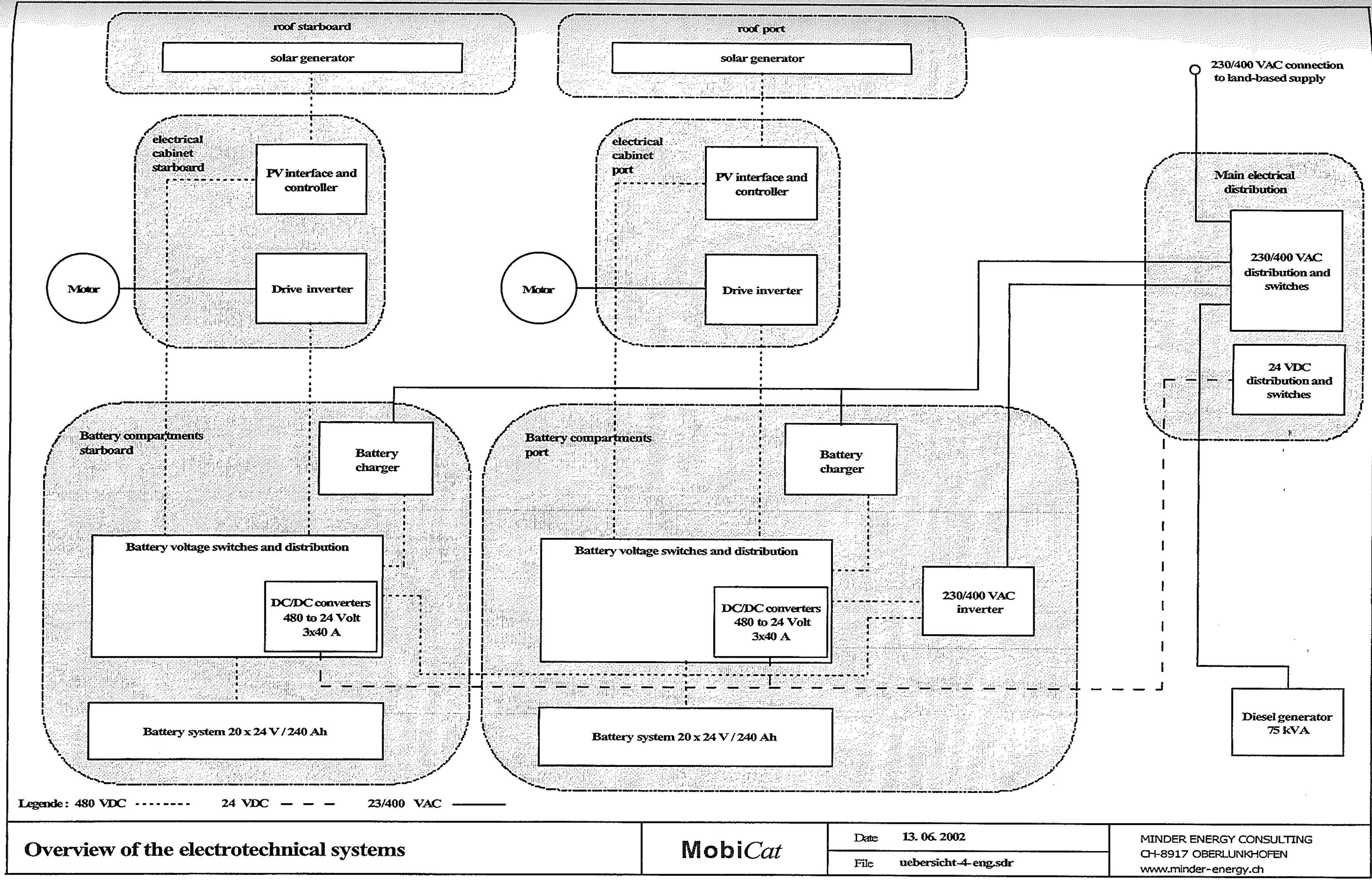

Figure 9 Schematic overview of the electrical installation, in courtesy of Dr. R. Minder, Minder Energy Consulting

4.4 **Battery charger**

Each battery system is has its own 25 A charger for the following functions:

- Semi or full charging of the batteries from the land net
- Charging of the backup generator – security system
- Periodical full charging as specified by the manufacturer

4.4 Electrical motor and drive inverter

The drive system consists of industrial propulsion components, with a compact a-synchronic motor by Siemens of 81 kW at 1150 rpm and a torque of 678 Nm. As mentioned in section 3.4, the motors are connected in the axis of the propeller shaft. Thrust transmission and alignment allowance of the stern gear is given by an Aquadrive system. This system also reduces vibrations and allows the air cooled motor to be mounted on silent blocks and to be running free of axial thrust. The drive inverter are installed in the rounded aft corner of the superstructure. They are also air cooled and have a nominal power output of 90 kW.

4.5 Electrical board supply and backup system

When calculating the electrical consumption of all the domestic systems, tests showed that they require nearly the same power as one of the propulsion systems at cruising speed. By installing a gas tank as a power sources for the heating, warm water, the stove, and the coffee machine, the electrical consumption was drastically reduced. The ship is supplied with two electrical board systems 230/400 VAC and 24 VDC. Apart from the light most of the domestic installations are powered by the tri-phase 230/400 VAC system. The following three power sources can be used:

- Supply of the batteries via inverter
- Supply of diesel generator (backup system)
- Land based supply in port

The inverter has a power output of 25 kVA and is supplied by the two batteries simultaneously, which consequently are equally discharged. Both the 230/400 VAC and the 24 VDC distributions are installed in the crew cabin on deck level. The 24 VDC system is mainly used for all navigation systems such as radar, GPS, hydraulic pumps for steering gear and lights. The diesel generator has a power output of 60 kW – try phase 230/400 VAC at 50 Hz. As it is part of the safety system, it has its own starter battery, a 700 liter diesel tank and is controlled from the cockpit.

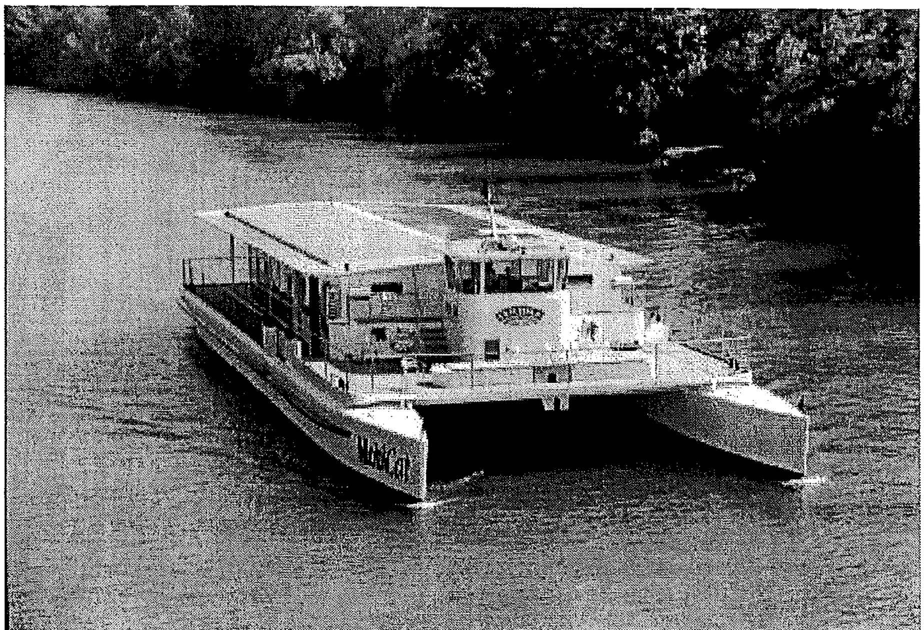

Figure 10 *MobiCat* in the canal without passengers at a speed of 10 km/h, the two halves of the solar generator can be seen.

5 Construction

As the project had to be built in nine months and was in many ways different to a general passenger ship, it did not seem possible to commission a standard type ship yard. It was therefore decided to use the shipping company as general contractor, which itself commissioned over 100 different companies specialised in their own field. As mentioned earlier, since the shipping company had only a launching site but no yard or sufficient workshop, the logistics of transporting and assembling the ship had to be respected from the beginning of the early design phase. The main structure of the ship was built in parts, by three different locksmiths. These companies are specialised in building large metal structures, however, none of them had ever built a ship before. This required solid project management and very detailed descriptive plans. Much care was taken in the accuracy of building, as all structural components of the different companies had later to be assembled within a margin of several mm. Due to this and time optimisation most steel plates were cut by laser. The required cutting patterns were all produced by the author and transmitted via email directly to the workshops.

Once the structural components were transported, they had to be put together in less than four weeks. This and all the subsequent work had to be done under difficult conditions with temperatures often below 0° Celsius, since it was winter and the ship was only covered by a tent. After all the welding was finished, the steel structure was sand blasted and covered with a corrosion protection system and then painted.

Since the project time was short, the detail planing of the interior and that of several systems was done during the above described construction phase. This had the slight disadvantage of having a finalised and built structure which could not have been alter if later required, for example to install a larger heating system. Once the steel structure was corrosion protected and painted, the insulation, the first systems and later the interior were installed all within three month. During this hectic building period there were often over ten different companies on place and a solid project management was essential.

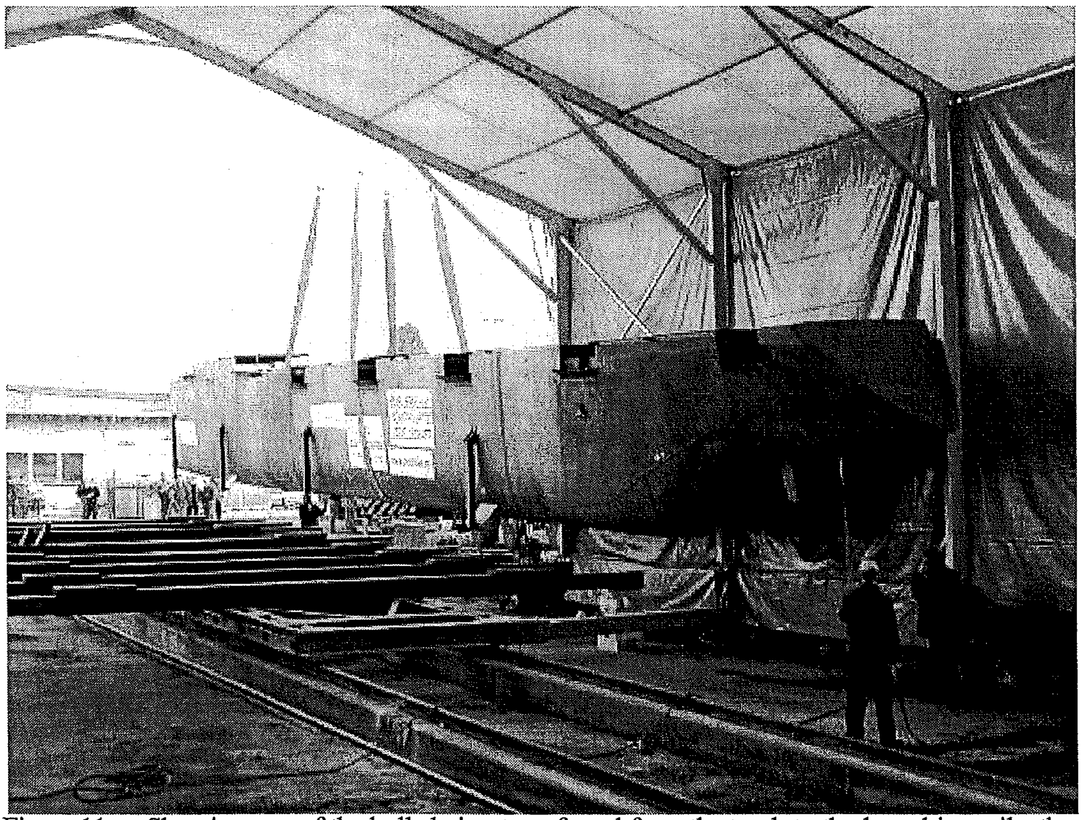

Figure 11 Showing one of the hulls being transferred from the truck to the launching rails, the insets for the seven crossbeams are well visible.

6 Operation

Since its launch, 5th July 2001, the company has been successfully running *MobiCat,* covering over 2,000 kilometres and transporting more than 5,000 passengers. Practice has shown that the characteristics of the ship are as specified in the design brief. Due to the strong public interest in the project, the ship is almost fully booked and should within the first few years result in a good return on investment. The passengers are fascinated by the nearly soundless ship "gliding" across the lakes. The crew is also fascinated by the operating of the ship. As the vessel is part of a fleet of 11 conventionally propelled ships, the energy management had to been learned and is an interesting task. For example the captain must decide whether the batteries are full enough or have to be charged by the land based supply before leafing the port. This decision is based on the charging conditions of the battery, the length of the cruise, the estimated energy input by the solar generator during the cruise and the estimated energy use which is a factor of sea and wind conditions, speed requirements, and the use of the domestic systems.

After observing the overall energy balance of the ship over a period of a year, the equation is clearly positive. As the ship is not in daily use during the off seasons and winter, the energy produced by the solar generator during this time is much greater than the energy required for operation. The resulting supplement of energy is also greater than the energy input of the land based supply during the peak season. Due to this, it was planned that the *MobiCat* would not only serve as a passenger ship but also as a small solar power plant. Since the Swiss regulations rate power of renewable energy much higher than power of non-renewable resources, this could be a further income for the shipping company. However, due to the needed investment for the required power inductor this option is momentarily not used.

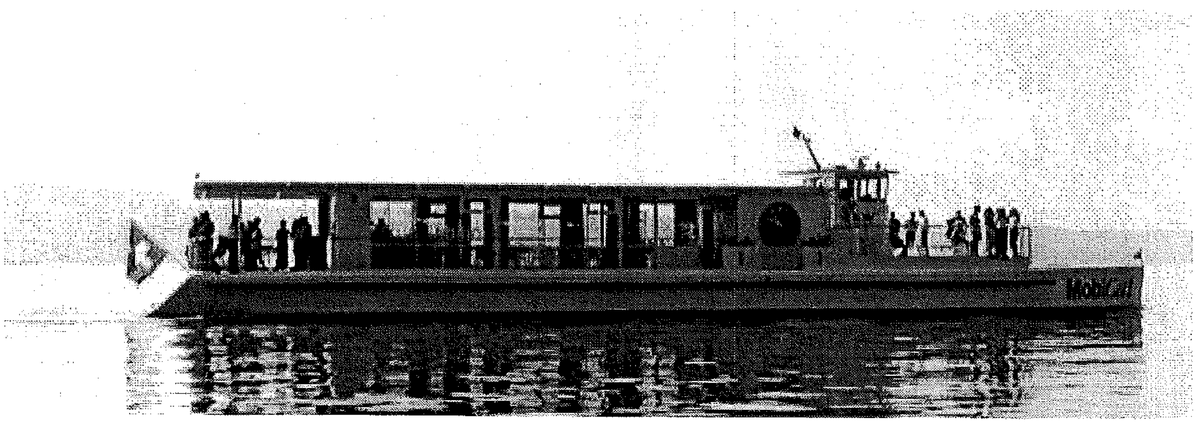

Figure 12 *MobiCat* at a speed of 11 km/h, with 53 Passengers in calm weather conditions.

As the ship is mainly used for charter, its cruising speeds are between 10 to 12 km/h. For this range the energy consumption is small enough, ensuring an autonomy of up to seven hours in bad weather or at night without using the diesel generator. The ship is supplied with a data logging system, connected to a GSM – modem. This allows the operational data to be downloaded via PC and modem. This system was particularly useful during the trial phase. Figure 13 was derived by data gained with the above described system and shows the power characteristics of the ship in flat sea with moderate wind conditions. It can be seen for a speed of 12.5 km/h the craft requires approximately 45 kW. As the solar generator has a maximum power output of 20 kW, a further 25 kW are used from the stored energy in the batteries to sustain this speed. Assuming the ship would only be driven by the direct energy output of the solar generator, its maximum speed would then be around 7.5 km/h.

The data for Figure 14 was gained in the same way as for the Figure 13. It is a graph of power requirements and accumulated energy for a measured test drive. The aim of the test was to establish the energy requirement per person when transporting 110 passengers over a distance of 10 km within a hour. It can be seen that approximately 25 kWh were used to cover the distance, this results in 22.8 Wh per passenger. In comparison to a combustion engine, this is equivalent to roughly 50 ml diesel per person for a distance of 10 km within an hour!

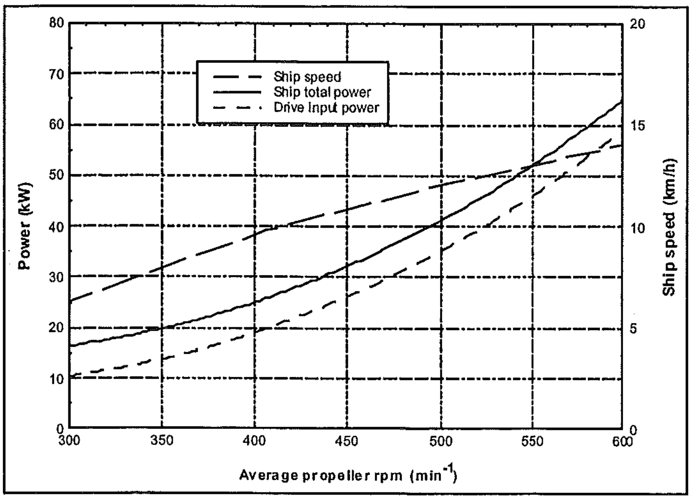

Figure 13 Power diagram for *MobiCat*, courtesy of Dr. R. Minder, Minder Energy Consulting

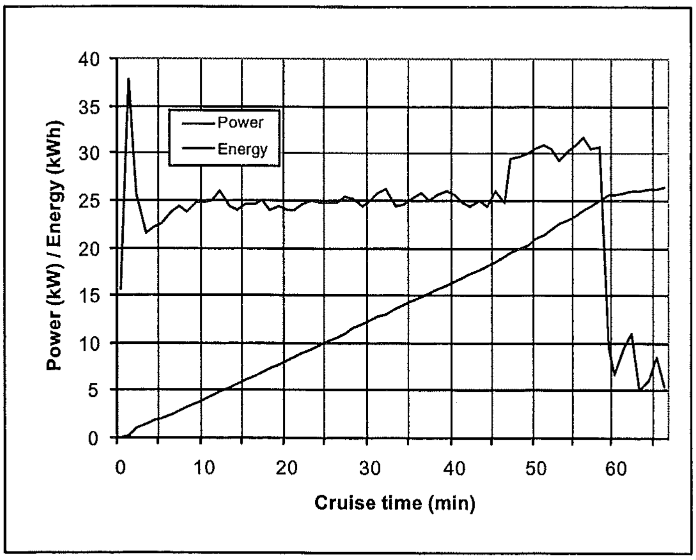

Figure 14 Cumulated Energy for a passage of 10 km within 1 hour, courtesy of Dr. R. Minder, Minder Energy Consulting

Apart from a few early "teething problems" of absolutely normal scope for a project of this size, all the earlier specified criteria's were meat. Testing in rough seas with waves of up to 1.5m and winds of over 60 km/h have shown that *MobiCat* is a safe ship for all possible conditions on the Swiss inland water lakes. Inevitably the required propulsion energy for these conditions rises up to 20% for equivalent speeds. However, as the ship is equipped with a backup generator its autonomy is not reduced and a secure arrival in port is certain.

7 Conclusions

A number of conclusions can be drawn and suggestions for possible refinements made. In retrospect clearly the most difficult circumstances were the short design and building time combined with the small budget. Although having accomplished the project on time and with only a few percentage over budget, the author is very interested in further solar powered projects but would hesitate to accept a project with these conditions in future. Larger financial resources and more time would allow further research into possible design configurations and refinements. Of special interest would be the optimisation of slenderness ratio and wetted surface area. This could be done by the combination of a well developed tank testing program, possibly in combination with CFD work. The full size data gained by the trials of *MobiCat* will most certainly contribute much to future designs.

Having fully succeeded with the goals specified in the beginning of the project, the author believes in the future of solar powered passenger ships. The operation over the past season and the public interest also shows that a ship of this kind is not only a technical success but also of financial interest for a shipping company. Since high speeds are generally not an issue for charter cruises on inland water lakes, solar powered passenger vessels are a good alternative to combustion propelled ships. However, still much work has to be done to show the possibilities of this environmentally friendly powering solution. Shipping companies have to be informed about the system and the possible economic gains. Further refinement in increase in autonomy could be obtained by a combination of solar power and a system of another renewable energy source.

The project has also shown the limitations of solar powered ships. The author believes for example that professionally operated solar powered vessels for coastal or off shore waters cannot be built within the near future. This project also showed that the solar power system increases in efficiency with increasing ship size. This is mainly due to a larger area for the solar cells compared to the increase in resistance. Furthermore the weight of the batteries becomes proportionally smaller with increasing size. However, the increase in size could be counterproductive from a financial point of view.

As a naval architect, the author is interested in all kinds of water crafts and propulsion systems. Although he strongly advises his clients to use the most suited powering system for the specific use, he wishes to be involved in further projects having a wise environmentally friendly power system.

8 Acknowledgement

The author wishes to thank Dr. R. Minder of Minder Energy Consulting and C. Dransfeld of dyne for providing their technical reports and data.

9 References

[1] O. Khattab (1998), *Prediction of the seakeeping of small craft*, Symposium on Yacht and Small Craft Design, La Spezia

[2] Dr. R. Minder (2001), MobiCat - solar elektrisches Fahrgastschiff für Binnengewässer, Oberlunkhofen Switzerland

Hydrodynamic Design and Analysis of Unconventional Fin Stabilisers

Stefano Brizzolara
University of Genova, Department of Naval Architecture and Marine Engineering
Via Montallegro, 1 - 16145 Genova - Italy
brizzolara@dinav.unige.it

Abstract

Active stabilisation of ship motions is an issue of primary importance in the design of modern high performance ships, to ensure the highest comfort level, largest operation capabilities and in some cases also improved safety.

Having introduced a preliminary survey on the state of the art of modern high efficiency fin stabilisers and existing design methods, the paper describes a modern practical approach for the hydrodynamic design and analysis of marine motion control surfaces, based on 2D/3D CFD methods. The theoretical methodology is presented by following up a study about the design and performance assessment of stabiliser fins with increased L.E. radius profiles, with respect to a standard NACA 0015 fin profile. Anyhow it is obvious that the devise method can be applied to the prediction of hydrodynamic characteristics of any fin configuration. In fact, once the 2D profiles are designed and their hydrodynamic viscous and cavitating characteristics are estimated, these data are used to correct the 3D fin characteristics predicted by a potential flow panel method, through an approximate method, which is shown to give satisfactory correlation with model tests results.

Conceptually the procedure does not differ to the classic one presented some thirty years ago by Cox (1977), but the use of different theoretical methods, based on modern CFD techniques, permits to overcome some uncertainties of the classical design practice and to more accurately predict the full scale fin lift force also in the near stall region and in cavitating environment. All these at much smaller expenses than a complete RANSE solution. On the other hand, the kind of approximation at the base of the proposed hybrid methodology limits its applicability to a restricted range of cases. Cases where the viscous 3D effects are most important and where other types of cavitation than laminar can influence the hydrodynamic characteristics of the fin, are excluded. The difference in the results obtained with this new methodology, respect to the traditional formulas and results from model tests in the case of the target fin are presented and critically discussed as well.

Introduction

Unconventional fin stabilisers

About 30 years ago a provoking paper of Capt. Kehoe (1973) revealed the better sea-worthiness of USSR destroyers that could sustain high speeds also in severe sea conditions, while the majority of USA DDGs, in comparable sea states, had to slow down due to the excessive roll and green water on deck. Russian warships, as well as the majority of the Royal Navy's, at those ages, were already equipped with anti-roll fin stabilisers, while only a very limited portion of the USA destroyers, could have the benefits of this active stabilisation. From those years on, a lot of research work was conducted about ship motion control surfaces that resulted in a series of experience and methods to design and assess the hydrodynamic performance of active fin stabilisers. The article of G. Cox and A. Lloyd (1977) offers a good synthesis of the state of the art of the now how reached in those years.

From that period, the hydrodynamic design of stabiliser fins was not substantially changed: the standard fin design actually features, in fact, a basic NACA 4-digit series profile; in high cavitation risk cases, profile of the NACA series 6x or 16 are used; only standard planform design are used, of rectangular or trapezoidal shapes. In particular applications, where higher fin lift is required, a splitted flap of 20-30% cord length is used to reach a higher maximum transversal stabilising moment.

Only in these last two decades, when the use of fin stabilisers has become a standard prescription also for many passenger and merchant ships to assure higher comfort and superior operability in rough seas, the applied hydrodynamic research on this subject registered again a new impulse. The goal, of course, is to improve the hydrodynamic efficiency of the fin (in terms of lift to drag ratio), even if sometimes it is accepted a (limited) efficiency decrement in spite of an higher maximum lift coefficient. For this purpose, various typologies of unconventional fin designs are being proposed in the shipbuilding world, based on different design philosophies.

It is perhaps of help, the attempt made to list all the possible areas of intervention to the increase the lift of a control surface in general from the hydrodynamic point of view, and group all the existing designs under main categories. The following scheme can then be conceived:

modification of the hydrodynamic load along the cord of the fin:

- unconventional high lift profiles
- auxiliary profiles at the L.E. or T.E. of the main profile, such as different kind of slats and flaps

modification of the load along the span of the fin:

- various fin tip devices: end plates, vortex breakers or tip fins
- unconventional design planforms (glove types and others)

boundary layer control:

- fluid blowing
- b.l. suction
- combined effects of vortex generators (V.G.)

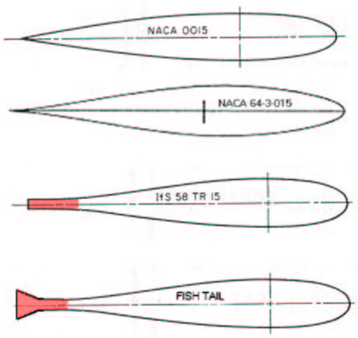

Figure 1: Example of conventional (first two) and non-conventional high lift profiles used for marine stabiliser fins

An example of unconventional high lift profiles with a blunt trailing edge is presented in figure 1, together with two standard NACA profiles commonly used for stabiliser fins. The fish tail profiles (derived as a concept from the IFS profiles) behave very similarly to the flapped profiles, having a steepest slope of the linear part of the lift curve (vs. a.o.a.) and an higher maximum lift of the order 15-20%, in general payed with a lower hydrodynamic efficiency. These profiles are mainly used for retractable fins stabilisers to avoid drag increase and cavitation/noise during normal ship operation.

Fixed T.E. ailerons are also used instead of moving flaps, mainly to give the same kind of effect without the complicated kinematics of the flap. Main disadvantage is the increased drag (and low efficiency) for lowest a.o.a., that can be more than compensated by the advantage of the highest maximum lift reached by the multiple profiles configuration.

Blade tip devices are used in some cases, like anti-vortex fin blades or more classical end plates. They do not increase as much the maximum lift of the fin but do increase the slope of the lift curve (against the a.o.a.) and the efficiency. The obtained reduction of the tip vortex, let the fin have a finite load at its tip and consequent lower induced downwash velocities on the whole fin surface.

An singular example of the application of b.l. control devices to obtain higher fin lift and stabilisation efficiency has been presented by Brizzolara and Calcagno (2000). This concept makes use of vortex generators of wedge or ramp type to delay separation of the turbulent b.l. at the trailing edge of the foil. This lets the lift curve to maintain its linear behaviour up to higher angles of attack and to reach a 10-15% higher maximum lift limit. The hydrodynamic principles and preliminary model test results, in the case of a simple fin configuration, have been presented in the referenced paper.

Hydrodynamic design and analysis methods

Although many example of new hydrodynamic fin design and devices have appeared in this last decade, the hydrodynamic design practice of these control surfaces still rely on direct extensive model tests and on the use of various approximate empirical formulas or data, such as those derived by the experimental works of Whicker & Fehlner (1958), Abbot and Von Doenhoff (1959), Kerwin et Al. (1972), Gregory and Dobay (1973) and others. Simplified analytical formulas, mainly derived by classical aerodynamic theory, are also widely used for the correction of 2D profile data.

Attempts to use modern CFD techniques for the analysis of practical rudder configurations have recently been made by several authors: Soeding (1998) well described the limit of potential flow theory for the analysis of rudder hydrodynamics; El Moctar (1998 and 2001) showed the potential of application of RANSE solvers to the hydrodynamic analysis of rudders, also in the near stall region. The RANSE approach, though, seems to be still a tool for specialised research, being the complexity and time required for the setup of the numerical model of practical 3D configurations, simply not compatible with the usual design time. A comprehensive review on the state of the art of current design methods and feasible CFD approaches is given by Bertram (2000).

The hydrodynamic problem of stabiliser fins is manysided and difficult to be entirely modeled by means of CFD tools: it includes the estimation of maximum lift at stall and the degradation of performance in cavitating environment, as well as the Reynolds scale effects, which are not negligible for both the previous mentioned phenomena.

Trying to provide for all of these phenomena, the author devised a simplified hybrid methodology based on 3D potential flow and 2D viscous numerical simulations. The methodology is detailed in the rest of the paper through an application example of the hydrodynamic design and analysis of fins with unconventional (non-NACA) profiles. Other references about the theoretical and numerical method used for this study and eventual alternative approaches are given along with the sections relative to each modeling case.

Design of fins with unconventional profiles

Profiles with increased L.E. radius for higher maximum lift

The investigations into the mechanism of boundary layer separation made by Prandtl (1928), firstly related the stall phenomenon of wing profiles to the characteristics of the boundary layer developed just up to the separation point. After this first findings, McCoullogh and Gault (1951) experimentally reproduced different types flow separation that are connected with stall of 2D wing profiles. In particular by the observation of a series of model tests on various profiles (NACA series 63) of different shape and thickness, they were able to define three different b.l. separation modes which cause to the stall. The analysis made by Thwaites (1960), well rendered in figure 2, highlighted two major two different types of stall for wing profiles: for thin profiles with $t/c<0.12$, a typical laminar separation bubble is triggered at the L.E. at high angle of attack and gradually proceed up the the T.E. of the profile up to the complete profile stall. In some cases the separation bubble is not able to reattach on the profile back surface, and stall is manifested with an abrupt loss of lift (in few degrees of a.o.a). For thick profiles with $t/c>0.15$ and rounded L.E., on the contrary, the separation usually proceeds from the T.E. up to the L.E. in a gradual manner, causing a typical flat pressure distribution after the separation point and a generalised lowering of the sucking pressure distribution on the back of the profile.

In large ships with draft of 6÷8m sailing at reduced speeds (15 knots) in rough seas, it is easy for the fins to work at high cavitation indexes such as σ_0=5÷6, with a typical operating point close to the maximum lift angles in low cavitating conditions. It is just in these conditions that the fins have to be effective and that usually for dimensioning reason, they are not able to give the necessary lift force to stabilise the ship. Then, increasing the maximum lift in these conditions, could give the opportunity to dimension the fin for higher speeds, while assuring good stabilising efficiency also in extreme sea states at lower speeds, where the fins are moved at their maximum angles of attack.

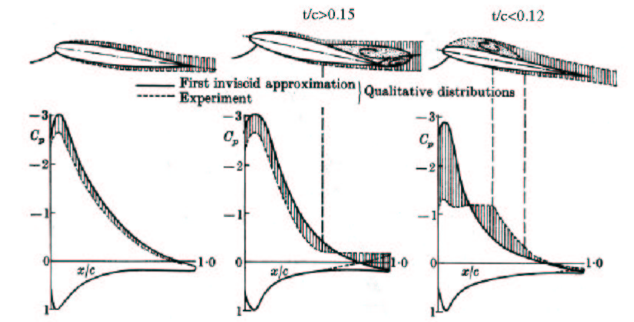

Figure 2: Effect of boundary layer and two types of separation experienced by airfoils (from B. Thwaites, 1960)

Following this requirement, alternative profile shapes to the standard NACA symmetric series were looked for, through a systematic variation of the L.E. radius, necessarily associated with an advancement of the point of maximum thickness over the chord. The modified profiles are presented in figure 3, against the original NACA 4 digit. The idea of having a large L.E. radius is to lower the sharp negative pressure peak at the highest a.o.a. typical of the flat plate pressure distribution; while the reduction in curvature of the sides after the max thickness is to keep the slope of the pressure recovery on the back of the profile (after the peak) as low as possible. The combination of these two effects should imply a delay in the turbulent boundary layer separation at the T.E. of the profile, according to thin boundary layer theory.

The modified profile M5 represent the extreme of the range and it has been added in the figure just for sake of completeness and to better show the adopted design criteria. It has been discarded, though, from the rest of the analysis, since too unpractical, due to its drastically smaller area and moment of inertia.

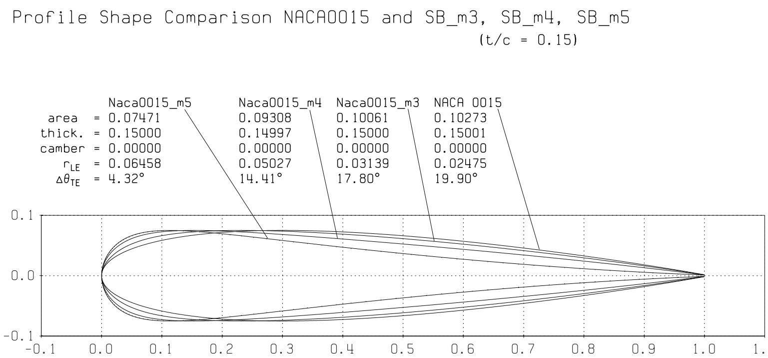

Figure 3: Unconventional profiles with systematic L.E. radius increase plotted against the original NACA0015

Different potential flow methods coupled with thin boundary layer methods has been tested for the analysis of the flow around the profiles. The most effective and reliable one, though, has been found to be that developed by Drela (1989) which is capable of giving accurate results also at the stall point and beyond. The inviscid formulation used in the method by Drela is a standard linear-vorticity panel method based on the stream function solution around the profile, adapted to treat a finite T.E. thickness, by means of an extra source panel. Explicit Kutta condition is imposed at the T.E. The boundary layer and wake are solved using a two-equation lagged dissipation integral b.l. equations (Drela, 1987) that permits to treat also the case of limited regions of separated flow. Transition is predicted with an envelope e^ncriterion, well described, for instance by Cebeci (1999). The viscous-inviscid coupling is performed by means of the transpiration velocity concept (Lightill,

1958) explicitly formulated and brought to convergence by a standard Newton-Raphson scheme. The drag is calculated in the Treffetz plane properly far down in the wake. Drela developed a special method for describing the viscous flow around blunt trailing edges, by which is possible to predict rather accurately the profile base drag (1989).

Another possible tested alternative method is that proposed by Norris (1991), which uses the elegant panel method developed by Kennedy and Mardsen (1977, 1978), conceived to treat multiple profiles, together with a simpler thin boundary layer integral method, based on Thwaites method (1960) and Falkner Skan velocity profile in the laminar region, while the integral method of Head is used in the turbulent b.l region. In his work, Norris proposes some analytical function correlating the integral parameters of turbulent b.l., based on experimental results on several wing profiles made by different authors which are useful in simplifying the calculations. Transition is triggered instantaneously by means of the Cebeci and Smith criterion (1989) which relates the length of the b.l. to the its momentum thickness at the separation point. A simple model for treating T.E. separated, based on very crude assumptions, flows is used by Norris, and permits to run the calculation also beyond the stall, with poor results though. An alternative model which try to reproduce the actual separation bubble at the T.E. of the profile is that proposed by Maskew and Dvorak (1978), which should give better results.

A number of other methods have been developed for the analysis of partially separated flow, such as that of Milgram (1977) based on the potential flow theory and others which only consider viscous-inviscid coupling with no separation, such as that well described by Cebeci (1998).

More recent method, which solve the viscous problem through RANSE modeling, show very good results also in 3D, as for instance shown by El Moctar (1998 and 2001). These models probably will be the future design tool for ship control surfaces, but at the moment their use in the design process is still inhibited by the long time and experience needed to generate good meshes and to set out the model.

The results of two methods were generally in agreement up to the beginning of flow separation, where the more elaborated wake model of Drela showed more realistic results. Interesting feature of the e^ncriterion is that one can play on the exponent coefficient (n) to reproduce the mean turbulence level of the incoming flow. This permits to calibrate the results on the characteristics of the different water or air tunnel turbulent qualities.

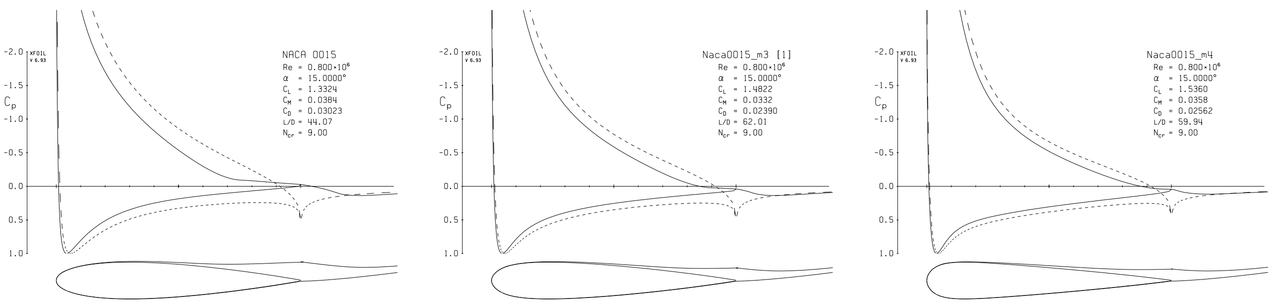

Figure 4: Prediction of viscous pressure distribution over NACA0015 and modified M3 and M4 profiles

An example of calculation, made with Drela's code, is given in figure 4 where the pressure distribution (perfect fluid and viscous flow) and b.l. displacement thickness (also in the wake) is presented at an high a.o.a., and a Reynolds number typical of model tests. From the figure the superior performance of the M4 modified profile at the highest angle of attack is evident: the separated region at the T.E. is almost absent. The displacement thickness at T.E. and in the wake, in fact, is sensibly less for M4 than for the other two. The predicted lift coefficient and length of the separated flow region (on the back of the profile) are ordered with respect to the L.E. radius dimension, as well.

The lift coefficient predicted in the complete angle of attack range and for two different Reynolds numbers representative of the model scale and full scale, is presented in figure 5, while the corresponding polars are given in figure 6.

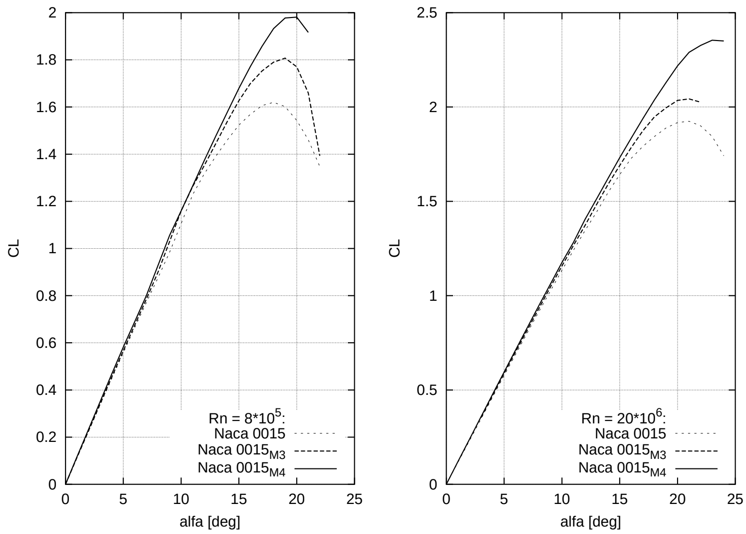

Figure 5: Comparison of the lift coefficients predicted for original and modified profiles at two different Reynolds numbers (model and full scale).

Main results of the calculations are summarised also in table 1 for numerical reference. The comparison show that the M4 modified profile is able to maintain the linear slope of the $C_L - \alpha$, for more than 5° respect to the original NACA 00 profile, achieving an increased maximum lift more than 20% higher in correspondence of a.o.a. about 2 degree higher. Moreover same ranking order and similar lift percentage increases hold in model and full scale for the three profiles, though the absolute values are, of course, different.

In terms of efficiency, the modified profiles pay, as expected, a limited drag increase at the lowest angle of attacks ($0° \div 5°$), while above a $C_L = 0.6$ they maintain the same efficiency of the original NACA 00 profile and overcome it after its deviation from the linear behavior. The substantial differences on efficiency and maximum lift predicted at the two different Reynolds numbers, highlight the caution that should be payed in calculating the corrections factor to extrapolate model test results to full scale (sometimes, the corrections are even not done at all !).

If only the potential flow results are compared, they do not show no appreciable changes in lift prediction connected to the different shapes of the three profile. This fact, again, confirm the importance of considering CFD methods based on viscous flow solution for the prediction of hydrodynamic characteristics of unconventional hydrofoils.

Naturally, considering the approximated numerical models used to solve the boundary layer flow and to schematise the separated regions, the numerical values predicted near the stall should not be taken acritically, while, of course, they can be used to give a ranking of the performance of the alternative designs.

Table 1: Predicted lift coefficients (C_L) for the original NACA profile and the modified ones.

Profile	$C_{Lv}(15°)$	$C_{Lpot}(15°)$	$C_L$max	$\alpha_{C_L max}$	$C_L$max	$\alpha_{C_L max}$
	$Rn = 0.8 * 10^6$		$Rn = 0.8 * 10^6$		$Rn = 20 * 10^6$	
NACA0015	1.33	1.83	1.33	15.0	1.92	21.0
NACA0015_M3	1.48	1.84	1.51	16.5	2.04	21.0
NACA0015_M4	1.53	1.84	1.57	16.5	2.36	23.2

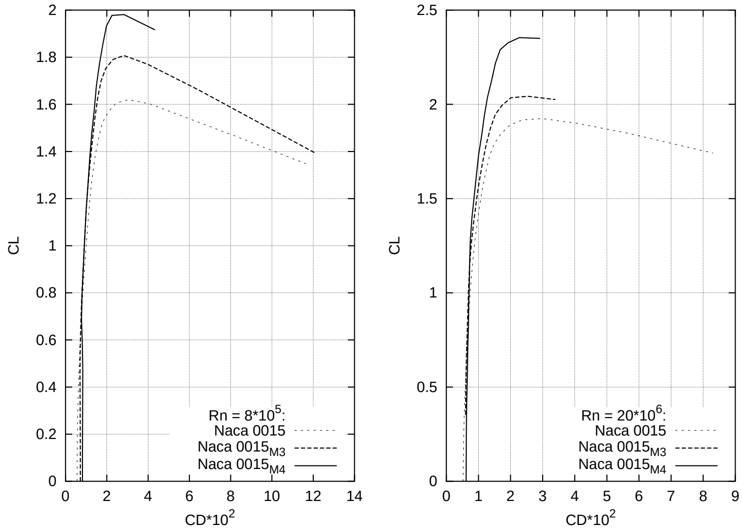

Figure 6: Comparison of the polar of the original and modified profiles predicted at two different Reynolds numbers representative of model and full scale working conditions.

Cavitation analysis

An important issue for the comparison of the hydrodynamic performance of hydrofoils is the different cavitation behaviour. Although in this case the cavitation performance of the profile is not a primary issue with respect to the target working conditions, it is advisable to predict the performance under cavitating conditions or at least to compare the incipient cavitation indexes at various angles of attack.

The simplest assessment of the cavitation limits for hydrofoils can be done comparing the coefficient of minimum relative dynamic pressure at different angles of attack.

Assuming that cavitation instantaneously occurs when the pressure on the profile reaches the water vapor pressure at ambient temperature (considered constant with temperature being two order of magnitude lower than ambient atmospheric pressure), then we can confuse the minimum pressure coefficient on the profile with the cavitation index: $Cp_{min} = \frac{p-p_\infty}{1/2\rho V^2} = -\sigma_0$.

The minimum pressure coefficient vs. angle of attack, calculated by means of the viscous-inviscid method introduced in the previous section, is present in figure 7 for the three different profiles considered in the study, at the two different Reynolds numbers (model and full scale).

As could be expected, the results indicate a better behaviour of the NACA 0015 profile at the lowest angle of attack, respect to the modified profiles that have the maximum thickness advanced towards the L.E.. Following the thin profile theory, in fact, at lower angles of attack the contribution of thickness to the total dynamic pressure has a dominant effect on total pressure distribution. The behaviour, instead, is inverted at the higher angles of attack when the minimum pressure contribution is primarily due to the flat plate (angle of attack) component: for this reason the greater L.E. radius of the modified profiles is able to sensibly effect the magnitude of the negative pressure peak on the back.

Anyhow, the comparison of Cp_{min} can only give a qualitative idea of the cavitation performances of the different profiles, since the existence of a total pressure lower than the vapour pressure on the profiles is not a sufficient condition to justify the actual presence of cavitation on the profile. Cavitation bubbles, in fact, usually need a certain extent of the low pressure region to develop and sustain.

For this purpose the cavitating conditions, in the case of laminar sheet cavitation, has been verified

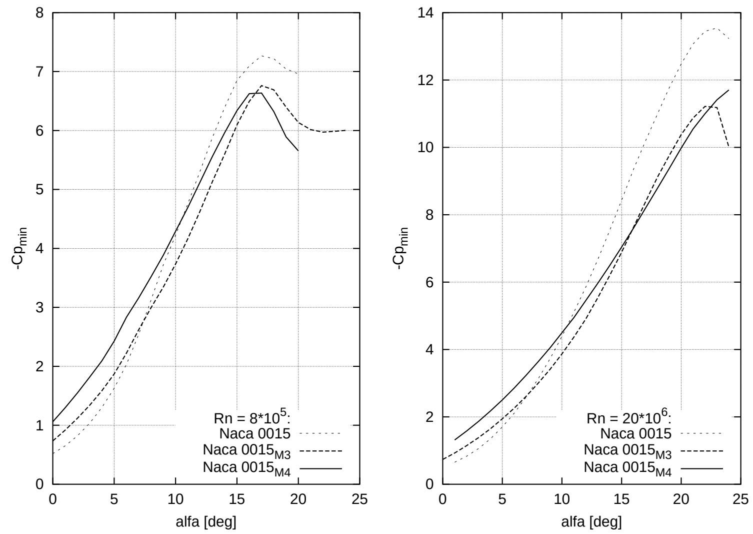

Figure 7: Comparison of the minimum pressure coefficient on the different 2D profiles at various angle of attack and two different Reynolds numbers (model and full scale)

through an ad hoc model. The model, developed by Brizzolara (2002), on the basis of the derivations of Caponnetto et al. (1993) on the original method proposed by Rowe et al. (1991), consider the potential flow around an hydrofoil with an attached laminar cavitation bubble. The solution is achieved by means of a linear boundary element method with constant sources and dipoles distribution over the profile and over the panels on the cavity contour. A kinematic boundary conditions is imposed over the profile and cavity surface (considered as streamlines) and a dynamic condition on the sheet cavity panels (constant pressure equal to the pressure inside the bubble). The pressure in the recovery region behind the cavity is supposed to vary linearly in space, while the Kutta condition at the T.E. is imposed by means of a panel in the wake aligned with the bisector angle of the sharp T.E..

Since the geometry of the cavity is initially unknown, the problem is solved iteratively fixing the cavity length and converging on the actual geometry by realignments of the cavity panels with flow predicted at each iteration. At convergence, then, the cavitation index (pressure coefficient) at which that particular geometry of cavity exists can be indirectly found, together with the inviscid pressure distribution on the cavitating profile and the relative lift force.

Some representative results of the calculations performed with this method are presented in figure 8 to 10, for the NACA 0015 profile and the modified M4, which represent the limit of the considered range of L.E. radius and longitudinal position of maximum thickness. An example of the cavitation behaviour at a lower angle of attack (7.5°) is given in figure 8, where the minor margin to cavitation of the M4 modified profile is evident respect to the original NACA: for an equal cavity length, the predicted cavitation index of the modified profile is higher, as well as the relative dimension (area or height) of the sheet cavity. For a.o.a as much as 15° (figure 9), the cavities predicted on the two profiles at same cavitation index, are similar with a slightly less area for the M4 modified profile. The better behaviour of the modified profile M4 respect to the original NACA one, occurs just at the highest angles of attack as for instance presented in figure 10, in which for the same cavity length the predicted cavitation index of the M4 profile results lower, as well as the cavity area.

It is obvious that the results obtained with the potential flow method for these thick profiles can be regarded only as indicative of the qualitative behaviour of the different profiles in cavitating environment, and a certain uncertainty margins should be considered when the cavity shapes at that particular a.o.a and cavitation index, are compared with model test results. In general, in fact, the prediction of cavitation inception or extent is a very complex phenomenon that should take into account a set of other parameters not considered in this model, such as cavitation nuclei, surface

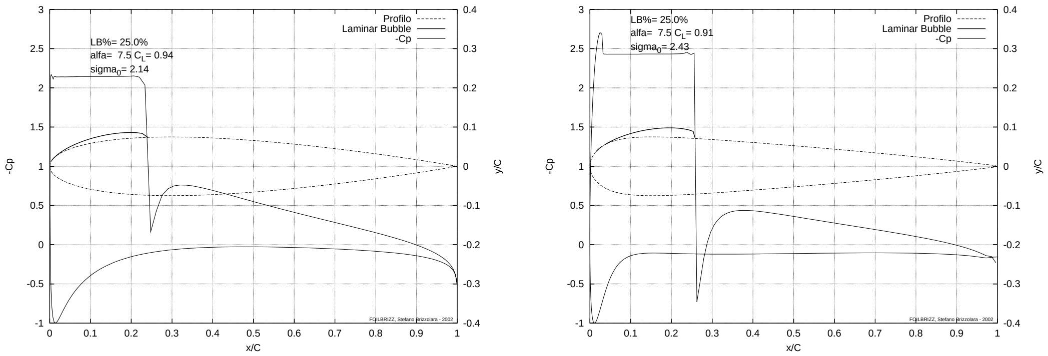

Figure 8: Laminar cavitation bubble predicted for NACA0015 (left) and modified M4 profiles (right) at $\alpha = 7.5^o$and a bubble length (from the L.E.) of 25%.

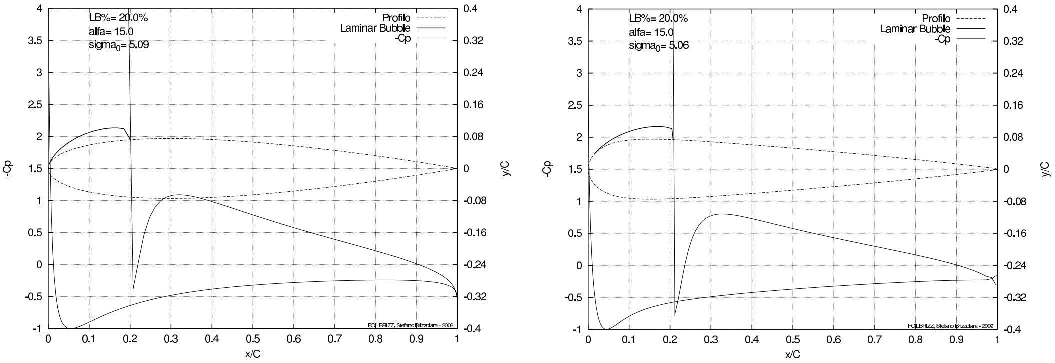

Figure 9: Laminar cavitation bubble predicted for NACA0015 (left) and modified M4 profiles (right) at $\alpha = 15^o$and a bubble length (from the L.E.) of 20%.

imperfections, and viscous effects. Especially in this case, where viscous effects were shown to be the main discriminant for the performance of the different profiles in non-cavitating conditions, it is believed that a method which can take into account also for the viscosity on cavitation development should represent better the reality. The method proposed by Kinnas (1994) could be interesting for this purpose and is currently under investigation.

Lift curve predictions up the maximum value for rectangular fins (with finite A.R.)

Having designed the base profiles for the fin and evaluated their performance in 2D, the designer needs to estimate the hydrodynamic characteristics in 3D, for any considered alternative planform shape. It is moreover clear that the hydrodynamic characteristics at the maximum lift angle need to be considered for the fin's structure dimensioning and actuating system design.

When the hydrodynamic characteristics of a fin of known aspect ratio are known, using classical wing theories it is possible to estimate the characteristics of a similar fin with different aspect ratio. Such theories, though, assume a certain load distribution along the span (as for instance the elliptical load distribution of Prandtl's classic theory) or a fixed planform shape (Glauert, Anderson, etc.) and are usually based on linear lifting line or lifting surface theory, which do usually not consider the effect due to the finite thickness of the profile.

3D panel methods can be considered, nowadays, as a mature design tool for naval architects and offer many advantages respect to the classical lifting line and surface theories. The limits of the application of pure potential flow theory in the case of ship rudders (and fins, for analogy), have been

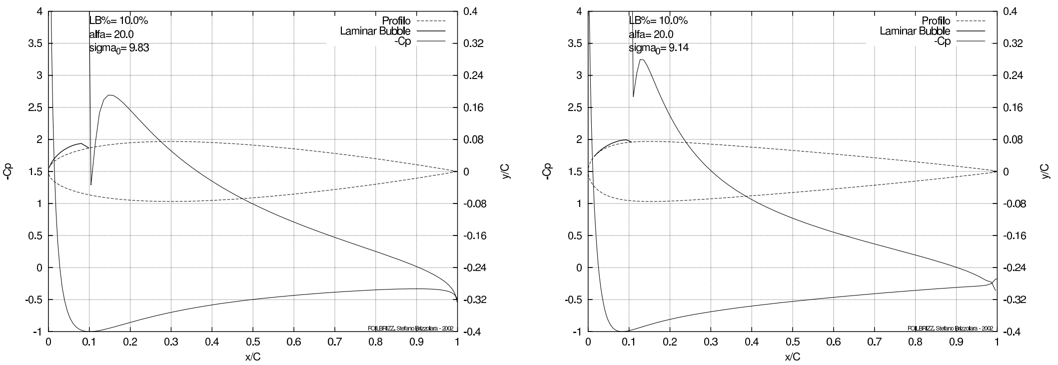

Figure 10: Laminar cavitation bubble predicted for NACA0015 (left) and modified M4 profiles (right) at $\alpha = 20^o$and a bubble length (from the L.E.) of 10%.

well described by Soeding (1998). Also in this case, as for the 2D cases, though, the limitation of the potential flow could be overcome with a coupled inviscid-viscous method. Some examples appeared in the literature, are the method developed by Cebeci (1999), which combine a 3D differential boundary element method to a standard Hess and Smith linear panel method, through the transpiration velocity concept; the method proposed Milewsky (1997) which couple to a low order boundary element method to an integral 3D boundary layer method; or the integral b.l. method developed by Mughal and Drela, which seems a valid alternative to the differential method of Cebeci. The above mentioned 3D boundary layer formulations are conceived for non separated flows, and go in defect in the near-stall region or (the integral b.l. methods) in presence of strong cross flows, such as those experienced near the L.E. of a stabiliser fin. Naturally also in this case the use of RANSE CFD tools could overcome completely the problem.

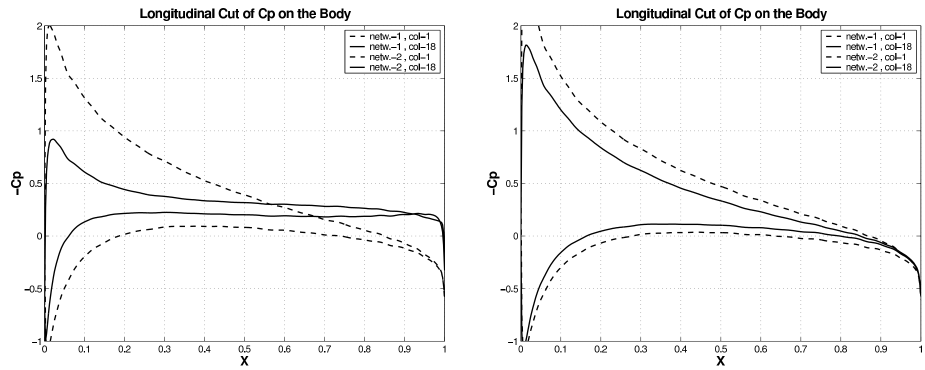

Figure 11: Pressure distribution along the chord of two rectangular fins with AR_g=1.0 (left) e 5.0 (right) at the same position along the span: y/c=0 (col-0) and y/c=0.8 (col-18).

An alternative approximated hybrid method, then, has been devised for the estimation of the 3D characteristics, which requires considerably less resources than a full 3D viscous approach. The method uses the 2-dimensional results of the viscous-inviscid solution for the chosen profile (M4) to correct the results obtained with an inviscid panel method for the 3D fin geometry. The 3D potential flow solver is based on a higher order linear boundary element method, as derived by Johson and Forrester (1980), with non flow-adaptive wake panels.

Rectangular fin planform shapes have been considered in this study, being they widely used for retractable fin arrangements. A systematic variation of the aspect ratio was done for the rectangular fin with NACA0015 base profile for a range of (geometric) $AR_g \in [0.25; 15]$. Some examples of used panel meshes and predicted pressure distribution on the back side of the fins are presented in figure

16. From the figure the gradual loss of negative pressure on the back of the fin due to the tip vortex is well evident. Moreover, the downwash velocity induced by free vortices close to the tip are uniformly distributed along the chord, as verified by the longitudinal cuts of figure 11 operated at two different spanwise position, for fins with $AR_g = 1$ and 5, respectively. This finding allow us to consider each transverse section of the fins as an isolated 2D profile working at an effective angle of attack, in general different from the geometric a.o.a. of the fin.

The normalised sectional lift distribution along the span is presented in the graph of figure 12, for the rectangular fins of different aspect ratios. The sectional lift is found by pressure integration over each longitudinal strip of panels. The panel mesh, in fact, is an orthogonal mesh made up by two family of curves obtained by the intersection of the fin surface with longitudinal and transversal planes. Since the calculations are performed with a linear panel method, the sectional lift coefficient is opportunely normalised by the fin aspect ratio and the total lift coefficient. As can be noted the shape of load distribution along the span varies considerably with the AR of the fin, and in particular cannot be considered to be elliptic at any AR as usually supposed in making 3D corrections.

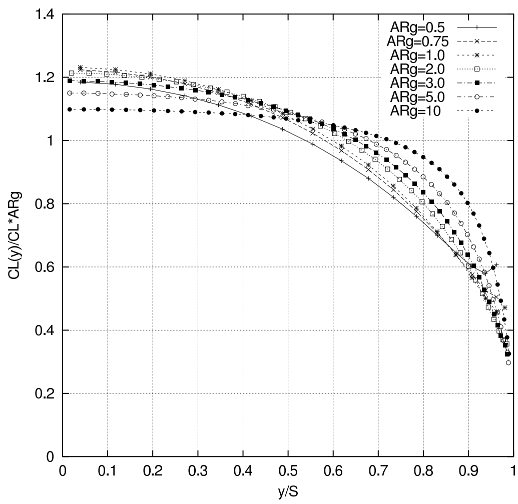

Figure 12: Normalised load distribution along the span for rectangular fins with different geometric aspect ratios (AR_g), calculated on the basis of the 3D linear panel method results.

Especially when the estimation of lift at a certain aspect ratio are based on 2D hydrofoil experimental data or numerical calculations, as in this study, it is important to consider the real shape of 3D load distribution along the span, in our case predicted by the 3D panel method. When the estimation, instead, is performed on the base of available data for fins with aspect ratio similar to that of the target fin, then the error made in confusing the two different spanwise load distributions is negligible.

A good idea of the order of approximation of the different correction methods is given in the graphs of figure 13, in which the results of the 3D panel method calculations have been elaborated in terms of slope of the linear part of the $C_L - \alpha$ curve and compared with the most often used formulas for the A.R. correction of aerodynamic wings and ship motion control surfaces. The linear slope predicted by the 2D inviscid panel method is also included in the figure, as it should represent the asymptotic limit of the 3D panel method for infinite AR. The other formulas plotted for comparison are reported here below for reference (expressed in rad^{-1}):

Glauert formula for rectangular wings: $\partial C_L/\partial\alpha|_{\alpha=0} = a_0/\left[1 + (1+\tau)\cdot a_0/\pi AR\right]$, in which $a_0$is the slope of the linear $C_L - \alpha$ curve for the 2D profile, and τ is a function of the ration AR/a_0, tabulated by Glauert (see Thwaites, 1960).

Jones formula valid for lifting surfaces of very low aspect ratios (A.R.<<1): $\partial C_L/\partial\alpha|_{\alpha=0} = \pi/2 \cdot AR$

Prandtl formula for elliptic wings of high aspect ratio: $\partial C_L/\partial\alpha|_{\alpha=0} = a_0 \cdot \frac{AR}{AR+2}$ (where in place of the theoretical $C_L - \alpha$ slope of 2π for thin wing profile, the numerical slope found for the 2D profile has been used)

Correction formula proposed by Soeding (1998): $\partial C_L/\partial\alpha|_{\alpha=0} = a_0 \cdot AR\frac{AR+0.7}{(AR+1.7)^2}$

Whicker & Fehlner formula: $\partial C_L/\partial\alpha|_{\alpha=0} = \frac{0.9\cdot 2\pi\cdot AR}{\left[\left(\cos(\Lambda)\sqrt{\frac{AR^2}{\cos^4(\Lambda)}+4}\right)+1.8\right]}$, devised on the base of systematic model tests on low aspect ratio tapered fins with NACA0015 profile, and where Λ is the sweep angle of the quarter-chord line. Reference of the works relative to the above formulas can be found in PNA (1989) and Thwaites (1960).

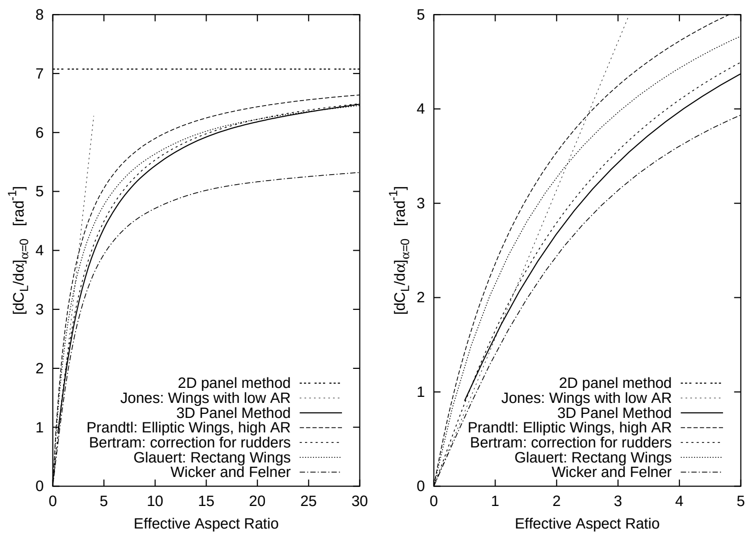

Figure 13: Effect of the effective aspect ratio (ARe) on the slope of the linear part of $C_L - \alpha$ curve. Together with the results predicted with the 3D panel method several classical formulas of wing theory are included for comparison.

The formulas of Glauert and Prandtl seem to overestimate the slope of the lift curve, respect to the panel method and Whicker and Fehlner results, especially at lower aspect ratios. The panel method results seem to better behave, in the mean, in the complete range of considered effective A.R, since they tend to the asymptotic 2D limit for higher aspect ratios (on the contrary of Whicker and Fehlner formula) and they are not so distant as the other theoretical formulas from the experimental results of Whicker and Fehlner for small aspect ratios. Moreover the results of the panel method agree quite well with the formula proposed by Soeding (1998) for the design of rudders, probably derived from potential flow methods as well. It is worth to note that Whicker and Fehlner experiments were all done for fins with base NACA0015 profile and $AR_e = 1 \div 3$, so their formula should not be extrapolated at higher AR.

Moreover the control surfaces of W&F have the same thickness of the profiles considered in this study, but not the same rectangular planform. For this reason a certain difference on the $C_L - \alpha$ curve slope, then, can be accepted, considering also that the formula of W&F is based on model tests results, and implicitly comprehends viscous effects that are obviously neglected in the inviscid panel method. Another possible deviation in the CL curve slope prediction could be due to the non relaxed wake model used in the 3D panel method.

In conclusion, to include viscous effects into the 3D results, and trying to predict 3D lift force up to the stall of the fin, the following approximate methodology is used:

- 2D inviscid and viscous calculations are performed for the fin base profile, up to some point beyond the lift breakdown angle;
- for the 3D fin with a certain aspect ratio and planform design (rectangular, in this case) the inviscid sectional lift distribution (along the span) is found by the 3D higher order linear panel method;
- for each angle of attack of the 3D fin, in the hypothesis of uniform downwash along the chord, the sectional lift coefficient are corrected (at each spanwise location) by viscous effects found in 2D: the sectional 3D potential flow lift coefficient is diminished of the difference found in 2D,

between viscous and inviscid calculations, for the profile working at a (2D) angle, such that the $CL_{2D}^{pot} = CL_{3D}^{pot}(y)$:

- in the hypothesis that the corrections applied to each fin's transverse sections do not affect any other section, the new spanwise load distribution in integrated to calculate the corrected 3D lift at the considered a.o.a.;

Following this calculation procedure, the $C_L - \alpha$ curves of figure 14, for rectangular fins having the modified M4 profile and different aspect ratios, have been predicted for the model scale Reynolds number. A guess of the maximum lift coefficient in non cavitating conditions can be done with this method. Of course the proposed methodology is only a crude approximation of the real flow, since it completely ignores the cross flow close to the fin tip and is stopped at the first order approximation with regards to the downwash velocity induced on the fin surface (or vortex intensities in the wake). The 3D coupled viscous-inviscid methods, previously introduced, overcome to these approximations, but they are not capable of modeling 3D separated flow and consequently not adapted for the estimation of maximum lift. The ultimate solution for this case would be the 3D RANSE modeling of the complete fin.

Another advantage of this approximate hybrid 2D-3D method is that, in principle, it can be used also for the estimation of maximum lift for the fin in cavitating conditions, as will be presented in the next section.

Prediction of lift curves in cavitating environments and comparison with model tests

A model fin with modified M4 profile (t/c=0.15) made of ABS synthetic material with a chord c=170mm and a span of 340mm, rectangular planform and squared tip, is still undergoing the tests in the cavitation tunnel of CEIMM in Rome. The cavitation tunnel of the research institute of Italian Navy (CEIMM) has a squared test section of 600mm x 600mm and a maximum velocity of 12 m/s.

The fin was tested at four different cavitation indexes σ_0: atmospheric (6.5), 4.0, 3.0, 2.0 and 1.0, at a Reynolds number Rn$\simeq 0.80 \cdot 10^6$.

Already in figure 14 the numerical lift curve predicted for non-cavitating condition was compared with the experimental lift curve, derived from model test at an high cavitation index $\sigma_0 = 6.5$.

A first difference that is noted in non-cavitating conditions (figure 14), is that the slope predicted by the numerical calculations results some 10-15% higher of the one found from the model tests. The lower slope of the $C_L - \alpha$ curve of the model tests could be due to the gap (inevitable) existing between the fin root and the tunnel wall that act for a reducing of the effective aspect ratio of the fin or on a overestimation of the slope of the panel method as already pointed out in the previous section.

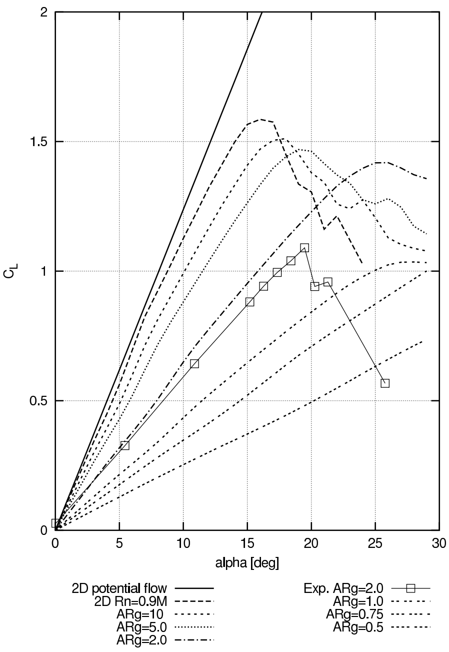

Figure 14: $C_L - \alpha$ curve for rectangular fins with finite AR and modified M4 profile,at model Reynolds number ($0.8 \cdot 10^6$). Experimental values from cavitation tunnel test at $\sigma_0 = 6.5$.

The high cavitation index of 6.5, moreover, is not sufficient to grant that no cavitation develop on the fin, especially at highest a.o.a. The appearance and burst of large cavities on the profile is believed to be responsible of the lower maximum lift experienced in experiments, respect to the non-cavitating predictions. This fact confirms the importance of considering the cavitational limits for the estimation of the maximum lift of stabiliser fins.

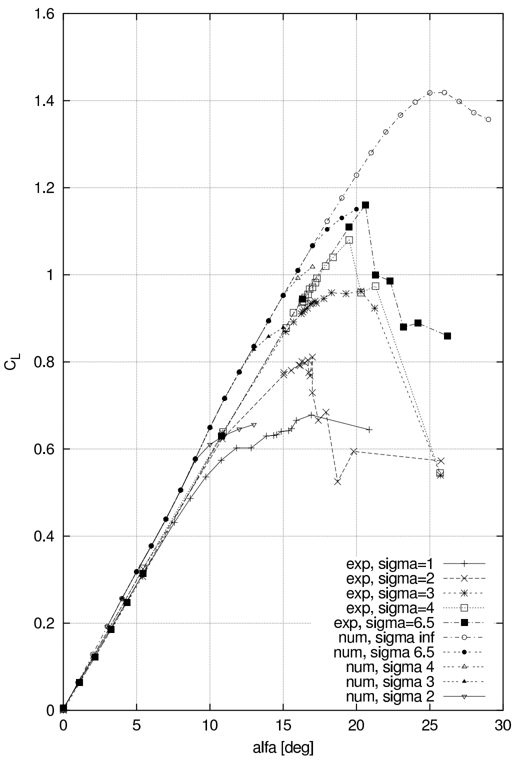

Figure 15: Experimental and numerical lift curves for the rectangular fin with AR_g=2 and modified profile M4, at different cavitation indexes.

For this reason, a procedure for correcting the 3D panel method sectional lift distribution, with the 2D results, similar to the one already introduced for the case of non-cavitating fin, has been devised. In this case, though, in addition to the correction for 2D viscous effects, the 3D sectional lift coefficient is limited by the maximum lift coefficient found at each cavitation index by the potential 2D flow model with laminar sheet cavitation. In particular the 2D potential flow code with sheet cavitation was interactively used to find, for each cavitation number σ_0, the maximum angle of attack and corresponding lift coefficient at which a certain "stable" cavity could be still predicted. This inviscid 2D lift coefficient is assumed as the maximum sectional lift coefficient for the fin in 3D, at the same cavitation index σ_0.

An example of the results obtained with this methodology in the case of the rectangular fin with modified base profile M4 and $AR_g = 2$ is presented in figure 15, together with the corresponding measured lift coefficient in the cavitation tunnel. The point on the lift curve where incipient cavitation occurs, at different σ_0 ranging from 2 to 6.5, predicted by the present hybrid 2D-3D methodology, correlated well to the model tests results. it is believed that the maximum lift coefficient, at the lowest cavitation index ($\sigma_0 < 3$), is influenced by other types of cavitation that are not considered in the devised methodology, which naturally fails to predict the correct value. Anyhow the results that can be obtained by such an approximate methodology are already of great help for the designer. Further improvements at this purpose could be obtained by the adoption of a 2D viscous method with laminar cavitation model.

Conclusions and further studies

A design method for unconventional fin profiles has been presented and tested. The method is used for the design and analysis of fins having profiles with increased L.E. radius respect to the NACA 4 digit profiles commonly used for stabiliser fins, with the aim to obtain higher maximum lift coefficients in non cavitating conditions, i.e. at lowest speed and largest a.o.a. The methodology is based on a numerical inviscid b.e.m. coupled with an integral thin boundary layer formulation, valid also for the near stall region, and a 2D inviscid b.e.m. with laminar sheet cavitation, to design the 2D hydrofoil. Results of 2D calculations are used to correct the 3D results obtained with an inviscid panel method. The unconventional hydrofoils show higher maximum lift, in non-cavitating conditions, but as expected less cavitation margins at the lowest a.o.a. The results obtained through the proposed methodology correlate in a satisfactory manner with model test results. The innovative aspects of the proposed approximate methodology are the inclusion of viscous and cavitation effects for the prediction of 3D hydrodynamic characteristics, with special regards to the maximum attainable lift and the possibility of taking into account the Reynolds scale effects on full scale predictions.

Further research work, still connected with the design of high efficiency fin stabilisers, is foreseen in the following areas:

extension and validation of the design methodology in the case of high lift configurations with multiple profiles, such as auxiliary profiles at L.E. of the fin (slats);

investigation of 3D b.l. methods to be coupled with the currently used inviscid 3D panel method;

2D/3D Cavitation model with non linear viscous effects;

further investigation on the combination of v.g. and unconventional profile design for obtaining higher stabilisation efficiencies at lower speeds.

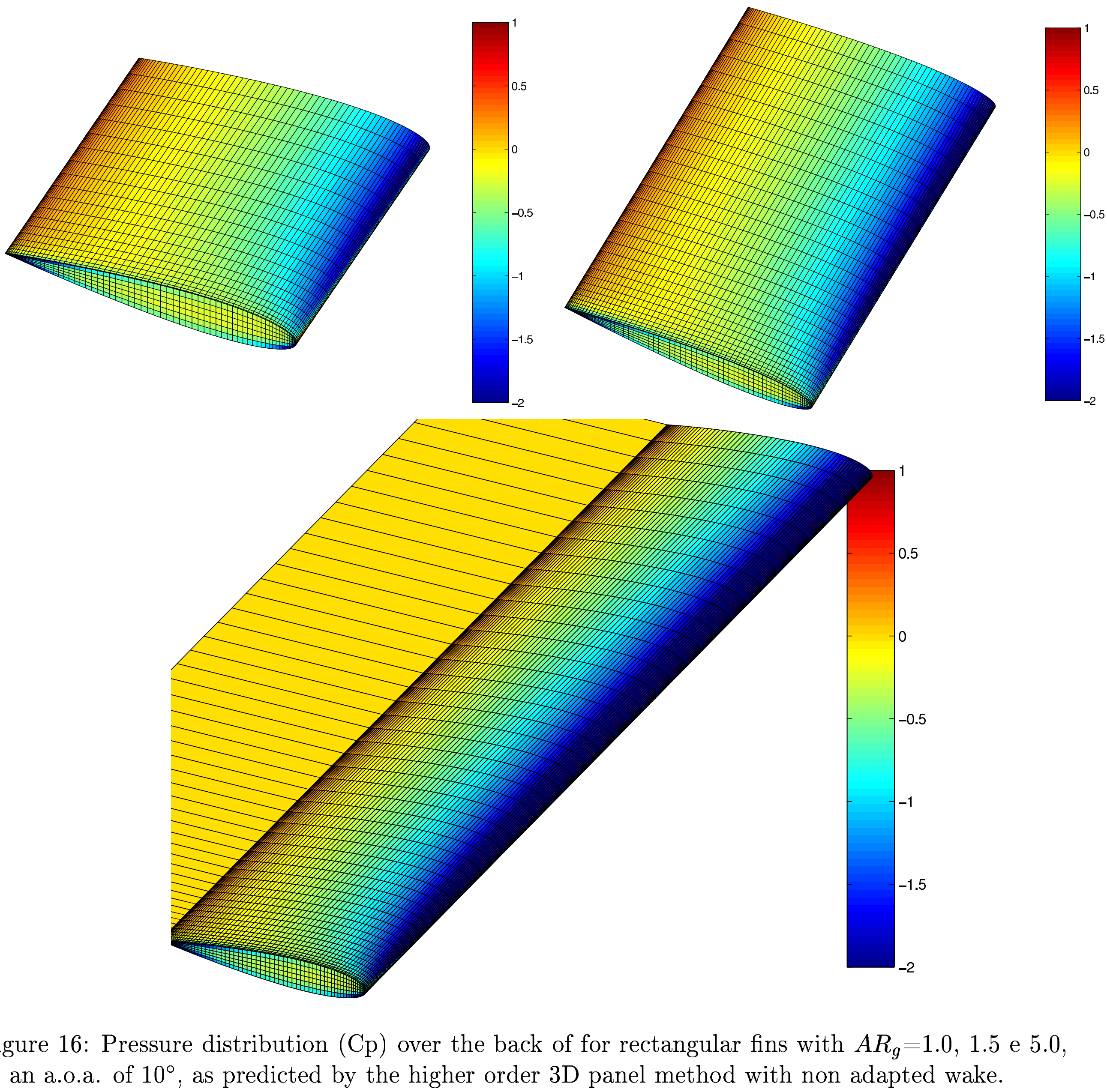

Figure 16: Pressure distribution (Cp) over the back of for rectangular fins with AR_g=1.0, 1.5 e 5.0, at an a.o.a. of 10°, as predicted by the higher order 3D panel method with non adapted wake.

References

KEHOE, J.W., *Destroyer Seakeeping: Ours and Theirs*, Proceeding, U.S. Naval Institute, 99-11, pp.849-864, (1973)

ABBOT, I., VON DOENHOFF, A., *Theory of Wing Sections*, McGraw Hill, 1949, Dover Edition, (1959)

BERTRAM V., *Practical Ship Hydrodynamics*, Buttenworth+Heinemann, Oxford, (2000)

BRIZZOLARA S., *Metodo a Pannelli per la Soluzione del Flusso Attorno a Profili Alari con Bolla di Cavitazione Laminare*, (in Italian) Report DINAV SB-01-02, (2002)

BRIZZOLARA S., CALCAGNO A., *New Types of Roll Fin Stabilisers with Increased Maximum Lift*, NAV 2000, Venezia, proceedings pp. 9.2.1-21, (2000)

CAPONNETTO et al., *Analysis of Partially Cavitating Profiles*, HSMV'93 - Napoli, pp.165-192, (1993)

CEBECI T., *An Engineering Approach to the Calculation of Aerodynamic Flows*, Springer-Verlag, Berlin, ISBN 3-540-66181-6, (1999)

COX G.G., LLOYD A.R., *Hydrodynamic Design Basis for Naval Ship Roll Motion Stabilisation*, SNAME Transaction Vol. 85, pp.51-93, (1977)

DRELA M., GILES M., *Viscous Inviscid Analysis of Transonic and Low Reynolds Number Airfoils*, AIAA Journal, vol.25 no.10, (1987)

DRELA M., *XFOIL an Analysis and Design System for Low Reynolds Number Airfoils*, Conference on Low Reynolds Number Airfoils, University of Notre Dame, (1989)

DRELA M., *Integral Boundary Layer Formulation for Blunt Trailing Edges*, Paper AIAA-89-2200, August (1989)

EL MOCTAR O., *Viscous Flow Computations Around Rudders*, First Numerical Towing Tank Symposium, Hamburg, (1998)

EL MOCTAR O., *Numerical Computation of Flow Forces in Ship Manoeuvring*, Schiffstechnik, vol.48, (2001)

GREGORY D.L., DOBAY G.F., *The Performance of High Speed Rudders in a Cavitating Environment*, presented at SNAME Spring Meeting, Florida, (1973)

JOHNSON F.T., FORRESTER J., *A General Panel Method for the Analysis and Design of Arbitrary Configurations in Incompressible Flows*, NASA CR 3079, May, (1980)

KERWIN J.E., MANDEL P., LEWIS S.D., *An Experimental Study of a Series of Flapped Rudders*, JSR, pp. 221-239, (1972)

KINNAS S.A., MISHIMA S., BREWER W.H., *Non-linear Analysis of Viscous Flow Around Cavitating Profiles*, Twentieth Sympusium on Naval Hydrodynamics, Santa Barbara, (1994)

LEWIS, E. V., editor, *Principle of Naval Architecture - II Edition,* SNAME, (1989)

MASKEW B, DVORAK A., *The Prediction of CL_{MAX} Using a Separated Flow Model*, Journal of the American Helicopter Society, 23(4):1-8, (1978)

McCULLOUGH G.B., GAULT D.E., *Examples of three Representattive Types of Airfoil Section Stall at Low Speeds*, NACA tech. note TN-2502, NACA, (1951)

MILEWSKI M., *Three-dimensional Viscous Flow Calculations Using the Integral Boundary Layer Equations Simultaneously Coupled with a Lower Order Panel Method,* PhD Thesis, Dept. of Ocean Engineering, MIT, (1997)

MILGRAM J. H., *Calculation of Attached or Partially Separated Flow around Airfoil Sections,* Journal of Ship Research, 21(2):69-81, (1977)

MUGHAL B., DRELA M., *A Calculation method for the three-dimensional boundary-layer equations in integral form*, 31st Aerospace Science Meeting Axhibit, AIAA, (1993)

NORRIS S., *Inviscid and Viscous Flow about thin and thick airfoils*, Master Thesis in Applied Mathematics, Univ. of Adelaide, (1991)

ROWE, MENDELSOHN, REBOUL, *Modelisation de la cavitation partielle par la methode du potentiel*, Association Technique Maritime et Aeronautique, (1991)

SAARIS, G., *A502 User's and Theory Manual, Panair Technology Program for Solving Problems of Potential flow about Arbitrary Configurations,* Boeing D6.74503 document, (1992)

SOEDING H., *Limits of Potential Flow Theory in Rudder Flow Predictions*, Proceedings XXII Symposium on Naval Hydrodynamics, Washington, (1998)

SWAFFORD T.W., *Analytical Approximations of Two-Dimensional Separated Turbulent Boundary Layer Velocity Profiles*, AIAA Journal, vol.21, pp. 923-926, (1983)

THWAITES B., *Incompressible Aerodynamics*, Oxford University Press, ISBN 0-486-65465-6, (1960)

WHICKER L.F., FEHLNER, L.F., Free Stream Characteristics of a Family of Low Aspect Ratio, All Movable Control Surface for Application to Ship Design, DTMB Report 933, (1958)

Numerical Prediction of High Speed Catamaran Behaviour in Waves

Dario Bruzzone, Paola Gualeni
Department of Naval Architecture - University of Genova -Italy
bruzzone@dinav.unige.it, gualeni@dinav.unige.it

Abstract

The proposed paper examines the application of a boundary element method for seakeeping computation to catamaran hulls at different separations. After a brief presentation of the methodology, which is based on Rankine sources into the frequency domain, the vertical motions and the added resistance are computed, for a combination of Froude numbers and hull separations in regular head waves. Also the single demihull case is considered. The catamaran investigated in this study was derived from the NPL series by Insel and Molland (1992). A quite comprehensive set of experimental data for seakeeping have been further published by Molland et al. (2000). In addition to evident validation purposes in terms of motion response amplitude operators and added resistance results, emphasis is posed in discussing the particular problem of the effects of interference caused by the reciprocal position of the demi-hulls into the various hydrodynamic problems. To this aim, comparisons at different separations of demihulls are performed for added mass, damping coefficients and exciting forces.

1 Introduction

Multihulls, catamaran vessels in particular, have gathered the interest of ship designers and operators for their specific efficiency in terms of wide transportation capabilities compared with relative propulsion power increase. Since several applications are spread in the passenger and vehicle transportation field, design efforts are devoted to the assessment of the comfort characteristics which are strongly influenced by the vessel behaviour in waves. The distance between demi-hulls is mainly investigated for resistance purposes but the different layout and distribution of weights in comparison to a monohull, together with the interference of the radiated and diffracted wave patterns, could also be of significant influence on motions. Because of this further degree of freedom in the design development, complete experimental investigations in towing tanks is even more expensive than for monohulls and the necessity of a previous investigation by mean of some suitable numerical methodology is more and more evident. Notwithstanding the common application of numerical methods based on the strip theory approach, 3-D methods are in principle more adequate to investigate the matter, since they are able to capture three dimensional effects as the complex wave field caused by the the interference among the radiated and the diffracted waves between the demi-hulls. On the other hand, since this kind of vehicles are often characterized by high speed, Rankine source methodologies, such that exploited for this paper, are able to inherently consider also the speed effects on the free surface boundary conditions. These are neglected into the strip theories, and sometimes also in certain other three dimensional theories. Seakeeping computations for twin hulls catamarans have been the subject of several papers in which motions have been evaluated with a variety of methods. To cite only few more recent examples, Shelling and Rathje (1995) face the problem using a three dimensional method, based on oscillating sources within high frequency and slender body hypotheses, in which the free surface boundary condition is modified accordingly. Bayley et al. (1999) examine the motions of high speed catamarans, the same used for the present paper, using a Green function based on translating pulsating sources. Comparing with the results from pulsating source only and with experimental data, they show the importance of properly taking into account speed effects, also into the free surface boundary condition. Van't Veer (1997) uses a Rankine source methodology showing improvements with respect to strip theory and high-lighting the importance of trim and sinkage corrections. Finally, Kring et al. (1997) present computations for catamarans at different separations and Froude numbers, using a Rankine source method in the time domain.

The method here employed, developed at the University of Genova, has proved its applicability to high speed vehicles in a number of cases and it has been further extended in order to deal also with seakeeping calculation of multihulls. Indeed it has already been verified for the computation of the motions of some high speed mono-hulls of practical interest, both round bilge and deep V types. Its results have been compared with strip theories, other Green function formulations and, where possible, validated with experimental data (Bruzzone et al., 2001). Recently also the added resistance problem for high speed hulls has been tackled (Bruzzone and Gualeni, 2001b).

The increased complexity of catamarans with respect to single hull ships, requires an adequate validation of the extended numerical method. In the case of multihulls not many experimental results are available in the open literature with systematically varied tests, well documented geometries and necessary mass and inertia data, to be used for seakeeping computation. The work of Molland et al. (2000) is a notable exception: after a large set of data regarding resistance of catamarans (Insel and Molland 1992, Molland et al, 1996), very useful experimental results are rendered available regarding seakeeping of some of the previous considered hull forms.

In this paper the adequacy of the proposed methodology to deal also with the motion in waves of catamarans is shown, by comparing its results with some of the cited experimental data. A brief outline of the numerical method is presented in the first section. In the following sections, computed vertical motion response amplitude operators are then presented, compared with corresponding experimental results and discussed also considering the computed hydrodynamic coefficients and exciting forces.

2 Computational method: the physical problem and its numerical solution

A right handed coordinate system is considered, proceeding at the vessel speed U_∞, with the x-axis coincident with the intersection of the symmetry plane of the whole body with the undisturbed free surface and directed afterwards. The z-axis is normal to the waterplane and is positive upwards. Under the hypothesis of incompressible and inviscid fluid the linear potential theory is applied for the solution of the flow, imposing the Laplace equation:

$$\nabla^2 \Phi = 0 \tag{1}$$

with appropriate boundary conditions:

i) a body impermeability condition

$$\nabla \Phi \cdot \vec{n} = \vec{V}_B \cdot \vec{n} \tag{2}$$

being $\vec{V}_B$ the rigid body velocity of a point on the hull wetted surface and $\vec{n} \equiv (n_x, n_y, n_z)$ the outward normal vector

ii) a kinematic condition on the free surface $\zeta = \zeta(x, y)$

$$\frac{\partial \zeta}{\partial t} - \Phi_z + \nabla \Phi \cdot \nabla \zeta = 0 \tag{3}$$

iii) a dynamic condition on the free surface

$$\frac{1}{2} \nabla \Phi \cdot \nabla \Phi + g\zeta + \frac{\partial \Phi}{\partial t} + \frac{p}{\varrho} = \frac{1}{2} \rho U_\infty^2 \tag{4}$$

Finally, a suitable radiation condition must be enforced, in order to ensure the uniqueness of the solution and a proper asymptotic behaviour of the numerical model. The linearisation of the boundary value problem is performed assuming the total velocity potential as the sum of the potential of a steady base flow, here indicated as Φ_S, and of a small perturbation unsteady potential Φ_{US}:

$$\Phi = \Phi_S + \Phi_{US} \tag{5}$$

Further, the unsteady perturbation potential can be written as a superposition of an incident wave potential, a diffraction potential and a set of radiation potentials:

$$\Phi_{US} = \Phi_0 + \Phi_7 + \sum_{j=1}^{6} \Phi_j \eta_j \tag{6}$$

The decomposition of the unsteady potential enables to study the total linearized boundary value problem as the outcome of separated problems, namely a set of radiation problems defined by the potentials $\Phi_{1\div 6}$ and the diffraction problem defined by the potentials Φ_0 and Φ_7.

Assuming $\Phi_j = \phi_j e^{i\omega_e t}$, where ω_e is the enconter frequency, the body boundary condition will be written as:

$$\begin{aligned} \frac{\partial \phi_j}{\partial n} &= i\omega_e n_j + m_j \qquad\qquad j = 1, ...6 \\ \frac{\partial \phi_7}{\partial n} &= -\frac{\partial \phi_0}{\partial n} \end{aligned} \tag{7}$$

where the m_j are the components of the vector $-\vec{n} \cdot \nabla\left(\nabla \Phi_S\right)$ for *j=1-3* and of the vector $-\vec{n} \cdot \nabla\left(\vec{x} \times \nabla \Phi_S\right)$ for *j=4-6*; $\vec{x} \equiv (x, y, z)$ indicates the position vector of a point on the body.

The free surface boundary conditions 3 and 4, after linearization, are combined as follows and are to be enforced on $z = 0$:

$$\begin{aligned} \partial^2\Phi_j/\partial t^2 + g\partial\Phi_j/\partial z + 2\nabla\Phi_S \cdot \nabla\left(\partial\Phi_j/\partial t\right) + \nabla\Phi_S \cdot \nabla\left(\nabla\Phi_S \cdot \nabla\Phi_j\right) + \\ + \tfrac{1}{2}\nabla\Phi_j \cdot \nabla\left(\nabla\Phi_S \cdot \nabla\Phi_S\right) = 0 \end{aligned} \tag{8}$$

Speed effects are intrinsically taken into account through the reference steady potential Φ_S. In the present methodology it may be assumed, at increasing order of approximation as: the free stream potential $-Ux$, the double model potential Φ_D, the steady free surface potential Φ_s.

For the numerical solution of the foregoing boundary value problems, flat quadrilateral panels on which a source distribution of density σ is applied, are adopted on the hull and on the free surface. From the discretization of the mathematical model, the relevant boundary conditions make up a system of N_t linear algebric equations into N_t unknown complex source strength for each radiation problem ($j = 1 \div 6$) and for the diffraction problem ($j = 7$). Three sections of the free surface are considered for the numerical enforcement of corresponding boundary condition: an outer section, a transom section and a inner section. Second order derivatives of the involved potentials are computed through a backward finite difference operator in the longitudinal direction and an outward operator in the lateral direction. Proper radiation conditions must be chosen at the foremost boundaries of each section of the free surface grid. At the outer and the inner sections the wave elevation and it first derivative are assumed null (the method is valid for $U_\infty \omega_e / g > 0.25$); at the forward edge of the section behind the transom it is assumed that the wave elevation is equal to the transom immersion and that its slope is the same of the ship buttocks at the very aft end of the hull.

The consequent independent calculation of the unsteady pressure components allows the evaluation of exciting forces, added mass and damping coefficients that, together with the linear hydrostatic restoring coefficients and with the mass matrix, permits the solution of the system of equations for the determination of ship motions.

The added resistance can be obtained considering time averaged values of second order terms of the longitudinal forces. These may be obtained from a perturbation expansion of the quantities related to the flow around the ship hull. In addition a Taylor's expansion of the pressure around the mean hull and free surface position is considered. In synthesis, the equation for the added resistance may be expressed as:

$$R_{aw} = \overline{R_p} + \overline{R_n} + \overline{R_S} = \overline{\int\limits_{S_H} \delta p\, n_x\, dS_H + \int\limits_{S_H} p\, \delta n_x\, dS_H + \int\limits_{\delta S_H} p\, n_x\, dS_H} \tag{9}$$

which is composed of three second order parts consisting in: quadratic terms of the dynamic pressure (δp), quadratic terms involving variations of the unit normal vector on the hull surface due to ship motions (δn_x), terms involving a differential wetted surface (δS_H) not considered into the first order integrations of pressure forces carried out only on the mean wetted hull surface S_H. After ship motions have been determined, equation 9 may be evaluated; difficulties that arise are mainly numeric. More details of the procedure may be found in Bruzzone and Gualeni (2001b).

3 Applications to a catamaran hull and results

The numerical method has been applied to a catamaran hull at different Froude numbers and hull separations with reference to experimental values drawn out from a systematic investigation available in literature (Molland and al., 2000). The selected form for each demi-hull is the round bilge transom stern from NPL series, which in the cited reference is denoted as model 5b. A representation of the discretised boundary surfaces is given in fig. 1

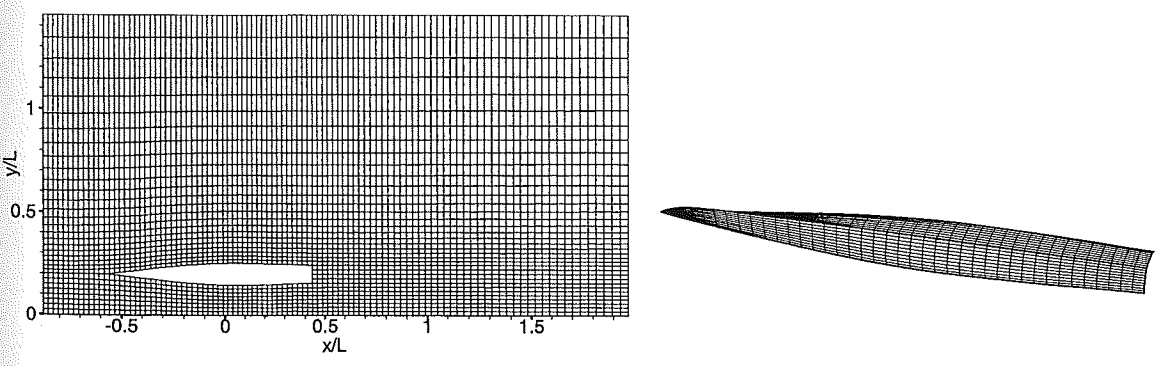

Figure 1: Hull and free surface grids

For Fn=0.5 calculations are presented regarding the monohull and the catamaran at the two separations $s/L = 0.2$ and $s/L = 0.4$. Comparisons with experimental values for the vertical motions are shown in Fig.2. The behaviour of the numerical results is similar for the monohull and for the $s/L = 0.4$ operators, showing a complete agreement with the experimental results for the pitch motion and a not negligible overestimation for the heave motion. On the contrary, for $s/L = 0.2$, a better agreement is shown for heave, whereas differences can be noted on pitch.

In order to put in evidence the influence of the demi-hull separation on the unsteady problem

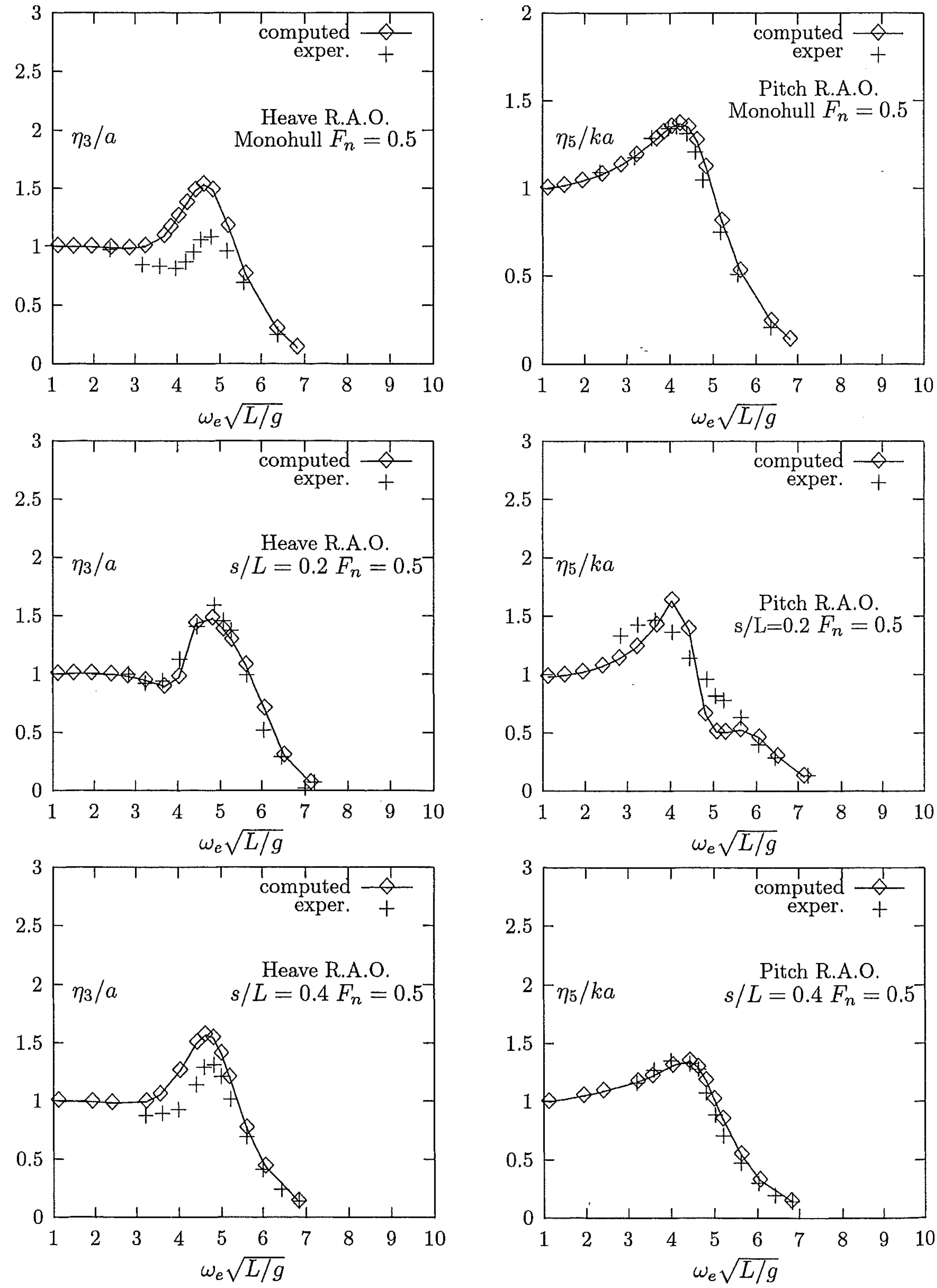

Figure 2: Heave and pitch response amplitude operators

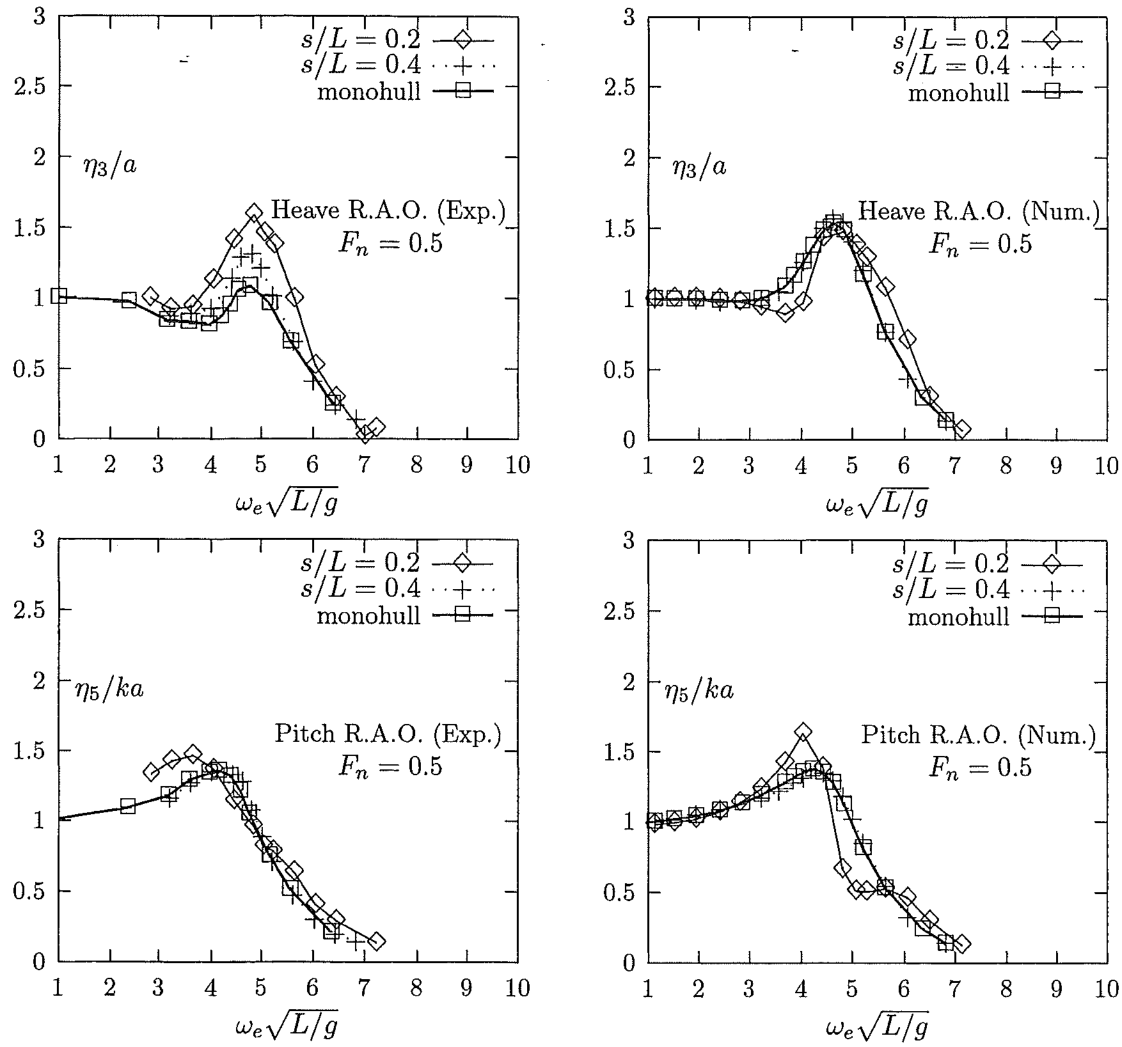

Figure 3: Numerical and experimental R.A.Os at different separations

and the capability of the numerical method to assess different configurations, the results are also presented altogether in Fig.3 for the experimental data and for the relevant numerical calculations. As it can be expected, experimental values for the wider separation are closer to the mono-hull values: in particular, considering the heave amplitude operator, the value of the peak frequency does not change appreciably with separation (due to the same predictable natural frequency) while the amplitude is affected by separation, with the highest value for $s/L = 0.2$. This may be related to a different damping which depends on the different interference pattern of radiated waves. Again, for $s/L = 0.2$, the experimental pitch amplitude operator shows a more pronounced different behaviour in comparison with the mono-hull both in terms of the peak frequency value and in terms of R.A.O. amplitudes. The numerical method seems to capture the peculiar behaviour of the $s/L = 0.2$ separation, especially for the peak frequency values, even if the heave amplitude operator is underestimated at the lower frequencies and the peak value of the pitch amplitude operator is slightly overestimated. A better understanding of the computational results is also possible by means of a comparative analysis of the added mass and damping coefficients and of the exciting forces which are reported in Fig. 4, where it is possible to remark a wavy behaviour of the diagonal terms A_{33}, A_{55}, B_{33} an B_{55} for the lower separation. The effects of the oscillations of the damping coefficient for $s/L = 0.2$ is directly recognizable on the R.A.Os behaviour.

Comparisons with additional experiments reported in the already cited reference, carried out on a

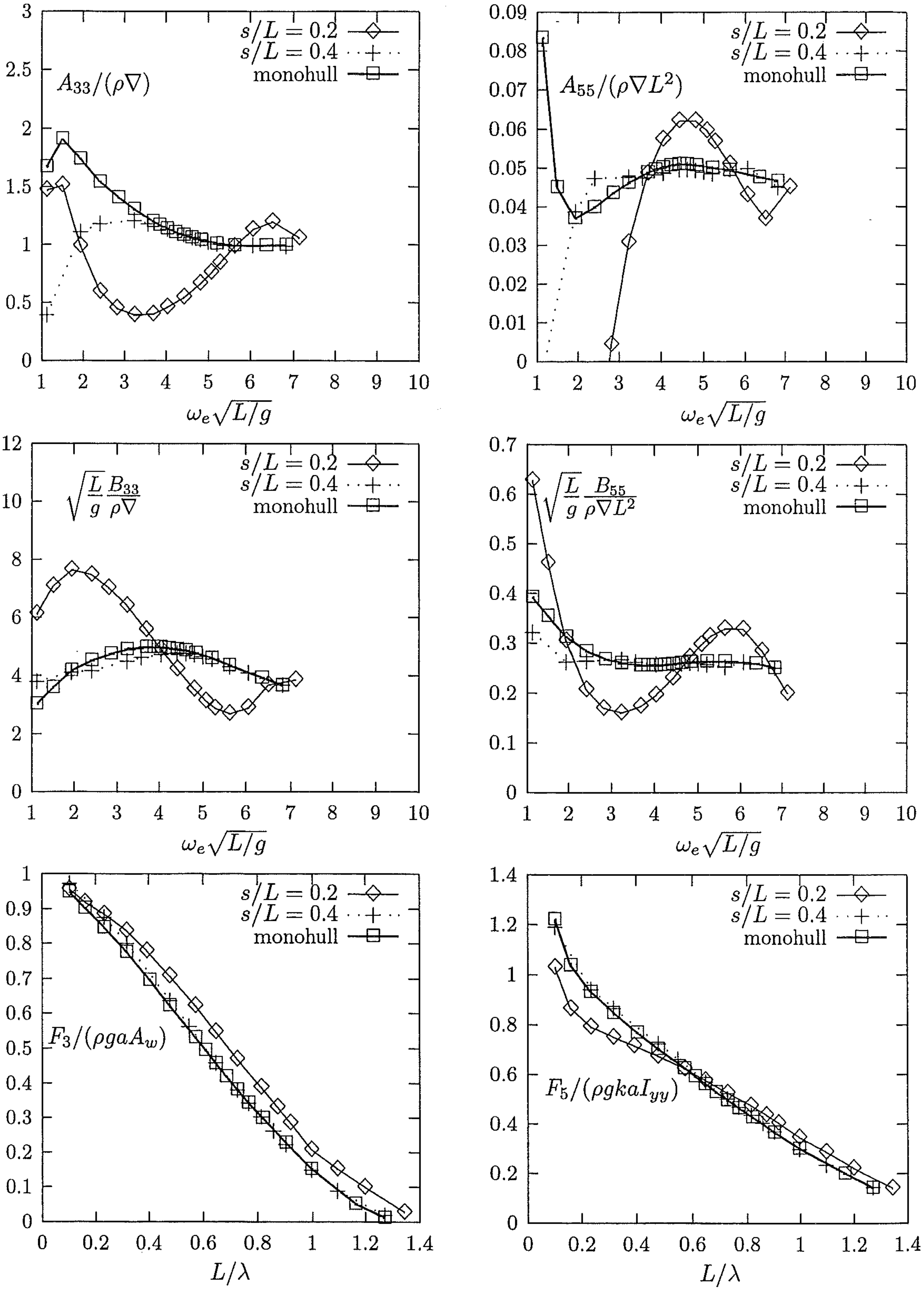

Figure 4: Hydrodynamic coefficients and exciting forces at various separations

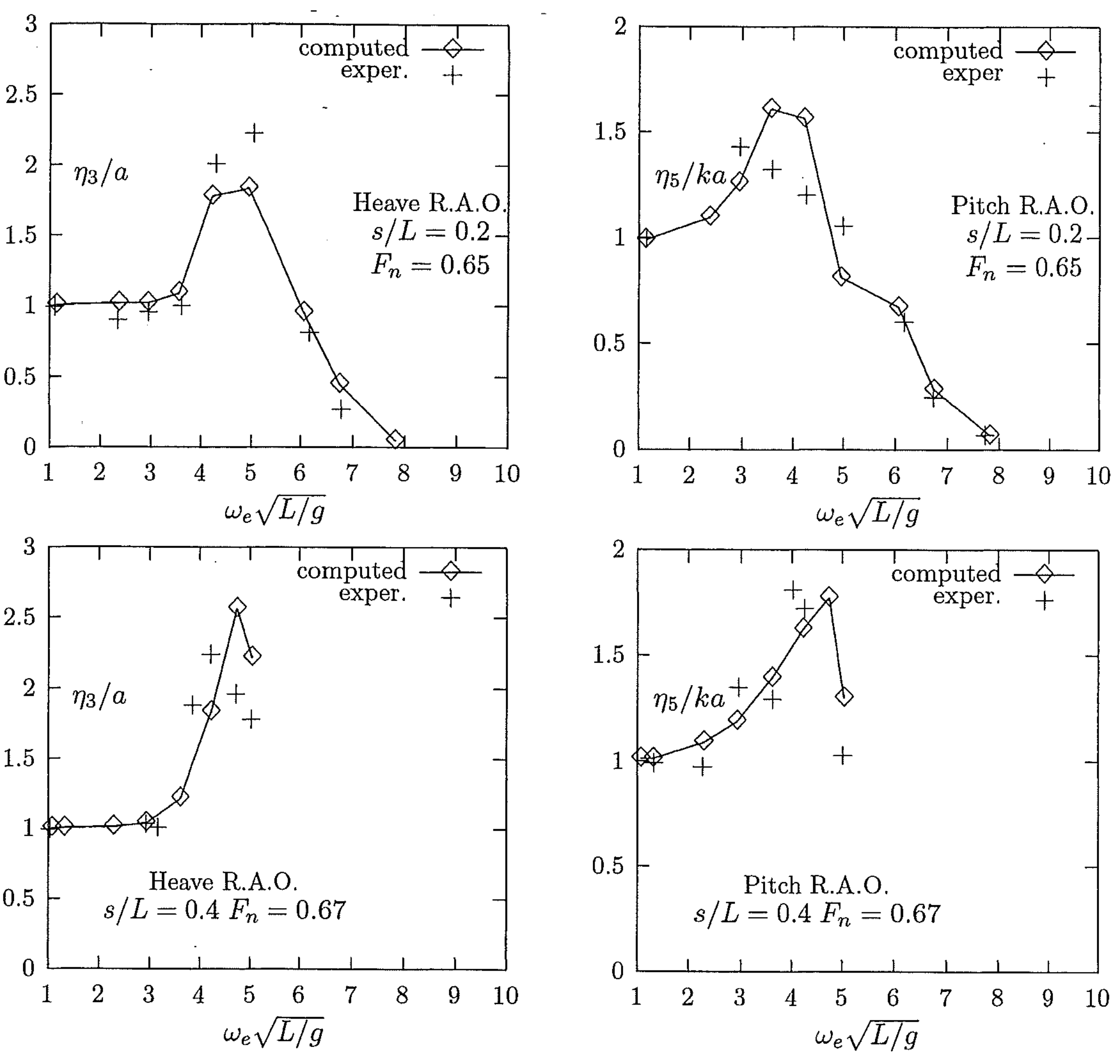

Figure 5: Heave and pitch response amplitude operators

larger scale model at $F_n = 0.65$ and $F_n = 0.67$ for $s/L = 0.2$ and $s/L = 0.4$ respectively, confirm a good performance of the numerical method as far as pitch and heave response amplitude operators in head waves are concerned.

The computation of the added resistance has also been examined with the application of the methodology to the test cases investigated for vertical motions: therefore in Fig. 6 numerical and experimental values are reported for the monohull and the two catamaran configurations s/L=0.2 and s/L=0.4 at Fn=0.5. To compare the relative behaviour of the various configurations, the data have been rendered non-dimensional in a way different from that presented by Molland (2000). This enables to present the results under a sort of interference factor point of view. While the behaviour of the curves related to the monohull are nearly satisfactory, some observations arise from those regarding catamarans: a strong overestimation of the added resistance can be noted for S/L=0.4 at the lower frequencies; in fact, looking at the relevant experimental curve, in that branch the values are definitely lower, even in comparison with the monohull. The numerical results for s/L=0.2 are more satisfactory with the exception of some points which present an overestimation that is, anyway, directly connected with the motion amplitude operators, especially with the pitch one.

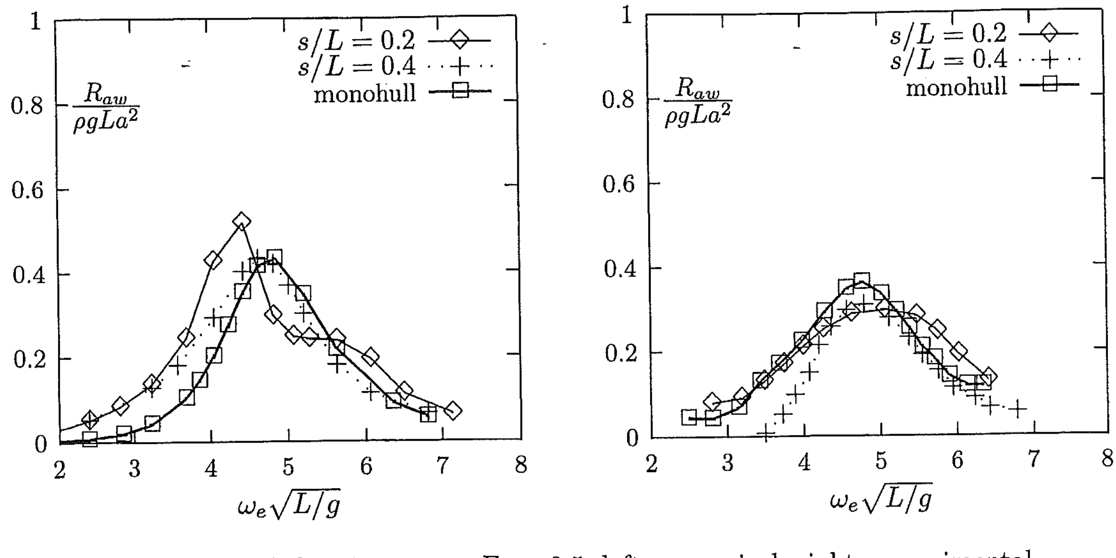

Figure 6: Added resistance at $F_n = 0.5$; left: numerical; right: experimental

4 Final remarks and conclusions

A three dimensional method based on Rankine sources for the evaluation of ship motions in waves has been extended to deal with catamaran hulls. Round bilge catamarans fitted with transom stern have been considered. By comparing with published experimental results, it has turned out that the proposed method delivers adequate results as far as response amplitude operators of vertical motions in head waves are considered. The method has been able to asses the different behaviour due the different configurations considered. Results for added resistance, even if manifesting a plausible behaviour, are more critical and require further applications for their validation. Computations in oblique waves and application to other kind of multihulls (as trimarans) might be a natural extension of this research.

5 References

BAILEY P.A., HUDSON D.A., PRICE W.G., TEMAREL P.(1999) *Theoretical and Experimental Validation of the Seakeeping Characteristics of High Speed Mono- and Multi-hulled Vessels* Proc. of the 5th International Conference on Fast Sea Transportation FAST 1999, Seattle, pp.429-441

BRUZZONE D., GUALENI P. (2001), *Different Three Dimensional Formulations for Evaluating Forward Speed Effects in Seakeeping Calculations of High Speed Hulls* Proc. of the 6th International Conference on Fast Sea Transportation FAST 2001, Southampton, vol. II, pp.235-241

BRUZZONE D., GUALENI P. (2001b), *Added Resistance in Waves for Ships and High Speed Marine Vehicles* 14th Int. Conf. on Hydrodynamics in ship Design, Szczecin Miedzyzdroje, pp.291-300

INSEL M. and MOLLAND A. F. (1992), *An Investigation into the Resistance Components of High Speed Displacement Catamarans.* Transactions of the Royal Institution of Naval Architects, Vol. 134, , pp. 1-20

KRING D. C., MANTZARIS D.A., TCHEU G.B., SLAVOUNOS P. D. (1997) , *A Time-Domain Seakeeping Simulation for Fast Ships* Proc. of the 4th International Conference on Fast Sea Transportation FAST 1997, Sydney, vol. I, pp.455-461

MOLLAND A. F., WELLICOME J. F., COUSER P.R. (1996), *Resistance Experiments on a Sys-*

tematic Series of High-Speed Displacement Catamaran Forms: Variation of Length-Displacement Ratio and Breadth-Draught Ratio Transactions of the Royal Institution of Naval Architects, Vol. 138, , pp. 59-71

MOLLAND A. F., WELLICOME J. F., TEMAREL P., CIC J. and TAUNTON D. J. (2000), *Experimental Investigation of the Seakeeping Characteristics of Fast Displacement Catamarans in Head And Oblique Seas* Transactions RINA, vol. 142.

SCHELLIN T.E., RATHJE H. (1995), *A Panel Method Applied to Hydrodynamic Analysis of Twin-Hull Ships* Proc. of the 3th International Conference on Fast Sea Transportation FAST , Lubeck-Travemunde, vol II, pp.905-915

Vant't VEER R. (1997) *Analysis of Motions and Loads on a Catamaran Vessel in Waves* Proc. of the 4th International Conference on Fast Sea Transportation FAST 1997, Sydney, vol. I, pp.439-445

Identification of Hydrodynamic Coefficient from Standard Manoeuvres

Roberta Depascale, CETENA, Genova/Italy, roberta.depascale@cetena.it
Mauro Elefante, MARICOGECAP, Roma/Italy, cp4rep@libero.it
Luca Sebastiani, CETENA, Genova/Italy, luca.sebastiani@cetena.it
Massimo Soave, MARISTAT CEIMM, Roma/Italy, ceimm@insean.it
Michele Viviani, FINCANTIERI Naval Business Unit, Genova/Italy, michele.viviani@fincantieri.it

Abstract

The purpose of the present paper is to outline a procedure for the identification of the hydrodynamic coefficients from experimental data, either full-scale or model-scale, on standard zigzag and turning circle manoeuvres. To this end a ship was selected for which experimental results from PMM model-scale tests and standard manoeuvres from full-scale tests were available and two sets of standard manoeuvres were considered, zigzag and turning circle. The most influent hydrodynamic coefficients (resulting from an initial sensitivity analysis) were the unknown parameters for the identification procedure. This procedure was based on the iterative use of our manoeuvring simulation program (SIMSUP) within the framework of a numerical optimization package (FRONTIER), having as objective to be minimized an error function made up of the main parameters of the two manoeuvres. The proposed identification procedure allows to refine the predictions based on the preliminary estimation of the coefficients through the regression formulas incorporated in SIMSUP, even if it was not yet possible to identify univocally a pre-determined set of hydrodynamic coefficients. Among the benefits of the proposed procedure is the feasibility to exploit any available experimental data-base of standard manoeuvres in order to extract a set of hydrodynamic coefficients, ready to be used for computer simulations or to build up regression formulas.

1. Introduction

The manoeuvrability of ships has increasingly grown in consideration in the last decade. A first step has been made with the adoption by IMO of the RESOLUTION A.751(18) in 1993 [1] and will be probably followed by new regulations (especially for naval vessels). In some particular fields, such as ships that carry dangerous loads, high speed crafts and passenger ships, it is likely that the requirements will become more restrictive. A reliable preliminary estimation of ship manoeuvring behaviour is therefore strongly needed. On the other hand the performances of the existing prediction tools are critically related to the accuracy in the determination of the hydrodynamic coefficients that specify the mathematical model of ship manoeuvring.

These coefficients are usually estimated from regression formulas [2] [3] [4] based on existing model-test data, which may lead to inaccurate predictions of the manoeuvring abilities of the ship in the case of non-conventional vessel or whenever the ship under examination exceeds the parametric range of the experimental data base, which is the case for High Speed Vessels. Presently the only alternative viable to the designer is to perform an extensive (and expensive) campaign of captive model tests, often not feasible in a preliminary stage of the design.

Therefore the object of the present study was the research of a procedure for the identification of hydrodynamic coefficients (at least the most influent ones) included in ship's motion equations, on the basis of experimental results, both in model and full scale.

In the past system identification techniques were applied in order to evaluate the coefficients from the free running manoeuvres. In [5] and [6] the authors used Extended Kalman Filter analyzing zigzag and turning circle manoeuvres. Other recent works have analyzed the application of different filtering techniques, the possible changes in the model used and the introduction of different trials [7].

For the present analysis a ship for which experimental results obtained with model free running and captive (PMM trials), and with sea trials are known was assumed; in particular the standard manoeuvres were considered, i.e. zigzag and turning circle, that are usually object of experimental tests. A procedure based on these manoeuvres is of particular interest because CETENA has got an experimental data-base of more than 400 ships from which very valuable data could be extracted.

The software utilized for this study is the simulation program for surface ships SIMSUP developed by CETENA linked with the program of numerical optimization FRONTIER developed by EnginSoft.
At first a sensitivity analysis was conducted in order to identify the coefficients that are more influent in ship's motion and these coefficients were the object of the following identification.
The procedure of optimization was based on the minimization of the error function made up of the main parameters of the two manoeuvres analyzed.

2. Programs utilized

Before explaining the procedure used, in the following paragraphs a description of the software utilized is reported.

2.1. Simulation program

The simulation program SIMSUP [8] [9], developed by CETENA, is capable of determining the ship manoeuvring characteristics in various functioning condition, taking into account also the influence of environment (i.e. wind, sea, current, shallow water)
The program allows to perform manoeuvrability simulations for surface ships with four degrees of freedom (surge, sway, yaw and roll) under the action of propulsion and steering system.
The simulation program SIMSUP has a specific calculation module which, on the basis of the characteristics of the ship, by means of statistical regression formulae developed by SSPA [4] on a great number of hulls tested at the PMM, permits to determine the hydrodynamic derivative coefficients.
In the following, a brief description of the mathematical model used is reported, with reference only to the equation of surge, sway and yaw since in this study the roll motion is neglected.

The mathematical model is obtained from the usual motion equations:

$$
\begin{aligned}
&m\left(\dot{u} - vr - x_G r^2\right) = X \\
&m\left(\dot{v} + ur + x_G \dot{r}\right) = Y \\
&I_{zz}\dot{r} + m x_G\left(\dot{v} + ur\right) = N
\end{aligned}
$$

where X, Y, N are forces and moment due to the hydrodynamic effect on the hull and to the propeller and rudder actions.
In particular, the forces and moment acting on the hull and generated by the rudder are expressed using an expansion in Taylor series of second and third order respectively [10] corrected in order to take into account some effects, such as the interaction between propeller and rudder, in accordance with SSPA mathematical model [4].

The employed mathematical model was validated through an extensive theoretical-experimental correlation analysis for single [11] and twin-screw ships with one or two rudders [12] (for conventional merchant ship hull forms).

2.2. Optimization program

FRONTIER is a software system for multi-objective optimization by EnginSoft, Trieste [13], which can be used as a platform for the management of all calculations associated with an optimization process. It manipulates the input files used to execute outside software tools in batch-mode, launches this program in a concerted manner and scans the output files produced during each run for desired data (for instance the current value of an objective function).

Between all the available solving algorithms offered by FRONTIER the following two are used in the present study:

- DoE Design of Experiments: with this algorithms the objective function can be calculated with different combination of input parameters given arbitrarily by the program (following certain rules) or chosen directly by the user;
- MOGA Multi Objective Genetic Algorithm: given an initial population of input data by the user, this algorithm makes a selection in order to find the population that solves better the optimization problem; the algorithm proceeds iteratively until convergence is reached.

The algorithms can be executed sequentially in any meaningful order to benefit to the specific features of each of them; the procedure utilized in the study is described in the following paragraphs.

2.3. Linking of the Programs

The flow diagram reported in figure 1 can represent, very simply, the scheme used to link the two programs.

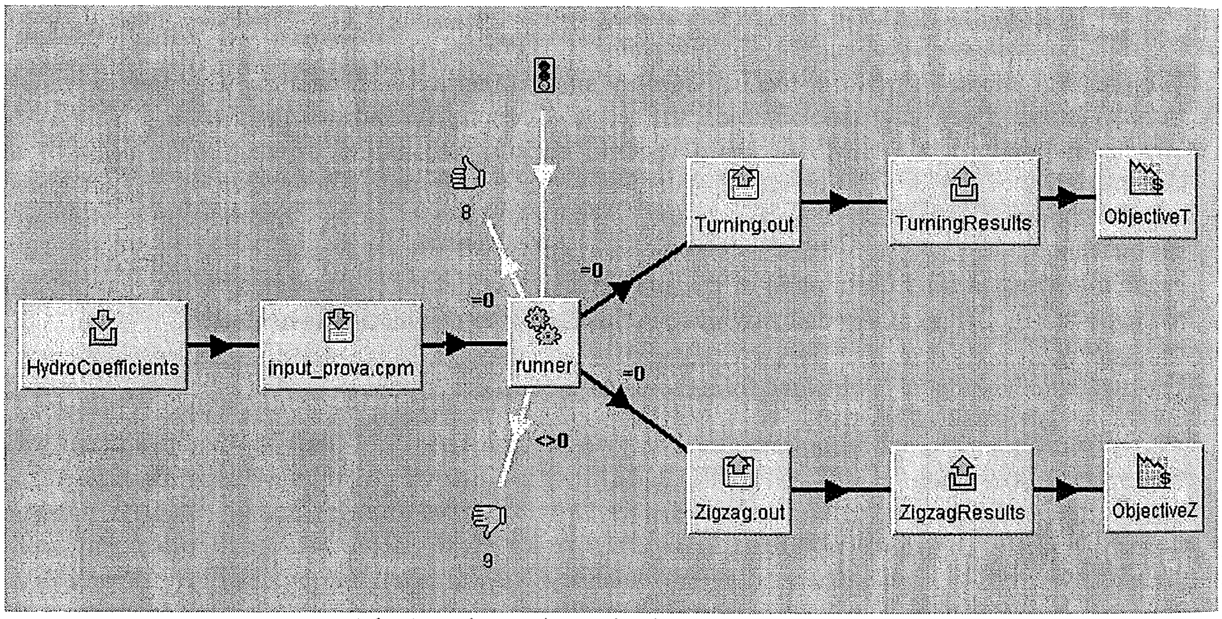

Fig.1 – Simsup/Frontier interface scheme

Reading the flow-diagram from left to right there are the following blocks:

- "HydroCoefficients": represents the blocks corresponding to hydrodynamic coefficients given in input;
- "input_prova.cpm": is the file containing all the hydrodynamic coefficients in the usual format as utilized by SIMSUP;
- "runner": this command starts the execution of SIMSUP in the version linked to FRONTIER;
- "Turning.out" and "Zigzag.out": are the output files respectively of turning circle and zigzag manoeuvres;
- "TurningResults" and "ZigzagResults": represent respectively the blocks corresponding to the output macroscopic parameters typical of turning circle and zigzag manoeuvres;
- "ObjectiveE" and "ObjectiveZ": are respectively the objective functions of turning circle and zigzag manoeuvres defined in different ways depending on the different application of the procedure (sensitivity analysis or identification).

3. Procedure followed

3.1. Sensitivity analysis

Sensitivity analysis was developed to identify the hydrodynamic coefficients that are more influent on the typical parameters of standard manoeuvres.
In particular, for the ship selected for the analysis, a 10°/10° zigzag and a 35° turning circle manoeuvres were considered.
In order to identify the most influent coefficients for turning circle and zigzag manoeuvres the procedure adopted is the following.

At first the following hydrodynamic coefficients were estimated using SIMSUP internal regression formulae:

Xvr, Xvv, Xdd, Xudot, Yv, Yuv, Yr, Yur, Yvmodv, Yvmodr, Yrmodr, Yd, Yddd, Ytd, Ytddd, Yntd, Yntddd, Yvdot, Yrdot, Nv, Nuv, Nr, Nur, Nvdot, Nrdot.

where, in general:

$$Y_v = \frac{\partial Y}{\partial v}$$

where:

u	is the surge velocity
v	is the sway velocity
r	is the yaw velocity
$d = \delta$	rudder angle

$$\text{Xudot} = X_{\dot{u}} \qquad \text{Yvdot} = Y_{\dot{v}}$$
$$\text{Yvmodv} = Y_{v|v|} \qquad \text{Yrdot} = Y_{\dot{r}}$$
$$\text{Yvmodr} = Y_{v|r|} \qquad \text{Nvdot} = N_{\dot{v}}$$
$$\text{Yrmodr} = Y_{r|r|} \qquad \text{Nrdot} = N_{\dot{r}}$$

and where Ytd, Ytddd, Yntd and Yntddd are used to take into account the interaction between rudder and propeller.

Using these coefficients a first simulation of the studied manoeuvres was performed, collecting the main parameters.

The following step consisted in a series of simulations assuming each time a variation of 10% or 20% of one hydrodynamic coefficient in order to identify its influence on the objective functions defined later; the resulting combinations of coefficients were used as input data for a Design of Experiment.
By the use of the mentioned algorithm, for each manoeuvre the value of the merit function was calculated; analyzing the results obtained it is possible to identify the coefficients that influence more ship's motion.

The objective functions utilized are written down for the two different manoeuvres considered.

For turning circle manoeuvre:

$$\left|\frac{A-A_S}{A_S}\right|+\left|\frac{T-T_S}{T_S}\right|+\left|\frac{D_T-D_{TS}}{D_{TS}}\right|+\left|\frac{D_F-D_{FS}}{D_{FS}}\right|+\left|\frac{V_R-V_{RS}}{V_{RS}}\right|+\left|\frac{T_{90}-T_{90S}}{T_{90S}}\right|+\left|\frac{(T_{180}-T_{90})-(T_{180S}-T_{90S})}{(T_{180S}-T_{90S})}\right|$$

with:

A = Advance;
T = Transfer;
D_T = Tactical Diameter;
D_F = Steady Turning Diameter;
V_R = Final Rotative Velocity;
T_{90} = Time corresponding to 90° change in the path;
T_{180} = Time corresponding to 180° change in path.

For zigzag manoeuvre:

$$\left|\frac{A_1-A_{1S}}{A_{1S}}\right|+\left|\frac{T_{e1}-T_{e1S}}{T_{e1S}}\right|+\left|\frac{(T_{O1}-T_{e1})-(T_{O1S}-T_{e1S})}{(T_{O1S}-T_{e1S})}\right|+\left|\frac{A_2-A_{2S}}{A_{2S}}\right|+\left|\frac{(T_{e2}-T_{O1})-(T_{e2S}-T_{O1S})}{(T_{e2S}-T_{O1S})}\right|+$$

$$+\left|\frac{(T_{O2}-T_{e1})-(T_{O2S}-T_{e1S})}{(T_{O2S}-T_{e1S})}\right|+\left|\frac{A_3-A_{3S}}{A_{3S}}\right|+\left|\frac{(T_{e3}-T_{O2})-(T_{e3S}-T_{O2S})}{(T_{e3S}-T_{O2S})}\right|+\left|\frac{(T_{O3}-T_{e3})-(T_{O3S}-T_{e3S})}{(T_{O3S}-T_{e3S})}\right|$$

with:

T_e = Time of rudder execution (1^{st}, 2^{nd}, 3^{rd});
T_O = Time required for yaw checking (1^{st}, 2^{nd}, 3^{rd});
A = Overshoot yaw angle (1^{st}, 2^{nd}, 3^{rd}).

In both the expressions the subscript "S" identifies the values of the parameters considered as obtained from the first calculation made by SIMSUP program with the initial hydrodynamic coefficients.

The results obtained can be illustrated by diagrams (Figures 2, 3, 4, 5) where each slice represents the coefficients which variation gives a deviation on objective function greater than 2%; other coefficients are grouped and indicated with "others".
It is to be noted that the deviations are "normalized" in order to obtain 100 as sum of the all percentages (so the error indicated with 2% doesn't represent effectively an error of 2% but only the relative importance of the coefficients); therefore, the values reported on the resuming diagrams are:

$$err_{normalized}(i)=\frac{err(i)}{\sum_{j=1}^{n} err(j)}$$

Analyzing the diagrams reported the most influent coefficients for each manoeuvre can be resumed as follows:

For turning circle manoeuvre: Yd, Nr, Nv, Yr, Yv, Yddd,

For zigzag manoeuvre: Nr, Yd, Nv, Yv, Nur, Yr, Nrdot

Manoeuvre: 35° Turning Circle

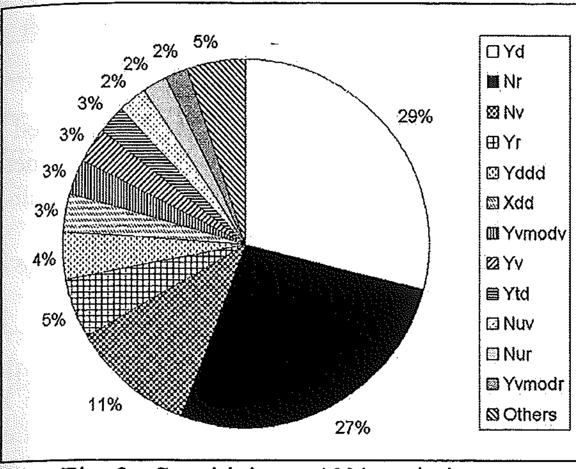

Fig. 2 - Sensitivity to 10% variation of each hydrodynamic coefficient

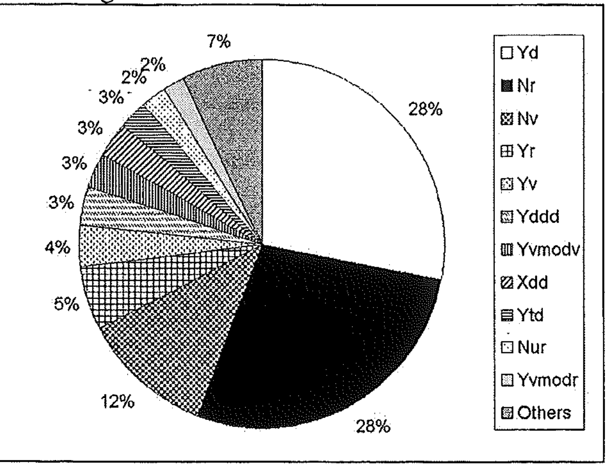

Fig. 3 - Sensitivity to 20% variation of each hydrodynamic coefficient

Manoeuvre: 10°/10° Zigzag

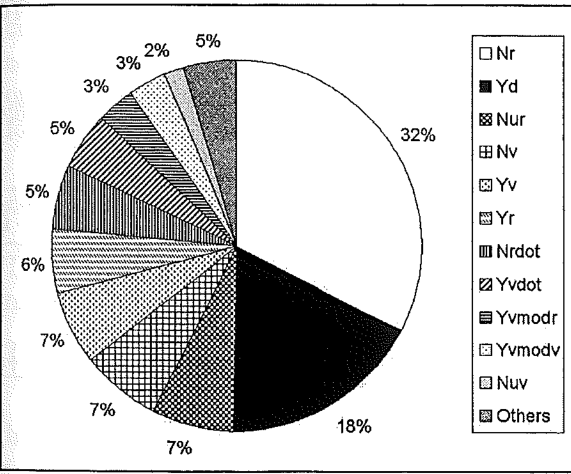

Fig. 4 - Sensitivity to 10% variation of each hydrodynamic coefficient

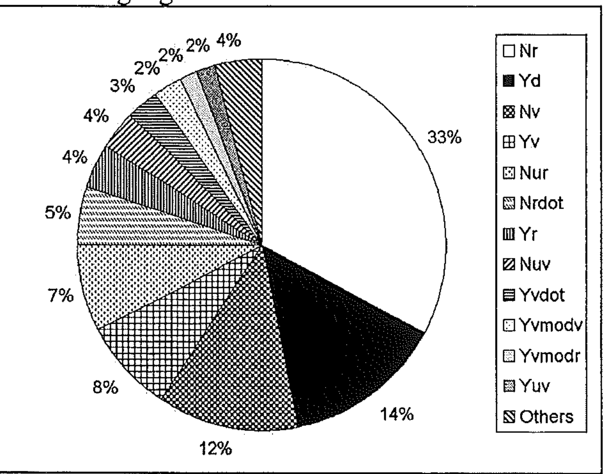

Fig. 5 - Sensitivity to 20% variation of each hydrodynamic coefficient

It is also possible to identify a set of coefficients that are significant for both the manoeuvres considered, in particular:

Nr, Yd, Nv, Yr, Yv, Nur, Nrdot, Yddd,

The hydrodynamic coefficients determined in this way were object of the procedure of identification.

3.2. Identification

Once the most significant coefficients have been identified using the sensitivity analysis, the sequent step was the research of a procedure to calculate their values utilizing as input data the results of experimental tests; the objective functions are the same utilized for the sensitivity analysis, measuring in this case the discrepancy between values of the typical manoeuvre parameters simulated and measured.

The identification procedure, in general, is structured as follows:

- Starting from an initial range of variation for the investigated coefficients a large number of combinations of hydrodynamic coefficients is generated randomly by the program;
- These combinations are used for a first optimization made with a Design of Experiment;
- The best 20 (about) solutions of this first calculation, easily identifiable by diagrams presented in FRONTIER, are assumed as input population for a second optimization made with a Genetic Algorithm; the range of variation of the coefficients given in input is limited to the values corresponding to the best solutions identified by the previous step of calculation;
- The procedure is repeated iteratively with a sequence of Genetic Algorithm reducing the range of investigation step by step until the optimization is completed.

At this step the intention was to validate the procedure before using it with experimental data; in order to do this, the procedure of identification was applied to a simulated manoeuvre and not to an experimental one, thus avoiding problems related to experimental data such as uncertainties, measurement errors and similar. The objective is therefore to obtain, starting from perturbed values, the coefficients used to generate the simulated manoeuvre. The coefficients, which were not object of the identification, were maintained as given directly by the regression formulae.

As a first approach, the procedure described was utilized to obtain the set of coefficients wanted by the intersection of the possible solutions resulting from two separate identifications applied to 10°/10° zigzag and turning circle manoeuvres.

The same procedure of identification was then applied considering the two manoeuvres together utilizing only one objective function obtained as sum of the two functions assumed before:

$$\left|\frac{A-A_S}{A_S}\right|+\left|\frac{T-T_S}{T_S}\right|+\left|\frac{D_T-D_{TS}}{D_{TS}}\right|+\left|\frac{D_F-D_{FS}}{D_{FS}}\right|+\left|\frac{V_R-V_{RS}}{V_{RS}}\right|+\left|\frac{T_{90}-T_{90S}}{T_{90S}}\right|+\left|\frac{(T_{180}-T_{90})-(T_{180S}-T_{90S})}{(T_{180S}-T_{90S})}\right|+$$

$$+\left|\frac{A_1-A_{1S}}{A_{1S}}\right|+\left|\frac{T_{e1}-T_{e1S}}{T_{e1S}}\right|+\left|\frac{(T_{O1}-T_{e1})-(T_{O1S}-T_{e1S})}{(T_{O1S}-T_{e1S})}\right|+\left|\frac{A_2-A_{2S}}{A_{2S}}\right|+\left|\frac{(T_{e2}-T_{O1})-(T_{e2S}-T_{O1S})}{(T_{e2S}-T_{O1S})}\right|+$$

$$+\left|\frac{(T_{O2}-T_{e1})-(T_{O2S}-T_{e1S})}{(T_{O2S}-T_{e1S})}\right|+\left|\frac{A_3-A_{3S}}{A_{3S}}\right|+\left|\frac{(T_{e3}-T_{O2})-(T_{e3S}-T_{O2S})}{(T_{e3S}-T_{O2S})}\right|+\left|\frac{(T_{O3}-T_{e3})-(T_{O3S}-T_{e3S})}{(T_{O3S}-T_{e3S})}\right|$$

Since the optimization algorithm needs an initial estimate of the coefficients object of the identification, a perturbation of 10% from the value calculated by SIMSUP was assumed, representing the possible error which could be made by the use of regression formulae in a real case. The range of variation for the first step of the procedure described was set to ±35% from those initial perturbed values.

3.2.1. Identification – Zigzag Manoeuvre

The objective of this first step was the identification of the most significant coefficients for the 10°/10° zigzag manoeuvre; the values calculated by SIMSUP for them were those reported in table I, while the range of variation of coefficients to which the final solutions belong, together with the best one, are reported in table II.

Tab.I: coefficients obtained by SIMSUP regression formulae

Coeff.	SIMSUP values
Yd	2.970E-3
Yr	5.014E-3
Yv	-14.050E-3
Nr	-2.920E-3
Nv	-4.132E-3
Nur	-2.499E-3
Nrdot	-0.389E-3

Tab.II: coefficients obtained by optimization of 10°/10° zigzag manoeuvre; final range and best value

Coeff.	Min. Values	Max. Values	Best Value
Yd	2.55E-3	2.75E-3	2.656E-3
Yr	4.50E-3	5.80E-3	4.811E-3
Yv	-18.00E-3	-15.50E-3	-17.50E-3
Nr	-2.60E-3	-2.30E-3	-2.50E-3
Nv	-3.90E-3	-3.00E-3	-3.667E-3
Nur	-2.50E-3	-1.50E-3	-1.944E-3
Nrdot	-0.35E-3	-0.29E-3	-0.30E-3

Because for some of the coefficients, the values given by SIMSUP weren't contained in the ranges obtained, it was concluded that the identification procedure considering separately the two manoeuvres was not the best solution, due to a probable ill-conditioning of the problem; the calculations therefore were repeated assuming the two manoeuvres simultaneously in order to constrain more the solution, and reducing the number of investigated coefficients.

Anyway it is important to underline that the time history (figures 6, 7, 8) of the 10°/10° zigzag manoeuvre simulated using the identified coefficients (indicated as "Frontier (Z)" in the figures) compared with the same obtained with the initial coefficients (indicated as "SIMSUP") are almost equal as expected; moreover, analyzing the 20°/20° zigzag and the turning circle manoeuvres obtained with the identified coefficients, the error is not significant, even if greater than that obtained for 10°/10° zigzag manoeuvre.

3.2.2. Identification – Zigzag and turning circle manoeuvres

The coefficients investigated in this step with the procedure already explained and applied to both the manoeuvres were:

Yd, Yr, Yv, Nr, Nv

In this case, the range of variation of coefficients to which the final solutions belong, together with the best one, are reported in table III:

Table III: coefficients obtained by optimization of 10°/10° zigzag and 35° turning circle manoeuvres together; final range and best value

Coeff.	Min. Values	Max. Values	Best Value
Yd	3.0E-3	3.2E-3	3.089E-3
Yr	5.0E-3	7.0E-3	6.159E-3
Yv	-13.7E-3	-10.0E-3	-11.25E-3
Nr	-3.4E-3	-3.1E-3	-3.149E-3
Nv	-6.0E-3	-4.5E-3	-4.927E-3

These results are different from that obtained with the optimization of the zigzag manoeuvre only, but also in this case for some coefficients the range obtained didn't contain the initial value. Nevertheless, the simulated manoeuvres (indicated as "Frontier (EZ)" in figures 6, 7, 8) result nearly coincident to the same obtained with the initial coefficients for the two manoeuvres on which the optimization is applied, and very similar for the 20°/20° zigzag, as wanted.
This can be due to the sensible improvement in the estimation of the two most significant coefficients (Yd and Nr).

3.2.3. Results

In the following diagrams the results of the simulations obtained with the initial values of the coefficients are compared with those obtained with the optimized values estimated by the two different procedures previously described.

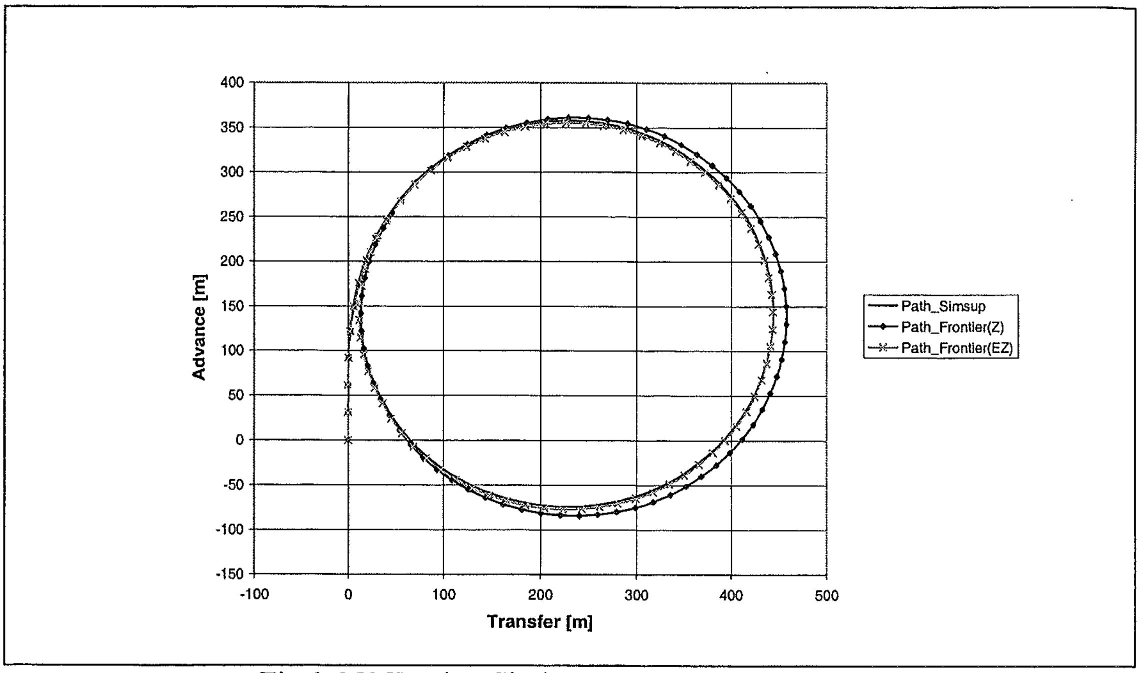

Fig.6: 35° Turning Circle Manoeuvre – Comparison

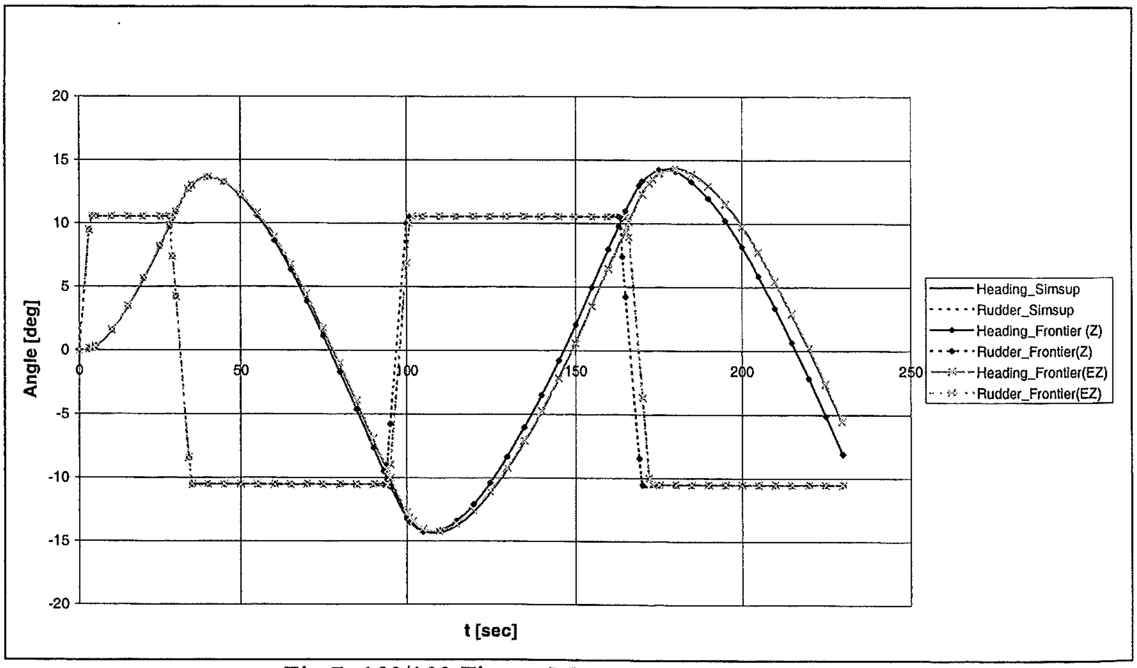

Fig.7: 10°/10° Zigzag Manoeuvre - Comparison

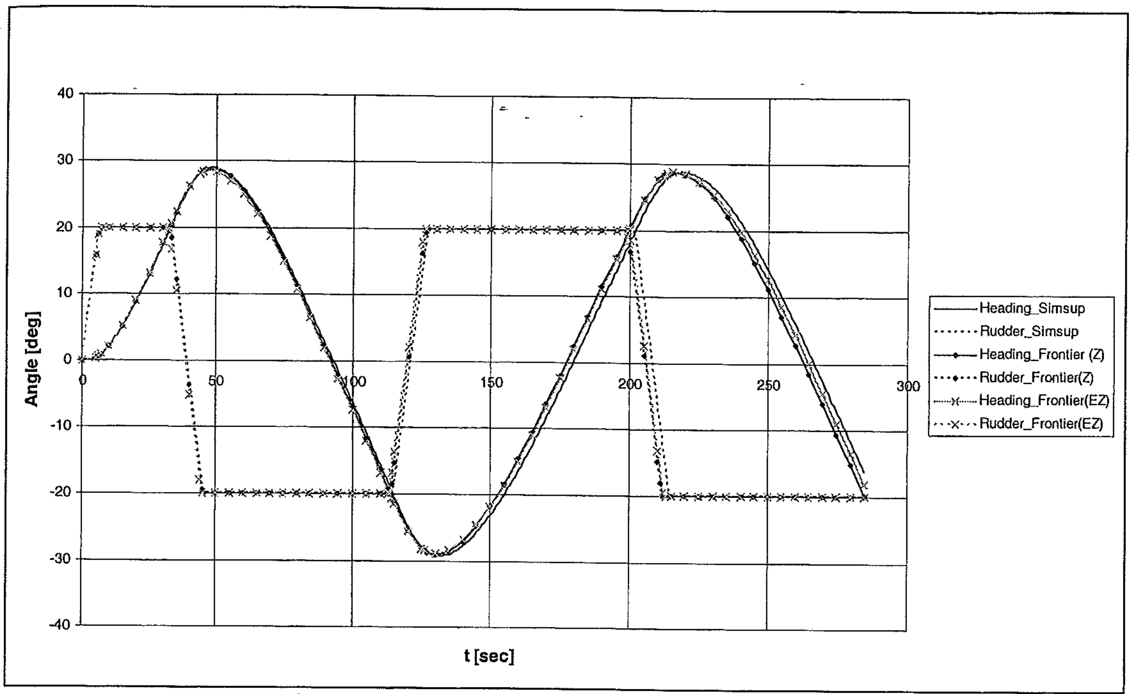

Fig.8: 20°/20° Zigzag Manoeuvre - Comparison

The results obtained suggest that the identification of coefficients could be a problem of non uniqueness, as already indicated by other similar studies [5] [6]; this implies that similar solutions can be obtained increasing or decreasing simultaneously some coefficients, and it is possible to obtain the optimization of the objective function and of the typical parameters of the manoeuvres with different combinations of hydrodynamic coefficients.
With the procedure applied, anyway, it is possible to obtain a simulation very close to the target one, and to reduce the error in the initial estimated range of variation of the coefficients; this latter result is particularly significant for the most influent coefficients using the second procedure described.
It was therefore interesting to apply the optimization to experimental results, as illustrated in the next paragraph, in order to obtain a complete analysis of the procedure.

4. Procedure applied to experimental results

In order to verify the accuracy of the procedure described in paragraph 3.3.2., identification of coefficients was applied to experimental data; in this case, the objective function for the optimization algorithm is the same reported before, in which the parameters indicated with "S" represent no more the values estimated by SIMSUP, but the values obtained by tests with ship at sea; the initial range for the values of the coefficients is centered on the values estimated with SIMSUP regressions (table I), allowing a possible variation of ±35%.

The resulting range of variation of coefficients to which the final solutions belong, together with the best one, are reported in table IV:

Table IV: coefficients obtained by optimization applied to experimental results of 10°/10° zigzag and 35° turning circle manoeuvres together; final range and best value

Coeff.	Min. Values	Max. Values	Best Value
Yd	3.08E-3	3.18E-3	3.172E-3
Yr	3.59E-3	4.05E-3	4.043E-3
Yv	-15.5E-3	-10.1E-3	-14.28E-3
Nr	-3.03E-3	-2.61E-3	-2.867E-3
Nv	-5.02E-3	-4.04E-3	-4.889E-3

In accordance with that made before, the time histories of manoeuvres, obtained by SIMSUP assuming the final coefficients identified by the optimization procedure are plotted in figure 9, 10 and 11 together with the experimental results and the simulations obtained directly using SIMSUP values for the coefficients; in those figures, moreover, the results obtained from the optimization of the 10°/10° zigzag manoeuvre only are also reported for comparison.
The curves pointed with "Sperim." correspond to experimental results, the curves pointed with "Frontier(Z)" and "Frontier(EZ)" represent the values obtained by SIMSUP assuming respectively the coefficients identified by optimization of the zigzag manoeuvre only and of the two manoeuvres together, while "Simsup" points the results obtained assuming directly the values estimated by the regression formulae.

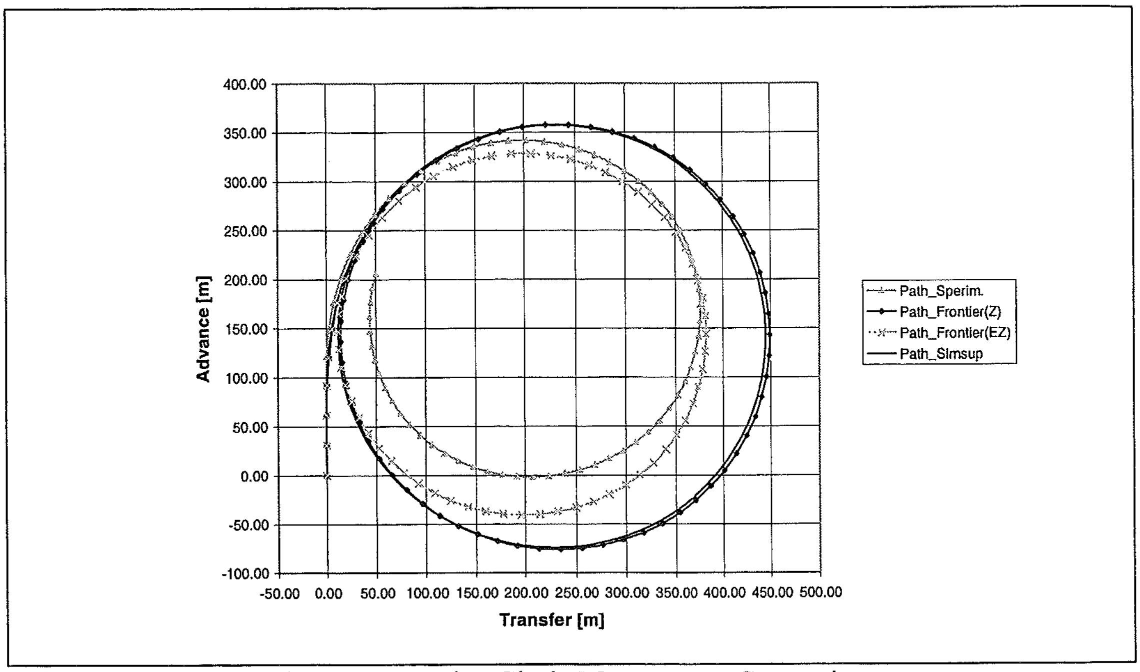

Fig.9: 35° Turning Circle Manoeuvre - Comparison

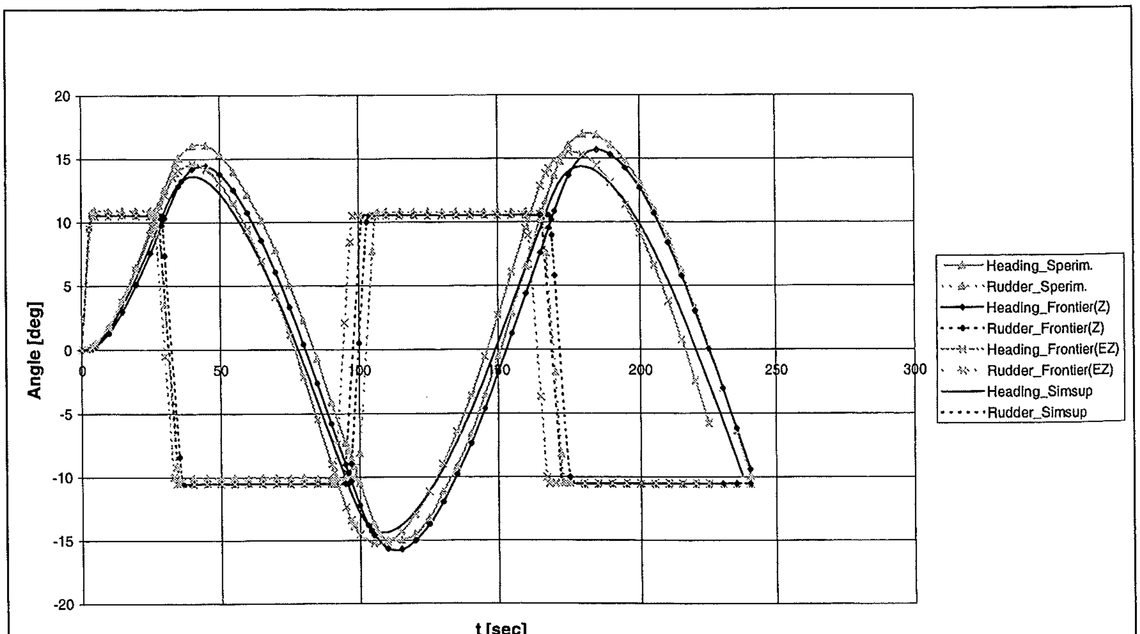

Fig.10: 10°/10° Zigzag Manoeuvre – Comparison

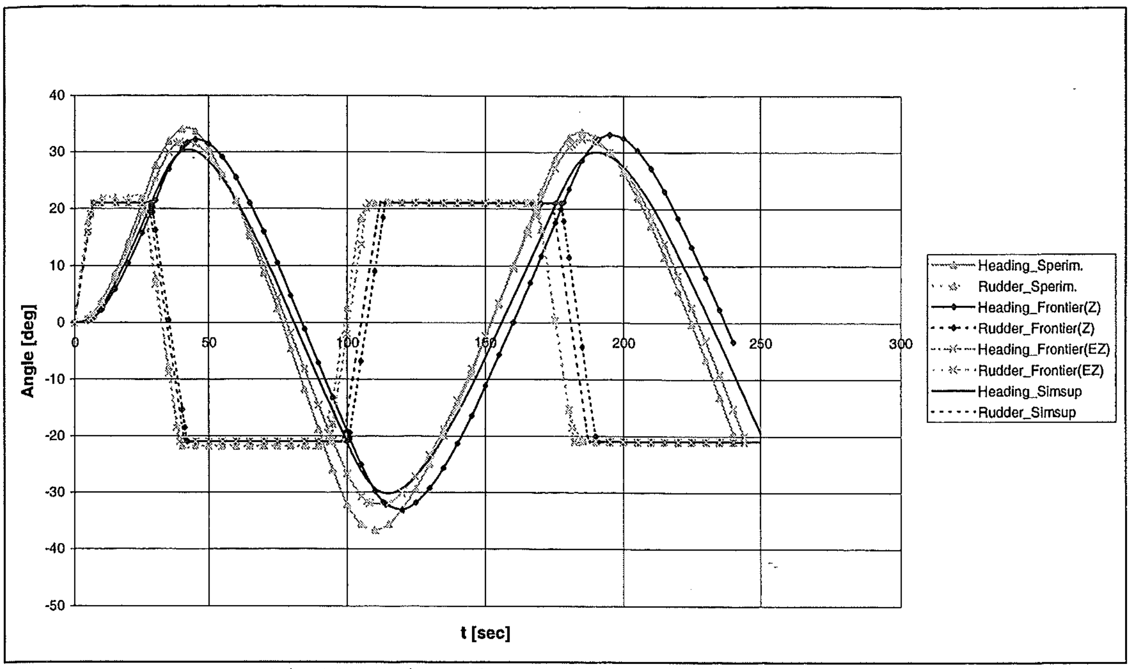

Fig.11: 20°/20° Zigzag Manoeuvre – Comparison

For what regards the 10°/10° zigzag manoeuvre, it can be observed that the time history estimated by the simulation program using both the procedures and that obtained during a test at sea are very similar and improve the results obtained with regression values. Similar results were obtained for 20°/20° zigzag manoeuvre, even if in this second case the use of the second procedure gives better correspondence to the experimental data.
It is to be observed, moreover, that the experimental results for the second manoeuvre are for an initial velocity equal to 15kn, while the coefficients were estimated from manoeuvres with an initial velocity of 12kn, therefore the effect of ship's velocity on hydrodynamic coefficients could be disregarded.

Regarding the turning circle manoeuvre, it can be noted that by the optimization of the zigzag manoeuvre only it wasn't possible to improve the simulation, which resulted very similar to the one obtained using SIMSUP regression values, while by the optimization of both the manoeuvres the estimation results were noticeably improved.

In conclusion of this analysis, it appears that it is possible to identify with the optimization of the zigzag and turning circle manoeuvres together hydrodynamic coefficients adequate to simulate the wanted manoeuvres with greater accuracy than assuming those given by the regression used by the program.
Moreover, it has to be considered that differences between the results obtained assuming the values estimated by optimization and that obtained experimentally can be attributed, partially at least, to inaccuracy of experimental data due to errors of measurements and to the influence of environmental conditions (current, wind, etc.) not considered, in this analysis, in the simulation made by SIMSUP.

5. Conclusion and recommendations

The analysis conducted doesn't allow concluding definitively on the possibility to identify univocally the hydrodynamic coefficients characteristic of a hull; instead, it can be already concluded that the procedure of optimization described can be useful to adjust the procedure of simulation made by the program; as found, in fact, it is possible to estimate, on the basis of experimental data, coefficients that if assumed in the calculation made by SIMSUP, give manoeuvres in accordance with experimental results also considering non-conventional ships or ships which geometrical parameters are out of the range covered by the regression actually used.

In order to obtain a more definite conclusion on the feasibility of this procedure, the field of analysis has to be extended to a series of "unconventional" vessels similar to the one used for this study; from this analysis it will be possible to verify the trend of results obtained and to adjust the regression formulae used by SIMSUP with different corrections for different ship's categories.

References

[1] IMO (International Maritime Organization) (1993), *Iterim Standards for Ship Manoeuvrability,* Resolution A.715(18)

[2] CLARKE, D.; GEDLING, P.; HINE, G. (1982), *The Application of Manoeuvering Criteria in Hull Design Using Linear Theory,* RINA Transaction

[3] INOUE, S.; HIRANO, M.; KIJIMA, K. (1981), *Hydrodynamic Derivatives on Ship Manoeuvering,* ISP

[4] BYSTROM, L.; OTTOSON, P. (1988), *SHICOF – Program for Calculation of Hydrodynamic Manoeuvring Coefficients for Merchant Ships,* SSPA

[5] HWANG, W.Y. (1980), *Application of System Identification to Ship Maneuvering,* MIT

[6] ABKOWITZ, M.A. (1980), *Measurement of Hydrodynamic Characteristics from Ship Maneuvering Trials by System Identifications,* SNAME Transaction

[7] KIM, K.; RHEE, K.P. (2000), *A New Sea Trial Method for Estimating Hydrodynamic Derivatives,* SOTECH

[8] CAPURRO, G.; CUOMO, G. (1994), *Programma di simulazione SIMSUP – Teoria e manuale d'uso (Versione 3.0),* CETENA

[9] CAZZANI, G.; DEPASCALE, R.; MONACI, P. (2002), *Programma di Simulazione SIMSUP 5.1 – Manuale d'uso,* CETENA

[10] *Principles of Naval Architecture,* SNAME

[11] CAPURRO, G.; PUCCIO, P. (1990), *Primi risultati del programma SIMSUP per navi monoelica. Confronto teorico – sperimentale,* CETENA

[12] CAPURRO, G.; PUCCIO, P. (1990), *Primi risultati del programma SIMSUP per navi bielica. Confronto teorico – sperimentale,* CETENA

[13] SPICER, D.; COOK, J.; POLONI, C.; SEN, P. (1998), *EP 20082 FRONTIER: Industrial Multiobjective Design Optimization,* ECCOMAS

Rudder Loads for a Fast Ferry at Unusually High Rudder Angles

Ould M. El Moctar, Germanischer Lloyd[1], Vorsetzen 32, D-20416 Hamburg, moct@germanlloyd.org
Volker Bertram, ENSIETA[1], 2 rue François Verny, F 29806 Brest, bertram@waves.insean.it

Abstract

HSVA used CFD to simulate the flow around a high performance rudder at angles up to 45°. The CFD simulations show that the maximum side forces on the rudder are not higher than for angles up to 35° both in forward speed and reverse speed. The computations used the commercial RANSE code Comet using steady flow simulations for small rudder angles and unsteady simulations for high rudder angles. The CFD results supported class approval for these exceptionally high rudder angles for one of the Superfast ferries of Flender Werft AG.

1. Introduction

Traditional practice for rudder design has often employed profiles of the NACA-00 series developed for aeronautical applications. More recently, there has been an increasing interest in concave profiles such as the HSVA profiles or the IfS profiles, Brix (1993), Bertram (2000). These profiles allow higher lift coefficients and are less susceptible to cavitation compared to NACA profiles, albeit at the cost of higher resistance. One recent example for the application of such high-performance concave rudder profiles is the Superfast ferry XII built by Flender Werft AG in Lübeck/Germany, Fig.1. The ferry design featured a twin-screw twin-rudder arrangement employing concave rudder profiles of the type HSVA MP 71.

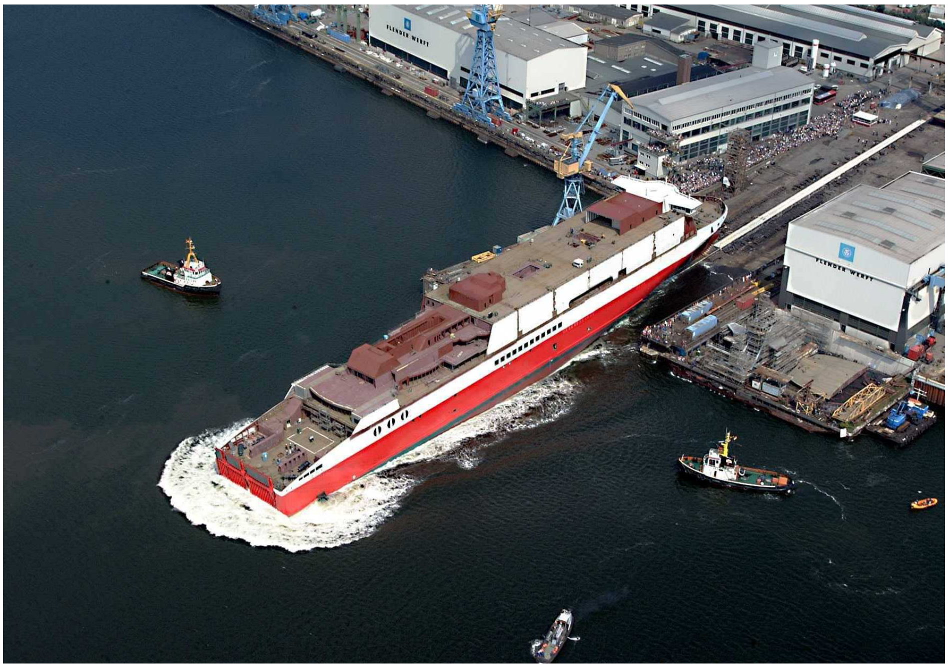

Fig.1: Superfast XI ferry of Flender Werft AG

During the project, the idea was generated to increase the maximum rudder angle to 45° to improve the course-changing ability particularly for low speeds. However, neither a change in rudder structural design or rudder gear, nor a sophisticated control of the rudder angle depending on speed was acceptable. The classification society (ABS) voiced justifiably concerns that the rudder gear may be overloaded at high speeds and rudder angles exceeding the usual 35°. ABS agreed to accept the high maximum rudder angles if evidence could be provided that the rudder forces would not exceed those encountered

1 Formerly Hamburg Ship Model Basin (HSVA), info@hsva.de, where this work was performed.

for rudder angles up to 35°. In this situation, HSVA was tasked to compute the expected forces on the rudder of the Superfast ferry resorting to its considerable experience in the field of CFD for rudder design.

Diagrams to estimate rudder forces such as given in Brix (1993) or Bertram (2000) have been popular in classical rudder design. These diagrams extrapolate model test results from wind tunnels or are based on potential-flow computations. However, the maximum lift is determined by viscous flow phenomena, namely flow separation (stall). Potential flow models are generally not capable of predicting stall and model tests predict stall at too small angles. Recently, computational fluid dynamics (CFD) has become the most appropriate tool to support practical rudder design, El Moctar (2001), El Moctar and Bertram (2001), El Moctar and Söding (2001). The underlying theory of the employed CFD approach using Comet, ICCM (2001), is documented in the following chapter.

2. Theoretical background

The flows around rudders are slow enough to be considered incompressible. The fundamental field equations describe conservation of mass (continuity equation) and conservation of momentum (Reynolds-averaged Navier-Stokes equations = RANSE). The time averaging is an ensemble averaging, i.e. the average is considered to be taken over a time span large compared to the turbulent fluctuations, but small compared to the large vortex shedding. In the following, all equations are to be understood as time averaged in this way.

The RANSE equations are given in integral form as the code is based on the finite-volume method approach:

$$\frac{d}{dt}\int_V \rho \, dV + \int_S \rho \, (\mathbf{v}-\mathbf{v}_s)\cdot d\mathbf{s} = 0 \qquad (1)$$

$$\frac{d}{dt}\int_V \rho \, \mathbf{v} \, dV + \int_S \rho \, \mathbf{v} \, (\mathbf{v}-\mathbf{v}_s)\cdot d\mathbf{s} = \int_S (\mathbf{S}-p\mathbf{I}-\rho\mathbf{v'v'})\cdot d\mathbf{S} + \int_V \mathbf{f} \, dV \qquad (2)$$

Bold symbols denote vectors and Tensors. ρ is the fluid density, V the volume, S the surface area of a control volume (CV), d**s** the outward normal on the surface. **v** is the (time averaged) velocity vector of the fluid, $\mathbf{v}_s$ the velocity vector of the CV surface, p the pressure, **v'** the turbulent fluctuation of the velocity, **f** a resultant body force per unit volume, *t* the time, **I** the unit tensor, and **S** the viscous part of the stress tensor. For incompressible (Newtonian) fluids the components of **S** are proportional to the fluid's rate of deformation:

$$\mathbf{S} = \mu \, (\mathbf{grad\ v} + (\mathbf{grad\ v})^T) \qquad (3)$$

μ is the dynamic viscosity. The Reynolds stress tensor $\rho v_i'v_j'$ is expressed as a function of time-averaged quantities using a turbulence model following the eddy-viscosity hypothesis of Boussinesq:

$$-\rho \, \overline{v_i'v_j'} = \mu_t \, (\partial v_i/\partial x_j + \partial v_j/\partial x_i) - (2/3) \, \rho \, \delta_{ij} \, k \qquad (4)$$

$\mu_t = C_\mu \, \rho \, k^2/\varepsilon$ is eddy viscosity which is a function of the local turbulence, C_μ an empirical constant, δ_{ij} the components of the unit tensor. We solve corresponding transport equations for the turbulent kinetic energy $k=0.5 \, \mathbf{v'}\cdot\mathbf{v'}$ and its dissipation rate $\varepsilon = (\rho/\mu) \, (\mathbf{grad\ v'} : (\mathbf{grad\ v'})^T)$:

$$\frac{d}{dt}\int_V \rho \, k \, dV + \int_S \rho \, k \, (\mathbf{v}-\mathbf{v}_s)\cdot d\mathbf{s} = \int_S \mathbf{q}_k\cdot d\mathbf{s} + \int_V (P-\rho\varepsilon) \, dV \qquad (5)$$

$$\frac{d}{dt}\int_V \rho \, \varepsilon \, dV + \int_S \rho \, \varepsilon \, (\mathbf{v}-\mathbf{v}_s)\cdot d\mathbf{s} = \int_S \mathbf{q}_\varepsilon\cdot d\mathbf{s} + \int_V (C_1 P\varepsilon/k - C_2\rho\varepsilon^2/k - C_4\rho \, \varepsilon \, \mathrm{div}\,\mathbf{v}) \, dV \qquad (6)$$

$\mathbf{q}_k$ and $\mathbf{q}_\varepsilon$ are the diffusion fluxes for k and ε:

$\mathbf{q}_k = (\mu+\mu_t/\sigma_k)$ **grad** k (7)
$\mathbf{q}_\varepsilon = (\mu+\mu_t/\sigma_\varepsilon)$ **grad** ε (8)

P is the production of turbulent energy by shear:

$$P = -\rho\, \mathbf{v'}\, \mathbf{v'} : \mathbf{grad\, v} \tag{9}$$

C_1, C_2, C_4, σ_k, σ_ε, σ_T, σ_{ci} are empirical constants. We employed the RNG-k-ε model of Speziale und Thangam (1992), which differs from the standard k-ε model in two aspects:

1. An additional source term in the transport equation for ε, which is associated with the effect of the rate of mean flow distortion on turbulence dissipation rate. This extra term is believed to be important when the nondimensional shear is large compared to unity.
2. Other empirical constants are chosen:

C_μ	C_1	C_2	C_4	C_5	C_6	σ_k	σ_ε	σ_T	σ_{ci}
0.085	1.42	1.68	1.42	4.38	0.012	0.72	1.3	0.9	0.9

The above described transport equations are discretized in a finite-volume method (FVM). The domain is discretized by control volumes of hexaedral shape.

The variables are stored at the cell center (colocated variable arrangement). The field equations are discretized employing assorted interpolation and differencing schemes. The resulting algebraic system of equations is solved numerically. Volume and surface integrals are determined using a second-order midpoint rule. The convective flux of the variable ϕ through cell side j is approximated as follows:

$$\int_{S_j} \rho\, \phi\, (\mathbf{v}-\mathbf{v}_s)\cdot d\mathbf{S} \approx \phi_j \int_{S_j} \rho\, (\mathbf{v}-\mathbf{v}_s)\cdot d\mathbf{S} \approx \phi_j \rho (\mathbf{v}-\mathbf{v}_s)_j \cdot \mathbf{S}_j = \phi_j\, \dot{m}_j \tag{10}$$

The mass flux $\dot{m}_j$ through the cell face is taken from the previous iteration following a simple Picard iteration approach. The remaining unknown ϕ_j at the center of the cell face j is determined combining a central difference scheme (CDS) with an upwind differencing scheme (UDS). The CDS employed a correction to ensure second order accuracy for arbitrary cell, Demirdzic and Muzaferija (1995). Second-order CDS can lead to unphysical oscillations if the Peclet number exceeds 2 and large gradients are involved. UDS on the other hand are unconditionally stable, but lead to higher unphysical diffusion. To obtain a good compromise between accuracy and stability, the schemes were blended as follows:

$$\phi_j = \phi_j^{UDS} + \lambda_j\, (\phi_j^{CDS} - \phi_j^{UDS}) \tag{11}$$

The blending factor λ_j was chosen between 0.9 and 0.95 near the rudder and 0.8 further away. This choice is motivated by the higher cell density near the rudder. The stability and computational efficiency is further increased in Comet following the deferred correction approach of Khosla and Rubin (1974). Only the first-order approximation contributes to the coefficient matrix, while the correction term is calculated explicitly using values from the previous iteration and is added to the source term. In the converged solution, explicit and implicit contributions of the UDS cancel each other and only CDS remains.

The diffusive fluxes through cell faces are approximated using a second-order midpoint rule. The Euler implicit method was used to integrate in time. This first-order fully-implicit approximation is unconditionally stable.

Pressure and velocity are coupled by a variant of the SIMPLE algorithm as derived in Ferziger and Peric (1996).

The system of equations are under-relaxed to dampen changes between iterations. All equations except the pressure correction equations were under-relaxed using a relaxation factor 0.6. The pressure correction equations were under-relaxed using a relaxation factor 0.04 for steady flow simulation, 0.1 to 0.5 for unsteady simulations finding in each case a suitable compromise between stability and convergence speed.

v, k, and ε are initialized at all cell centers. For parameter studies (i.e. rudder angles), the values of the previous parameter are taken which typically saves 20% CPU time. At the inlet, **v**, k, and ε are specified. At the outlet all gradients in flow direction are set to zero. At symmetry boundaries (rigid water surface) normal velocities and normal derivatives of parallel velocity components and scalar quantities are set to zero. On the rudder, we enforce the no-slip condition via a standard wall function (following capacity restrictions rather than physical insight) and set the kinetic energy to zero. The dissipation rate ε is fixed at the first point near the wall to a value corresponding to the computed kinetic energy following the assumption of local balance of turbulence.

The propeller is modelled using axial and tangential body forces. These are external forces distributed over the cells which cover the location where the propeller would be in reality. The sum of all axial body forces is the thrust. The body forces are assumed to vary in radial direction of the propeller only. This procedure is much faster than geometrical modelling of the propeller (by two orders of magnitude) at a negligible penalty in accuracy (about 1%) as shown in benchmark tests by El Moctar (2001). Propeller data and average wake were taken from propulsion tests. The distribution of axial and tangential forces follows Stern et al. (1988). The ship hull is not modelled. The procedure has been extensively validated for rudder flows both with and with-out propeller modelling, El Moctar (2001).

3. Application to Superfast ferry rudder

The flow was simulated for design speed (29 knots) and rudder angles from 0° to 45° (in steps of 5°) for full-scale Reynolds number. This is decisive for the determination of the lift maximum. The computations were performed for steady flow up to rudder angles of 25° and unsteady (in time simulations) after 30°, because the flow became considerably unsteady for higher angles of attack. Forces and moments are then to be understood as time-average over short-term fluctuations. In the computations, "rudder angle of attack" is the angle assuming that the ship moves straight ahead and the rudder is laid to the specific angle. This is a worst case scenario. Typically the large angles occur when the ship is already turning which reduces the rudder angle to a smaller (hydrodynamic) angle of attack.

The semi-balanced rudder was completely modeled, Fig.2. The computational model extended 10 chord length ahead and aft of the rudder of the rudder and to each the ship hull. The grid extended in vertical direction 6 rudder heights below the rudder. The grid had in total 1.8 million cells. Figs.2 and 3 show details of the grid. Forces are made non-dimensional with the stagnation pressure, lateral area of the movable part of the rudder, the moment in addition with the average chord length of the rudder.

The maximum side force appeared for 35° in the curve, Fig.4. The actual maximum may be slightly higher at perhaps 36° or 37°. The decline of the side forces beyond 35° is due to increasing flow separation as illustrated for a cross section in Fig.5. The flow in the upper part of the rudder with the fixed fin is still sufficiently accelerated to avoid largely flow separation in this part. With increasing rudder angle, the flow separation zone extends further and covers approximately 90% of the profile length for 45°. The shaft moments show a monotonous growth and reach maximum at the maximum angle of 45°

The rudder was also investigated for the case of reversing ship. In this case the propeller operates downstream of the rudder and has hardly any influence on the rudder which justified to omit the propeller in the CFD model. The flow feature change considerably as qualitatively expected. The maximum lift appears for 20° in the curve, Fig.6, much earlier than in the usual forward-speed inflow conditions. The actual maximum may be slightly lower at perhaps 19°. The decline of the lift force beyond 20° is due to massive separation as illustrated by Fig.7. The lift forces are generally lower than for forward speed. In reverse flow condition, as the flow separates over the whole rudder height. The shaft moment features a very shallow maximum region between 20° and 35°. The resistance increases again monotonously.

4. Conclusion

The case study shows that CFD analyses for rudders are by now mature enough to serve as a practical design aid for rudder design including discussions with classification societies concerning realistic load assumption even for unusual cases. Such computations should be performed as a matter of standard in an early design stage.

Acknowledgement

We appreciate the good cooperation with Flender Werft AG in the project and the unbureaucratic permission to publish these results.

References

BERTRAM, V. (2000), *Practical ship hydrodynamics*, Butterworth&Heinemann, Oxford

BRIX, J. (Ed.) (1993), *Manoeuvring technical manual*, Seehafen Verlag, Hamburg

DEMIRDZIC, I.; MUZAFERIJA, S. (1995), *Numerical method for coupled fluid flow, heat transfer and stress analysis using unstructured moving meshes with cells of arbitrary topology*, Computer Methods in Applied Mechanics and Engineering 125

EL MOCTAR, O.M. (2001), *Numerical computations of flow forces in ship manoeuvring*, Ship Technology Research 48, pp.98-123

EL MOCTAR, O.M.; BERTRAM, V. (2001), *Selected topics of CFD for ship manoeuvring,*36th WEGEMT School, Rome

EL MOCTAR, O.M.; BERTRAM, V. (2002), *Computation of viscous flow around fast ship superstructures*, 24. Symp. Naval Hydrodynamics, Fukuoka

EL MOCTAR, O.M.; SÖDING, H. (2001), *Numerische Vorhersage des Manövrierverhaltens,* Hansa 138/8, pp.23-25

FERZIGER, J.H.; PERIC, M. (1996), *Computational methods for fluid dynamics,* Springer

KHOSLA, P.K.; RUBIN, S.G. (1974), *A diagonally dominant second-order accurate implicit scheme,* Computers Fluids 2, pp.207-209

SPEZIALE, C.G.; THANGHAM, S. (1992), *Analysis of an RNG based turbulence model for separated flows,* Int. J. Eng. Science Vol. 30

STERN, F.; KIM, H.T.; PATEL, V.C.; CHEN, H.C. (1988), *A viscous flow approach to the computation of propeller hull interaction*, J. Ship Research 32

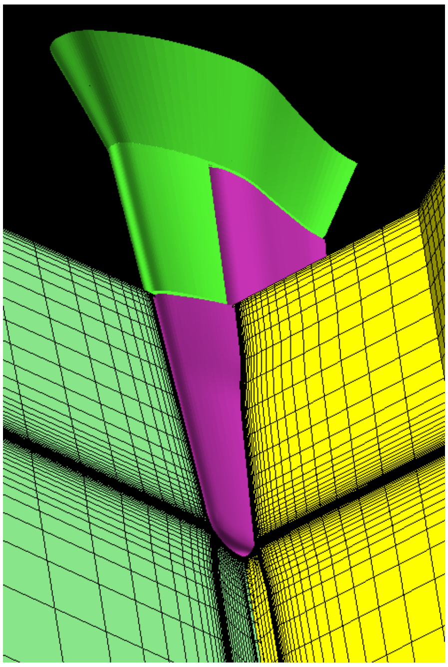

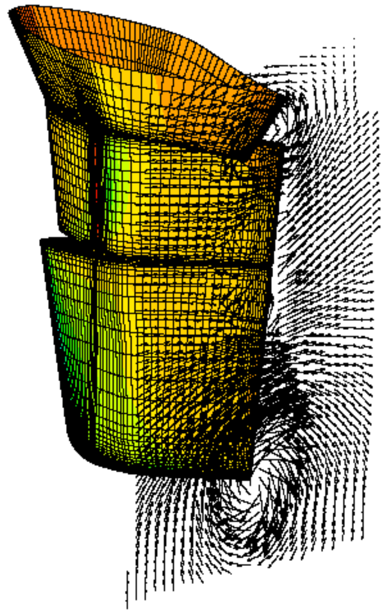

Fig.2: Grid on rudder Fig.3: Vortex formation behind rudder for 25° angle of attack

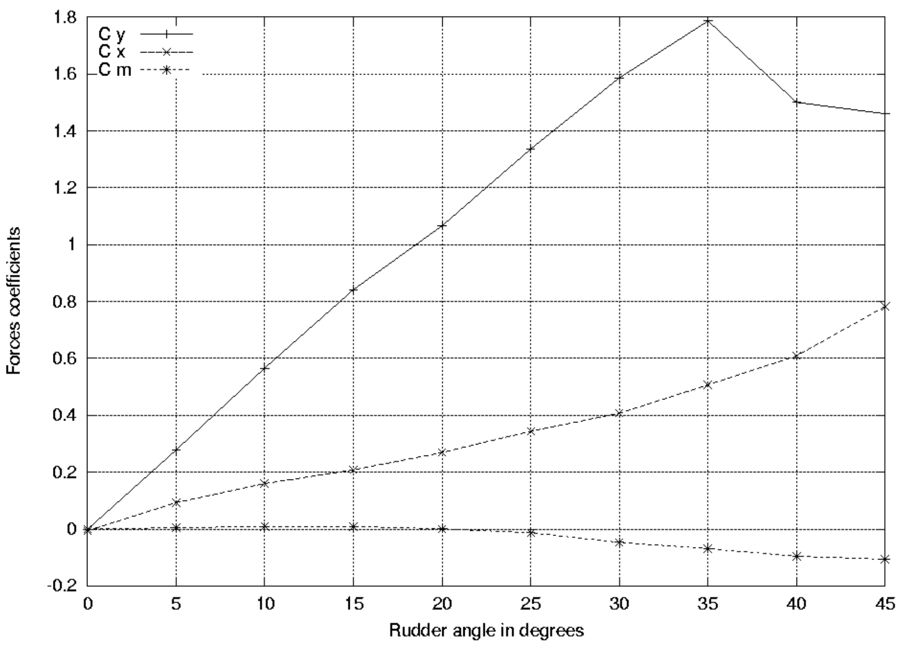

Fig.4: Force and moment coefficients for rudder

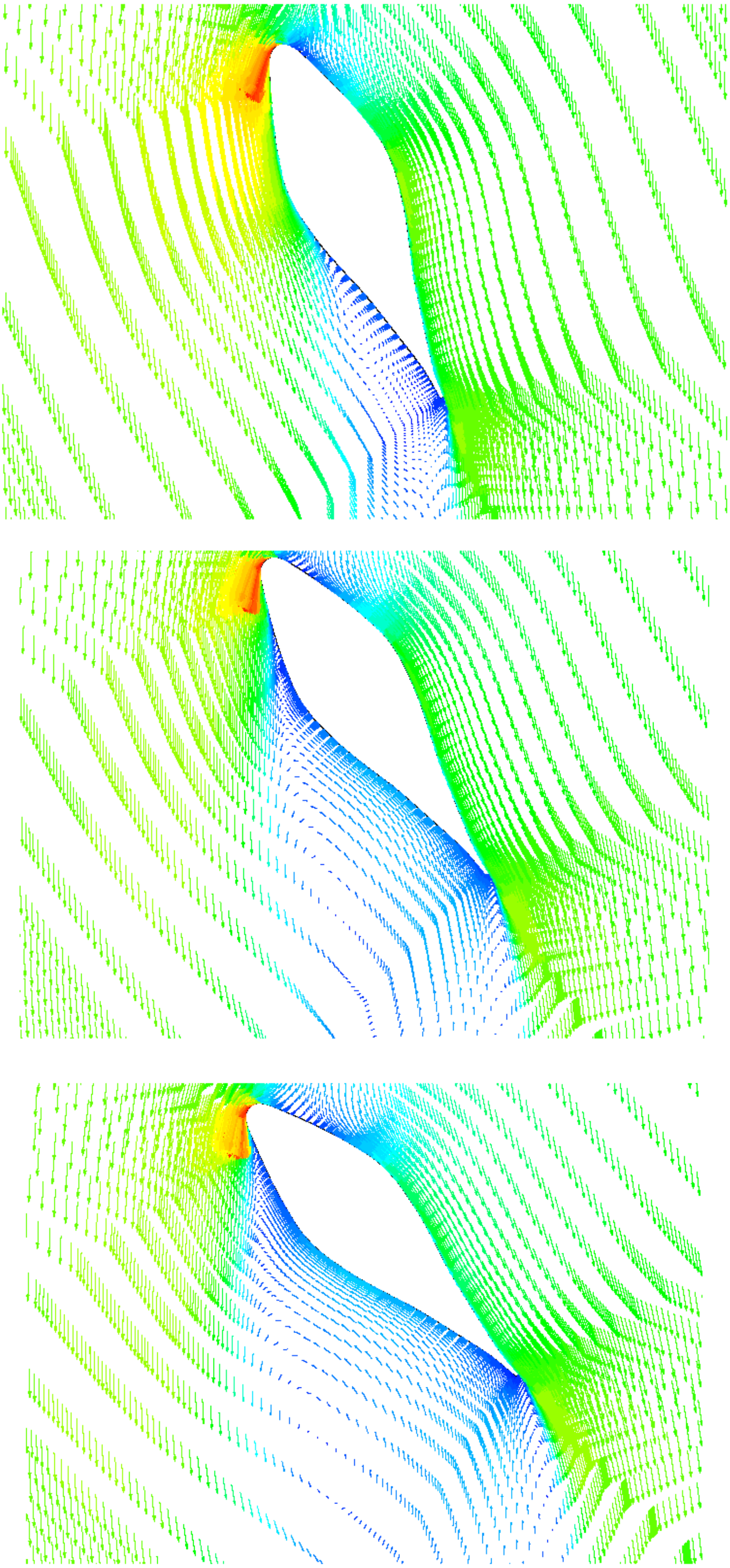

Fig.5: Velocity distribution on profile section 2.6 m above rudder base;
Rudder angles 25° (top), 35° (center), 45° (bottom)

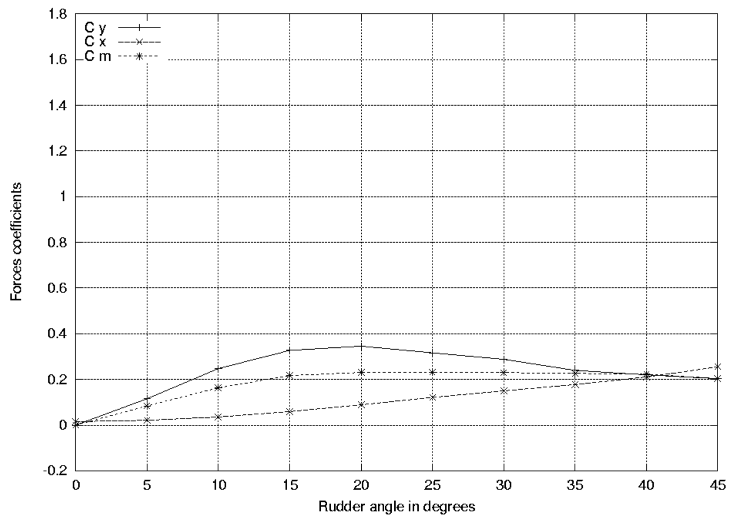

Fig.6: Force and moment coefficient in reverse flow

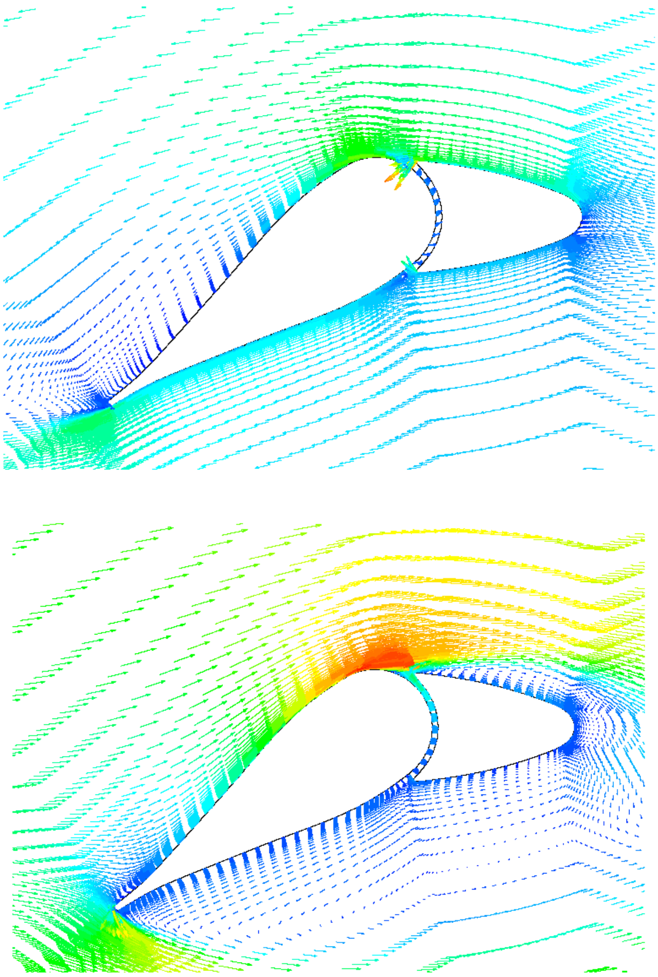

Fig.7: Velocity distribution on rudder profile at rudder top for rudder angle 35°; forward speed (top) and reverse flow (bottom)

The Excitation of Ships by Wave Wash Generated by High Speed Craft

Björn Elsäßer, Trevor J.T. Whittaker

School of Civil Engineering, Queen's University Belfast, David Keir Building, Stranmillis Road, Belfast BT9 5AG, Northern Ireland, UK, t.whitttaker@qub.ac.uk

Abstract

The wash waves produced by fast ships can create problems for other vessels which are either moored or under way. The risk imposed must be considered when evaluating existing routes or when planning new routes. A preliminary investigation of this topic was undertaken by the Fast Ferry Research Group at Queen's University Belfast as part of the research project 457 completed in 2001 for the Maritime and Coastguard Agency in the UK. A series of 50^{th} scale model experiments were undertaken and analysed. In addition the motions of a cargo carrier berthed on a jetty were measure at full scale.
The paper discusses the effect on other vessels of wash waves generated by fast ships operating at super critical and near critical depth Froude numbers. The two most significant conclusions reached are the importance of good mooring procedures when fast ships are operating in the vicinity of moored ships at open jetties and the wide range of vessels which are effected by the wash, often at considerable distance from the track of the fast ship.

1. Introduction

Ship wash can be classified by the depth Froude number which is simply the ratio of the speed of the vessel to the maximum speed a gravity wave can travel in a given water depth. The classical Kelvin wash pattern with both divergent and transverse waves is produced when the depth Froude number is less than one. When the vessel velocity and depth limited wave speed is equal the wash is critical and at higher ratios super-critical. Consequently when a ship operates at higher speeds and the velocity of the waves in the wash become depth limited, the wave pattern will change significantly. The transverse waves disappear because they can not travel fast enough to keep up with the ship. The first crest becomes straight energy is not dispersed to subsequent waves with the following wave crests being continuous, curved in plan view and divergent. The length, speed and energy of the leading waves is much longer than that observed in the Kelvin wave patterns.

Consequently it is the critical and super-critical wash which is of most interest due to the amount of energy conserved in the leading wave group. The following situations have been considered,

- a fast ship overtaking another vessel,
- a fast ship approaching an on-coming vessel,
- the effect of fast ship wash on moored vessels.

As part of the MCA 457 (2001) project, a series of experiments were conducted in a 50m long and 17m wide shallow tank to observe the behaviour of vessels under the conditions outlined above. Video was taken of the experiments to enable observation of both the fast ship and the other vessel. Also the motion of the full size ships was evaluated using video.

2. Ship Motions

In general the excitation processes caused by the wash of high speed craft are similar to those considered in sea keeping predictions due to gravity wave excitation. The waves generated by high speed craft operating in shallow estuaries are small in amplitude but are very long with a period of up to 40s. The most energetic waves have a period between 12 and 15s and are comparable in length to ocean swell. Unlike wind seas, the initial wave group in super-critical ship wash is composed of regular sequences of waves, which progressively vary with time in terms of wave period and wave height. Although the direction of the initial waves changes with both wave period and distance from the ship, wave refraction aligns the wave crests with the sea bed contours close to the shore. Consequently at the shoreline the wash looks like a train of parallel crested waves steadily varying in height and period.

In many cases the linearised equations for small amplitude ship motions in regular waves are applicable. However, most sea keeping theories are limited in their application to high speed super-critical wave wash because,

- in most sea keeping calculations the waves are assumed to be sinusoidal. Linear wave theory represents and predicts the properties of the wave pattern well.

- the waves in most sea keeping calculations are assumed to be deep water waves. It is necessary to prove that the equations take the general functions for wave and group velocities c and cg for any water depth into account.

2.1 Encounter Frequency

The wave frequency ϖ has direct influence on the motion of a floating object with no speed through water. However if the ship is moving the excitation is more dependent on the frequency at which the ship encounters the waves.

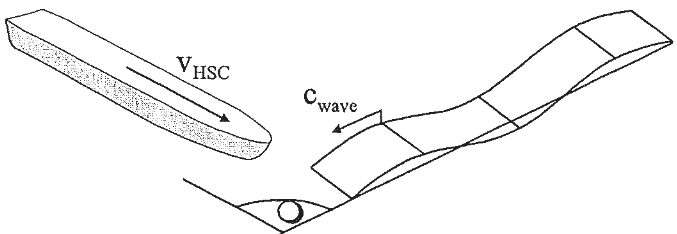

Figure 1: Definition of heading angle of a ship in regular waves

The encounter frequency, ω_e is a function of the heading angle μ. defined as the angle between the ship's course and the direction of wave propagation, figure 1. The corresponding encounter frequency can be calculated using the following equation

$$\omega_e = \omega - kV_S \cos\mu \qquad \text{with} \qquad k = \text{wave number}$$

Furthermore for a high speed craft approaching another ship from any direction in constant water depth at a depth Froude number above 1 the heading angle can be estimated for the first wave using the following equation.

$$\mu = \gamma - \arccos\frac{\sqrt{gH}}{V_{HSC}} \qquad \text{with} \qquad \gamma = \text{course}_{ship} - \text{course}_{HSC},$$

H = mean water depth,
V_{HSC} = speed of the HSC.

For the following waves the divergence in angle can be taken from the graphs or calculated using the mathematical model described by Whittaker et al 2001.

Transfer functions (or response amplitude operators) are graphs of the excitation or response of one particular ship at a range of encounter frequencies. The response function is made dimensionless by dividing by the wave amplitude (for linear motions) or wave slope (for angular motions). In deep water the wave amplitude is equal to half of the horizontal and vertical maximum displacement of a particle at the water surface. In shallow water however the orbital motions become elliptic and the horizontal displacement is greater than the vertical displacement.

The horizontal amplitude or half of the displacement of a particle at the water surface, can be calculated using the following equation:

$$\eta_{x\max} = \eta_0 * \coth(kH) \qquad \text{with} \quad \eta_0 = \text{wave amplitude}, \; H = \text{water depth}, \; k = \text{wave number}.$$

The natural frequencies, which can be obtained more easily than the transfer functions in many cases, can be used to estimate the point of harmonic response of a vessel in regular waves with small amplitude, but not the amplitude of the response.

In the following sections some general characteristics of conventional monohull ships will be used to describe the motions of the ship's centre of gravity in high speed wash. Absolute motions will be discussed in a later section of this paper.

Often the wave pattern generated by a high speed craft in a coastal area consists of several groups of waves and a range of frequencies, as shown in figure 2. As a result, a wide range of ships is effected by these waves, each by a different group in the wave pattern. In the wave cut shown in figure 2 the first zone shows the very long period leading waves in the super-critical wash. Zone 2 are waves of between 4 and 8s and are similar to those produced in a sub-critical wash. The third zone shows a set of 3s waves close to the breaking limit which are peculiar to fast ships with immersed transom sterns.

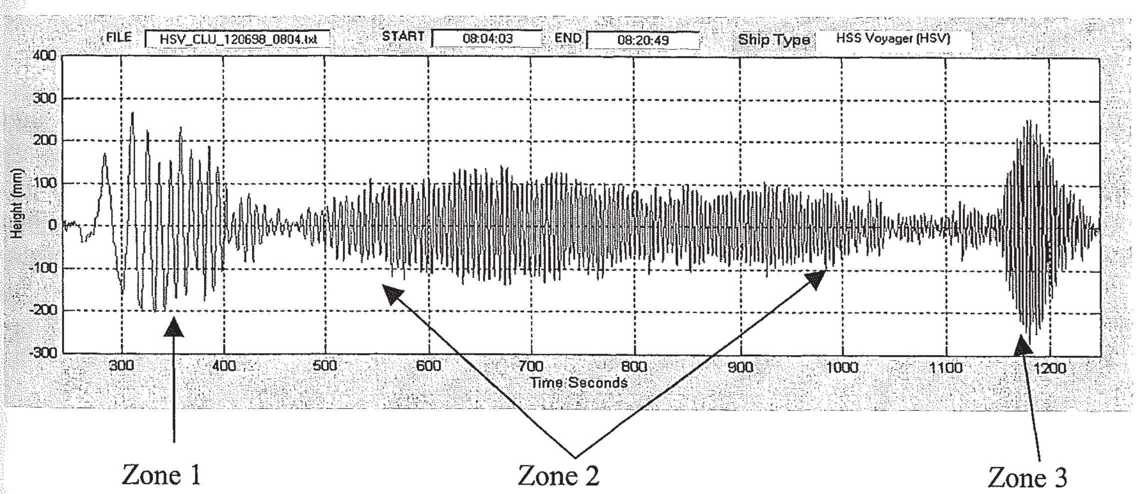

Figure 2: wave trace of HSC at super-critical depth Froude number and zones in wash

3. Ships Encountering Wash from High Speed Craft

3.1 Ships Passing and Overtaking

Motions in following or head waves (μ=180° or 0°)

In figure 3 one example is shown of a ship encountering high speed wash from the stern. The ship navigates in the same direction as the wave travels. If the wave celerity is substantially greater than the ship speed, it will experience similar motions to a particle of water at the surface. The maximum surge will occur in the wave crests and troughs and will reach the same value as the horizontal particle amplitude ($\eta_{x\ max}$).

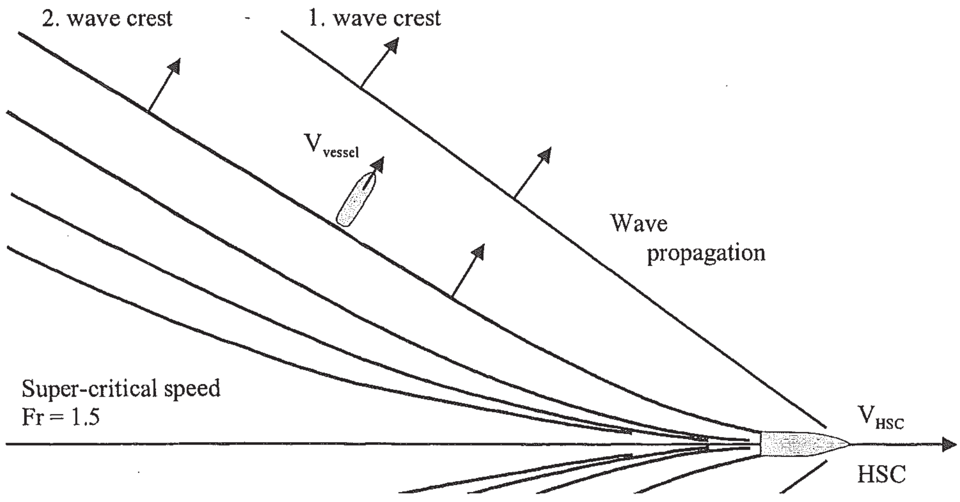

Figure 3: Wave pattern (crest lines) of HSC at supercritical speed and smaller vessel encountered by wash

The encounter frequency is always positive for a high speed craft, (HSC), overtaking the vessel. In following waves (caused by a passing HSC) the heave amplitude is not bigger than the wave amplitude (η_0). In head seas (caused by an overtaking HSC) this is in general the same case. However, at higher speeds some vessels tend to a heave / wave amplitude ratio bigger than 1 for encounter frequencies between 1 and 1.5. This is the case of a HSC passing another HSC either during or shortly after one of them has passed through the critical speed range. The high speed craft will hit a critical wave which will most likely be a head wave. (critical wave: $c_{wave} = V_{HSC} = \sqrt{gH}$)

The simplified heave transfer function for a slender long monohull is shown in figure 4. For higher speeds (above 20 knots) the ratio of heave to wave amplitude is bigger than 1 with a slight negative phase shift. It is possible that the ship speeding into the critical wash wave will partially emerge from the water at the bow and slam into the following wave. This has been observed in Belfast Lough and Loch Ryan and was accommodated by the masters of HSC warning each other about the existence of a critical wave. Therefore the master of a HSC has to be vigilant when passing through other high speed wash while operating at high speeds.

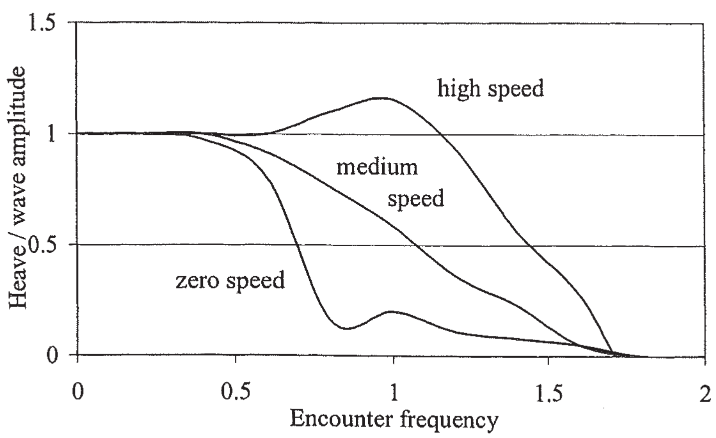

Figure 4: Transfer functions of a long slender monohull in regular head waves at different speeds

Table 1: General relationships between wavelength, ship length and heave amplitude in following or head waves	
Wavelength / ship length > 5	Heave / wave amplitude ~1
Wavelength / ship length between 5 & 1	Heave / wave amplitude depending on ship speed
Wavelength / ship length < ¾	Heave / wave amplitude Small to zero

The pitch transfer functions of many ships are similar to the heave transfer functions in following or head waves.

By considering the buoyancy forces along the hull a simple illustration for the motions can be given:

- For long waves the maximum heave will occur at the troughs (max. negative heave at the crest). The maximum pitch is reached after one quarter of the encounter period from the trough (max. negative pitch occurs ¼ period before the crest).
- For a wave being as long as the ship the buoyancy forces induce a moment causing pitch. Dynamic effects and the coupling of motions alter the simple relationship for longer encounter periods.
- If the wavelength is short compared to the ship length the different buoyancy forces in the crests and troughs of the waves eliminate each other.

3.2 Motions in beam waves (μ=90°)
A ship travelling towards or away from the track of the HSC as shown in figure 5 will be excited by beam waves. Similar to the motions in head or following waves a ship with a beam smaller than the wavelength will follow the orbital motions of a particle at the surface. As a consequence the heave amplitude is a first approximation equal to the amplitude of the wave. For a small craft (e.g. a leisure craft) the supercritical waves are not very important, the passengers will experience hardly any motion, as the acceleration is very small. However, for a draft limited ship operating in a channel with small bottom clearance, the large but slow motions can be vital. The maximum ratio of heave to wave amplitude is reached at this course for a VLCC. This increases the risk of a grounding situation. The sway is again equal to the horizontal particle motions or the horizontal wave amplitude ($\eta_{x\ max}$). The maximum heave will be experienced at the crest and trough and maximum sway at the zero crossing points of the wave.

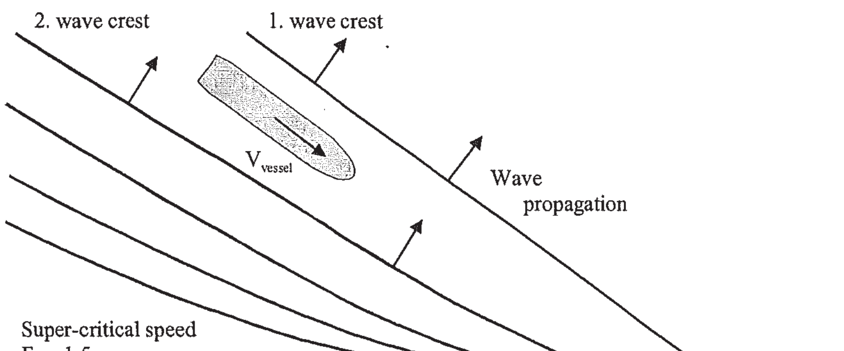

Figure 5: Wave pattern (crest lines) of HSC at supercritical speed and larger vessel encountered by wash

Roll motions are particularly strong in beam waves and at zero vessel speed. With a higher forward speed, the roll damping increases. The maximum roll amplitude (maximum harmonic response) occurs at slightly lower wave frequencies (natural frequency). Again the natural frequencies can be used to predict the frequency of the harmonic response of the ship. The amplitude of the roll motions is dependant on the metacentric height of a ship, meaning that for one ship encountered by the same wave but with different loading situations the roll amplitude will be different.

A report prepared by SSPA (1998) states that the wash from high speed ships is only a potential problem for VLCC's if the distance between the ships is less than 0.1 to 0.3NM. However, beyond this distance there may be a problem as a result of shoaling and energy concentration.

3.3 Motion in oblique waves - overtaking

When passing in channels or fairways, the course of the overtaking ship and the HSC are parallel. In figure 6 a situation is shown, where a vessel is being overtaken by a fast craft at super-critical speed. The ship will experience motions caused by oblique waves. The curved line in the diagram illustrates the lateral displacement due to the orbital motions of a particle at the water surface. Small craft (ship length < $\lambda/4$) behave like a particle on the water surface. The dominant motions will be surge, sway and heave, depending on the encounter angle and the ratio of wave amplitude to horizontal wave amplitude. Roll and pitch are small because of the wave slope being small.

A ship with a length of between $\lambda/4$ and λ will alter its course significantly. When the first wave reaches the ship the stern will be lifted and shifted away from the High Speed Craft. This results in a turn of the ship towards the overtaking vessel at the first zero crossing point of the wave. The maximum yaw will occur when the centre of gravity is at the crest of the wave. As the wave progresses underneath the moving ship this will be reversed. Approaching the first trough the ship will yaw to the other side. The stern is moved towards the overtaking ship while the bow is displaced away from it.

Due to these course alterations there is the possibility of collision if the ships have almost the same speed and are very close to each other. It has to be stated that a good helmsman or autopilot will adjust these course changes and minimise them. If the ship length is longer than one wavelength the motions become small compared to the wave amplitude and wave slope.

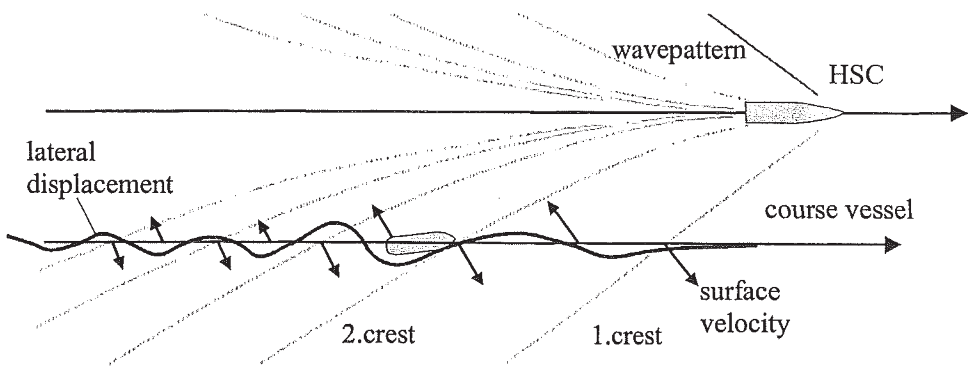

Figure 6: Wave pattern (crest lines) of HSC at supercritical speed and vessel encountered by oblique wash

Figure 6 illustrates the problem of defining one particular type of ship, that is effected by high speed wash. At the 4th wave the wavelength has reduced to half the length, consequently a range of vessel sizes is effected by different parts of the wave train.

The oblique angle of the waves advancing underneath the ship causes rolling due to the asymmetry of the forces resulting from the wave elevation. Hull shapes with a high overall beam to length ratio, like catamarans, are more effected than other conventional ships. Again it depends on the response of a particular hull design and their roll damping. For example catamarans have a high rate of roll damping, which results in the vessel following the water surface without motion amplification..

However, the strongest effect on larger vessels can be expected from the first waves of the supercritical wash, as these waves are the biggest in the wave pattern. However, small boats are more effected by the tail waves, which are generated by the combination of the hydraulic jump behind immersed transom sterns and jet plumes, plunging into the water at the rear of the high speed craft.

3.4 Motions in oblique waves - Passing

The effect of the high speed wash on an oncoming ship is similar to the response during overtaking. The wave pattern and the wavelength will be the same at similar speeds and water depths, but the encounter frequency will be higher. The risk of collision is less, as the ship will yaw away from the high speed craft at the first wave while abeam.

4. Motions of Moored Ships

The movements of moored ships are different to the motions of a free moving ship. The motions are constrained by the mooring, which is a flexible system. This adds another set of springs and dampers to the natural dynamic system of the ship. The eccentric mooring couples heave, surge and roll and introduces additional roll motions. The strength of the coupling depends on the eccentricity of the mooring and the angle of the mooring lines.

The wave pattern reaching the moored ship is usually more complicated compared to open waters due to the influence of coastal structures and the local bathymetry. The angle of propagation is due to wave refraction, reflection and diffraction around solid obstacles and, unless the berth is open to the incoming waves, these changes need to be considered. The wavelength can be shorter due to diffraction, which can increase the height at the same time. For illustration purposes a wave reaching a quay and the resulting wave crest bending is shown in figure 7.

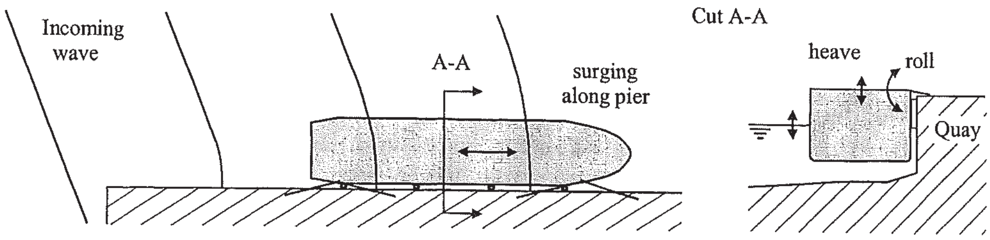

Figure 7: Moored ship encountered by stern waves on a pier

If the ship shown in figure 7 were alongside the pier with no moorings the movements would be surge and heave. Due to the mooring the ship will perceive additional rolling motions due to the coupling effect. Moorings consist of a set of different ropes with varying length and elasticity. It is important that the mooring lines facing in one direction are of similar length, similar elasticity and similar tension. Otherwise one rope could take excessive strain and can eventually fail. Short transverse lines are not recommended at a berth, which is subject to long period waves from the wash of high speed ships. If loading or discharge processes are taking place, which are sensitive to ship movements, it is recommended to interrupt these processes. It is good practice for the master of the HSC to notify the personnel in charge of the loading process via VHF prior to the approach.

4.1 Other Wash Induced Effects

Apart from the effect on moored ships discussed in MCA 420 (1998) there are other problems such as surge in marinas and small craft harbours due to the leading long period waves in the super-critical wash. However, during the course of this study other phenomena have either been observed or reported by users of the coastal zone. These fall into two categories;

- the dynamic response of floating structures such as link-spans and pontoons in harbours and marinas,
- relative motion of supply ships or pilot boats and another ship.

These are summarised in table 2.

Table 2: Wash induced effects at moorings

Ship type/mooring situation	Effected by	Counter measures
Cruise liners, large ships at freight and ferry terminals	Long period swell, dislocation of link span, ramp or gangway	
Small boats in yacht harbours	Steep crested tail waves	Floating breakwater
Working ships, pilot embarkation	Huge relative motions due to different behaviour in waves	Cease work process, secure equipment
Freight discharge and loading at anchorage, Replenishment at anchorage	various groups	Awareness and knowledge about existence of the problem

5. Absolute Ship Motions

The six motions so far discussed were the movements of the centre of gravity of a ship in regular waves. In many cases the motions of the ship at a particular location within the ship is more important Typical examples are movements in the restaurant of a passenger ferry, excursions of the ejector chute from a conveyor discharging cargo or the minimum bottom clearance of a large vessel.

While the three angular motions are the same at any point of the ship the linear displacements depend on these angular motions. However the linear displacements can be easily calculated for any point in the ship with co-ordinates in respect to the centre of gravity. The minimal bottom clearance for example at the chine shoulder at $^{Lwl}/_2$ of the ship is composed of the clearance with no motions less the heave as well as the lever arms of pitch and roll. The angular motions are in phase with the linear movements for intermediate encounter frequencies. For head waves, pitch and heave are synchronised for many ships. This causes large absolute motions, which are significantly greater than the wave amplitude.

6. Summary

With reference to the wave zones shown in figure 2, the processes presented can be summarised as follows:

Type of marine vehicle	Effected by group of pattern	Risks
Leisure craft / small boat / tug	Surging long waves in harbour entrances Short tail waves near craft	Grounding Capsizing/broaching (only very small craft)
Pilot boat / small fast craft	Short tail waves and medium waves (zones 2 & 3) if effected boat is travelling at high speed	Emergence / slamming / propeller emergence / propeller racing

Coastal and river cargo ship & bulk carrier	Head waves (zone 1) Beam waves (zones 1 & 2) Group Oblique waves (zone 1)	Distinct pitch and heave causing deck wetness or freeboard exceedance Distinct roll Yaw and partial loss of manoeuvrability
Ocean going container vessel / tanker	Beam waves (zone 1)	Roll and heave cause grounding
High speed craft / Fast ferry	Head waves at high speed / in particular critical wave Oblique waves (zone 1)	Critical encounter frequency emergence/ slamming/ air ingestion in water jet unit Distinct roll in particular for wide beam ships passenger experience unexpected motion
Working barge / jag up rig / platform / pontoon	Short period tail waves Surging long waves in very shallow water Any long period wave 1. & 2. group	Unexpected freeboard exceedance at calm day grounding in shallow water Shifting of equipment or building material due to unexpected movement of working platform

7. Conclusions

High Speed Vessels Passing Other Ships: The effect of the wash of high-speed craft on other moving vessels is dependent on size, displacement and hull form. Consequently the risk to each vessel must be assessed individually. However, there are a number of general observations which have been made:

(a) All vessels are effected by some part of the super- or trans-critical wash due to the spread of wave periods.

(b) Small craft are particularly at risk from the steep sometimes near breaking waves produced by fast craft in the trans-critical zone. They are particularly at risk of broaching and capsize when being overtaken.

(c) Long period wash waves cause large vessels to yaw and alter course, which can be problematical in a confined channel posing the risk of grounding, or when passing other ships in close proximity posing the risk of collision.

(d) Vessels operating at high speed are more effected by high speed wash than at low speed.

(e) Maximum pitch motions are expected for most craft, when the super-critical wash encounter the ship as head or following waves.

(f) Maximum heave motions are expected for bigger craft, when the super-critical wash encounter the ship as beam waves.

(g) Wash induced roll of deep draft wide beam ships such as container vessels operating in confined channels run the risk of grounding at the turn of the bilge.

(h) Compared to normal sea-keeping calculations it is important to consider, that the orbital motions are elliptic in shallow water, therefore the horizontal motions are much bigger, than the vertical.

Moored Ships and Super-critical Wash: Moored ships will surge on the long period super-critical or near-critical waves. As with any damped mass spring system, the response of the ship will depend on size, displacement and the elastic constraint of the mooring system. Large ships will respond to the long period waves while small vessels will respond to the shorter wave components. Consequently each ship and mooring configuration has to be analysed individually to assess the problems caused by fast ferry wash. A range of general observations can be made:

(a) It is important that the mooring lines facing in one direction are of similar length, similar elasticity and similar tension to avoid individual ropes taking excessive strain and breaking.

(b) The fact that mooring lines are attached to one side of a vessel results in induced roll when the vessel surges. However the motions are usually very complex.

(c) Field observations have shown that incidence of mooring rope breakage can be reduced if the crew of the moored vessels is aware of the imminent arrival of high speed craft and its wash.

(d) If loading or discharge processes are taking place, which are sensitive to ship movements, it is recommended to interrupt these processes. It is good practice for the master of the HSC to notify the personnel in charge of the loading process via VHF prior to the approach.

8. Acknowledgements

The authors wish to acknowledge the support of the Maritime and Coastguard Agency (MCA) in the UK, Stenaline, Belfast Harbour Commissioners and the support staff of the Department of Civil Engineering, Queen's University Belfast.

References

MCA 420, 1998, 'Investigation of High Speed Craft on Routes Near to Land or Enclosed Estuaries', Maritime and Coastguard Agency, Res. Project. 420, published July 1998

MCA 457, 2000, 'A Physical Study of Fast Ferry Wash Characteristics in Shallow Water', Maritime and Coastguard Agency, Res. Project. 457, published Nov. 2001

WHITTAKER, T.J.T., DOYLE, R., ELSAESSER, B., 2001, 'An experimental investigation of the physical characteristics of fast ferry wash', Proc. 2. Int. Conf. on High-Performance Marine Vehicles HIPER, HSVA, Hamburg, May. 2001, 14 pages.

LLOYD, A.R.J.M., 1998; Seakeeping, Ship Behaviour in Rough Weather, Gosport

SSPA MARITIME CONSULTING, 1988; Motions of VLCC due to wash waves from Stena HSS 1500, report No. 9744333-1, Feb 1998, commercial report.

High Speed Craft in Service

Karsten Fach, Germanischer Lloyd, fa@germanlloyd.org

Abstract

Based on GL a review of recent developments in high-speed craft (HSC) including wing-in-ground craft with particular focus on feedback from problems in service of fast ships is given, covering aspects of structures, machinery, and equipment.

Introduction

For many years we were talking on HSC conferences all over the world about new HSC developments. Up to 1995 the DSC Code (Dynamically Supported Craft) was used for HSC. It was followed by the HSC code and since July 1 st, 2002 the HSC code 2000 is effective.
About 7 years ago speeds of 36 knots were high, nowadays the speed exceeds 40 and 50 knots. We are learning more and more to handle load-, fatigue-, speed-, noise- and vibration predictions but normally we are not talking about the problems owner have when operating their vessels.
This paper will start with a short overview of existing GL classed vessels, typical materials will be described and structural and machinery problems will be discussed.

Significant ships

Fig. 1 shows the Fincantieri built monohull "Pegasus One". In Figs 2 and 3 the sisterships "Euroferrys Pacifica" and the "Westpac Express" built by Austal Ships in Western Australia, are shown. A very interesting vessel, built in Germany at Abeking & Rasmussen is described in Fig. 4, one of the two SWATH type Aluminium pilot tender for the German Bight. Flightship 8, see Fig. 5, was built in Germany and completed in Australia.

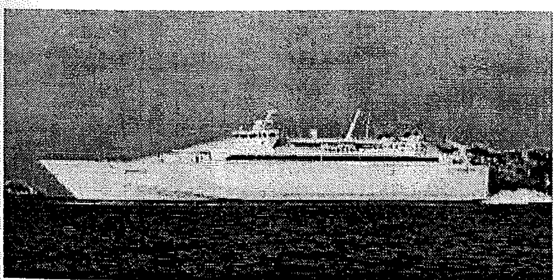

Fig. 1

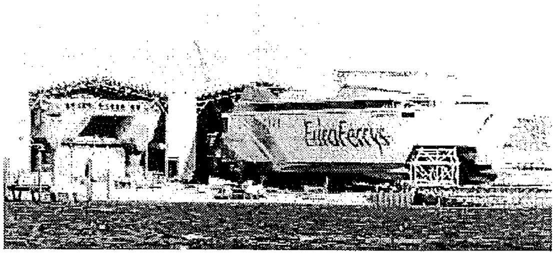

Fig. 2

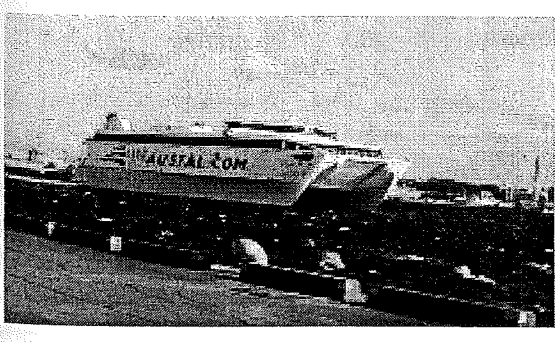

Fig. 3

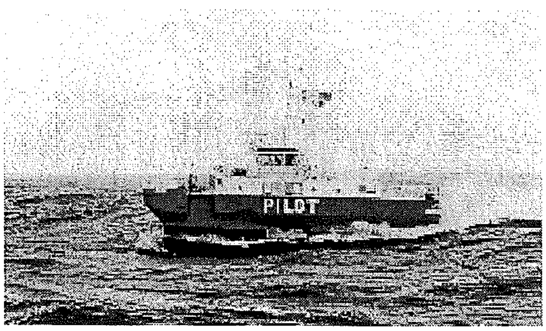

Fig. 4

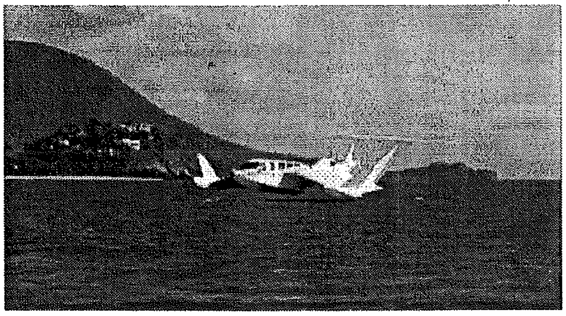

Fig. 5

Lightweight Design

Lightweight construction has always been of great significance in shipbuilding. Especially for high speed craft, which have in recent years been increasingly developed, savings in weight are absolutely essential. Given careful selection and application of design and calculation methods, materials as well as of manufacturing processes and conditions, it is possible to obtain high-strength structures with a prolonged service life. The additional efforts required will result in increased cost compared to conventional ships of conventional design and construction.

Reducing the weight of ship structures - aimed at for several reasons - increases the risk of underdimensioning with respect to possible failure modes.

For specific ship types lightweight construction is a basic requirement, e.g. for high speed craft and naval vessels, where it has a decisive influence on displacement and draught and consequently speed and power consumption. Also the mass centre - for reasons of floatability in damaged condition a decisive design parameter - is of relevance in lightweight construction. In the case of passenger and Ro/Ro vessels lightweight construction helps gain valuable, useful space in way of the superstructure.

Reduction in light-ship weight will as a rule be achieved by minimization of the scantlings, by innovative design and construction as well as by the use of higher-tensile hull structural steels or other materials, such as aluminium alloys or composite materials (fibre-reinforced plastics, FRP). In the endeavour to obtain structures of increasingly lighter weights adequate strength must, of course, be ensured with respect to possible failure modes.

In the past, stringent fire protection regulations rendered the use of aluminium and FRP as lightweight construction materials possible to a limited extent only. The savings made in the weight of structures were cancelled out by additional fire protection insulation. Once the IMO High Speed Craft (HSC) Code was adopted, which provides for a special safety, greater possibilities were opened up for the use of aluminium and FRP.

Materials:

Higher-Tensile Steel

Ordinary and higher-tensile steels, materials traditionally employed in shipbuilding, are also frequently used in present-day lightweight structures. For seagoing ships of approx. 150 m in length and over, higher-tensile hull structural steels with a minimum yield strength of up to 390 N/mm^2 are used particularly in continuous deck longitudinals. This enables not only the material required to be considerably reduced, but also excessive plate thicknesses and the problems associated therewith, e.g. in connection with forming and welding, to be avoided. In the case of lightweight and fast vessels, naval vessels as well as very large seagoing ships complete hull structures are made of higher-tensile steel. An example of this is the hull of the high speed passenger ferry "Pegasus One" built at the Italian shipyard Fincantieri; see Fig. 1.

When employing higher-tensile steel, special attention must be paid to fatigue strength. In welded structures with a relatively high notch effect fatigue strength is generally acknowledged to be only slightly superior to that of ordinary steel. Also in view of the heavy dynamic loads acting on fast vessels and the magnitude of load cycles it becomes increasingly important to ensure adequate fatigue strength both in the design and plan approval phases. In this context, the assessment of cross joints of continuous longitudinal structural members with fillet weld connection as well as of welded joints of highly stressed transverse frames and longitudinal girders in the upper and lower flange of the hull girder has to be considered.

Another problem associated with the use of higher-tensile hull structural steel is that of ensuring adequate buckling strength, particularly of continuous longitudinal structural members. In order to prevent buckling of plate panels, stiffeners and girders, these will frequently have to be dimensioned such that the scantlings determined in accordance with the respective local sea loads of the structural members concerned will be exceeded. Nowadays finite element models of individual sections and/or global hull structures are often used to accurately determine and assess critical areas within the hull. The stress analysis results obtained form the basis for assessment of the structure with regard to strength, fatigue strength and buckling strength.

Steel / Aluminium Connections

The passenger ferry "Pegasus One"(Fig. 1), the hull of which consists of higher-tensile steel and the superstructure of aluminium alloy, is a good example of consistent implementation of the lightweight construction principle. Explosion-bonded or extrusion-bonded steel / aluminium welding transition joints have proved successful in joining the different materials. Because of the generally reduced specific strength of the pure aluminium zone of the steel / aluminium joint, a larger surface is required for force transmission. During welding it has to be ensured that the boundary layer will not be unduly heated (max. 300°C), as this will entail embrittlement implying the risk of separation. Therefore, for reasons of uniform force transmission and heat exchange, weld connections at the edges of the welding transition joints are inadmissible. Moreover, owing to the necessity of avoiding undue heating of the boundary layer, it is not possible to fully weld together the transition joints and consequently achieve an absolutely tight joint. Therefore and because of the corrosion risk implied (contact element), additional sealing and/or anti-corrosion measures are required to be taken

Aluminium Alloy Structures

Aluminium alloys are from today's point of view no doubt the materials most commonly used for fast lightweight ships. Whereas in the sixties initially only a few small monohull vessels for commercial and private use were built of aluminium, today mainly large passenger ferries as well as combined passenger/car ferries attract our attention.
In shipbuilding, aluminium alloys of the 5000 series (AlMg alloys) and the 6000 series (AlMgSi alloys) are employed both for ships' hulls and superstructures. These aluminium alloys are characterised by good weldability and excellent corrosion resistance in a marine environment. Additional coatings and/or cathodic protection are therefore not required for part structures of ships, such as the underside of the transverse structure of catamarans.

Aluminium-magnesium alloys are primarily employed for plates of the shell, decks and built-up girders. Their strength properties can be enhanced by forming processes (mainly cold and/or hot rolling) subsequent to fabrication. In the recent past new, high-strength aluminium-magnesium alloys have been introduced into shipbuilding.

Aluminium-magnesium-silicon alloys are relatively soft, so that they require a limited extent of forming work only. They are therefore particularly suited for the production of extruded sections, with (almost) no limits being set for the design engineer in terms of shaping; see Fig. 6. By subsequent heat treatment it is also possible to improve the strength properties of AlMgSi alloys. An example of this is the increase in the 0.2 % proof stress of EN AW-6082 from 85 MPa in condition 0 (soft) to 260 MPa in condition T6 (solution treated and artificially aged). When using high-strength aluminium alloys in welded structures, the strength properties in the heat-affected zone will be reduced due to the input of heat.

Although the EN AW-7075 aluminium alloy is not weldable and consequently it is an untypical material for marine applications, it has been used in construction of the riveted airfoil framing structure, see Fig. 6, of FLIGHTSHIP 8. This alloy has a special resistance to crack corrosion and is more common in the aviation industry.

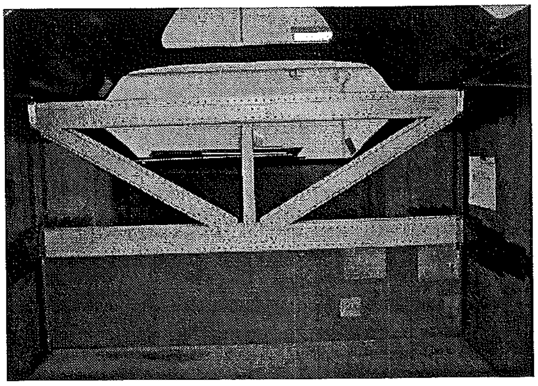

Fig. 6

FRP Structures

It is extraordinary that fibre-reinforced plastic (FRP) materials are still considered to constitute a novel material in shipbuilding. Glass-fibre reinforced plastics (GRP) have been in use for about forty years. Moreover, FRP materials are also employed in aerospace technology.
One of the most common applications of FRP on board high speed craft is the fabrication of carbon-fibre laminate shafts. Fig. 7 shows a typical shafting arrangement in an aluminium high speed craft.

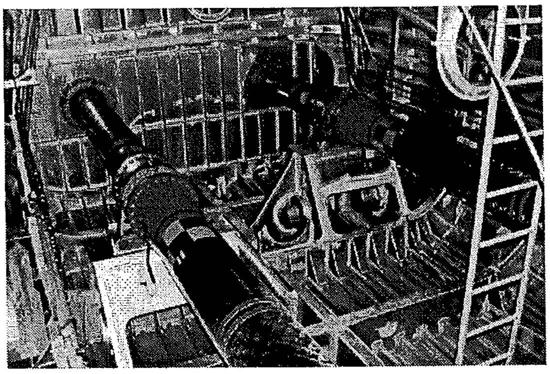

Fig. 7

The upper decks of the wheelhouses of these fast ferries are made of GRP sandwich laminate. FBM Marine in Cowes, Isle of Wight, use GRP for numerous components of the open deck structure of the HSC catamarans built by them.
Another interesting example is the wing in ground effect ship FLIGHTSHIP 8 which was built in Germany at Airflow Development for Australia; see Fig.5.
There are a variety of different FRP materials. For reinforcement generally glass, carbon and aramide fibres are used. Carbon and aramide fibres have very high-tensile strength values. Compared with compressive strength, the tensile strength of aramide fibres is low; however, on account of their tenacity, aramide fibres are used to increase impact strength. Carbon fibres displaying different

properties (HM - High Modulus; HT - High Tenacity; HST - High Strength) are supplied, depending on their intended purpose.
The fibres are available in the form of rovings, mats, fabrics and non-woven fabrics and combinations of these. The advantage offered by these materials is the possibility of producing laminates which, depending on the fibre direction, display desired strength properties, but also quasi-isotropic behaviour achieved by the respective laminate construction.
The main laminating resins used are polyester, vinylester and epoxy resins. The two latter-mentioned resins are characterized by particularly high resistance to hydrolysis, i.e. they absorb insignificant amounts of water and the risk of osmosis is practically excluded.

Core materials available for sandwich laminates are generally PVC foams, polyurethane (PUR) foams, polymethacryl (PMI) foams, balsa wood and honeycombs (thin aluminium or stainless steel plate honeycombs) as well as aramide paper (Nomex honeycomb). PUR foams are rarely used [1].

Discussion of Problems:

A problem in connection with aluminium structures in shipbuilding that becomes more and more critical is the failure under dynamic loads as sea loads acting on the shell, of pressure fluctuations in the waterjet inlet ducts and/or of loads due to vehicles acting on the deck structures and ramps. In view of the high rates of utilization of present-day lightweight structures special regard has to be paid to fatigue strength in areas exposed to high dynamic loads. Smooth transitions of transverse joints soft toy brackets, single-bevel and/or double-bevel welds with full root penetration instead of fillet welds as well as well rounded free edges will improve the fatigue strength properties of highly stressed aluminium structures. For special structures, such as the waterjet inlet ducts of waterjet powered high speed vessels, assessment of structural details on the basis of the results of finite element analysis performed is required to ensure adequate fatigue strength.

Following the problems on buckling mentioned for lightweight steel structures, aluminium structures have carefully to be checked as well in the design and structural plan approval phase. Buckling of highly loaded longitudinal and transverse structures located at the fore end of high speed crafts has been surveyed several times, especially on vessels sailing frequently in rough sea condition. Fig. 8 shows buckling of a longitudinal bulkhead due to slamming events on the wet deck structure of a high speed catamaran operating at the Baltic Sea.

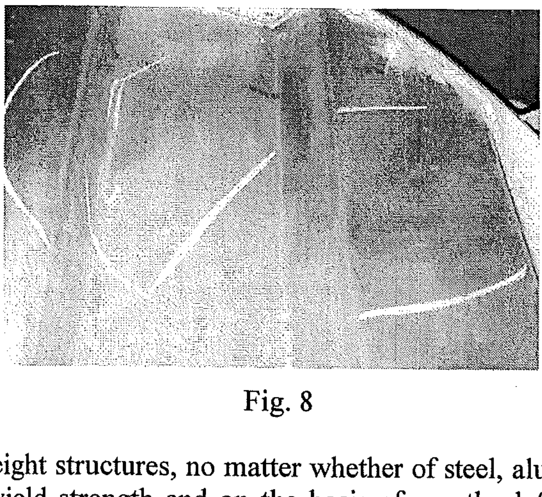

Fig. 8

Due to the fact that lightweight structures, no matter whether of steel, aluminium or FRP, are usually dimensioned close to the yield strength and on the basis of exactly defined load cases, unforeseen events may cause damages of partial hull structures. Such an event may be, for example, the collision of the vessel with harbour facilities. Fig. 9 shows the damaged aft structure of an aluminium catamaran. Extensive repair work was required to restore the original shape. Traditionally built structures may have less damage, on the other hand the higher weight of the conventional ship will result in a higher impact force.

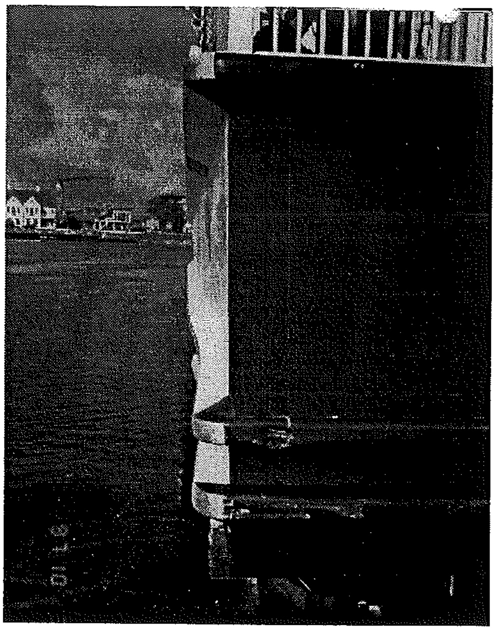

Fig. 9

Special consideration must also be given during the design phase to the vibration behaviour of lightweight structures. Because of the possibility of reduced scantlings with unchanged unsupported length achieved by use of increased strength materials for transverse and longitudinal girders or alternatively an increased girder length with unchanged scantlings, the natural frequency of these large "weak" structures can lie within the resonance range of low-frequency exciters, such as propellers. Vibration analyses of critical structures during the design phase are nowadays more or less a matter of routine and are increasingly performed, using the finite element method.

In this connection the noise behaviour of light-weight structures has also to be mentioned. The reduction of weight and stiffness often lead to uncomfortable noise levels which is well known on HSC. Additional stiffeners and material at the main engine foundation can reduce the noise level considerable. The additional weight for this matter is often less than the weight for insulation necessary for comparable noise reduction. A noise prediction performed by a competent partner can optimise the noise behaviour of light-weight structures.

More and more windows on HSC and passenger ships were glued to the superstructure to reduce the weight of the construction. Up to now the experience with this procedure is positive. It is important to use trained staff for this work, failures in the working procedure cause significant loss of the strength of the connection. It has to be noted that glued windows are only allowed in areas which are not affected by International Load Line.

The most common failure of sandwich laminates is undoubtedly attributable to shear fracture in the core. Often, when designing the core material, insufficient attention will be given to shear stressing. Damages due to lack of adhesion between core and skin laminate are less frequent. Problems may also be caused by local introduction of forces not known at the time of construction; in that case, expensive modification work will in some instances have to be carried out subsequently, so that the sandwich laminate will be capable of resisting the additional forces introduced.

A general problem faced in FRP processing is non-compliance with manufacturers' specifications, such as temperature, humidity of the air, mixing ratios and cleanliness. Even with apparently completely cured resins reduced strength may be the result of failure to observe the respective requirements. Non-destructive testing of FRP materials is unfortunately possible to a limited extent only.

Corrosion of Aluminium

As mentioned before, traditional and new developed high-strength aluminium alloys of the 5000 and 6000 series have an excellent corrosion resistance in a marine environment. However, in the recent past we surveyed extensive corrosion defects on car deck planking extruded from EN AW-6082 alloy. The reason is the intensive contact of the non-coated deck planking with saline melted snow and ice from cars. This special problem of vessels servicing countries in North Europe will be faced by additional requirements of Germanischer Lloyd on coating. Normally the aluminium alloys which are used for marine purpose have no corrosion problems in seawater, see Fig. 10 shows the loss of material for aluminium in different media. It is obvious that for the media (water) HSC are used there is no loss of material.

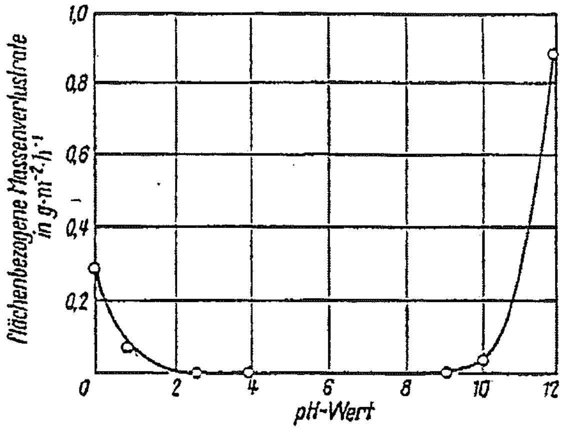

Fig. 10

Nevertheless corrosion is one of the major problems for Aluminium structures due to contact corrosion or selection of wrong materials. Fig 11. shows the typical problem of contact corrosion having aluminium and stainless steel without proper insulation.

Fig. 11

Damage Statistic

GL's statistic about structural damages on HSC since 1996 for ships operating in the Skagerak, Baltic Sea, North Sea, Irish Sea, Mediterranean Sea, Red Sea, Indonesia, South America, Polynesia shows that most of the reported damages are caused by collision or grounding. Most of these accidents happen during harbour manoeuvring (collision with harbour facilities). About 20% of the damages are caused by unexpected loads during operation in normal conditions and about 15% are reported as overload, operating above the design limits. The remaining are caused by bad workmanship, material failures or unknown reasons. All of these damages were local and most of the repairs were done without longer interruption of operation.

Machinery Aspects

Most of the reported machinery problems are caused by the following facts:

- Wrong Rating Selection

  Each vessel on each specific route has its own load profile for the engines. From this profile the manufacturer can calculate a load factor and an appropriate engine can be selected for the vessel. Sometimes this load profile was not investigated sufficiently and a wrong engine was selected.

- Engine Room Environment

  Due to the small size of some engine room compartments and the restrictions to the exhaust system regarding noise the ventilation of some engine rooms is not enough for the installed power. Very often this is coupled with high outside air and cooling water temperature. In this moment the power output of the engines is reduced and to achieve the service speed the engines may be overloaded.

- Maintenance

  Very often engine manufacturer requirements were not observed. Fuel oil and lubrication oil quality sometimes is very poor and does not meet the preconditions of the engine manufactures.

  In cold regions corrosion in cooling system is a minor problem, as the antifreeze contains a corrosion protection remedy. In warm areas a corrosion protection should be used.
  Special care has to be taken to the qualification of maintenance personal. In some area this qualification is not the best and damages may be the result.

References

[1] Classification Experience with Lightweight Ship Structures; Karsten Fach, Falk Rothe, Germanischer Lloyd.

Slamming Induced Pressures on HSC

Rasmus Folsø

RINA, Innovation Research and Products Section, via Corsica 12, Genoa, Italy.
Rasmus.Folso@rina.org

Francesco Torti

Rodriquez Engineering, Piazza della Vittoria 15/9, Genoa, Italy, ftorti@rodriquez.it

Abstract

Initially the calculation procedure for assessment of slamming induced pressures on HSC proposed by Stavovy and Chuang (1976) will be recited. It order to make this procedure more applicable for design purposes, some modifications to the theory will be introduced. Secondly, the model test results will be applied in order to demonstrate how calibrated values of the pressure coefficient Cp, which enters in the Stavovy and Chuang procedure, can be determined. Finally, with these values of Cp, slamming induced pressures will be determined and compared to the pressures obtained from model tests. The result of this comparison is that the modified Stavovy and Chuang procedure is applicable and that it is capable of yielding results that are in good agreement with the model tests results.

1 Introduction

One of the basic problems a designer of HSC (High Speed Craft) has to face early in the design phase is the determination of the design loads. The first, and probably the most important, design load that is determined is the amidships vertical bending moment. This moment consists of both a still water and a wave induced part. The wave induced bending moment can be estimated e.g. by application of classification society rules, whereas the still water bending moment can be determined by means of a hydrostatic calculation once the ship's hull geometry and longitudinal weight distribution are known. At this point the value of the wave induced bending moment can be further analysed by means of e.g. sea-keeping calculations or quasi-static "frozen wave" calculations.

The above approach has proved to yield reliable values of the design bending moment, or, more in general, the design sectional forces. However, these loads are not the only design loads needed. For HSC slamming induced pressures are important design loads for the dimensioning of bow/bottom structure. Unfortunately, these pressures are a lot more difficult to determine, as they are dependent on many factors and quite sensitive to even small modifications of these. Again classification society rules can be applied to obtain design values, but due to the complexity of slamming many designers prefer to expand this by performing e.g. model tests, calculations or a combination of these. This paper shows how improved values of slamming pressures can be obtained by combining calculations and model tests.

In more details this paper will start by reciting the Stavovy and Chuang (1976) procedure for estimation of max impact pressures on HSC, and then this approach will be slightly modified in order to make it more simple and flexible. Then it is shown how a limited number of model tests can be used to obtain calibrated values of the pressure coefficient Cp to be used in the modified Stavovy and Chuang procedure, and finally this procedure for prediction of max slamming pressures will be tested. The testing will consist of following steps:

1. The time histories of the measured pressures during the irregular wave tests will be analysed and for each impact registered, the corresponding measured vertical relative velocity will be determined. By application of both the original and the modified Stavovy and Chuang procedure, also the respective impact velocities are calculated. This way it is possible to assess the correlation between:

- The vertical relative velocity and the measured impact pressures,

- The original Stavovy and Chuang impact velocity and the measured impact pressures,

- The modified Stavovy and Chuang impact velocity and the measured impact pressures.

The velocity that shows the best correlation with the impact pressures is the velocity best suited for calculation of the impact pressure.

2. The max measured impact pressures in the irregular wave tests will be compared to results from frequency domain strip theory calculations combined with both the original and the modified Stavovy and Chuang procedure.

The work presented in this paper was carried out in the MONITUS research project. This project is a 3 year EUREKA financed project with the partners: Rodriquez Cantieri Navale (Italian ship yard), RINA (Italian classification society), MARIN (Dutch research institute) and DTU (Technical University of Denmark).

2 Stavovy and Chuang method

An accurate and theoretical rigorous prediction of impact loads is very complicated and time consuming. In order to fully describe impact forces and resulting structural response, various phenomena (entrapped air, hydroelastic interactions, compressibility effects and non linear effects) should be modelled. However, there is a lack of understanding on the basic modelling in each of them, which implies that slamming is far from being accurately modelled by presently available theories. As a result, marine structures must be designed based on a number of assumptions about the spatial and temporal distribution of forces and pressures as well as about their intensity. A widely adopted approach is to correlate the impact velocity with the slamming induced pressure. The simplest description of the impact velocity is the relative vertical velocity between the hull and the sea surface. This velocity can be derived from sea-keeping calculations both in the frequency and the time domain. However, for HSC this velocity is usually not capable of reflecting the dynamics of the impact. This is due to first of all the high forward speed of the ship, and secondly due to the typical deep-V hull forms of this kind of vessel.

Stavovy and Chuang (1976) developed a methodology for HSC which both considers the forward speed and the effective deadrise angle. This approach can be considered as a 3D expansion of more traditional 2D approaches such as Wagner (1931) and Von Karman (1929), as it not only considers the deadrise angle of the hull, but also buttock, heel and trim angles. The maximum impact pressure, p_{max} is given by:

$$p_{max} = \rho C_P \frac{V_r^2}{2} \qquad (1)$$

where ρ is the water density, V_r is the component of the relative velocity of the craft perpendicular to the impact surface at the point of impact, from now on referred to as the *impact velocity*, and C_P is the coefficient of maximum pressure, which can be taken as proposed by Stavovy and Chuang (1976) or be based on ad hoc experiments. In the present paper the latter approach will be adopted, and in chapter 3 it is described how C_P can be determined based on model tests. The following relationships are used:

$$V_r = V_r\,(V_{z\alpha}, V_h, \xi(\alpha, \beta_e, \tau, \delta)) \qquad (2)$$

Where: α is the buttock angle, $\xi(\alpha, \beta_e, \tau, \delta)$ is the effective impact angle, β_e is the effective deadrise angle, δ is the heel angle, τ is the trim angle, $V_{z\alpha}$ is the value of vertical relative speed between the craft and the wave having α probability of exceedance and V_h is the craft forward speed.

Without entering into details about how to determine the effective impact and deadrise angles it will here be recited that the impact velocity is defined as:

$$V_r = V_{h\omega} \cos\beta_e \sin\xi + V_{v\omega} \cos\xi \tag{3}$$

where $V_{h\omega}$ and $V_{v\omega}$ are the velocity components of the impact body perpendicular to the wave surface, and defined as:

$$\begin{aligned} V_{h\omega} &= V_h \cos\theta - V_{z\alpha} \sin\theta - V_{ot} \\ V_{v\omega} &= V_h \sin\theta + V_{z\alpha} \cos\theta + V_{on} \end{aligned} \tag{4}$$

where θ is the wave slope at the point of impact and V_{ot} and V_{on} are respectively the tangential and normal component of the wave particle velocity, which are again function of the wave slope! It is obvious that for design purposes it is not convenient that the wave slope and the wave particle velocity components, at the point of impact, must be known in order to estimate the impact pressure, as this requires exact knowledge of the wave the vessel is encountering, and where the impact will take place. To overcome this problem, $V_{h\omega}$ and $V_{v\omega}$ will here be defined as:

$$\begin{aligned} V_{h\omega} &= \overline{V}_h \cos\theta_S - V_{z\alpha} \sin\theta_S \\ V_{v\omega} &= \overline{V}_h \sin\theta_S + V_{z\alpha} \cos\theta_S \end{aligned} \tag{5}$$

where θ_S is the max slope of a wave with the height H_S, corresponding to the significant wave height of the considered sea state, $\overline{V}_h$ is the forward speed of the vessel relative to the travelling waves, and defined as:

$$\theta_S = \frac{2\pi^2}{gT_P^2} H_S \tag{6}$$

$$\overline{V}_h = V_h - C\cos\phi \tag{7}$$

where ϕ is the heading angle between ship and wave (180° being head sea), and C is the velocity of the travelling waves (wave celerity) defined as:

$$C = \frac{gT}{2\pi} \tag{8}$$

This definition of the velocity components perpendicular to the wave surface has the advantages that;

1. The exact wave slope is not needed. Instead a characteristic wave slope is used, such that it is sufficient to know the characteristics of the sea state in which the vessel is travelling.

2. The heading angle between ship and wave is introduced explicitly. The original Stavovy and Chuang procedure only includes the effect of the heading angle through the relative vertical velocity. The horizontal relative velocity is very much affected by the heading angle, and the above modifications take this into account in an approximate way.

3 Experimental determination of C_P

If measurements of slamming pressures from model tests are available, it is possible to obtain "true" values of the pressure coefficient Cp that enters the Stavovy and Chuang approach. An example for the Rodriquez built and designed TMV114 fast ferry, with main particulars shown in Table 1, is given in the following:

Length overall (L_{oa})		114.0 [m]
Length between perpendiculars (L_{pp})		96.0 [m]
Breadth moulded (B_{mld})		16.5 [m]
Breadth at waterline (B_{mwl})		13.8 [m]
Depth (D)		10.8 [m]
	V = 0 [kn]	*V = 35 [kn]*
Draught at aft perpendicular (T_{app})	2.47 [m]	2.84 [m]
Draught at fore perpendicular (T_{fpp})	2.72 [m]	2.06 [m]
Displacement (Δ)		1727 [t]
Design speed (V)		35 [kn]
Froude number (F_n)		0.59

Table 1: Main particulars of TMV114.

The maximum impact pressure is in the Stavovy and Chuang approach defined as:

$$p_{max} = \rho C_P \frac{V_r^2}{2} \tag{9}$$

Now, assuming that p_{max} is known from model tests, the coefficient of max pressure can be determined as:

$$C_P = \frac{2p_{max}}{\rho V_r^2} \tag{10}$$

The problem now becomes to determine the impact velocity V_r, which can be done in two ways; one based on the statistical results from the model tests, another based on an analysis of the time histories from the model tests. These two approaches will be demonstrated in the following.

Determination of Cp based on statistical model test results

In order to determine the pressure coefficient Cp based on the statistical results from model tests, following approximate procedure can be adopted:

1. a characteristic value, e.g. the significant $p_{1/3}$ (mean of the largest 1/3), of the measured impact pressures in a given sea state is determined
2. the relative vertical velocity is then determined, in the same sea state as the tests were carried out in, by means of sea-keeping calculations.
3. based on the results from the sea-keeping calculations, which is a RMS (standard deviation) value of the relative vertical velocity in the considered sea state, a characteristic vertical velocity $V_{Z,1/3}$ corresponding to the characteristic pressure determined in 1., is determined.

4. by application of the buttock, deadrise and trim angles, the characteristic vertical relative velocity $V_{Z,1/3}$ is transformed into the characteristic impact velocity $V_{r,1/3}$, by application of the Stavovy and Chuang procedure.

By following this procedure it is obtained that for a given location on the hull, a given sea state and a given heading angle, corresponding values of impact pressure and impact velocity are determined. It is then straightforward to obtain the coefficient of max pressure C_P. In Figure 1 a comparison between the experimental derived values of Cp and the Stavovy and Chuang values are shown. The tests considered are all tests with irregular waves, and the sea states are described in Table 2. The vertical relative velocity applied in the calculations have been determined with RINA's in-house sea-keeping code SGN, which is based on the linear frequency domain strip theory according to Salvesen et al. (1970), including modifications in order to take into account the effect of passive and active ride control systems (anti-roll fins, T-foils), described by Folsø and Torti (2001).

Test	Hs [m]	Tp [s]	Heading [deg]
1	2	10.3	180
2	3	10.3	180
3	2	10.3	135
4	4	10.3	135
5	2	6.4	180
6	2	6.4	135

Table 2: Modelled sea states during the model tests.

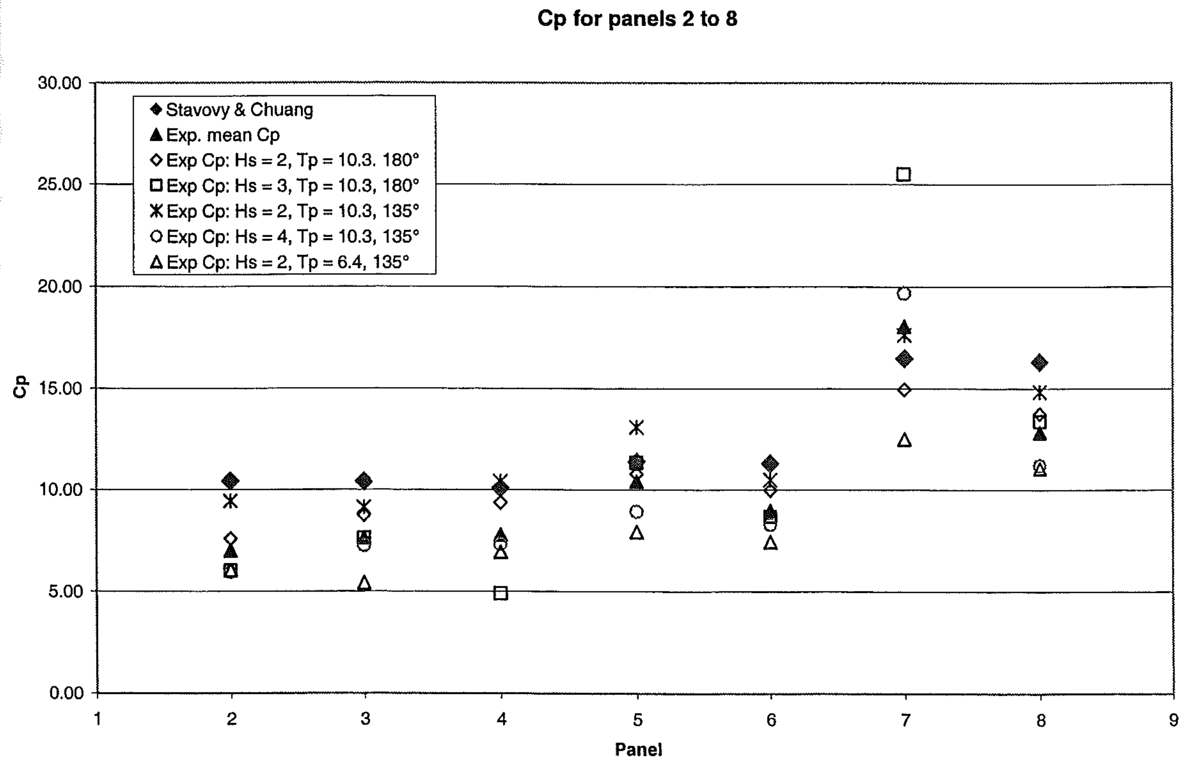

Figure 1: Experimental derived Cp values compared to Stavovy and Chuang values, based on original description of the impact velocity.

In Figure 1 it can be seen that the Cp values based on the original Stavovy and Chuang method compares rather well to the experimentally derived ones, maybe with the exception of panel 7 where the discrepancy is noteworthy. It can also be noted that the experimental values show quite some scatter around their mean values. The explanation for this is, at least partly, the stochastic nature of the slamming; the characteristic pressure values are based on the measured slams during the tests, whereas the characteristic velocity is based on sea-keeping calculations. Due to time limitations when performing the model tests, they have been terminated when approximately 150 waves have been encountered. This is considered to be sufficient for obtaining statistical estimates of the responses, but it is also well known that if the exact same test is repeated, somewhat different statistical estimates are obtained.

However, the results in Figure 1 also reveals that for all panels but one, the smallest C_P values are found in the sea state with the lowest wave period, Tp = 6.4 s. This can be considered as a sign that the original definition of the impact velocity does not model correctly the effect of the wave period; the Cp values should be independent of the wave period if the impact velocity modelled this correctly. Therefore, as described in chapter 2, a modified impact velocity definition that takes into account the propagation velocity of the waves and their heading angle relative to the ship direction, has been developed. In Figure 2 the experimentally derived C_P values based on the modified impact velocity are shown. **It can be seen that these C_P values are all significantly smaller than the Stavovy and Chuang values, but this is not really a problem as they are also intended for application with a different impact velocity; the derived pressures are similar!**

What is interesting to note is that the C_P values derived in the test with Tp = 6.4 s are no longer biased with respect to the C_P values derived from the other tests. This is a clear indication that the modified impact velocity reflects the dynamics of the impact better than the original velocity. This can also be seen in Figure 3, where the Coefficients of variation (CoV) of the derived C_P values at each panel are shown.

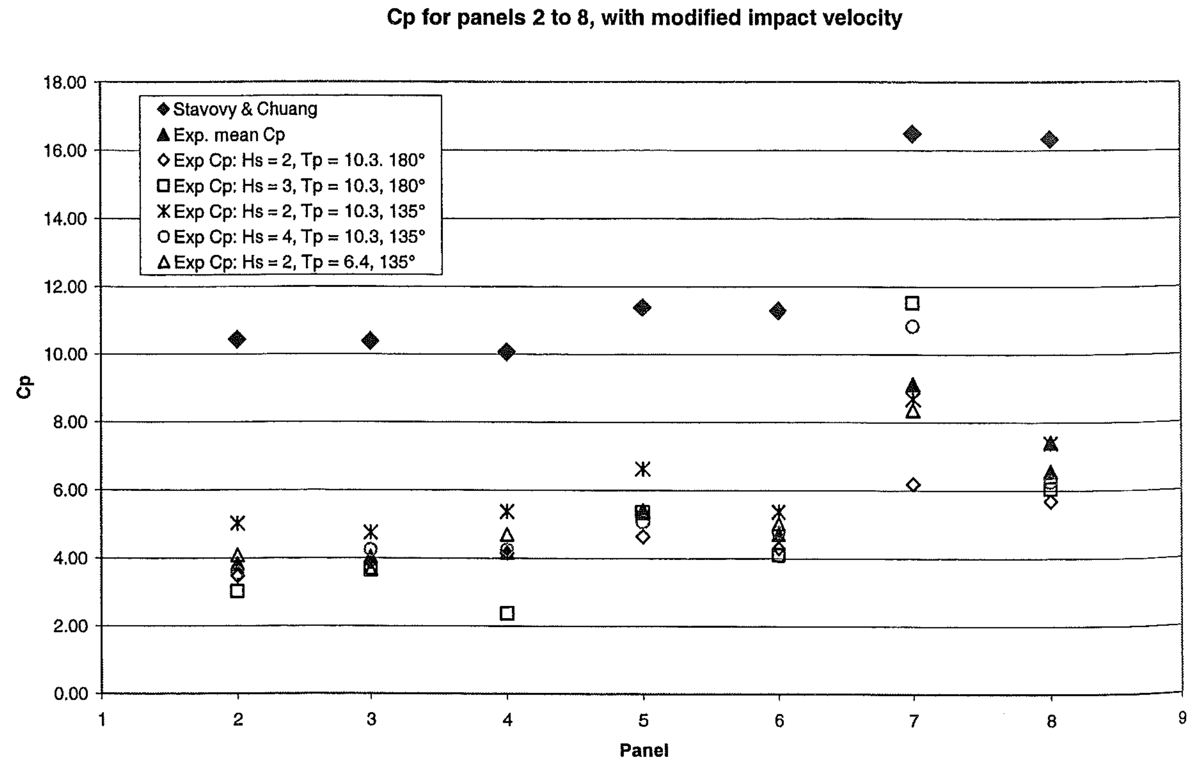

Figure 2: Experimental derived Cp values compared to Stavovy and Chuang values, based on modified description of the impact velocity.

In order to verify that it is more correct to estimate slamming pressures based on the impact velocity than on the usual relative vertical velocity, the CoV's of the Cp's at each panel have been calculated. The CoV is defined as;

$$CoV = \frac{Standard\ deviation}{Mean\ value} \qquad (11)$$

and thus describes the non-dimensional average scatter of the values around their mean. This means that the more correlated the velocity is with the pressure, or, in other words, the better it describes the slamming dynamics, the smaller will the Cp be.

In Figure 3 the CoV's of the Cp's obtained with the two impact velocities, and for reference also for the Cp's obtained with the more traditional relative vertical velocity, are shown. It can be seen that the Stavovy and Chuang impact velocity correlates much better with the measured slamming pressures than does the relative vertical velocity. Furthermore, it can also be seen that the modified impact velocity correlates slightly better with the measured pressures than the Stavovy and Chuang velocity, and it is therefore concluded that the modified impact velocity yields a more accurate modelling of the slamming dynamics.

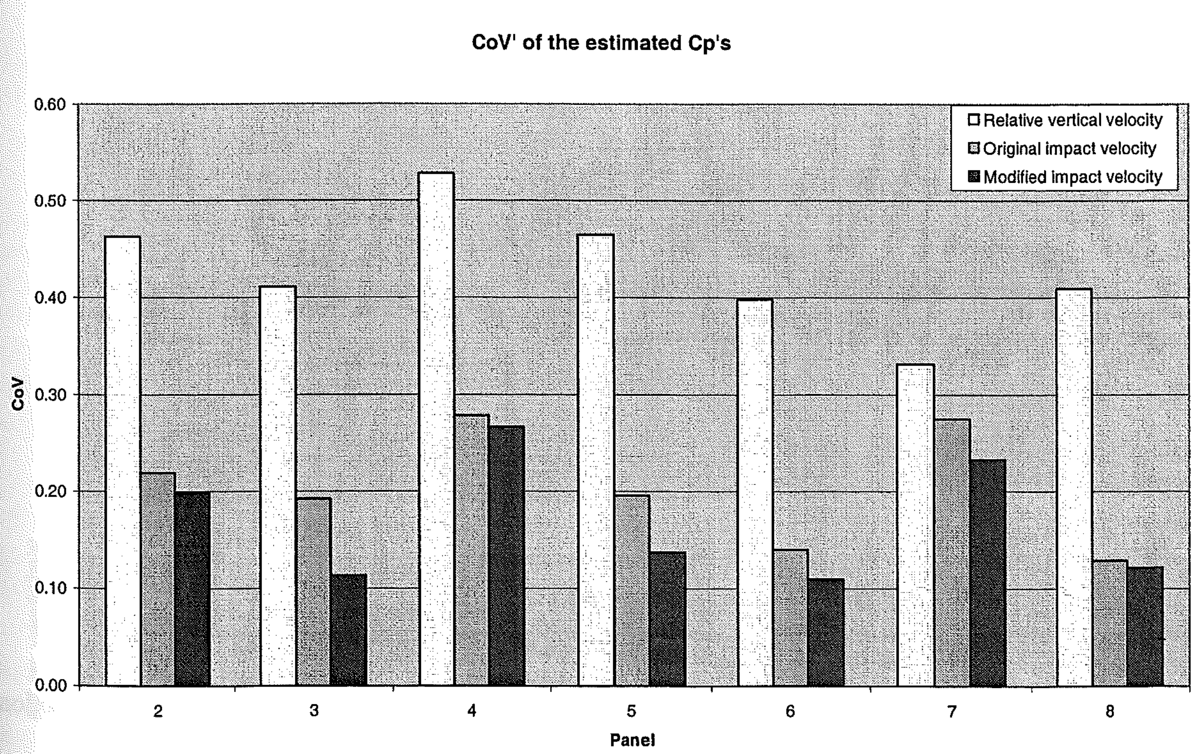

Figure 3: Coefficients of variation (CoV) showing pressure correlation with respectively the vertical relative velocity, the Stavovy and Chuang impact velocity and the modified impact velocity.

Determination of Cp based on time series from model tests

In order to determine the pressure coefficient Cp based on an analysis of the time series from model tests, following time histories must be available:

1. Time history of the measured pressure on the hull,
2. Time history of the relative vertical velocity, at the same location as where the pressure is being monitored.

During the model tests performed in the MONITUS project it was ensured that the above information would be available. The model was instrumented with an experimental device for measuring the relative motion at station 17, where also a force panel measuring the force acting on a 1 m^2 (full scale) area was installed. A picture of this instrumentation is shown in Figure 4. With this instrumentation it has been possible to obtain corresponding time series of the relative vertical motion and the pressure at panel 2, both located at station 17. By taking the time derivative of the relative motion the relative velocity has been obtained.

The time histories of the measured pressure has been analysed and all the pressure peaks (impacts) has been identified. In Figure 5 through Figure 7 the measured relative vertical velocity is shown together with the measured pressure peaks. It can be noted that there is a very good correlation in time between the peaks of the relative vertical velocity and the pressure peaks. I.e. the general applied assumption that slamming occurs when the relative vertical velocity exceeds a certain threshold value, Ochi and Motter (1973), seems to be correct.

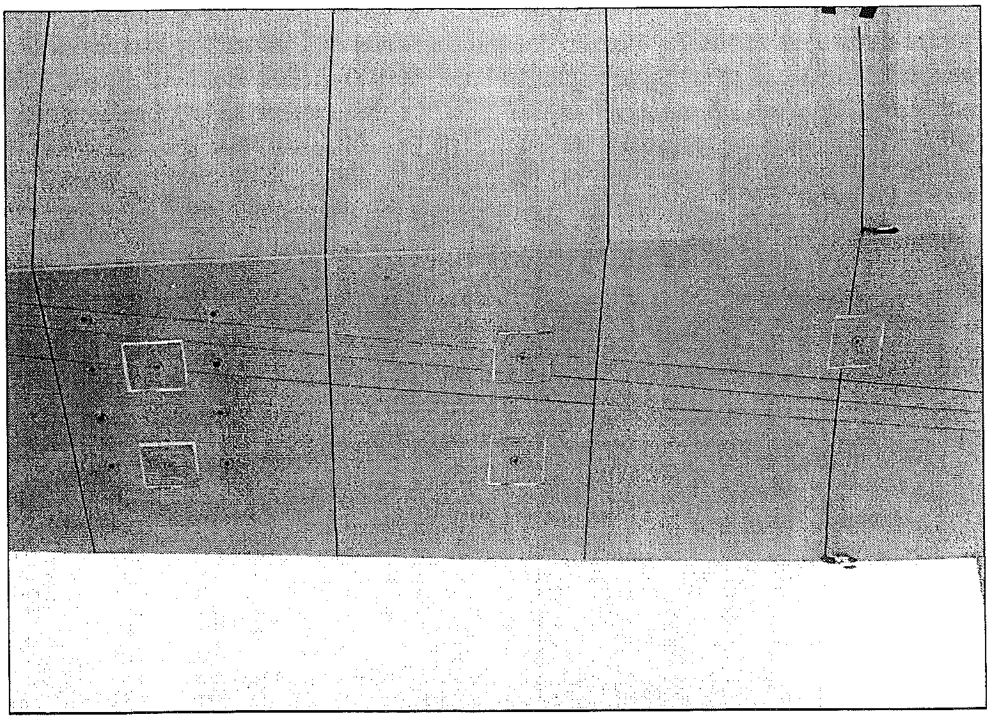

Figure 4: Picture of installed force panels and the experimental device measuring the relative motion at station 17 (foremost station in picture above).

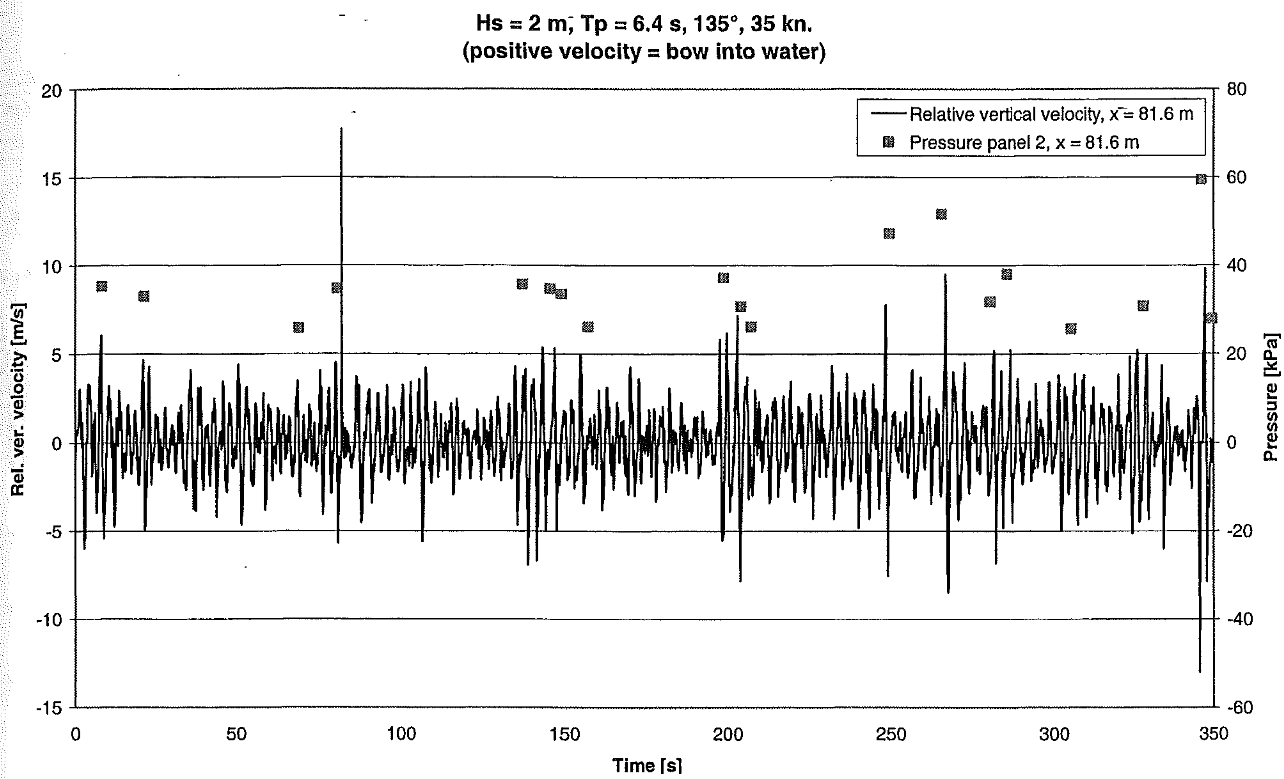

Figure 5: Measured relative vertical velocity and impact pressures.

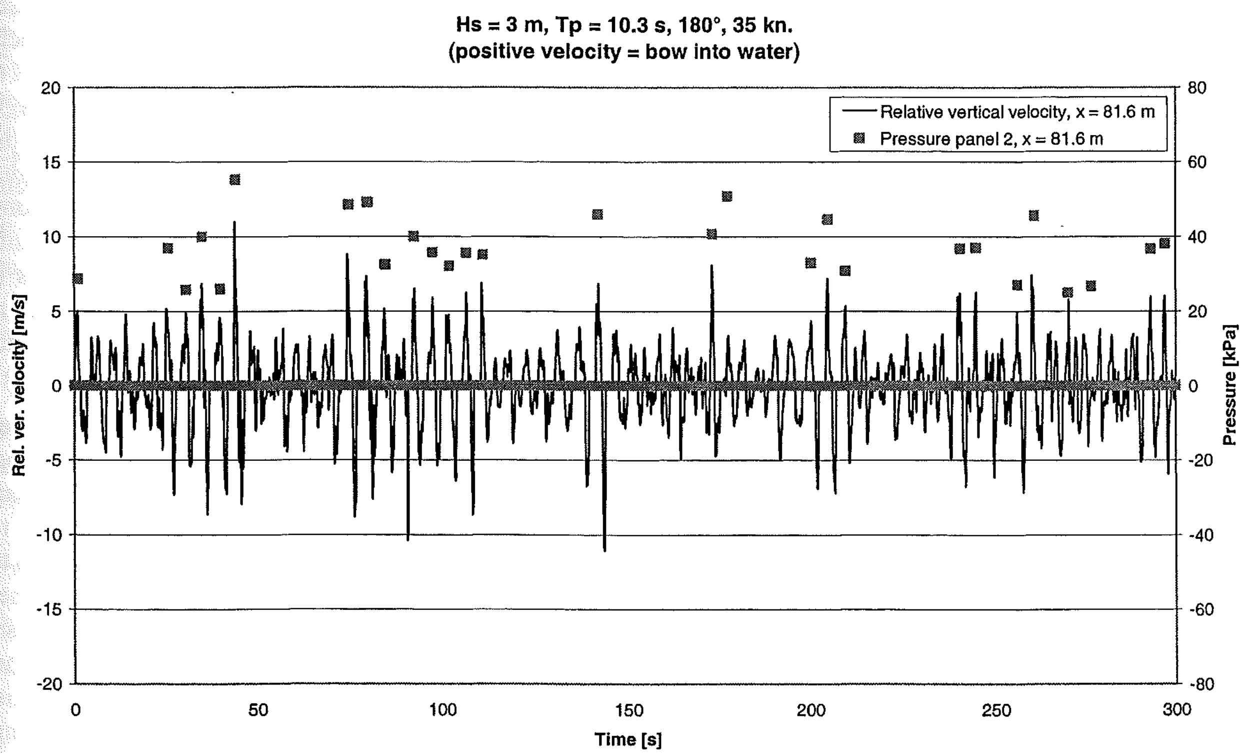

Figure 6: Measured relative vertical velocity and impact pressures.

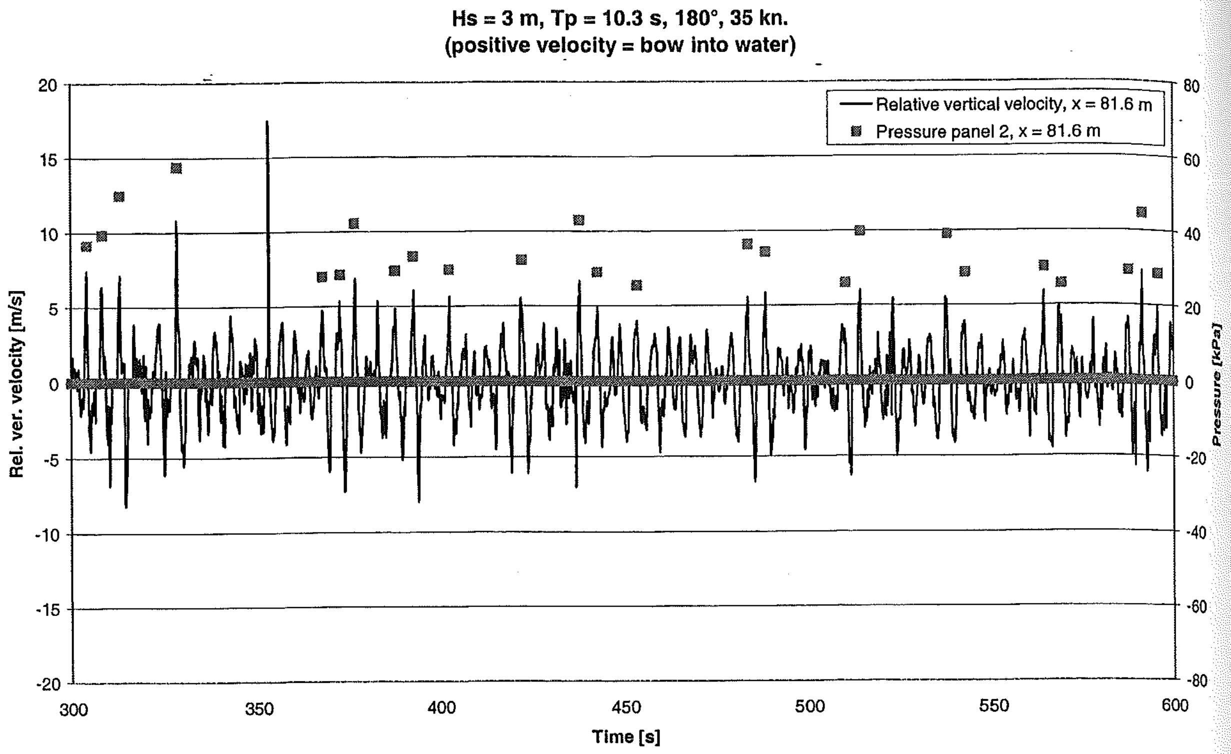

Figure 7: Measured relative vertical velocity and impact pressures.

Now, by pairing the corresponding values of relative vertical velocity and pressure, the pressure coefficient Cp can be estimated, as described previously, by calculating the modified impact velocity. This rather elaborative approach has been performed for model tests in two sea states, and the resulting Cp values are shown in Figure 8. It can be seen that there is a discrepancy between the Cp values derived from the two tests. The test with Hs = 2 m yield consistently values that are larger then those from the test with Hs = 3 m. This is in very good agreement with the results in Figure 2, obtained by considering the characteristic values of pressure and impact velocity, see comparison in Table 3. The positive aspect of this is that it seems that the two approaches are congruent, meaning that the much simpler approach based on the statistical values can be applied safely, whereas the negative side is that this is clear evidence that the current description of the impact velocity does not include correctly the effect of wave height, wave length or heading angle. Further work is therefore needed.

It can also be noted that the experimentally derived Cp's have quite some scatter, mostly in the head sea test. In this case this cannot be explained by the stochastic nature of the slamming, because both the pressure and the velocity have been measured in the exact same wave conditions and at the same time. More likely, this scatter is evidence that the slamming pressure depends on the pitch and roll angle at the instance of impact. This also explains why there is much more scatter in the head sea test than in the bow quartering sea test; depending on the sign of the roll angle the impact pressure in head sea will be greater on one side of the bow than on the other. In bow quartering sea the impact pressure is almost always largest on the side of the incoming wave, where panel 2 was in fact located. It is here appropriate to remind that even though there theoretically should be no roll in the head sea condition, in reality the model did roll during the tests. Probably due to the fact that obtaining and maintaining a heading angle of exactly 180° during the test is impossible with a self-propelled model.

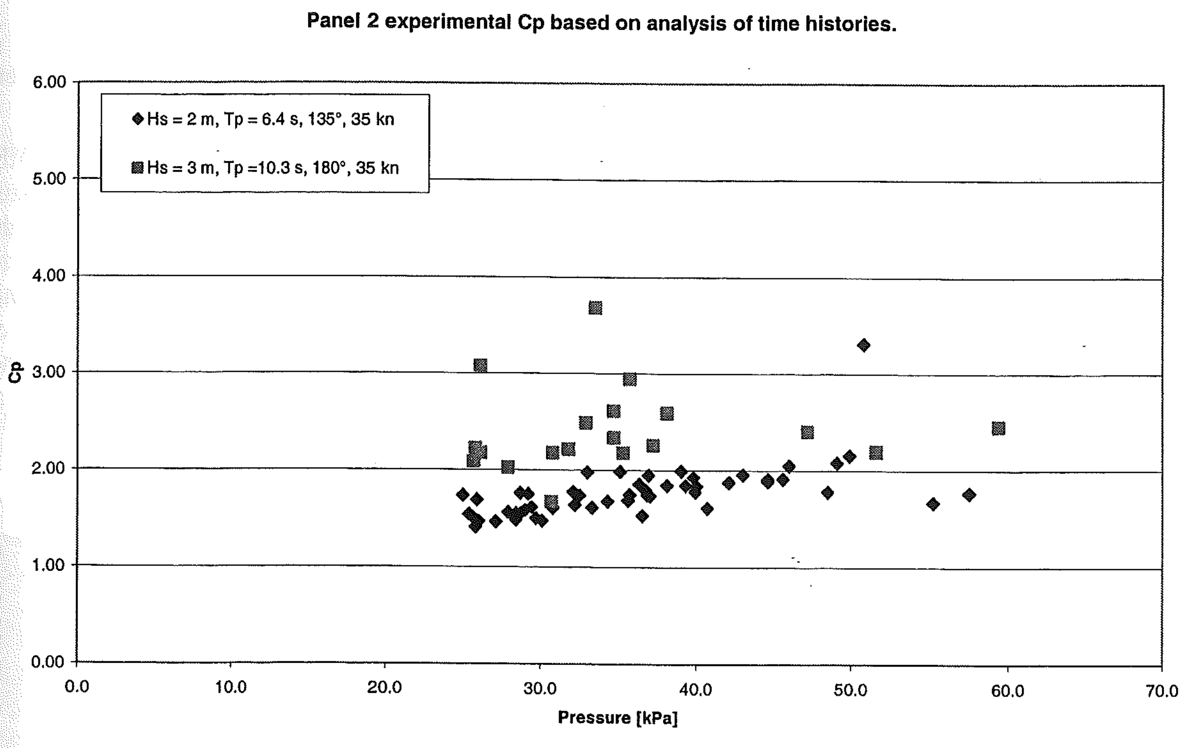

Figure 8: Experimentally derived Cp values for panel 2, based on analyses of time histories.

	Hs = 2 m, Tp = 6.5, 135°	Hs = 3 m, Tp = 10.3, 180°
Cp based on characteristic values of velocity and impact pressure	4.1	3.0
$Cp_{1/10}$ based on analysis of time histories(1)	3.4	2.3

(1) Taken as the average of the 1/10 largest Cp's determined in each test, as this is deemed appropriate for design purposes.

Table 3: Experimentally derived Cp's.

Application of experimentally derived Cp's

The Cp's derived based on the statistical results from the model tests have been used to calculate the max impact pressures in those sea states. The Cp values applied are the mean experimental values in Figure 2, and their values are given in Table 4.

	Panel 3	Panel 4	Panel 5	Panel 6	Panel 7	Panel 8
Cp	4.04	4.16	5.41	4.71	9.12	6.55

Table 4: Calibrated Cp values.

The max pressure have been determined by calculating the most probable max relative vertical velocity in 150 wave encounters with the sea-keeping code SGN. 150 wave encounters are chosen because this was the approximate number of wave encounters realised during the model tests for each sea state. In Figure 9 a comparison between the measured and calculated max pressures are shown. In the figure following legends are used:

- Calculated: the max impact pressure calculated according to Stavovy and Chuang,

- Measured: the max measured impact pressure during the model tests,
- Calibrated Cp: the max impact pressure calculated according to Stavovy and Chuang, but with modified impact velocity definition and calibrated values of Cp.

It can be seen that generally the pressures estimated with the modified impact velocity and the calibrated Cp agrees better with the measurements than does the traditional Stavovy and Chuang estimates. This is particularly true for high sea states, and the reason for this is obviously not the calibrated Cp values – they calibrate the results independently of the wave height – but likely the modified impact velocity. The fact that the propagation velocity of the waves is included means that in head and bow quartering seas the horizontal relative velocity is increased considerably, which on the other hand means that the vertical relative velocity has less influence on the impact velocity. This is seen to be justified by the measured impact pressures that does not increase linearly with Hs, as does the relative vertical velocity.

Hs = 2m, Tp = 6.4s, Heading 135°, 35 knots

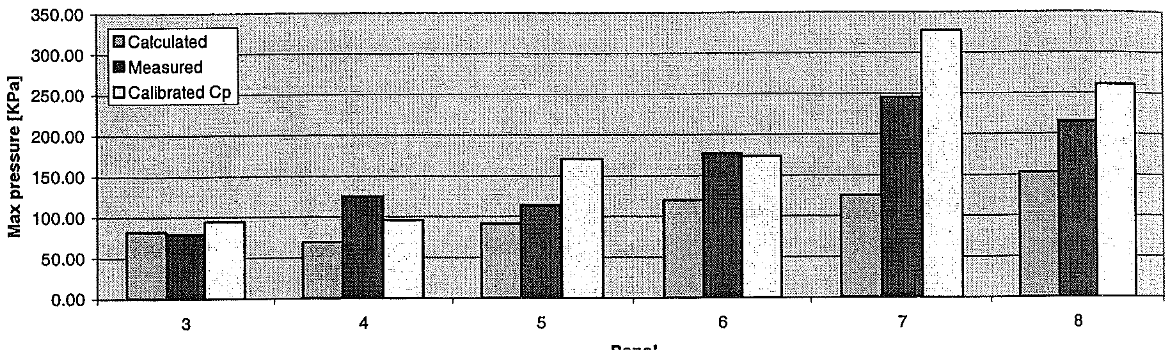

Hs = 2m, Tp = 10.3s, Heading 180°, 35 knots

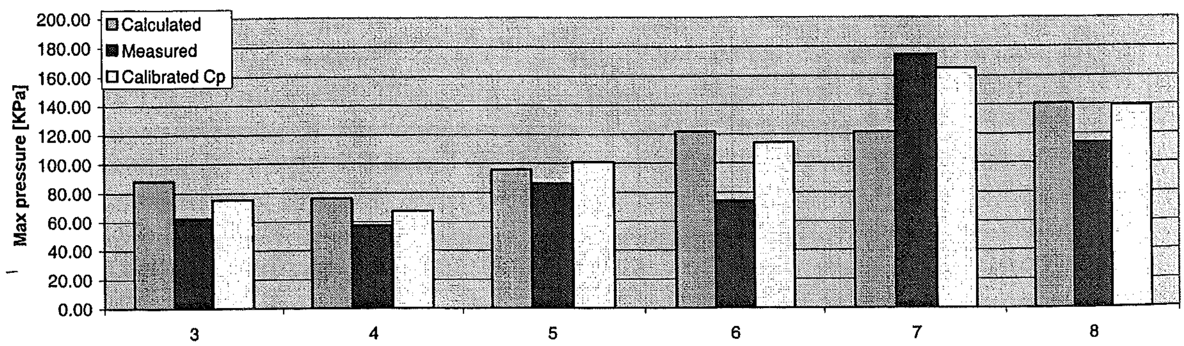

Hs = 3m, Tp = 10.3s, Heading 180°, 35 knots

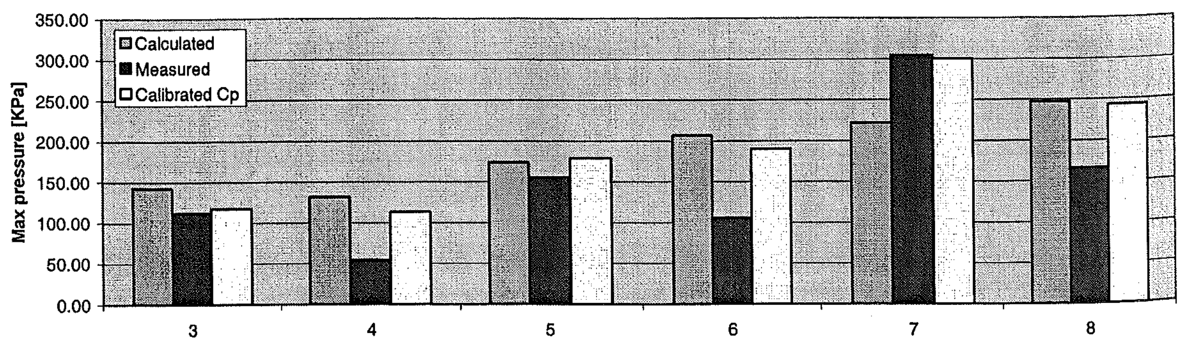

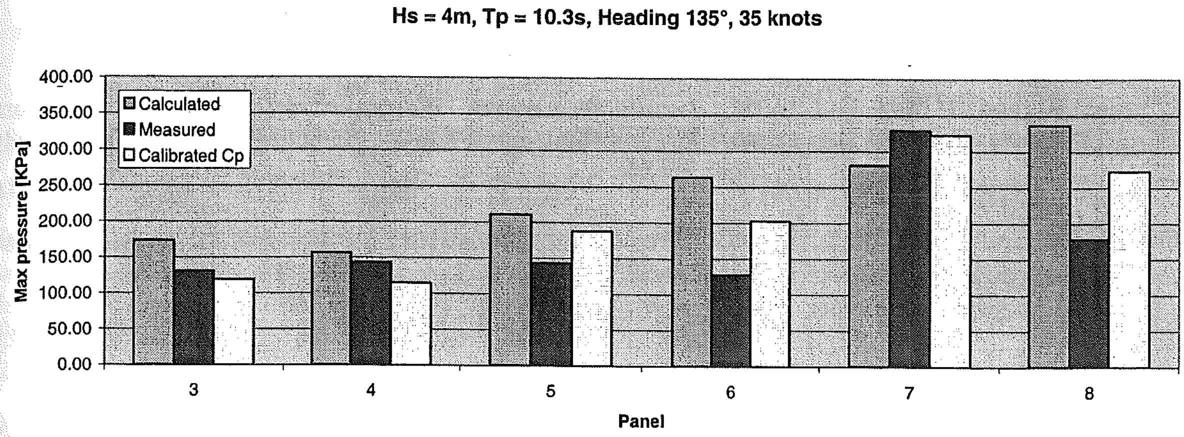

Figure 9: Comparison of measured and calculated max impact pressure.

4 Conclusion

It has been shown how model tests in combination with sea-keeping calculations can be used to obtain improved estimates of slamming induced impact pressures on the bow flare of HSC. The method applied for the assessment of slamming pressures is based on the Stavovy and Chuang (1976) procedure, however with some modifications in order to make it more simple and flexible to use. The modifications to the Stavovy and Chuang procedure are:

- The exact wave slope at the point of impact is not needed; instead the max slope of a wave with the height Hs, which is the significant wave height of the sea state considered, is applied.
- The wave particle velocity components at the point of impact are not needed; instead the propagation velocity (celerity) of a wave with the period Tp, which is the peak period of the sea state considered, is applied.

These modifications yield the major advantage that detailed information about the encountered wave at the exact time of impact is not needed; it is sufficient to know two basic parameters of the sea state in which the vessel is travelling.

In addition it is also shown how a relatively limited number of model tests can be used to obtain calibrated values of the pressure coefficient Cp.

Finally, application of the above shows that the modified and simpler procedure yield good predictions of the slamming pressures.

Acknowledgement:

The authors wishes to thank Dr. R. Van't Veer from MARIN for supplying us with the needed model test results, Mr. A. Sculati from Rodriquez Engineering for allowing the publication of the results and Professor J. J. Jensen from DTU, Mr. G. K. Kapsenberg from MARIN and Dr. M. Dogliani from RINA for their comments.

References:

FOLSØ, R. and TORTI F. (2001), *Operational Control of Comfort on HSC*, 2nd International EuroConference on High-Performance Marine Vehicles, HIPER'01, Hamburg 2-5 May 2001, pp.149-163.

OCHI, M.K. and MOTTER, L.E. (1973), *Prediction of Slamming Characteristics and Hull Responses for Ship Design*, Proceedings of annual SNAME meeting 1973, New York, 15-17 November 1973.

SALVESEN, N.; TUCK, E.O.; FALTINSEN, O. (1970), *Ship Motion and Sea Loads*, Trans. SNAME, Vol.78, pp.250-287.

STAVOVY A.B. and CHUANG S.L. (1976), *Analytical Determination of Slamming Pressures for High-Speed Vehicles in Waves*, SNAME, JSR, Vol. 20, No. 4.

VON KARMAN, T. (1929), *The Impact on Seaplane Floats during Landing*, NACA, Tech. Note 321, SITDL TR 1854.

WAGNER, H. (1931), *Landing on Sea Planes*, NACA Tech. Memo 622, SITDL TR 2102.

Hydrodynamic Design Aspects for Fast Conventional Vessels

Manfred Fritsch, HSVA, Bramfelder Str 164, D-22305 Hamburg, fritsch@hsva.de
Volker Bertram, ENSIETA, 2 rue François Verny, F-29806 Brest Cd 9, bertravo@ensieta.fr

Abstract

Resistance and power prediction procedures for fast displacement, semi-displacement and planing monohulls and catamarans are outlined giving some new empirical relations and diagrams for early design purposes. Guidelines for employing spray rails, trim wedges, interceptors and arrangement of appendages are given to improve designs further. The practical examples are taken from extensive HSVA experience.

1. Fast monohulls

Most fast ships operate at Froude numbers $0.3<F_n<1.7$. There is considerable overlap in operational speed ranges for various fast ship types. Compromises are not always good. E.g. planing hulls operated at $F_n<0.6$ require more power than round-bilge non-planing hulls of same displacement. The displacement for fast ships reaches an approximate maximum of 5500t for modern frigates. We focus here on the most common representatives of fast ships: displacement, semi-displacement and planing monohulls, Fig.1.

Typical examples of fast displacement ships are corvettes, frigates, working boats and similar ships. These are characterized by straight V-shaped sections in the forebody, slender waterlines, round bilge with decreasing radius going to the transom stern and centerline skeg. They are frequently fitted with an integrated trim wedge. The LCB positions usually lie between 2% and 3% aft of $L_{pp}/2$ for larger ships. Displacement ships operate up to F_n=0.4...0.6, i.e. they approach only the begin of the planing condition. Advantages of this hull form are good seakeeping behavior, good course-keeping ability, and – if the vessel operates above the resistance hump – relatively low dynamic trim at top speed. The steep run of the power curve at higher speeds caused by the fact that little hydrodynamic lift is produced, is a main disadvantage and determines the operational limits of this type.

Semi-displacement ships integrate the attributes of displacement and planing hulls. Semi-displacement ships achieve higher speeds than displacement ships due to increased dynamical lift and corresponding reduction in resistance. The most common examples of this type are patrol boats, special navy craft, pleasure yachts, pilot boats, etc. Vessels can reach the planing condition with speeds of up to $F_n\approx1$. The course-changing and course-keeping behavior is similar to that of pure displacement ships. The seakeeping is in general good. At high speeds, roll-induced transverse instability can arise under certain circumstances, *Codega and Lewis (1987).*

Real planing hull designs should normally be used for high-speed vessels only. The stations have straight sections and knuckle lines (with a bilge knuckle running from the stem over the entire length to the transom), relatively large deadrise angles in the forebody decreasing further aft to about L/2 and continuing at nearly constant angles of not less than 10° to the transom. Early planing hull designs with warped deadrise are not very common today. The forward part of the longitudinal knuckle is designed to work as a spray rail. Trim wedges with adjustable tabs are often installed to control the dynamic trim. These become less effective for $F_n>1$ as there is generally a reduction in dynamic trim in that speed range. Typical examples are fast patrol boats, racing yachts, S&R boats, fast small passenger ferries, and similar vessels. For lower speeds, the resistance of this hull form is slightly higher than that of a semi-displacement vessel with the same length and displacement. The typical advantages of this hull form develop at speeds $F_n>1$. The seakeeping qualities of these vessels are not as good as for displacement and semi-displacement hulls. This disadvantage can be partially compensated by selecting relatively high L/B (L/B≈7...8) and deadrise angles $\tau>10°$ in the aft part. The high-speed stability problem of semi-displacement hulls may also occur with planing hulls.

In one particular project, HSVA investigated alternatively a semi-displacement and a planing hull design for a 45-knot yacht. The planing hull had lower calm-water resistance for high speeds, but the semi-displacement hull performed better in waves.

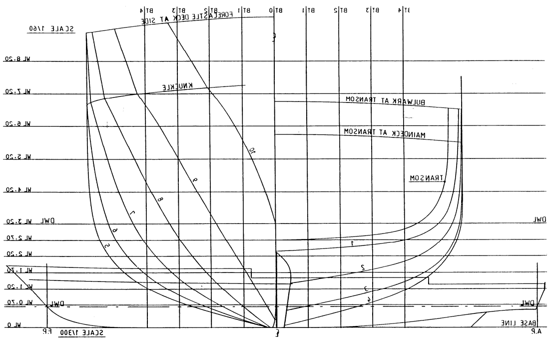

Displacement hull, F_n=0.62

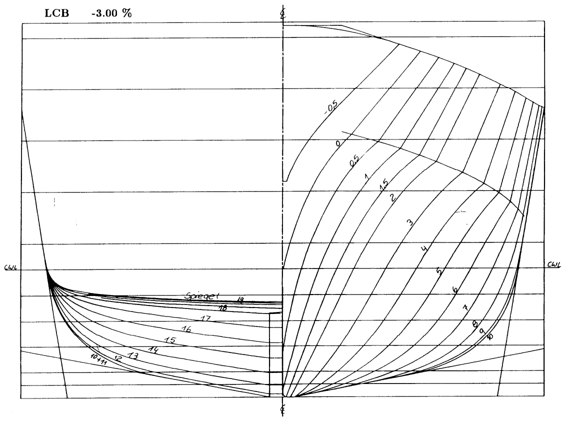

Semi-planing hull, F_n=0.67

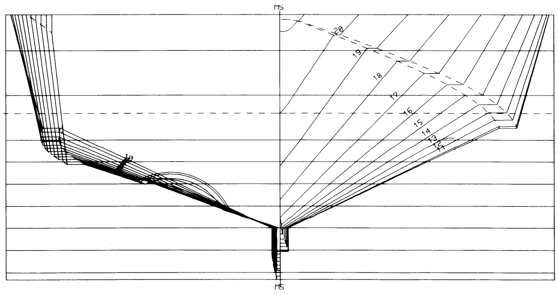

Planing hull , F_n=1.0

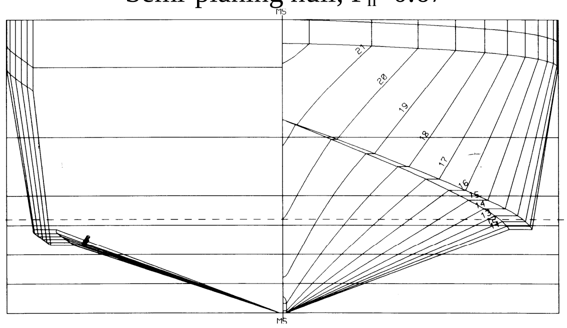

Planing hull, F_n unknown

Fig.1: Body plans of typical representatives of fast monohulls

2. Resistance and power prediction

After the general hull type has been selected, the main dimensions of the hull are settled and the hull form can be worked out based on the designer's experience, data for comparable ships or systematical series of hull forms. A speed/power prediction is needed early in the design to select the engine. This prediction is usually based on a resistance computation and an estimation of overall efficiency. Closely connected with the propulsion plant are also details of the appendages such as shafts, brackets, propellers, stabilizer fins and steering system. Based on a general arrangement plan, more detailed computations of LCG and LCB as well as stability are carried out. Static trim can significantly influence power consumption.

The resistance of high-speed vessels is primarily a function of the vessel's displacement, wetted length and surface, speed and additionally breadth for planing hulls. Therefore significant parameters are the slenderness $L/\nabla^{1/3}$ and the specific resistance R_T/∇. The total resistance R_T is decomposed as usual with notation following ITTC unless otherwise specified, *Bertram (2000)*:

$$R_T = R_F + R_R \tag{1}$$

$$R_F = C_F \cdot \rho/2 \cdot V^2 \cdot S \tag{2}$$

$$R_R = R_W + R_{APP} + R_{AA} + R_{PARAS} \tag{3}$$

ρ denotes the water density, V the ship speed, S the wetted surface (at rest except for planing hulls as described in more detail below), C_F follows ITTC'57 with Reynolds number is based on L_{wl}. The appendage resistance R_{APP}, the air and wind resistance R_{AA}, and the parasitic resistance R_{PARAS} (resistance of hull openings such as underwater exhaust gas exits, scoops, zinc anodes, etc.) can be estimated globally with 3-5% R_F for a projected vessel, but the determination of R_W (which includes wave, wave-making, spray and viscous pressure (or separation) resistance) is more difficult. It is common practice to take data from one of the systematical series, e.g. *Bailey (1976)* or *Blount and Clement (1963).* However, these prediction methods are more or less time-consuming and semi-empirical formulae are more helpful for design engineers. Considering the propulsive efficiencies yields the necessary engine power P_B from effective power $P_E=R_T \cdot V$:

$$P_B=P_E/(\eta_D \cdot \eta_M) \quad (4)$$

η_M =95% is the mechanical efficiency of gear box and shaft bearings. The propulsive efficiency is $\eta_D=\eta_H \cdot \eta_R \cdot \eta_0$. Since $\eta_H \approx 1$ and $\eta_R \approx 1$for these hull forms, the main influence is the propeller efficiency η_0. Modern propeller designs and water jet propulsion systems can reach values of more than 70% under good operational conditions.

2.1. Speed/power prediction for planing hulls

The selection of the main engine(s) influences the fuel consumption, the total weight, and the LCG position of the vessel. Different test series are available for the necessary reliable power prediction in the early design phase. The most useful is the DTMB Series 62, *Clement and Blount (1963).* With the help of these test series, a favorable hull form can be selected and the speed-power curve predicted relatively reliably. Some semi-empirical power prediction methods are available, partly developed from conclusions and combinations of the above mentioned reports and partly based on data from sea trials of high-speed planing hulls. Of the methods, the Polar Curve Method of *Angeli (1974)* is presented as an example in the following.

The basic coefficients describing the hydrodynamics of planing hulls are the lift and resistance coefficients:

$$C_L = \Delta/[(\rho/2) \cdot B^2 \cdot V^2] = 0.0723 \cdot \Delta/(B^2 \cdot V_K^2) \quad (5)$$

$$C_D = R/[(\rho/2) \cdot B^2 \cdot V^2] = 0.0723 \cdot R/(B^2 \cdot V_K^2) \quad (6)$$

Here B is the mean of the maximum beam at chines and the chine beam at the transom. V_K is the speed in knots. Empirical design formulae are:

$$L = 0.580 \cdot \Delta^{1/3} \quad (7)$$

$$B = 0.215 \cdot \Delta^{0.275} \quad (8)$$

$$C_D = 0.0053+0.0978 \cdot C_L \quad (9)$$

The specific resistance $\Gamma=R/\Delta$ is expressed as a function of the volume Froude number F_∇:

$$\Gamma=0.0978+ 0.0125 \cdot F_\nabla^2/\Delta^{0.117} \quad (10)$$

$$F_\nabla=0.5207 \cdot V_K/\Delta^{1/6} \quad (11)$$

Taking P_B as delivered by the engines, the ship’s resistance coefficient is:

$$C_{DS} = 10.537 \cdot P_B/(B^2 \cdot V_K^3) \quad (12)$$

We find from sea trials:

$$C_{DS} = 0.01+0.19 \cdot C_L \quad (13)$$

Finally, the brake horsepower P_B [kW] required by a ship of displacement Δ [kg] at maximum speed V_K [kn] is:

$$P_B = 0.7354 \cdot (\Delta \cdot V_K/765.2+ B^2 \cdot V_K^3/1051.1) \quad (14)$$

The accuracy of this formula has been confirmed by many high-speed vessels tested at HSVA. One of the advantages of this equation is obviously the simple application when compared with other methods based on systematical series.

2.2. Speed/power prediction for semi-displacement hulls

The procedure for estimating resistance and power is very similar as for planing hulls. The NPL High Speed Round Bilge Displacement Hull Series, *Bailey (1976)*, is available to aid the selection of main dimensions, lines design, resistance and power prediction. This series also deals with examples for practical application.

At HSVA, statistical data has been compiled for the prediction of the bare hull effective power P_E. These statistics are based on a slenderness coefficient $C_\nabla = \nabla/L^3$. The resistance coefficient $C_{T\nabla}$ is defined by:

$$R_T = C_{T\nabla} \cdot \rho/2 \cdot V^2 \cdot \nabla^{2/3} \qquad (15)$$

$C_{T\nabla}$ is a function of the Froude number, found by means of the diagrams in Fig.2.

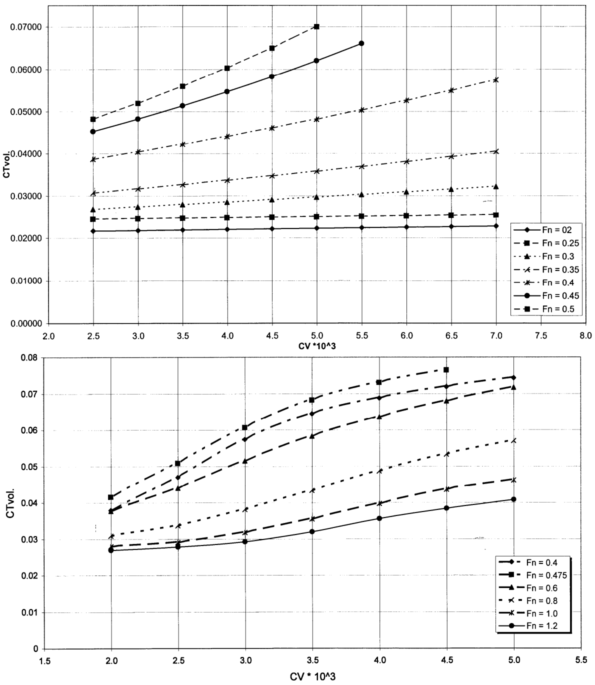

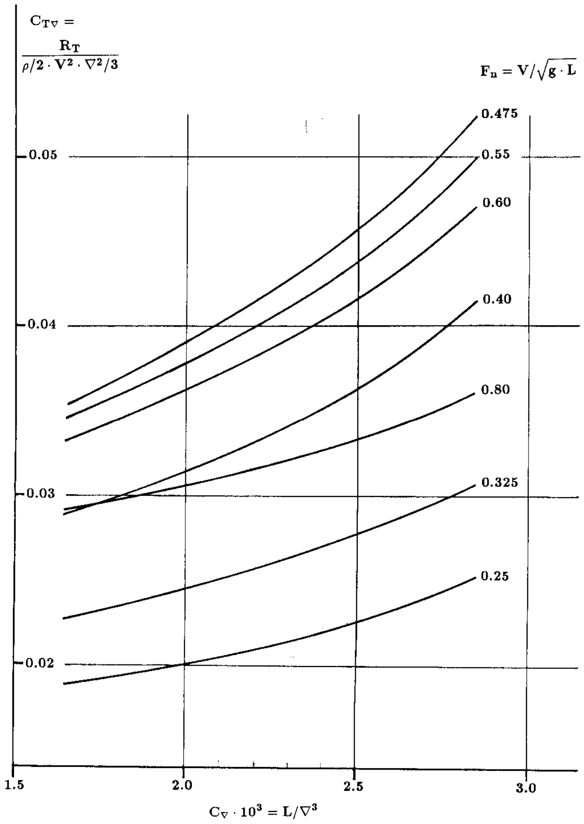

Fig.2: Bare hull resistance coefficient for high-speed vessels (top) and for frigates/corvettes (right)

Since the value found for the effective power is valid for the bare hull only, allowances for R_{APP} and R_{AA} must be added. R_{APP} can be estimated from statistical data, Fig.3, or calculated directly, e.g.*Bailey (1976).*

However, these formulae do not include interference effects from the individual parts of the appendages. R_{AA} can be calculated following *Schneekluth and Bertram (1998).*

3. Improvements of a present design

Even when the hull design for a fast vessel complies with all the fundamental design criteria, there are still numerous measures to improve it. From our experience in testing hundreds of fast vessels, there was not one design which could not be improved. In a recent project for a 96m yacht, the power requirement could be reduced by 14%. This figure may not be representative for all fast ship projects at HSVA, but it is by no means an exception. Some of the most successful methods for improving a design for calm water operation are described in the following.

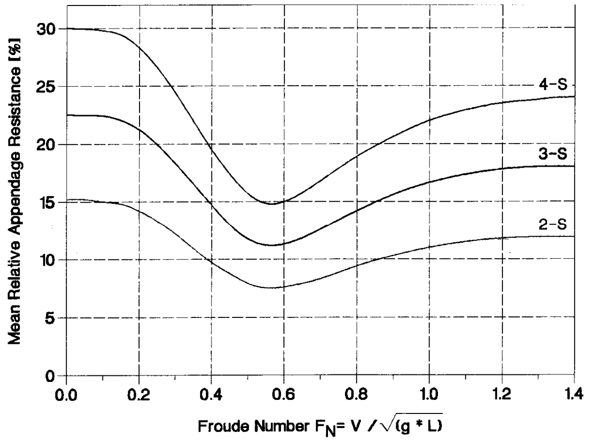

Fig.3: Mean relative appendage resistance R_{APP}/R_T for 4-screw, 3-screw and 2-screw vessels

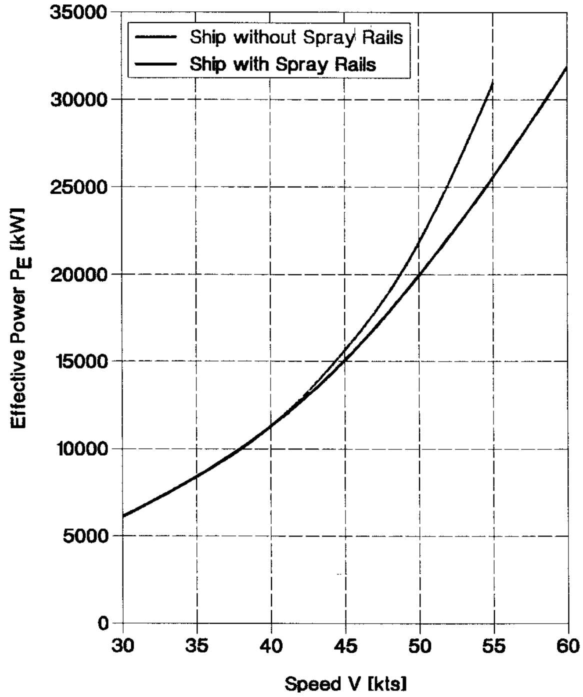

Fig.4: Influence of spray rails on required power

Fig.5: Fast patrol boat; initial design (left) and final design with spray rails and modified trim wedge (right)

3.1. Spray rails

Many fast displacement, semi-displacement, and also planing hulls are characterized by moderate to severe spray generation. The spray comes from the bow wave rising up the hull with speed. This is particularly caused by the relatively blunt waterlines and hard buttock forward when $L/\nabla^{1/3}$ is unfavorably small or the beam too large. Severe spray generation has a number of disadvantages:

- The increase of frictional (due to larger wetted surface) and wave making resistance.
- Wetness of deck and superstructures, unfavorable for yachts and unacceptable for gas turbine powered ships (due to their demand for very dry and salt free combustion air)
- Increased radar signature (for navy craft)

Spray generation can be taken into account when designing the hull before entering the construction phase. Sometimes hull changes are not possible. Then spray rails can often be an effective and relatively cheap measure to reduce spray generation. Spray rails can improve also the performance of existing fast ships. Typical spray rail arrangements either use an additional triangular profile or integrate a two-step knuckle line into the form. These run from the stem to about amidships. In both cases a horizontal deflection area with a sharp edge must be created. Fig.4 shows the influence of spray rails on the vessel's resistance. Spray rails also influence the dynamic lift on the forebody, thus improving often the resistance also indirectly.

3.2. Trim wedges and interceptors

The resistance of a fast ship is fundamentally linked with the dynamic trim. Fig.6 gives optimum trim angles for fast vessels based on older designs. More recently, we recommend values approximately 30% lower than the values found in the diagram.

Fixed trim wedges, Fig.7, or moveable trim flaps can be used to optimize the dynamic trim for a given speed and slenderness. Trim wedges should normally be considered during the design phase, but they are also acceptable for improving craft already in service. Trim wedges are most effective at speeds in the resistance hump range at $F_n \approx 0.4...0.5$. They have almost no effect for $F_n > 1.2$. Reductions in total resistance of more than 10% are possible in the resistance hump range. The most effective trim wedge for a certain craft and operational range is best found in model tests. A further advantage of stern wedges is that they can reduce the height of the stern wave. This effect is similar to that known from the application of duck tails.

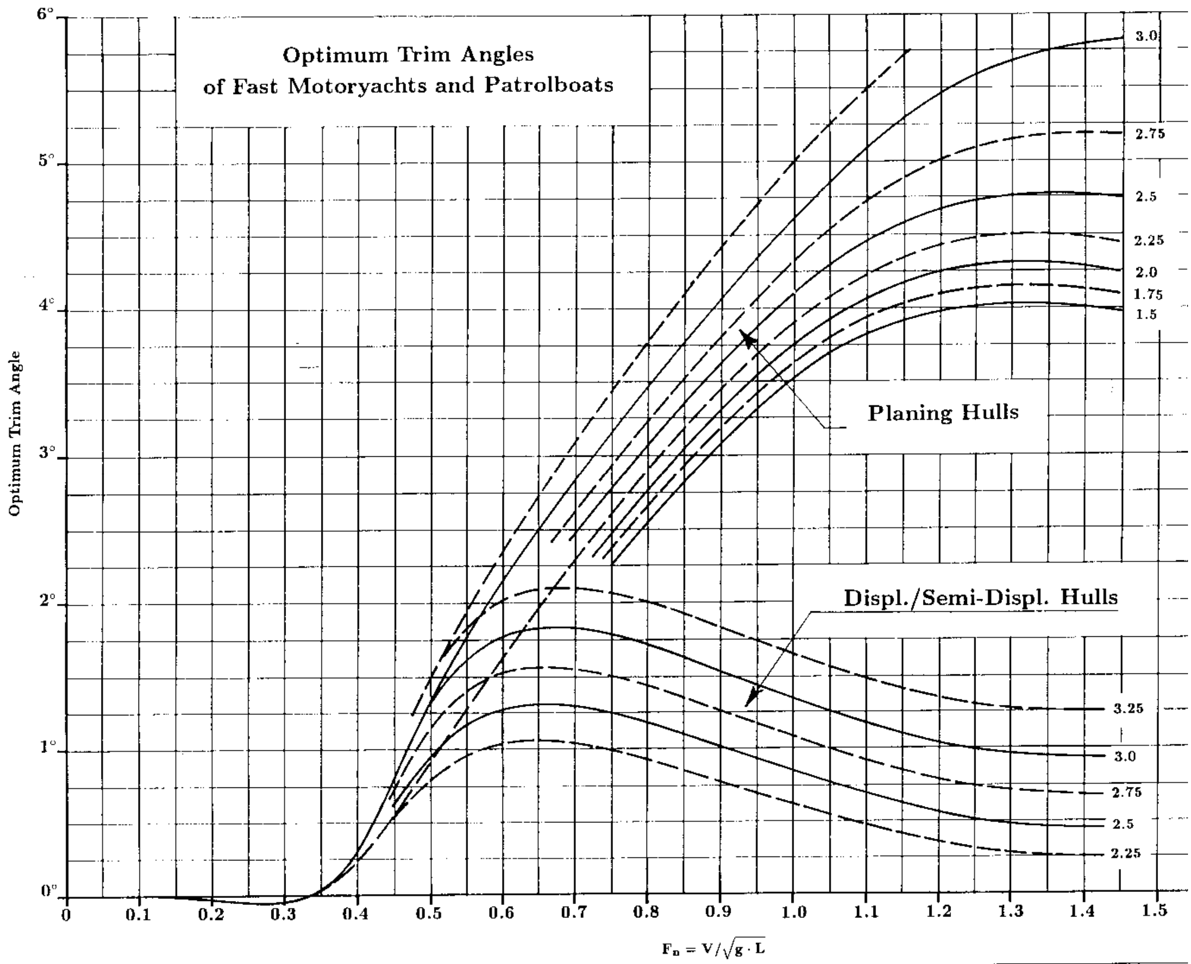

Fig.6: Optimum trim angles for fast vessels depending on parameter $\nabla^{2/3}/B \cdot T$

Fixed or adjustable interceptors, Fig.8, offer an alternative to control the dynamic trim of a vessel. An interceptor is basically a vertical extension of the transom beyond the shell plating. Forward of the interceptor plate the flow is decelerated and the local pressure is increased which generates a lift force to the vessel's stern. The effect is identical to that of a conventional stern wedge. However, the height of the interceptor needs only to be 50% of that of a wedge for the same effect on the dynamic trim and resistance. This is an advantage at lower speed due to the smaller immersed transom area.

Fig.7: Trim wedge at model (upside down)

Fig.8: Interceptor at model (upside down)

3.3. Arrangement of appendages

Appendages influence strongly resistance and propulsive efficiency of fast ships (R_{APP}=6%...15% R_T). Recommendations are:

- Avoid oversizing the shaft brackets, bossings, and rudder profiles.
- V-bracket designs may have approximately 5-7% higher R_{APP} than I-bracket designs.
- If V-brackets are obligatory for whatever reason the inner and outer legs should be aligned with the flow to minimize resistance and wake disturbance (vibration, cavitation). Optimization of the brackets may employ CFD or model tests (three-dimensional wake measurements).
- For twin-screw vessels, power consumption may differ by 3%...5% changing the sense of propeller rotation, depending the aftbody lines. The propulsive coefficient η_D is also influenced by the degree of shaft inclination ε, expressed by an additional efficiency η_ε, *Hadler (1966)*:

  $$\eta_\varepsilon = 1-0.00187\cdot\varepsilon^{1.5} \qquad (16)$$

  The decreasing tendency of at increasing shaft angles ε indicates that the shaft arrangement should be considered carefully in the design. The phenomenon is due to the inhomogeneous flow to the propeller blades which reduces the propeller efficiency. Also cavitation may be increased to a certain degree.
- For twin-rudder arrangements, an inward inclination of the rudders' trailing edges by 2°...3° can increase the propulsive efficiency by up to 3%.
- Strut barrels should be kept as small as possible and their noses should be rounded or have parabolic shapes.
- Bilge keels should generally be aligned with the flow at the bilge. The line of flow may be determined in paint tests or CFD.
- If non-retractable stabilizer fins are projected, the angle of attack with least resistance can be determined in model tests (with different adjusted fin angles) or employing CFD.

4. Catamarans

One of the advantages of catamarans vs. monohulls is the up to 70% larger deck area. On the other hand, catamarans have typically 20% more weight and 30%-40% larger wetted surface. Catamarans require usually 20%-80% (the higher values near F_n=0.5) more power than monohulls due to higher frictional resistance and higher wave resistance, Rutgersson (1986). Catamarans feature high transverse stability, but roll periods are similar to monohulls due to high moments of inertia. Catamaran designs come at low, medium and high speeds. Thus catamaran hull forms range from pure displacement up to real planing hulls, Fig.9.

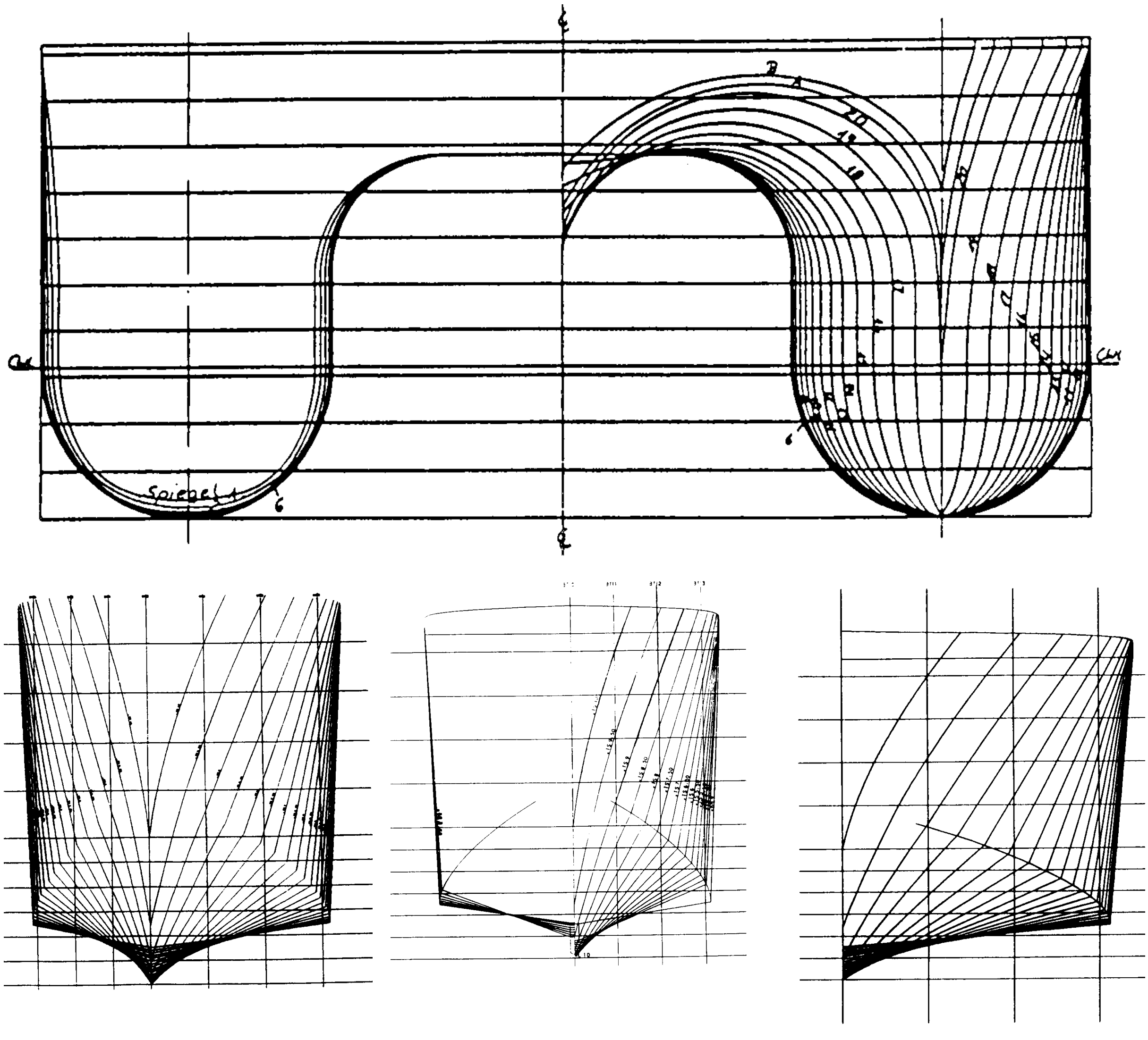

Fig.9: Typical catamaran hull forms, semi-displacement (top) and planing (bottom)

Displacement catamarans usually operate near the hydrodynamically unfavorable hump speed ($F_n \approx 0.5$). The design is then usually driven by the demand for a large and stable working platform, high transverse stability and shallow draft where speed is not so important, e.g. for buoy layers, sightseeing boats, etc. There is no typical hull form for displacement catamarans. Round bilge, hard chine, and combinations of both are used. Asymmetric hull forms are common to reduce the wave interference effects between the hulls. For catamarans with low design sped, a relatively large $L/\nabla^{1/3}$ should be selected to minimize the resistance. The majority of displacement catamarans are driven by fully immersed conventional propellers. Due to the frequent shallow draft requirements for catamarans the clearance for the propellers becomes rather small. Then arrangements of tunnels and propeller nozzles are usual.

Semi-displacement catamarans operate at higher speeds, frequently at the begin of the planing condition at $F_n \approx 1$ or slightly above. Again, no typical hull characteristic is to observe; both round-bilge and hard-chine sections are common. For rough seas (like the North sea), round-bilge sections are more advantageous with respect to ride comfort. Most wave-piercer catamarans have also round-bilge sections. Semi-displacement catamarans may have propeller drives or waterjet propulsion.

Planing catamarans operate at speeds up to 50 knots or more and F_n up to 2.0 and higher. Typical knuckled planing hull forms dominate. Symmetric and asymmetric hull forms show only marginal performance differences. For high speeds, waterjets offer better efficiencies than conventional propellers with lower cavitation risk. Thus for planing catamarans, water jets are the most favorable propulsion system. Surface-piercing propellers are also an option which has been employed by some racing boats and navy craft.

Foils may reduce resistance and improve seakeeping. Foil-assisted catamarans (FAC) have forward and aft foils, supporting part of the total weight, Fig.10. The bow is usually lifted clear of the water, but the stern remains partially immersed which is necessary for waterjet operation and stability. Fig.11 shows the influence of different types of foils on the ship's resistance. Increasing the foil area decreases the resistance, e.g. Fig.12. For modern FACs, the foils are equipped with efficient ride control systems which usually adjust a movable flap on the forward foil and in more advanced systems also on the rear foils. Controllable flaps are recommended for several reasons. The risk of broaching in quartering or side waves can be reduced, especially when operating with foils in maximum lift condition. Controllable flaps also help to tune dynamical trim and foil adjustment for maximum lift and minimum resistance. For FACs, wetted length and surface of the model change very much with speed. At HSVA, test results are corrected as follows for this effect and the scale effect for the foils.

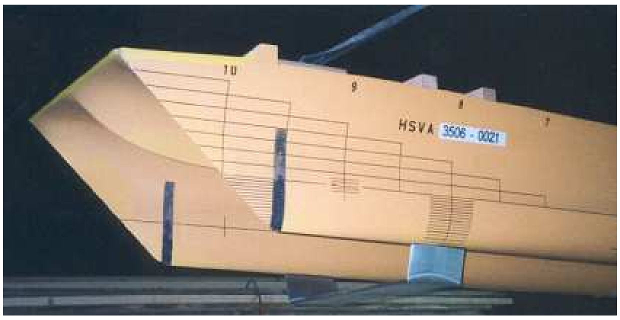

Fig.10: Foil arrangement on foil-assisted catamarans in model test at HSVA; forward foil (top) and aft foil (right)

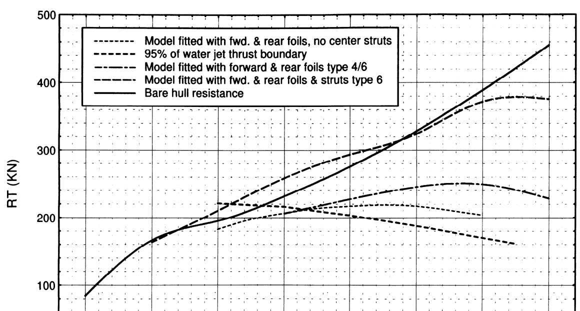

Fig.11: Resistance of a 45m catamaran with and without foils

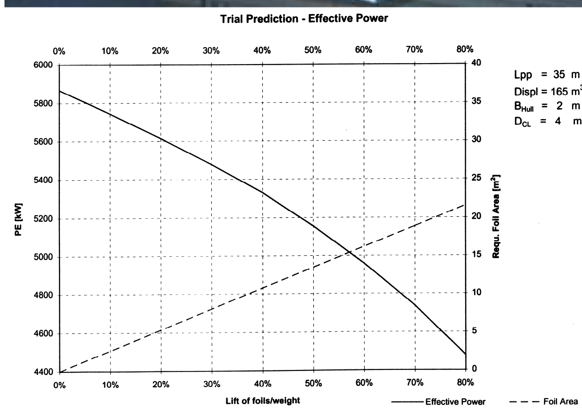

Fig.12: Prediction of P_E as function of foil area and lift at V=45 knots

Total model resistance $R_{T,m}$, dynamic trim angle θ and sinkage z_v are measured directly at the model. From the dynamic trim and sinkage, the dynamic wetted length L_{OS} and dynamic wetted surface S of the hull and wetted length l_i and wetted surface s_i for each appendage are determined. The frictional model is computed as:

$$R_{F,m} = 0.5\, \rho_m\, V_m^2\, (C_F(L_{OS},V_m)\cdot S_m + \sum C_F(l_i,V_m)\cdot s_i) \quad (17)$$

C_F is computed following ITTC'57. For appendages, C_F=0.004 is assumed for $1.10\cdot 10^5<R_n<2.14\cdot 10^6$ and for $R_n<1.10\cdot 10^5$ laminar flow can be assumed with C_F following the Blasius line: $C_F=1.327/(R_n)^{0.5}$.

The residual resistance is then scaled to the ship:

$$R_{R,s} = R_{R,m}\cdot \lambda^3\cdot(\rho_s/\rho_m) = (R_{T,m}-R_{F,m})\cdot\lambda^3\cdot(\rho_s/\rho_m) \quad (18)$$

Frictional and residual resistance give total ship resistance:

$$R_{T,s} = R_{R,s} + R_{F,s} = R_{R,s} + 0.5\, \rho_s\, V_s^2\, ((C_F(L_{OS},V_s)+C_A)\cdot S + \sum C_F(l_{i,s},V_s)\cdot s_i) \quad (19)$$

With correlation allowance C_A=0.0025 for fast round bottom boats. For trial prediction, R_{AA} and an additional viscous resistance R_{AV} (to account for openings and appendages not present on the model) are added. Typically R_{AV}=4% R_F.

Based on its extensive experience with foil systems, HSVA can recommend profiles with respect to high lift, sufficient strength and low drag. Table I shows the influence of foil parameters near the free surface.

In general, seakeeping of catamarans in moderate seas is similar and in some aspects better than that of comparable monohulls due to the more slender hulls and the much higher transverse stability. This changes drastically in heavy head sea conditions. The highest stresses for fast catamarans are slamming impacts on the fore part of the wetdeck. The most common anti-slamming device (ASD) is a deep-V part in the forward wetdeck above the calm waterline, as in wave-piercing catamarans, Fig.13, can reduce impacts significantly. The wave energy in slamming events remains unchanged by ASDs, but is smeared over a longer period thus reducing peaks. Another ASD arranges longitudinal rails and steps on the bottom of the wetdeck, Fig.14. This reduces the slamming impacts as air-water cushions are formed between the longitudinal rails. Also longitudinal stiffeners with holes have been proposed.

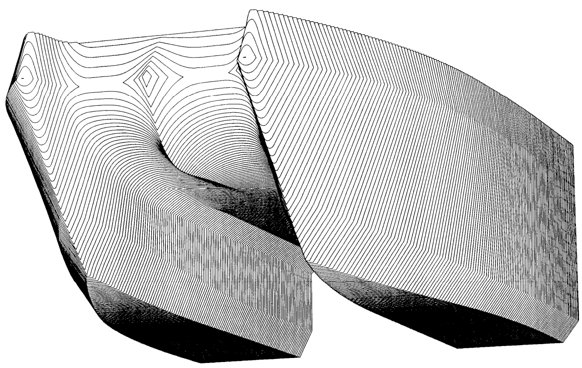

Fig.13: ASD form with faired deep-V addition

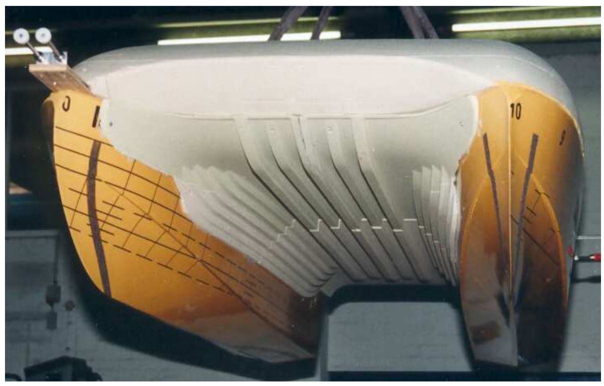

Fig.14: ASD longitudinal rails at model

The resistance for catamarans needs basically the same parameters as for monohulls, i.e. L, ∇, F_n. Hull spacing, breadth, deadrise, symmetric or asymmetric hull form have less importance. Based on many model tests, HSVA derived a simple prediction formula for the bare hull resistance coefficient:

HSVA formula for round-bilge catamarans:

$$C_{T,Vol} = R_T/(0.5\rho\cdot V^2\cdot\nabla^{2/3})\approx 0.2/(L/\nabla^{1/3})+2.05/\{[1+25(F_n-0.45)^2]\cdot(L/\nabla^{1/3})^2\} \tag{20}$$

HSVA formula for hard-chine catamarans:

$$C_{T,Vol} \approx 0.25/\{[1+(F_n-0.45)^2]\cdot(L/\nabla^{1/3})\}+ 2.5/\{[1+25(F_n-0.45)^2]\cdot(L/\nabla^{1/3})^2\} \tag{21}$$

R_{APP} and R_{AA} must be added separately.

Table I: Estimate of drag and lift coefficients for 2-d hydrofoil near the free surface; c = chord length, t= thickness, w=camber, T_p=profile draft, F_{nc}=chord-based Froude number

			F_{nc}=3, T_p/c=1		F_{nc}=5, T_p/c=1		F_{nc}=3, T_p/c=0.4		F_{nc}=5, T_p/c=0.4	
t/c	w/c	α	C_L	C_L/C_D	C_L	C_L/C_D	C_L	C_L/C_D	C_L	C_L/C_D
0.10	0.01	1°	0.135	12.929	0.143	13.915	0.092	10.551	0.096	11.153
0.10	0.02	1°	0.216	15.925	0.223	17.549	0.162	14.308	0.168	15.816
0.10	0.03	1°	0.297	17.000	0.304	19.115	0.232	15.852	0.239	18.083
0.10	0.04	1°	0.378	17.060	0.384	19.439	0.303	16.185	0.311	18.837
0.10	0.05	1°	0.459	16.616	0.465	19.085	0.373	15.903	0.383	18.735
0.10	0.06	1°	0.540	15.944	0.545	18.393	0.443	15.330	0.454	18.186
0.10	0.01	-2°	-0.082	-9.646	-0.081	-9.391	-0.084	-10.693	-0.091	-11.328
0.10	0.01	-1°	-0.010	-1.144	-0.007	-0.776	-0.026	-3.431	-0.028	-3.753
0.10	0.01	0°	0.063	6.963	0.068	7.552	0.033	4.294	0.034	4.357
0.10	0.01	1°	0.135	12.929	0.143	13.915	0.092	10.551	0.096	11.153
0.10	0.01	2°	0.207	16.377	0.218	17.807	0.151	14.477	0.158	15.671
0.10	0.01	3°	0.279	17.859	0.292	19.645	0.210	16.346	0.221	18.032
0.10	0.01	4°	0.351	18.106	0.367	20.114	0.269	16.839	0.283	18.850
0.10	0.01	3°	0.279	17.859	0.292	19.645	0.210	16.346	0.221	18.032
0.06	0.01	1°	0.129	13.698	0.128	13.387	0.096	11.755	0.091	11.215
0.08	0.01	1°	0.133	13.410	0.138	13.854	0.095	11.238	0.095	11.385
0.10	0.01	1°	0.135	12.929	0.143	13.915	0.092	10.551	0.096	11.153
0.12	0.01	1°	0.134	12.283	0.144	13.609	0.088	9.711	0.093	10.552
0.14	0.01	1°	0.131	11.492	0.142	12.971	0.081	8.732	0.087	9.611

References

ANGELI, J.C. (1974), *Prediction of planing boat smooth water horsepower requirement by the polar curve method*, Note 1115

BAILEY, D. (1976), *The NPL high-speed round bilge displacement hull series*, Maritime Technology Monograph 4, RINA, pp.491-579

BERTRAM, V. (2000), *Practical ship hydrodynamics*, Butterworth+Heinemann, Oxford

BLOUNT, D.L.; CLEMENT, E.P. (1963), *Resistance tests of a systematic series of planing hull forms*, SNAME 71, pp.491-579

CODEGA, L.; LEWIS, J. (1987), *A case study of dynamic instability in a planing hull*, Marine Technology 24/2, pp.143-163

HADLER, J.B. (1966), *The prediction of power performance of planing craft*, SNAME Trans., pp.563-610

RUTGERSSON, O. (1986), *Catamarans versus single-hull concepts*, RINA's Warship

SCHNEEKLUTH, H.; BERTRAM, V. (1998), *Ship design for efficiency and economy*, Butterworth+Heinemann, Oxford

Damage of Composite Cylinders under Low-Speed Impact

Papa B. Gning[(1)(2)], Mostapha Tarfaoui[(1)], Francis Collombet[(2)], Peter Davies[(3)]
(1) ENSIETA / MSN, 2 rue F. Verny, 29806 Brest Cedex, gningpa@ensieta.fr; tarfaomo@ensieta.fr
(2) IUT Paul Sabatier de Toulouse, 133 avenue de Rangueil, 31077 Toulouse cd 4, Francis.Collombet@gmp.iut-tlse3.fr
(3) IFREMER Centre de Brest, 29280 Plouzané, Peter.Davies@ifremer.fr

Abstract

The composite materials find more and more marine and underwater applications, and for hydrodynamic reasons the cylindrical form is often favored. Tubes manufactured by filament wounding are used for containers of instrumentation, piping for transport of oil fluids, and are considered for many underwater machines. The behavior in impact of composite materials was the subject of many studies but one was interested especially in the answer of plates. For the applications quoted here one put several questions concerning the behavior of composite cylinders during and following an accidental impact. More precisely, this presentation is interested in the following aspects:

- which is the response of a cylinder subjected to a low speed impact ?
- can one evaluate and predict the extent of the induced damage ?

In order to answer these questions a program was put in œuvre for an analysis and trial run of the results. This program contents tests of punching, indentation, impact by falling weight, a fine study of the damage mechanisms introduced and development of methods of ultrasonic inspection.

1. Introduction

Many authors worked on the modeling of the laminated plates and in particular their behavior with the shock. The studies, rather many, related as much to the response of the structure than the characterization and the prediction of the damage after impact. Concerning the composite cylinders, the investigations made until now were not also numerous and their susceptibility to the shock remains still little studied.

The objective of this work is to study the response to the impacts of the structures of the cylindrical shape in composites (tanks, tubes...). Such structures find many applications but the harmfulness of the impacts is not taken into account during their dimensioning (Figure 1). However, during their handling or in service the damage introduced by accidental impact can blame the capacity to fulfill the dedicated function. Indeed, taking into account the low velocity of displacement by gravity of the object immersed, it will be a question of seeing the behavior with the impacts at the time of a shock of weak energy having a null incidence with the projectile. The cylinders are thick (diameter report/ratio on thickness higher than 10) and consist of reinforcement out of glass and epoxy matrix.

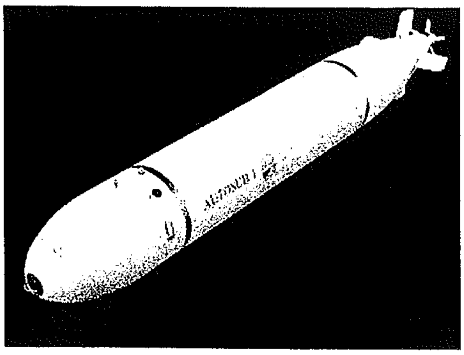

Figure 1: Convey underwater autonomous (L=7m, Ø=0.9m)

2. The Composite Material

The tubes are carried out on a machine of rolling up filament (Figure 2). This method for realization makes it possible to obtain an important fiber volume fraction, (62%), for our material. The fibers are directed with ±55°. Indeed calculations in static's show that the angle of orientation of 55° is the optimal slope for the behavior in external pressure. The realization of the test-tubes requires 40 return tickets of the drum carry-wire. An observation under the optical microscope makes it possible to distinguish that it is about a stacking of 10 ply woven in the thickness of the laminate (Figure 3). Le reinforcement consists of glass-E fibers and the matrix is resin epoxy LY556 with a hardener HY917.

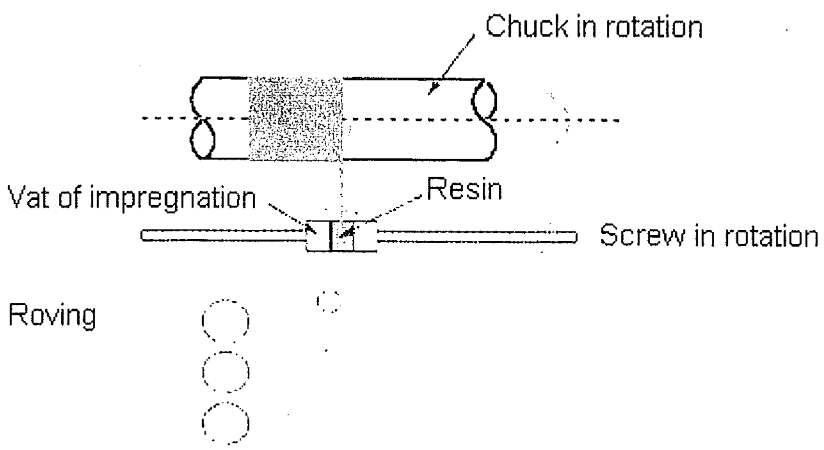

Figure 2: Principle of rolling up filament

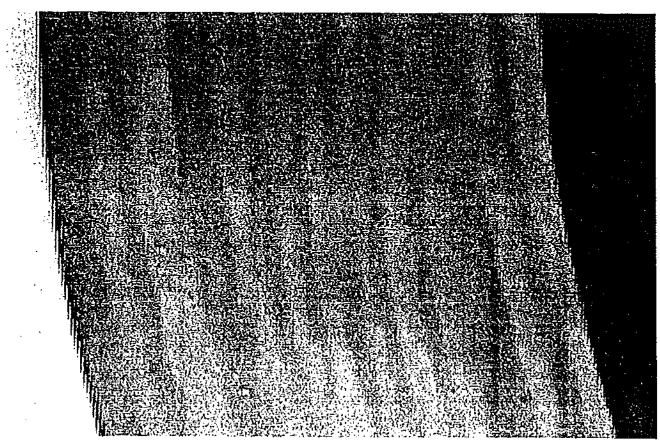

Figure 3: Sequencing of the folds in the thickness of a test-tube

The tubes (Figure 4) have as an interior diameter of 55 mm, an external diameter of 67.7 mm and its length is of 110 mm.

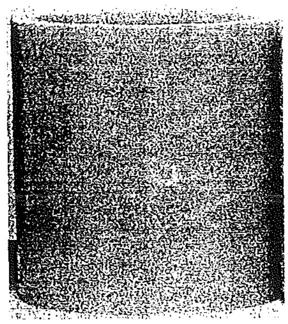

Figure 4: Tube out of glass-E / LY 556

The mechanical characteristics of the laminate (Table 1) were determined by Davies and al. [1].

Masse volumique (kg/m^3)	2050
Longitudinal modulus E_l (GPa)	49.9
Transversal modulus E_2 (GPa)	17.4
Out-plan modulus E_3 (GPa)	17.4
In-plan shear modulus G_{12} (GPa)	6
Out-plan shear modulus G_{23} (GPa)	6.2
Out-plan shear modulus G_{13} (GPa)	6
Poisson's ratio ν_{12}	0.266
Poisson's ratio ν_{23}	0.4
Poisson's ratio ν_{13}	0.266
Limit Values	
Longitudinal tensile strength X_t (MPa)	1200
Transverse tensile strength Y_t (MPa)	35
Out-plan tensile strength Z_t (MPa)	35
Longitudinal compressive strength, X_c (MPa)	600
Transverse compressive strength Y_c (MPa)	12
Out-plan compressive strength Z_c (MPa)	120
In-plan shear strength S_{12} (MPa)	60
Out-plan shear strength S_{23} (MPa)	80
Out-plan shear strength S_{13} (MPa)	60
Inter-laminate shear strength (MPa)	39

Table 1: Mechanical properties of the test-tubes

3. Experimental Study

The phenomena concerned at the time of an impact low speed are several and varied. The damage mechanisms are complex. In order to apprehend the damage mechanisms and their evolution during the impact, we initially tried a static approach by tests of quasi-static punching, then of the quasi-static indentation in the thickness then tests of impact to low incidental energy.

3.1. Quasi-static punching

The tests of punching are carried out on a tensile testing machine. The test-tube puts back in a cradle of diameter 100 mm. The instrumented cross slide of a hemispherical end with a diameter 50 mm which represent the impactor, comes in contact with the tube. The test is carried out with imposed displacement (Figure 5) and the displacement rate is of 1mm/mn.

The damages identified during such a test are a local hammering in the contact with the punch, intra-laminar cracking of fold and interlaminar failure. Hammering is detected in a tactile way. It is about the crushing of the layer of surface resin as well as crushing in the thickness. A transverse section of punched tube shows a healthy part localized under the point of impact in the thickness; around this healthy volume, interlaminar failure as well as the cracking of ply is propagated. Such a cut makes it possible to observe the cone of interlaminar failure whose angle following the axis of the cylinder is more important than in the direction of the circumference.

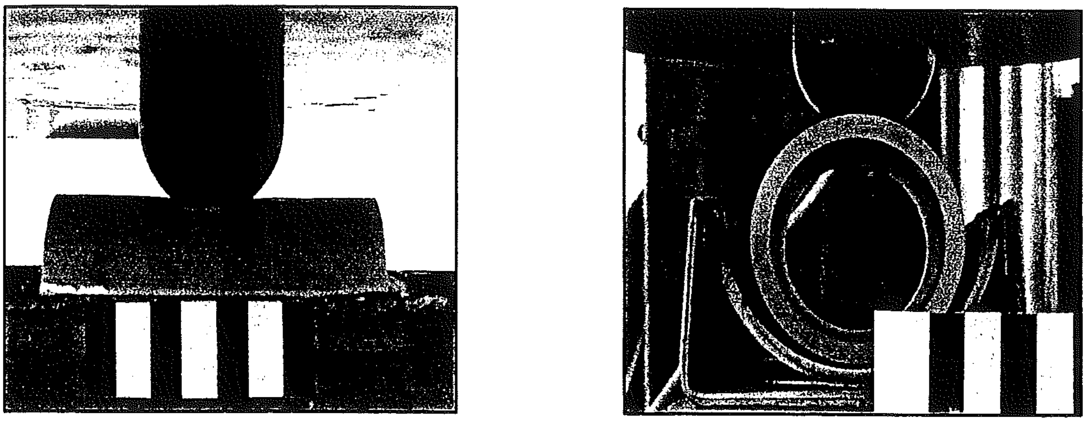

Figure 5: Device of indentation quasi-static

The results of punching (figure 6) show a good repeatability of the test. One notices at the beginning of the test, a small nonlinear part due to crushing of the surface layer of resin. The total stiffness of the test-tube, equal to the initial slope during the test, seems constant until the first damage. The break of slope interpreted as introduction of defect is at the neighborhoods of 6 kN. Beyond that, one notes an abrupt reduction in the stiffness who seems to keep the same slope for all the remainder of the test. The evolution of the surfaces damaged for various levels of loading makes it possible to conclude that there is an effort threshold of creation of interlaminar failure; beyond that, this surface grows with the load.

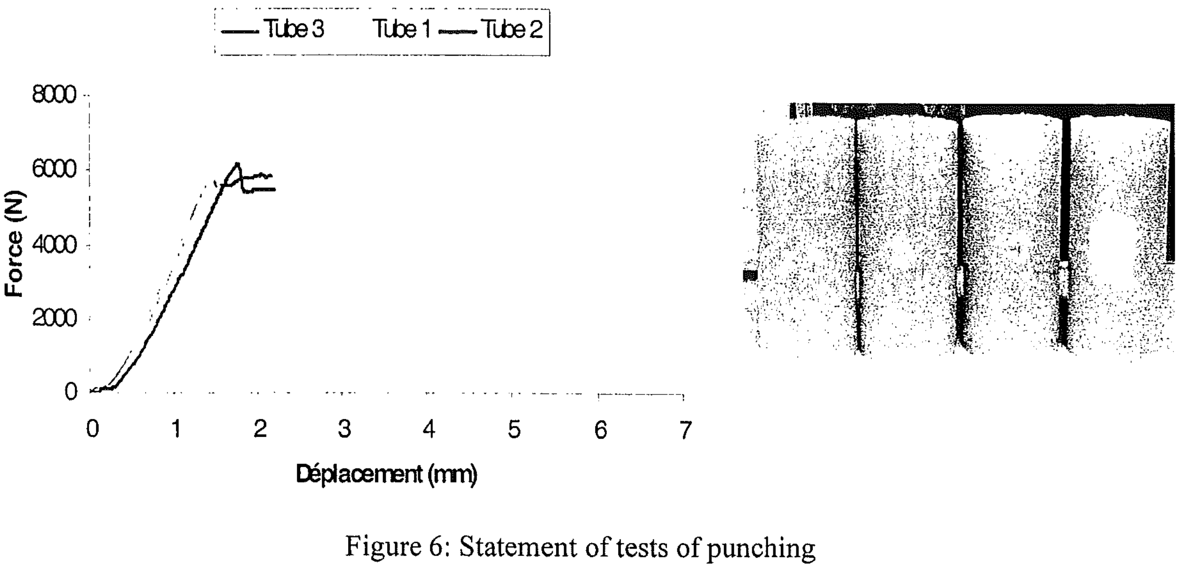

Figure 6: Statement of tests of punching

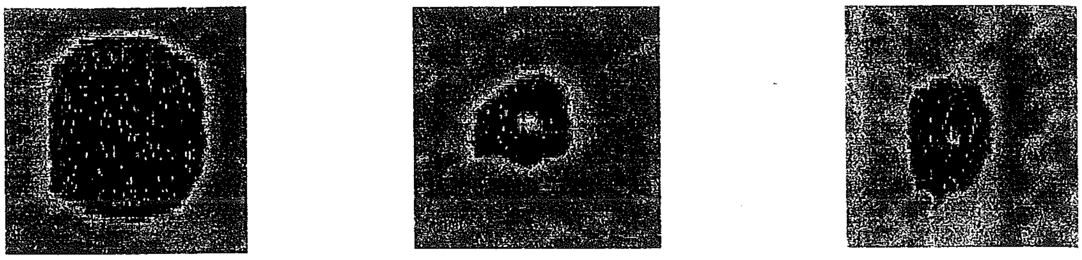

Tube 1 Tube 2 Tube 3

Figure 7: Faces of the damages by ultra sound

A cycle of load followed by a unloading (figure 8) makes it possible to identify a permanent crushing of the test-tube on the level of the contact with the hemispherical end. It is about a residual indentation which represents the localization of phenomena that will be underlined during the tests of quasi-static indentation of the laminate.

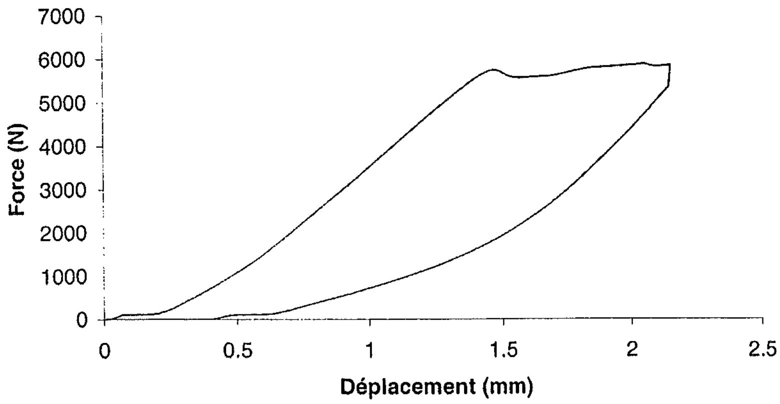

Figure 8: Cycle of load followed by a discharge during punching

3.2. Quasi-static Indentation

The tests of punching underlined the existence of a crushed zone which can be due to a local politicization of the sample. To understand these phenomena, tests of quasi-static indentation are realized on tensile testing machine similar to the preceding one. The goal of these tests is to study the behavior of the tube in its thickness in order to determine the laws of the contact. The behavior in the thickness being independent of the limiting conditions at the time of the impact, we put in œuvre an experimental device made up of the tube assembled on a rigid plain mandrel which rests on two ve placed on both sides (Figure 9). The inflection of the chuck is negligible. Because of the distribution of the constraints in the thickness of the laminate, the response of the latter is not affected by the difference in rigidity with the treated steel chuck. The hemispherical end assembled on the cross slide has a diameter of 50 mm. Various speeds of load application are used (0.2, 1 and 5 mm/min). The tests are with displacement imposed for various values thresholds of effort.

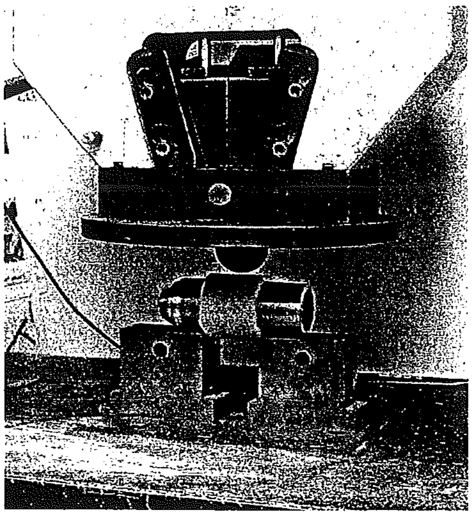

Figure 9: Device of quasi-static indentation

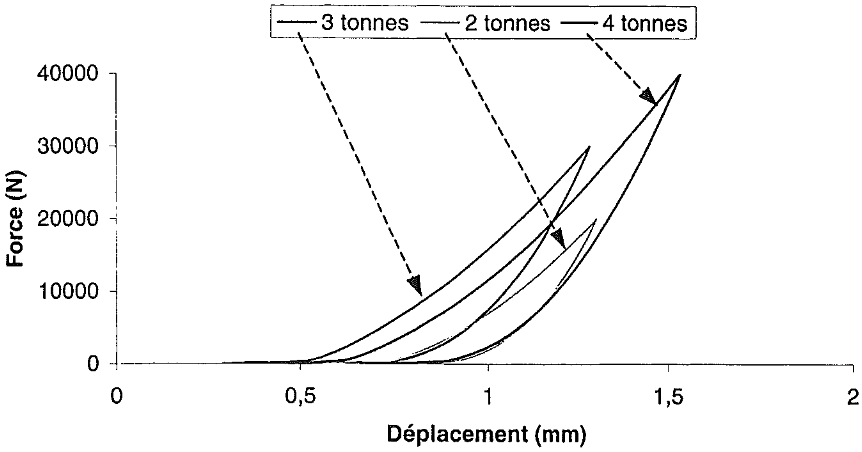

Figure 10: Load and unloading diagrams for a test of indentation

The zone of contact presents an elliptic form due to the intersection half-sphere / cylinder. One detects a local hammering which, according to the incidental effort, would act of the crushing of the surface layer of resin or a hammering in all the thickness of the laminate. This layer of resin is about 0.5 mm of thickness. The ways at the time of the load and the unloading are nonlinear (figure 10). They seem to correspond to the hertzian modified contact laws as those identified in the literature [2] for the case of the laminated plates. Some is the level of the loading effort, one notes a residual permanent indentation. That is due to the elastoplastic behavior of the laminate following the normal direction to the ply.

Comparative measurements are in hand in order to estimate the sensitivity at the speed of deformation as well as the influence of the diameter for hemispherical indenters.

3.3. Tests of impact

The tests of impact by falling weight (figure 11) were carried out on a device of well of fall. It consists of a tower of which is released an instrumented impactor. It is guided by a tube of centering in order to fall to the right of the highest generator of the test-tube, in the medium of the length of the tube. The tube rests in a cradle maintained on a rigid bench. The Associated metrology to this test is specific and it comprises the following instrumentation:

1) One piezoelectric accelerometer fixed in the end of the impactor at 10 mm of the point of contact. It makes it possible to collect the time laws of acceleration, of force, displacement and duration of interaction projectile - structure during the shock.
2) Two laser aiming, interdependent of the tower of fall, which give speeds incidental and of rebound.
3) Two gauges of deformation laid out on interior surface of the tube under the point of impact. It inform about the average local deformation rate about the impact.
4) Acquisition with NICOLET system 16 ways makes it possible to sample at a frequency of 1 MHz.

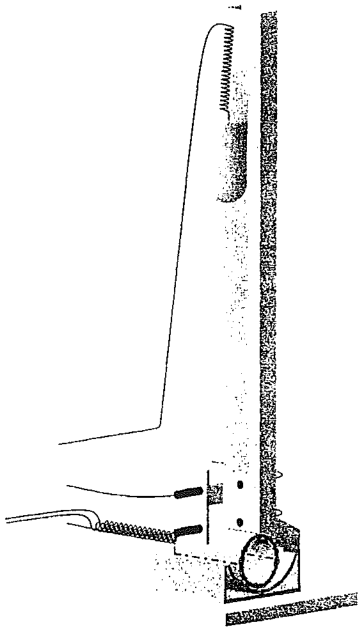

Figure 11: Device of the impact by weight falling

The damages observed during the tests of impact on the composite thick tubular structures are comparable with those observed in the case of test of quasi-static punching. One notes a local hammering at the point of contact with the impactor, the intra-laminar cracking of ply and interlaminar failure.

The evolution of the delaminated area, measured from the stereotypes ultrasound shows the existence of a threshold value of incidental energy for the initiation of interlaminar failure. Other studies are in hand in order to determine the evolution of the damage for increasing incidental energies.

3.2. Test results

	Test 1	**Test 2**
Incidental velocity (m/s)	2.28	3.53
Incidental energy (J)	4.2	10.03
Coefficient of restitution	0.88	0.52
Time impact (ms)	2.06	2.26
Maximum effort (N)	6669	12313
Maximum displacement (mm)	1.14	2.07
Surface delaminated (mm^2)	0	637
	Without damage	**With damage**

4. Conclusion

The tests of quasi-static punching and indentation, and impact allowed the identification of types of damages. This damages are local hammering at the impact point, delamination induced by inter-laminar shearing and also intra-laminar cracks of the ply. The scenario which will trace the history of the listed damage is not yet well-known.

The comprehension of the initiation and the propagation of damage are a fundamental factor to evaluate the mechanical behavior of the structures damaged during their service.

In this study we can raise the points according to:
- existence of a localized healthy part in the center of the damaged part,
- around this healthy volume, it has a propagation of interlaminar failure and cracking,
- existence of an effort threshold of creation of interlaminar failure,
- the laws of increasing and decreasing load is nonlinear

Other studies are in hand in the sight of better apprehending all the events which occur at the time of impact low energy. The finite element method part will be perform for better prediction of the damages.

References

[1] Davies et al, *Matériaux composites pour véhicule sous-marin 6000 mètres*, Proc. JNC10, p525

[2] Kim, S.J.; Nam, S.G., Kim, T.W., *The effect of curvature on the dynamic response and impact-inducted damage in composite laminates*, Composite Science and Technology, 1997, p 763-773

Design Criteria for the Use of Very High Tensile Steel in Fast Ships

Thomas Gosch
Flensburger Schiffbau-Gesellschaft mbH, Flensburg/Germany, gosch@fsg-ship.de

Abstract

Fast High Performance Marine Vehicles require a very lightweight but strong structure. Flensburger Schiffbau-Gesellschaft (FSG) has designed a fast monohull within the framework of a European research and development project. The steel design of the midship section was conducted utilising very high tensile steel (HT69) in order to reduce the steel weight as much as possible. To estimate the loads and calculate the scantlings first principle methods were used.

The main focus of the work carried out was to identify design criteria for the development of steel structures made of HT69. When using HT69 material, buckling strength, fatigue strength and permissible deflections are the dominant parameters to determine local scantlings. Looking on the global strength, dynamic problems like springing and whipping overrule the common longitudinal strength parameters.

1. Introduction

Within the R&D-project FasdHTS, Flensburger Schiffbau-Gesellschaft (FSG) was in charge of developing a fast ferry design. The project FasdHTS relates to design, construction and fabrication of large high-speed craft. One of the main targets of the project is the reduction of the steel weight by introducing high tensile steel HT69. Savings of 40 % in steel weight are to be achieved. To make detailed studies on possible steel designs, a target ship was designed. This was a HSC of about 200 m length and 50Kn speed.

The project is supported by the EC within the 5th framework program under the PRODIS cluster "New Concepts of Ships and Ship Systems". The consortium consists of engineering companies, shipbuilding and repair shipyards, a steel mill, several research institutes as well as classification societies.

The following paper will focus on the steel design of the midship section.

2. General arrangement of the target ship

The ship was designed for operation in the Mediterranean sea. The deck arrangement as follows:
A truck deck at maindeck level, a car / cabin deck as upperdeck and a pax-deck above that. All machinery is located beneath the main deck. The ship is propelled by six waterjets. Four of them are powered by gas turbines. The other two jets are powered by medium speed diesel engines. These are used for the manoeuvring in harbour. Intensive investigations using CFD methods have been made to optimise the hydrodynamic behaviour of the ship. After several design circles, taking into account also the loading unloading process, engine room arrangement with redundant propulsion, evacuation of passengers etc., the basic design finally resulted in a ship with the following main particulars :

Table 1 Main particulars of the design

Length betw. perp.	205m
Breadth	24.70m
Draught	5.55m
Lightship	6900t
Deadweight	3000t
Passengers (without AC)	1500+(500)
Officers/Crew	10/64
Passenger cabins (4 Pers.)	50
Crew cabins (4 Pers.)	16
Officer cabins (1 Pers.)	10
Cars	170
Car lanemeter	900m
Trucks	71
Truck lanemeter	1075m
Lane width cars	2.50m
Lane width trucks	3.10m
Installed power	4GT 27.600kW each/ 2DE 8200kW each
Operational speed	47kn
Range	400nm

The details of the design were presented by Schöttelndreyer at the *Hiper (2001)*.

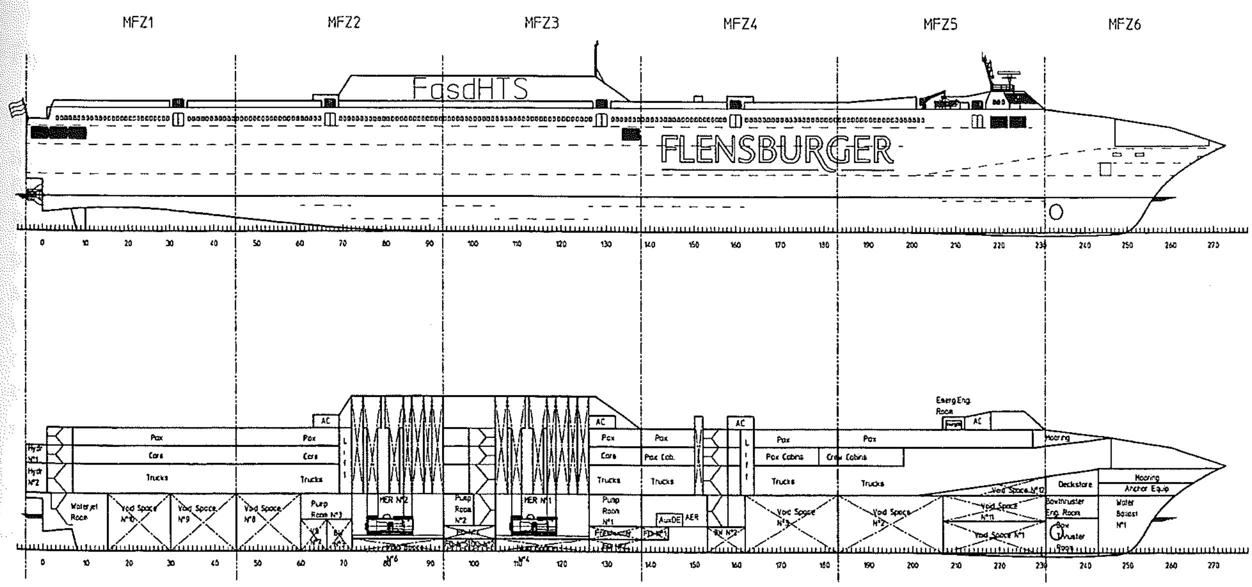

Fig.1 Side view of target ship

2. Steel design of the midship section using the HSC Code of Germanischer Lloyd

2.1 Permissible stress

A first approach to determine the scantlings for the midship section was made using the *Rules for Construction and Classification of High Speed Craft* of Germanischer Lloyd *(GL HSC).* Permissible stresses with regard to longitudinal strength were defined using the equation :

$$k = \frac{295}{R_{eH} + 60}$$

given in *GL (1997).* With $R_{eH} = 690\frac{N}{mm^2}$ the *k*-factor results to $k = 0.393$ with leads to a permissible stress of $\sigma_{per} = \frac{150}{k} = 380\frac{N}{mm^2}$. It should be mentioned here that the equation for the *k*-factor shown above was developed for the interpolation of *k*-factors for steel with a yield strength between $R_{eH} = 235\frac{N}{mm^2}$ and $R_{eH} = 390\frac{N}{mm^2}$. A extrapolation of the *k*-factor as shown here, or even the complete use of the *k*-factor concept, for a steel with a yield strength of $R_{eH} = 690\frac{N}{mm^2}$ is very questionable. Here, this concept was used to determine a first set of scantlings for the midship section as a starting point for further investigations.

2.2 Design Loads

Design loads for the decks were applied as shown below. For the truck deck no mafi trailer loads were considered because it seems to be reasonable to assume that on a ship with such a high speed only exclusive and time critical load will be carried, with trucks driving directly onto the vessel.

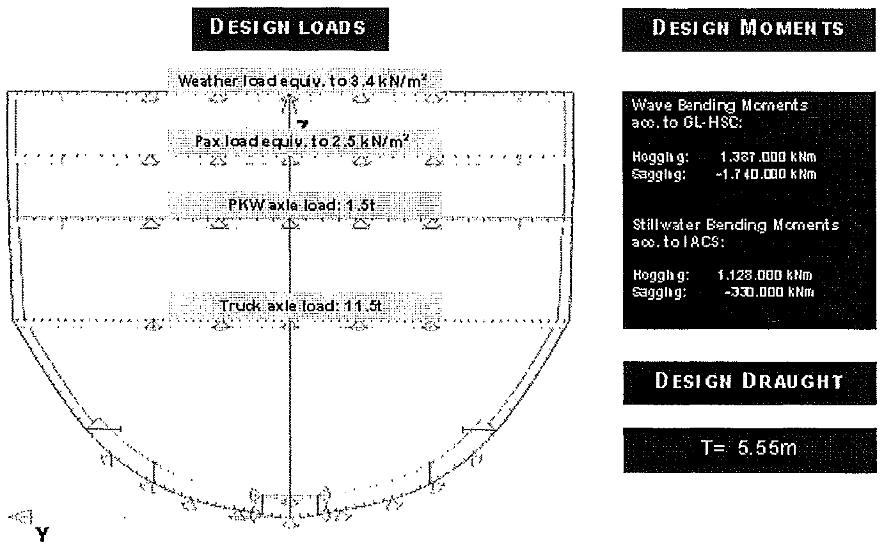

Fig.2 Design loads

For the longitudinal strength, the wave bending moment was calculated according to *GL-HSC.* Stillwater bending moment was calculated according to IACS. Again these moments were, as the k-factor concept mentioned above, only used to determine a first set of scantlings for further investigations. More sophisticated methods to calculate longitudinal strength values will be discussed later.

2.3 Scantlings according to HSC-Code

Making use of the permissible stresses and the loads determined above, a first set of scantlings was calculated, using the rules given in *GL-HSC.* The calculated scantlings for the plating and the applied scantling criteria used shown in the figure below. They relate to a weight of 12.7 t/m for the longitudinal members.

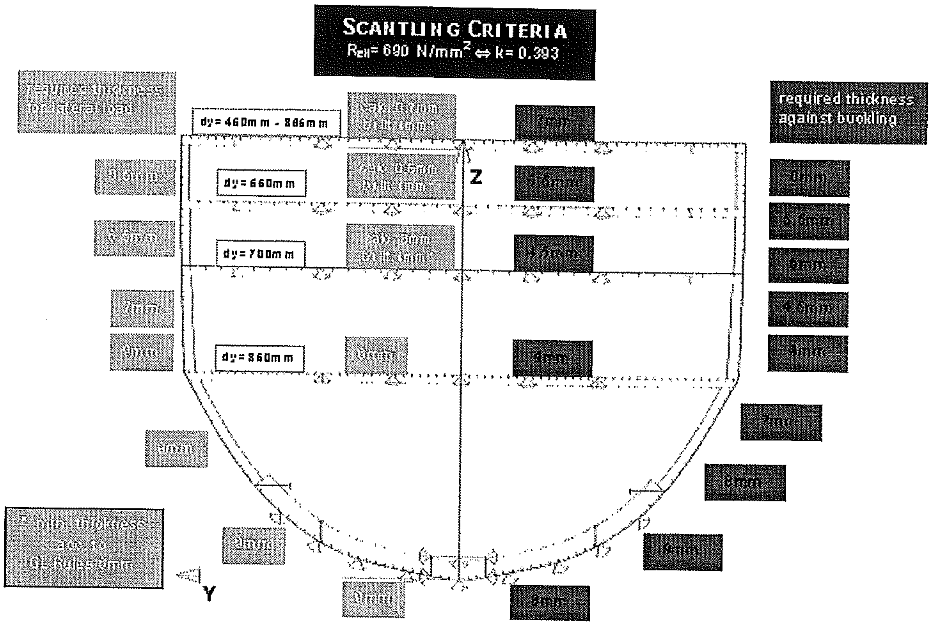

Fig. 3 First scantlings of plating and design criteria

For the plating below the car deck the lateral pressure is the design criteria for the scantlings. In the upper region of the ship, the buckling criteria is the decisive criteria for nearly all scantlings. Here, a first difference to a design made of "common" high tensile steel in ship building, HT36, can be seen. Because of the high permissible stresses of the HT69 steel the plate thickness calculated due to lateral pressure are relatively thin. Also the section modulus due to longitudinal strength comes out to very small values. This leads to high pressure stresses in the upper and lower flanges of the ship compared to designs made of common steel. The combination of thin plates and high compressive stresses in designs using very high tensile steel (VHTS) makes the buckling behaviour a major design driver for the scantlings of the plating. Further research to the buckling behaviour of VHTS plate fields are necessary to optimise such structures.

The transverse structures, especially the deck and side girders, were calculated according to the *GL-HSC* code. In the area of the pax-decks a minimum height of 450 mm was used for the girders, in order to allow for the arrangement of for the installation of pipes and wires. Again, as found for the longitudinal plate structure, the check against buckling of the web or even tripping of the flange has to be examined carefully, since the compressive stresses are very high due to the high permissible stress of HT69. The scantlings of the transverse members are shown on figure 4.

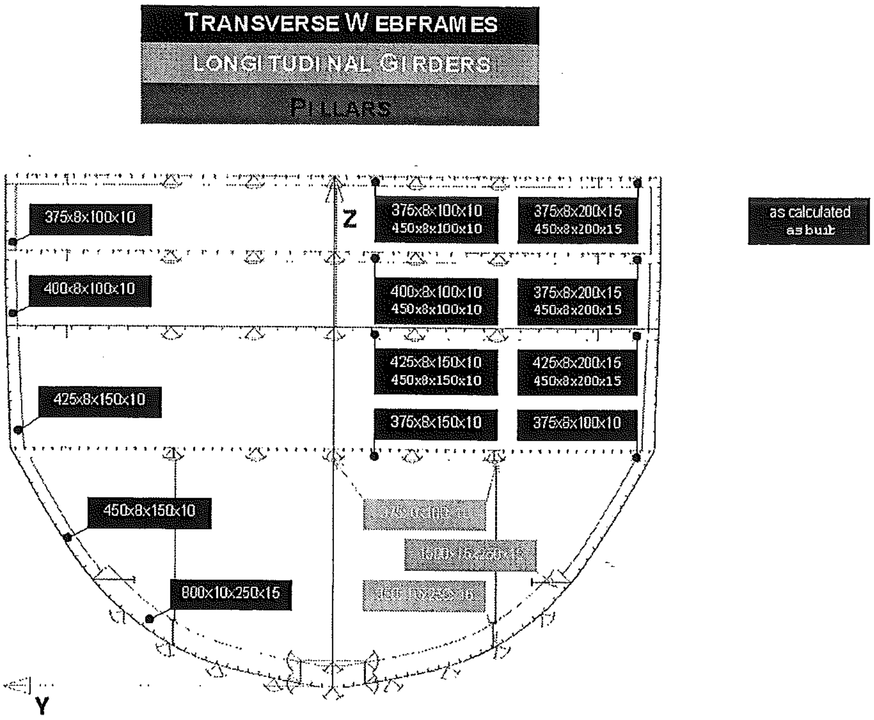

Fig. 4 Scantlings of transverse structure

3. Validation of the first design, direct calculations

3.1 Racking calculations

To validate the scantlings estimated using the *GL-HSC,* a finite element model of the midship area was launched. The main target of this FE-calculations was to get an indication on the racking behaviour of the transverse structure. The model was generated as shown in the figure 5.

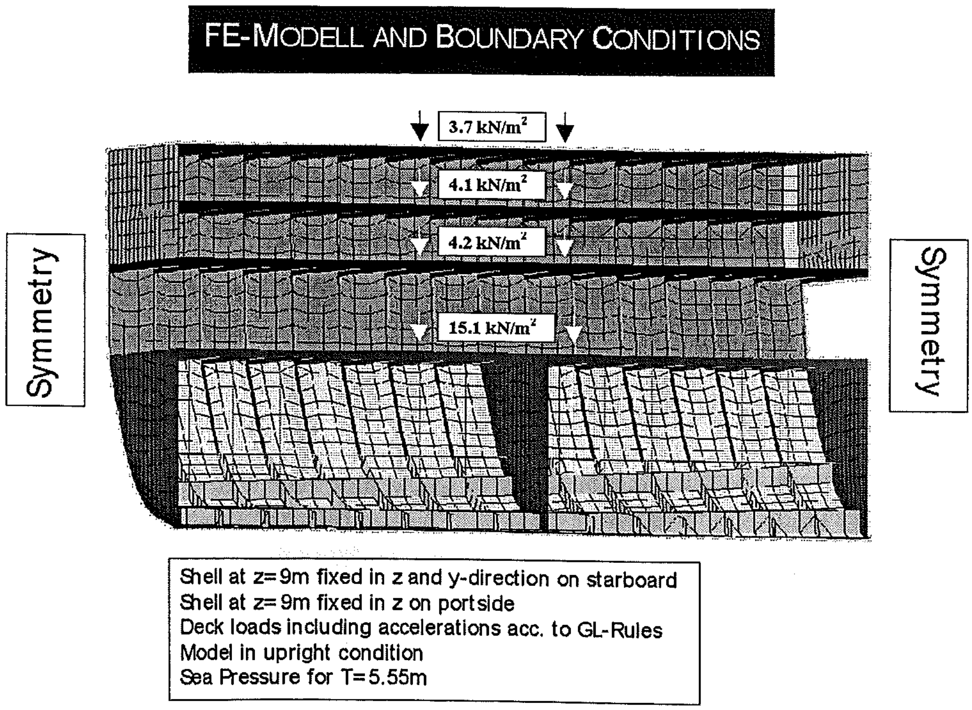

Fig. 5 FE-model

For the midship model, an area of the ship without center casing was chosen to determine maximum stresses and deformations at the transvers members. Upright and heeled conditions were calculated. The upright condition was found to be the one giving the higher stress levels in the transvers members. Thus the following research was focused on the upright condition. The resulting deformations are shown in figure 6.

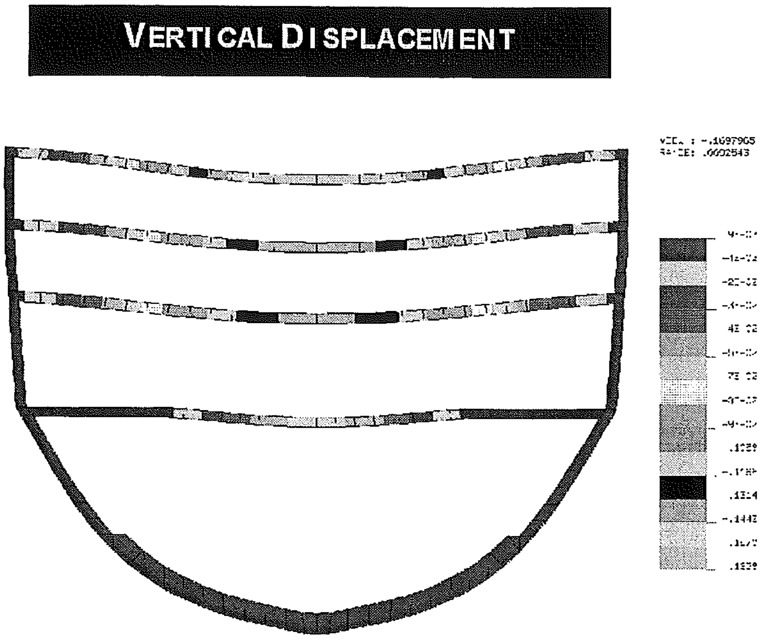

Fig. 6 Vertical displacement FE calculation

The results for HT69 show a dramatically weak structure. The maximum vertical deformation in the girder system was calculated to be 170 mm. In most applications, this is an unacceptable high value. The bending stresses calculated in the deck girder system are shown in figure 7. They are well below the permissible stress.

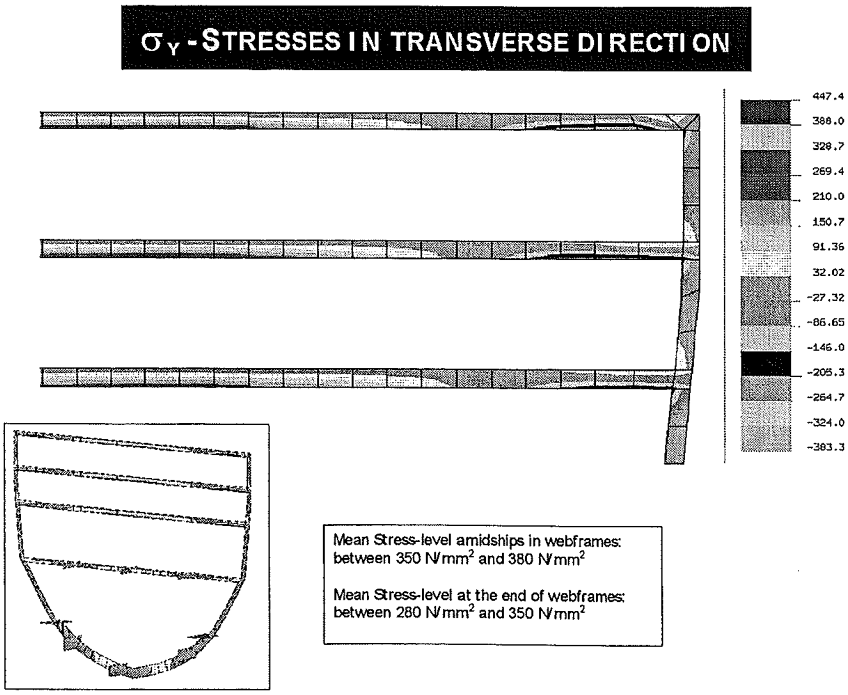

Fig. 7 Bending stress in deck girders

The scantlings of the deck girder system were designed using the permissible stresses as design criteria. This is common practice within the ship steel design process. For ship structures made of VHT-steel the permissible deformation have to be used as an additional design criteria.

A practical way for designing the scantlings for such structures could be to define permissible deflections. For these deflections the resulting stresses in the girder system could be calculated. Using permissible stresses allows to select the best fitting steel grade, leading to an optimised structure with regard to weight, stress usage of the steel and deflections.

3.2 Direct calculations on global strength

Most of the work with regard to global strength was done by the colleagues of Germanischer Lloyd. To check the global strength behaviour by direct calculations, a global FE-model of the ship was launched. This model is shown in figure 8.

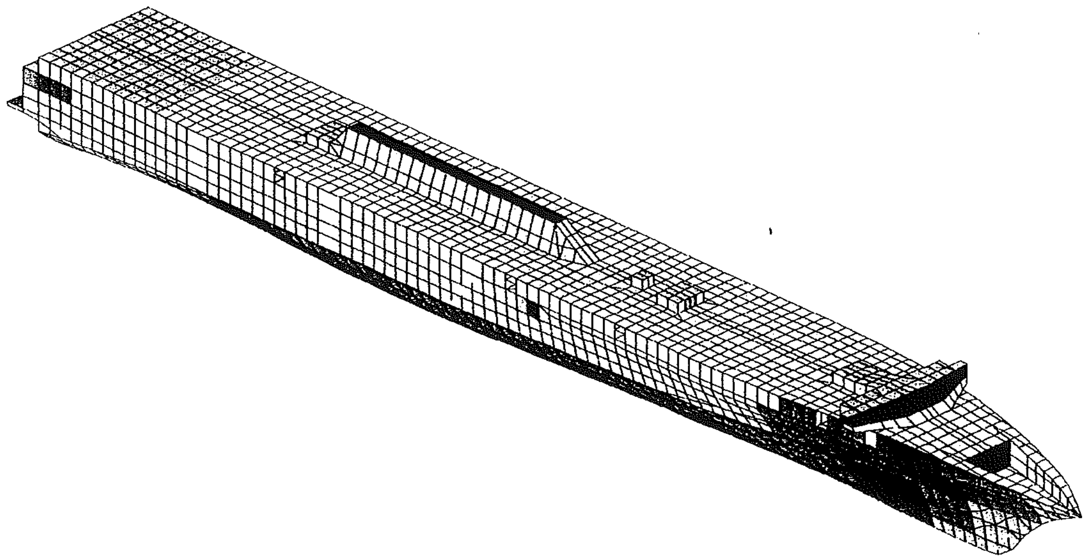

Fig. 8 Global FE-Model

For a first indication to the longitudinal strength behaviour the stillwater bending moment and wavebending according to *GL-HSC* code, moments were applied as calculated above. The resulting deformations of the hull are shown on the figure 9.

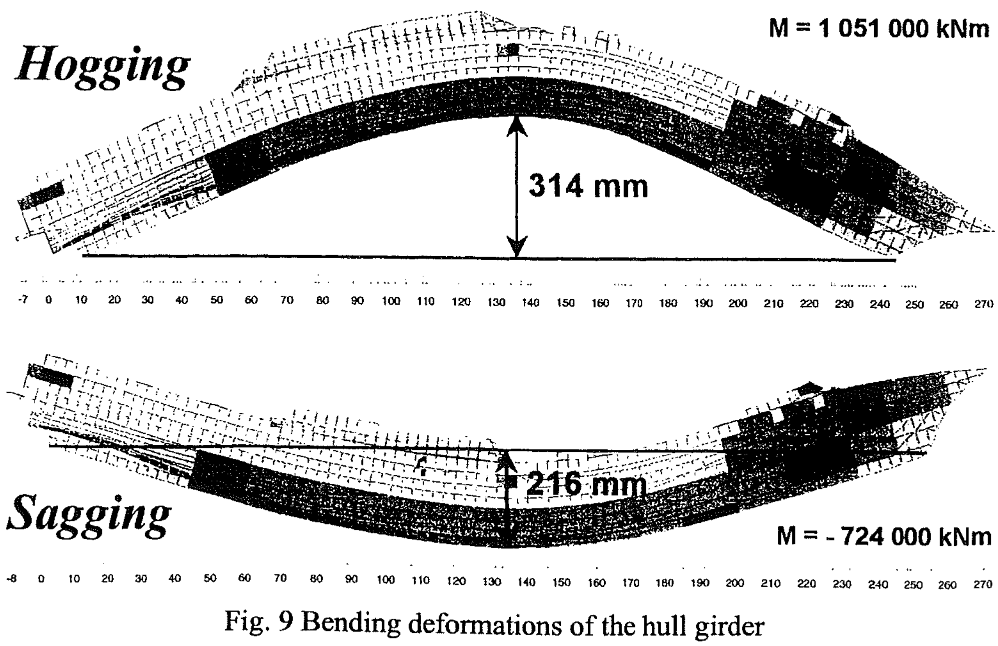

Fig. 9 Bending deformations of the hull girder

Like seen in the racking calculation before, the deformations are very high compared to designs made of "common" steel. They are in the range known from the very large post panmax container vessels. The results show again that structures of VHT-steel will end as a very weak structure.

Before discussing how to limit these deformations, a look should been taken at the load side. The calculated deformations are based on bending moments derived from *GL-HSC* code for world wide operation of ships. When optimising a fast ship structure, the area of operation of the ship should be taken into account as a new design criteria. The bending moment, and thus the hull girder bending deformations, could be reduced noticeable when limiting the area of operation e.g. to the Mediterranean sea.

The hull forms of very fast ships are not comparable to "common" hull forms. The hydrodynamic effects of cruising at 50 Kn are different to the ones at slower speed. Since the formula of the *GL-HSC* code are made by extrapolation of values from "common" ships with "common" speeds, the hull girder bending moments calculated while using these formulae are doubtful. Direct calculations for the bending moments, taking into account the actual hull form and pressure distribution on the hull for a given speed, would give more certainty to the steel design. The different longitudinal bending moments derived from *GL-HSC* code for world wide operation, direct hydrodynamic calculations for world wide operation and direct hydrodynamic calculations for operation in Mediterranean sea can be seen in figure 10.

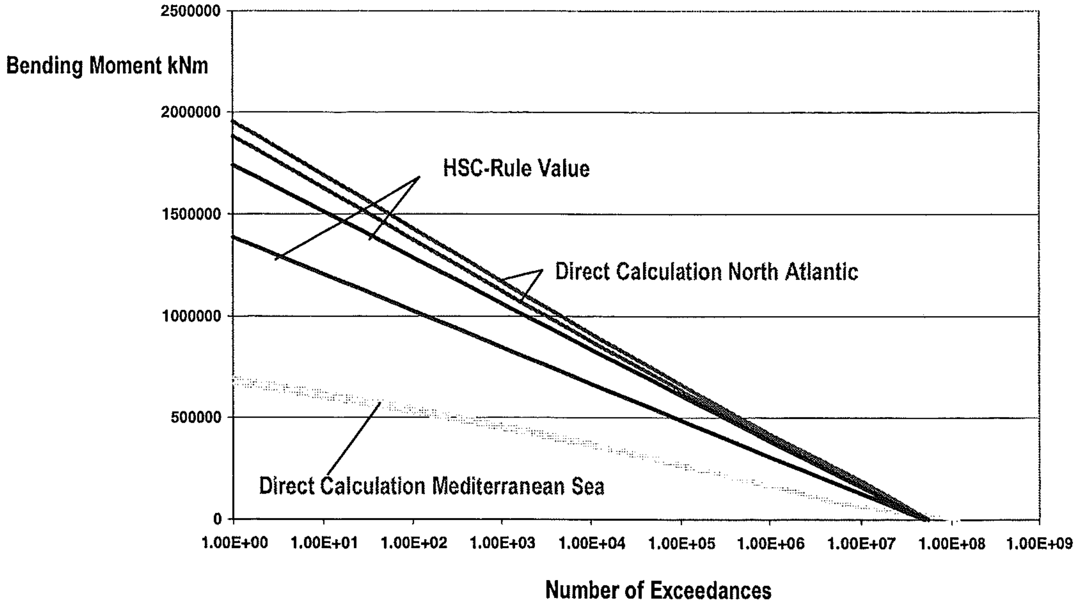

Fig. 10 Hull girder bending moments

Dynamic effects to the hull girder could change the design bending moments too. The stiffness of the hull girder with regard to bending is reduced drastically by the use of VHT-steel. Thus the eigenfrequencies for bending of the hull girder comes out very low. Contrary to that the frequency of the encountered waves increases due to the high speed of the ship. So the risk of effects like springing and whipping of the hull girder increases dramatically. Springing is a high frequency phenomenon whereby elastic vibration modes are periodically exited by the encountering waves. Whipping is a high frequency flexural vertical vibration of the hull girder exited by a slamming impact. Both, springing and whipping can increase the wave inducted midship bending moment dramatically. Thus, avoiding these effects could be a design criteria for the steel structure as well. Further investigations on these effects is needed to find proper methods for the steel designers to keep control of this phenomenon during the design process.

An other design criteria influencing the longitudinal strength of a fast ship could be the comfort of the passengers on board. A ship travelling at 50 Kn in 8 m significant wave height will cause very high accelerations on board. Passengers on board will get seasick or even injured. Therefor the maximum speed for the ship needs to be limited for a certain significant wave hight to keep accelerations to a tolerable level for the passengers. Of cause, the wave induced midship bending moment is reduced by this as well. A typical "speed limitation curve" is presented on figure 11.

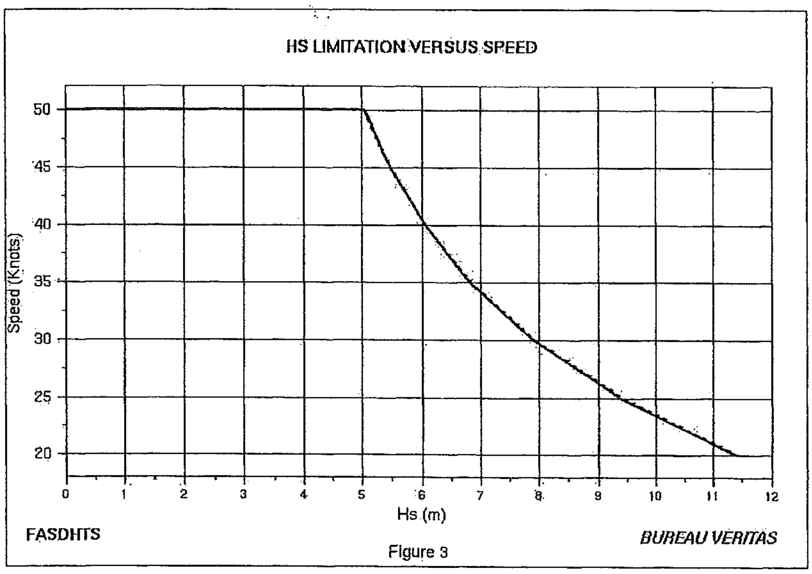

Fig. 11 speed limitation curve

Further investigations are needed to make it possible to consider the speed limitation due to passenger comfort when determining the wave induced midship bending moment.

4. Conclusions

For a large high speed craft a first design of a steel structure utilising HT69 steel was generated applying the rules of *GL-HSC* code. This first design was validated by direct calculations. A set of new criteria to be considered during the steel design process were found :

For the calculation of the midship bending moment the specific hull form, the area of operation and the passenger comfort (speed / acceleration limitation) have to be taken into account. Direct calculation methods need to be used for these calculations. Methods have to be developed to make it possible for the steel designers to take care of avoiding springing and whipping effects.

For local strength calculations in VHT-steel structures, permissible deflections come out as a major design criteria. For a given permissible deformation the steel grade needed has to be determined. Buckling strength is getting a much more dominant parameter than known from "common" designs utilising HT-steel.

Within this report no investigations were made with regard to fatigue strength and vibration behaviour. But it should be clear that ship structures made of VHT-steel, which are weak and highly loaded, will be very sensitive to fatigue and vibrations. Therefor fatigue and vibration behaviour will be major design criteria as well. Further investigations are needed to get a sound technological basis for the designers. An extensive program for fatigue tests has been set up within the FasdHTS R&D project to get more information about the fatigue strength of very high tensile steel.

References

Hiper (2001), *2nd International Euro Conference on High-Performance Marine Vehicles, report of Friedrich Schoettelndreyer*

GL-HSC, *Rules for Construction and Classification of High Speed Craft, Part 1, Chapter 5, High Speed Craft*

GL (1997), *Rules for Classification and Construction, Ship Thechnology, Part 1, Capter 1, Seagoing Ships*

Environmental Performance of Land and Marine Transportation in Inland Shipping – Impact of ship speed

Kazuhiko Hasegawa[1] **, Kho Shahriar Iqbal**[2]

[1]Dept. Naval Architecture & Ocean Engineering, Osaka University, hase@naoe.eng.osaka-u.ac.jp

[2]Dept. Naval Architecture & Marine Engineering, Bangladesh Univ. of Engineering & Technology

Abstract

It was found that the marine transport is more environmental friendly than land transport in inland cargo shipping[1,2]*. Fet*[3] *also showed the superiority of marine transport in trans border cargo transportation. In all of these cases, the researchers considered moderate operating speeds for ships. But other researches showed that fast ship was not competitive in this respect*[4,5]*. This paper is to discuss about a methodology to find the critical speed of a ship up to which the marine transport will be favorable for sustainable development to the environment.*

1. Introduction

The climate of the earth is changing. Inland and coastline disappearing under water, more frequently occurring fiercer hurricanes and typhoons, heat wave, melting polar ice caps, shift of agricultural zones, coral bleaching in the Pacific Ocean as well as the Indian Ocean and Caribbean Seas are some of the evidences which show the certainty of climate change. Scientists believe that in all of the human history climate has never changed as fast as it is changing today. Plenty of reasons are behind this change. Some of them are natural and some are human induced. Ever increasing human activity is having a negative effect on the climate.

Industrialization and technological development causes people to use ever increasing quantities of gas, electricity, petrol and diesel, and leads to emit increasing volume of CO_2 with some other gases such as methane (CH_4), nitrous oxide (N_2O), CFCs, PFCs, and SF_6 to the atmosphere. These gases enhance the natural greenhouse effect leading to the Earth gradually becoming warmer. Since the industrial revolution, the global mean surface temperature has risen by 0.3^O C to 0.6^O C[6], which is the effects of increased atmospheric concentrations of various greenhouse gases. It has been found that during this period carbon dioxide (CO_2) concentration in the atmosphere has increased nearly 30%, methane (CH_4) concentration has more than doubled and nitrous oxide (N_2O) concentration has risen by about 15% [6].

The governments of industrialized countries and the countries with economies in transition have been trying to convince those sectors, companies and sources, which are involved in emitting greenhouse gases, so that they adopt new methodologies to reduce these emissions. The Kyoto Protocol[7] has been a turning point in this regard for future economical and environmental policies for both industrialized and developing countries. In this circumstances, environmental friendly and economically feasible transportation system planning has become a very essential subject matter in recent days.

Among the human activities causing the climate change, use of transports and burning the fossil fuel for energy are vital. Table 1 shows some emissions and the share of transport sector in Japan[8]. So especial attention is being paid to the transport sector to reduce the emissions caused by this sector. Measures, which are being considered, include raises in excise duties, stepping up enforcement of speed limit, finding alternative transport modes and infrastructures.

Table 1: A few emissions and the share of transport sector in Japan

Emission	In year	Japan national total ('000 ton)	Japan transport sector (%)
CO_2	1990	1,124,532	18.29
	1997	1,230,831	20.42
CH_4	1990	1,543	4.93
	1997	1,389	3.24
CO	1990	3,873	52.78
	1997	3,751	53.56
N_2O	1990	58	22.41
	1997	66	22.73
NO_x	1990	1,851	49.49
	1997	2,051	49.73
SO_2	1990	900	20.67
	1997	796	12.44

Modal shifting of cargoes from road transports to ships may be an achievement in finding a less emitting alternative transport mode from the existing types[1,2]. One of the significant barrier to attract users to water transport is the speed. Conventional ships sail at speeds much lower than that of road and rail transports. To improve the customer service quality and to attract the user towards water transport, the general trend is to introduce high-speed water-craft or fast ship. But some of the recent research showed that the fast ship is not a better solution as it consumes more energy and emits more gases harmful to the environment compared to the conventional ships and other mode of transports[4,5]. That is why, some researchers including Isensee *et al*[4] and Kristensen[5] suggested not to introduce fast ship, but fast shipping through better cargo/passenger handling and improved navigation. Considering all these, it is logical to believe that there is one certain speed for a certain ship which is critical, that is below that speed that ship is competitive to the land transport. This paper is to find an easy and handy method to find that critical speed for a ship. Hasegawa and Iqbal[1] proposed an easy method to compare the water transport with the relevant road vehicles. In that comparison process, three important factors related to transportation system – environmental impact, economic benefit, and customer service quality, are considered. Using the similar comparison process, a methodology of finding the critical speed for a water transport is discussed here.

2. Methodology

For a specific transportation model, life cycle impact assessment, required freight rate and service time are estimated for both road and inland water transport to find their impact on environment, economic superiority and customer service quality respectively. Then comparing these characteristic parameters, the benefit of modal shifting of cargo/passenger from road vehicles to ship is analyzed. Three different indices – environmental index, economic index, and customer service index, are estimated to find the superiority of one transport type over other in three different fields. Then a single comparison index is found to show the overall superiority. The critical speed will be that speed at which the comparison index will be 1, that is, at that particular speed the road vehicles and the ship will be equally beneficial for the society considering all three mentioned factors.

2.1. Transportation model considered

A transportation system model similar to the inland courier service is considered for the comparison here. Two alternative transportation systems are shown in Fig. 1. For this comparison, the transportation task only between the stock points is considered, because the rest of the systems for both alternatives are similar. A specific amount of cargo is assumed to be carried by both road vehicles and ships for shipment through a particular route.

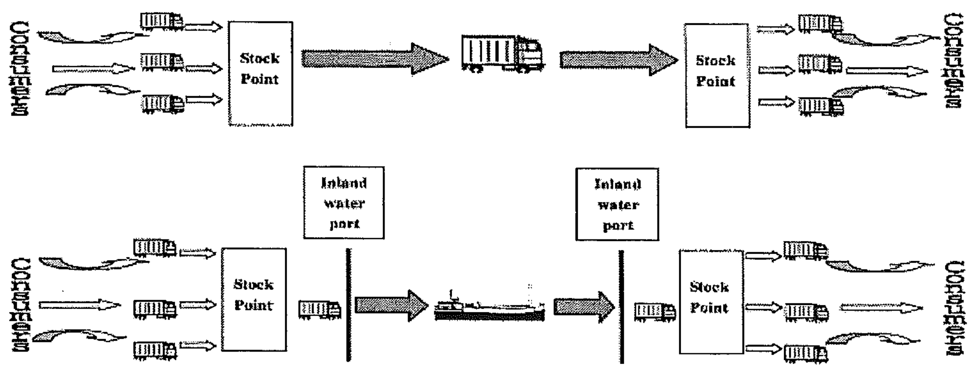

Fig. 1 Alternative transportation model

The route and trip particulars are calculated according to the following equations:

Trip time,

$$t_{trip} = \left(\frac{R}{v} + t_{load}\right)\left(1 + \frac{t_{delay}}{100}\right)$$

where, R = route distance, v = velocity (km/h), t_{load} = loading and unloading time, t_{delay} = delay in time (%)

Maximum possible round trip per annum (RTPA) per transport is calculated from the trip time and total number of hours available in a year for operation according to the following equation,

$$\text{RTPA} = \frac{(24D)}{(2t_{trip})}$$

where, D = days in operation per annum = (365 – off hire days)

Round trip required per annum (RTRA) is the minimum required number of round trip that is required to perform the whole transportation task. It is calculated as follows,

$$\text{RTRA} = \frac{L}{(2C_{ap})\left(\frac{\delta}{100}\right)}$$

where, C_{ap} = capacity (ton), δ = loading condition (%), L = total amount of cargo carried (ton/year)

Amount of fuel consumption per annum (in kg),

$$\text{F}_c = \frac{(2R)(RTRA)(g)}{(f)}$$

Where, g = specific gravity of fuel used, f = fuel consumption rate (km/l),

Annual transportation task in ton-kilometer,

$$\text{A}_t = (L)(R)$$

Where, $L = (2)(365)W$, W = cargo to be carried (ton/day each way)

Number of transport required to perform the task,

$$T = \frac{RTRA}{RTPA} \text{, when } \frac{RTRA}{RTPA} \text{ is an integer}$$

$$INT\left(\frac{RTRA}{RTPA}\right)+1 \quad , \quad \text{when } \frac{RTRA}{RTPA} \text{ is not integer}$$

2.2 Life cycle impact assessment and the environmental destruction index

In considering the life cycle impact assessment of the transportation system, the environmental impact of whole life cycle of the transportation system should be considered. But the data related to the whole life cycle is rarely available. So, on the basis of the available data such assessment is recommended. Calculating the total amount of substances and compounds released for the transportation task by both transportation systems, the environmental impact of the transportation system in different impact categories (for example, fossil fuel exhaustion, local warming, global warming, acid rain, eutrophication, air pollution) are estimated by multiplying the total amount of emissions by respective characterization factors according to the following equation[3].

$$EP(j) = \sum (Q_i \times EF(j)_i)$$

where, $EP(j)$ is the sum of the potential contribution from the impact category, Q_i is the emissions of compound I, $EF(j)_i$ is the characterization factor of compound i related to the impact category j

The environmental destruction index is calculated multiplying the ratio of the amount of potential impact by road transportation system to that of the marine transportation system with some specific weighting factors for each impact category according to the following equation.

$$I_E = \sum \omega_j \frac{(EP(j))_{road}}{(EP(j))_{water}}$$

ω_j is the weighting factor for impact category j. The values of the weighting factors (ω_j) for various impact categories may be estimated by analytic hierarchy process (AHP)[9] by a survey with a questionnaire.

2.3 Required freight rate

To find the economic superiority, required freight rates (RFR) at a certain rate of return for the investment to the transportation systems are calculated and compared. RFR is the minimum freight rate required to meet the expected rate of return (i) on the principal investment or initial price (P) and the annual cost (C) within a specified length of period (N). Here annual cost includes the fuel cost, maintenance cost, crew cost, insurance etc. The RFR is calculated using the following equation[10].

$$RFR = \frac{\left[\frac{P}{spw} + C\right]}{L}$$

where, RFR = Required freight rate, P = Price of the transport or first cost, C = Annual cost , L = Amount of cargo carried (ton/year),

$$spw = \frac{(1+i)^N - 1}{i(1+i)^N}$$

where, spw = Series present worth factor, i = Rate of return (compound interest), N = Number of year in operation

Series present worth factor, also called annuity factor, is the multiplier to convert a number of regular (annual) payments into the present sum[10].

The economic index, $I_F = \frac{(RFR)_{road}}{(RFR)_{water}}$

2.4 Customer service index

Customer service is an important factor to be considered during the transportation system planning. Here only the 'service time', that is, the time taken by the transport company to serve their customer is considered as 'customer service quality' to compare the transportation modes.

In the service time, the time required to accumulate the cargoes/passengers at the stock point should be included with the trip time.

The ratio of this service time of truck transport to the ship transport is taken as the customer service index.

That is, customer service index, $I_S = \frac{(t_{accum} + t_{trip})_{road}}{(t_{accum} + t_{trip})_{water}}$

where, t_{accum} is the average cargo/passenger accumulation time.

2.5 Single comparison index

To find a single comparison index, three different indices i.e. environmental index, economic index and customer service index, are added up after multiplying with respective weighting factor according to the following equation,

$$I = \alpha_1 I_E + \alpha_2 I_F + \alpha_3 I_S$$

α_1, α_2 and α_3 are the weighting factors for environmental index, economic index and service index respectively may be calculated by AHP in the similar fashion described earlier.

It is generally believed that the water transport is environmentally more friendly than other mode of transports. Hasegawa and Iqbal[2] showed that for inland shipping in Japan, cargo ship is about 4 times less detrimental to the environment compared to truck transportation system.

Most of the factors considered here for this comparison are very much related to the time taken by the transportation system. The customer service index is directly related to it. The speeds of the transports considered play a significant role in the time consumption. For the betterment of the customer service in the water transport, introduction of fast ship in many sectors, specially passenger transportation, is recently become popular. But some recent research works showed that fast ship is not environmentally competitive with land transports. Only the water transports with moderate speed are found competitive from the environmental point of view. It means, there is a critical speed for a particular ship type that shows equally beneficial with other particular land transport. Obviously the speed with the comparison index 1 will be that critical speed. It may easily be found using the comparison index-speed relation. An arbitrary curve of comparison index-speed relation is shown in Fig.2. The ship speed at index 1 in this arbitrary curve is that critical speed at which the ship will be equally beneficial to the society compared to the road transport considered.

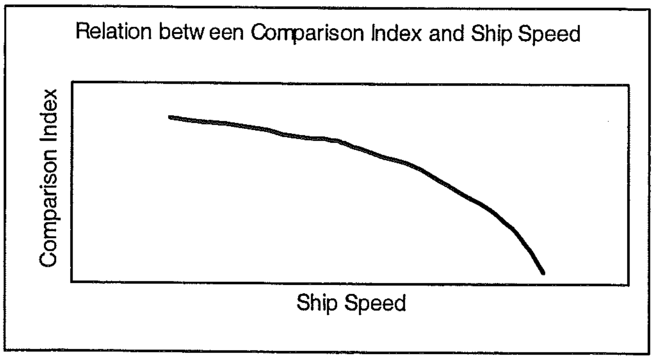

Fig. 2: Relation between comparison index and ship speed

As the ship speed increases, the environmental emissions and energy consumption increase. Though it will improve the customer service quality, the comparison index considering all the factors will apparently go down.

3. Conclusion

A handy method to find the critical speed of ship is shown here. With this critical speed the ship is equally beneficial to the society with particular road transportation system. Shipping is not only carrying by transport, but the whole system involved from receiving the cargo up to delivery to the recipient. So while comparing two transportation systems, the whole systems should be included in the comparison. This method should be studied with real life data of two particular transportation systems to check whether it is acceptable.

References

1. Hasegawa K and Iqbal K S (2000); Inland Transportation System Planning by Life Cycle Impact Assessment: A Case Study. Journal of Marine Science and Technology, Springer-Verlag Tokyo, Vol. 5, pp. 1-8.
2. Iqbal K S and Hasegawa K (2001); Inland Transportation System Planning by Life Cycle Impact Assessment: A Case Study, (second report: single comparison index). Journal of Marine Science and Technology, Springer-Verlag Tokyo.
3. Fet A M, Michelsen O, Karlsen H (2000); Environmental Performance of Transportation – A Comparative Study. ENSUS 2000, Newcastle upon Tyne.
4. Isensee, J., Bertram, V., Keil, H. (1997); Energy efficiency and air pollution of ships and other vehicles, Proceedings of FAST'97, Sydney.
5. Kristensen, H. O. (2001); Transport by ship a 'green' alternative. Cruse & Ferry Info.
6. USEAP (United States Environmental Protection Agency) (1998); Global Warming, The climate system. http://www.epa.gov/globalwarming/climate/intro.html
7. UNFCCC (1997); Kyoto Protocol, Third conference of the {Parties, Kyoto, Japan. http://cop3.unfccc.int/
8. UNFCCC (1997); Greenhouse Gas Inventory database. http://62.225.2.23/
9. Saaty T. L. (1980); The Analytic Hierarchy Process. McGraw-Hill International Book Company, USA.
10. Buxton I. L. (1987); Engineering Economics and Ship Design. British Maritime Technology Limited, UK.

Exploiting the Non-linear Response of Sandwich Panels in High Speed Craft Design

Brian Hayman[1], Harald Osnes[2], Asle Skiple[3] and Dag McGeorge[4]
[1,4]Det Norske Veritas AS, Høvik, Norway
[2]University of Oslo, Norway, and Det Norske Veritas AS, Høvik, Norway
[3]Norwegian University of Science and Technology, Trondheim, Norway
[1]Brian.Hayman@dnv.com, [2]osnes@math.uio.no, [4]Dag.McGeorge@dnv.com

Abstract

In sandwich construction, with fibre-reinforced plastic (FRP) skins separated by a lightweight core, the core must provide an effective structural connection between the skins, and it must carry the major part of the out-of-plane shear forces that occur under transverse loading of the panel. The paper focuses on two non-linear effects in the response of sandwich panels under lateral loading:

- *Geometric non-linearity as deflections increase and membrane effects are developed.*
- *Material non-linearity in the core, some core materials being much more ductile than others.*

Currently, the acceptance criteria in classification rules are generally based on linear assumptions, with allowable stresses related to the respective material strength. It has been suggested that geometric non-linearity may significantly increase the load-bearing capacity of a sandwich panel as compared to what is predicted by use of linear analysis, and that such benefits should be exploited in design. It has also been suggested that design codes and classification rules should give credit for high ductility in the core material.

The paper reviews relevant work carried out previously in this field. Results are presented from more recent research into the effects of both material and geometric non-linearity, and recommendations are made concerning the possible implementation of improved acceptance criteria.

1 Introduction

Sandwich construction, with fibre-reinforced plastic (FRP) skins separated by a lightweight core, has been used extensively in high speed and light craft and in certain types of naval vessels. The applications range from sailing yachts to passenger ferries, and high-performance marine vehicles such as patrol, rescue and fast attack craft. The sandwich core must provide an effective structural connection between the skins, and it must carry the major part of the out-of-plane shear forces that occur under transverse loading of the panel. Design criteria for such panels thus include requirements to the shear strength of the core as well as to the strength of the skins and the stiffness of the panel.

Four types of non-linearity are relevant when considering the ultimate strength and deflections of sandwich panels under lateral loading:

- Geometric non-linearity as deflections increase and membrane effects are developed.
- Material non-linearity in the core, some core materials being much more ductile than others.
- Material non-linearity in the skin laminates, as the material progressively degrades under increasing loading.
- Local buckling (wrinkling) of a sandwich skin experiencing in-plane compressive stress.

The paper focuses on the first two of these non-linear effects.

Currently, the acceptance criteria in classification rules are generally based on linear assumptions, with allowable stresses for cores and skin laminates that are a given fraction of the respective material strength. (For skin laminates the acceptance criterion may also be expressed in terms of a laminate failure criterion, such as Tsai-Wu, with a required failure strength ratio.) It has been suggested in earlier papers and reports that geometric non-linearity may significantly increase the load-bearing capacity of a sandwich panel as compared to what is predicted by use of linear analysis, and that such benefits should be exploited in design. It has also been suggested that design codes and classification rules should give credit for high ductility in the core material (indeed, some classification rules already do so, but a more rational basis for this has been sought).

The paper begins with a review and evaluation of some relevant work carried out previously in this field. Then results are presented from more recent research into the effects of both material and geometric non-linearity. Finally some recommendations are made concerning the possible implementation of improved acceptance criteria.

2 Review of previous work

2.1 Geometric non-linearity

2.1.1 Studies by Hildebrand and co-workers

Hildebrand and Visuri (1996) and Riihentaus and Hildebrand (1997) studied the capacity of a sandwich panel as predicted by linear and geometrically non-linear analysis. The panel had face laminates containing five plies of stitched 0°/90° E-glass reinforcement. Each ply weighed 600 g/m^2, with a fibre content 47% by volume, and had a thickness of 0.48 mm. The core was made of 50 mm thick end-grain balsa (100 kg/m^3). A key question was whether structural dimensions might be reduced when the optimisation process was based on non-linear methods.

Usually sandwich panel structures are designed by considering a single panel subjected to simply supported and/or clamped boundary conditions on the panel edges, neglecting the effects of possible in-plane restraint. The authors point out that such conditions do not reflect the behaviour of real panels which are generally connected to neighbouring structural elements. Furthermore, the predicted maximum deflection and stresses are highly dependent upon the applied boundary conditions. In order to avoid, or at least reduce, the influence of boundary conditions, the team investigated a stiffened panel structure in which the panel of particular interest was surrounded by eight other panels, with two stiffeners in each direction (similar to Fig. 2 in Section 3 of this paper). "Hinged" boundary conditions (fixed displacements in all directions, free rotations) were applied at the outermost edges of the stiffened panel. Using symmetry, only a quarter of the total stiffened panel was analysed. Several load cases were considered – lateral load on the central panel, lateral load on the entire stiffened panel, and a combination of in-plane compressive and lateral loads. In the present paper only the results obtained for lateral loading on the central panel are discussed.

The panel was analysed by both linear and non-linear finite element (FE) methods, and maximum allowable loads were calculated based on allowable stresses broadly in line with the DNV Rules for High Speed and Light Craft (DNV, 1991). Linear FE analysis showed a maximum allowable applied pressure of approximately 32 kPa. At this load level the maximum values of all stress components in the centre panel were close to their upper limits. However, the maximum deflection of the centre panel, or, more accurately, the difference between the maximum deflection (at its centre) and the minimum deflection (at its edges), was approximately 2.7% of the shorter in-plane dimension of the panel. This is considerably greater than the 1% allowed by the DNV Rules. Linear analysis of the centre panel in isolation showed relative deflections in the order of 1% and 3% in the clamped and simply supported cases, respectively. It should also be noted that the allowable pressure reported above is in close agreement with the value obtained using the formulae in the DNV Rules based on traditional, linear analytical methods.

When the problem above was analysed using geometrically non-linear FEM, with the same allowable stresses, a maximum allowable pressure of 37 kPa was found. This is approximately 16% higher than obtained by linear analysis. However, the shear stress in the core is now by far the most limiting factor: the in-plane stresses in the skin laminates are well below their allowable values.

Based on the discussion above, three preliminary conclusions/statements may be drawn:

1. The panel of investigation is optimised with respect to linear analysis methods.
2. The load carrying capacity of the panel may be increased using a thicker core layer (or a stronger core material).
3. The thickness of the panel skins, and thus the panel mass, may be reduced without considerable loss in the load carrying capacity.

A careful analysis was made of the last statement above. Five different panels were investigated – the original one and panels where the number of plies in each skin was reduced from five to four, three and two, and finally a panel with three plies in the outer layer and two in the inner layer. Reducing the number of plies in each skin from five to two only reduced the allowable load from 37 kPa to 34 kPa, which is higher than the allowable load predicted by linear analysis of the original panel. The corresponding reduction in panel mass was 38%. However, the maximum relative deflection increased from 2.7% to 4%. The core shear stress remained the limiting stress component, but the predicted values for the remaining stress components were also close to their allowable levels, indicating a more balanced design than the original based on linear analysis.

2.1.2 Optimisation studies by Rasmussen

Rasmussen (2001) investigated the effect of including geometrically non-linear effects when optimising an isolated sandwich panel with respect to its mass. Both clamped and simply supported boundary conditions were considered. The analysis was based on data applicable for the hull structure of a naval vessel. Allowable stress, allowable deflection and minimum skin thickness criteria were applied in accordance with the DNV Rules. For a design slamming pressure of about 250 kPa, appropriate to the vessel in question, Rasmussen established that the panel design was so thick that membrane effects were negligible. However, a lower design pressure of about 75 kN/m^2 gave an appreciably thinner panel for which membrane effects were more significant.

Rasmussen concluded nonetheless that the potential for weight reduction based on the use of non-linear analysis was very small for the cases considered. This seems to have been largely due to his retention of the minimum skin thickness requirement for hull bottom panels, together with the maximum allowable deflection (1% of smaller panel dimension) in the optimisation. Relaxation of the deflection limit to 2% gave a negligible benefit for the case of clamped edges and about 6% weight reduction for the simply supported case. These very limited weight reductions appear to be caused by the retention of the minimum skin thickness criterion in all cases. Possibly the potential for weight reduction would have been greater if the minimum skin thickness requirement had been removed, or relaxed to a level appropriate to decks or internal bulkheads.

2.1.3 Conclusions – geometric non-linearity

The differing conclusions from the studies described in Sections 2.1.1 and 2.1.2 appear to be due to Rasmussen's retention of the DNV minimum skin thickness requirement for hull bottom panels, combined with the maximum deflection requirement (although the latter was increased from 1% to 2%). These requirements ensure that the stress levels in the skins are far below their allowable values. Hildebrand and co-workers applied only stress criteria and were able to reduce considerably the thickness of the skins.

It may be concluded that, if existing restrictions on the skin thickness and relative deflection are retained, the gain by using non-linear methods is small. However, if both such requirements are relaxed, the possible mass reduction connected to non-linear analysis may be considerable.

2.2 Material non-linearity

Hayman et al. (2001) performed a study aimed at establishing to what extent sandwich panel behaviour depends on the type of material behaviour shown by the core, and whether the ratio of allowable stress to ultimate strength should depend on the degree of ductility or type of non-linear behaviour. Non-linear FE modelling was carried out to obtain a thorough understanding of the way ductility in the core influences panel behaviour. A series of cores having typical stress-strain relations varying from brittle to extremely ductile was considered (Fig. 1). The modelling covered the two extremes of aspect ratio (square and very long panels). In each case the panel was considered to be a part of a larger, stiffened panel arrangement in which the panel of interest was surrounded by a number of similar panels all subjected to the same, uniform pressure loading. This was modelled by using symmetry conditions at the panel boundaries. However, in most cases the edges were allowed to "pull in" in the in-plane direction, while remaining straight.

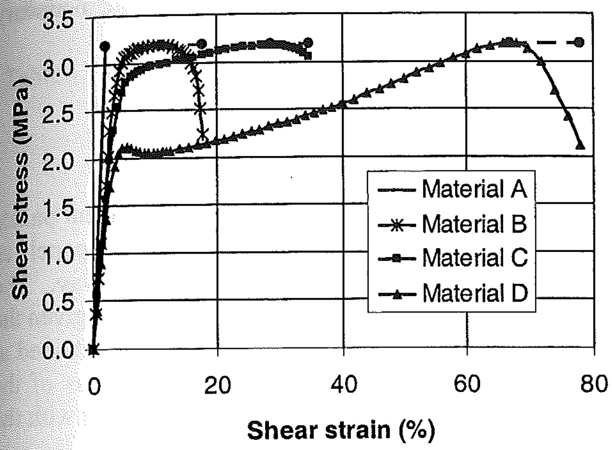

Material	Ult. shear strength τ_u (MPa)	Ult. shear strain γ_u (MPa)
A	3.18	2
B	3.18	12
C	3.18	30
D	3.18	67

Fig. 1 Assumed shear stress-strain curves for the core materials (Hayman *et al.*, 2001)

For square panels with the edges allowed to pull in, the predicted load-carrying capacity increased considerably with increased ductility (strain to failure) in the core. (This was considerably enhanced if the edges were fully fixed in the in-plane direction.) However, the benefit was very much less for the infinitely long panels. Furthermore, for the very ductile material D representing a linear PVC foam, the deflections became so large as the failure load was approached that the panel would be far outside its useful range of use. With this core material the panel deformations increase quite rapidly when the initial peak in the stress-strain curve is exceeded. The ultimate shear strength, as measured at the second peak in the stress-strain curve, has little relevance for the practical capacity of a panel.

The main conclusion was that there is some justification for giving credit for ductility in the sandwich core material when determining safety factors for sandwich panel design. However, the extent to which such credit may be given will depend not only on the core ductility but also on the boundary conditions and the panel aspect ratio. In addition it will be necessary to consider the possibility that skin laminate failure will become governing.

3 New studies on geometric non-linearity

3.1 Approach adopted

To be able to exploit geometric non-linearity it is necessary to satisfy the following conditions:

- The non-linear behaviour of the sandwich panel must be correctly described in the design calculations.
- The boundary conditions on the real panel must be sufficiently similar to those assumed in the design calculations to keep the modelling errors within acceptable limits. This means that the adjoining/supporting structure must have the requisite stiffness to enable the membrane effects assumed in the design to be developed in practice.
- The adjoining structure must also be dimensioned such that it has sufficient strength to withstand the loadings that result from the in-plane membrane forces developed in the panel.

It is widely recognised that a rectangular panel supported at its edges (whether simply supported or with rotations prevented at the edges) will not develop substantial membrane forces unless the edges are fully or partially prevented from "pulling in", i.e. from in-plane movement normal to the edges. In practice it is impossible to prevent the edges completely from pulling in – that would require an infinitely stiff adjacent structure. Thus it is impossible to exploit fully the potential increase of load-bearing capacity that full in-plane fixity would give over the case when the edges are allowed to pull in freely. A question that presents itself is what proportion of the theoretical maximum increase in load-bearing capacity can be achieved readily by conventional structural arrangements.

To answer this question a 3 m x 2 m rectangular sandwich panel has first been analysed under lateral pressure loading with all four edges simply supported and with the following in-plane boundary conditions at all four edges:

- edges allowed to pull in freely
- edges allowed to pull in but while maintained straight
- edges fully prevented from pulling in.

Then, the same panel was considered as part of a larger panel arrangement by adding adjacent panels as shown in Fig. 2. The simple supports were continued out to the edges of the adjoining panels as shown. The outer edges of the adjacent panels were not supported or restrained in any way. The pressure loading was applied only to the 3 m x 2 m area in the middle. The dimension c was given the values 375, 750, 1500 and 3000 mm, and the aspect ratio of the entire panel structure maintained at 3:2. Thus the in-plane stiffening at the edges was provided only by the in-plane stiffness of the adjoining panels. The analysis of the panel field with c equal to 3000 mm was then repeated with the outer edges simply supported in addition to the previously imposed conditions.

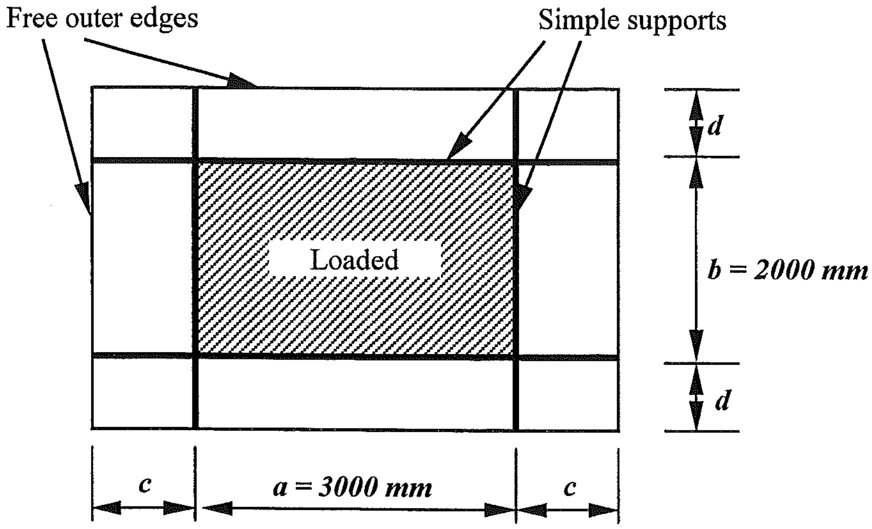

Fig. 2 Sandwich panel geometry and supports for studies of geometric non-linearity.

A problem that arises in analysis of sandwich panels is that of hard and soft boundary conditions (Zenkert, 1995). Soft boundary conditions imply that the two skin laminates can move relatively to each other in the direction parallel to the edge. With hard boundary conditions such relative displacements are prevented; for analysis with a single layer of shell elements this requires fixing of the rotational degree of freedom about an axis in the plane of the panel but normal to the edge. The use of hard and soft boundary conditions is investigated for the test cases without adjacent panels.

In order to make comparisons with a relevant analysis meaningful, the basic sandwich lay-up was the same as assumed by Hildebrand and co-workers (see Section 2.1.1). In the first set of analyses the outer and inner laminates each had five 0.48 mm layers. In order to investigate the consequences of reducing the panel mass, a series of analyses was then performed with three layers in each face.

The analyses were performed using the FEM software ABAQUS with layered, four-noded shell elements of type S4R, which is applicable for layered, orthotropic materials. The number of layers in each element was three – one for each of the skins and one for the core. Three integration points were applied through the thickness of each layer. Using symmetry, only a quarter of the total panel was modelled. Thorough numerical testing suggested that a discretisation of the quarter of the mid-panel in 48×32 elements offers reasonable accuracy of local stresses, strains and deflections. This gives 31.25 mm square elements. The same element size was applied for the adjacent panels. In each case a constant pressure load was applied to the mid-panel, and the stresses in each layer of the mid-panel as well as the deflection were investigated. The stress values were compared with the allowable stresses from Riihentaus and Hildebrand (1997). Both the ultimate strength and the allowable stress values are reported in Table 1.

Table 1 Assumed ultimate strength and allowable stress values (MPa) for face laminates and core.

Face laminate		
Stress component	Ultimate strength	Allowable stress
$\sigma_{x,\,ten}$	427	139
$\sigma_{x,\,comp}$	269	88
$\sigma_{y,\,ten}$	464	151
$\sigma_{y,\,comp}$	285	93
Core		
Stress components	Ultimate strength	Allowable stress
τ_{xz} and τ_{yz}	1.85	0.47

For each set of boundary conditions and size of adjacent panels, both linear and geometrically non-linear simulations were run for the lay-up with thick (five ply) face laminates. The geometrically non-linear analyses were repeated for the lay-up with thin (three ply) skins. In the non-linear simulations the applied load was increased in a step-wise manner from 0 to 60 kPa. For the stress components that reached their allowable values for a pressure load within this interval, the corresponding capacity was obtained by interpolation. However, for those components allowing external load above 60 kPa, the load limits were approximated by extrapolation, resulting in a somewhat decreased accuracy. Fig. 3 shows the FE mesh and out-of-plane shear stress contours for a typical case. In Tables 2-4, the capacities obtained by linear and non-linear analyses are presented.

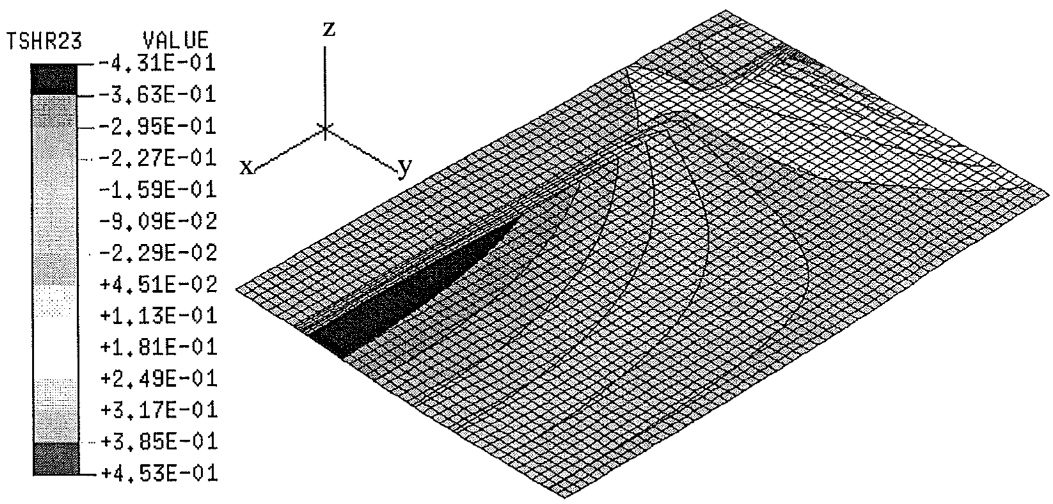

Fig. 3 Finite element mesh for geometrically non-linear analysis of sandwich panel, with contours of out-of-plane shear stress τ_{yz}.

Table 2 Applied pressures at which respective allowable stresses and deflection are reached, and deflection at lowest of these applied pressures: sandwich panel with thick skins (5 layers), by linear analysis.

Dimensions of adjacent panels (mm)		Bound. conds.	Loads at which respective allowable values are reached, for various stress components and panel deflection (kPa). Sandwich panel with $a = 3000$ mm, $b = 2000$ mm							Deflection at lowest load
c	d		$\sigma_{x,\,ten}$	$\sigma_{x,\,comp}$	$\sigma_{y,\,ten}$	$\sigma_{y,\,comp}$	τ_{xz}	τ_{yz}	w (1%)	w/b
0	0	S, 1	79.4	50.3	47.3	29.2	30	**25.6**	8.8	0.03
0	0	S, 2	79.4	50.3	47.3	29.2	30	**25.6**	8.8	0.03
0	0	S, 3	79.4	50.3	47.3	29.2	30	**25.6**	8.8	0.03
0	0	H, 1	84.4	53.4	50.7	31.2	36.1	**28.5**	9.4	0.03
0	0	H, 2	84.4	53.4	50.7	31.2	36.1	**28.5**	9.4	0.03
0	0	H, 3	84.4	53.4	50.7	31.2	36.1	**28.5**	9.4	0.03
375	250	4	90.3	57.1	55.6	34.3	32	**28.6**	10.4	0.028
750	500	4	100.1	63.4	62.9	38.7	30.2	**29**	11.8	0.025
1500	1000	4	114.3	72.4	72.1	44.4	31.1	**27.8**	13.8	0.02
3000	2000	4	118.4	75	77.8	47.9	32.3	**27**	15	0.018
3000	2000	5	118.4	75	79.4	48.9	32.5	**26.8**	15.3	0.018

Key to boundary conditions (Tables 2-4):
H = hard, S = soft.
1 = prevented from pulling in, 2 = allowed to pull in but as straight line, 3 = free to pull in;
4 = outer edges completely free, 5 = outer edges simply supported.

Table 3 Applied pressures at which respective allowable stresses and deflection are reached, and deflection at lowest of these applied pressures: sandwich panel with thick skins (5 layers), by non-linear analysis.

Dimensions of adjacent panels (mm)		Bound. conds.	Loads at which respective allowable values are reached, for various stress components and panel deflection (kPa). Sandwich panel with $a = 3000$ mm, $b = 2000$ mm							Deflection at lowest load
c	d		$\sigma_{x,\,ten}$	$\sigma_{x,\,comp}$	$\sigma_{y,\,ten}$	$\sigma_{y,\,comp}$	τ_{xz}	τ_{yz}	w (1%)	w/b
0	0	S, 1	103.7	inf.	63.5	inf.	46.6	**46.2**	9.9	0.028
0	0	S, 2	83.7	95.2	56.3	59.8	34	**32.7**	9.2	0.029
0	0	S, 3	72	59	54.6	35.3	31	**26.7**	8.8	0.028
0	0	H, 1	107.2	inf.	65.2	inf.	52.7	**49.3**	10.4	0.028
0	0	H, 2	89.7	106.5	58.6	64	39.2	**35.8**	9.8	0.03
0	0	H, 3	74.4	68.5	57.2	37.8	36.1	**29.5**	9.3	0.029
375	250	4	83.2	133.5	64.6	47.3	33.1	**30.7**	10.5	0.027
750	500	4	95.3	154.3	71.1	60.5	**31**	31.2	12.1	0.024
1500	1000	4	109.7	120.7	78.4	78	31.7	**29.4**	14	0.02
3000	2000	4	118.1	143.8	84.2	96.5	33	**28.2**	15.3	0.018
3000	2000	5	118.1	132.6	84.4	98	33.3	**28**	15.6	0.017

Table 4 Applied pressures at which respective allowable stresses and deflection are reached, and deflection at lowest of these applied pressures: sandwich panel with thin skins (3 layers), by non-linear analysis (but values with asterisks, *, were obtained by linear analysis). Values in brackets define the capacity when artificial stress peaks near the outer corner are neglected.

Dimensions of adjacent panels (mm)		**Bound. conds.**	**Loads at which respective allowable values are reached, for various stress components and panel deflection (kPa). Sandwich panel with $a = 3000$ mm, $b = 2000$ mm**							**Deflection at lowest load**
c	d		$\sigma_{x,\,ten}$	$\sigma_{x,\,comp}$	$\sigma_{y,\,ten}$	$\sigma_{y,\,comp}$	τ_{xz}	τ_{yz}	w (1%)	w/b
0	0	S, 1	64.6	inf.	37.4	inf.	**33.2** (52.3)	34.4 (57.8)	6.2	0.03
0	0	S, 2	51.4	58.2	33.1	35	**22.4** (34.5)	23.1 (37.0)	5.8	0.031
0	0	S, 3	43.9	38.5	32.4	21.5	**19.6** (30.3)	20.4 (27.6)		0.032
0	0	H, 1	67.2	inf.	**38.1**	inf.	59.4	62.1	6.5	0.031
0	0	H, 2	54.1	62.7	**34.1**	36.7	40.2	40.9	6.1	0.039
0	0	H, 3	45.3	43.0	34.1	**22.2**	35.4	30.1		0.034
375	250	4	51.8	78.0	38.6	**28.2**	32.9	32.6	7.0	0.036
			55.4*	35.1*	34.2*	**21.1***	31.3*	28.4*	6.9*	0.031*
750	500	4	59.5	74.9	42.6	35	**30.1**	32.6	8.1	0.033
1500	1000	4	66.3	65.5	47.1	43.4	30.6	**29.9**	9.5	0.028
3000	2000	4	69.8	71.7	50.0	53.4	31.9	**28.4**	10.5	0.025
3000	2000	5	69.1	69.6	51.1	54.5	32.1	**27.9**	10.8	0.024

All values in these tables, except those in the last two columns, define the applied loads (in kPa) at which the stress components of consideration reach their allowable limits. The boldface numbers show the lowest pressure values for which allowable stress levels are reached. For example, for the linear analysis (see Table 2) with the smallest adjacent panels (c = 375 mm, d = 250 mm) it is seen that the capacity is 28.6 kPa, which in this case is connected to the core shear stress τ_{yz}. The last column shows the maximum deflection at this load level, divided by the smaller mid-panel dimension b. The last but one column shows the applied loads that cause 1% relative deflection ($w/b = 0.01$).

From the tables it is seen that τ_{yz} (in the core) is the governing stress component in most cases. However, there are several important exceptions. For example, τ_{xz} is the most critical component for the non-linear analyses when the adjacent panels have c = 750 mm and d = 500 mm, as well as for the panels with the thin face laminates (and no adjacent panel) when the soft boundary conditions are applied. Also, for the panels with the thinner skins, the laminate stresses $\sigma_{y,\,ten}$ and $\sigma_{y,\,comp}$ are the governing stresses in certain cases. This is a consequence of the fact that reducing the thickness of the skins increases the face stresses. It should also be remarked that when adjacent panels are included and geometrically non-linear effects are taken into account the allowable pressure loads are almost the same for the panels with skins containing 5 and 3 layers. A corresponding linear comparison predicts a decrease in panel capacity of the order of 25% when the number of plies in the faces is reduced from 5 to 3. Thus, based on non-linear analysis it is possible to reduce the thickness of the skins by 40% (in this example), leading to a decrease in total panel mass of 26%, without substantial loss in capacity. However, this requires relative deflections (w/b) of the order of 3.5% to be allowed.

3.2 Conclusions from studies of geometric non-linearity

The following conclusions may be drawn from the analyses performed on geometric non-linearity:

1. As should be expected, the extent to which the edges are allowed to pull in) makes no difference to the results predicted by linear analysis. However, the change between hard and soft boundary conditions does make a difference to the linear results.

2. A change from soft to hard boundary conditions has little effect on the skin laminate stresses (whether predicted by linear or non-linear analysis). The main effect is on the core shear stresses.

3. For the panel with thin skin laminates and no adjoining panels, high values of core shear stresses are found locally near the panel corners when soft boundary conditions are assumed. Such boundary conditions are considered unrealistic in practical terms since the skin laminates are normally connected either by a laminate wrapped around the panel edge or by other adjoining structure. Changing to hard boundary conditions removes these local core shear stress peaks and the results become similar to those for the corresponding cases with thick skin laminates, with the skin laminate stresses governing.

4. For cases where out-of-plane core shear stresses are governing,
   - if the edges are fully prevented from pulling in, a non-linear analysis indicates a significantly larger load-bearing capacity than a linear analysis;
   - if the edges are allowed to pull in, but constrained to remain straight, a non-linear analysis indicates a somewhat larger load-carrying capacity than a linear analysis, but the difference is not as great as when the edges are fully prevented from pulling in;
   - if the edges are allowed to pull in freely, a non-linear analysis shows only a slightly larger load-carrying capacity than a linear analysis;
   - connection to adjacent panels gives values of load-bearing capacity similar to those for an isolated panel with hard boundary conditions.

5. If core shear is not governing, and the panel edges are either fully prevented from pulling in or kept in a straight line, the stress component $\sigma_{y,tens}$ is the one that governs.

6. If core shear is not governing, and the panel edges are either unrestrained in the in-plane direction or restrained only by adjoining panels,
   - the stress component $\sigma_{y,comp}$ is generally the one that governs;
   - the stress component $\sigma_{y,tens}$, governs, however, for the case with the largest adjoining panels;
   - increasing the size of the adjoining panels increases the load-bearing capacity in relation to both the $\sigma_{y,tens}$ and the $\sigma_{y,comp}$ criteria, but that for $\sigma_{y,comp}$ increases more rapidly than that for $\sigma_{y,tens}$;
   - a non-linear analysis indicates a larger load-carrying capacity than a linear analysis, the increase being larger as the size of the adjoining panels is increased.

7. As long as the panel is connected to adjoining panels (whatever their size, within the range considered), the panel with thin skin laminates (3 layers) has roughly the same predicted load-bearing capacity as that with thick skins (5 layers) when only stress criteria are considered. However, the panel deflections are greater for the panel with thin skins.

8. To be able to utilise the material strength fully in the load range where geometric non-linearity is advantageous, it is necessary to accept panel deflections up to about 3% of the smaller panel dimension b for the panel with thick skins, and about 4% for the panel with thin skins. It may also be necessary to relax any minimum thickness requirements that apply at the location concerned.

3.3 Overall conclusions from studies of geometrically non-linear response

The boundary conditions assumed by Hildebrand and Visuri (1996) and Riihentaus and Hildebrand (1997) are somewhat unrealistic and unconservative in that they include full restraint of the outer edge of the stiffened panel structure in the in-plane direction. The new analyses relax this restraint and are conservative in that they include only the in-plane restraint due to the presence of the adjacent panels themselves. The new analyses also have the advantage that the boundary conditions are rather simple and well described.

Even with this more conservative approach, the new analyses show considerable benefits from the use of non-linear analysis, provided the deflections are allowed to be as high as 3% - 4% of the smaller panel dimension, and provided minimum thickness requirements do not govern.

4 New studies on core ductility

4.1 Extent and purpose of studies

The analyses reported by Hayman *et al.* (2001) have been extended by Skiple (2002) as follows:

- An improved, more rigorous procedure has been used for obtaining the direct stress-strain curve for the core material from the results of the block shear test.
- To provide a simpler way of characterising the non-linear core material, analyses have been carried out with bi-linear approximations to the material stress-strain relations.
- To provide a conservative treatment of possible in-plane restraints provided by adjoining panels (or their absence), additional boundary conditions in which the edges are allowed to pull in freely (without remaining straight) have been included for the square panel.
- Intermediate aspect ratios, between a square plate and an infinitely long one, have been considered.

For the infinitely long panel a beam model has been used as in Hayman *et al.* (2001). For all other cases one-quarter of the panel has been analysed, implying a different mesh from that used previously for the square panel (for which one-eighth of the panel was modelled). The core is modelled with solid elements as previously.

The aim of the studies with bi-linear stress-strain curves and intermediate aspect ratios has been to provide a quantitative description of the potential benefits of ductility.

4.2 Effect of improved procedure for obtaining direct stress-strain curves

The details of the improved procedure for obtaining the direct stress-strain curve from the nominal shear stress-strain curve obtained in a block shear test will not be discussed here. Briefly, the new procedure is more consistent than the old one in that the shear test data are converted from nominal stresses and strains to true values before converting to direct stress and strain values. The original and improved stress-strain curves are shown in Fig. 4. The difference between the initial parts of the curves for material D is largely due to a difference in the way the stress-strain curve has been scaled to give an ultimate strength similar to that for material C.

Table 5 Predicted applied pressure loads at failure (i.e. when maximum shear strain reaches ultimate value) for square and infinitely long panels with materials A, B, C and D as predicted using various material stress-strain curves. The long panels have been simulated with a beam model.

Core material	Panel case	In-plane boundary conditions	Load at γ_u (bar)			Load at τ_u (bar) from linear design calc.
			Previous analysis	Improved material curve	Bi-linear material curve	
A	Long	Straight	2.52	-		2.81
	Square		3.26	-	-	4.23
B	Long	Straight	3.22	3.51	3.48	2.81
	Square		5.62	5.82	5.76	4.23
C	Long	Straight	3.24	3.45	3.41	2.81
	Square		7.18	7.20	7.14	4.23
	Long	Fixed	5.34	-	-	2.81
	Square		8.56			4.23
D	Long	Straight	3.53	3.45	3.50	2.81
	Square		15.55	14.06	13.14	4.23

The results of introducing the new procedure are shown in Table 5 and (for materials B and C) Fig. 5. The effect on the predicted applied pressure at failure is generally a few percent. The largest effect (9%) is for the long panel of material B. These changes are not sufficient to alter the conclusions drawn by Hayman *et al.* (2001), as outlined in Section 2.2 above.

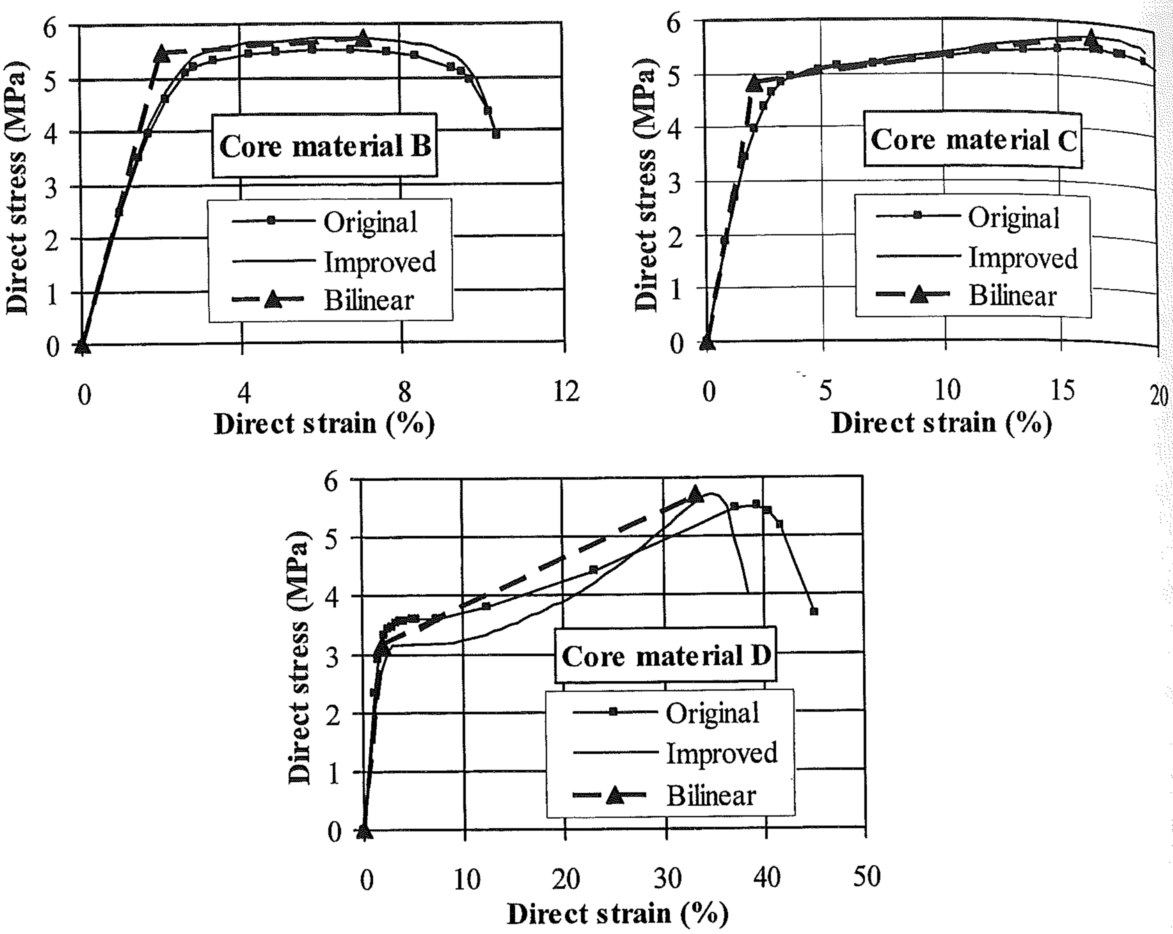

Fig. 4 Direct stress-strain curves from Hayman *et al.* (2001) and as derived by improved method, for materials B, C and D. Also shown are bi-linear approximations used in Section 4.3.

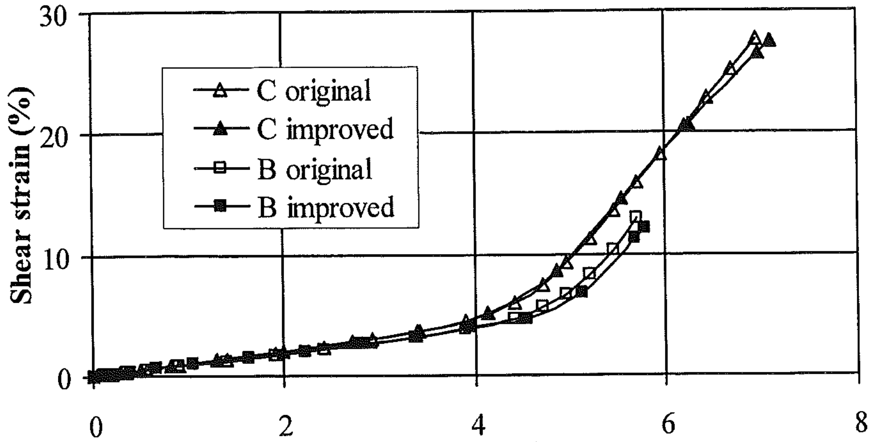

Fig. 5 Maximum transverse shear strain plotted against applied pressure for square panels with materials B and C using original (Hayman *et al.*, 2001) and improved stress-strain curves.

4.3 Effect of adopting simplified bi-linear stress-strain curves

The extent to which the capacity of a sandwich panel is enhanced by core ductility, and the extent to which this enhancement can be utilised in practice, is a function of the shape of the stress-strain curve as well as the ultimate strength of the material. In order to describe real stress-strain curves in terms of a small number of parameters, analyses have been performed using bi-linear approximations to the real curves. Such curves can be described in terms of the following parameters:

- Elastic modulus E
- Stress σ_p or strain ε_p at proportional limit
- Ultimate strength σ_u
- Ultimate strain ε_u

Note that it is possible to apply the bi-linear approximation either in terms of the shear stress-strain curve as obtained in a block shear test or in terms of the derived direct stress-strain curve. Here the latter procedure has been adopted.

In conventional, linear-elastic design the only material parameter used is either σ_p or σ_u (unless buckling is a criterion, in which case E may also be required). If it is assumed that the panel capacity is not strongly dependent on E, then for strength assessment that utilises bi-linear material curves one will need in addition measures of only

- the ductility (such as ε_u - ε_p) and
- the difference between σ_p and σ_u (such as $(\sigma_u - \sigma_p)/\sigma_u$).

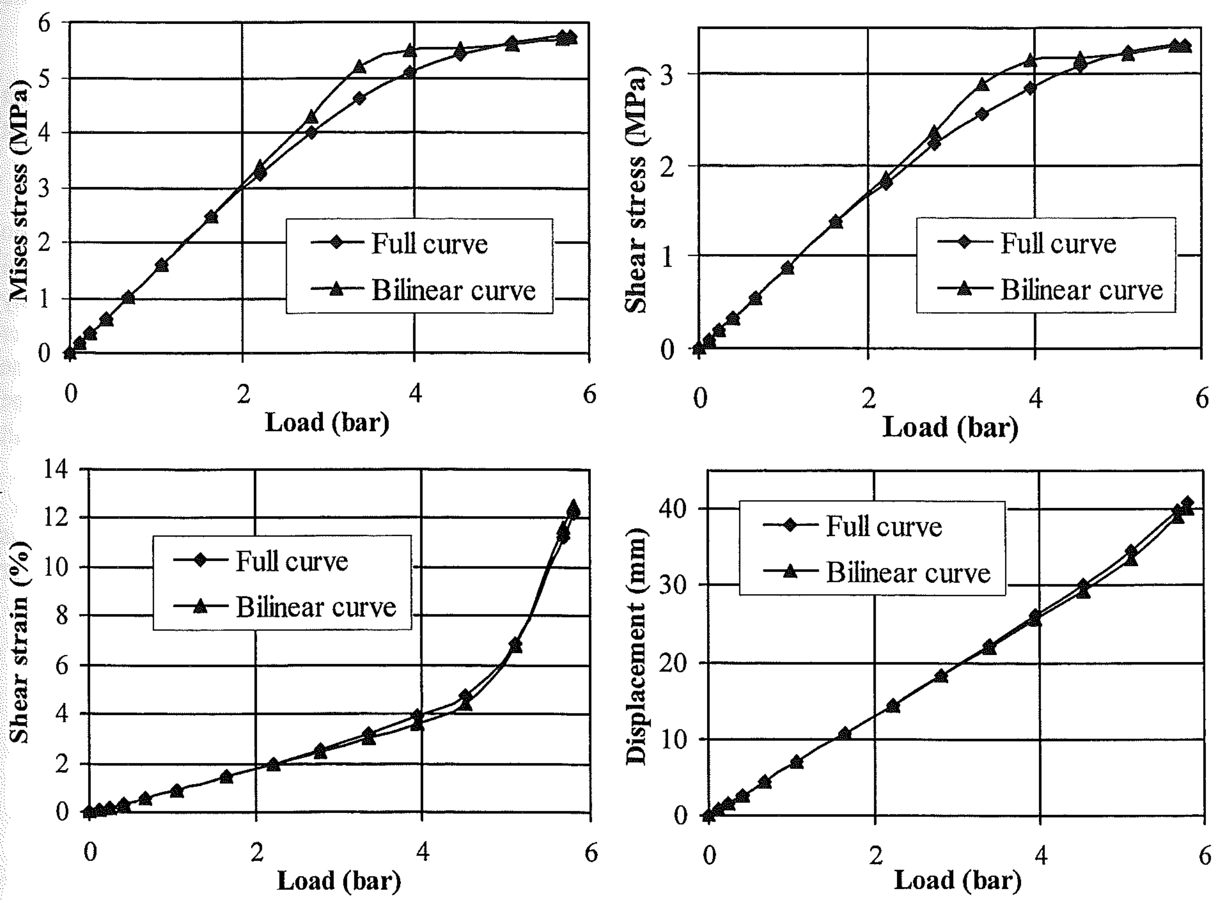

Fig. 6 Response curves for square panels with core material B for full stress-strain curves and bi-linear approximations.

To test the use of bi-linear approximations, bi-linear curves have been generated that approximate to the direct stress-strain curves for materials B, C and D. These are shown in Fig. 4. Fig. 6 (for material B only) and Table 5 show the results of these analyses compared with those based on the full material curves.

The response curves for material B show some deviations in the stresses in the region of the "knee" of the stress-strain curve, but the bi-linear approximation gives responses very close to the true curves for strains and displacements. Similar results are found for material C, the differences being even smaller (since the full stress-strain curve is close to bi-linear). For material D there are more noticeable differences in the plastic response, as might be expected from the larger difference between the bi-linear and full stress-strain curve, but again they are not large. The results in Table 5 show changes in predicted failure load within about 1% for B and C, somewhat more for D.

The bi-linear approximation to the full material stress-strain curves appears to give a sufficiently accurate description of the panel behaviour for use in future parametric studies to establish the influence of the core material ductility on the load-bearing capacity of sandwich panels.

4.4 Intermediate aspect ratios

Hayman *et al.* (2001) concluded that the ductility of the core material gave a significant increase in load-bearing capacity for square panels but little, if any, for very long panels unless the edges were fully restrained from pulling in. For long panels the load increased only very slightly as the plastic strains increased. For square panels the plastic zone starts off small but grows as the load is increased. Also some membrane effects are generated for square panels even without full in-plane restraint at the edges.

New analyses have been performed by Skiple (2002) for various intermediate values of the aspect ratio a/b, where a is the longer panel dimension and b the shorter dimension. The edges are kept straight but allowed to pull in. The results are shown in Table 6 and Fig. 7.

For design based on conventional linear analysis the strength is scarcely dependent on the aspect ratio for panels with aspect ratios above about 2; the strength of a panel with aspect ratio 2 is only 7% greater than one with infinite aspect ratio. However, the dependence on aspect ratio is appreciably greater when non-linear analysis is performed. While the benefits of core ductility are small or negligible for infinitely long panels, they are significant for aspect ratios up to 3 or 4, at least for the more ductile core materials considered, C and D. Thus the case of the infinitely long panel can be misleadingly pessimistic. (Note that for material D the deflections become large, so a deflection limit criterion must be applied, as noted previously.)

Table 6 Applied pressure load (bar) on a sandwich panel when the ultimate shear strain in the core is reached, for various aspect ratios. Also shown is the load at which the ultimate shear strength is reached based on the linear calculation procedure in the DNV Rules.

Panel aspect ratio *a/b*	Load at γ_u (bar) for panel with core material:			Load at τ_u (bar) from linear design calc.
	B	C	D	
1	5.82	7.20	14.06	4.23
1.2	4.83	6.14		3.83
1.5	4.12	5.27	10.97	3.34
2	3.73	4.67	9.52	3.03
3	3.65	4.33		2.93
4	3.64	4.16	6.74	2.83
Infinite	3.51	3.45	3.45	2.81

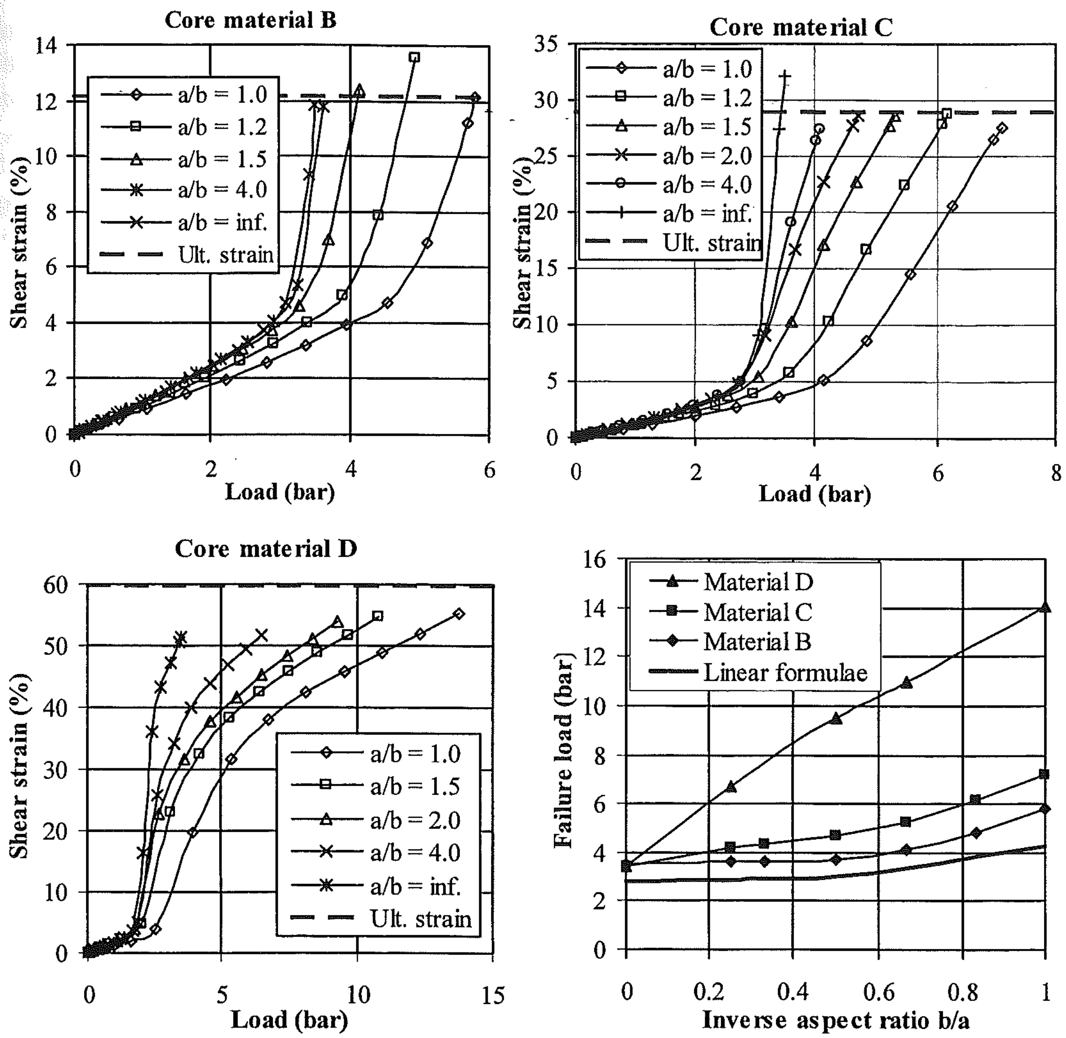

Fig. 7 Maximum transverse shear strain plotted against applied pressure load for panels with different core materials and aspect ratios *a/b*, and panel ultimate failure loads plotted as a function of inverse aspect ratio *b/a*.

4.5 Skin laminate stresses

Additional stresses are induced in the skin laminates as the sandwich core yields and the deformations increase. These stresses are essentially of two types:

- In-plane membrane stresses due to stretching of the panel and its skin laminates as the panel deflection increases. This is very similar to what happens with linear-elastic core materials (see Section 3), and leads to a reduction in the primary bending stresses.
- Local, secondary bending stresses induced close to the panel edges as the skins follow the local shear deformation in the core. Associated with these bending stresses are out-of-plane shear stresses, which supplement the out-of-plane shear stresses in the core.

The main increases in laminate stresses occur close to the panel edges, where in practice the skins are usually thickened by tapered secondary laminations. Thus safe utilisation of the core ductility may also be dependent on the provision of adequate laminations of this type.

4.6 Conclusions from studies on core material non-linearity

An improved conversion of block shear test data to obtain the direct stress-strain curves for use in FE analysis has been implemented and shown to give some small differences in predicted responses.

The use of bi-linear curves in place of the full material stress-strain curves would allow a quantitative description of the benefits of core ductility. The studies have shown that substitution of bi-linear curves gives only minor errors in the panel responses for materials B and C. The errors for material D are more substantial (because the full curve cannot be properly represented by a bi-linear curve), but the overall picture of the responses is still broadly correct. A more quantitative description of the effects of core material ductility can thus be obtained by performing a larger series of analyses with a range of bi-linear curve parameters. These should consider necessary limitations on deflections and laminate stresses, taking account of tapered secondary laminations at the panel edges.

The studies on intermediate aspect ratios have shown that significant benefits from core ductility are possible for aspect ratios up to about 2. For the more ductile materials (ultimate shear strain greater than about 20%) this applies even for aspect ratios of 3 or 4.

5 Further discussion and recommendations

The new studies on geometrically non-linear response of sandwich panels have confirmed that substantial savings of weight are possible if the non-linear membrane effects are taken into account in the design analysis. However, this requires relaxation of the deflection limit to 3-4% of the smaller panel dimension, and may also require relaxation of minimum thickness requirements. Because of uncertainty about the ability of the adjoining structure to provide sufficient in-plane stiffness (and strength) to develop membrane effects fully, it is recommended that only the influence of adjoining panels in the same plane as the panel in question be taken into account. At present this requires non-linear analysis on a case-by-case basis, but the potential savings of weight are significant.

The studies on non-linear core material have confirmed that the ductility of the core material may influence considerably the ultimate capacity of a sandwich panel, but that the benefit of such ductility is strongly dependent on the panel aspect ratio as well as the extent of the material ductility. It is recommended that further analyses be carried out with bi-linear material stress-strain curves to establish a parametric dependence.

Acknowledgements

The work was carried out as part of the Nordsandwich project, which is a Nordic research collaboration on sandwich technology, co-ordinated by VTT Manufacturing Technology. Financial support was provided by the Nordic Industrial Fund and the Research Council of Norway.

References

DET NORSKE VERITAS (1991). Rules for Classification of High Speed and Light Craft, Part 3 Structures, Equipment, Chapter 4 Hull Structure Design, Fibre Composite and Sandwich Construction. Det Norske Veritas, Høvik, Norway.

HAYMAN, B., HOFFMANN, P., MCGEORGE, D. and NOURY, P. (2001). Non-Linear Core Behaviour in Sandwich Panels for High Speed Craft. Proc. 5th International Conference on Fast Sea Transportation (FAST 2001), Southampton, UK, September.

HILDEBRAND M. and VISURI M. (1996). The Non-Linear Behaviour of Stiffened FRP-Sandwich Structures for Marine Applications. Technical Report VTT VALB 155, VTT Manufacturing Technology, Espoo, Finland..

RASMUSSEN J. F. (2001). Membrane Effects for Flat Composite Sandwich Panels (in Danish). Student Project Report, Technical University of Denmark (DTU), Lyngby, Denmark.

RIIHENTAUS J. and HILDEBRAND M. (1997). Utilising Non-Linearities in Stiffened Sandwich Panels. Technical Report VALB 180, VTT Manufacturing Technology, Espoo, Finland.

SKIPLE, A. (2002). Accounting for the Effect of Core Material Ductility on the ultimate capacity of sandwich panels. M.Sc. Thesis, Norwegian University of Science and Technology, Trondheim, Norway.

ZENKERT, D. (1995). An Introduction to Sandwich Construction. Engineering Materials Advisory Services Ltd., United Kingdom.

Evacuation Analysis as a Design Tool

Åsmund Hellesøy
Flensburger Schiffbau Gesellschaft mbH, Flensburg/Germany, hellesoy@fsg-ship.de

Abstract

High-Performance Marine Vehicles require high safety performance. The abandonment of fast ships has unfortunately been necessary several times over the last decade, and efficient evacuation of a vessel is crucial to eliminate or reduce the number of casualties. IMO requires an evacuation analysis to be performed for vessels carrying passengers. There is currently one evacuation analysis guideline for High Speed Passenger Craft and a different set of guidelines for other passenger vessels. We have been observing that the evacuation analysis often have been scheduled very late in the design process and therefore the possibility for implementing needed changes are significantly hindered. New guidelines from IMO opens for the use of advanced evacuation analysis, and thereby the door is opened for increasing the use of evacuation analysis in the early part of the design phase.

This paper presents experience obtained at Flensburger Schiffbau Gesellschaft regarding integrating evacuation analysis in the early part of the design process. One of the important reasons for conducting evacuation analysis is to identify congestion points and to take action to solve possible problems as appropriate. Based on the discussion in this paper it is concluded that evacuation analysis using the advanced method aided by one of the commercially available software packages is the best way to impact the layout of a vessel and thereby obtaining improved evacuation scenarios.

Much of IMO's effort on this subject has been focused on the assembling of persons onboard, that is to say the reaction time and travel time needed for all persons to reach their assembly stations. The embarkation and launching phase on the other hand has received less attention. Work done at FSG in close cooperation with liferaft developers and manufacturers includes simulation of the entire assembly and embarkation process of a High Speed Craft carrying 2000 passengers. The method and results are presented in this paper.

1. Nomenclature and Definitions

CAD	Computer Aided Design
Circ.	Circular
FSG	Flensburger Schiffbau Gesellschaft mbH & Co. KG
GA	General Arrangement Plan
HPMV	High-Performance Marine Vehicles
HSC	High Speed Passenger Craft
HSC Code	International Code of Safety for High-Speed Craft
IMO	International Maritime Organization
MES	Marine Evacuation System(s)
min	Minutes
MSC	Maritime Safety Committee
MVZ	Main Vertical Zone
PS	Port Side
SB	Starboard Side
sec	Seconds
SFP	Structural Fire Protection Time
Std. Dev.	Standard Deviation
TraffGo	TraffGo GmbH
GL	Germanischer Lloyd

Simplified Evacuation Analysis: As described in IMO Circ. 1033 Annex 1. This method has historically been referred to as the simplified, macroscopic, hydraulic or hydrodynamic method.
Advanced Evacuation Analysis: As described in IMO Circ. 1033 Annex 2. This method has historically been referred to as advanced, microscopic or computer based method.

2. International attention to evacuation analysis

Several tragic disasters at sea have put international attention to the matter of evacuation analysis. The HSC Code was the first IMO publication to request an evacuation analysis to be performed. Later a regulation considering ro-ro passenger ships came into force, and all such vessels built after July 1st 1999 are required to undertake evacuation analysis at the early stage of design. The MSC, at its 75th session in May 2002 adopted MSC/Circ.1033 which for the first time opens for computer based advanced evacuation simulation. MSC/Circ.1033 lets the designer choose from either simplified or advanced evacuation analysis. Evacuation tools complying with the new IMO guidelines are currently available from several different companies.

3. Short theoretical description of an evacuation tool

FSG is using the evacuation simulation software AENEAS derived from the cooperation between TraffGo and GL. The background theory and approach of the various available software programs differs. In the following a short description of the AENEAS software is provided.

3.1. AENEAS

The vessel's GA is imported from the users CAD system to the AENEAS Editor. Walls, doors, stairways, escape routes, and locations of passengers are automatically identified by the editor, and manual adjustments to the imported layout can be made if necessary.

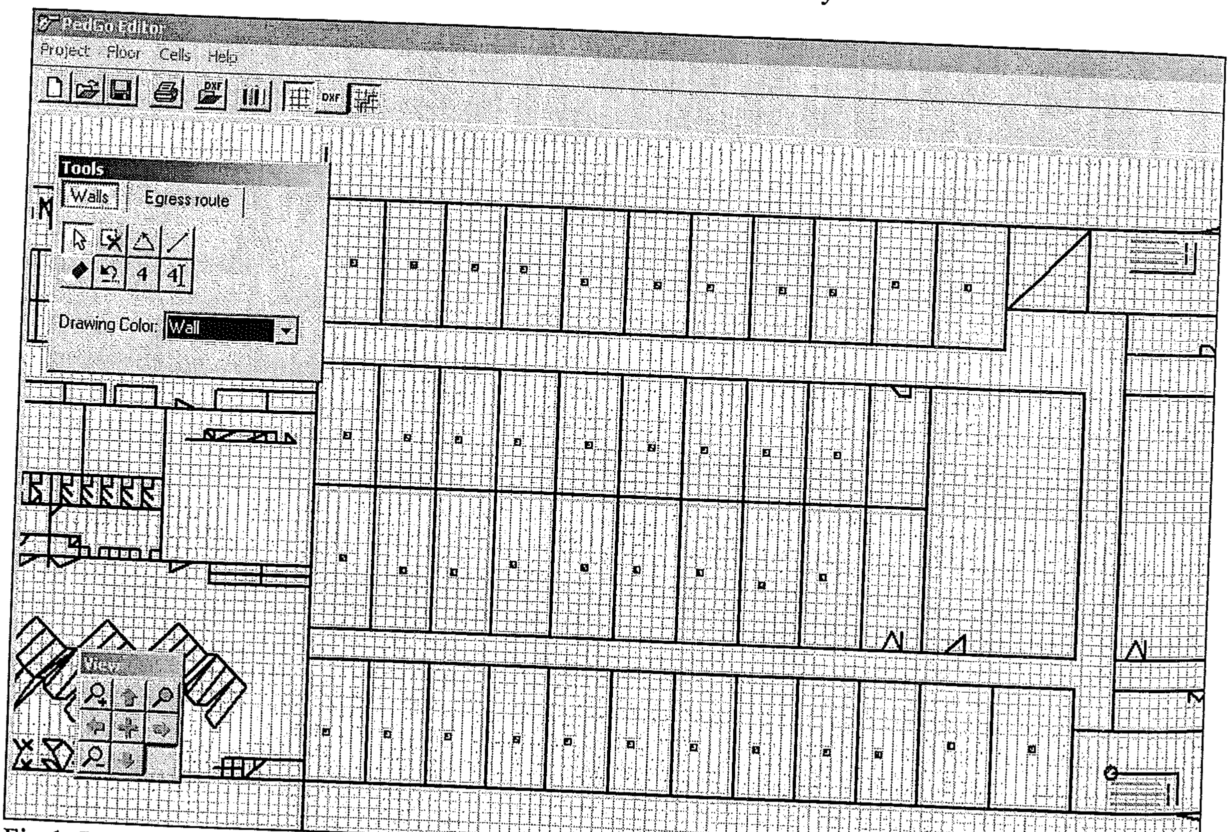

Fig.1: Part of the GA for a Ro-Pax vessel being edited in the AENEAS Editor, © TraffGo

The approach used in AENEAS is the so called microscopic or advanced simulation model. The decisions and movement of every single person is simulated. A multi-agent-model in discrete time and space is used. Therefore the floor-plan of the investigated ship is divided into square cells of a size of 0,4 by 0,4 meters as represented by the grid on Fig.1. Each square represents approximately the space occupied by one person when standing in a queue. The direction in which a person has to move in order to reach her goal is contained in the cells. A person moves along the escape-route by the given cell-information and then jumps from one cell to the next one, avoiding obstacles and other persons.

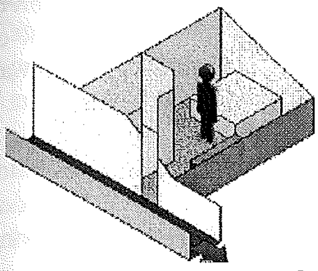

Fig.2: Room Geometry, © TraffGo

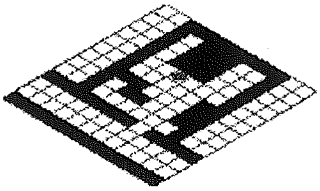

Fig.3: Grid, © TraffGo

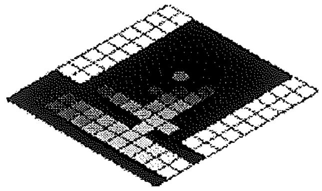

Fig.4: Potential, © TraffGo

Fig.2. is showing a cabin and a small corridor as a simplified geometry example. The geometry is transformed into cell information as seen in Fig.3. The model is considering the five cell-types; walls, obstacles, doors, stairs and free cells. Persons are represented with dots travelling on the grid of cells. Potentials for orientation spread out from the appointed exits according to the given escape-routes as indicated in Fig.4. The gradient of the blue color marks the potential value and thereby the resulting direction of movement.

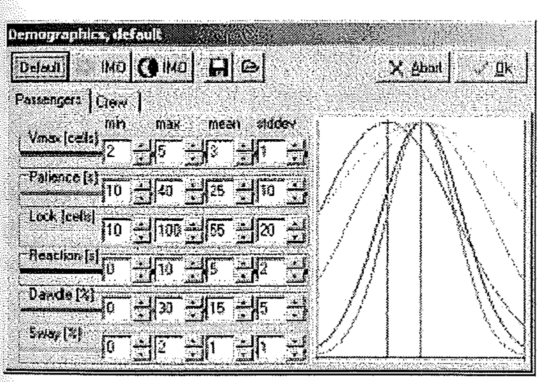

Fig.5: AENEAS Demographics, © TraffGo

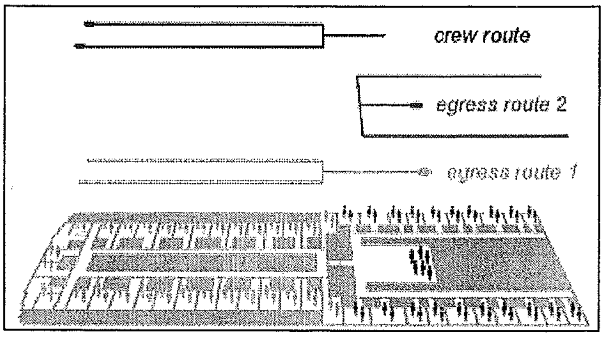

Fig.6: Multiple Escape Routes, © TraffGo

Variation of personal abilities is taken into account by assigning every person a set of parameters influencing her behavior. The list of factors affecting the movement of a person is nearly endless. However, from a physical point of view the movement of a person is only characterized by her speed and direction.

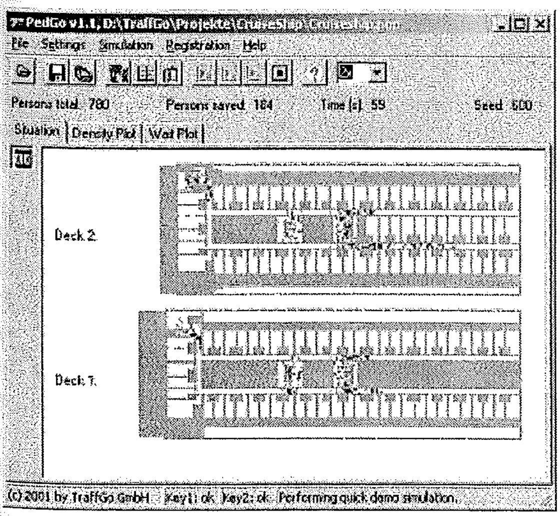

Fig.7: AENEAS Simulation, © TraffGo

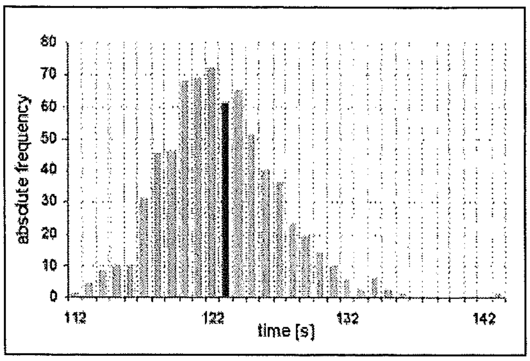

Fig.8: Distr. of multiple simulations, © TraffGo

The number of parameters characterizing the abilities of a person in AENEAS was reduced to the six parameters shown in Fig.5. All parameters are assigned by normal distributions with cutoffs for minimum and maximum values. The parameters are: Speed (the speed of the person in cells/s), Patience (maximum waiting time until a person seeks an alternative route), Look (maximum number of cells that a person is looking to decide the direction of movement), Reaction (the reaction time of the person), Dawdle (the probability that a person stands still for the rest of the time-step) and Sway (the probability that a person diverge from her direction of movement).

Various escape routes can be assigned as demonstrated in Fig.6. Along these routes, the editor automatically spreads the potentials. An egress route can be seen as a self-contained layer, by which the person following this route orientates, but at the same time interacting with persons following alternative escape routes.

The evacuation simulation generates a large amount of data. This comes from the many simulation runs which are necessary for a statistical analysis and because the data of every single person is collected. The distribution of evacuation times shows you how much the result spreads and how it is distributed. An example is provided in Fig.8.

4. Flensburger Schiffbau Gesellschaft's approach to Evacuation Analysis

FSG has been engaged in Evacuation Analysis since its beginning in the Nineties, and analyses have been performed according to the simplified evacuation analysis of MSC/Circ. 909. It was early concluded that analysis according to MSC/Circ. 909 was too time-consuming and not flexible enough to satisfy the ship designer needs in the early part of the design process. The naval architect needs a quick and accurate way to investigate the escape routes. Over the last couple of years FSG has been active in testing evacuation simulation tools and providing user's feedback to the developer. FSG has also been engaged in extensive local, national and international work as an effort to move forward IMO's approval of computer based evacuation simulation tools. From February 2002 FSG has been official user of the simulation tool AENEAS described in chapter 3.

Time has always been an important factor in the marine industry, and the ship designer is faced with the demand for even higher productivity and effectiveness to shorten the project response time. FSG provides very detailed and firm offers for optimized designs within 4 weeks. During these first 4 weeks of a project several rounds of evacuation analysis are conducted. The move from simplified to advanced analysis is enabling FSG to use evacuation analysis as a true design tool, and not only a service to satisfy the authorities.

Few days after the start of a project the first GA sketches are developed and the first ideas regarding escape routes and life saving appliances are in place. At this point the first evacuation analyses are conducted. The CAD drawing is imported to the simulation editor as described in chapter 3, and after few hours of effort the first results are ready. Possible congestion points have now been located, and action can be taken as appropriate. Currently the evacuation simulation tools are accurately locating the bottlenecks of the escape routes. It has been pointed out by critics that very little data exists regarding the individual parameters of the passengers, and thereby the trustworthiness of the results is weakened. We have to agree with those criticizing that it is impossible to know if the simulation times are "on the Second" correct. However, we know that the congestion points are in most cases precisely located using advanced analysis, and this is usually the most important information for the ship designer in the early part of design. It is stated in the IMO interim guidelines that the scope will be to assess the evacuation process through benchmark cases rather than trying to model the evacuation in real emergency condition. One of the very important consequences from the advanced analysis is therefore putting awareness to points of trouble in the geometrical layout of the vessel and the escape routes. After locating congestion points several changes to the layout are considered. By doing this at the very early design stage significant layout changes can be made resulting in only minimal setback in the time-progress of the project.

4.1 Evacuation of High Speed Crafts

Currently IMO has not opened for the use of advanced evacuation analysis on HSC. MSC/Circ. 1001 requires escape routes in HSC to be evaluated by an evacuation analysis early in the design process, according to the 2000 HSC Code, section 4.8.2. It is written in MSC/Circ.1001, section 1.2; "The purpose of the Interim Guidelines is to provide guidance on how to execute a simplified (hydraulic) analysis and use the results to plan the evacuation demonstration required in section 4.8.5 of the 2000 HSC Code." The introduction of advanced analysis has brought several benefits compared to simplified analysis, and it is believed that these benefits also apply to evacuation analysis of HSC. Advanced analysis provide statistical results based on the given individual parameters and the unique population for every new run. Congestion points are located and improvements can be incorporated.

Table I: Comparison of selected items for simplified and advanced evacuation analysis.

Item for Comparison	**Simplified Evacuation Analysis**	**Advanced Evacuation Analysis**
Flow	Depends only on density and escape route width.	Determined by the simulation.
Walking Speed	Either fast walking speed when no congestion, or slow walking speed in queue.	Varies individually.
Counter Flow	Not possible.	Possible.
Visualization	Not possible as a function of time.	Sequence oriented and thereby possible.
Reaction Time	Only global reaction time	Varies individually.
Embarkation	Only one constant time for the entire embarkation process.	Simulation of all individual persons possible.
Result	One time.	Statistical results, Standard Deviation, Minimum, Maximum, Graphics, Animation.
Density	Only at transition points.	Available everywhere.
Geometry	Problems with furniture and large public spaces.	Described in detail.
Use of the method.	Somewhat difficult and in some areas illogical.	Intuitive and easy.
Effort implementing changes in GA	Incorporation of small changes can take a very long time.	Changes to the GA are quickly done by using the editor or importing a new dxf-file from the CAD system.
Automation	Quite difficult.	Relatively easy.
Overall time for complete analysis	Long.	Quick as long as a prepared dxf-file is available.

Some classification societies and individuals have claimed that the travel time in the case of evacuation of HSC is insignificant and need not be analyzed. The reader is hereby warned that this might not be true, especially when dealing with large HSC with grand number of passengers. It is in our opinion always important to investigate the persons movements from original location to embarkation, even if the MES slide or chute often is the bottleneck during the evacuation of HSC. We never know where a troublesome congestion point in the vessel's layout might occur, and therefore the travel through the ship is of significant importance, not only for passenger vessels and ro-ro passenger vessels, but also for HSC.

5. FasdHTS Research Project Evacuation Analysis

FSG was asked to develop a fast ferry design within the R&D project FasdHTS. The research work was mainly aimed at high tensile steel in fast ship structures, and the evacuation analysis is a voluntary addition by FSG not directly linked to the FasdHTS project.

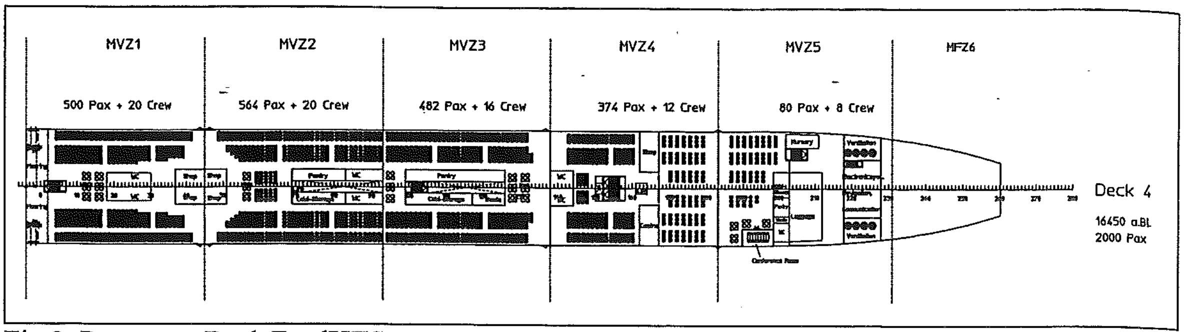

Fig.9: Passenger Deck FasdHTS

The vessel is carrying 2000 passengers and 76 crew. In this research project the two following scenarios have been analyzed:

Alternative 1: All 2076 persons located on Deck 4 distributed over five MVZ as shown in Fig.9. Deck 4 is arranged with 1st Class in the forward part of the vessel, and therefore the person density is highest in the MVZ 1 to 3.

Alternative 2: Passengers are located on Deck 3 and Deck 4. Cabins are located on Deck 3 in MVZ 4 and MVZ 5 accommodating 200 passengers in 50 four-bed cabins, and 74 crew in 10 single-bed cabins and 16 four-bed cabins. The remaining persons are located on Deck 4. See Fig.10.

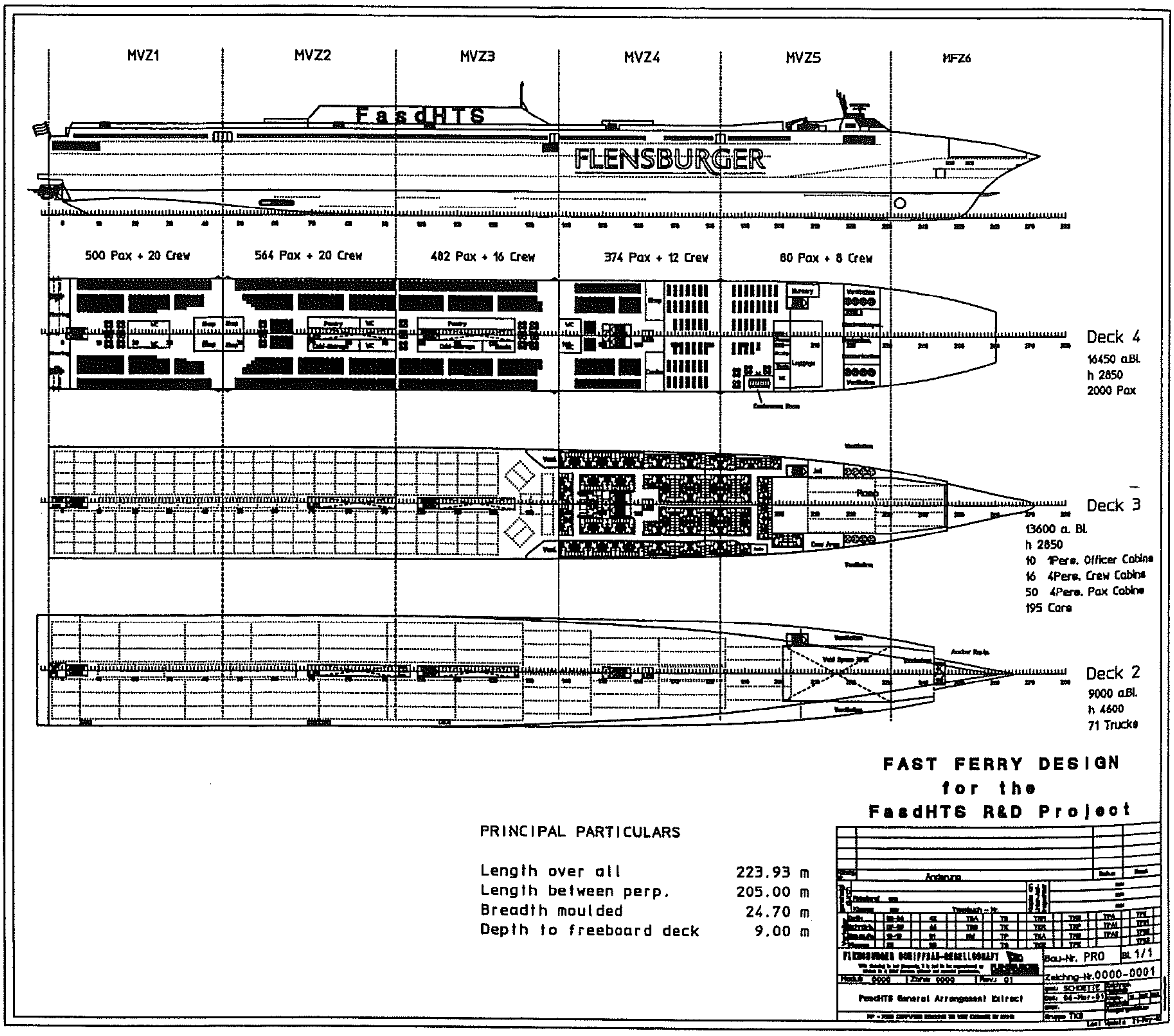

Fig.10: FasdHTS General Arrangement Extract

The current guidelines do not open for passenger cabins on HSC, however vessels in the future might develop in a way that will introduce passenger cabins on vessels falling into the category currently defined as HSC. Alternative 2 is included to investigate some of the consequences of cabins on a HSC.

5.1 Close cooperation with life-saving equipment manufacturers

FSG has worked closely with the two life-saving equipment manufacturers Viking Life-Saving Equipment (Viking) and Liferaft Systems Australia (LSA). Viking developed several different MES arrangements for the vessel. Some of the arrangements are shown in Fig.11.

Version 1 is having two 300 person MES per MVZ (10x300=3000) providing a large over-capacity of ca 45%. The two forward zones are having less number of persons compared to MVZ 1 to 3, and therefor it is suggested to let the two forward zones share MES as shown in Fig.11, Version 2. Such an arrangement is shown in detail in Fig.13.

Version 3 (Fig.11) provides for the same number of persons as version 1. Some sources claim that version 3 is safer than version 1 since the MES are evenly distributed over the length of the vessel. However, version 3 has less space for dropping of liferafts compared to version 1. The MES arrangement proposed in version 3 can be seen in more detail in Fig.14.

Version 4 (Fig.11) are utilizing only shared MES. Such an arrangement is shown in detail in Fig.13. Version 4 can not be used because of insufficient capacity in MVZ 1.

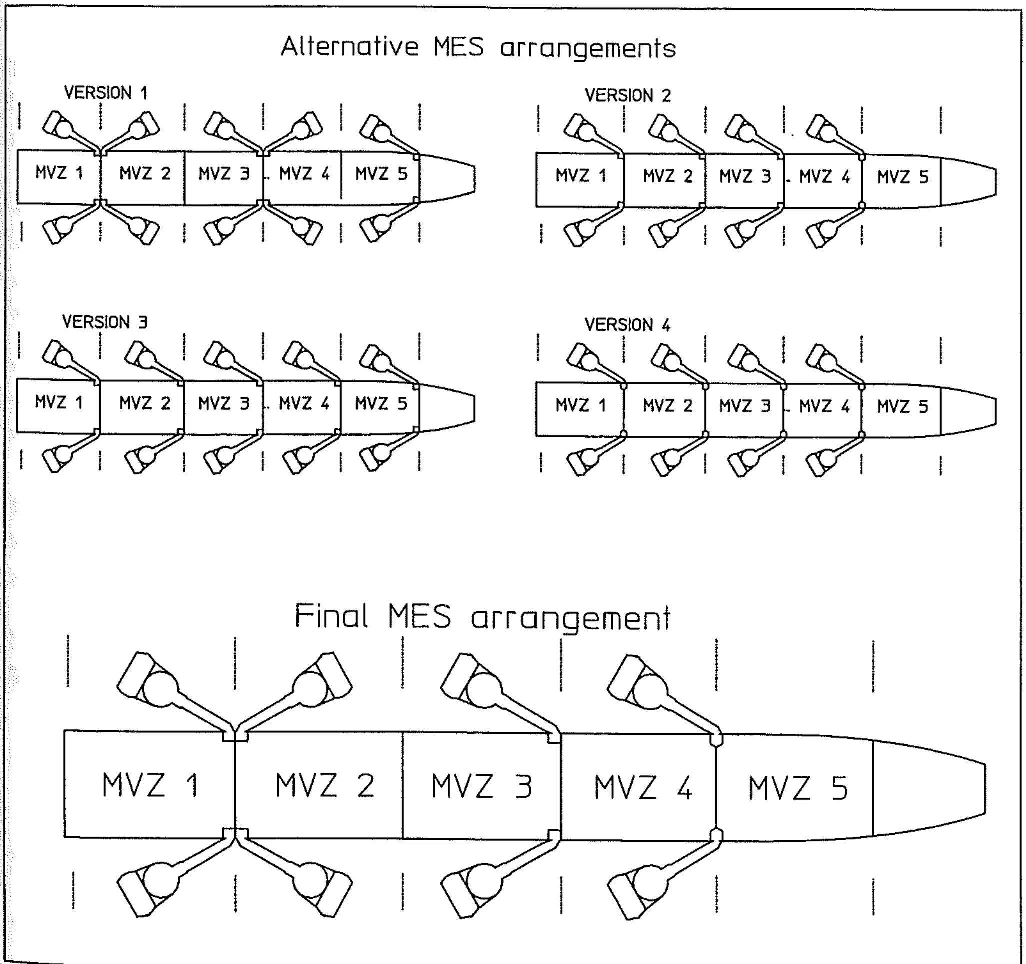

Fig.11: MES arrangement alternatives proposed by Viking Life-Saving Equipment

The chosen MES arrangement is shown in Fig.11. The final version is designed as a combination of the 3 solutions described in figures 12, 13 and 14. An MES over-capacity of 10% is required , and the vessel is having an over-capacity of ca. 16%. All MES are equipped with double slides (Fig.15).-

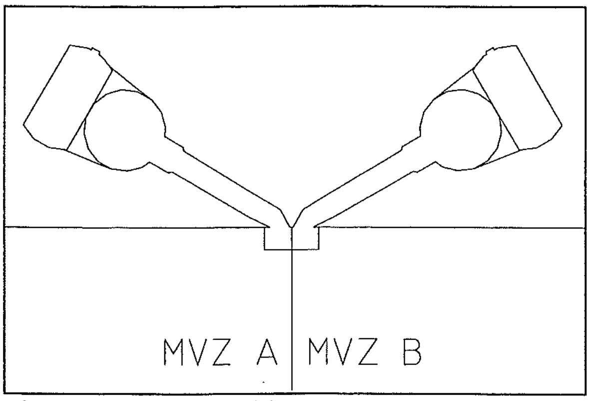

Fig.12: Two zones with one MES each

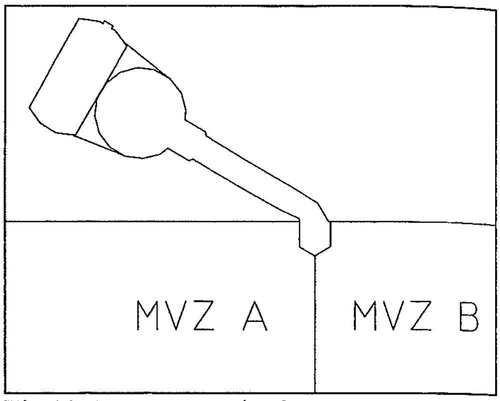

Fig.13: Two zones sharing one MES

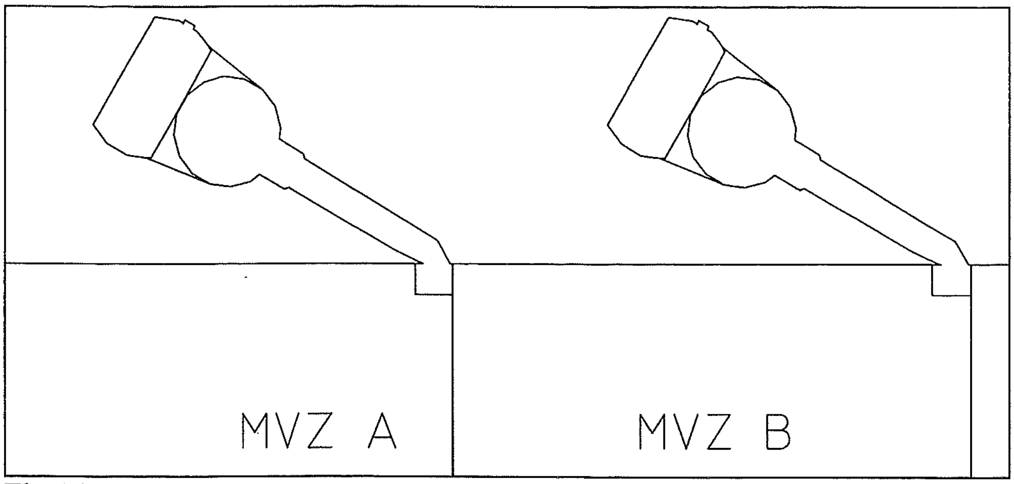

Fig.14: Two zones with one MES each

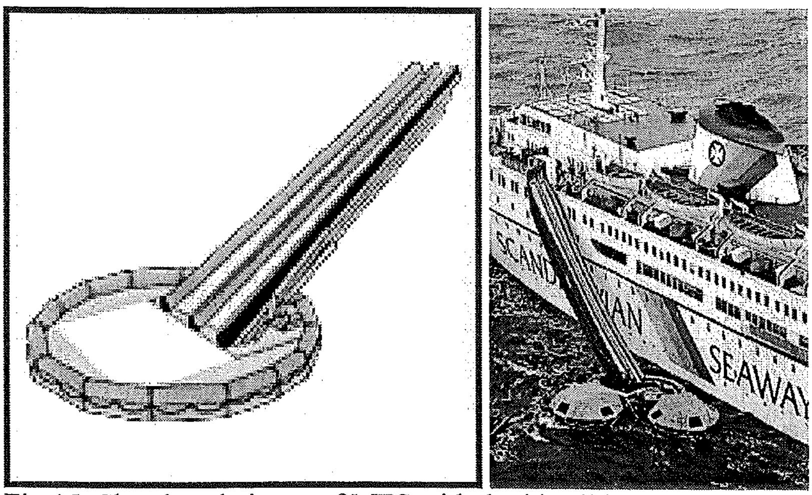

Fig.15: Sketch and picture of MES with double slide
© Viking Life-Saving Equipment A/S

For evacuation analysis MSC/Circ. 1001 is defining the following times:

1. t_M is the ideal deployment time needed for preparation and launching of the MES and the first survival craft in water.
2. t_I is the ideal travel time needed for the slowest group of people to reach the embarkation point in calm water.
3. t_E is the ideal embarkation time needed for all passengers and crew to board the survival craft in calm water.

The performance standard is given in ideal condition mainly because the full scale evacuation tests are conducted under ideal conditions, and also to provide for easier comparison of evacuation times of different vessels. Please note that evacuation analysis for HSC based on IMO's guidelines is not modeling the evacuation in a real emergency condition. The ideal situation is simulated. However, the analyses are providing very useful information for developing the vessel to better cope with a possible abandonment. One of these items is identifying congestion points. The following two performance standards should be complied with for calculating the overall evacuation time according to MSC/Circ.1001:

$$t_M + t_E \le \frac{SFP - 7}{3} [\text{min}] \qquad \text{and} \qquad t_I + t_E \le \frac{SFP - 7}{3} [\text{min}]$$

We will show in the following that we have reached an even higher performance standard of:

$$t_M + t_I + t_E \le \frac{SFP - 7}{3} [\text{min}]$$

The value for t_M was obtained from Viking Life-Saving Equipment. The information is stated in a DNV approved certificate for the slide system of the DNV witnessed function test held on board the HSC vessel "Silvia Ana":

t_{m1} :	1 min 30 sec inflation of slide *
t_{m2} :	15 sec raft container in water, pulled to slide platform and connected **
t_{m3} :	30 sec inflation of liferaft (100 persons) inflated ***
t_m :	2 min 15 sec

* Inflation times are depending on slide length, liferaft size, and temperature.
** Depending on distance from drop of liferaft to platform.
*** Depends on raft size and temperature.

The embarkation time t_E needed for all passengers and crew to board the survival craft is simulated by blocking the slide a time $t_{E\text{-PER-PERSON}}$. Extensive tests have been conducted and $t_{E\text{-PER-PERSON}}$ is set to 3 sec based on data obtained from Viking Life-Saving Equipment and Liferaft Systems Australia.

Five-hundred simulation runs were conducted for each of the two alternatives. The total simulation time for the 500 runs were 59 minutes.

5.2 Analysis according to Alternative 1 without cabins

The SFP of the FasdHTS vessel is 60 minutes, and thereby according to MSC/Circ.1001, section 3.2.8 the maximum allowable evacuation time is t_{max} = 17 min 40 sec.

The actual number of passengers to be evacuated per MES is shown Table II.

Table II.

MES LOCATION	**NUMBER OF PASSENGERS**
PS MVZ 1	260
SB MVZ 1	260
PS MVZ 2	292
SB MVZ 2	292
PS MVZ 3	249
SB MVZ 3	249
PS MVZ 4 and 5	237
SB MVZ 4 and 5	237
TOTAL	**2076**

The ideal travel time and embarkation time have been simulated to the following values:

T_{MEAN} $= t_I + t_E =$ 10 min 10 sec
$T_{MINIMUM}$ $= t_I + t_E =$ 09 min 53 sec
$T_{MAXIMUM}$ $= t_I + t_E =$ 10 min 32 sec
Std. Dev. = 6 sec

The ideal deployment time t_M = 2 min 15 sec as described in chapter 5.1.

When choosing the maximum travel and embarkation time the total evacuation time T becomes: $t_M + (t_I + t_E) = 2\,\text{min}\,15\,\text{sec} + 10\,\text{min}\,32\,\text{sec} = 12\,\text{min}\,47\,\text{sec}$

The requirements are therefore fulfilled.

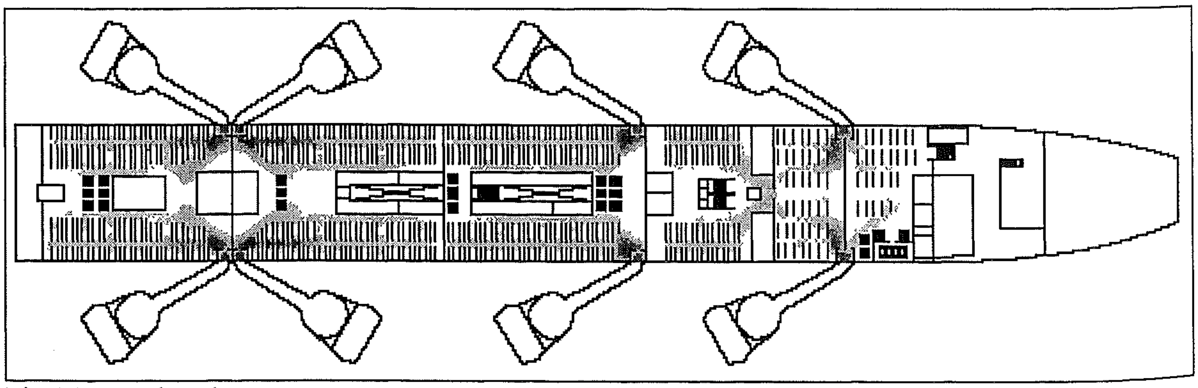

Fig.16: Density plot.

The density plot in Fig.16 is included only to illustrate one of the possible outputs from the analysis. This paper is in black and white, but in the original image the colors red, yellow and green are representing high, medium and low person densities respectively. For the FasdHTS the highest person densities are located directly in front of the MES exits as expected. It was also seen high person density in some of the alleyways. Somewhat wider aisles would give the persons more space, and possible panic might be reduced or eliminated.

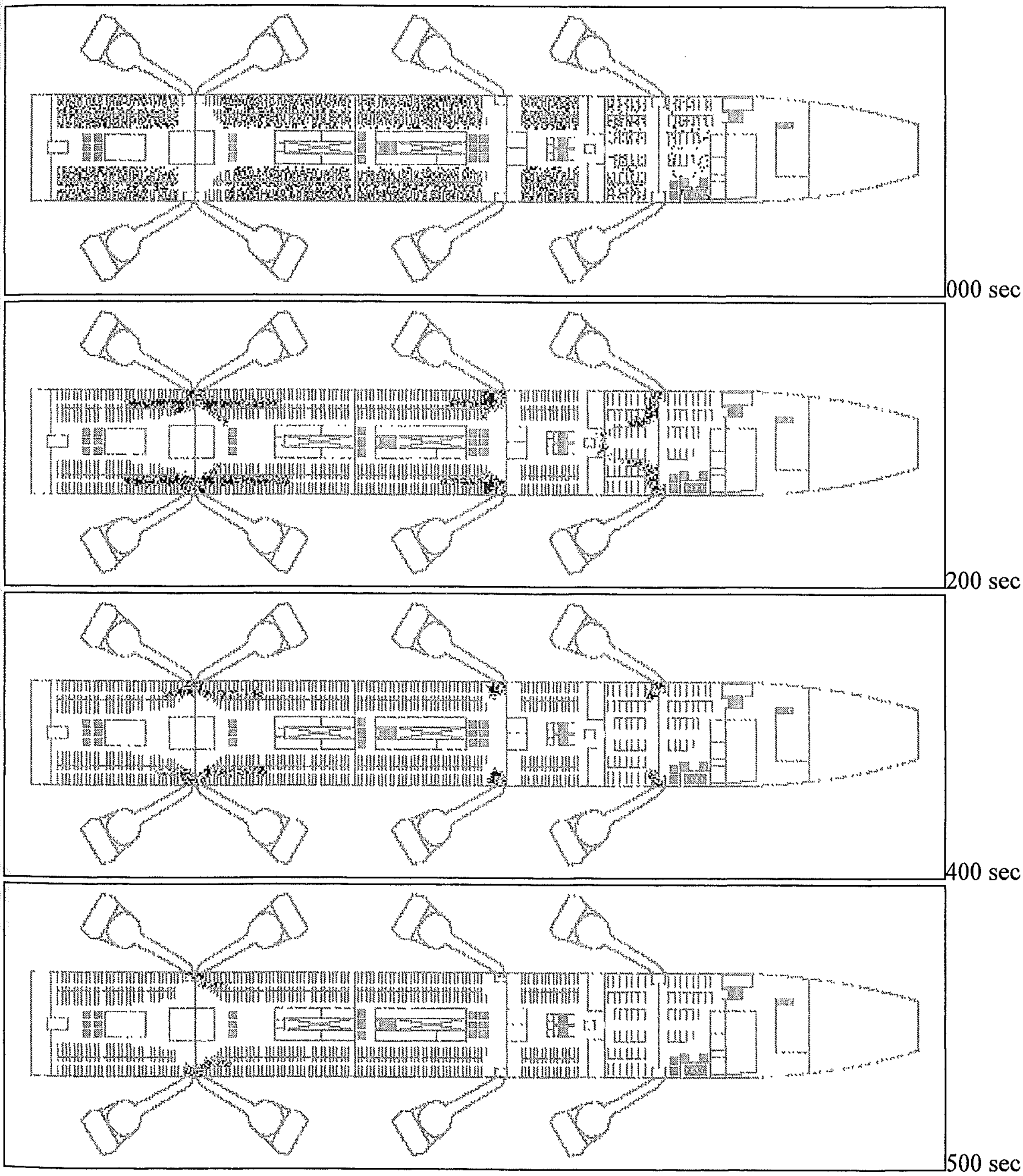

Fig.17: Location of persons at 0, 200, 400 and 500 sec. Persons represented as dots.

It is seen in Fig.17 that MVZ 2 is the last zone to empty.

5.3 Analysis according to alternative 2 with cabins

Actual number of passengers to be evacuated per MES is shown Table III.

Table III.

MES LOCATION	NUMBER OF PASSENGERS
PS MVZ 1	260
SB MVZ 1	260
PS MVZ 2	292
SB MVZ 2	292
PS MVZ 3	249
SB MVZ 3	249
PS MVZ 4 and 5 coming from Deck 3	137
SB MVZ 4 and 5 coming from Deck 3	137
PS MVZ 4 and 5 coming from Deck 4	100
SB MVZ 4 and 5 coming from Deck 4	100
TOTAL	**2076**

The ideal travel time and embarkation time have been simulated to the following values:
T_{MEAN} $= t_I + t_E =$ 10 min 09 sec
$T_{MINIMUM}$ $= t_I + t_E =$ 09 min 50 sec
$T_{MAXIMUM}$ $= t_I + t_E =$ 10 min 29 sec
Std. Dev. = 6 sec

The ideal deployment time t_M = 2 min 15 sec as described in chapter 5.1.

When choosing the maximum travel and embarkation time the total evacuation time T becomes:
$t_M + (t_I + t_E) = 2\,\text{min}\,15\,\text{sec} + 10\,\text{min}\,29\,\text{sec} = 12\,\text{min}\,44\,\text{sec}$

The requirements are therefore fulfilled.

Interestingly the PS forward MES has been serving a larger number of persons than the SB forward MES (Fig.18). This is due to the decisions of the population of this certain simulation run. All the 500 runs result in slightly different results based on the individual parameters and decisions of the evacuating persons.

5.4 Comparing the results of alternative 1 and 2

Table IV: Comparing the results of alternative 1 and 2

	Alternative 1	**Alternative 2**
T_{MEAN}	10 min 10 sec	10 min 09 sec
$T_{MINIMUM}$	09 min 53 sec	09 min 50 sec
$T_{MAXIMUM}$	10 min 32 sec	10 min 29 sec
Std. Dev. [s]	00 min 06 sec	00 min 06 sec
t_M	02 min 15 sec	02 min 15 sec
T	12 min 47 sec	12 min 44 sec

MVZ 2 is yielding the longest total evacuation time for both alternatives. MVZ 2 remains identical for alternative 1 and 2, and the 3 sec difference of T is due to the statistical distribution of individual person parameters.

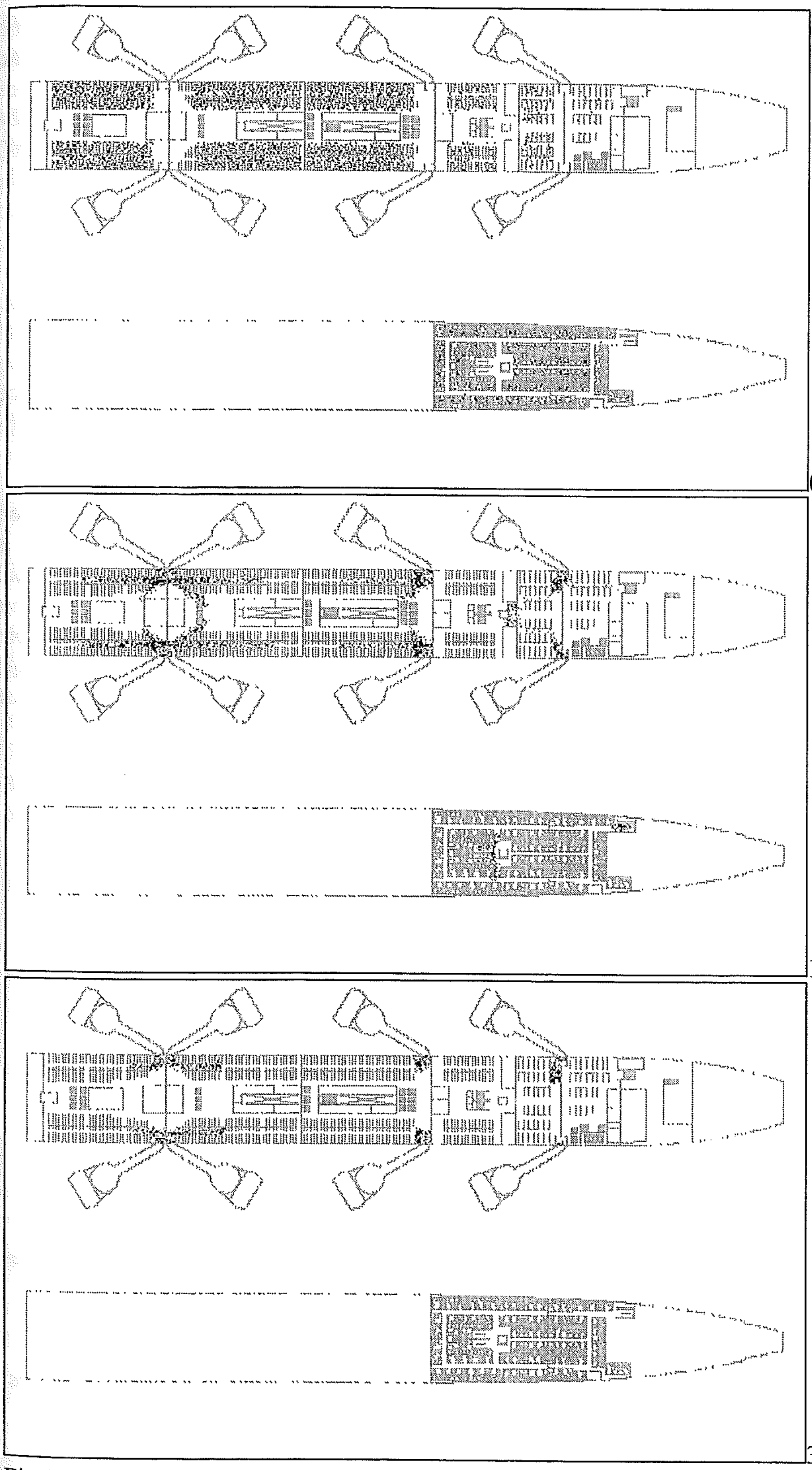

000 sec

100 sec

350 sec

Fig.18: Location of persons at 0, 100, 350 sec. Persons represented as dots.

5.5 Effect of passenger cabins

The introduction of passenger cabins on the FasdHTS does not lengthen the overall evacuation time based on the evacuation analysis presented in this paper. As mentioned earlier MVZ 2 yields the longest evacuation time for alternative 1 as well as for alternative 2. The passengers on Deck 4 are provided with "aircraft-seats" situated in large sitting rooms as seen on Fig.9. A total number of 474 persons are located in MVZ 4 and 5. In alternative 2 the 474 persons are split with 274 and 200 persons on Deck 3 and Deck 4 respectively. The introduction of passenger cabins results in lower person densities in MVZ 4 and 5. The distance of travel is somewhat longer from the cabin areas to the embarkation point, but not enough to obtain the longest evacuation time of the vessel.

Providing cabins for all passengers on a HSC would have resulted in very different evacuation scenarios, and also probably weight problems for a HSC. We are concluding that the introduction of cabins for all crew and 10% of the passengers is not problematic from the evacuation point of view, with an arrangement as presented in this project. Issues like structural fire protection time might be more interesting in the discussion of passenger cabins on HSC. A successful introduction of high tensile steel in HSC could be an important step towards the approval of passenger cabins on HSC.

Many items need further investigation in the area of evacuation analysis on HSC. We have to mention in particular that reaction time for the persons in the cabins has not been considered. Reaction time is clearly defined for day and night scenarios for other vessels carrying passenger, but not for the ideal scenario required for HSC. The parameters used are presented in Table V. We are aware of this problem, and hope we can spark a debate regarding cabins in general on HSC. It is our hope, as more data becomes available, that evacuation analysis will move away from the "ideal" or "benchmarking" philosophy to modeling closer to reality. Nevertheless, the ongoing benchmarking process is one important step in the development of advanced analysis.

Table V: Person Individual Parameters. Normally Distributed.

Parameters	**Minimum**	**Maximum**	**Mean**	**Std. Dev.**	**Unit**
V_{max}:	2	5	3	1	cells/s
Patience:	10	40	25	10	s
Look:	10	100	55	20	cells
Reaction:	0	0	0	0	s
Dawdle:	0	30	15	5	%
Sway:	0	2	1	1	%

6. Closing comment

Hereby including two chilling remarks helping us seeing the importance of evacuation analysis.

"The boat tipped, there was panic and shoving out on the overcrowded sun deck. Then the boat went over, and I was fighting for my life in the ice-cold dark water."
Sleipner disaster survivor.

"The rescue leaders now see no hope for finding more survivors. It is cold. There are large waves."
Spokeswoman at the Norwegian Rescue Coordination Center at Sola after the Sleipner disaster.

Acknowledgements

We would hereby like to warmly thank the following institutions for their cooperation, interest and help in this project.

TraffGo GmbH
Viking Life-Saving Equipment A/S
Liferaft Systems Australia
Gerhard-Mercator Universität Duisburg
Federal Ministry of Transportation, Building and Housing, Germany
Color Line A/S
Norwegian Maritime Directorate
Swedish Maritime Administration

References

1. IMO. *Interim Guidelines for a simplified evacuation analysis on ro-ro passenger ships*. IMO, 1999. MSC/Circ.909
2. IMO. *Interim Guidelines for a simplified evacuation analysis on High-Speed Passenger Craft*. IMO, 2001. MSC/Circ.1001
3. IMO. *Interim Guidelines for evacuation analysis for new and existing Passenger Ships*. IMO, 2002. MSC/Circ.1033
4. IMO. *International Code of Safety for High-Speed Craft*. IMO, 2000.
5. M. Schreckenberg and S.D. Sharma. *Pedestrian and Evacuation Dynamics*. Springer, Berlin, 2001.
6. Fairplay. *Rina pioneers safety system*. Page 23-24, April 18, 2002.
7. Lloyd's Ship Management. *Broadening the Horizons*. Page 25-26, May 2002.
8. Speed at Sea. *Marine Evacuation Systems*. Page 27, February 2002.
9. TraffGo GmbH. *Instruction Manual AENEAS*. TraffGo GmbH, 2002.

Full-Scale Measurements of Global Loads on SES Vessels Built in FRP Sandwich Materials Using Networks of Fibre Optic Strain Sensors

Alf Egil Jensen, FiReCo AS, Mossevn. 39b NO-1610 Fredrikstad, Norway, alf.e.jensen@fireco.no
Jon Taby, FiReCo AS, Mossevn. 39b NO-1610 Fredrikstad, Norway, jon.taby@fireco.no
Karianne Pran, Light Structures AS, PO.Box 109, NO-2027 Kjeller, Norway, karianne.pran@lightstructures.biz
Geir Sagvolden, Light Structures AS, PO.Box 109, NO-2027 Kjeller, Norway, geir.sagvolden@lightstructures.biz

Abstract

This paper presents some results from full-scale sea keeping trials performed with the new Royal Norwegian Navy, pre-series fast patrol boat, "KNM Skjold", which is a surface effect ship (SES) built in FRP sandwich composites. A method for estimating global loads based on extensive finite element analyses and networks of fibre optic Bragg strain sensors are presented. The sensor system was tested and applied during sea keeping trials in the North Sea. Measured global loads and accelerations are compared with design loads given by Det Norske Veritas, High Speed Light Crafts(HSLC)-rules (1993/1996)[3] and Allan et. al.[1].

Nomenclature

$\boldsymbol{\varepsilon}$	Vectors of measured strain values
$\mathbf{k}$	Matrix of calculated strain values
$\mathbf{f}$	Vector of time dependent scaling factors
ε	Strain component
a-e	Time dependent scaling factors
M	Global load
$M_{Sagg/Hogg}$	Sagging/hogging moment
$M_{H.Bending}$	Horizontal bending moment
$T_{Twisting}$	Twisting moment
V_{Shear}	Shear force
N_{Normal}	Longitudinal compression force
$\boldsymbol{\varepsilon}_{\mathbf{normal}}$	Vector of strain values for determination of: $M_{Sagg/Hogg}$, $M_{H.Bending}$, and N_{Normal}
$\boldsymbol{\varepsilon}_{\mathbf{shear}}$	Vector of strain values for determination of: $T_{Twisting}$ and V_{Shear}
$\mu\varepsilon$	10^{-6} (microstrain)

1. Introduction

In April 1999 the Royal Norwegian Navy (RNoN) received the new pre-series fast patrol boat, "KNM Skjold", which is a twin hull surface effect ship (SES) made of fibre reinforced polymer (FRP) sandwich composites, see Figure 1. The vessel is 47m long, 13.5m wide, it has a displacement of approximately 270ton, and capable of a speed in excess of 55 knots. The vessel was built by the yard Umoe Mandal AS in Norway.

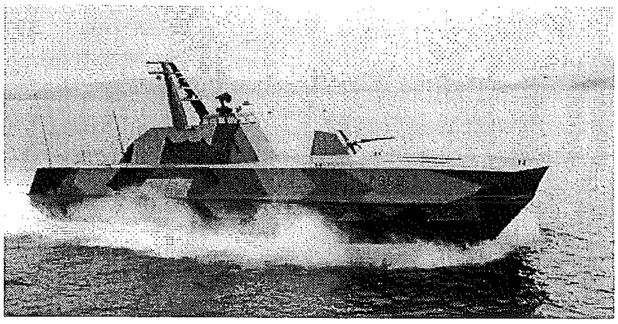

Figure 1: The RNoN pre-series fast patrol vessel,
"KNM Skjold"

This paper presents some important results from full-scale measurements of global response in SES vessels. The hull concept of SES vessels is not new, but the influence from sea loads on this particular hull concept is not fully established yet. The reason for this is that few ships of this type are, or have been in service, and consequently, thorough investigations have been limited. For the present design of "KNM Skjold" the loads are measured and compared with the DNV High Speed and Light Crafts(HSLC)-rules of 1993 and 1996[3]. The HSLC-rules are based on experience and numerical analyses of generic catamaran hulls. However, in some cases relatively large deviations between predicted and measured values for catamaran vessels have been reported (Roberts et al.[10]). For SES vessels in particular even larger deviations can be expected due to the complex influence from the air cushion. The cushioning effect is very difficult to model, both in numerical hydrodynamic simulations and in experiments with scaled models. Another uncertainty is connected to the influence of the very high speed of this particular vessel. It was therefore of interest to measure some of the global loads in order to verify the assumptions that formed the basis for the design of "KNM Skjold", and to see whether the DNV-rules could serve as a design basis.

A method for estimating global loads applied to multi-hull vessels in service is presented. It is based on online strain measurements using networks of strain sensors adhered to the inside of the hull and detailed FEM calculations. The sensors should be distributed over a cross-section at carefully pre-selected locations and orientations in order to maximise the measured strain response of the loads of interest, and to minimise the amount of interference between the strain signals from the different deformation patterns caused by the local loads. In this paper only a brief presentation of the method for global load estimation is given. A more thorough presentation is given in Jensen et. al.[5].

2. Global load measurements

2.1 Theoretical background

In the DNV HSLC-rules extreme design values for the sagging moment, hogging moment, horizontal bending moment and longitudinal twisting moment are given. On a vessel these extreme load will appear at a cross section close to amidships. Thus, in order to be able to measure the extreme values a cross section close to amidships has to be instrumented.

For vertical shear force the extreme value appears near the quarter lengths of the hull beam. But, in order to be able to estimate the global moments amidships the strain components due vertical shear force have to be known as well. Furthermore, in extreme sea conditions where the vessel dives into a head wave, longitudinal accelerations and hence compression forces could become significant. Therefore the response of a longitudinal normal force is also included. The effects from vertical shear force and normal force are only included in order to "complete" the set of loads and corresponding responses at the cross section.

Linear elastic material properties are assumed, which is valid for the strain level of interest. Further, a linear dependency between the applied loads and the respective strain components is assumed, and the response of the loads applied to the hull beam is assumed to appear simultaneously over the hull cross section where the sensors are attached. Based on these assumptions a detailed FEM model with idealised load cases for each global load component has to be made, and from the FEA the local strain values were determined.

In order to measure global loads based on the network of strain sensors and the FE model data the following system of linear algebraic equations is suggested:

$$\boldsymbol{\varepsilon}^{T} = \mathbf{k}\,\mathbf{f}^{T} \qquad (1)$$

$\boldsymbol{\varepsilon}^{T}$ is a vector containing measured strain from strain sensors. **k** is a matrix containing strain values from FEA with idealised load cases, where the number of columns is equal to the number of global loads to be estimated. The number of rows is equal to the number of sensors attached to the structure. The strain values are taken from the FE model at the same positions where the different sensors are located on the real structure. Vector **f** contains time dependent scaling factors between the applied global loads of interest and the respective static loads applied in the FEA. For the estimate of the measured loads presented in this paper, the following **f**-vector is used

$$\mathbf{f} = [a, b, c, d, e] \qquad (2)$$

To be able to determine the factors in vector **f**, the **k**-matrix has to be invertible. Thus, the **k**-matrix must be quadratic[14]. A solvable system of linear algebraic equations can now be constructed by choosing strain signals from a number of sensors equal to the number of global loads to be estimated. The scaling factors in vector **f** are now determined by solving the expressions,

$$\boldsymbol{\varepsilon}^{T} = \mathbf{k}\,\mathbf{f}^{T} \;\Rightarrow\; \mathbf{f}^{T} = (\mathbf{k})^{-1}\,\boldsymbol{\varepsilon}^{T} \qquad (3)$$

When the scaling factors in **f** are determined, the strain components caused by the five distinct loads can be obtained for each sensor signal by multiplying the respective factors, *a-e*, with the calculated strain values.

$$\varepsilon_{Sagg} = \varepsilon_{Sagg,\,FEM} \cdot a\,,\; \varepsilon_{Hogg} = \varepsilon_{Hogg,\,FEM} \cdot b\,,\ \text{etc....} \qquad (4)$$

Since linear dependency between the applied loads and the respective strain components are assumed the following expression holds for all load cases,

$$[M/\varepsilon_{sensor}]_{Measured} = [M/\varepsilon_{sensor}]_{FEM} \qquad (5)$$

Here M represents one of the global loads. By a substitution of the measured strain components from Equation (4) into Equation (5), a relation between the actual load, $M_{Measured}$, and the applied FEM load is determined.

$$M_{sagg,\,Measured} = M_{Sagg,\,FEM} \cdot a\,,\ \text{etc...} \qquad (6)$$

The global loads are obtained by a multiplication of the loads applied in the different FEM analyses with the corresponding factors, *a-e*. This gives the measured global loads for each sample. The global load components can now be continuously measured by repeating the calculations given by Equations (3) and (6) for each sample. Since the **k**-matrix is known the inversion of the matrix can be done in advance, which makes the computational effort to solve Equation (3) and Equation (6) very modest. Thus, the calculations can be done in real-time by an online system.

2.2 Experiments

Full-scale sea keeping tests have been performed with "KNM Skjold". The objective with the experiments was to estimate the extreme values for the sagging moment, hogging moment, horizontal bending moment and longitudinal twisting moment at different Sea States and headings and to see whether the actual strength of the vessel is sufficient for the intended purpose. The results were also compared with the load values given by the DNV HSLC-rules of 1993 and 1996[3].

2.3 Fibre optic sensor system

A network of fibre optic Bragg strain sensors was installed on "KNM Skjold". Fibre Bragg gratings have been successfully used as strain sensors on a range of structures including aircrafts[2]. The gratings are formed by exposing an optical fibre to a pattern of UV light creating an integrated sensor in an optical fibre with a typical diameter of 250nm[7]. The sensor works by reflecting a specific wavelength of light, and this wavelength is linearly dependent on the axial strain in the fibre. Incorporating several Bragg gratings that reflect different wavelengths and illuminating them with a broadband source easily achieve multiplexing of several sensors in a single fibre.

The light source and read-out electronics were placed in the operations room on board the vessel, and cables of up to 60m were drawn to the sensor locations. The sensors that were employed in the moment/force estimation were distributed on four fibres.

The performance of a Bragg grating based strain sensing system depends mainly on the read-out technique. For the sea keeping tests a scanning fibre Fabry-Perot filter for the wavelength to strain conversion was applied [6, 8]. The principles of this technique are shown in Figure 2. A light source that emits a wide range of optical wavelengths illuminates the sensors which each reflects a specific wavelength. When the reflected light is passed through a scanning optical filter, the detectors will register a short burst of light whenever the filter transmission wavelength matches the wavelength reflected from a sensor. Knowing the relation between the scan drive voltage and the filter transmission wavelength, the reflected wavelength from the time of detection can then be determined.

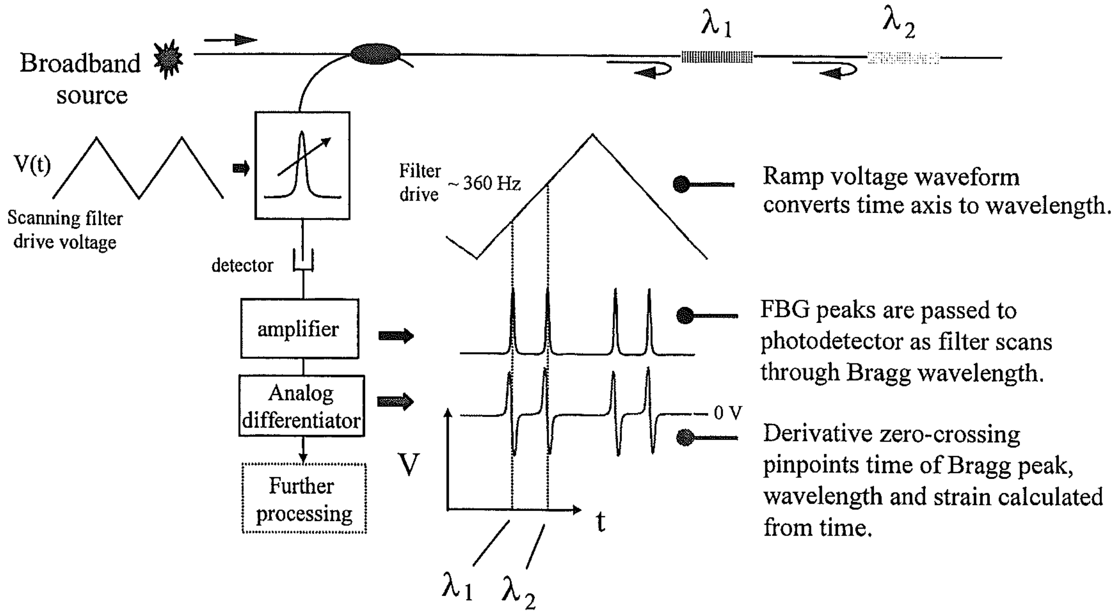

Figure 2: The scanning Fabry-Perot filter read-out technique

With this technique up to 64 Bragg grating sensors distributed in four fibres can be simultaneously sampled. The system noise floor lies below 0.2με/(Hz)0.5, and it is possible to measure strains up to ±13000με with a resolution of 0.5με (με = 10^{-6}).
The maximum scanning frequency of the filter that was used for these tests is 360Hz, which determines the sampling rate. This is more than sufficient for measuring global moments and forces. The signal processing was more conveniently performed on data that had been filtered to remove all frequency components above approx. 20Hz and down-sampled to a sampling rate of 45Hz.

2.4 Sensor locations

The global moments of interest were estimated by the method presented in this paper. A network of fibre optic Bragg strain sensors was attached on the inside of hull panels. The sensors were adhered to the inner skin of the sandwich panels, and to protect the sensors a 5.0cm wide strip of a 100g/m^2 CSM (Chopped-Strand Matt) layer of glass fibre was laminated on top of the optical fibres. The same matrix material as in the structure was used. Ten strain sensors were attached at a cross section located approximately 1.0m in front of the deckhouse. Figure 3 shows the sensor location at the cross section.

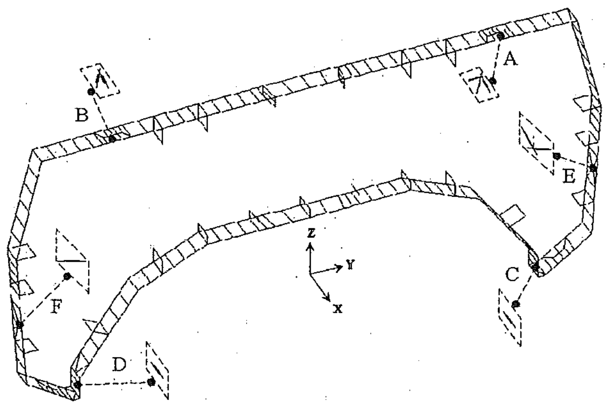

Figure 3: Fibre optic sensor positions at a cross section amidships

Care must be taken when the locations for the sensors are determined. The influence from local lateral loads can cause unwanted responses. However, since we are interested in dynamic strain values at relatively low frequencies (0-10Hz), and the local dynamic strain values due to vibrations that appear at significantly higher frequencies, it is possible to low pass filter the strain signal to remove the local strain components. Further, it is important to avoid attaching the sensors on overlap laminas used for the T-joint between the hull panels and the different stiffeners etc.. A global FEM model of the entire vessel that take details like overlap laminates into consideration would become far too large for practical applications.

In order to achieve the best possible estimate for the loads, two sets of five sensors were chosen. For the selection of sensor locations at the cross section the following factors were important:

- High strain response caused by the load to be estimated in comparison to the other global loads.
- The mutual position of the sensors at the cross section.
- Avoiding misinterpretation of the strain field from global loads due to local conditions.

At this stage of the analysis the hull was looked upon as a mechanical beam. From classical beam theory the highest strain response from bending moment is achieved far from the neutral axis and parallel to the beam. The locations of the sensors used for estimating the three bending moments are position A, B, C, and D, see Figure 3. Four sensors were aligned parallel to the length of the vessel and a fifth sensor was positioned perpendicular to the other four at location A. The orthogonal relation between the vertical sagging/hogging moments and the horizontal moment makes them fairly easy to separate by the sign of the strain values. The normal force was also measured using this set. Thus, the following five strain signals formed the $\boldsymbol{\varepsilon}$-vector in Equation (3):

$$\varepsilon_{\mathbf{Normal}} = [\varepsilon_{Ax}, \varepsilon_{Bx}, \varepsilon_{Cx}, \varepsilon_{Dx}, \varepsilon_{Ay}] \qquad (7)$$

The five sensors belonging to the second set are located at position A, B, 2 sensors at E, and F, see Figure 3, and at an angle 45° with respect to the cross section. This was done to maximise the strain response from the shear stresses due to the twisting moment and the transversal shear force acting on the cross section. Thus, the following five strain signals formed the $\boldsymbol{\varepsilon}_{\mathbf{Shear}}$ -vector in Equation (3):

$$\varepsilon_{\mathbf{Shear}} = [\varepsilon_{A45}, \varepsilon_{B45}, \varepsilon_{E45}, \varepsilon_{E\,-45}, \varepsilon_{F45}] \qquad (8)$$

2.5 Fem model and analyses

Sea loads act on the hull of a vessel through continuous variations of distributed water pressure in balance with inertia forces, and it is not practical to try to copy these load distributions in refined FEM models for detailed design. However, the locations on the hull beam where the different global loads have their extreme values are relatively well known. By modelling simple and idealised load cases and calculating the strain values at the cross section where the loads have their extreme values, the total load applied to the structure can be estimated from the load/strain relation determined by FEA.

A detailed FEM model of the SES vessel was made with the computer program DISPLAY III, and the strains were calculated by the program NISA II. The model contained 179 different material specifications and 721 842 degrees of freedom (dofs), and were assembled from sub-models used for detailed design purposes. A general 3D laminated composite shell element (isoparametric with 8th nodes) with 2nd order shape functions was chosen for the element formulation. The model includes hull panels, bulkheads, longitudinal- and transversal stiffeners, and cut outs. The main reason for creating such a detailed model was to achieve a best possible representation of the forces and moments responses (strain values) at the cross section where the sensors are located. Furthermore, in the FEM-model it is important to apply forces, or moments, as far from the cross section of interest as possible, in order to reduce the influence from local stress concentration around the nodes where the loads are applied. In Figure 4 a schematic presentation of the idealised static load cases is given. The only difference between the strain values due to sagging and hogging moment is the sign of the applied moment. In the calculations of the global loads the strain values corresponding to hogging is simply the strain values from sagging with the opposite sign.

The vertical shear force was found by a subtraction of the strain due to the bending moment at cross section A:A, a distance L from the force, see Figure 4. The expression used was:

$$\varepsilon_{shear} = \varepsilon_{cantilever} - \left(\frac{\varepsilon_{Hogg}}{M_{Hogg}} \right) \cdot M_{cross\,section} \qquad (9)$$

M_{Hogg} is the bending moment from the FEM model for sagging/hogging and $M_{cross\ section} = FL$ is the bending moment due to the vertical force, F, applied in the model.

In all the five models presented in Figure 4 the global load of interest is kept constant through the entire beam length. For the real hull beam this is obviously not correct. However, it assures that the model load at the cross section of interest is known and that the strain response is fully dominated by the applied model load. The different loads applied in the FEM calculations were:

$$M_{Sagg/Hogg} = M_{H.\ Bending} = T_{Twisting} = 1.0\ MNm,$$
$$N_{Normal} = 1.0MN, \text{ and } V_{Shear} = 100kN \qquad (10)$$

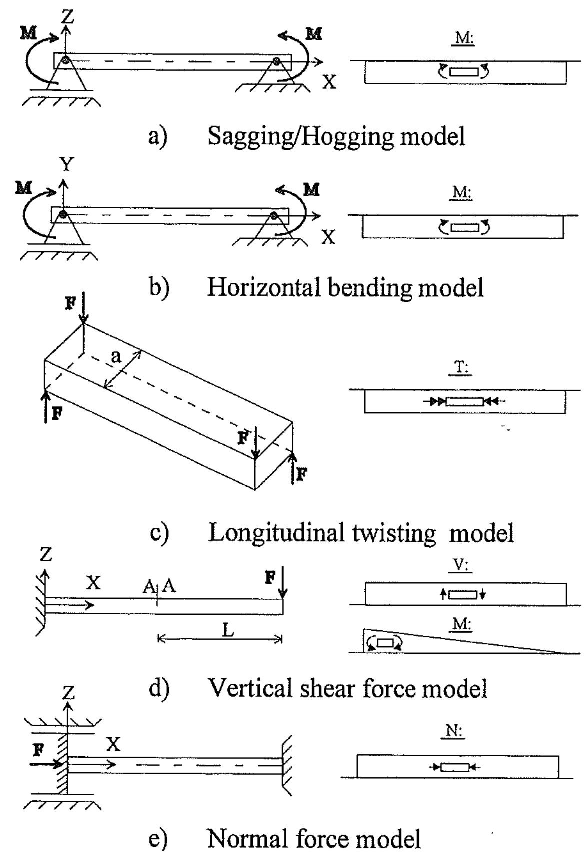

Figure 4: Idealised static models for the load cases applied in the FEM model

From the FEA with load cases as presented, the different columns of the k-matrix in Equation (1) are found. The load constants *a, b,* and, *e* in vector **f**, see Equation (2), were calculated for each sample using the expression

$$\boldsymbol{\varepsilon}^{T}_{\mathbf{Normal}} = \mathbf{k}\,\mathbf{f}^{T} \;\Rightarrow\; \mathbf{f}^{T} = (\mathbf{k})^{-1}\,\boldsymbol{\varepsilon}_{\mathbf{Normal}}{}^{T} \qquad (11)$$

The load constants *c* and *d* were calculated for each sample using the expression,

$$\boldsymbol{\varepsilon}^{T}_{\mathbf{Shear}} = \mathbf{k}\,\mathbf{f}^{T} \;\Rightarrow\; \mathbf{f}^{T} = (\mathbf{k})^{-1}\,\boldsymbol{\varepsilon}_{\mathbf{Shear}}{}^{T} \qquad (12)$$

Finally, the three constants from Equation (11) and the two constants from Equation (12) were substituted into Equation (6) in order to estimate the global loads. The calculation in Equations (11), (12), and (6) were repeated for each sample of strain values during the test runs.

2.6 Experimental test program

The sea keeping tests with "KNM Skjold" took place in May/June 1999, outside the western coast of Norway. 25 different runs, each of approximately 15-20 minutes duration were performed. The duration time was chosen equal to the time required for wave measurements, used for determining the short time distribution of wave heights. From this distribution the significant wave height, Hs, can be found and the Sea State determined. A wave radar, mounted at the bow of the vessel, and the Motion Reference Unit (MRU) of the vessel were used in the experiments to measure the wave motions and consequently the Sea State[4]. The following parameters were systematically varied during the test program: heading, speed, on/off cushion, and the Sea State. The measured Sea States were 3, 5 and upper 6 -7, where Sea State 6 represents the operational limit.

2.7 Results

From the DNV HSLC-rules (1996)[3] a set of characteristic loads for sagging-, hogging-, and longitudinal twisting moment and transversal shear force were determined. For the horizontal bending moment the moment capacity of the hull was determined by calculating the horizontal bending moment that gave a Tsai-Wu[11], last ply failure (LPF) factor equal to a safety factor of 3.3. Furthermore, four of the experimentally measured global loads were normalised by a division of the respective HSLC loads, and the horizontal bending moment was normalised by the horizontal bending capacity. Thus, a measured load equal to 1.0 is identical to the DNV characteristic rule load. However, the basis for the design of the present vessel is different from the DNV requirements. The comparison with the DNV requirements is only done to see whether this can be used as design basis for the present type of vessel.

The normalised measured maximum values for the global loads at different Sea States are presented in Figure 5. During the test runs significant wave heights of 4.5-6.5m and wave periods of 6.0-6.4s were measured for Sea State 6. In the scatter diagram for the North Sea[4] this combination of wave heights and wave periods are only experienced 4 times out of 100 000 observations, so this Sea State is an extreme Sea State 6 with relatively steep waveforms. The same steep waveforms were also experienced in Sea State 5. Since the maximum values in Figure 5 are measured during tests in extreme Sea States they are believed to be representative as maximum values for Sea State 5 and 6.

The forward speed in the three Sea States: 3, 5, and 6 were approximately 45 knots, 42 knots, and 11 knots respectively. From Figure 5 it is seen that the loads increase due to an increase in wave height, or Sea State. For Sea States 5 and 6 the hogging moment exceeds the DNV rule value by 1.4 and 1.8 respectively, and the same is seen for the sagging moment in Sea State 6. In Figure 6 the maximum values are plotted against heading in Sea State 6. Here, the forward speed was 11-, 18-, 25-, 25-, and 25 knots for the respective headings: 0°, 45°, 90°, 135°, and 180°. Figure 6 shows that for head sea (0°) both the extreme sagging- (2.1) and hogging- (1.8) moment exceeds their respective DNV values. These results show that the load prediction given by the DNV HSLC-rules (1996)[3] provides significant non-conservative loads for sagging/hogging when the most extreme combinations of Sea State, forward speed, and heading are present.

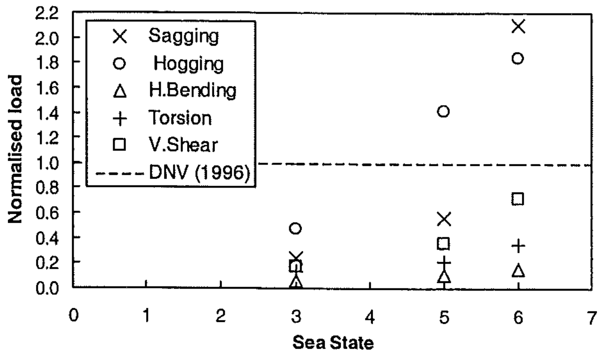

Figure 5: Normalised extreme global loads with respect to DNV HSLC(96) at different Sea States.

A very interesting result was found when the measured extreme sagging and hogging moments were compared with the DNV, HSLC-rules from 1993. The global design loads given by the 1996 revision of the DNV HSLC-rules were reduced significantly from the 1993 revision. The HSLC-rules of 1996 and 1993 give the following values for sagging and hogging moments:

DNV HSLC version	Sag (MNm)	Hog (MNm)
1996	11.1	6.3
1993	27.1	13.0

By comparing the measured extreme sagging and hogging moments with respective HSLC-rules values of 1993, one see that the measured extreme values are lower than the extreme values given by the rules. The normalised extreme values become 0.86 for sagging and 0.89 for hogging. This clearly shows that one should use the HSLC-rules of 1993 for prediction extreme global sagging and hogging moments rather than the 1996 version.

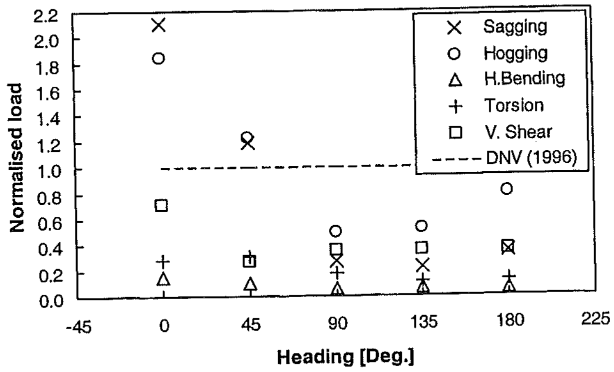

Figure 6: Normalised extreme global loads with respect to DNV HSLC(96) at different headings and Sea State 6

The four maximum global moments for on- and off-cushion states in Sea State 5 are presented in Figure 7. In these test runs only the diesel engines were used to produce thrust, simulating a survival condition with forward speeds varying from approximately 5 to 9 knots. From Figure 7 it is seen that the moments are increased when the air cushion is deactivated, except for slightly decreased in the hogging moment at 45° heading. This general tendency can be explained due to the evenly load distribution effect of the air trapped between the side hulls and the compliant seals at the bow and stern of the vessel. In the off-cushion state the height between the wet deck and the water surface will also be lower, and consequently, the wet deck will experience slamming at an earlier stage in comparison to the on-cushion state. One reason for the decreased hogging value in head sea (45°) may be that the forward speed in the off-cushion state was 5.1 knots, while the forward speed in the on-cushion state was 7.3 knots.

Another general tendency, which is seen in both Figure 6 and Figure 7, is the rapid increase in the sagging- and hogging moment as the heading angle is reduced. This is expected due to the nature of the sagging/hogging motion. However, in Figure 7 it is seen for the off-cushion state that the sagging moment at 45° heading and the hogging moment at 90° heading are not following this tendency. A closer examination of the time series revealed that slamming impacts caused the two maximum moments. A bow flare slamming-like impact, where the bow dives into a large on-coming wave caused the maximum sagging moment. On the other hand a wet deck slamming at amidships caused the maximum hogging moment. This can be seen in Figure 8 as a rapid increase in the moment, followed by a transient whipping condition where the vessel vibrates with a frequency equal to the first sagging/hogging mode of the vessel. The bow flare slamming-like impact is not followed by whipping, which is normally expected and observed in other test series with higher forward speed. The relatively low forward speed during this particular test can be an explanation of the non-existence of whipping.

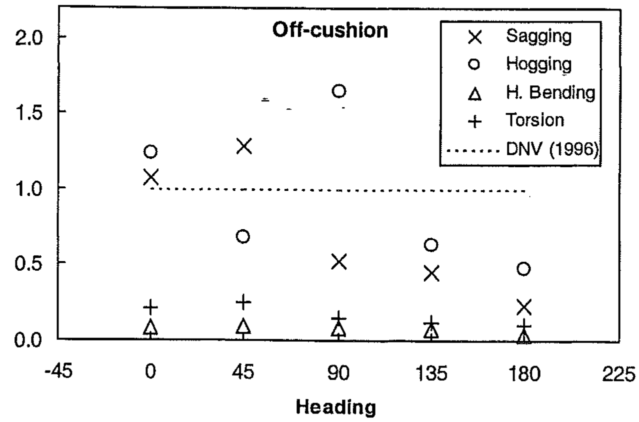

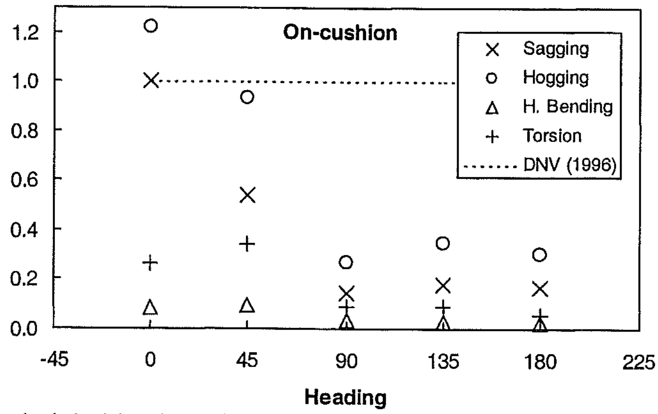

Figure 7: Measured global loads at different headings normalised with respect to the DNV HSLC(1996). The speed varied from 5 to 10 knots depending on the heading.

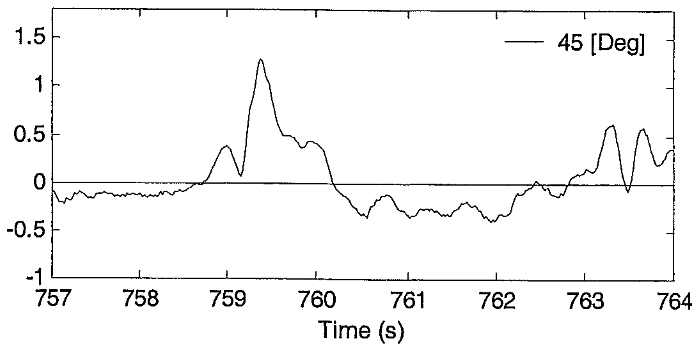

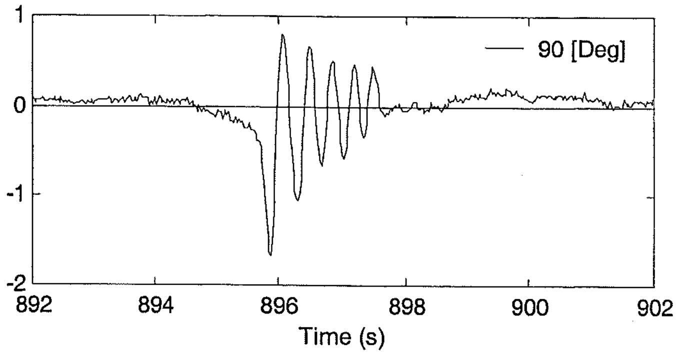

Figure 8: Normalised maximum values for sagging at 45° and hogging at 90° at off-cushion state

The vertical shear force was also measured. The values were small as expected since the maximum shear force has its maximum values near the quarter lengths.

In the extreme Sea State 6-7 with head sea, the vessel experienced a serious wave impact, which could be characterised like something between bow flare and "frontal"/wet deck slamming. The word frontal is used because the upper part of the bow is almost flat and vertical. When this part runs into a large on-coming wave, both the wet deck at the bow and the flat vertical part slam into the wave simultaneously. This impact initiates large vertical and horizontal forces at the bow, followed by a shudder or whipping of the entire ship. This can be seen in Figure 9, where time series of the sagging/hogging moments for the two most extreme bow impact events are shown. All the maximum loads that exceeded the HSLC values were caused by these frontal- or bow flare slamming-like impacts. The results from the full-scale measurements with the SES vessel show that these impact loads have a significant influence on the required maximum global strength of the entire hull, and have to be taken into consideration in global analyses as well. To the author's opinion, this will be highly relevant to ordinary catamaran hulls as well.

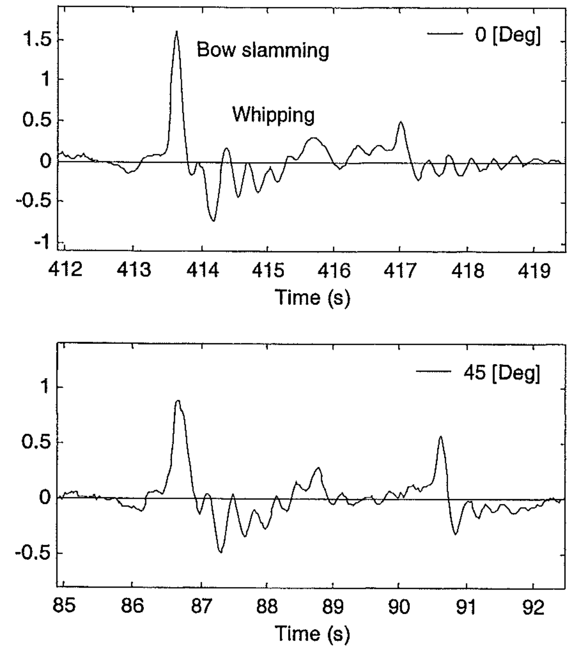

Figure 9: Normalised time series of the sagging moment for the two most extreme bow impact events.

The estimated twisting moments are less than 50% of the moment equal to 9.0MNm given by the HSLC-rules, see Figure 6 and Figure 7. An explanation for the relatively low values may be the extreme Sea State with relatively steep waveforms. A Sea State with longer wave periods may induce larger twisting moments in the 45° and 135° direction, due to increased roll and yaw motions, and it also implies a possibility for an increase in speed. However, to expect that the twisting moment should increase to values close to the DNV moment is not realistic. From experiments with a scaled model, performed by MARINTEK in a towing tank, the pitch connecting (PC) moment was estimated. The PC-moment can, to some extent, be made comparable to the longitudinal twisting moment by dividing with the keel length and multiplying with the distance between the keels. The modified PC-moments and the measured twisting moments, both normalised with respect to the dimensioning moment based on the HSLC-rules, are presented in Figure 10. The results indicate that the HSLC-rules are too conservative with respect to this load component.

Based on examination of the influence strain responses from local panel loads have on the estimated global loads an error of approximately 10% of the measured extreme sagging/hogging moments and twisting moments are to be expected. For further details related to the interrogation system, see Jensen et. al.[5].

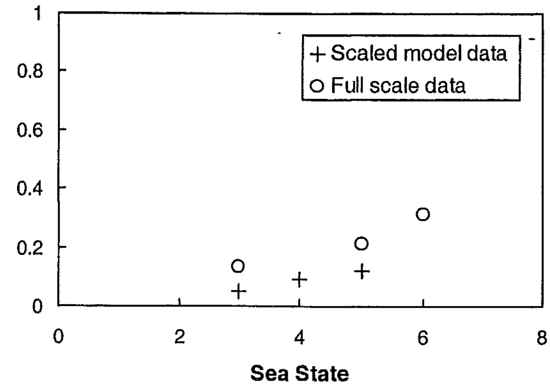

Figure 10: Modified pitch connection moment from a scaled model performed by MARINTEK and estimated longitudinal twisting moment at different Sea States. The moments are normalised with respect to the DNV HSLC(96) dimensioning twisting moment

3. Front panel slamming pressure

In Sea State 6 and in head sea the vessel experienced some impacts that could be described like something between bow flare slamming and frontal/wet deck slamming. The bow dived into a large on-coming wave and green sea was observed on the weather deck. During one of these events the maximum sagging moment was measured.

Another extreme value that was measured during these impacts was a horizontal retardation parallel to the vessel, a_x of 1g ($9.81 m/s^2$). Due to the stealth properties required for this particular vessel the front panels are flat and with a relatively steep angle in relation to the horizontal plane. This blunt bow section will experience large slamming pressure during frontal impacts.

By assuming a linear pressure distribution with the maximum value, P_R, at the centre of the vessel, the following relation between the retardation force and slamming pressure yields:

$$P_R = \frac{2F_R}{BL} \tag{13}$$

B is the height and L is the width of the front panel section. The retardation force, F_R could be determined from Newton's second law.

$$F_R = ma_x \tag{14}$$

The maximum retardation, P_R can now be estimated by setting the displacement of "KNM Skjold" equal to the mass, m=270 000kg and the acceleration, $a_x = 9.81 m/s^2$, in Equation (14), and B = 2.0m and L = 10m in Equation (13). By substituting Equation (14) into Equation (13) the maximum retardation pressure acting on the front panels at the centre becomes

$$P_R = 265\,kPa$$

In local structural design of panels subjected to slamming a constant equivalent slamming pressure is distributed over the whole panel area. The following characteristic impact pressures for the front panels of "KNM Skjold" are given by DNV HSLC(1993) and Allan et. al. (1978):

DNV, HSLC(1993)	$P_{sl} = 105kPa$
Allan et. al. (1978)	$P_{sl} = 272kPa$

By comparing the retardation pressure, P_R with the characteristic impact pressures a large deviation is seen between the value given by Allan et. al.[1], which is approximately equal to the estimated pressure based on the measured retardation, and the pressure given by HSLC(1993).

4. Conclusions

A method for measuring the global loads on a full-scale SES has been successfully applied. The method uses networks of fibre optic Bragg strain sensors attached on a cross section amidships together with pre-established strain values provided by extensive finite element calculations. The system presented can be constructed to continuously, and in real-time, predict global loads.

The measured loads: sagging/hogging moment, horizontal bending moment, and longitudinal twisting moment were compared with characteristic load values given by DNV HSLC-rules (1996). In Sea State 6-7, which represents the operational limit, and in head sea the vessel experienced some impacts that could be described like something between bow flare slamming and frontal/wet deck slamming. During one of these impacts the measured global sagging moment amidships exceeded the DNV design value by a factor of as much as 2.1. This shows that the HSLC-rules (1996) do not provide conservative loads for these extreme events. Furthermore, the dimensioning hogging moment is also underestimated by the HSLC-rules, but it is much smaller than the dimensional sagging moment.

However, a comparison of the measured extreme sagging and hogging moments with the characteristic values in the HSLC-rules of 1993 gives a safety factor equal to 1.1-1.2. This clearly shows that the design sagging and hogging moments as given in the 1993 HSLC-rules looks to be more relevant than the 1996 values for this case.

The longitudinal twisting moment of the hull was never higher than 50 % of the DNV characteristic value. This indicates that the values given by the HSLC- rules (1996) do overestimate the longitudinal twisting moment for SES vessels. The additional experimental data from a scaled model presented in the paper do confirm this. There is also a physical mismatch with respect to the values between the vertical and torsional moment as given by DNV.

Based on measurements of retardation during sea trials the design slamming pressure for the front panels of SES vessels similar to "KNM Skjold" should be in line with figures given by Allan et. al.(1978).

The exciting design basis for "KNM Skjold" were not changed in order to meet the DNV-HSLC rules (1996).

5. Acknowledgements

The authors are grateful to the Norwegian Navy Material Command (SFK) for the permission to publish the results from the tests with "KNM Skjold". The co-operation from SFK is highly appreciated.

6. Rreferences

1. ALLAN, R. G., JONES, R. R., and TAYLOR, D. W., 'A simplified method for determine design-limit pressures on high performance marine vehicles', AIAA/SNAME Advanced Marine Vehicles Conference, USA, 1978.
2. CHANG F.-K., Ed., 'Structural Health Monitoring 2000', Technomic Publ. Co, USA, 1999
3. DNV CLASSIFICATION A/S, 'Rules for classification, High Speed and Light Craft', 1993/1996
4. FALTINSEN, O. M., 'Sea loads on ships and offshore structures', Cambridge University Press, 1990

5. JENSEN, A. E., TABY, J., PRAN, K., SAGVOLDEN, G., AND WANG, G., 'Measurements of global loads on a full-scale SES vessel using networks of fiber optic sensors', J. of Ship Research, 2001(Accepted for publication)
6. JOHNSON G. A., PRAN K., WANG G., HAVSGÅRD G. B. and VOHRA S., 'Structural monitoring of a composite hull air cushion catamaran with a multi-channel fiber Bragg grating sensor system', Structural health monitoring 2000, Technomic Publ. Co, USA, 1999
7. KASHYAP, R., 'Fiber Bragg Gratings', Academic Press, 1999
8. KERSEY A.D., BERKOFF T. A. and MOREY W. W. , 'Multiplexed fiber Bragg grating strain-sensor system with a fiber Fabry-Perot wavelength filter', Optics Letters, 1993
9. KREYSZIG, E., 'Advanced engineering mathematics, 6th ed.', Wiley, 1988
10. ROBERTS, T. J., WATSON, N. L. and DAVIS, M. R. 'Evaluation of sea loads in high speed catamarans', FAST'97, 1997
11. TSAI, S. W., 'Theory of composite design', Think Composites, USA, 1992.

R&D on an advanced ride control system for a high speed mono hull

A.J. Jurgens, MARIN, The Netherlands, a.j.jurgens@marin.nl
F van Walree, MARIN, The Netherlands, f.v.walree@marin.nl
M.X. van Rijsbergen, MARIN, The Netherlands, m.v.rijsbergen@marin.nl
P.G.M van der Klugt, Imtech Marine & Offshore, The Netherlands, pgm.vd.klugt@imtechmarine.nl

Fig. 1: High speed monohull ferry AMD2400

Abstract

The paper describes the hydrodynamic research into the development of an Advanced Ride Control System for a high speed mono hull ferry: the HSF-ARCoS project. The principles of the ride control system will be briefly described, because this is treated in other papers, Klugt et al (2002). The emphasis of the paper will be on hydrodynamics.
For the development of the ride control system it was required to develop a simulation model for a high speed craft operating in waves and/or performing manoeuvres. The basis of a suitable simulation tool was already available in the form of Fredyn. Fredyn is a non-linear motion simulation package for investigating the performance of frigates in moderate to high sea states. For the present purpose Fredyn was adapted to high speed mono hulls by replacing the manoeuvring model for frigates by a dedicated high speed mono hull manoeuvring model and by adding control surface characteristics for T-foils, stabiliser fins, interceptors, trim flaps and waterjet propulsor characteristics. The manoeuvring and several control surface characteristics were obtained from an extensive experimental program in which a series of static and dynamic (PMM) captive model tests were conducted.
A reduced version of the simulation model was developed for use in the control system environment. The performance of the developed control system was judged by connecting the control system software to the Fredyn simulation environment. Thus, a very powerful simulator was obtained which enabled the development and evaluation of advanced motion control systems for fast mono hulls.

1 Introduction

The monohull has always been a very attractive solution as a high-speed vehicle, Keuning et al (2001). Despite competition from advanced marine vehicles such as SES, SWATH, catamarans and others, a vast amount of monohulls is dominating the market of fast vessels.

To extend the capabilities, Van der Giessen-de Noord, Imtech Marine & Offshore and MARIN co-operated in a research project on how the operability of a monohull could be enhanced. Therefore, a new monohull has been designed, combining many aspects in one realistic design. In particular when such a vessel has to be designed for a harsh environment, this leads to a different design than used previously. The inclusion of an advanced ride control system is a feature that can be used to achieve all goals in one design. Thus, Van der Giessen-de Noord may claim to be the first company to have a design environment that enables efficient tailoring of a fast ferry design for any route taking into account all design aspects (including control) and all design requirements (including safety).

In this paper, the necessity of this advanced motion control system is discussed. To tune and design such a control system, an advanced 6 degrees of freedom mathematical model of a point design vessel is made.

2 Maximising the operability

The objective of the ship design is to have an economic feasible concept, capable of achieving sufficiently large earnings for the ship operator in harsh environments. To achieve this, at a target speed of around 50 knots, the design had to be revolutionary. To achieve the speed, an arrangement consisting of 3 water jet propulsion units is designed. These are incorporated under a flat aft body.

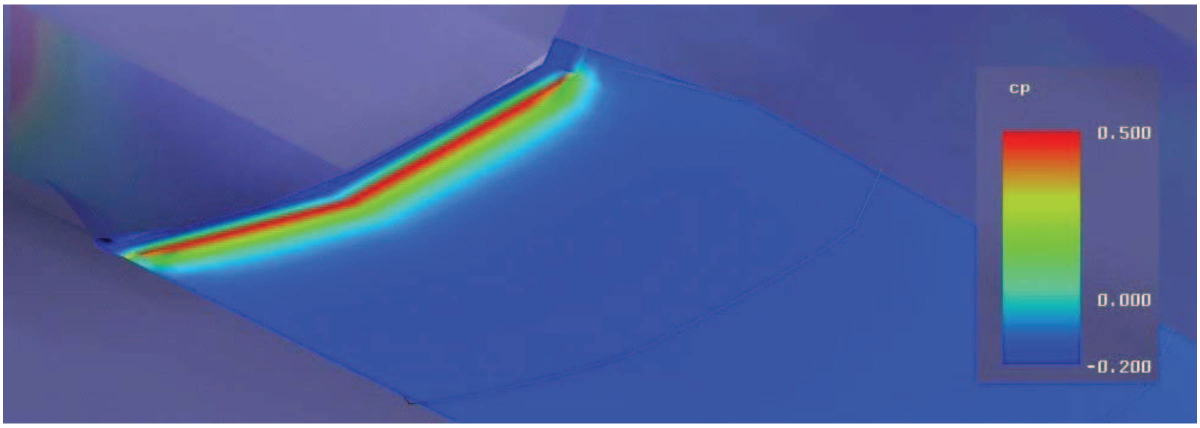

Fig. 2: Pressure distribution at trim wedge

The fore body of the vessel had to have very pronounced V shape. The forefoot is made extremely deep, without going to an axe-bow, see Keuning et al (2001), which was for the present design regarded as impractical. The presently chosen forefoot is a compromise between the maximum draught requirements and the maximum bow flare supposedly present. A vertical bow below the full load waterline gives the underwater hull shape more buoyancy forward, which results in a smaller wetted surface for the same relative displacement. This results in a significant reduction of the viscous resistance. Also the hull maintains a long waterline length in various running trim conditions. Such a vertical bow minimises the amount of bow impacts and added resistance in waves.

The flat aft body results in a deceleration of the flow in the aft area, as can be seen in Fig. 2. This deceleration will result in a reduction of the local wave trough, which results in a wave making resistance. To avoid this at the high speed of 50 kn, a trim wedge was designed. The performance of the trim wedge is validated by RAPID[1] calculations, see Fig. 2, and by means of model tests. Table 1 details the principal characteristics of the vessel and Fig. 3 presents the body plan.

[1] RAPID calculates the steady inviscid flow around a ship hull, the wave pattern and the wave resistance. It solves the exact, fully non-linear potential flow problem by an iterative procedure, based on a raised-panel method.

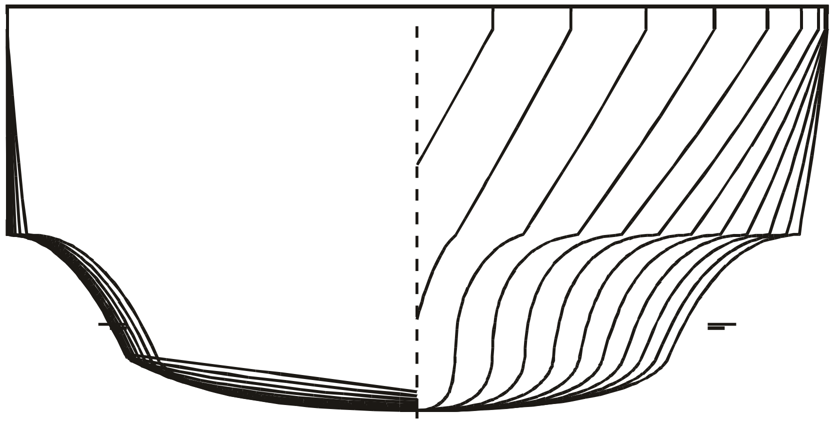

Fig. 3:AMD2400 body plan

In assessing the limits of the operability of the high speed ferry in waves, an operability analysis with and without ride control system is performed. Two routes were considered, one crossing the Irish Sea between England and Ireland and one from Northern France to Ireland.

The tools used were: Wasco and Gulliver. Wasco performs an analysis based on global wave statistics and provides the average sustained speed and inoperability percentages, while the Gulliver tool uses actual hind cast data for wind and waves and produces time domain results. These results can be analysed to produce a wealth of operability data, for instance the variation in trip duration due to both voluntary and involuntary speed reductions. Such data may be of high interest to operators for scheduling routes.

Table 1: Principal characteristics of the vessel

Dimension	Unit	Magnitude
Length between perpendiculars	[m]	123.7
Length overall	[m]	142.0
Breadth	[m]	22.0
Design Draught	[m]	2.60
Deadweight	[ton]	1365
Length-Breadth ratio	[-]	7.52
Breadth-Draught ratio	[-]	8.46

Because of the propulsion system, a skeg was not desired. The shape of the aft end with a B/T ratio of 7, and the shape of the forefoot lead to an inherent directionally instable vessel. This is not strange compared to modern vessels. A course keeping / ride control system can cope with this very well. The challenge might be to operate this course instable vessel in stern quartering waves. The speed, wave frequency and wave direction may result in a low wave encounter frequency with large excitation forces. In these cases, high performance is asked from the control system.

3 Controls and the control system

In principle each control surface may be configured to control any motion as long as it can influence that motion. However, to simplify the research and to improve the fundamental understanding during the first phase of the project, a distinction has been made between the primary responsibility of a control surface and the secondary responsibility.
To steer the vessel, a number of controllers are defined:

- Interceptors; will be used for steering the vessel primary and secondary for roll stabilising,
- Buckets; of the water jet are used for jet thrust deflection and hence for steering and braking,

- Trim flaps; are used primarily to reduce heave and pitch motions and hence reduce accelerations and bow impacts and secondary for controlling the roll motions,
- Fin stabilisers; are used to control the roll motions,
- T-foil; at about 1/5 of the length from the bow will be used to control heave and pitch motions.

The motions of the vessel are controlled by a combination of these actuators The challenge is to operate this kaleidoscope of actuators in such a way that the motions are improving and the earning capacity of the vessel is maximised. An advanced computer model is designed to do so. The parallel between the modern fighter airplanes can be made. Only by including advanced control systems, these fighters can operate at the maximum of the capabilities. This philosophy is also used for the vessel under consideration. By the introduction of the Advanced Ride Control System, the operability is maximised to a level that cannot be reached by human control.

In the system design of the ride control system, a ship model plays a crucial role. The mathematical model of the ship is used in the control domain, as the prediction part in the Kalman filter, to calculate the controller settings and the allocation coefficients and as core of the ship motion simulator.
The filter algorithms are designed to reject undesired frequency components. In case of roll control, they remove the low-frequency roll. In case of heading control they remove high-frequency heading fluctuations. The filter gains are derived on-line from the coefficients of the internal hydrodynamic model and the properties of the disturbances. Besides filtered motions, the filter algorithms provide derived signals such as the current estimation, the mid-ship position and the mid-ship u-v speed.
The control algorithms use fuzzy-set algorithms to adjust themselves to changing conditions. They take into account not only the impact of the disturbance, but also the changing limitations of the control surfaces. Thus, in all weather conditions they are automatically adjusted for optimal performance within the constraints posed by either the control surfaces or the operator.
The allocation algorithm distributes the control actions over the available control surfaces. It takes into account variations of limitations such as the T-foil cavitation limit that depends on the forward speed. When control surfaces fail or are disabled by the operator, the allocation algorithm automatically re-distributes the control actions.

It goes without saying that to design and test such a ride control system, an adequate description of the functions of all the actuators and of the subject vessel itself is of importance. In the following section, these forces and their particulars are dealt with.

4 Model tests to determine forces

One of the main challenges of such a high-speed vessel is that forces are linked to each other. Examples are the influence of the trim angle on the destabilising forces. A bow-down trim causes a destabilising moment and vice versa. When the vessel encounters trim changes during sailing or as function of trim flap and interceptors, this will effect the motions. Instabilities have been reported in both longitudinal and lateral directions with motions ranging from rapid loss of running trim, progressive heeling, broaching or a sudden combined roll-yaw motion, possibly resulting in crew injury to craft loss. Therefore, incorporating all six degrees of freedom into the mathematical model becomes increasingly important, see Plante et al (1998) and Toxopeus et al (1997).

Secondly, it is the intention to steer the vessel primarily with the interceptors. If steered, the interceptors are mainly generating a heeling moment. This heeling moment causes a heel angle, and the heel angle causes a turn. Consequently, the ship is steered with the so-called heel-yaw-coupling. Information on how to do this was not present. These are therefore investigated.

To quantify the characteristics of control surfaces and hull, model tests and calculations are carried out. A model has been built to a scale of 1:23.86. Control surfaces are mounted on the vessel and the resulting control forces are recorded. So-called captive model tests are performed able to measure the forces that the control surfaces generate on the vessel. The large unknown factor were the reaction forces of the vessel itself. The reaction forces of the ship hull due to motions such as drifting and yawing had to be quantified. The performance of the actuators T-foil and fins stabilisers was obtained from existing computational methods, since much confidence was placed in the calculation algorithms for these actuators, see Walree (1999). In view of the high speed of the vessel, the effects of cavitation on the characteristics of the T-foil were investigated. Cavitation observations and force measurements have been conducted for a generic T-foil model in the cavitation tunnel.

The wave excitation forces are calculated using different sources. The Froude Krilov component of the wave excitation force is obtained by the integration of the pressure distribution over the wetted surface of the hull using the undisturbed actual wave height (non-linear) and the instantaneous trim and sinkage. In Keuning (1994) and Quadvlieg and Keuning (1993), it is shown that this has an important effect. For the wave radiation forces (wave diffraction) the so-called strip theory is used.

The high frequent reaction forces are thought to be mainly influenced by potential flow effects. Hence also for these forces, the potential theory, and in particular the strip theory, is used to calculate strip-wise the added mass and the damping of each section in the frequency domain. To achieve the forces in the time domain, retardation functions are created based on the added mass and damping. The high-frequent reaction forces are hence linearised.

4.1 Experimental scheme

In total, 201 tests were conducted to determine the mathematical model of the vessel with all its control surfaces. These tests have been divided into 20 series. Each series had its specific purpose of measuring the influence of a certain variable. Only those aspects that could not be determined using calculation methods are tested in the model basin. For other aspects only parts of the calculations methods could be used, and several factors had to be derived from these tests to fill in the unknowns. In Table 2, the test series are identified and their objectives are explained.

Table 2: Measured conditions

Series	Type of test	Values of variables	Speeds [kn]	Objective = determination of….
		Resistance		
0	Resistance tests	Speeds from 0 – 45 kn in 6 steps	Var.	.. resistance, lift and trimming moment as a function of Fn
10	Under / overload tests of waterjet	Speeds from 0 – 45 kn in 5 steps	Var.	.. thrust-speed relation for waterjets
11	Heel angles	ϕ = 5, 10, 15 deg	22.5 – 45	.. asymetry in steering due to heel angles
15	Trim angles	θ = -0.5, 0.5, 2.5 deg	22.5 – 45	.. changes in resistance due to trim
		Pure Drift		
1	Drift tests	β = -10, -5, -2.5, 2.5, 5, 7.5, 10, 20, 30 deg	18, 25, 35, 45	.. destabilising forces due to drifting
	Thrust influence on lateral force	β = -20, -10 deg	25	.. drifting influence on thrust
12	Drift and heel tests	ϕ = 5, 10, 15 deg; β = -10, 5, 2.5, 0, 2.5, 5, 10, 20 deg	25	.. heel effect on the destabilising force
16	Drift and trim tests	θ = -0.5, 0.5, 2.5 deg; β = -10, 5, 2.5, 0, 2.5, 5, 10, 20 deg	25	.. trim effect on the destabilising forces
		Pure Yaw		
2	Yaw tests	γ = 0.1, 0.2, 0.4, 0.6	18, 25	.. stabilising forces due to rotating
17	Yaw and trim tests	θ = -0.5, 0.5, 2.5 deg; γ = 0.2, 0.4, 0.6	25	.. trim angle effect on the stabilising forces
13	Yaw and heel tests	ϕ = 5, 10, 15 deg; γ = 0.2, 0.4, 0.6	25	.. heel effect on the stabilising force
		Yaw with drift		
3	Yaw tests with drift angles	γ = 0.2, 0.4, 0.6; β = 10, 20 deg	18, 25	.. combination of stabilising and destabilising forces
18	Combination of drift, trim and yaw	θ = -0.5, 0.5, 2.5 deg; β = 10 deg; γ = 0.4	25	.. verification
14	Combination of drift, heel and yaw	ϕ = 10 deg; β = 10 deg; γ = 0.4	25	.. verification
		Control aspects		
4	Bucket deflection angles	δ = -10, -5, 0, 5, 10, 15, 20 deg	25, 45	.. waterjet steering forces
5	Static trim flap tests with opposite angles	α = -10, -5, 0, 5, 10, 15 deg	45	.. trim flap forces
6	Static interceptor execution tests	zi = 25, 50, 75, 150, 200, 300, 500 mm	45	.. interceptor forces
7	Static trim flap tests with equal angles	α = -10, -5, 0, 5, 10, 15 deg	45	.. trim flap forces
8	Dynamic trim flap tests	f 0.25 to 2.0 Hz, α = 5, 10, 15, 30, 45 deg	35, 45	.. frequency dependence of trim flap forces
9	Dynamic interceptor tests	f 0.25 to 2.0 Hz, α = 50, 125, 250 mm	35, 45	.. frequency dependence of interceptor forces

4.2 Experimental set-up

The measurement instruments comprised one six-component transducer fixed into the model, positioned above the centre of floatation, as can be seen in Fig. 4. The tests were carried out with the ship captive in all directions. Using the components of the transducers, three forces and three moments about the centre of reference could be found. Additionally, the actuation forces on the control surfaces were measured to obtain the reaction forces as well as the hydrodynamic pressure in front of the trim flaps.

Fig. 4: Model of AMD2400 under Computerised PMM

5 Hull forces

In this section, some particularly interesting results of the measured forces and moments will be presented.

The drift-heel relations are illustrated in Fig. 5, in which Y' N' and K' are given versus the drift angle for six heel angle conditions. It is observed that the Y-forces as function of heel angle are slightly influenced, with larger influences at higher drift angles. The yawing moment N' is equally influenced for all drift angles. The largest influence is on the roll moment K', but this is mainly non-linear.
So, a heel angle of 5° causes a significant turning moment on the vessel.

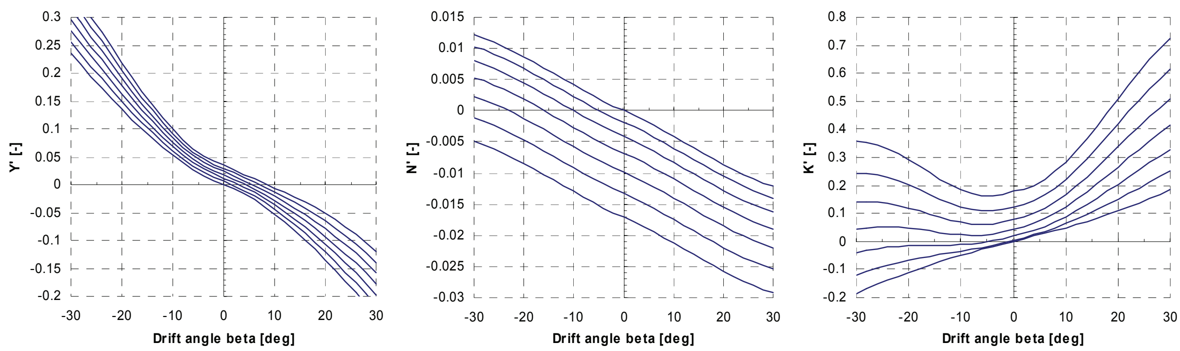

Fig. 5: V_s = 35kn; β = -30:30; θ = 0.5; ϕ = 0, 2.5, 5, 7.5, 10, 12.5, 15

It can be concluded from the figures in Fig. 6 that the hydrodynamic forces acting on a ship hull change remarkably as function of the heel angle ϕ. Fig. 6 shows that values of the lateral force Y' linear change with the heel angle ϕ. Fig. 6 also shows that value of the yaw moment N' become large as heel angle ϕ becomes large.

As a result the point of application of lateral force shifts forward as the heel angle ϕ increases. This results in a reduction in directional stability.

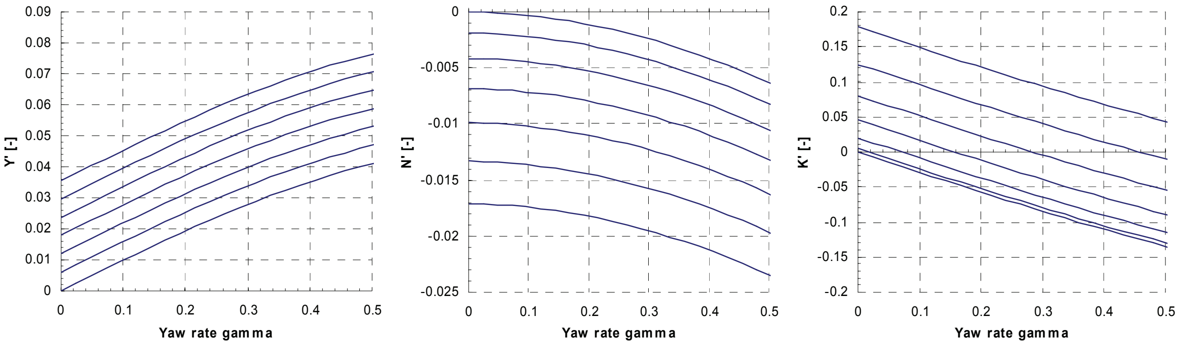

Fig. 6: V_s = 35kn; γ = 0:0.5; θ = 0.5; ϕ = 0, 2.5, 5, 7.5, 10, 12.5, 15

Fig. 7 shows the yaw-drift relation, indicating that these are significant non-linearities in combining drift and yaw motions.

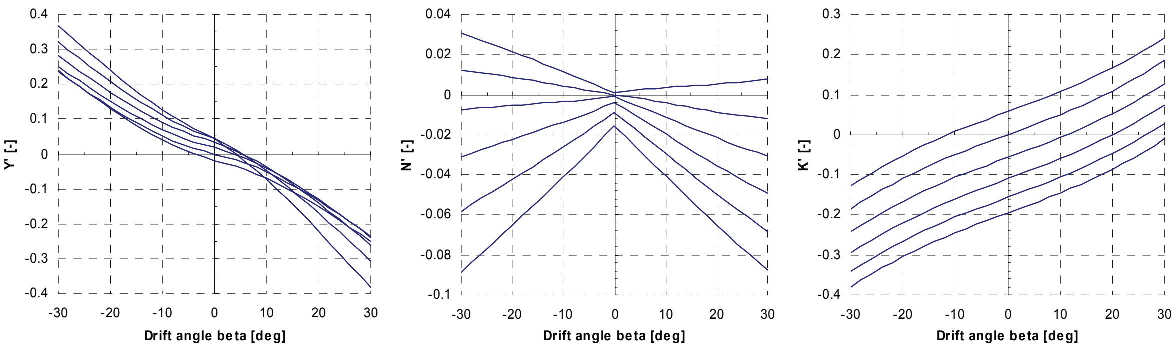

Fig. 7: V_s = 35kn; β = -30:30; γ = -0.2, 0.0, 0.2, 0.4, 0.6, 0.8; θ = 0.5; ϕ = 0

It was already indicated that trim-yaw coupling will be important for directional stability. In Fig. 8, the influence of trim angle on the stabilising forces is given. The side force is influenced a lot, contrary the yaw and roll moment.

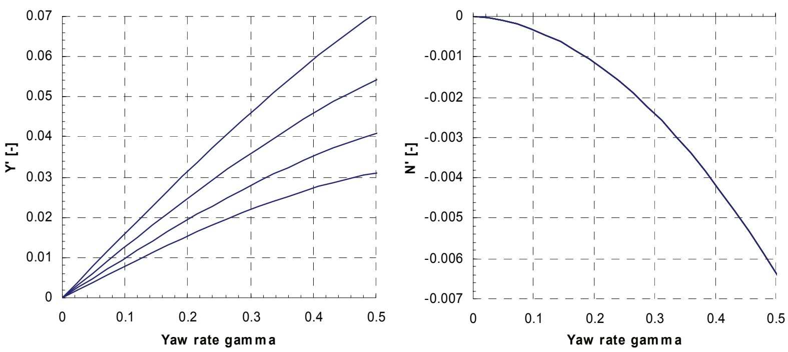

Fig. 8: V_s = 35kn; β = -30:30; θ = -0.5, 0.5, 1.5, 2.5; ϕ = 0

For a range of Froude numbers, the lever arms of stabilising and destabilising moments can be calculated based on the fits. This way, the straight-line stability of the vessel is expressed. In Fig. 9, the straight-line stability is indicated. The graph indicates that at lower speeds, the vessel is directionally stable, for the trim by stern condition, but at higher speeds, the instability grows. The amount of instability is, however, limited, so with a sufficiently good autopilot, the vessel should be kept on course without any problem. Note that this is a function of the trim angle. For different trim angles, the arms will change. This has an advantage for the higher speeds, as there will be a larger trim by stern, which is positive for the directional stability. The bow-down trim condition should be avoided since the vessel is straight-line instable in this condition.

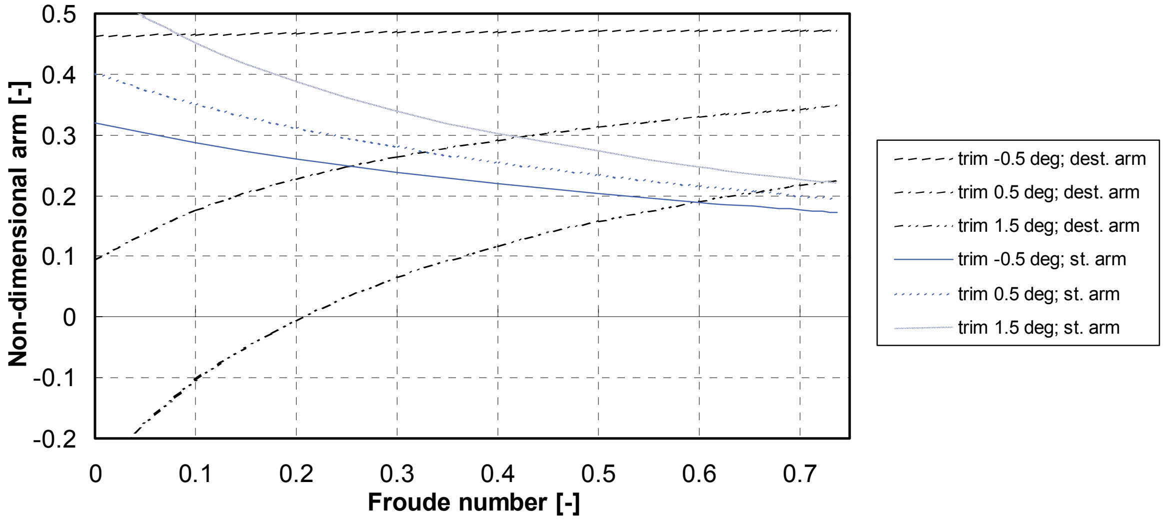

Fig. 9: Stabilising and destabilising arms

6 Control surfaces

To quantify the impact of control surfaces, a set of model tests are performed with the vessel equipped with these control surfaces. So-called captive model test are performed enabling to measure the steering and control forces. As a result of the high velocity of the vessel, the risk of cavitation on certain control surfaces is realistic.

Fig. 10 shows the relation between the lateral force and the yaw and roll moment as a function of interceptor immersion. Mark the large linear influence on the roll-moment as function of interceptor immersion.

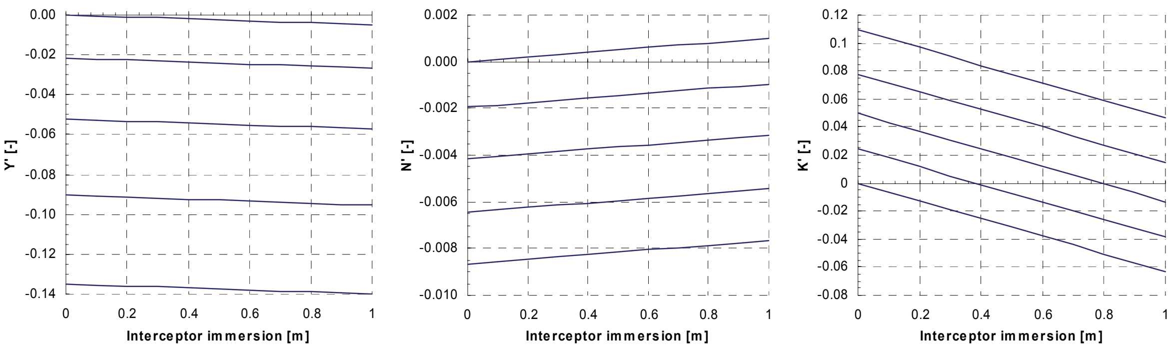

Fig. 10: V_s = 35kn; z_i=0:1 m; β = 0, 5, 10, 15, 20 deg; θ = 0.5 deg; ϕ = 0 deg

6.1 Frequency dependency

The frequency dependency of forces generated by trim flaps and interceptors is investigated. Test results described so far were essentially steady tests which results can be used for low frequency manoeuvring in a quasi-steady manner. However, during operation in waves the frequencies of motion are an order of magnitude larger resulting in frequency dependent forces. The same can be expected for hull forces exerted by control surfaces. Therefore, a series of tests has been performed to determine the frequency dependency of hull forces due to oscillatory trim flap and interceptor excursions. The time series of the forces were harmonically analysed to obtain the amplitude of the force and moment components and their phase leads relative to the oscillatory motion. Fig. 11 shows for the trim flap that the dependence of the longitudinal force (Cx) and pitch moment (Cm) coefficients on both the amplitude (a_i) and frequency (ω) of oscillation is significant. The force and moment coefficients have been made non-dimensional on basis of the dynamic pressure, the control surface area, deflection angle and position relative to the reference point. The maximum frequency corresponds to high speed operation in head waves. The efficiency of the trimflap increases with frequency and so does the resistance. Since the frequency dependence of the vertical force was found to be small, most of the variations in pitch moment is due to variations on the vertical force centre of effort. The variations in phase angles were found to be relatively small. For interceptors the frequency dependence was found to be smaller than for the trim flaps shown here.

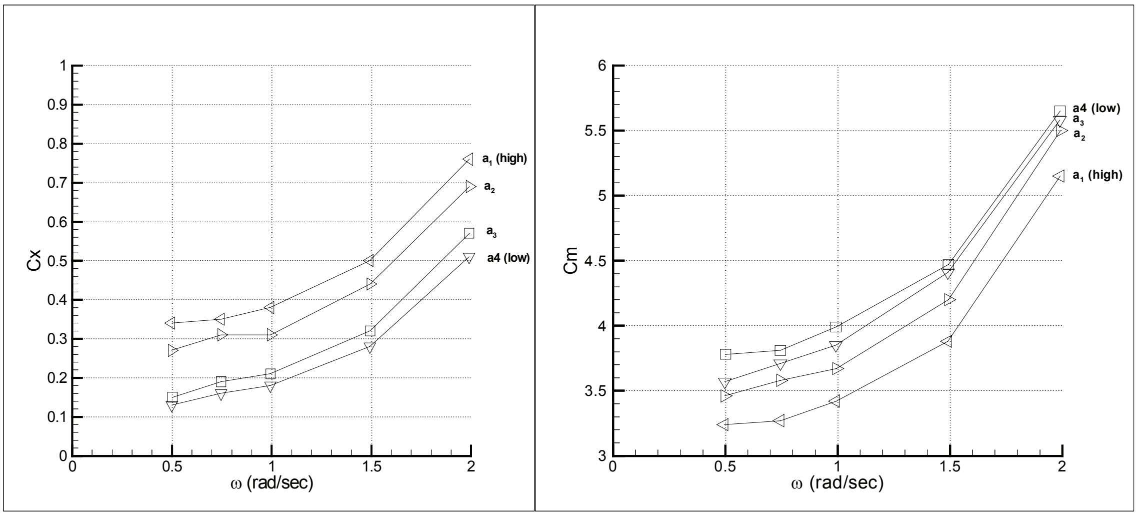

Fig. 11: Dependence of longitudinal force and pitch moment vs. frequency of oscillation

6.2 Unsteady cavitation

At speeds above about 28 knots, cavitation may have a significant effect on the characteristics of stabiliser and T-foils. In order to quantify these effects of cavitation on the forces and moment of a T-foil, a series of model scale cavitation tests was conducted.

A semi span of a T-foil with an aspect ratio of 1.56 was manufactured at a scale of 1:25. NACA 66-012 sections were chosen as a compromise between good cavitation and good drag characteristics. The foil was mounted horizontally on the wall of the test section of MARIN's Large Cavitation Tunnel. Turbulence of the flow over the foil was induced by strips at the leading edge and at 40% of the chord length with carborundum grains with an average diameter of about 60 μm. The forces (normal and tangential to the chord of the foil) and moment on the foil were measured by a 3 component balance. Fig. 12 shows the sign convention as used for the cavitation tests.

The cavitation tests were conducted at three cavitation numbers σ = 4.47, 1.00 and 0.68, simulating ship speeds of 15.8, 33.4 and 40.5 knots respectively. Both steady and unsteady pitch angles were tested. In the unsteady tests the pitch angle was varied sinusoidally with in total 11 combinations of amplitude and frequency as shown in Table 3. In the steady tests 6 angles of attack (α) were tested between -5 and 20 degrees. The average Reynoldsnumber of the foil during the tests was $6.5 \cdot 10^5$.

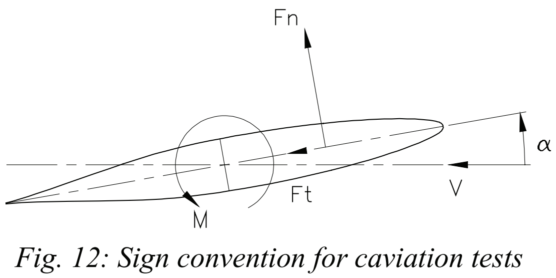

Fig. 12: Sign convention for caviation tests

k [-]	T [s]	ω [rad/s]	A [deg]
0.0375	6.90	3.64	5, 10, 15
0.0750	3.45	7.28	2.5, 5, 10
0.1125	2.30	10.93	2.5, 5, 7.5
0.1500	1.73	14.57	2.5, 5

Table 3: unsteady test conditions

Observations of the foil have been made at all cavitation numbers. Only at σ = 1.00 and 0.68 cavitation was observed. Fig. 13 shows the foil in a steady condition at α = 10 degrees. Developed sheet and tip vortex cavitation is present. The structure of the sheet shows that risk of erosion is present at this angle of attack. Fig. 14 shows that in an unsteady condition, the cavitation extent lags relative to the angle of attack.

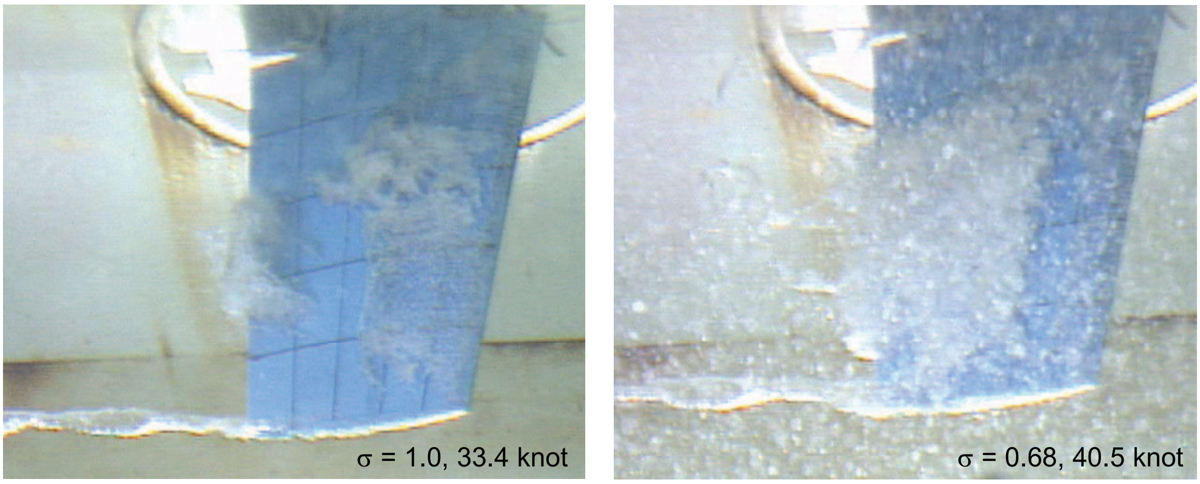

Fig. 13: Cavitation observation in steady condition, α = 10 degrees

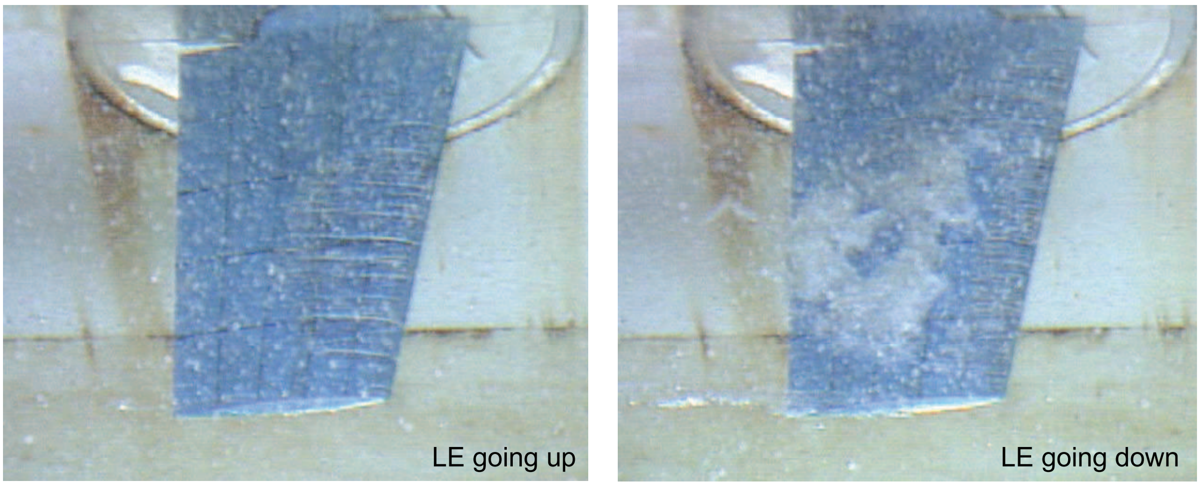

Fig. 14: Cavitation observations in unsteady condition: k = 0.075, A = 10.0 degrees, σ = 0.68 (40.5 kt), α = 7.5 degrees

Fig. 15 and Fig. 16 show a comparison of the normal force (C_N) and moment (C_M) coefficients in steady and unsteady conditions. The unsteady coefficients are synthesized from 5 harmonic coefficients which explains their smooth appearance. Clearly, a significant effect of cavitation on the normal force coefficient (C_N) is present at the highest speed for α > 10 degrees. The α - C_N relation changes from a line in the steady condition into a clock-wise rotating loop in the unsteady condition, which corresponds with a phase lead of C_N relative to α. Preliminary calculations show that this phase lead is caused by a combination of the position of the pitch axis (at 0.5 of the maximum chord) and 3D effects related to the small aspect ratio of the foil. Due to the fact that the cavitation extent has a phase lag relative to C_N in the unsteady condition, 15% higher maximum values are reached than in the steady condition.

The effect of cavitation on the moment coefficient is even larger and starts above α = 5 degrees. Due to unsteady effects, the α - C_M relation becomes an anti clock-wise rotating loop, which corresponds with a phase lag of C_M relative to α.

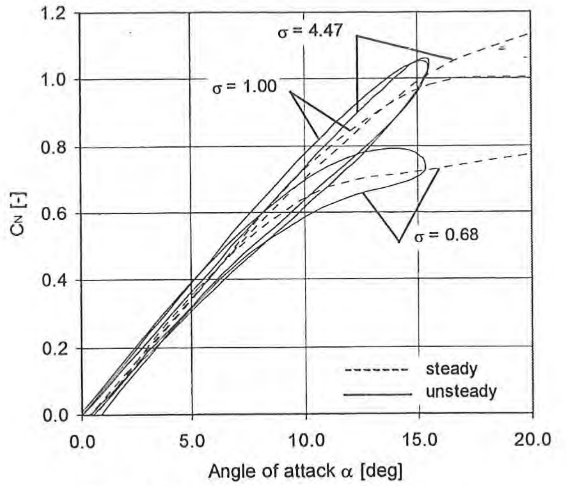

Fig. 15: Normal force coefficient

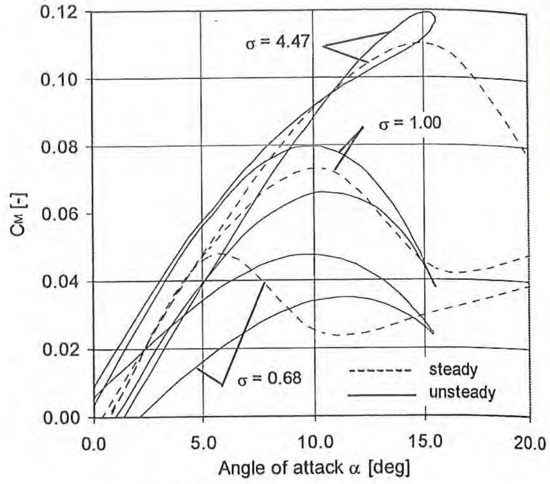

Fig. 16: Moment coefficient

Some interesting effects can be seen in the time signal of the normal force as shown in Fig. 17 and Fig. 18. At the lowest speed (the non cavitating condition), no significant variations in C_N are measured. At the highest speed however, a strong vibration which is caused by the periodic shedding of sheet cavitation is recorded. Measurements at lower oscillation amplitudes indicate that a risk of vibrations is present from $\alpha > 10$ degrees.

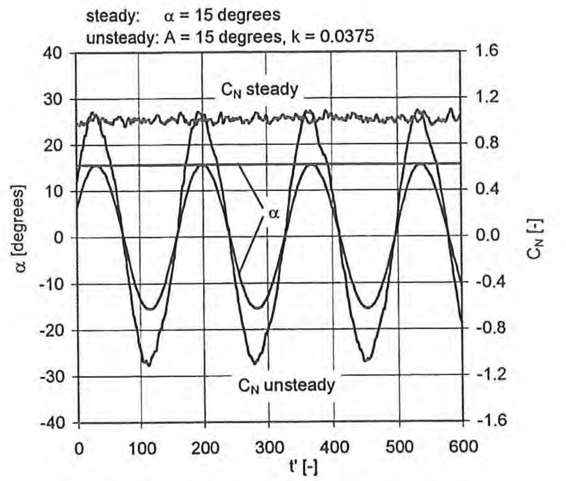

Fig. 17: Time signal at $\sigma = 4.47$

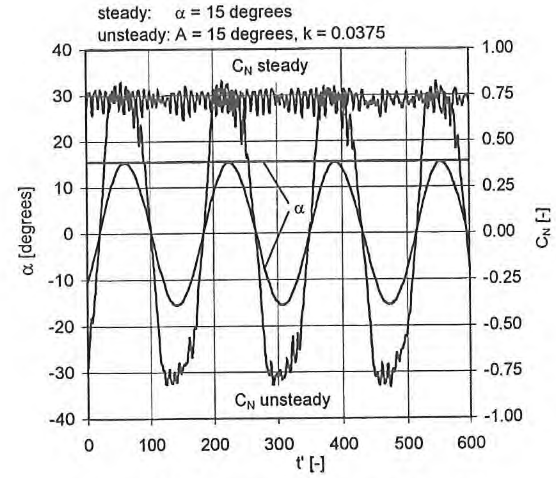

Fig. 18: Time signal at $\sigma = 0.68$

Concluding, it can be stated that cavitation tests with stabiliser or T-foils in both steady and unsteady conditions are essential for high speed ferries. The present tests give a good indication which hydrodynamic characteristics can be expected in general, but it is recommended that for a specific foil with a different position of the pitch axis, aspect ratio or an additional heave motion, specific model scale tests should be conducted.

7 Example cases and simulations

After having carried out the model tests, a mathematical model is developed in 6 degrees of freedom. This mathematical model has been incorporated in the time domain computer simulation program Fredyn. Fredyn is a time domain model based on a strip theory analysis of the ship's motions. The control surface and manoeuvring models are also included in a non-linear time domain simulation tool, which will subsequently be linked to the Imtech ride control system running on a separate computer, which was in turn linked to the computer program on which Fredyn is operating. This is

1. Sensitivity analysis
2. Change in initial position or velocity to determine the ability of the modelled ship to return to the equilibrium position
3. Change in manoeuvring mode
4. Change in seakeeping mode
5. A ride control case study
6. Correlation to free-sailing manoeuvring and seakeeping tests

<u>Ad 1. Sensitivity analysis</u>
The program seems to be stable for the different input changes, i.e. small changes in input results in a small change in output.

<u>Ad 2. Change in initial position or velocity</u>
For the changes in initial position or velocity, the model has to return to its initial equilibrium state. After a slight disturbance in the initial sway, yaw or roll velocity the model will keep a certain rate of turn and will not go back to her initial position. This behaviour corresponds to a directional instable vessel. For the other changes in initial position, the model returned to its initial equilibrium state.

<u>Ad 3. Change in manoeuvring mode</u>
Results of the spiral test simulation conducted using the Fredyn simulation at an approach speed of 35 kn and a stern-trim angle of 0.5 are presented in Fig. 19.

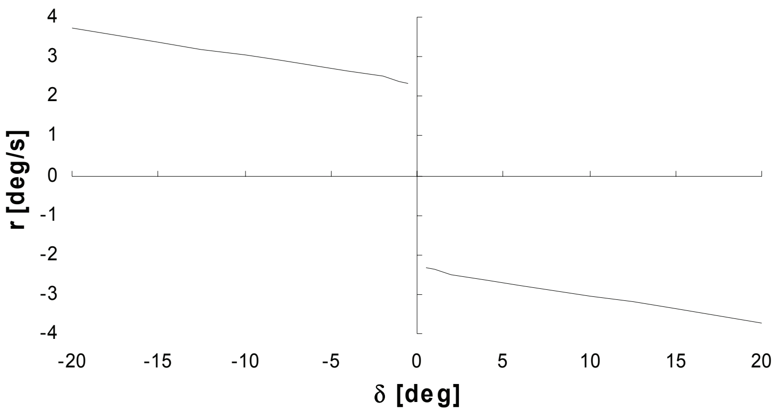

Fig. 19: Spiral test

From the spiral test it can be concluded that the model is straight-line unstable. The instability loop for bucket angles resulting in rates of turn between 0.75°/s and -0.75°/s was not determined.

<u>Ad 4. Change in seakeeping mode</u>
A number of seakeeping simulations has been performed in head and bow quartering seas. Which are generally considered as the most critical sea condition for high speed craft. The reduction in vertical accelerations due to control of the pitch motion by means of trim flaps and T-foil was the main target of the investigation. The course keeping in stern quartering waves which is a combined seakeeping and manoeuvring problem is investigated as well. This proved to be very useful since this wave condition turned out to be critical with respect to course keeping and broaching.

<u>Ad 5. A ride control case study</u>
As expected the fast ferry model seems to be rather sensitive to a large roll motion. The roll motion induced by the interceptor immersion has a larger impact on the rate of turn than the interceptor immersion it self. The control system can only stop such a yaw velocity in an adequate manner if it activates the buckets as well. This behaviour could be solved in different ways:

– By more gradually changing the heading, the initial roll angle remains low enough so that this large coupling does not occur, i.e.. lower interceptor immersion rates.
– By using the buckets in addition to the interceptors, enough yawing moment is available to counter-act the yaw velocity.
– Or simultaneously use the interceptors to reduce the roll angle as well as to steer.

Thus, these early experiments indicated that it is possible to obtain excellent manoeuvring behaviour with advanced autopilot.

Ad 6. Correlation to free-sailing manoeuvring and seakeeping tests
To get an impression of the results and the order of magnitude of the accuracy of the mathematical description of the model and its control surfaces, free-sailing model tests are scheduled.

8 Conclusions

In this paper, a time domain computer simulation program to predict the behaviour of a high-speed ferry in real life conditions for six degrees of freedom is described. The formulations used in the program were based on experiment data, additional theoretical and empirical descriptions.
The manoeuvrability characteristic changes remarkably depending on speed, heel and trim.

By the introduction of an advanced combination of autopilot, speed pilot and ride control system its possible to stretch the envelope of the operability of a directional instable high-speed ferry.

Although the validation of the tool with the free-running model tests has yet to be conducted. The present tool is supposed to be of value. The computer program can act as a powerful test bed for the development and extensive testing of the advance motion control system.

References

Keuning, J.A., Toxopeus, S.L. and Pinkster, J. (2001). "The Effect of Bowshape on the Seakeeping Performance of a Fast Monohull". *Proceedings of FAST 2001 Conference*.
Keuning. J.A. (1994). “The non-linear behaviour of fast monohulls in head waves”. *PhD-thesis*, Delft.
Klugt, P.G.M. van der, Walree, F. van and Pauw, P.M. (2002). “The HSF-Arcos research project”. *HSMV Napels*.
Plante, M, Blok, J.J., Toxopeus, S.L. and Keuning. J.A. (1998). "Hydrodynamic manoeuvring aspects of planing craft”. *International Symposium and workshop on Force Acting on a Manoeuvring Vessel*, Val de Reuil, France
Quadvlieg, F.H.H.A and Keuning. J.A. (1993). “Dynamic behaviour of fast monohulls” *RINA Conference on high speed passenger craft*.
Toxopeus, S.L., Keuning, J.A. and Hooft, J.P. (1997). "Dynamic stability of planing ships" *International symposium and seminar on the Safety of high speed craft. RINA, London*, United Kingdom.
Walree, F. van (1999). ”Computational Methods for Hydrofoil Craft in Steady and Unsteady Flow”. *Ph.D. Thesis, Delft University of Technology*.

Nomenclature

In this report the following definitions and sign conventions are used:

DESIGNATION	SYMBOL	UNIT	POSITIVE FOR
Froude number $Fn = V_s * (g\ L_{pp})^{-0.5}$	Fn	-	Forward speed
Ship speed $V_s = (u^2 + v^2)^{0.5}$	V_s	m/s	Forward speed
Roll angle	ϕ	deg	SB down
Trim angle	θ	deg	Bow up
Yaw angle	ψ	deg	Bow to SB
Longitudinal velocity $u = V_s * \cos\beta$	u	m/s	Directed forward
Transverse velocity $v(x) = V_s * \sin\beta + x * r$	v(x)	m/s	Directed to SB
Yaw rate	r	deg/s	Turning bow to SB
Bucket deflection angle	δ	deg	Trailing edge to PS
Trimflap angle	α		Downward positive
Interceptor immersion	z_i		Downward positive
Drift angle $\beta = \arctan(v/u)$	β	deg	Positive transverse speed
Dimensionless rate of turn $\gamma = (r\ L_{pp})/V_s$	γ	-	Turning bow to SB
Global transverse force on the ship	Y	kN	SB positive
Global roll moment on the ship w.r.t. waterline	K	kNm	SB down
Global yawing moment on the ship w.r.t. midship	N	kNm	bow to SB
indication for non-dimensional coefficient	‘		
Centre of reference, positioned at crossing half L_{pp}, centreline and waterline	O		
amplitude of oscillation	A	deg	
average chord length	c	m	
pitching moment coefficient = $M/(½\rho V^2 Sc)$	C_M	-	
normal force coefficient = $F_N/(½\rho V^2 S)$	C_N	-	
tangential force coefficient = $F_T/(½\rho V^2 S)$	C_T	-	
normal force	F_N	N	
tangential force	F_T	N	
acceleration of gravity	g	m/s^2	
shaft submersion	h	m	
reduced frequency = $\omega c/(2V)$	k	-	
pitching moment	M	Nm	
cavitation tunnel ambient pressure at pitch axis	P_A	Pa	
atmospheric pressure	P_0	Pa	
vapour pressure	P_V	Pa	
Reynolds number = Vc/ν	Re	-	
lateral surface foil (projected area)	S	m^2	
dimensional time	t	s	
non dimensional time = 2Vt/c	t'	-	
period of oscillation	T	s	
test section velocity	V	m/s	
kinematic viscosity of water	ν	m^2/s	
density of water	ρ	kg/m^3	
cavitation number = $(P_0 - P_V + \rho gh)/(½\rho V^2)$	σ	-	
angular frequency	ω	s^{-1}	

Wake Wash Minimisation by Hull Form Optimisation Using Artificial Intelligence

Kourosh Koushan; Sverre Steen; Rong Zhao

MARINTEK, Norwegian Marine Technology Research Institute
P.O.Box 4125 Valentinlyst, 7045 Trondheim, Norway
Kourosh.Koushan@marintek.sintef.no Tel. +47 73595913 Fax +47 73595870

Abstract

This paper describes the procedure developed at MARINTEK for automatic optimisation of hull lines to reduce the wake wash generated by a ship within the given constraints. The methodology, developed computer programs and used constraints are described. Methodology is exercised using lines of the RedJetIII, which is a low wash catamaran. A numerical comparison is performed between the wash performance of original RedJetIII hull and that of an optimised hull. Artificial neural networks are used to simulate wash criterion and vessel displacement whereas genetic algorithm is applied in optimisation procedure.

Introduction

Wake wash generated by ships concern more and more authorities and environmental agencies. Laws in some European countries already restrict the allowable wash generated by a ship. More countries are going to ratify legislatives to define limitations of allowable wake wash. It is expected that tougher restrictions will follow. Therefore ship operators and ship builders are interested in ships, which are "low wash" designs, especially in case of ferries and coastal vessels.

In an effort to assist designers towards low wash ship designs, MARINTEK has developed an automatic procedure for optimisation of hull form in terms of wake wash. MARINTEK is participating in the EU project FLOWMART, which aims towards better understanding of wash phenomena and development of tools for prediction of wash generated by ships. The project included also model and full scale validation of computational tools, which may be subject to future papers. The main focus at MARINTEK is dedicated to practicability of the procedure in a way that it is easy-to-use and possible to perform within a reasonable time. Since many iterations are inevitable during an optimisation, it is important that involved computational tools are fast and user friendly. Available commercial programs are therefore impractical. A new wash prediction computer program developed at MARINTEK is used. Artificial neural networks are applied to achieve even faster calculations. Genetic algorithm is applied for optimisation procedure.

Lines of RedJetIII, an already low wash catamaran, are optimised in terms of generated wake wash using developed procedure. Results of optimisation are presented and discussed. These results shall be validated with model test within year 2002.

Hull optimisation methodology

This methodology describes automatic optimisation of hull lines to reduce the wake wash generated by a ship. The methodology shall be valid for both mono-hull and catamaran vessels in deep water as well as in shallow water.

Geometry manipulation

First step towards hull optimisation is to parameterise the hull form. This is done using the mod_geo program. Figure 1 shows a schematic representation of hull parameterisation. Currently 10 equidistant points on each curve along the ship are used. In the optimisation of the forward part of the ship the fore half of the ship is used whereas the foremost point is kept constant. Draught and beam multiplication factors are used so that a total of 12 parameters are varied. The parameter variations are kept within certain constraints. Currently, parameters are allowed to vary ±15%. A similar procedure can be applied to optimisation of the aft part of the ship.

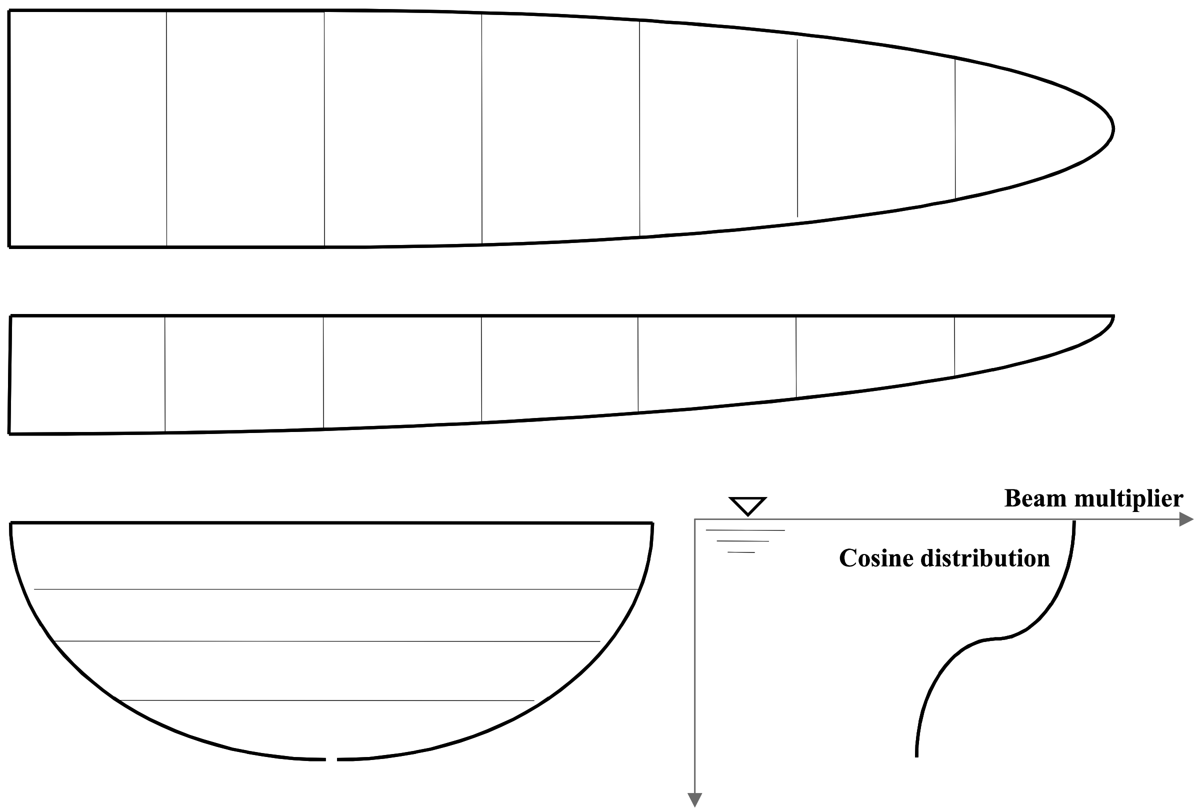

Figure 1 schematic representation of hull parameterisation

Program mod_geo is part of an automatic hull lines optimisation package developed by Marintek. Mod_geo reads the hull element file and modifies the hull geometry according to information specified. The modification is performed as a multiplication of the y (transverse) and z (vertical) co-ordinates of each point on each element. The multiplication factor is dependent on the position of the elements. The multiplication factor in every point is found as an interpolation/smoothing of the coarse grid specified as input. After modifying the elements, mod_geo checks the displaced volume and wetted surface, and also checks that all elements have non-zero area and the normal vector pointing outwards.

First, a global scaling in x (longitudinal), y and z directions is carried out. Then, multiplication of z and y co-ordinates of each element point is carried out, dependant on x-position.

The z-multiplication factor is a function only of x (longitudinal position). A number of fairly evenly spaced longitudinal points are defined, and a value of the z-multiplication factor is specified for each point. To find the multiplication factor to be applied at each element point a smoothing/interpolation procedure is used. Different smoothing algorithms can be selected. Cubic splines are recommended.

The y multiplication factor is dependant on both x (longitudinal position) and z (draught). The vertical (z) variation is in terms of a cosine distribution, where the wave length of the cosine wave is the maximum overall draught and the amplitude is specified as function of length in exactly the same manner as the z multiplication factor. In addition, a factor not dependant on z is added, so that a fairly general multiplication factor distribution can be expressed with a minimum of parameters. The y-multiplication factor can be expressed as:

$$ymult = yamp(x) \cdot \cos(\pi \cdot z/T) + yconst(x)$$

Available smoothing functions are given in Table 1.

Table 1 available smoothing functions

Type	Min. number of points
No smoothing	1
Cubic spline	2
Cubic spline – anti wiggle	4
Cubic spline - preserves concavity	4
B-spline - 2nd order	2
B-spline – 3th order	3
B-spline – 4th order	4
B-spline - 5nd order	5
B-spline - 6nd order	6
Interpolating cubic spline	4
Polynomial of order 1 (linear)	2
Polynomial of order 2	3
Polynomial of order 3	4
Polynomial of order 4	5
Polynomial of order 5	6
Polynomial of order 6	7
Polynomial of order 7	8
Average	1

Parameters and constraints

Optimisation is performed for a speed of 34 knots in shallow water with a depth of 14.6 m. Optimisation is based on minimisation of wash criterion in the interesting longitudinal range of a 30 m (from catamaran centreline) longitudinal cut. The trim and displacement used are the same as during model tests at MARINTEK. Trim is kept constant (It is assumed that weight distribution will be arranged in a way that trim can be kept constant).

Displacement shall be ±0.4% of original displacement.

Ship length is kept constant.

Maximum beam shall not be wider than the maximum beam of original hull.

Other geometric parameters used are given in the Table 2.

Table 2 Geometric parameters and their limitations

Parameter	Initial value	Minimum	Maximum
ZMULT1	1	0.85	1.15
ZMULT2	1	0.85	1.15
ZMULT3	1	0.85	1.15
ZMULT4	1	0.85	1.15
YAMP1	0	0	0.15
YAMP2	0	0	0.15
YAMP3	0	0	0.15
YAMP4	0	0	0.15
YCONST1	1	0.85	1.15
YCONST2	1	0.85	1.15
YCONST3	1	0.85	1.15
YCONST4	1	0.85	1.15

Generation of a random database

A random database of input geometry parameters is generated, which has currently 6000 datasets. The geometry modification program mod_geo.exe is applied to generate 6000 hulls using these input parameters. This program calculates at the same time displacement, wetted surface area and LCB of each hull. Calculated values are returned to the database.

The wash calculation program wash.exe is used to calculate a long longitudinal cut with a transverse distance of approximately one ship length from ship centreline. This program, which is developed at MARINTEK, is described in the paper of Koushan et al. (2001). This calculation is performed with original hull lines to identify the interesting longitudinal interval for further calculations. Results of this calculation are presented in the Figure 2. The interval 270 m to 420 m is identified as the interesting longitudinal interval. All further calculations use only this interval.

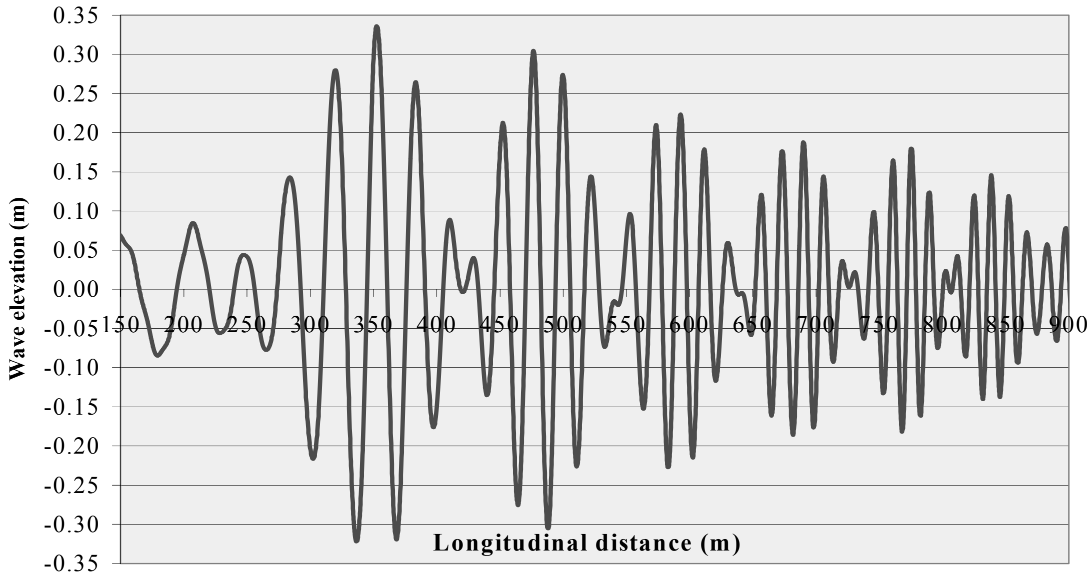

Figure 2 Wave elevation calculated for a longitudinal cut 30 m from catamaran centreline at 34 knots speed and 14.6 m water depth. Original hull lines are used.

Next, wave elevation is calculated within identified interval for all randomly selected 6000 hulls. This calculation takes approximately 1.5 minutes per hull on a pc with one 850 MHz processor. Then the program ReadWrite.exe is applied to post process the wave elevations. This program calculates different wash criteria using output file of the wash calculation program. Wash criteria calculated are:

- Maximum wave elevation
- Maximum wave height
- Sum of four largest wave heights
- Integration of wave elevation

$$W = \sqrt{\frac{1}{x_2 - x_1} \int_{x_1}^{x_2} \zeta(x)^2 dx}$$

with ζ wave elevation

x abscissa on the chosen longitudinal cut

x_1 starting point for the integration

x_2 ending point for the integration, chosen at a zero crossing point

x_2-x_1 = L = constant during all the process

These calculated criteria are then returned to the database. The database is now completed.

Pre-processing using Artificial Neural Networks

Artificial Neural Networks is used to simulate the displacement as well as the selected wash criterion, which currently is the integration of wave elevations.

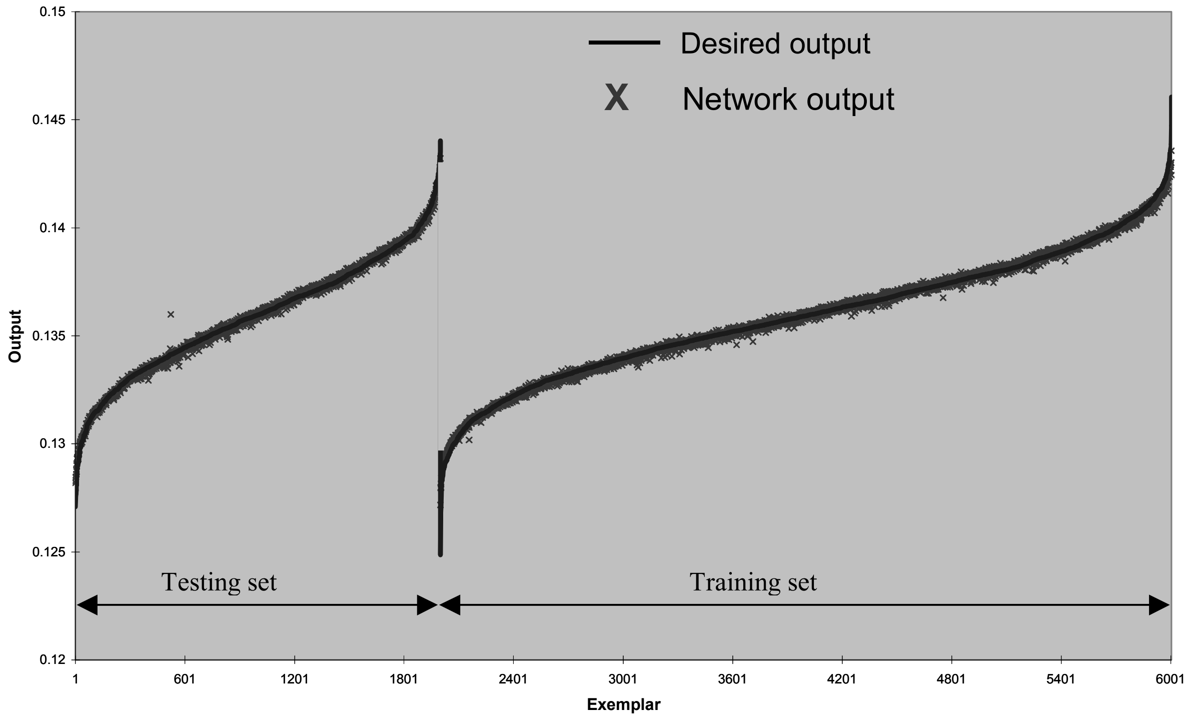

Figure 3 Desired and network output for wash criterion

The main idea of using Artificial Neural Networks (ANN) is to reduce the required time per iteration. ANN reduces the calculation time per run from 1.5 minutes to 0.015 seconds. The design of the ANN is done very fast as the data are well "behaved". Accuracy of the prediction of both wash criterion and displacement by ANN are very high as illustrated in Figure 3 and Figure 4. These two figures present desired outputs, which are the calculated wash and displacement, and the network outputs, which are the values predicted by the ANN.

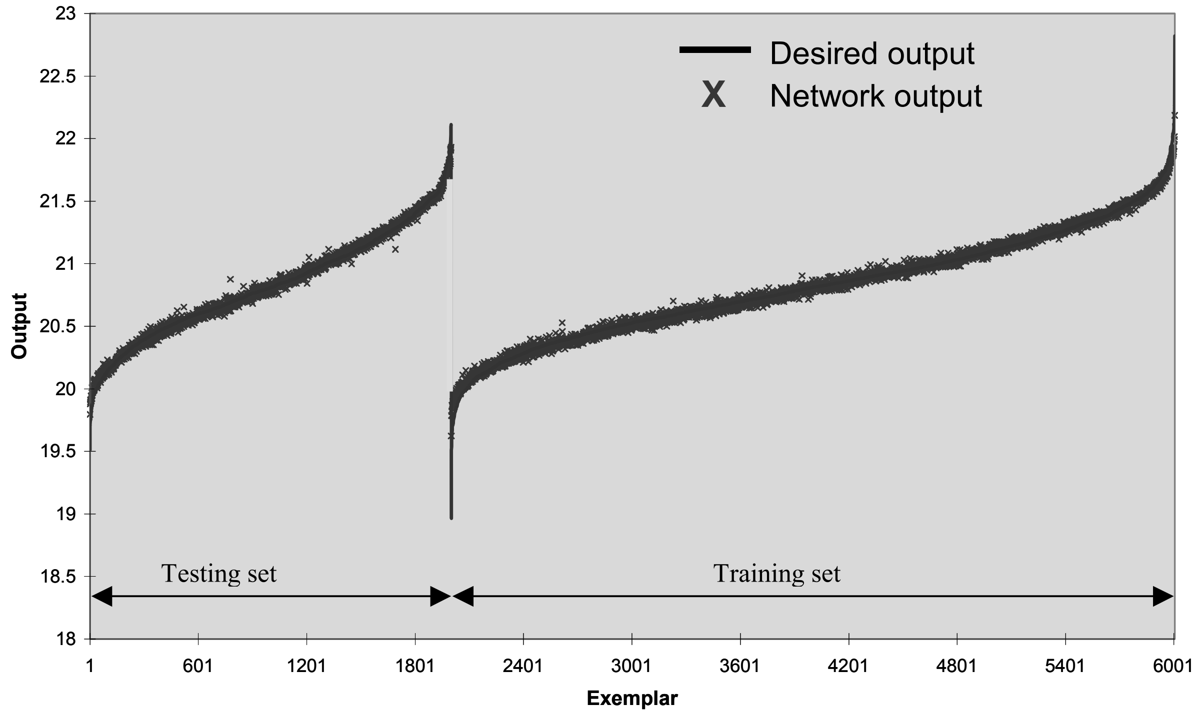

Figure 4 Desired and network output for displacement

Figure 5 presents schematically the flowchart of pre-processing.

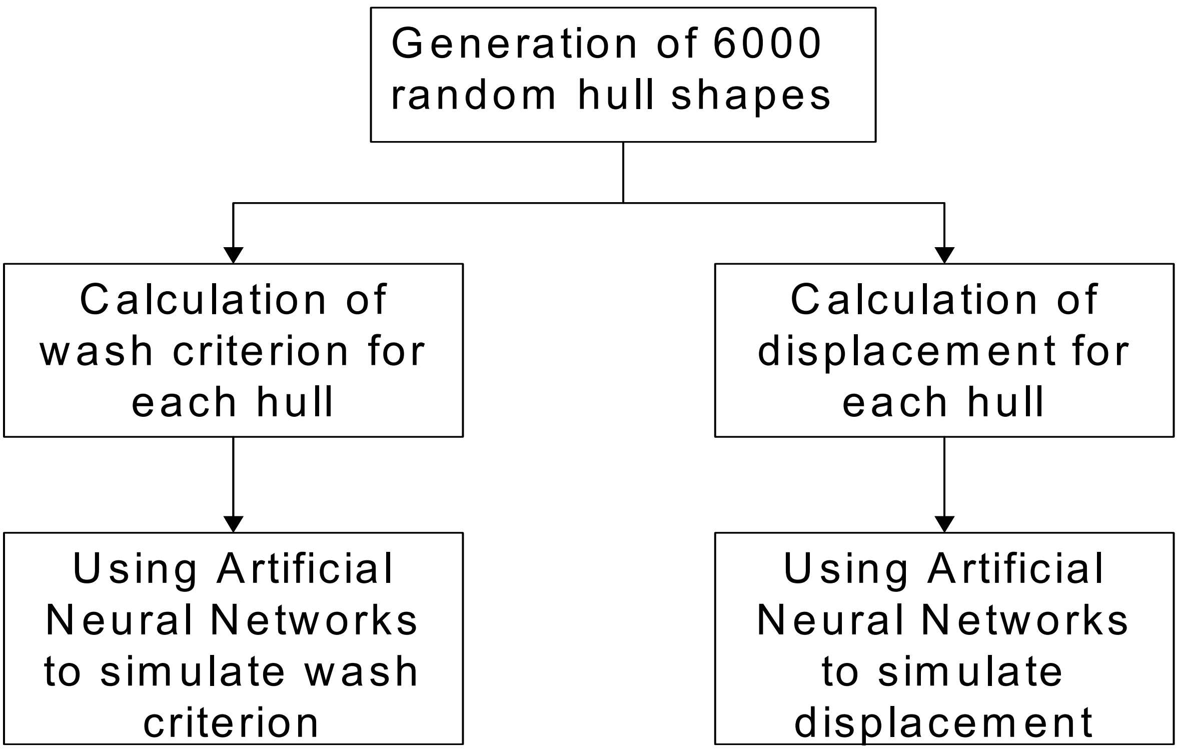

Figure 5 schematic flow chart of pre-processing

Optimisation using genetic algorithm

After design of prediction networks, optimisation procedure can be started. Figure 6 presents a schematic flow chart of the hull optimisation procedure. Starting with the first generation, a random set of hulls (geometric parameters) are created, displacements and wash criteria are calculated using ANN, Genetic algorithm is applied to define the next generation and the procedure is iterated. Iteration can be terminated using a termination parameter, which could be for example specified number of evolutions or convergence of members of a generation or convergence of best fitness of subsequent generations. Genetic algorithm uses also different parameters, which needs to be selected properly to result in best optimised hull. One of the parameters is the number of members in a generation. As the time required per iteration is very short, it is possible to do a parameter study to find the best suitable parameters for genetic algorithm. It is shown that 200 members per generation is a good compromise between calculation time and achieved optimisation results.

Applied genetic algorithm is single objective. Whereas optimisation has two objectives namely minimisation of the wash criterion and constant displacement. To achieve both objectives, an optimisation criterion is defined, which is the multiplication of wash criterion times displacement change powered n.

$$WashCriterion*ABS((new\ displacement - original\ displacement)/original\ displacement + 1)^{n}$$

Power n is selected so that genetic algorithm converges towards the same displacement while minimising wash criterion. It is shown that power n can be set to 0.1 and the optimisation converges still towards constant displacement while minimising the wash criterion.

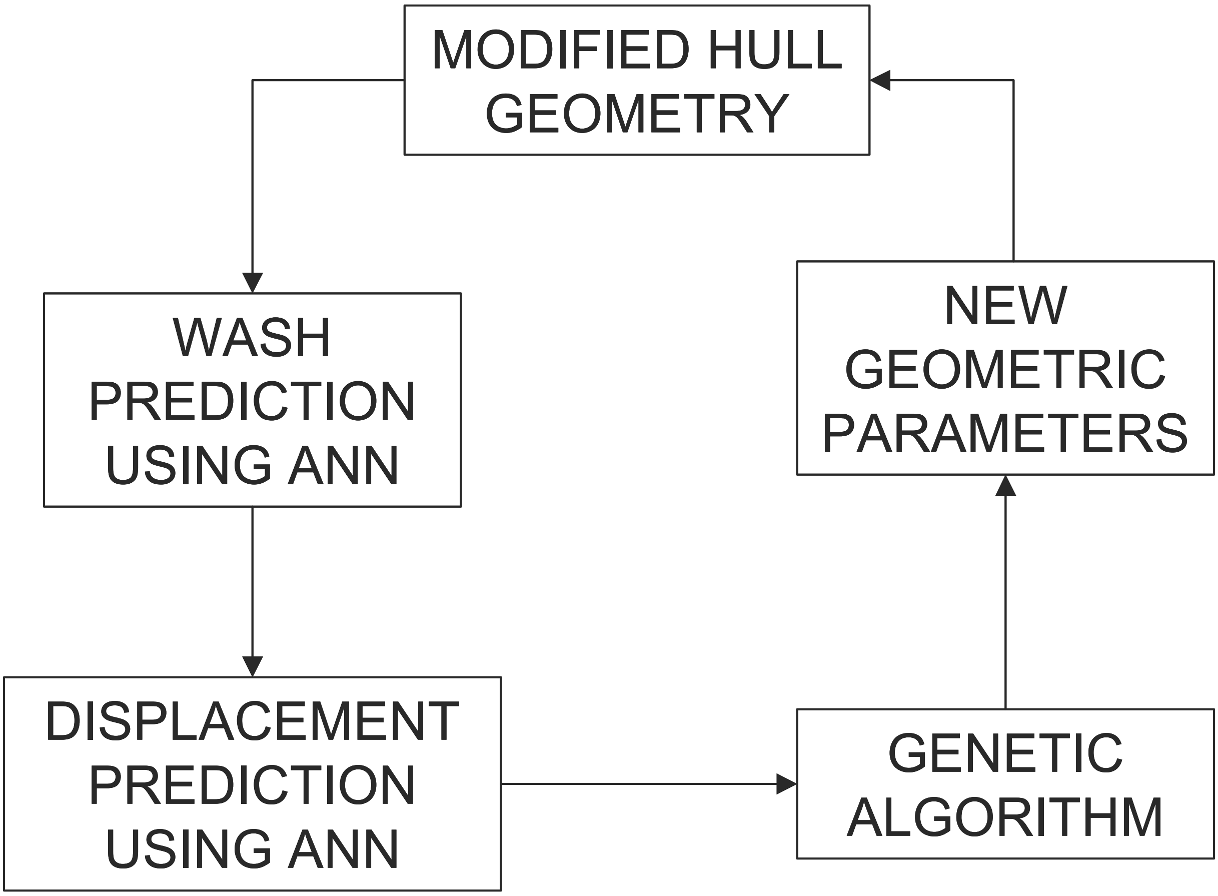

Figure 6 Schematic flow chart of optimisation procedure

After an optimisation procedure is finished and the best geometric parameters are selected, the new optimised hull shape is generated using mod_geo.exe. Actual displacement, wetted surface area and LCB are also calculated. The wash prediction program is applied to calculate the actual wave elevation at the given longitudinal cut. Displacement and wash criterion are compared to original hull.

Optimised hull

After running through 300 generations with 200 members each, an optimised hull is selected, which is called optimised5 hull. This is result of optimisation of fore part of the ship only. Same methodology can be applied to optimise aft part of the ship.

The displacement is remained almost constant (only 0.2% larger than original displacement). Whereas wetted surface area is increased by 0.9% only. Other design parameters like ship resistance, stability and seakeeping are not considered during this optimisation.

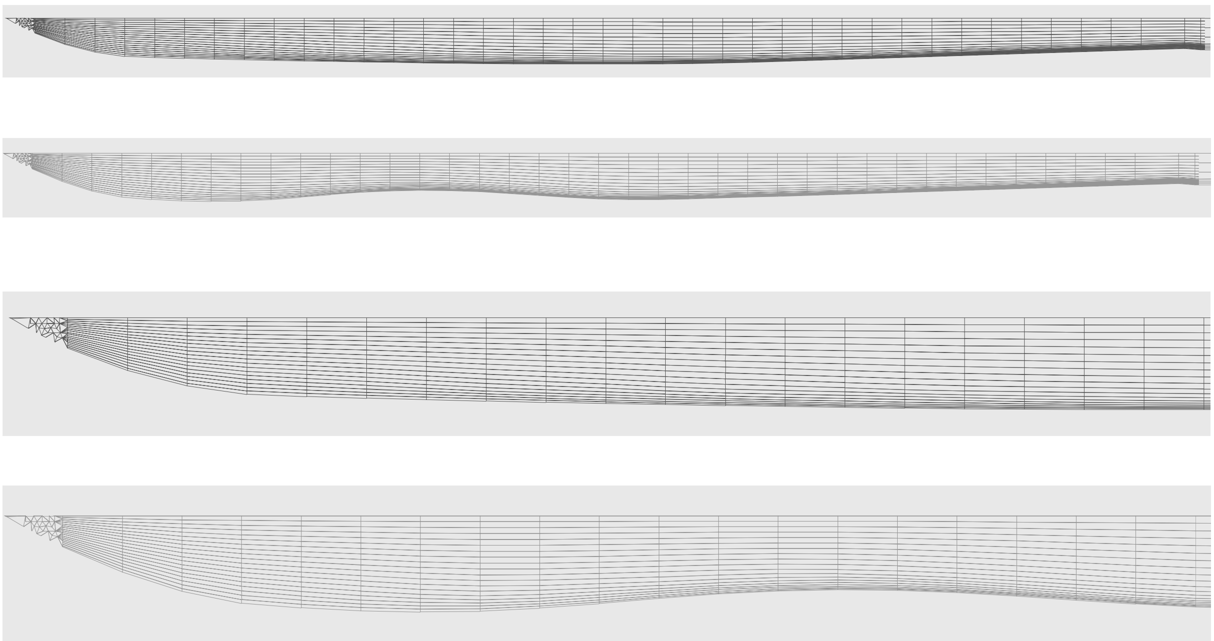

Figure 7 Side views of original hull in black, optimised5 hull in grey (only submerged part is shown, lower drawings show forepart only)

Figure 7 shows side view of the optimised and original hulls. It shows that draught of foremost part is increased whereas draughts of sections aft of that are decreased.

Same trend can be seen also on top view presented in Figure 8. Entrance angle is increased, whereas the beam of sections right behind the foremost part are decreased. Similar type of hulls were achieved in other optimisation runs.

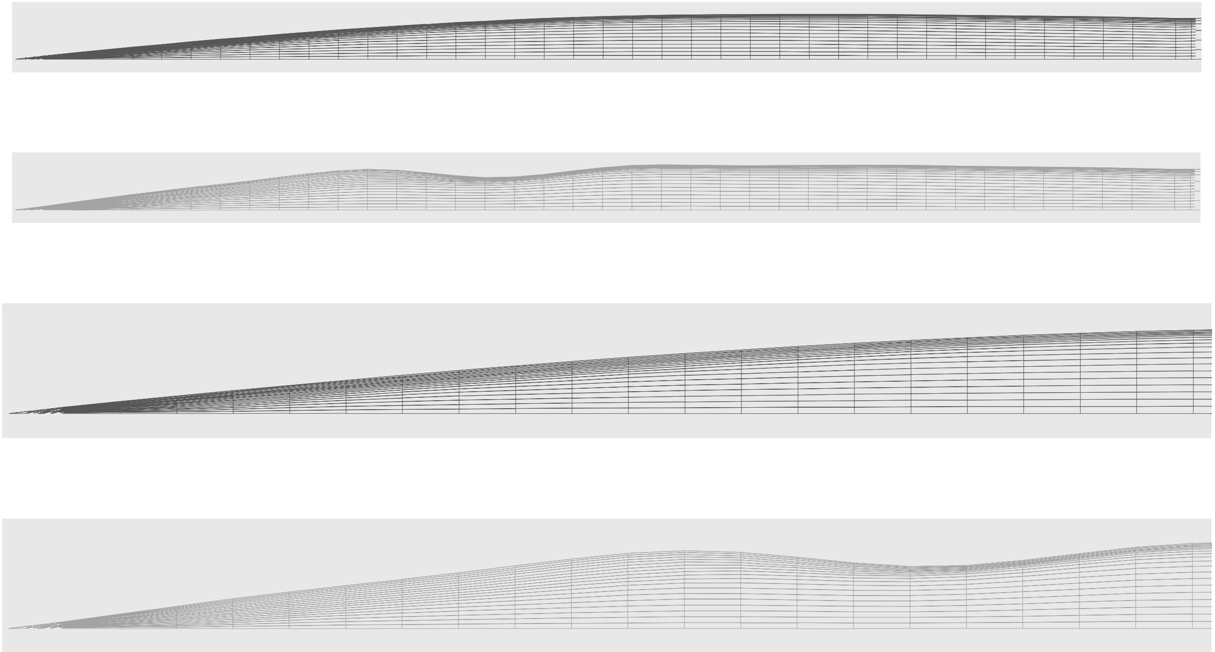

Figure 8 Top views of original hull in black, optimised5 hull in grey (only starboard half of one demi-hull is shown, lower drawings show forepart only)

Figure 9 shows wave elevations of a 30 m longitudinal cut generated by original and optimised5 hulls at 34 knots speed and 14.6 m water depth. Distance between demi-hulls is not changed. It shows that maximum wave height is reduced by approximately 13%. This means a large reduction in generated wave energy. Same trend can be seen in 60 m cut as presented in Figure 10. Optimised5 hull shows a better wash performance also in deep water. This comparison is shown in Figure 11.

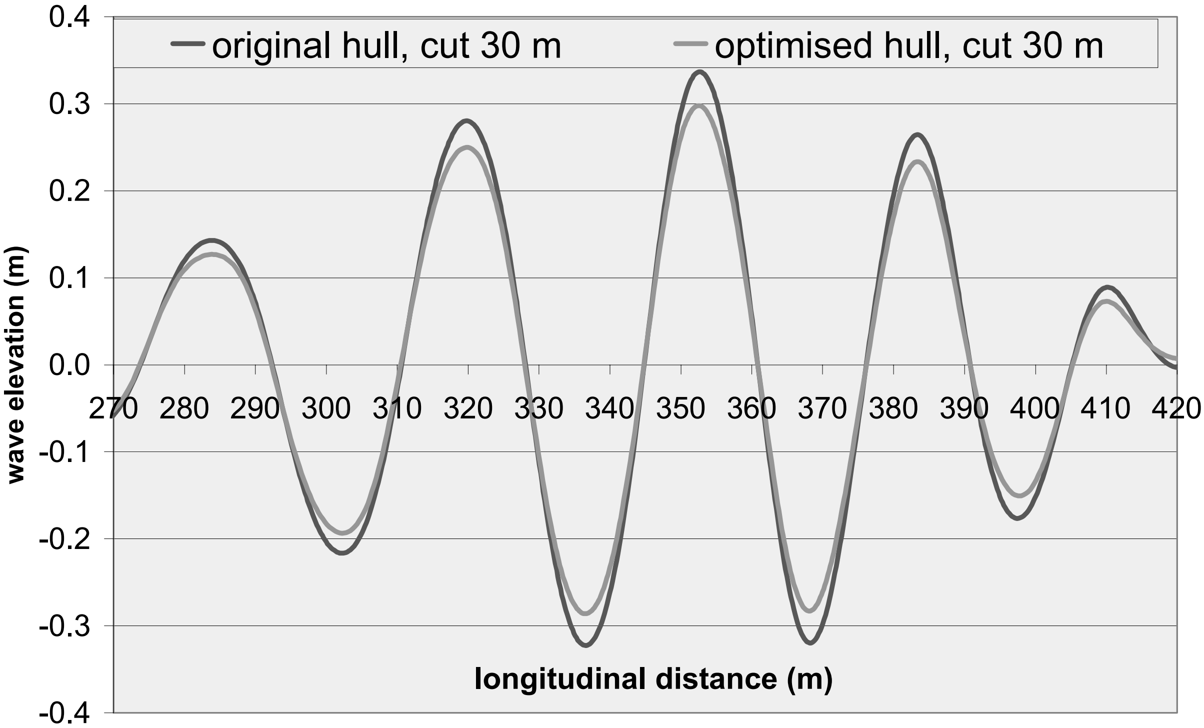

Figure 9 Wave elevations of original and optimised5 hull at 30 m longitudinal cut, 34 knots speed and 14.6 m water depth

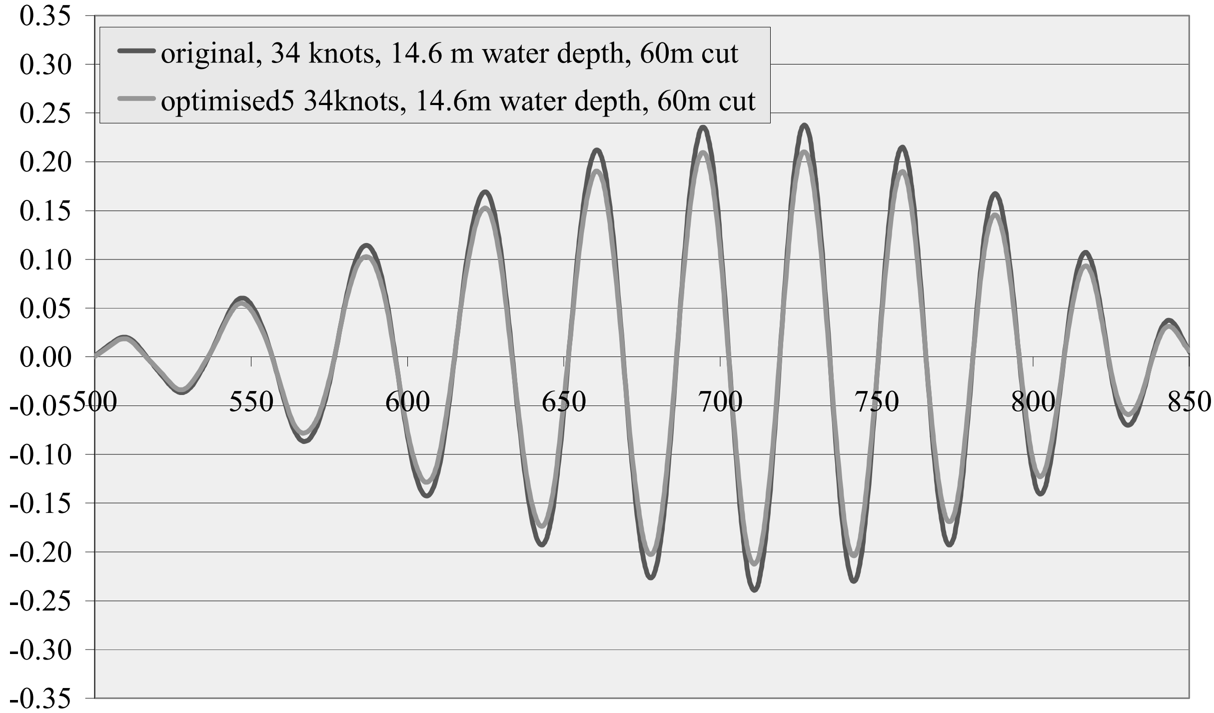

Figure 10 Wave elevations of original and optimised5 hull at 60 m longitudinal cut, 34 knots speed and 14.6 m water depth

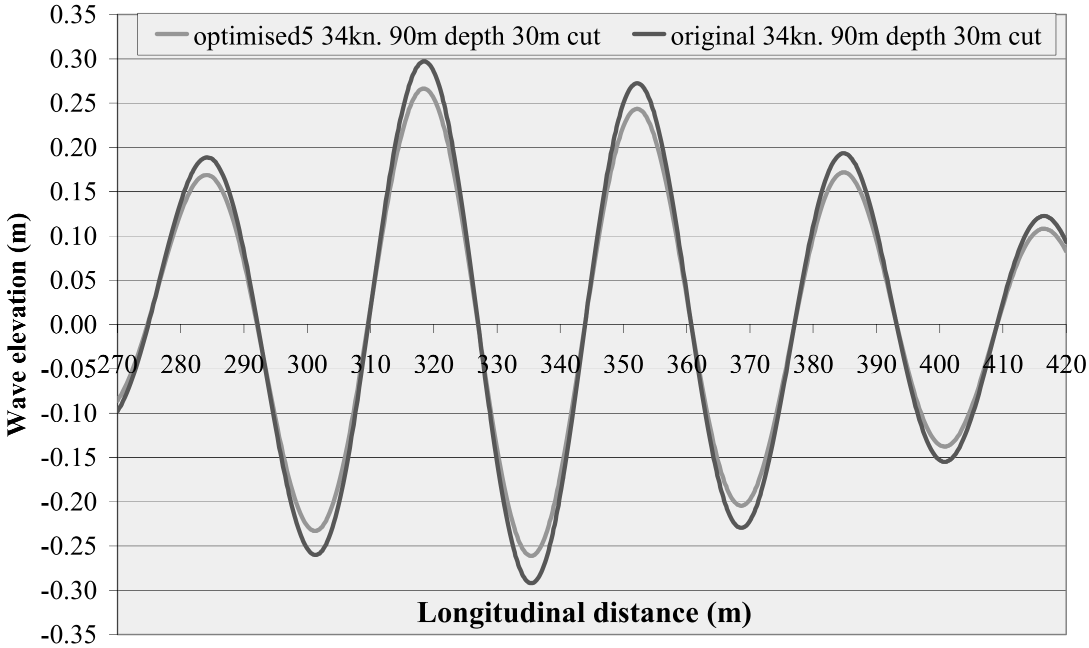

Figure 11 Wave elevations of original and optimised5 hull at 30 m longitudinal hull, 34 knots speed and 90 m water depth

Effect of hull distance on wash

Figure 12 presents calculated wave elevations generated by optimised5 hull with different hull distances. Calculations are performed for 30 m longitudinal cut, 34 knots speed and 14.6 m water depth. It shows that hull distance has a significant effect on the generated waves.

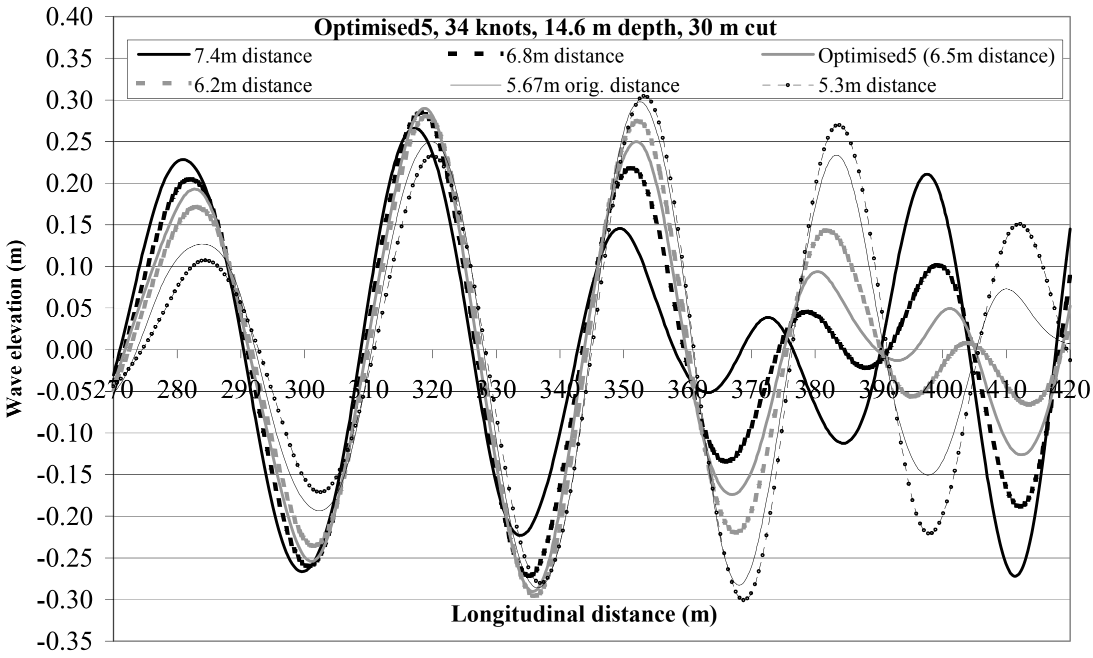

Figure 12 Wave elevations of optimised5 hull with different hull distances at 30 m longitudinal hull, 34 knots speed and 14.6 m water depth

Figure 13 shows relative wash criterion based on wave integration for original and optimised5 hull, where original hull with original distance is used as reference. It shows that hull distances shorter than the original hull distance of 5.67 m increase the wash whereas larger distances reduces the wash until a hull distance of 6.8 m is reached. Wash criterion starts increasing with hull distances larger than 6.8 m. Reduction in wash is quite significant; with a hull distance of 6.8 m, wash criterion is reduced by approximately 8%. Increasing the hull distance by 0.5 m results already in 5% reduction of wash energy.

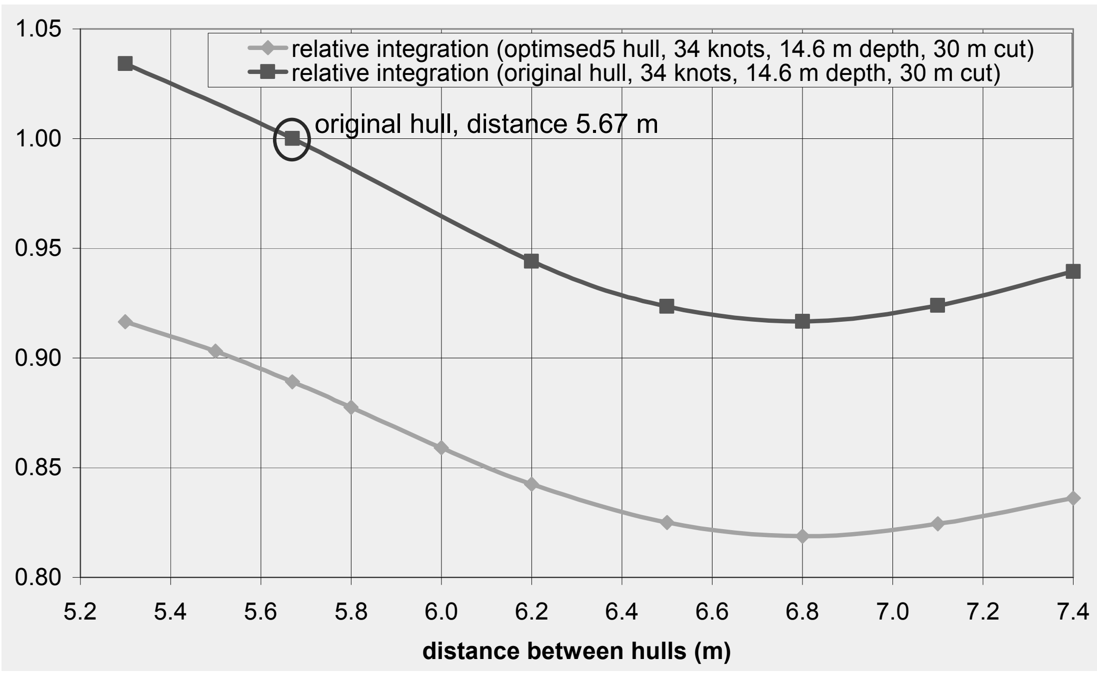

Figure 13 Relative wash criterion based on wave integration for original and optimised5 hull. Original hull with original distance is used as reference

Summery of used applications

Table 3 presents a summery of used applications during the hull optimisation procedure. All these applications are developed at MARINTEK as part of FLOWMART EU-project based on available codes at MARINTEK.

Table 3 A summery of used applications

APPLICATION	TASK
Mod_Geo.exe	Generation of modified geometry, calculation of displacement, wetted surface area and LCB
Wash.exe	Numerical calculation of wash
ReadWrite.exe	Processing the output of Wash.exe and Mod_Geo.exe, calculation of wash criteria, generation of database
Wash.dll	Prediction of wash criterion using Artificial Neural Networks
Displacement.dll	Prediction of displacement using Artificial Neural Networks
Optimisation.exe	Optimisation using genetic algorithm

Conclusions

Presented hull optimisation procedure works successfully. Though the catamaran used is already a low wash design, wash is reduced by ca. 13% by optimising the fore part only. Allowing the trim and total length to be varied could result in further improvement in terms of wash. Distance between hulls has also significant effect. Increasing distance between hulls by 0.5 m only results already in further 5% reduction of generated wash.

Geometric manipulation has potential for further improvement to achieve more construction friendly hulls. Other constraints could be added to the procedure, which are of importance. The first one could be the total resistance of the vessel.

It should be noted that currently only the wash behaviour of the vessel is investigated. The effects on stability, sea keeping, passenger comfort etc are not yet included. In a realistic design work, all different criteria need to be considered.

Acknowledgment

The materials presented are based upon the activities of MARINTEK within FLOWMART project (Contract No: GRD1-1999-10959) sponsored by the European Commission. The authors would like to acknowledge kind permission granted by the Commission and following project partners: University of Strathclyde (SSRC), Alpha Marine Ltd, ALSTOM Leroux Naval, FBM Babcock Ltd., LMG Marin AS, Newcastle University, National Technical University of Athens, Sirehna, SSPA and Tjarno Marine Biological Laboratories.

References

Koushan, K.; Werenskiold, P.; Zhao, R.; Lawless, J. (2001) “Experimental and Theoretical Investigation of Wake Wash”, Proceedings of FAST2001 Conference, Vol. I, pp. 165-180, ISBN 0903055708, Southampton UK

A New Tool for Assessing the Cost-Benefit of Emerging Technologies for Naval & Commercial Ships

David R. Lavis
Band, Lavis & Associates
A division of CDI Government Services
900 Ritchie Highway, Severna Park, MD 21146, U.S.A.
david.lavis@cdicorp.com

Abstract

The paper describes an engineering tool and a process that is being used to help assess the value of new technology for surface ships.

An overview of the approach is followed by examples of its applications.

1. Introduction

Every new ship acquisition and major upgrade program is faced with the problem of determining how to provide the warrior, or commercial operator, the needed mission capabilities within the limits of budgetary pressures.

A key element of this process is the capability of playing "what if" games very early in the evolution of a ship design.

These "what if" games address mission requirements and also attempt to determine what technologies are necessary to support the desired mission within the state of technology and within budget.

Shown in Figure 1 is a concept ship designed with this tool in 1993 and war-gamed in 1996 to assess and showcase the emerging HM&E technologies then being considered by ONR.

This is just one of many examples of studies over the years that have benefited from the approach described in the paper.

Figure 1: Vision of the Future – How Do We Get There?

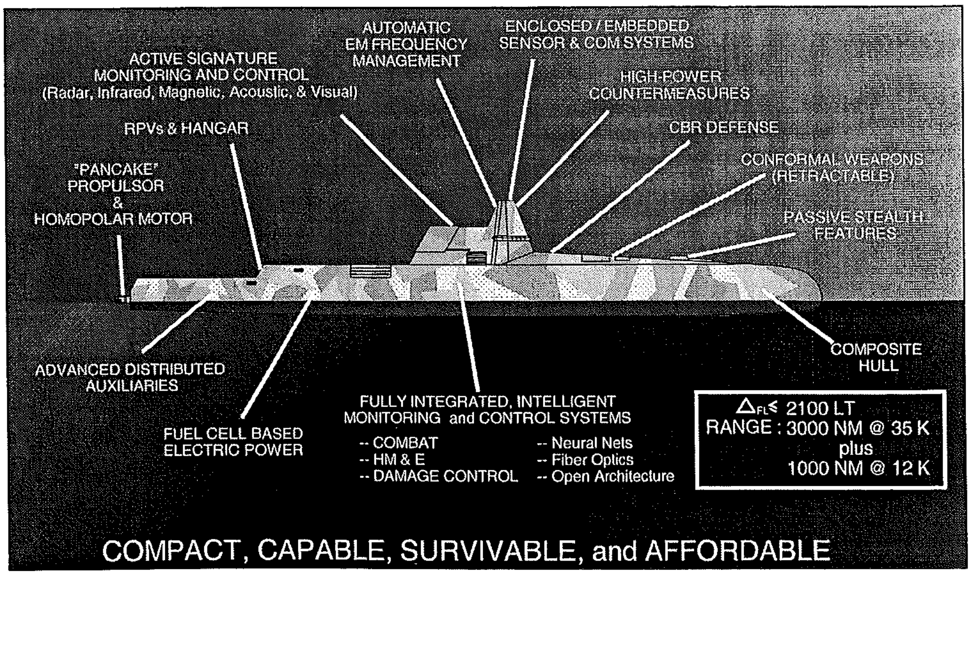

The applications of the approach are of three basic types:

1. Establishing affordable requirements,
2. Designing to common requirements, and
3. Comparing & assessing innovations.

The tool and method has been used and continually improved over a period of more than two decades.

In the mid-1990s, it underwent a major upgrade to a Windows-based environment.

This was thanks to an SBIR contract from the Office of Naval Research with technical oversight by NAVSEA Carderock.

2. Features

The main feature of the tool is its ability to rapidly automate the traditional ship-design spiral with emphasis on the use of physics-based algorithms. This has been achieved to ensure that extrapolations to new "out-of-the-box" designs will be accomplished with a higher degree of confidence than could be expected with methods that rely heavily on both empirical and historical trends.

Hullforms that are modeled are shown in Table 1 and include various types of Monohulls and Multihulls including SWATH.

Versions for ACVs and SES are available, but not yet integrated with the others.

Table 1: Capabilities in Advanced Hullforms

• Displaced Monohulls • Planing Monohulls • Semi-Planing Monohulls • Catamarans • Trimarans • Semi-SWATH & SWATH
Models for ACVs & SES are available but not yet integrated with the main tool.

Figure 2 is a screen capture showing a Monohull, Figure 3 shows a Catamaran, and Figure 4 shows a Trimaran.

Once a design is complete, a wire frame or its solid model can be viewed from any angle. Profile and deck plans can also be viewed, if required.

The program can examine almost any shape one may wish to explore. It is not limited to ship data based on prior experience.

Figure 2: Monohull

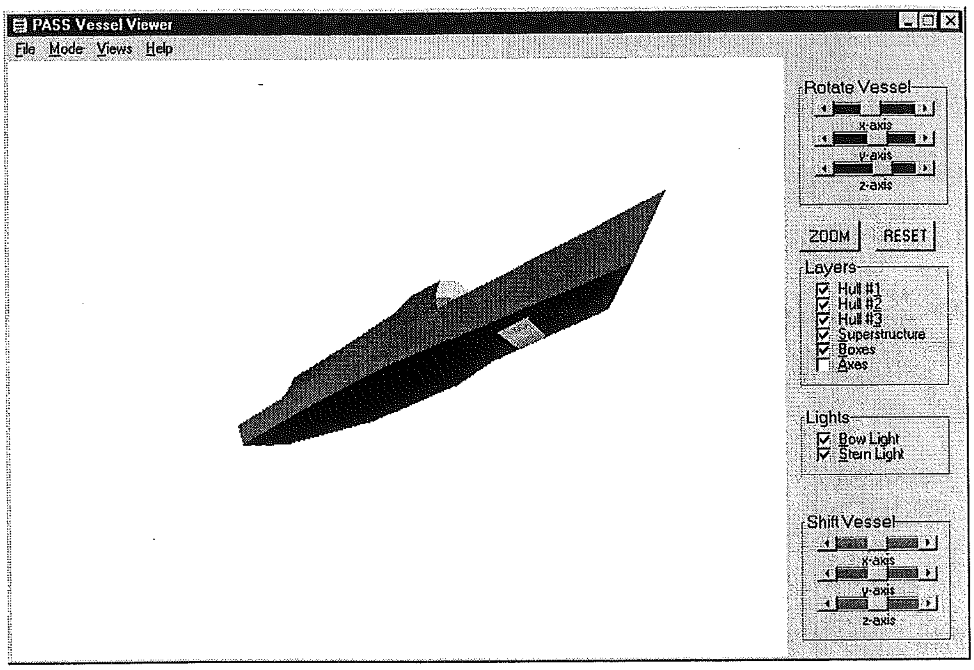

Figure 3: Catamaran

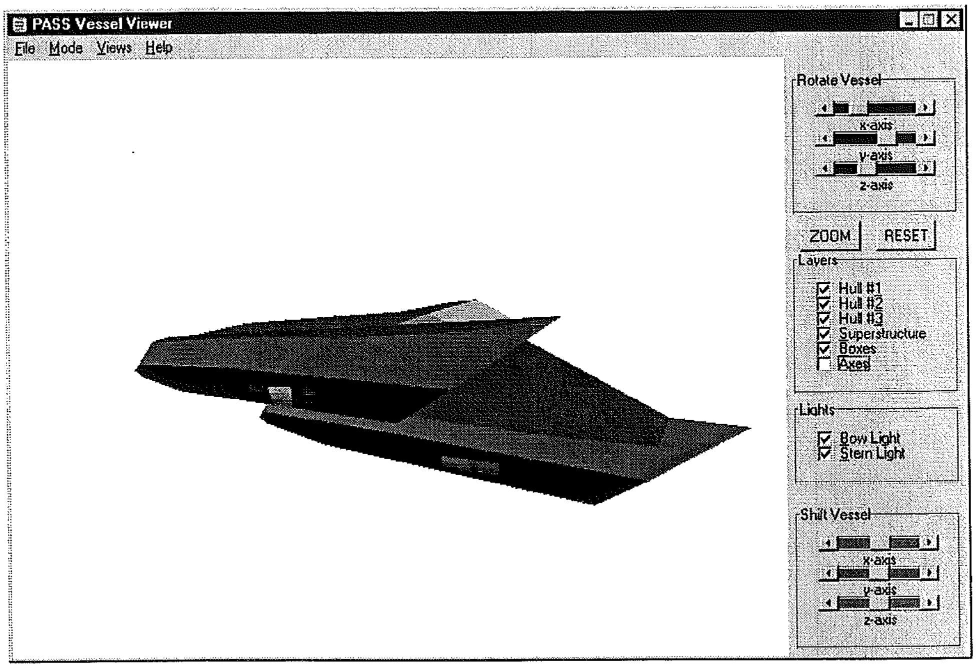

Figure 4: Trimaran

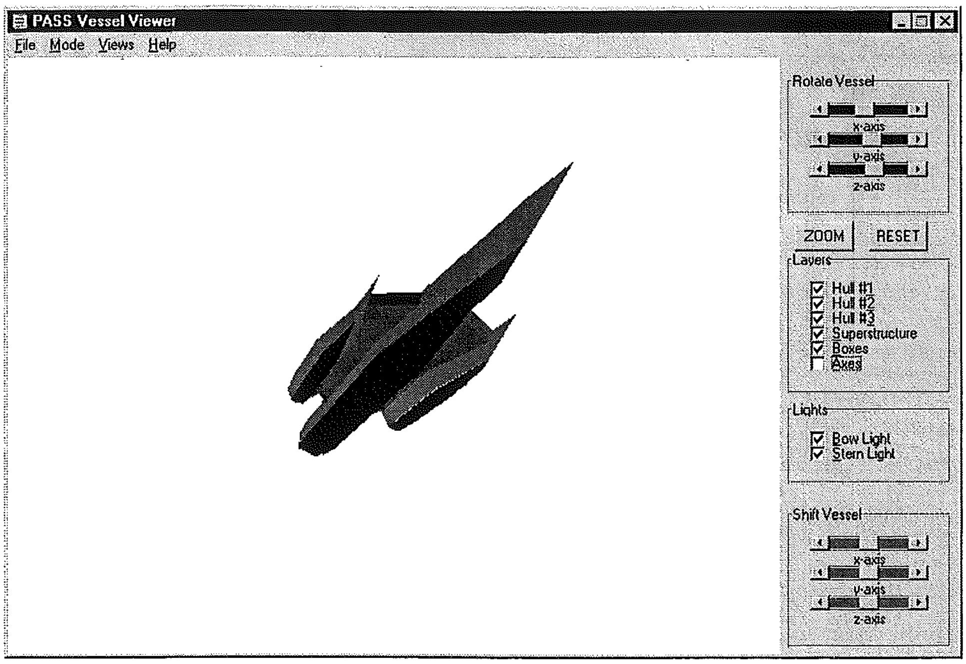

3. Validation

Efforts to validate the tool have been extensive, ranging in scope from the Coast Guard's 47-ft motor lifeboat to an SL-7 sealift ship as shown in Table 2.

Table 2: Scope of Validation

16 Combatants
• 3 Patrol Boats (MLB47, PC-1, 450 LT Trimaran Design)
• 3 Corvettes (SAR 5, 1400 LT & 2000 LT Designs)
• 1 USCG Cutter (Hamilton Class)
• 3 Frigates (FFG7, NFR 90, and 5400LT Trimaran Design)
• 3 Destroyers (DD963, DDG51, DDS Design)
• 1 Maritime Prepositioning Ship (86,000LT MPF 2010 Design)
• 2 Arsenal Ships (ONR and NG Designs)
• 1 Mobile Offshore Base (MOB)
6 Commercial Vessels
• 1 Container Ship (35,000 LT Vessel)
• 2 Sealift Vessels (SL-7, 6,000 LT Design)
• 3 Fast Catamaran Ferries (INCAT 81, 86, and 91)

Figure 5 shows examples of the % error on predicted displacement for various vessels.

For any studies involving vessels similar to these, the model could, of course, be fine-tuned to achieve even greater precision than that shown here.

Figure 5: Validation

- ❑ Benchmarking against existing designs demonstrates accuracy

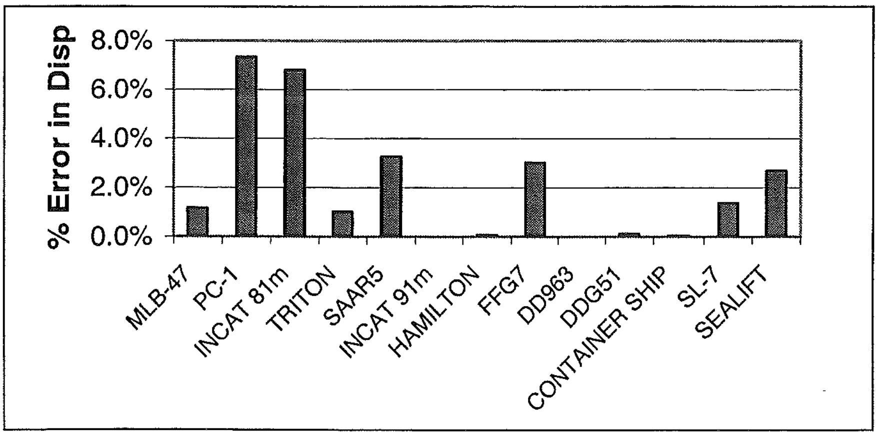

4. Modeling

The user has considerable scope in exploring the impact of requirements. Figure 6 is one of 8 input windows for required ship performance. For example, the user can define a mission profile by using up to 8 unique mission segments. For each segment, the user can specify ship speed, wave height, seaway modal period, sea spectrum, wind speed, and % of time operating in that segment. In this way, the impact of the environment can be changed and realistically assessed with inputs from the warrior.

Figure 6: Modeling the Mission Profile

- ❑ Modeling real-world mission requirements adds realism to results
- ❑ Enhances ability to assess impacts of requirements
- ❑ Lets the warrior make an input

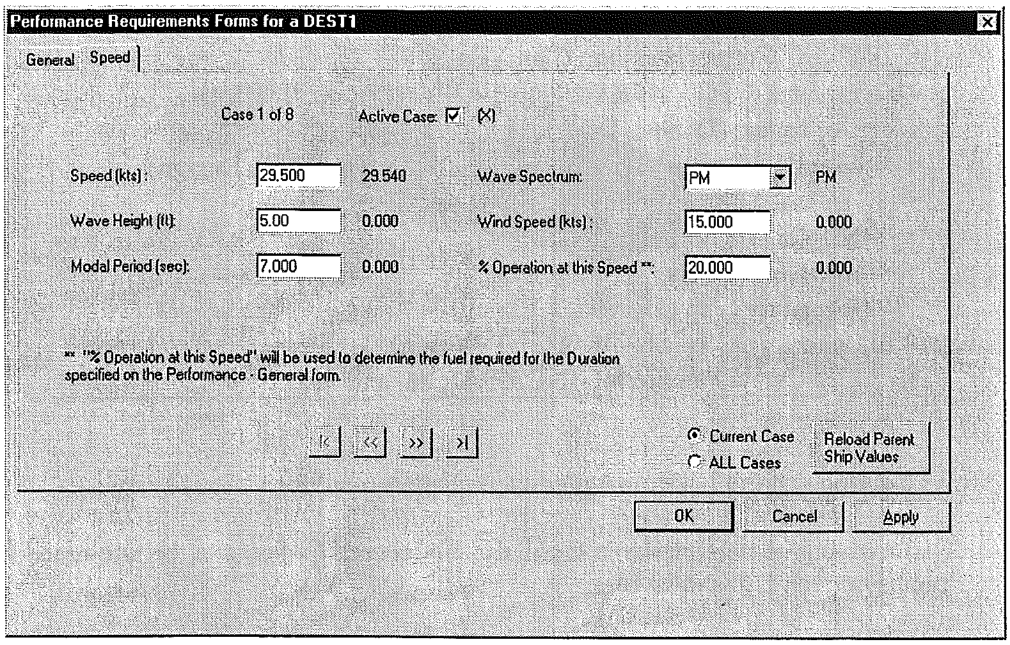

Figure 7 is one of numerous windows used to compose a ship design. In this case, it shows the selection of what choices of main propulsors could be made. Where a zero is provided as an input in the table, the value for that particular characteristic will be calculated by the program. Choices can be made from up to 8 different types of marine screws or 4 different types of waterjets, or the user can specify a new type of propulsor. Similar input windows exist for hullform, hull structure, and power plants, etc.

Figure 7: Composing a Ship Design

- ❑ Capture critical design parameters
- ❑ Input designer's technical expertise to the design

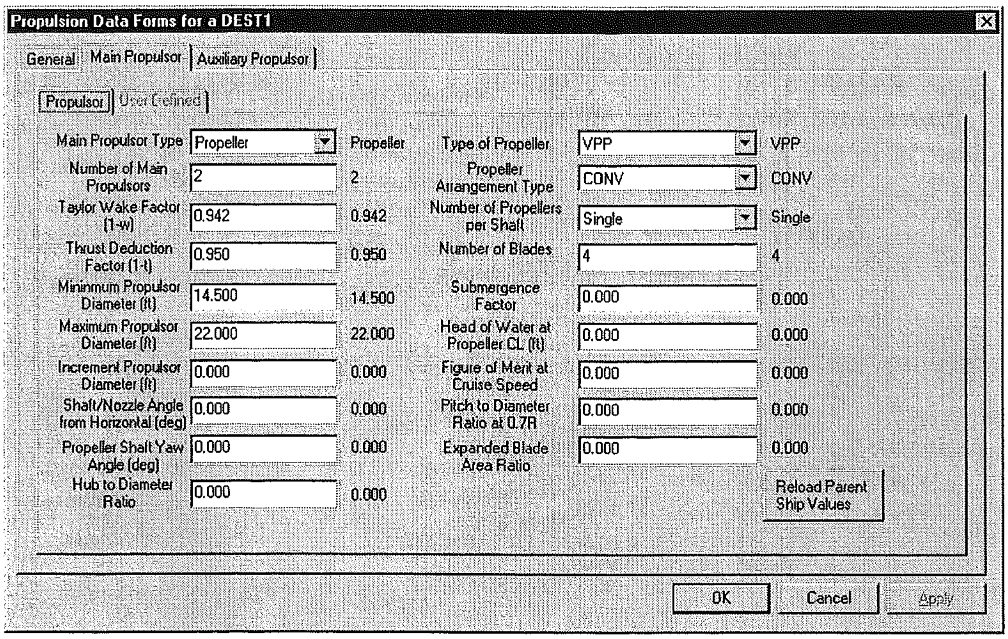

5. Applications

Examples of past applications are numerous. Some are listed in Table 3.

Table 3: Examples of Applications

Establishing Affordable Requirements	
Swedish Visby-Class High-speed Patrol Vessel	1993
U.S. 2000-Ton High-Speed Corvette	1994
U.S. Slender Monohull Fast Atlantic Freighter	1998
U.S. Army Theater Support Vessel	2000
Comparing & Selecting Concepts to Meet Common Requirements	
U.S.C.G. Deepwater Semi-SWATH Cutter	1998
U.S. T-ADC(X) AMMO Dry Cargo Ship	2000
Finnish T-2000 Coastal Patrol Boat	2001
U.S. University Research Vessels	2001
Middle East Coast Guard Patrol Vessel	2001
Finnish T-2000 Coastal Patrol Boat	2001
European High-Speed RO/RO Ferry	2001
Comparing Subsystem Innovations	
U.S. Fuel-Cell Propelled Future Frigate	1993
Distributed Battle-Space Force Architecture of Small Single-Mission Ships	1996
U.S. DDG51 Podded Propellers vs. Marine Screws vs. Waterjets	1997

They cover vessels from advanced patrol craft to Coast Guard cutters to corvettes and destroyers, cargo ships, research vessels, plus the exploration of new types of hullforms and propulsion systems, etc.

The software has now been used for over 40 individual programs. The examples shown in Table 3, with dates of completion, are listed under the 3 categories of application defined earlier.

A good example of success in helping to set affordable requirements and exploring different hullforms and subsystem options was the 1993 study conducted for the Swedish Navy. This eventually led to the fast Visby-Class Patrol Vessel shown in Figure 8.

Here, the effort was performed within, essentially, an IPT environment responding, real time, by phone to "what if" questions to find solutions that would meet a specified acquisition budget.

Figure 8: Selecting Affordable Requirements for the Mission

- Examining the impact of requirements (payload, range, speed, etc.) on cost

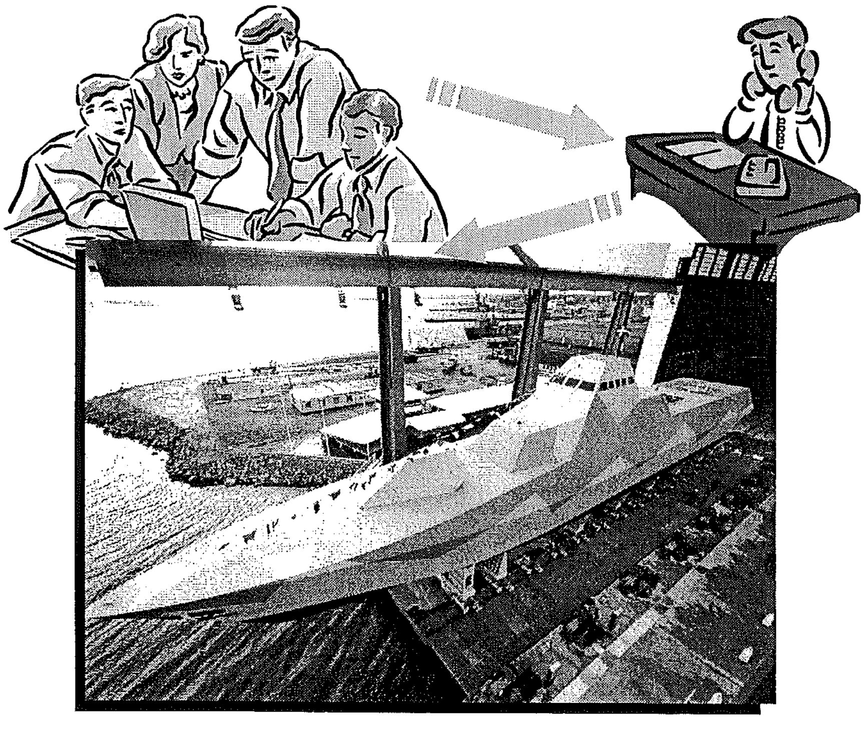

Another example is the Finnish Navy's T-2000 patrol boat. This is currently undergoing sea trials by Aker Finnyard. For this program, numerous cost trade-offs were conducted, as illustrated in Figure 9, to zero in on a preferred solution.

Figure 10 shows the impact on operating cost of varying payload and range for a sealift ship. Getting an early understanding of what you can afford to build can save a lot of headaches later.

Figure 9: Evaluation of Alternate Designs

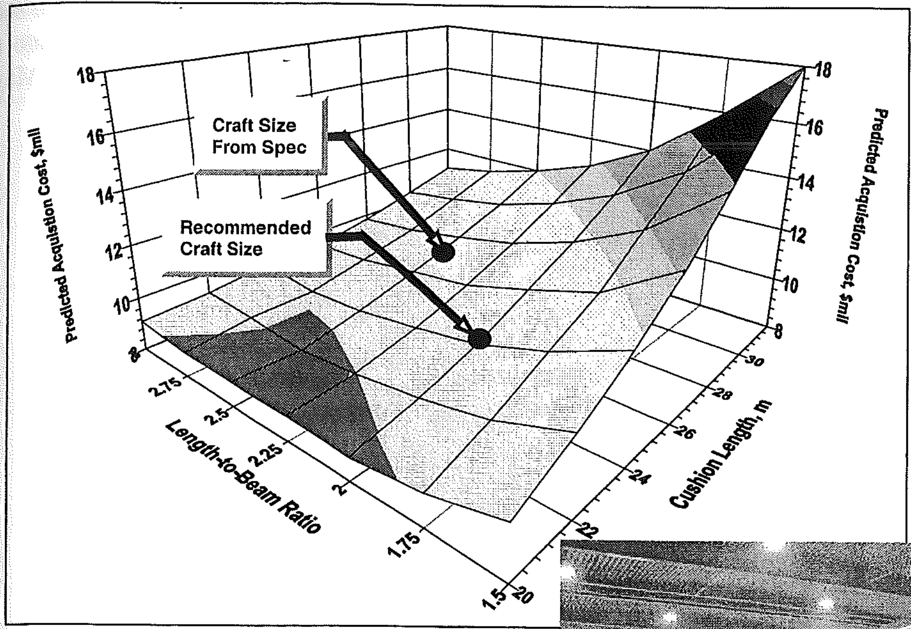

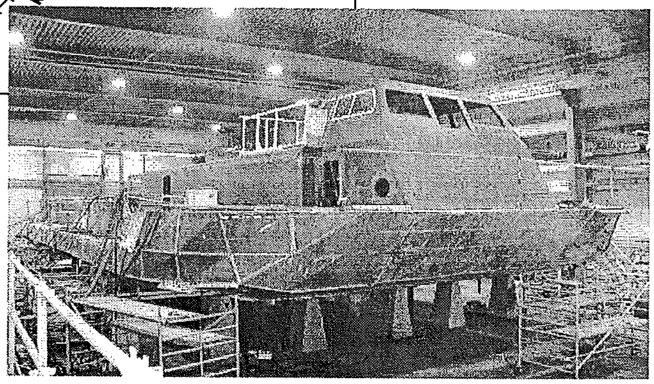

Figure 10: Matching Performance to Budget

- ❑ Parametrically match budget constraints to achievable performance

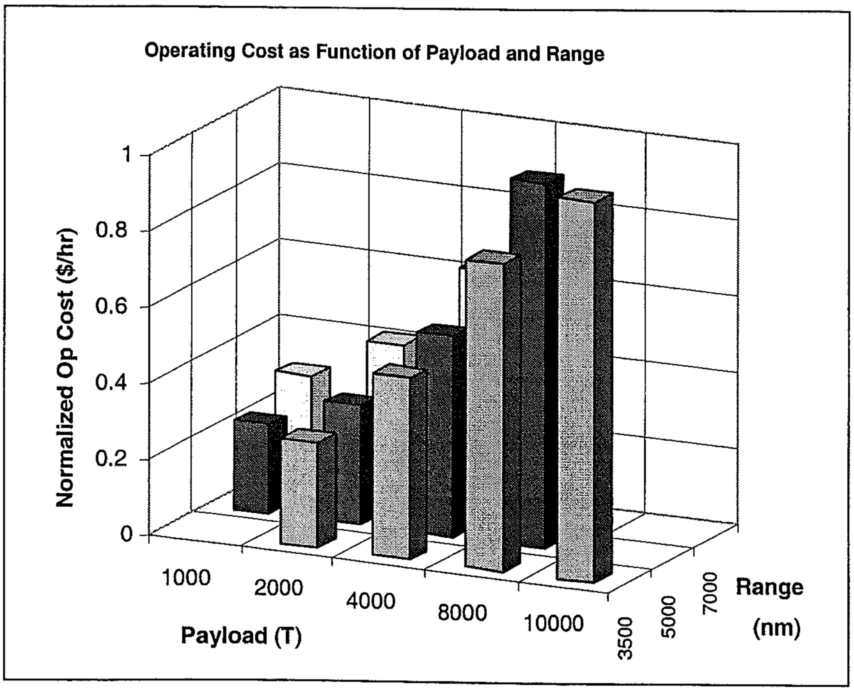

Figure 11 is an example in which having a vessel with acceptable seakeeping was of paramount importance. The figure shows how the vessel must increase in size and, hence, cost as the design sea state is changed. The vessel, in this case, was a passenger ferry and the cost was converted into a retail ticket price. The seakeeping module for the tool was described in an ASNE-Day paper in May of 2001.

Figure 11: Influence of Seakeeping

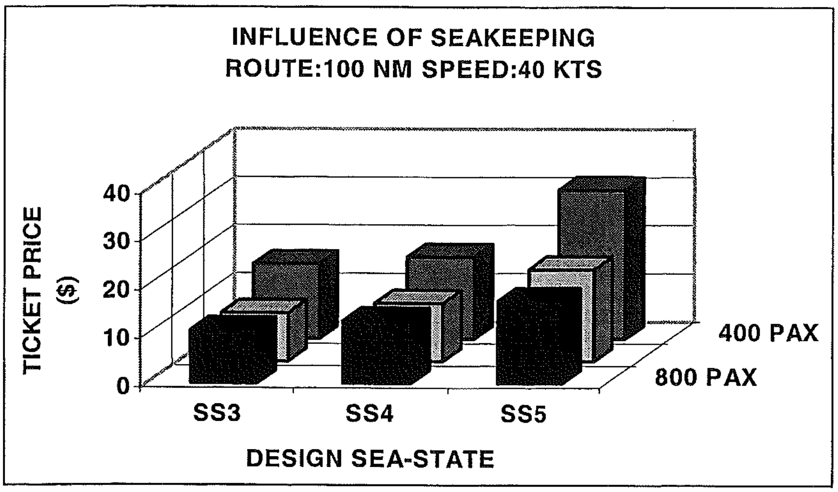

Figure 12 is an example of results for a large cargo ship, the T-ADCX (X). Life-cycle cost is shown as a function ship length and ship length-to-beam ratio. Specified limits on ship beam and draft, including ship stability, define a window of acceptable solutions within which a least-cost ship can be found.

Figure 12: Rapid Identification and Optimization of Cargo Ship Design Space

- Overlaid constraints quickly limit the design space

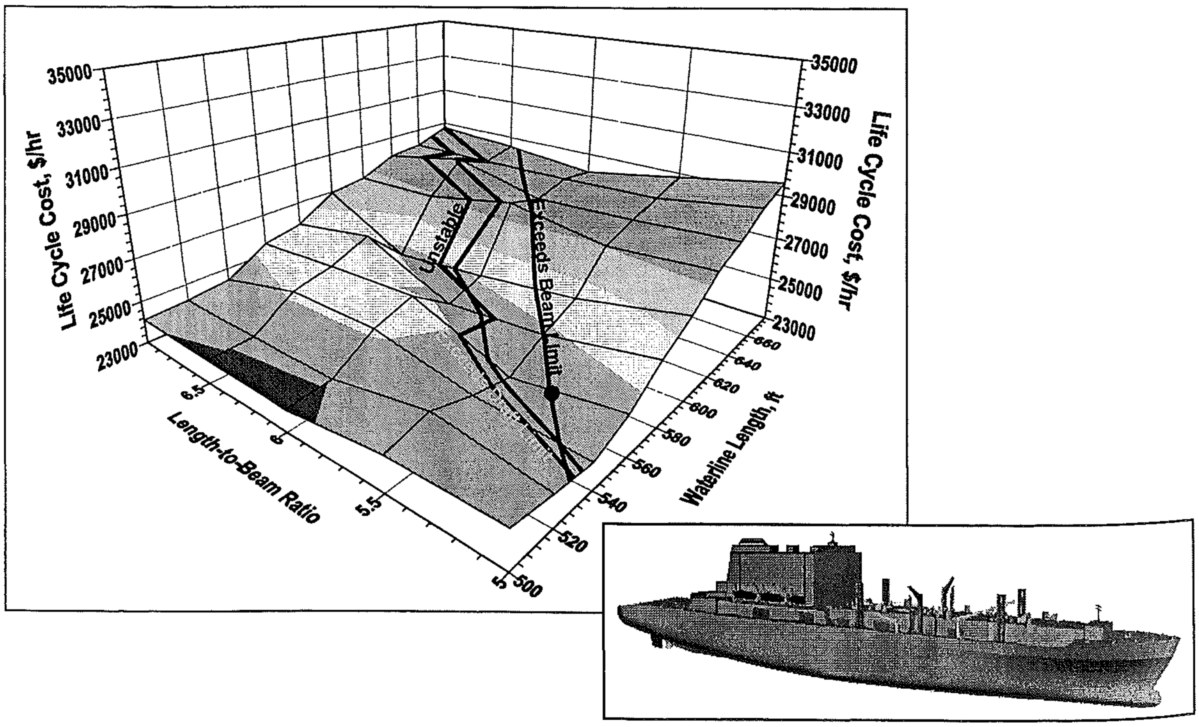

Figure 13 is an example of a recent research vessel study to assess the cost impact of hullform, powerplant, seakeeping, and workspace choices. The insert shows the vessel viewer; in this case, a catamaran.

Figure 13: Comparison of Research Vessel Design Options

- Assess the cost of hullform and powerplant choice and seakeeping and work space impact

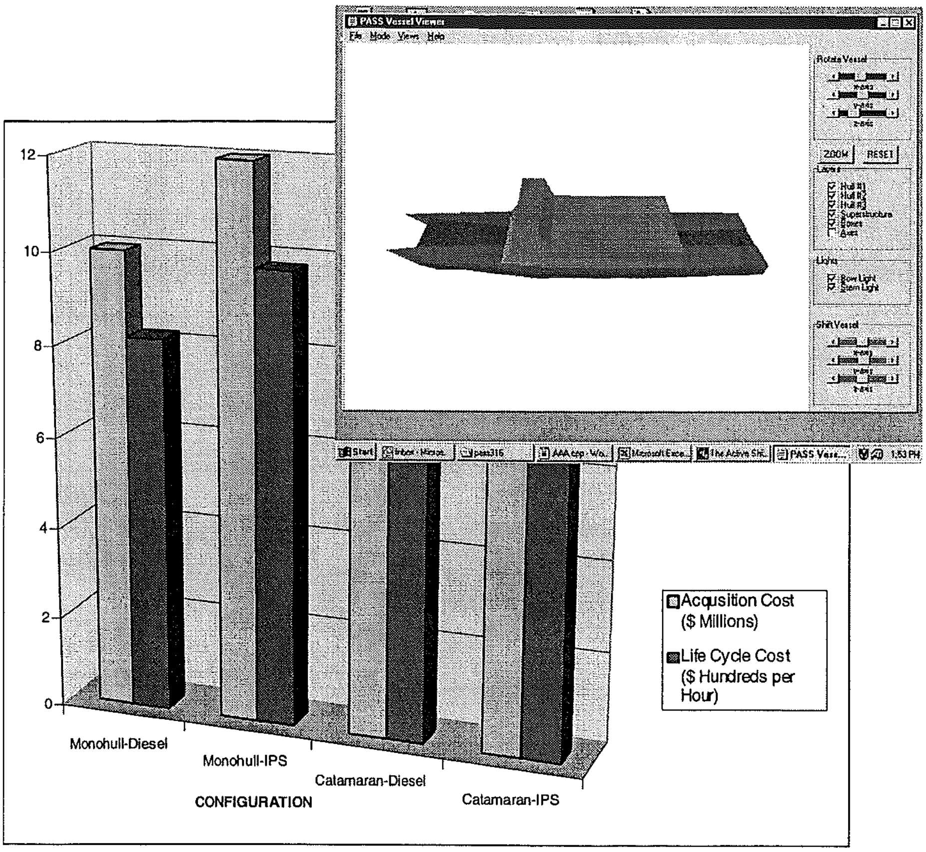

Figure 14 is from a recent study for a patrol vessel of a foreign coast guard. Here, ship displacement was of interest and the ship with least displacement could be found within limits of draft, beam, and available power.

Figure 15 is from a quick study conducted in 2001 to define a high-speed RO/RO SES for a European shipyard. The size of this vessel was driven by the number of vehicle lanes and available engine power.

Figure 14: Investigation of Powerplant Impact on Design Space

❑ Installed power and beam limits constrain design space

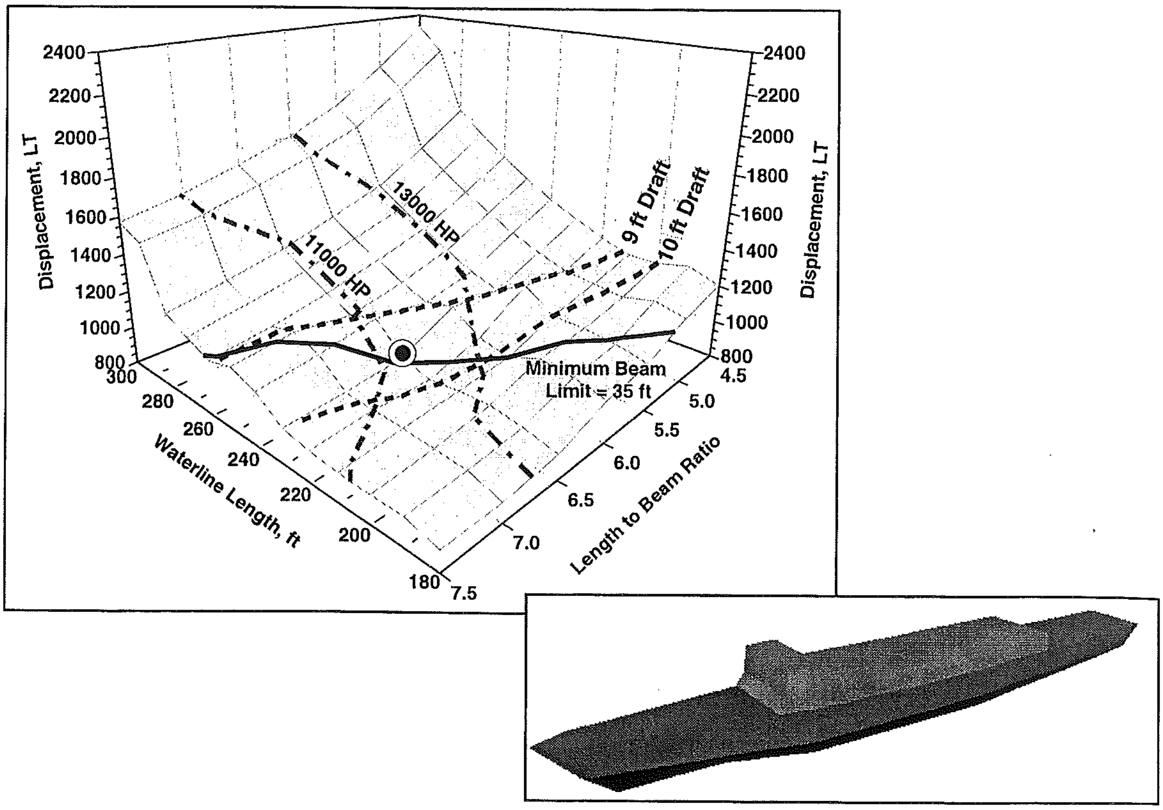

Figure 15: Assessing the Impact of Payload Arrangement

❑ Determining the impact of below-deck arrangements

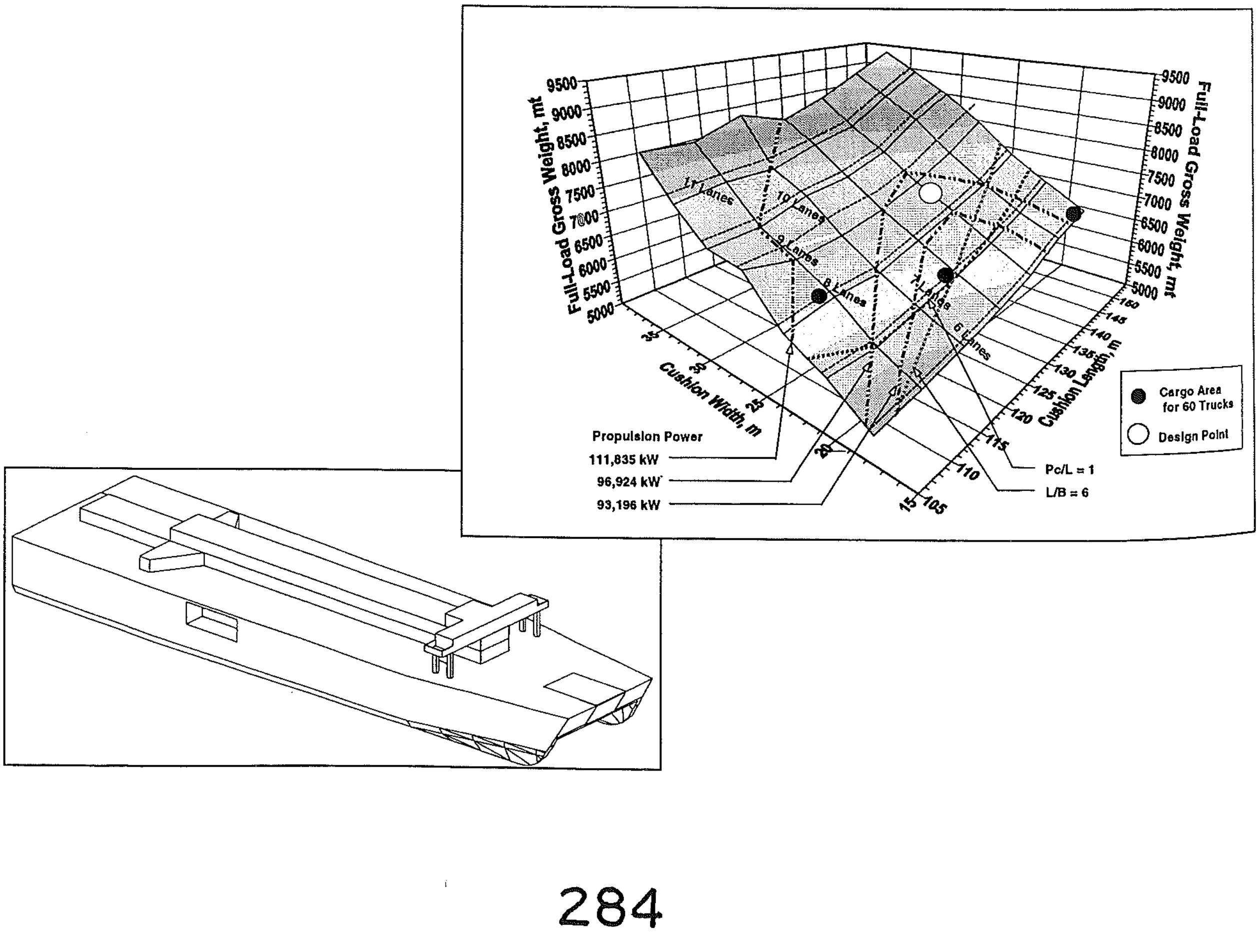

Figure 16 shows the acquisition cost of a fast semi-SWATH that was explored for the U.S. Coast Guard Deepwater Program. The graph insert shows how cost is impacted by the choice of block coefficient and slenderness of the ship's demi hulls.

Figure 16: Use by the Naval Architect

❑ Designing an affordable ship

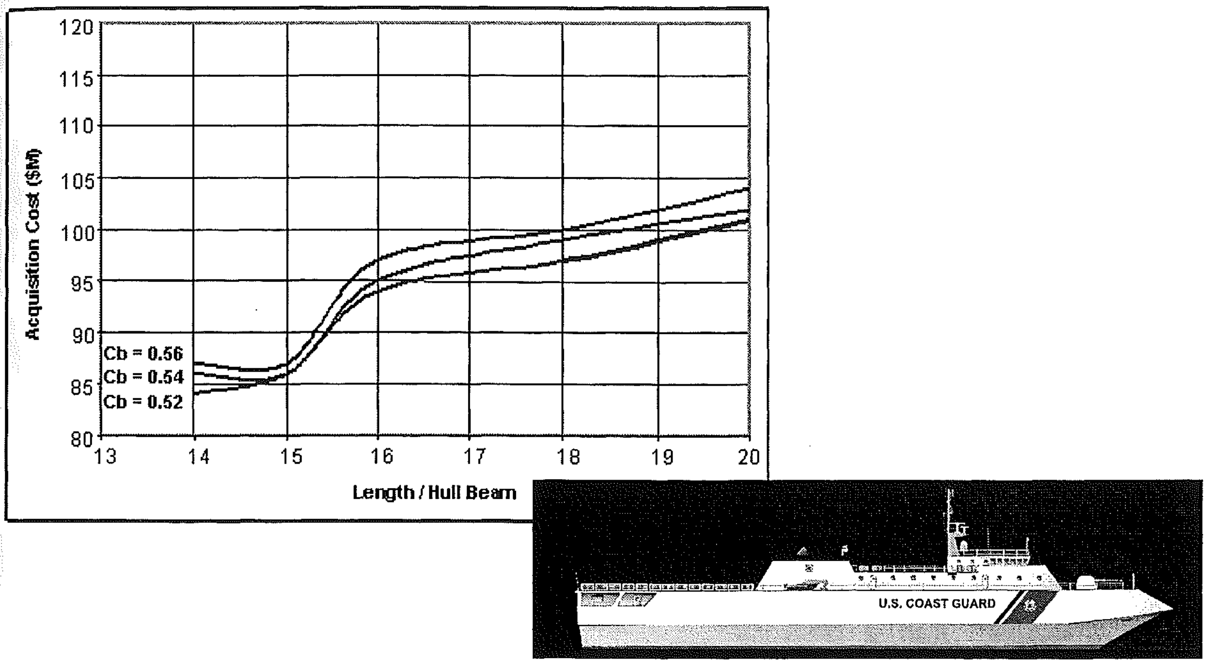

Other applications (Table 4) have included investigating the cost impact of new types of hull structure, new types of diesel engines, and new types of pollution control equipment. New types of electrical systems for an all-electric combatant have also been evaluated including an electric gun. The impact of new technology can be examined individually or in combination to provide a first look at potential benefits.

Table 4: Benefits of Whole Ship Design Synthesis – to the Technologist

•	Investigate HM&E technologies such as: Composite structures Composite diesels Pollution control equipment All electric ship systems Electric Gun
•	Individually or in combination
•	Provide first look at potential payoff

Figure 17 is an example where a new type of waterjet was compared to an AZIPOD and a conventional marine screw for an all-electric DDG51.

Figure 17: Whole-Ship Assessment of Alternate Technologies

- ❑ Competing technologies can be fairly assessed only at the whole-ship level
- ❑ Example: DDG51

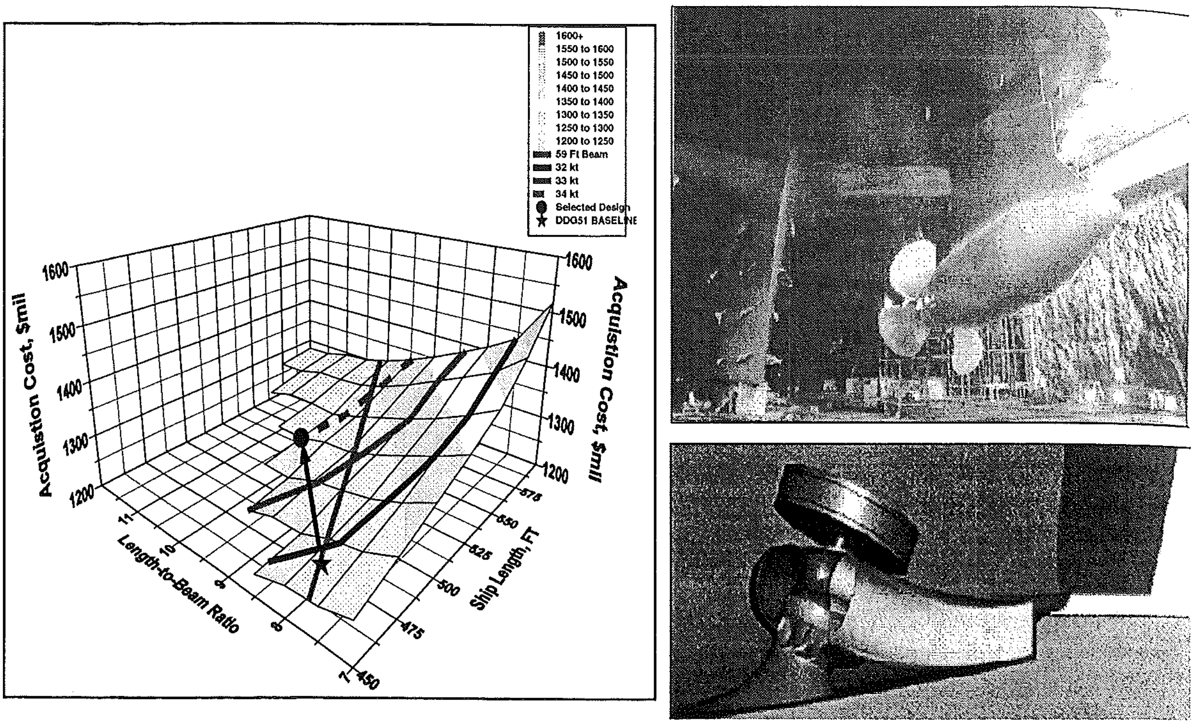

Figure 18 shows results where various types of fuel cell plants were modeled for main propulsion and ship service. By running the tool with various assumed fuel-cell capabilities and various ship types, one can determine the combinations of specific weight and fuel consumption that should be targeted:

1. To be of benefit to all naval applications
2. To be of benefit to some, and
3. To be of no benefit to any.

In this way, developers of fuel-cell plants can be given meaningful goals for future development.

Figure 18: Matching Technology to Requirements

- ❑ Setting goals for the technology developers

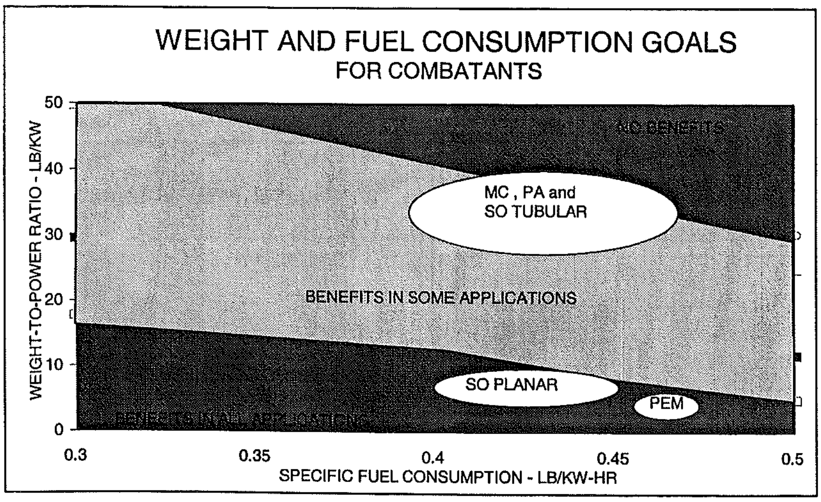

A study that actually included a war-gaming exercise was conducted in 1996 for NSWC Carderock. Here, we explored the cost benefits of a distributed battle-space force architecture of many small single-mission ships to replace fewer large multi-mission ships, as illustrated in Figure 19.

The larger multi-mission ships are shown in Fig. 19 as ghosts. Their smaller replacements are shown in black. This, we understand, was the genesis of the "street fighter" concept now being explored by the U.S. Navy as a Littoral Combatant Ship (LCS).

Figure 19: Examining Unconventional Force Architectures

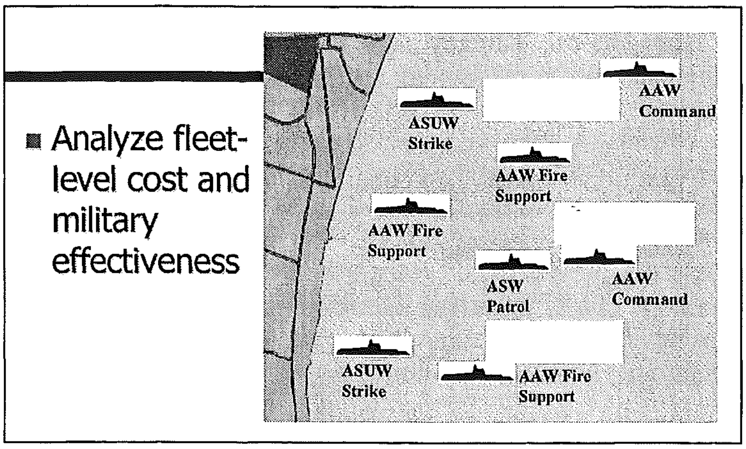

It was this exposure, coupled with the rapid turn-around work done to help the Swedish Navy find affordable requirements for the Visby-Class ship, that gave impetus to the idea of using the whole-ship assessment tool in a war-gaming environment.

Figure 20 illustrates a screening process of first harvesting promising technologies that could be assessed in an early-stage IPT environment using the synthesis tool pass. Results would then be passed to the U.S. Navy's asset and leaps tools for refined analysis leading to an assessment of "–ilities", including vulnerability and survivability. This would then characterize ship attributes that could be subjected to a war game to help assess overall capability and mission needs. Promising concepts would then be recycled for further refined analysis.

Note that the U.S. Navy's asset program can actually be run in a seamless fashion with inputs generated by PASS.

Figure 20: Integrating Technology with Mission Needs

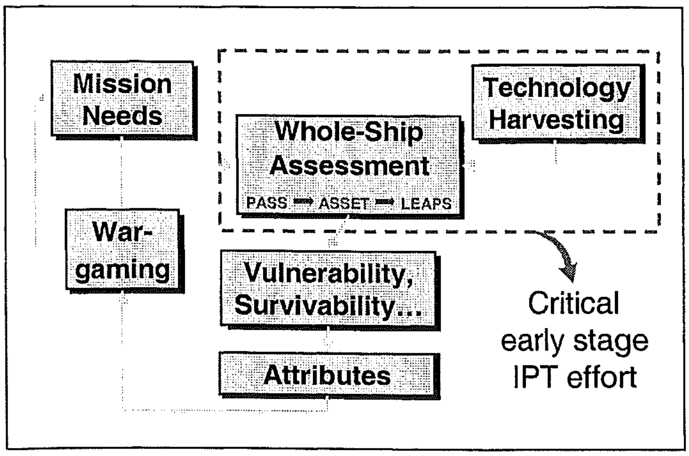

6. Conclusion

In conclusion, this paper has focused on two areas:

To show a method of assessing new technologies for naval ships in a total ship context, and to show a process that, with the aid of a design synthesis tool and an out-of-the-box thinking small IPT, the ship acquisition process can be jump-started (see Figure 21). This is achieved by rapidly examining early-on the possible mission and technology opportunities and the benefits including cost of requirements. With the suggested future ship concept development approach, the concepts are developed at increasing levels of fidelity if warranted and examined in assessment war games. If the answers are positive, technology managers can factually show the benefits of the application of their technology. Or, they can show the benefit of a technology needing further development, but providing a leap in operational capability.

Figure 21: Real-Time Examination of Options by IPT

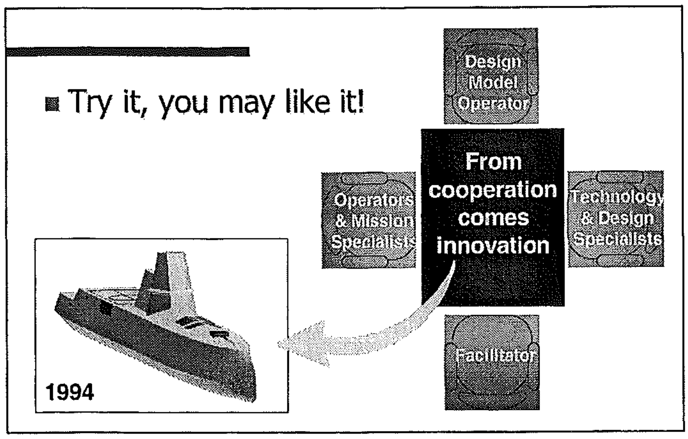

The process is win-win for the warrior or mission analyst, win-win for the technologies, for the naval architect and for OPNAV and the appropriate PEOs.

The pieces of the suggested future ship concept development approach are in place, but it needs to be utilized as a process. The process then needs to be scrubbed for lessons learned, changes made as appropriate and re-used, hopefully becoming an approved process by the Navy.

The process has been used in a few projects up to the level of the reporting out to the executive steering committee. In these cases, the committee was the customer.

It has not been integrated into the broader Navy community involving in-depth design studies by NAVSEA or recent assessment war games conducted by the Navy War College.

Again, all pieces are in place.

One just needs to try it.

You may like it.

Aerodynamic Flow Simulations for an SES Employing Virtual Reality Post-Processing Techniques

Olaf Lindenau, TU Hamburg-Harburg, lindenau@tu-harburg.de
Volker Bertram, ENSIETA, bertram@waves.insean.it
Ould M. El Moctar, Germanischer Lloyd, moct@germanlloyd.org
Scott Gatchell, HSVA, gatchell@hsva.de

Abstract

A commercial RANSE solver is applied to compute the flow around ship superstructures of the AGNES 200 surface effect ship. The water surface is approximated by a flat surface. The surface effect ship is quite simple in geometry and the grid employs only hexahedral elements. Results are shown for various angles of attack using unsteady flow simulations. The flow results show a very complex structure with corkscrew streamlines behind the superstructure towards the helicopter deck. Virtual reality techniques are employed to visualize the flow. The techniques to export results from CFD models to the VRML model are not straight-forward and experience is reported. CFD grids are usually too detailed to be used directly as Virtual Reality models. An automatic downsizing routine has been developed reducing the polygon count in this application by one order of magnitude without losing geometrical details. A Java application is presented that allows to interactively blend in and out streamlines.

1. Introduction

Wind forces are increasingly of interest as speed and surface area above the waterline increase. Other aerodynamic properties of interest here are working conditions on helicopter decks. The traditional approach to study aerodynamic flows around ships employs model tests in wind tunnels. Computational fluid dynamics (CFD) is increasingly used drifting from research to practical consulting work also for ship aerodynamics. As one of the first such applications, Førde et al. (1992) applied CFD to a surface effect ship (SES). The air resistance accounted for 25% of the total resistance for this 50 knot ship. The CFD guided improvement of the forebody of the superstructure reduced the wind resistance by 40%. We present here also an application to an SES, but naturally a decade later, our analysis employs a more sophisticated physical model (including viscosity and turbulence) and a finer resolution of flow and ship geometry. We employed the code Comet. The fundamental theory and main employed options are described extensively in El Moctar and Bertram (2002).

We selected for our application the French SES "AGNES 200", Table I. As a first step, a CAD description of the SES was generated in ICEM-CFD, which served as basis for further grid generation. The finite-volume grid used an inner cylindrical domain surrounded by an outer block-shaped domain, Fig.1. The grid extended from 1 ship length L=Lpp ahead of the forward perpendicular to 1.5 L behind aft perpendicular, 1.5 L in vertical direction, and 1.5 L to each side from the plane of symmetry. The inner cylindrical domain was designed such that a for each rotation by 5° cell nodes would again coincide with cell nodes in the outer domain, i.e. for each 5° increase in relative wind angle we could again work with matching interfaces in the code. The relatively simple geometry of the SES superstructure allowed to use hexahedral elements for the whole domain. Results shown here were obtained with a grid using 2.9 million cells.

Table I: Main data "AGNES 200"

Displ.	250 t	L_{pp}	45 m	Cushion length	41.4 m	T (on cushion)	1.1 m
L_{oa}	51 m	B_{oa}	13 m	Cushion width	8.0 m	Speed V	40 kn

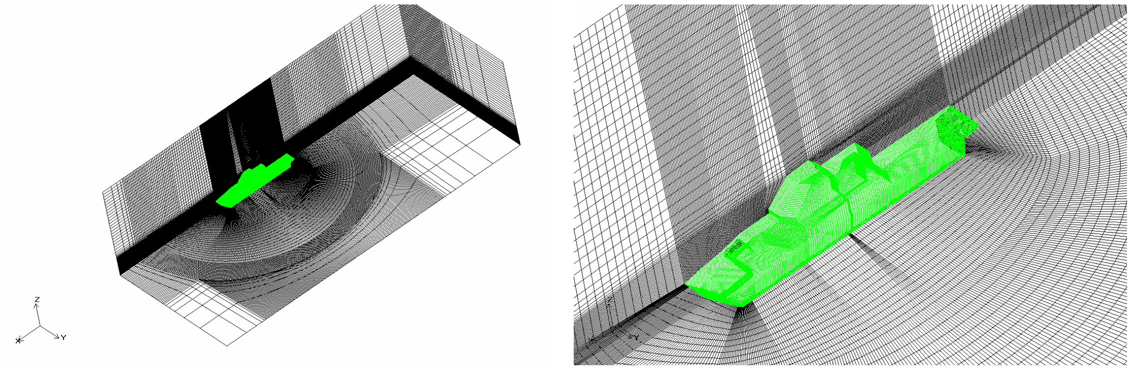

Fig.1: Grid detail for SES with inner cylindrical domain

2. Virtual Reality for CFD post-processing

The predominant role of post-processing for CFD is visualization of the complex flow structures and ship geometries under investigation. The visualization serves a twofold purpose:

- To aid the CFD expert in understanding the flow and thus derive conclusions on either how to improve his computational model (quality control) or on how to aid the customer in his design.
- To communicate his findings to the customer, e.g. by pointing out where, how and why to modify a design to improve its aero- or hydrodynamic characteristics.

CFD methods and post-processing have both become more and more sophisticated in time, a development which was enabled to a large extent by the rapid growth in computer power available to engineers in industry and academia. State of the art in CFD post-processing are color plots showing the flow from assorting angles with selected details and quantities to avoid confusion. This does not always succeed. E.g. for streamlines in complex flows with considerable cross-flows or rotation, plots turn quickly into "spaghetti" diagrams as the number of visualized streamlines increases. For unsteady flows, sometimes electronic videos (avi) are created, but these require considerable file size for longer simulations and decent resolution. Again, the perspectives and quantities are prescribed by the creator of the post-processing.

For complex 3-d flows and/or unsteady flows, Barcellona and Bertram (2000) proposed "virtual reality" techniques as a better alternative to conventional post-processing, presenting several applications. Virtual Reality (VR) enables to view (and zoom) in space and time an 'enhanced' world showing ship structures and flow properties. We use here the term 'Virtual Reality' for the "poor man's" version of Virtual Reality, i.e. a usually mouse-controlled fly-through navigation through a three-dimensional environment on a plain graphics monitor. This is far from what fully immersive Virtual Reality envisions, but can be realized on computer hardware widely available in industry and is sufficient for most applications we have. We implemented our models in the Virtual Reality Modeling Language VRML, which has become an international ISO/IEC standard. The resulting models are often surprisingly small, typically 0.1 to 5 Mbytes, i.e. a size that allows easy internet communication. VRML viewers ('browsers') are public domain and available for all common platforms. However, VRML capabilities are limited and in our application here we employed also JavaScript to add features. While the original programming is not so simple (compared to VRML), the script sources can be downloaded together with the VRML model, www.ssi.tu-harburg.de/VR/index.html, and serve as master copies to be included in similar models as black-boxes.

As a first step, we exported the geometry of the SES from the Comet RANSE grid. This resulted in a model with very many polygons which made the model extremely slow due a size of 43000 polygons and 2810 KByte. We then wrote a Fortran routine to merge faces lying (almost) in one plane which resulted in a considerably reduced polygon count to 900 polygon and 85 KByte, Fig.2, and a corresponding size of 130 KByte. The geometric model of the SES exploited then again the smoothing capabilities of VRML creating a realistic model of the hull. The streamlines were computed using the public domain IBM tool DX. The streamlines were exported and simplified similar to the SES geometry before they were converted to VRML format.

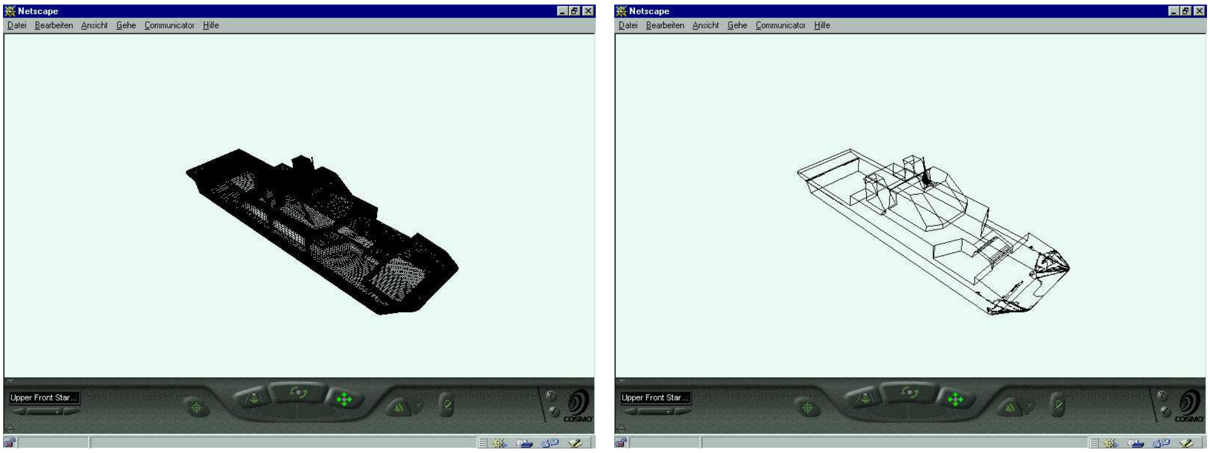

Fig.2: Original model exported from CFD grid (left) and model with automatically reduced polygon count (right)

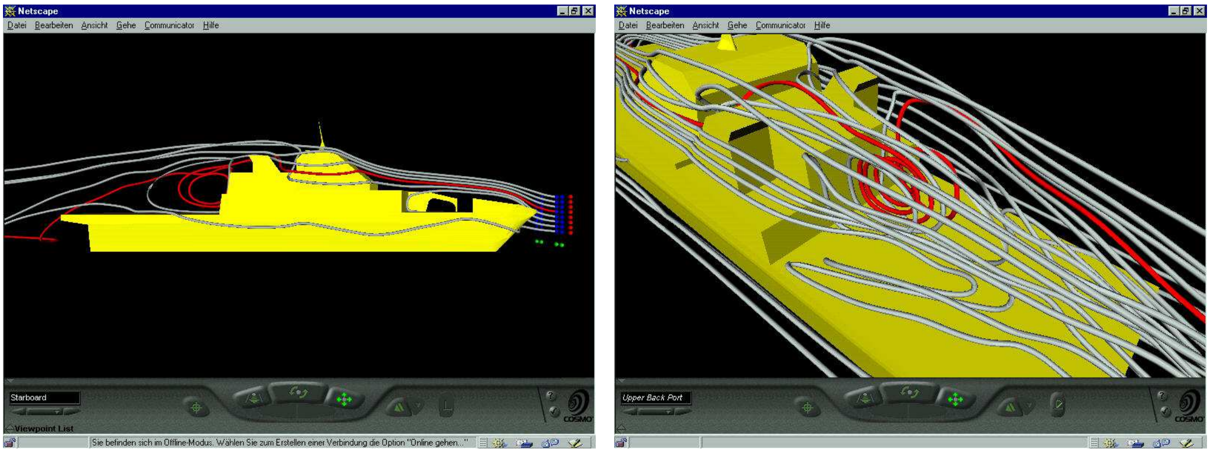

Fig.3: Streamlines with one selected streamline in red

We employed JavaScript to allow interactive selection (blending in and out) of streamlines. We also included a feature which highlights one selected streamline in red when moving the cursor to that streamline, Fig.3. The resulting model including streamlines has a size of 330 KByte (!) making it very easy to handle or download. (The zipped version has a size of 160 Kbyte.) Details of the process to create the VRML model will be presented in Lindenau and Bertram (2003).

3. CFD computations

For wind coming from relative wind angle μ=180° (e.g. pure wind resistance due to the moving ship), the computed pressure distribution looks as expected, Fig.5. At the skirt front, the flow is retarded to almost stagnation resulting in high pressures. Smaller high-pressure regions appear on the funnels in areas not in the wind shade of the cabin and on the forward inclined front of the cabin. At the edges and particularly on the cabin top and foredeck, there are corresponding low pressure zones. Fig.4 shows streamlines starting after the cabin. There are large recirculation regions above the helicopter deck and behind the stern. Between the funnels there are strong vortices as visualized by “cork screw” streamlines. Fig.6 shows streamlines starting in the foreship. The two layers differ by 0.55m in height of the starting points. The starting height yields here totally different streamline characteristics which is an indication of the strong three-dimensionality of the flow. The VRML modeling allows here easily to blend streamlines out at will and to view at an angle and distance at will. For the lower layer, the outer streamlines are sucked into the recess between foreship and cabin. Afterwards the follow largely the side of the ship. The center lines hit the lower edge of the cabin, and are then diverted to the sides where the speed is reduced to such an extent that the streamline tracing breaks down. For the upper layer, the center streamlines are diverted upwards over the cabin forming recirculation areas behind the cabin. The streamlines at the side are no longer sucked into the recess between cabin and foreship, but follow on the upper deck sideways around the cabin.

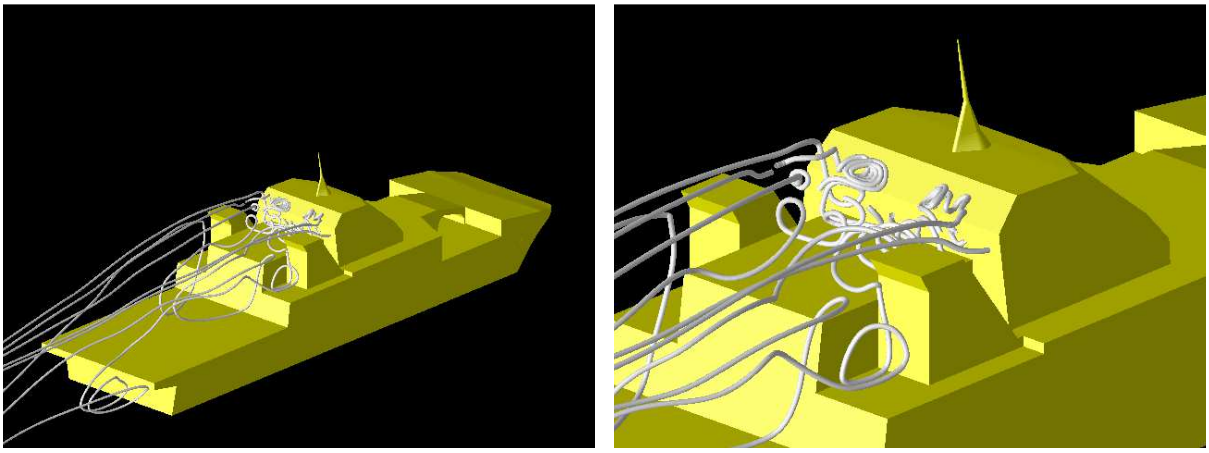

Fig.4: Streamlines behind cabin for μ=180°; side view (top) and detail between funnels (bottom)

A moderate oblique flow direction of 170° changes the flow noticeably, Figs.7 and 8. The high-pressure region at the forward cabin incline is increased. On the luff side, the low-pressure regions disappear almost, on lee the low-pressure regions are more pronounced. This tendency increases with angle of attack. The flow changes observed for 170º become more pronounced with increasing angle as demonstrated for 150º, Figs.9 and 10. There is a distinct blockage effect of the superstructure expressed in the pressures on the lee side. The flow is now predominantly in transverse direction and less complicated as there are hardly any superstructure elements downstream of other superstructure elements. The flow resembles somewhat the flow around a foil. On the lee side, the flow is sucked partially along the ship sides before it detaches approaching its original flow direction again, as becomes apparent when zooming out to a larger perspective, Fig.11.

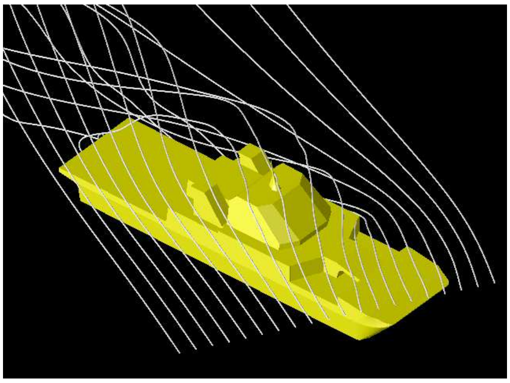

Fig.11: Streamlines for a larger region around the SES for μ=150°

4. Conclusion

RANSE computations help to understand the flow around the superstructures of fast ships. They may well aid the design in the future. Virtual reality techniques offer superior post-processing possibilities in understanding complex three-dimensional flow pattern such as streamlines with vortices and cross flows. Continued research is needed now to reduce time and cost for such analyses and to develop standard VRML post-processing interfaces.

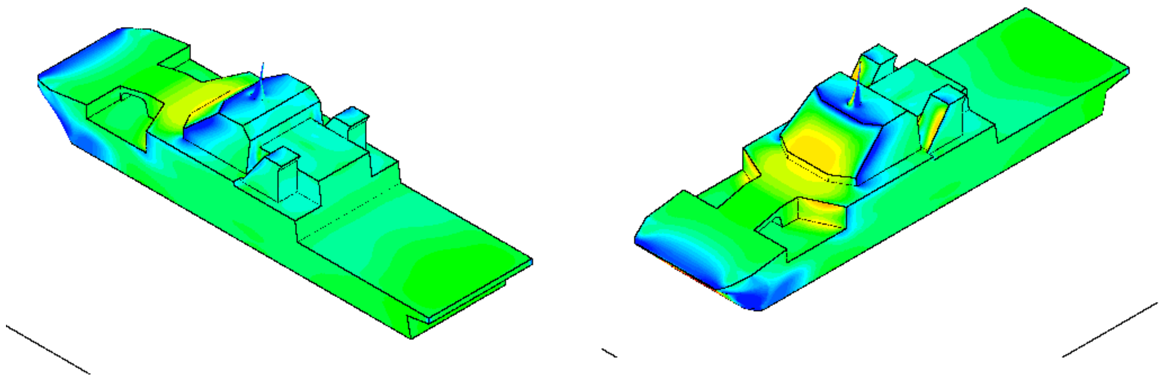

Fig.5: Pressure on SES for μ=180°

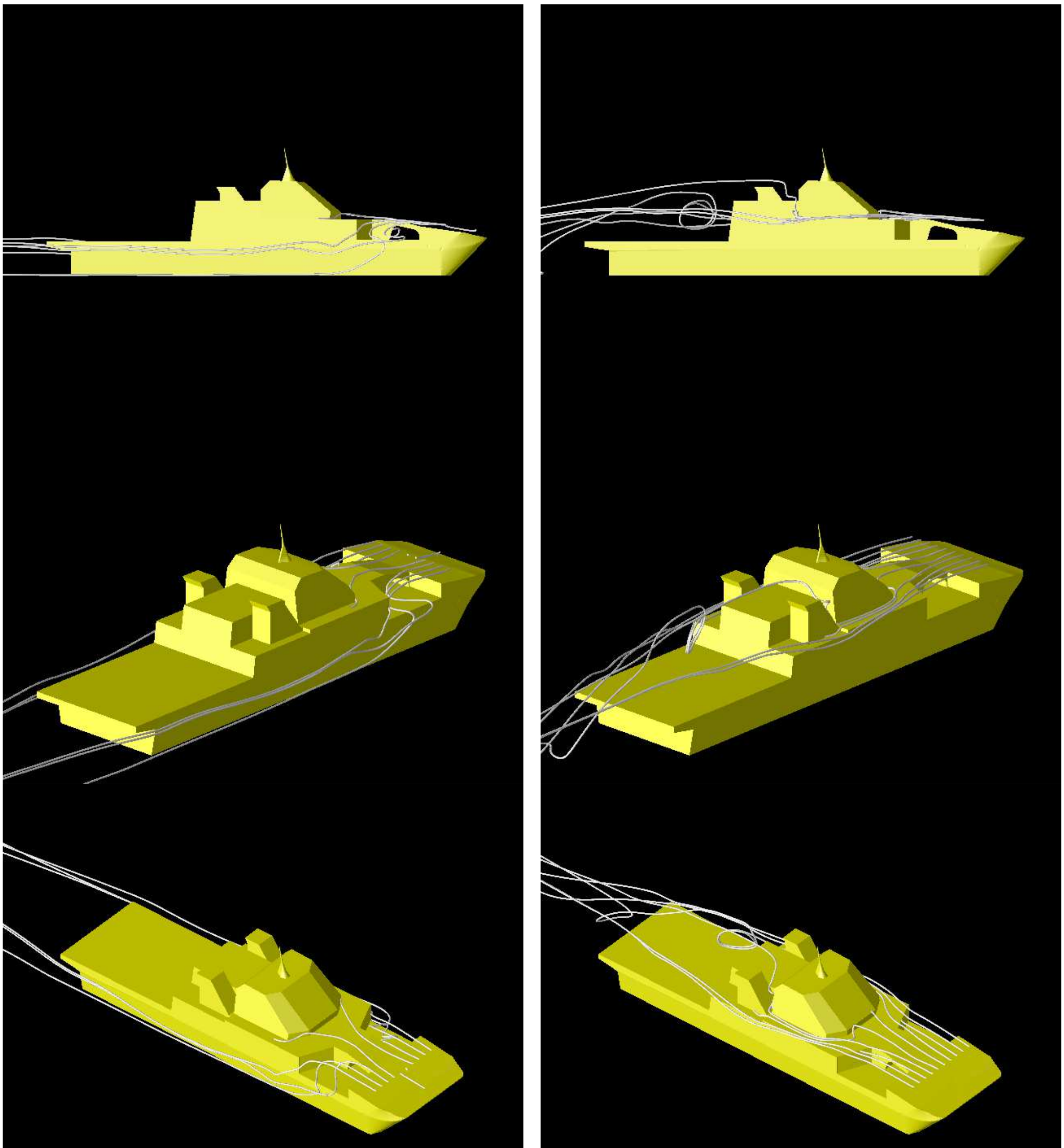

Fig.6: Streamlines starting in foreship μ=180º, lower layer (left) and upper layer (right)

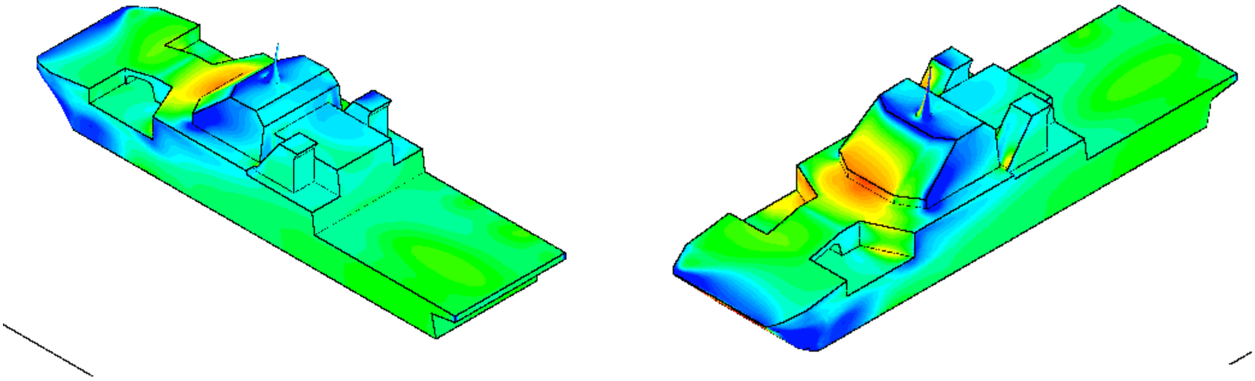

Fig.7: Pressure on SES for μ=170º

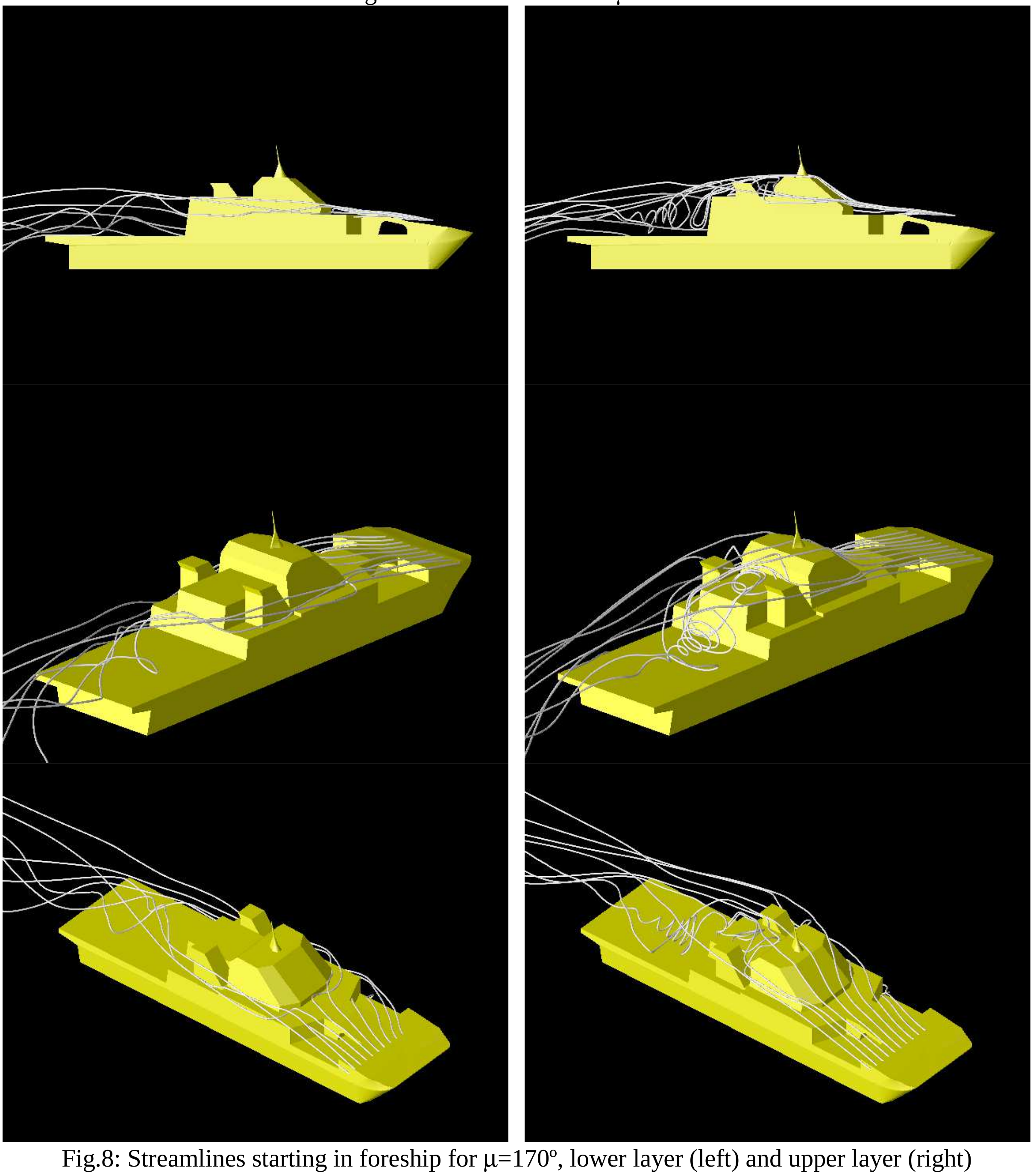

Fig.8: Streamlines starting in foreship for μ=170º, lower layer (left) and upper layer (right)

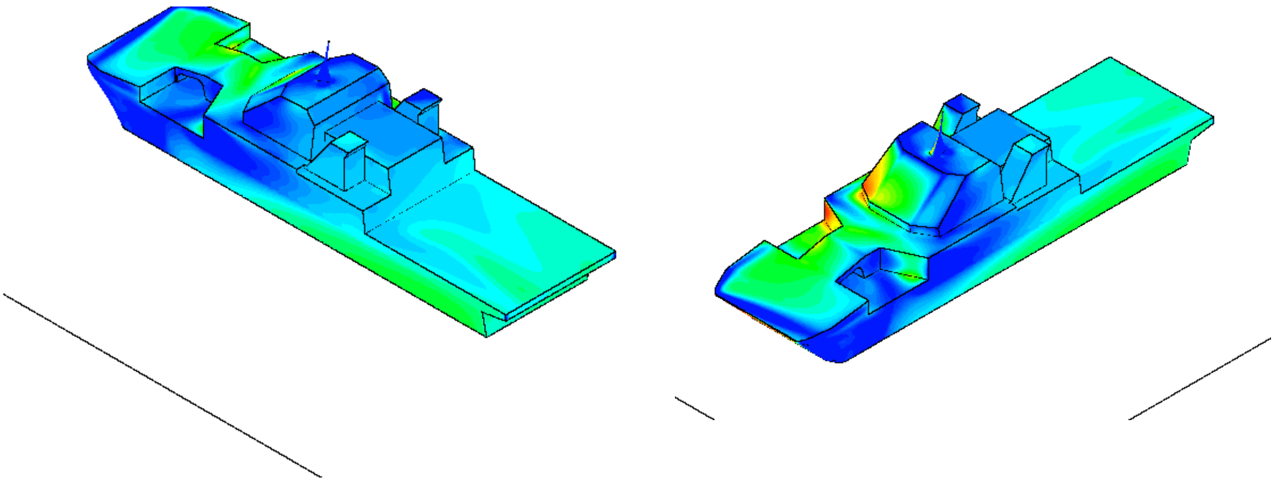

Fig.9: Pressure on SES for μ=150º

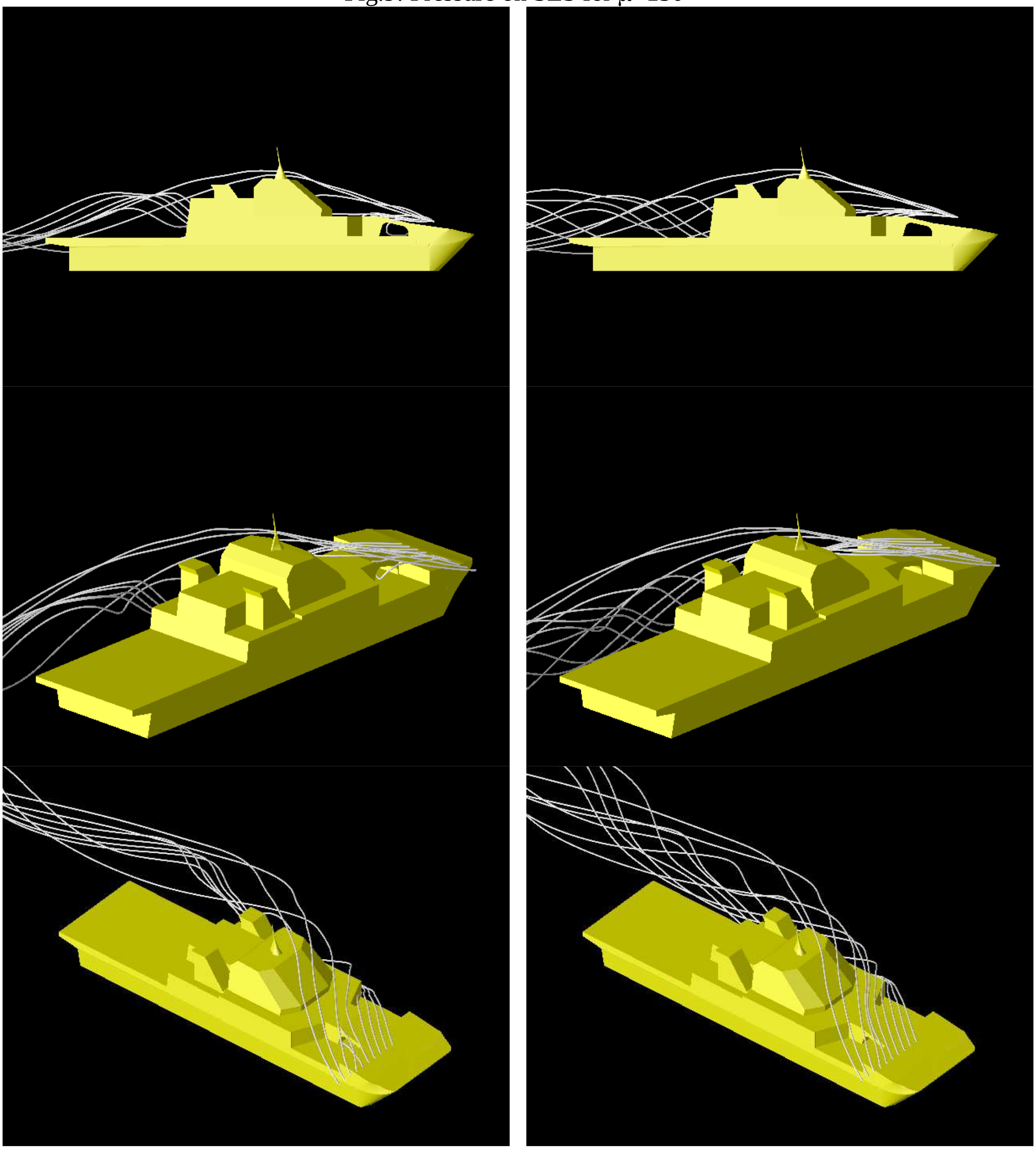

Fig.10: Streamlines starting in foreship for μ=150º, lower layer (left) and upper layer (right)

References

BARCELLONA, M.; BERTRAM, V. (2000), *Virtual Reality for CFD Post-Processing,* 1st Int. Conf. Comp. IT Appl. Maritime Ind., COMPIT, (Ed. V.Bertram), Potsdam

EL MOCTAR, O.M.; BERTRAM, V. (2002), *Computation of viscous flow around fast ship super-structures*, 24th Symp. Naval Hydrodyn., Fukuoka

FØRDE, M.; ØRBEKK, E.; KUBBERUD, N. (1992), *Reduction of aerodynamic drag of a high speed catamaran by using advanced CFD calculations,* 1st Int. Conf. Appl. CFD, Basel

LINDENAU, O.; BERTRAM, V. (2003), *The making of VRML models with streamlines and pressure distribution*, 2nd Int. Conf. Computer and IT Applications in the Maritime Industries, COMPIT, Hamburg (in preparation)

Finite Element Structural Modelling of a Composite-Material Multihull

Richard Luco*; **Marcos Salas***; **Mostafa Tarfaoui****; **Volker Bertram****

* Institute of Naval and Maritime Sciences, University Austral of Chile, rluco@uach.cl
** ENSIETA, Brest, France.

Abstract

The structural modelling of composite materials is not a straightforward procedure. Materials can be combined in a large number of ways, fibre orientation, i.e. strength, can be modified taking full advantage of orthotropic materials. The percentage of reinforcement material in the laminate is variable and finally material quality and properties also depend on the fabrication procedure. The reliable determination of materials mechanical properties is therefore not a trivial matter. Usually testing of samples is required, again due care is required in order to reproduce the material that would be obtained in hull-production conditions. Alternative methods for the estimation of mechanical properties are also available.

The present paper presents a practical approach to the calculation of composite materials structures, specifically PVC foam core and fibreglass in multihull vessels. Material properties are estimated in base of individual layers of composite materials. Some experimental results from testing samples are also provided. Different boundary conditions and static load cases are studied in order to provide a preliminary overview of the stress distribution of the multihull.

1. Introduction

The dynamic behaviour of a composite-material multihull travelling in waves presents several challenges to ship design science. The nature of the materials involved is complex and much research is required in order to fully predict the mechanical properties of composite materials under different, and often simultaneous, type of loads. The present state of the art in this field is, at best, in a developing stage and most authors agree in the need of experimental testing to validate composite materials mechanical properties.

Another source of uncertainty is the adequate consideration of sea loads. In this paper a static approach is employed as a suitable starting point to evaluate the stress-distribution over a multihull. Standard classification societies loads are introduced to simulate simple loading conditions. Despite the simplicity of the analysis “hot spots” are clearly identified providing valuable qualitative information. Determination of accurate realistic stress values requires dynamic sea loads to be introduced, including wave impact loads if a seakeeping analysis shows slamming is likely to occur in the prescribed seaway.

2. The Composite-Material Multihull

The composite-material multihull to be analysed is a catamaran designed by Crowther Multihulls (Australia) and built by Alwoplast Ltda. (Chile). Figure 1 shows a general view of the vessel. Main particulars of the catamaran are:

Length over all:	16.76 m
Beam:	6.00 m
Depth to main deck:	2.40 m
Draught:	0.80 m
Displacement:	18 tonnes
Material:	sandwich GRP
Service speed:	28 knots

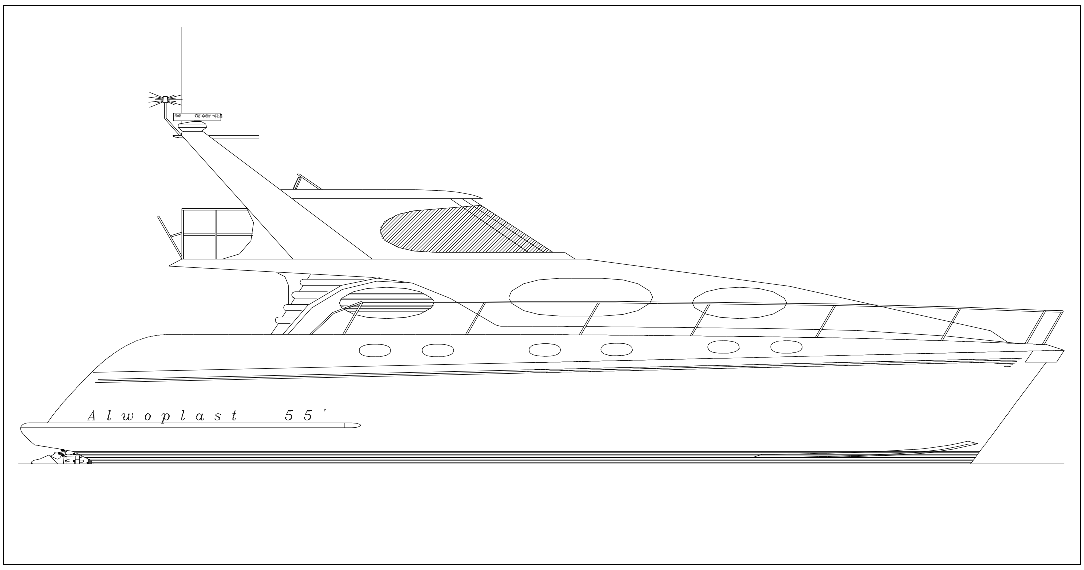

Figure 1: Composite-material Catamaran

The catamaran is built of sandwich Glass Reinforced Plastic (GRP) with Polyvinyl Chloride (PVC) core. Hull material is not unique as several types of glass fabrics are laminated in layers at different parts of the hull, namely unidirectionals, bi-axials and tri-axial glass fabrics.
The lay-up is a vacuum process to the maximum practical possible extent, this is about 60% of laminated structures. The remaining 40% corresponds to traditional manual lay-up techniques.

3. Mechanical Properties

One key aspect of the Finite Element Analysis of a composite-material marine structure is the determination of actual material properties. Composite-material mechanical properties are by no means a settled matter. Almost endless combinations of fibres and matrix (resin) can be chosen, furthermore, the orientation of fibres relative to main loads is also important in determining relevant material properties such as tensile, compressive and flexural modulus. Theoretical procedures to estimate composite material properties are described in the technical literature (Al-Quieshi 1984; Divinycell 1991; Miravete et al. 2000). Theoretical methods offer valuable preliminary information to determine composite materials mechanical properties, however, they are not reliable for complex laminates including several layers of fibres in different orientations. Moreover sandwich laminates introduce new complications related to the core behaviour.

Composite materials properties characterisation is a very difficult problem and there are no reliable theoretical methods available to estimate them. In general, theoretical expressions are usually severely restricted by one or more of the following assumptions:

- The laminate is thin
- The strain distribution is linear along the thickness direction
- Strains perpendicular to mid-surface are negligible
- Out-of-plane shear strains are zero.

Assumptions that in general do not apply to marine structures. It must be concluded that sample testing is the most reliable method to obtain mechanical properties of composite materials and therefore this will be the procedure followed to characterise material mechanical properties required in the finite element modal analysis of the multihull. Special care is necessary in order to reproduce similar working conditions as the fabrication techniques are by no means stable.

Normally, composite materials mechanical properties are obtained experimentally according with some recognised standard procedure, for example the American Standard for Material Testing rules C 393-94 or alternatively the European Standard EN 63 for testing Glass reinforced Plastics. Testing of composite material requires that samples must be fabricated, as far as practically possible, with the same techniques used in the fabrication of the full scale structure, a number of samples have to be tested to calculate average material properties and discard extreme results due to defects in the samples fabrication process. This results in Testing of composite materials being expensive and time consuming. For this very good reason mechanical properties are often estimated theoretically in order to carry out a structural stress analysis.

3.1 The Rule of Mixtures or Tsai – Halping Method

A simple theoretical method, the Rule of Mixtures or Tsai – Halping Method (Smith 1990;Spyrakos and Raftoyiannis 1997), relates the volume of component materials and their individual properties. The method, restricted to linear behaviour, allows several material properties to be estimated, including thermal conductivity. Main composite-material properties are calculated as follows.

Density

The rule of mixtures expression for composite-material density (ρ) is as follows

$$\rho = V_m \rho_m + V_f \rho_f$$

where *m* and *f* indicates properties corresponding to the matrix (resin) and the fibres respectively, for instance V_f correspond to the volume of fibres present in the laminate.

Young´s modulus

Young´s modulus for loads applied parallel to the direction of unidirectional fibres E_1 is calculated according to the expression

$$E_1 = V_m E_m + V_f E_f$$

The 1 sub index indicates properties in the direction parallel to the fibres.

When loads grow and the material behaviour is non-linear, the matrix contribution to stiffness can be neglected and Young's modulus is simply determined by fibre properties.

$$E_1 = V_f E_f$$

When loads are applied perpendicularly to unidirectional fibres, i.e. in direction 2, each component acts independently and the following expression is valid.

$$\frac{1}{E_2} = \frac{V_m}{E_m} + \frac{V_f}{E_f}$$

Poisson's ratio and Shear Modulus

Poisson's ratio ν and the Shear Modulus *G* in the 1-2 plane, can be obtained as follows,

$$\nu_{12} = V_f \nu_f + V_m \nu_m \qquad G_{12} = \frac{G_f * G_m}{V_m G_f + V_f G_m}$$

The expressions of E_2 and G_{12} are usually a lower bound for the transverse and Shear Modulus of unidirectional laminate and therefore experimentation is required to obtain reliable values.

Chopped Strand Mat (CSM) fibres are oriented in aleatory directions in the matrix, i.e. the material can be considered isotropic, at least in the plane parallel to fibres. In this case Young's modulus, Poisson's ratio and Shear modulus are described by

$$E = \frac{3}{8}E_1 + \frac{5}{8}E_2 \qquad \nu = \left(\frac{E}{2G}\right) - 1 \qquad G = \frac{1}{8}E_1 + \frac{1}{4}E_2$$

3.2 Validity of Theoretically calculated material properties

Is was mentioned before that applicability of theoretical methods is restricted to linear behaviour. To illustrate this, deflection of sandwich composite-material samples was determined experimentally. Additionally, a Finite Element Model of the sample was also evaluated, mechanical properties obtained theoretically according to the rule of mixtures were prescribed in the Finite Element Model.

Figure 2 shows the Sandwich Finite element Model. Skins corresponds to unidirectional glass in a vinyl ester resin matrix were modelled with 1200 shell elements while the core material is PVC foam of 80 kg/m^3 density modelled with 2400 brick elements.

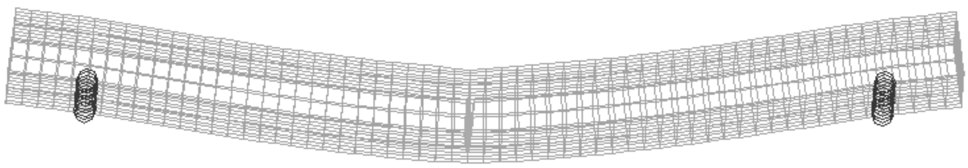

Fig. 2: Finite Element Model of Sandwich Sample

A concentrated load was applied in the middle of the unsupported span (250 mm) to produce a deflection. Deflection results are shown in figure 3.

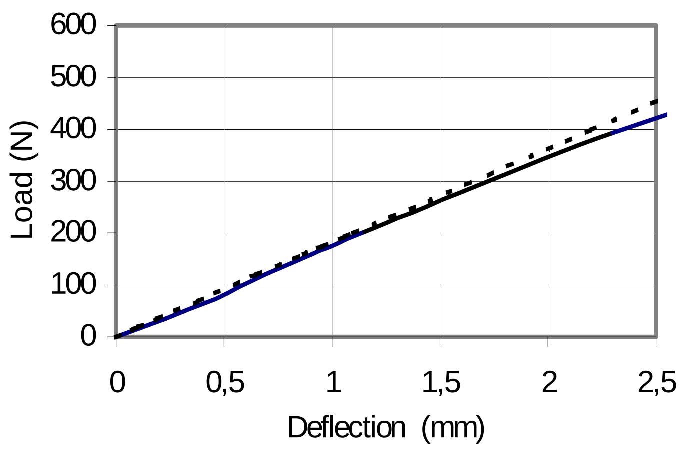

Fig. 3: Deflection of sandwich composite-material laminate. FEM(- - - -) and Experiment (——)

It is clearly seen that good agreement is obtained for lower loads, i.e. in the linear region. The agreement increases as the load increases. This result clearly shows that theoretically calculated composite-material properties are no longer valid when loads induce a non-linear material behaviour.

4. Finite Element Modelling

The catamaran is symmetric, relative to both, the centre line of each demihull and the vessel's centre line. Nevertheless introducing the forms of the multihull into the Finite element model is still a laborious task. To complete the geometric model a semi-automatic method was employed. Key points were defined at the intersection of transverse sections prescribed at suitable positions (mainly bulkheads) and longitudinal stiffeners. Key points coordinates (x,y,z) were then exported to the Finite Element program and finally nodes were defined at the corresponding coordinates. Figure 4 shows the definition of nodal coordinates.

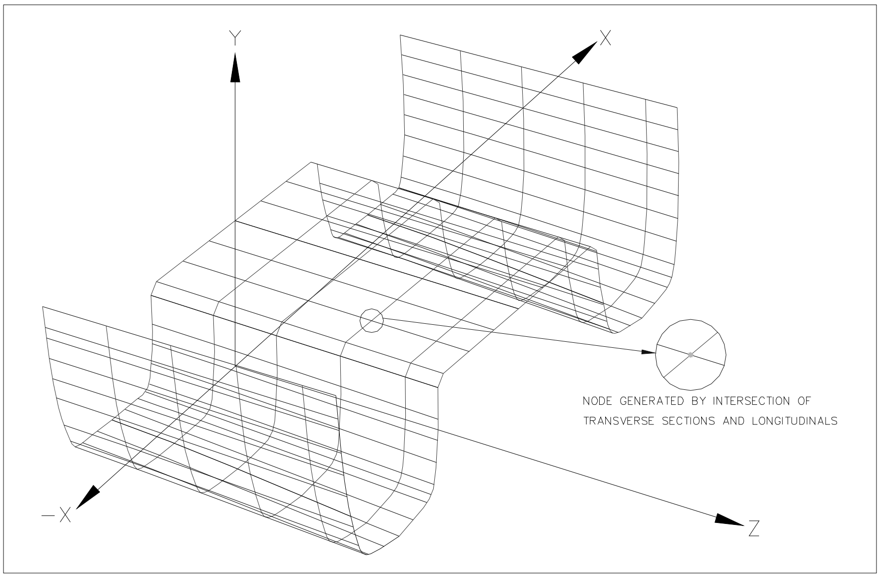

Fig. 4: Node generation

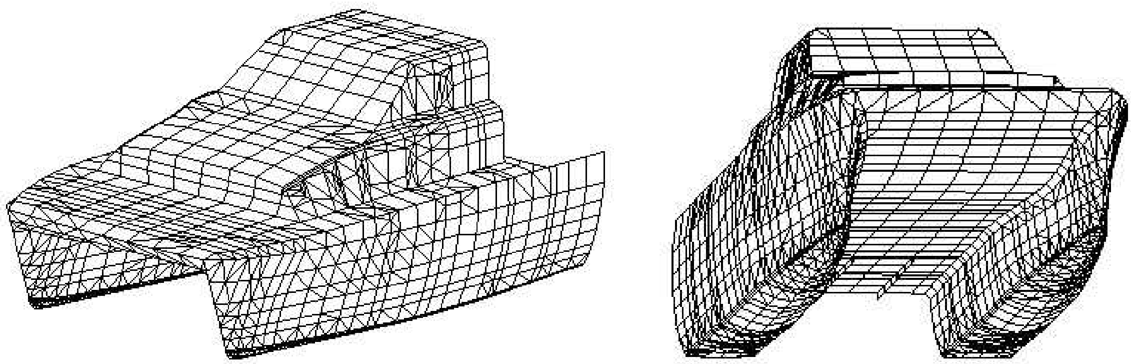

Fig. 5: Two views of the catamaran Finite Element Model

Additional model features such as elements, plate thickness and material properties were incorporated directly in the ANSYS pre-processor. This simple method allowed the creation of the Finite Element Model geometry at a reasonable cost. Complete (both sides) model, as shown in figure 5, required 2992 nodes and 4791 elements.

Composite-material properties were obtained theoretically. DAC, a code specially developed for this purpose (Zaragosa Composite-Materials Research Group) was used to calculate these properties. Results are presented in Table 1.

Table 1: Material properties of multihull structures

Structural Component	E_1 (GPA)	E_2 (GPA)	G_{12} (GPA)	υ_{21}	υ_{12}	thickness (mm)
Hull bottom and sides	1.391	2.702	0.733	0.243	0.472	34.33
Wetdeck	1.113	2.146	0.584	0.244	0.470	44.33
Deck and cabin sides	1.941	1.941	0.329	0.170	0.170	22.17
Cabin roof	1.378	1.378	0.239	0.173	0.173	32.17
Non-watertight bulkheads	0.851	0.851	0.778	0.420	0.420	21.39
Watertight bulkheads	3.311	1.781	0.330	0.189	0.102	23.79
Inner decks	2.162	1.047	0.573	0.419	0.238	22.95
Keel and longitudinal girders	1.392	0.440	0.147	0.361	0.114	10.590

4.1 Applied Loads

Three static load conditions were studied, hydrostatics pressure, prying moment and torsion. Loads were calculated according to (DNV) Det Norske Veritas (2000) Rules for high speed craft.

To ensure fulfilment of the hydrostatic pressure boundary condition, nodes at the bottom centre line were prescribed nil vertical displacements. Rotations (θ_x, θ_y, θ_z), were all kept free. The vessel is floating in calm water, therefore the procedure consist in balancing forces due to hydrostatic hull pressure and displacement weight. Reactions at the constrained nodes must be nil or practically nil.

Prying moment, i.e. transverse bending moment, equilibrium condition consist in applying load to one hull and, in order to produce a prying moment, nodes in the opposite hull are constrained (Figure 6-a) Prying moment load M_s is given by

$$M_s = \frac{\Delta * a_{cg} * b}{s} \text{ (kN*m)}$$

Where Δ is the Displacement tonnes, a_{cg} is vertical acceleration at centre of gravity, s is an operational zone factor and *b* is the distance between both demihull centrelines.

Finally, to introduce torsion loads in the finite element model, torsion moment M_t prescribed by DNV was applied to one hull and restrains to nodes located in the opposite hull, (Figure 6-b). The corresponding load is calculated form the following expression

$$M_t = \frac{\Delta * a_{cg} * b}{4} \text{ (kN*m)}$$

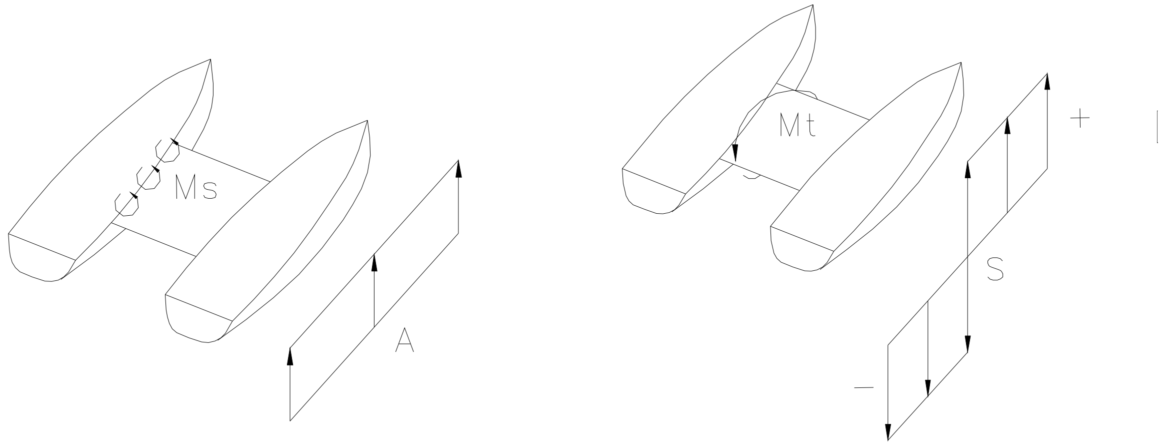

a) b)

Fig. 6: Applied static loads in prying moment a) and torsion b)

5. Results

5.1.- Deflections

Deflections at different areas of the multihull were obtained. For illustrative purposes those corresponding to the static floating condition are presented in Table 2. Figure 7 show deflections at the hulls, deck and cabin 7-a) and hulls and wetdeck 7-b).

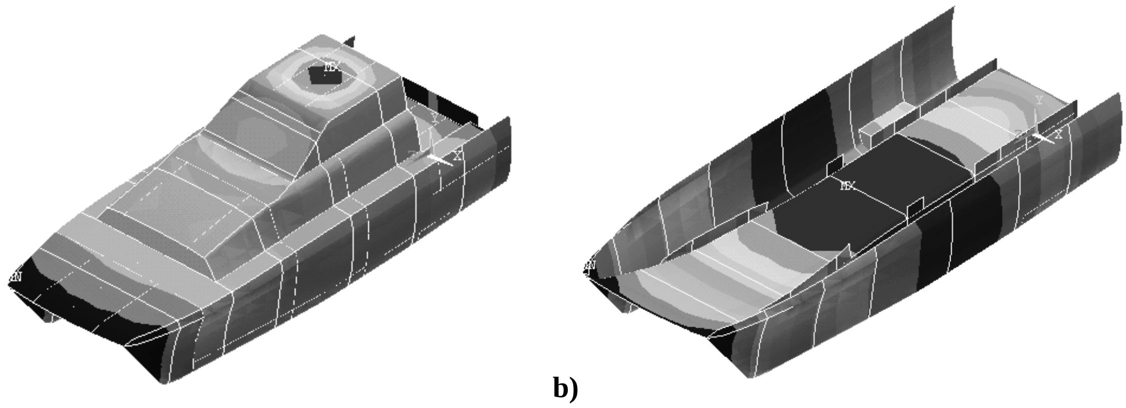

a) **b)**

Fig. 7: Deflections in the static floating condition. a) Hulls, deck and cabin; b) Hulls and wetdeck
Dark regions represent highly deflected areas of the catamaran

The cabin roof is the region most deflected. This is expected because the cabin roof is a light structure not intended to carry significant loads. Stiffening of the cabin resulted in much lower panel deflections.

5.2. Stress distributions

The static floating conditions does not show significant stresses, as expected, and therefore will not de discussed in this section. Table 3 shows maximum stresses for the prying moment loading condition and Table 4 for the torsion loading condition. Tabulated stresses correspond to maximum principal stresses, i.e. “hot spot” stresses as shown in figure 8 where stress distributions for prying moment and torsion are illustrated.

Table 2: Static floating condition deflections

HULL AREA	DEFLECTION (mm)
Hull bottom and sides	18.79
Wetdeck	19.36
Deck and cabin sides	31.86
Cabin roof	36.70
Non-watertight bulkheads	18.95
Watertight bulkheads	18.93
Inner decks	21.70
Keel and longitudinal girders	18.36

Table 3: Maximum stresses under prying moment loading

Stresses →	Principal Stresses (MPa)			Shear Stresses (MPa)		
Structural Component	S_1	S_2	S_3	S_{XY}	S_{YZ}	S_{XZ}
Wetdeck	38.9	18.5	43.7	20.5	9.19	13.8
Non-watertight bulkheads	7.37	1.66	4.35	1.75	3.78	0.332
Watertight bulkheads	105	54.6	107	28.9	1.72	0.04
Inner decks	12.2	4.46	10.9	-	-	3.74

Table 4: Maximum stresses under torsion loading

Stresses →	Principal Stresses (MPa)			Shear Stresses (MPa)		
Structural Component	S_1	S_2	S_3	S_{XY}	S_{YZ}	S_{XZ}
Wetdeck	361	125	362	180	31.3	26
Inner decks	2.97	1.78	2.8	-	-	0.868

6. Conclusions

Further research is required in order to improve the accuracy of theoretical methods to predict composite-material properties. At present the safest approach is to perform experimental tests, specially if non linear material behaviour is expected or multi-axial glass fabrics are included in the laminate. Fabrication of samples requires extreme care in order to reproduce full scale fabrication conditions, if possible, samples taken from the actual hull (cut-outs material) should be tested.

Theoretical methods are a simple and cheap way to estimate composite-material properties required in a Finite Element Analysis. Confidence in the results however is severely restricted due to the inherent restrictions of these methods. The procedure is anyway qualitatively useful because “hot spots”, i.e. regions where stress is highly concentrated, can be identified and appropriate course of action (additional reinforcement for instance) can be taken.

Finite Element Modelling of Sandwich plates requires combined use of shell and brick elements. Core material shear properties should be properly accounted for by brick elements.

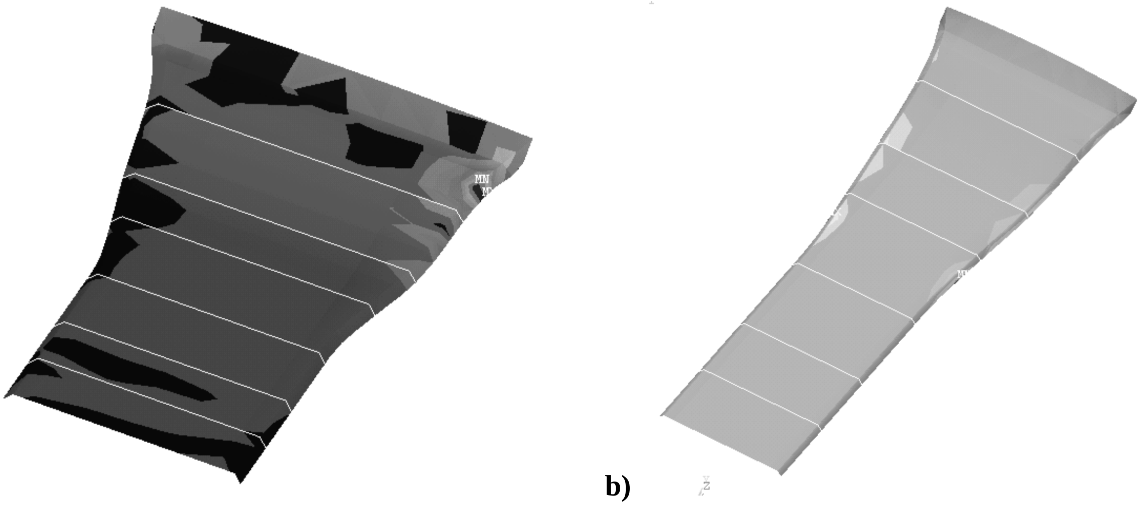

a) **b)**

Fig. 8: Wetdeck direct principal S1 stress distribution for a) prying moment and b) torsion. Dark regions represent highly stressed areas.

Acknowledgements

The authors are grateful for the financial support of DID/UACH (Research and Development Dept. University Austral of Chile). Thanks also are due to Alwoplast-Chile for fabricating test samples, Crowther Multihulls Australia, for providing technical data and DAC-Spain for computing material properties.

References

Al-Quieshi, H. (1984) "*Composite Materials: Fabrication and Analysis*". Inst. Tec. Aero, SJ Dos Campos Brazil.

Det Norske Veritas (2000). *Rules for high speed craft*.

Divinycell (1991). *Technical Manual*.

Miravete, A. et al. (2000) "*Composite Materials*" vol. I. Edited by Antonio Miravete. (in Spanish).

Smith, C.S. (1990) "*Design of Marine Structures in Composite Materials*". Elsevier Science Publishers.

Spyrakpos, C. and Raftoyiannis J. (1997) "*Linear and Non-linear Finite Element Analysis in Engineering Practice*". Algor Publishing Division.

Fatigue of High Speed Craft - In Service Experience

Odd Arne Lyngstad, Det Norske Veritas
Odd.Arne.Lyngstad@dnv.com

Abstract

DNV has during the last 35 years classed close to 600 High Speed Craft. About the half of these craft are still in-service with DNV. There is a great variety with regards to size and type of craft, everything from 12-15 m length rescue boats to 120 m long passenger catamarans for up to 1500 persons.A very brief introduction into DNV' philosophy for how to define fatigue loads and general in-service experience is presented in this paper.

Introduction

Most of the high speed craft built to DNV class are made of aluminium. Hull plating and frames are "normally" made of the 5083 grade while stiffeners and profiles are in extruded 6082. The standard design loads used for checking the strength of the hull are not material dependent. I.e. a craft made of aluminium is to withstand the same loads as a craft made of steel or GRP.

When it comes to fatigue calculations for high speed craft compared to the more traditional types of ships, both the loads and loading pattern may be completely different.

The traditional approach has been to keep the extreme stresses below a certain level knowing that below this level fatigue will not become a problem. This has worked well for traditional vessel where weight is not important.

For high speed craft where weight is of primary concern, extreme stresses and fatigue stresses must be dealt with separately. DNV has therefore established a procedure in order to do a more standardised fatigue analyse of high speed craft.

Loads

When defining the long term distribution of the loads it is not the intention to find the worst case, but rather the worst "normal" operational case. I.e. loads that the craft will experience during its lifetime. Standard lifetime is regarded as 20 years.

Type of craft	Operating Hrs. pr year
Large Passenger Ferry	7000
Small Passenger Ferry	4000
Cargo	8000
Crew boats	4000
Yachts	2500
Patrol boats	4000

Table 1 Definition of standard operating time for different types of craft

Dynamic load calculations should include:

- Wave loads from scatter diagrams.
- Motion induced loads including sloshing and slamming
- Steering forces
- Pulses from impellers/propellers

A craft hull consists of thousands of details which may lead to fatigue cracks. For simpler constructions it may be possible to calculate every detail separately, but for a high speed craft this is not possible. DNV has therefore tried to develop a calculation procedure that will give a "reasonable" approximation. It has been our intention to develop a procedure that is reasonable simple and not necessarily being 100% theoretically correct.

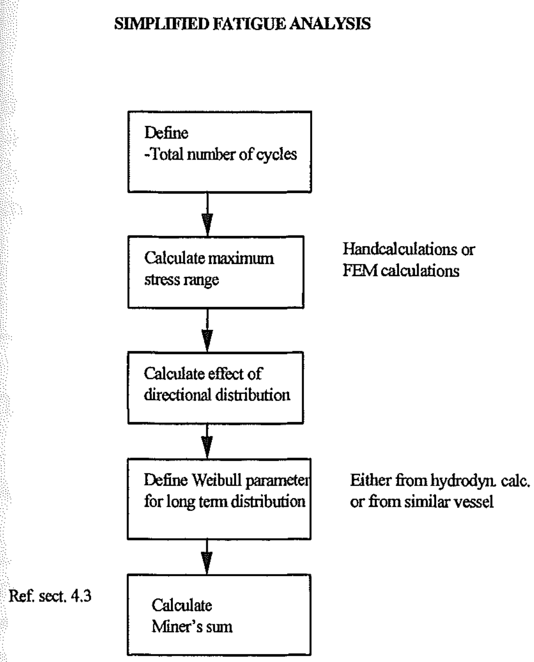

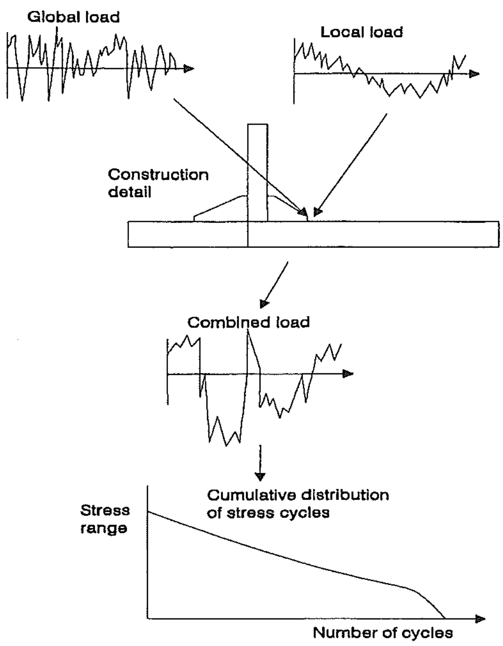

Figure 1 Simplified calculation procedure.   Figure 2 Combination of stresses

3. Defining S-N curve

DNV has established S-N curves that are applicable for standard details in shipbuilding. The S-N curves will differ depending on material, environmental conditions welded detail e.t.a. Note that for high speed crafts constructed in GRP fatigue do not need to be considered as long as allowable stresses are within the rule requirements.

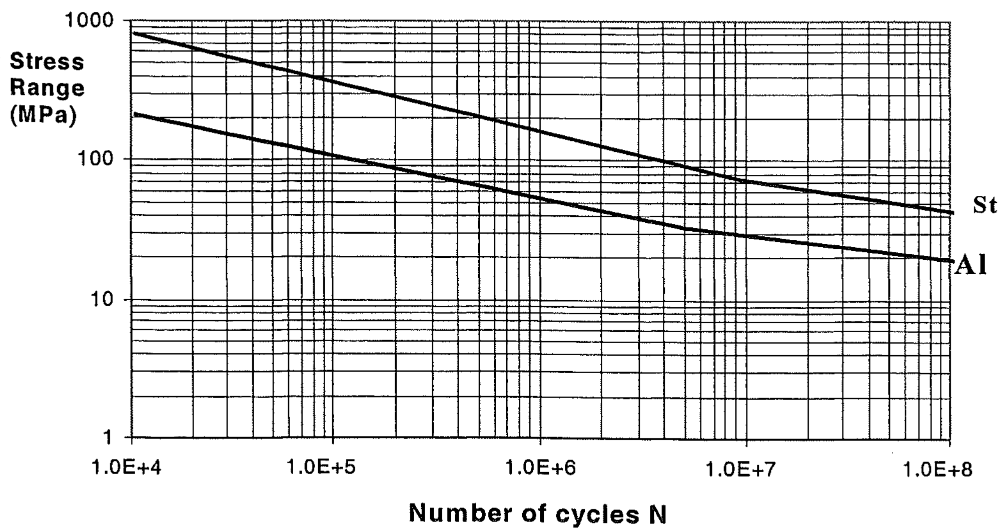

Figure 3 Basic S-N curves for welded joints in Aluminium and Steel, K = 1.0

The S-N curves used by DNV are based on curves for smooth specimen with a notch stress concentration factor K = 1.0 This factor is a result several stress raisers such as:

- Stress concentration due to gross geometry of the detail
- Stress concentration due to weld geometry
- Stress concentration due to eccentricity
- Stress concentration due to angular mismatch
- Factor for plate thickness exceeding 25mm.

The stress range to be used in the calculations will be the nominal or combined stress in way of the detail multiplied with the notch stress concentration factor. Other standards are using separate S-N curve for each detail. DNV has chosen to use the notch stress approach because this makes it simpler to use FEM analysis's to determine K-factors for details not covered any standard. In other terms giving more flexibility in the choice of joint parameters.

Note that identical details in steel and aluminium have different notch stress concentration factors.

<table>
<tr><th>Detail</th><th>Steel</th><th>Aluminium</th></tr>
<tr><td>Full penetration
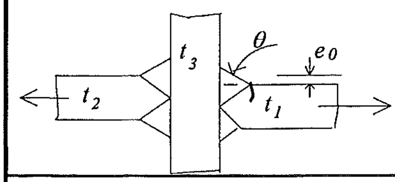
</td><td>K = 1.8</td><td>K = 2.0</td></tr>
<tr><td>Crossing of flanges
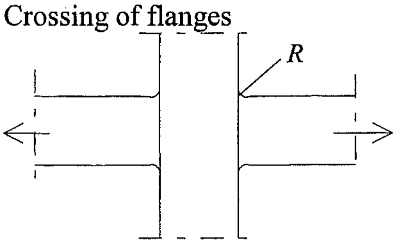
</td><td>K = 2.2</td><td>K = 2.2

(Radius ground welded from two sides)</td></tr>
<tr><td>Crossing of flanges
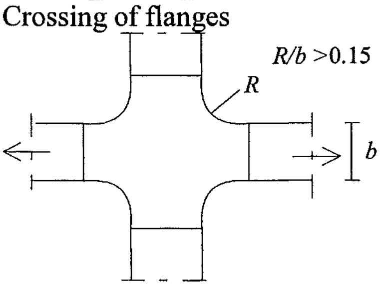
</td><td>K = 1.9</td><td>K = 1.9

Note : In the radiused area S-N curve for base material is applicable</td></tr>
<tr><td>Sniping of top flanges:
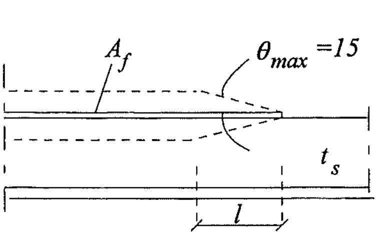
</td><td>$K = \frac{3A_f}{lt_s}$

$K = \min 3.0$</td><td>$K = \frac{3A_f}{lt_s}$

$K = \min 3.0$</td></tr>
</table>

Stiffener support	For rolled or built-up profiles	Built-up stiffeners.
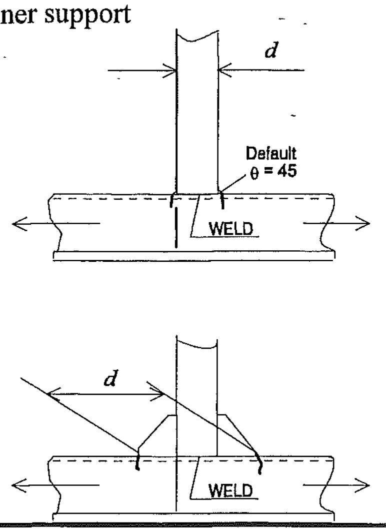	$K=1.9 \quad 50<d\le 100$ $K=2.0 \quad 100<d\le 150$ $K=2.2 \quad d>150$	$K=2.2 \quad 50<d\le 100$ $K=2.3 \quad 100<d\le 150$ $K=2.5 \quad d>150$ Extruded stiffeners $K=1.8 \quad 50<d\le 100$ $K=1.8 \quad 100<d\le 150$ $K=2.0 \quad d>150$

Table 2 K-factors for some details frequently used in shipbuilding.

4. Casualties and hull damages

DNV has collected in-service experience for each craft with DNV class in a database. Based on these data we may draw the following conclusions :

- Serious accidents are relatively few world wide
- Structural failure has never been the main cause for a serious accident
- Cracking is by far the most common failure mode

Some isolated craft however, have higher occurrence of damages. This may be due to factors such as:

- novelty of design and size
- Vibrations
- inexperienced yard

The majority of the structural failures are failures of local details due to fatigue, but it has also been seen few damages caused by extreme loads. I.e. when the craft has been operated outside its operational restrictions.
The graph below shows this situation where most craft have little or no damages, but a few craft have more damages as discussed above. It should also be noted that 70% of the recorded damages have occurred within one year after delivery.

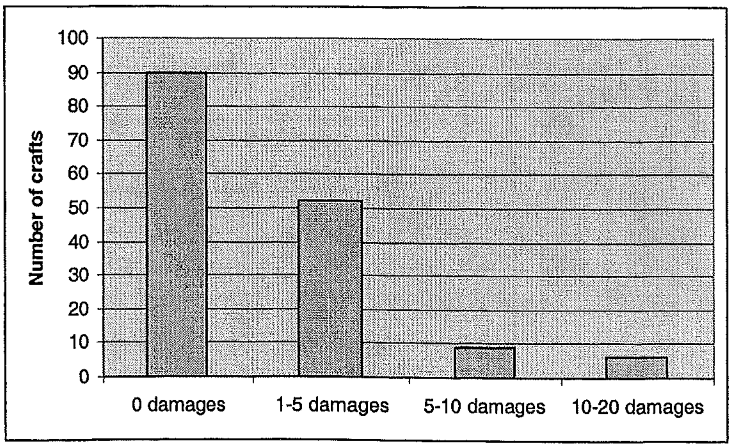

Figure 4 Damage distribution related to cracks for craft built after 1991

5. Common damages and main influencing factors

Below is given a brief description of the most common damages that are recorded for high speed craft and their reasons. This kind of information is evidently very useful in developing and improving rules and instructions

Aft ship	Hull general	Fore ship	Superstructure

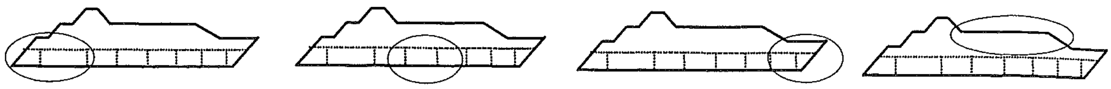

Damages	**Damages**	**Damages**	**Damages**
- Cracks	- Cracks	- Cracks	- Cracks
- Corrosion	- Corrosion	- Corrosion	- Loosening of windows
	- Buckling	- Buckling	
Loads / factors	**Loads / factors**	**Loads / factors**	**Loads / factors**
- Vibrations	- Cyclic bending	- Cyclic sea loads	- Global Deflections
- Cyclic loads	- Cyclic sea loads	- Slamming loads	
- Galvanic currents	- Humid environment	- Contact	
		- Humid environment	

As can been seen the above cracking is the most common damage type. This information can be further broken down into probable cause and occurrence.

AREA	DAMAGE / CAUSE	OCCURENCE
Aft Ship	Fatigue cracking in local details after relatively short time. Common cause is unfavourable detail design for the actual stress level and frequency of the cyclic loads in area. High cycle pulses from the waterjet impellers	Common
Aft Ship	Fatigue cracking in critical details due to resonance in structure to vibrations from machinery and propulsion installations. Typical engine and gearbox foundations	Common
Hull general	Overload and cracking of local detailing shortly after delivery. Common cause is unfavourable detail design with respect to transferring design loads between main structural members.	Quite Common
Hull general	Failure of general structure due to overload from operating outside operating restrictions	Rare

6. Some typical damages

The engine room area will always have a certain level of vibrations. It is therefore important to have smooth transitions and low stress concentrations. Scallops and sniped flanges are stress risers. To reduce possible problems in this area all welds are required to be continuous.

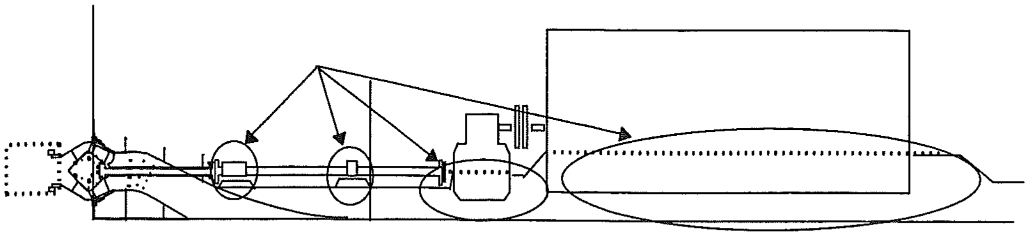

Figure 5 Showing problem areas in the engine room

Typical damage	Picture
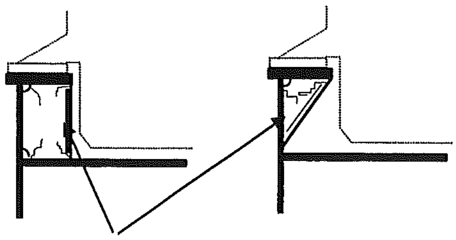 Cracks in bracket supports starting from bracket ends and scallops	
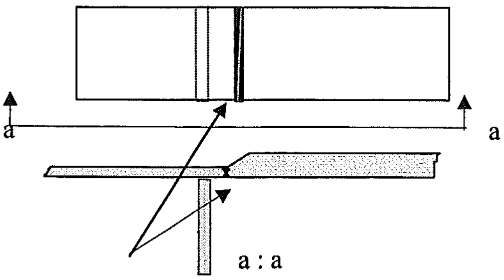 Cracks in foundation flanges in way of thickness transitions	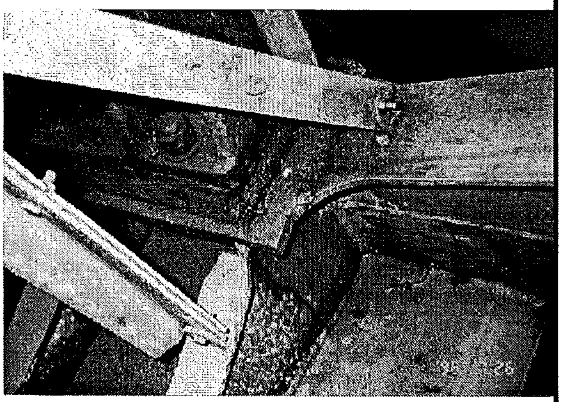

In way of the bottom structure high speed craft are exposed to high slamming loads. Global bending stresses from the hull beam are also present, but are low compared to the stresses caused by slamming. As slamming may give extreme high local loads scallops and intermittent welding should be avoided in these areas.

Typical damage	**Picture**
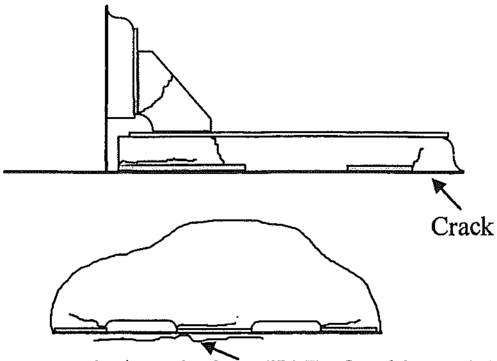 Cracks in web along HAZ of weld, crack in bottom plating	 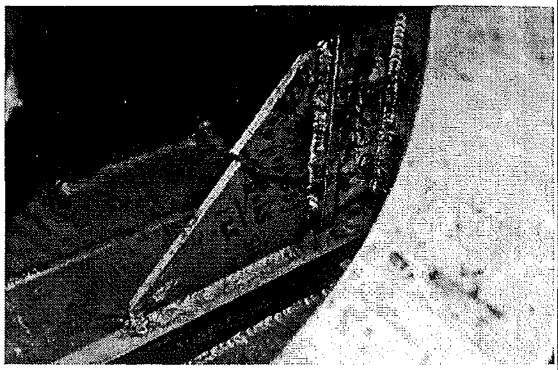

Some damages initially believed to be caused by global hull stresses have shown to be caused by poor local design. Cracks in transverse frames may be caused by "weak" end connections. The frame and side plate is forming an I-beam. In way of the upper turn of the bilge, spray chines or stringer bar the efficient flange is lost. This means that the loads are transferred to the web. To add damage to injury the web is normally fitted with some scallops in this area.

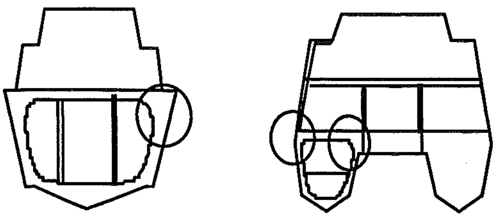

Figure 6 Change of shape

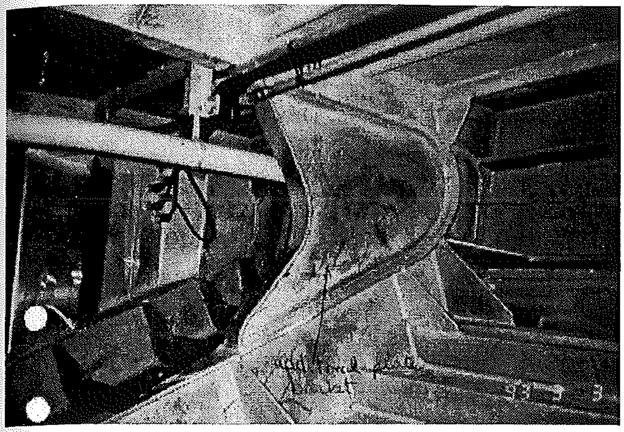

Figure 7 Is showing a typical example of a substantial bottom frame where the outer flange is the original connection and the inner flange is marking a later modification to make an more efficient end connection.

This is to show that proper design and understanding of the loads acting on a craft structure cannot be underestimated. Far to often fatigue problems could have been avoided already on the drawing table.

7. Concluding remarks

For craft with length less than 50m fatigue cracking may arise from local vibrations or poor detail design. No separate fatigue calculations are considered necessary for a "standard" construction.

For craft with lengths 50–100m it is advisable to carry out a fatigue check , specially for novel designs.

For craft with lengths longer than 100m fatigue may be determinable in deciding the scantlings in some critical areas. However, larger crafts often have less operational restrictions than smaller crafts. This means that these craft will have to be able to survive severe sea conditions i.e. very high extreme loads. This gives an "unused" hull girder capacity, which is increasing the fatigue life of the craft.

References

/1/: DNV Classification Notes no. 30.7 Fatigue assessment of Ship Structure, 2001

/2/: DNV Technical Report Proposal for Classification Note: Fatigue assessment of High Speed and Light Craft, rev.05, 1995

/3/: DNV Rules for Classification of High Speed, Light Craft and Naval Surface Craft, 2002-06-13

NOTE: High Speed Craft have up to now been designed based on extreme stresses for load conditions such as global loads, sea pressure, slamming pressure etc. These design cases and allowable stresses are found in Classification Rules. Such Rules are based on in service experience where also the fatigue aspect is implicitly included.

Fire Safety Assessment of Equivalent Design Solutions

Stefan Nusser, Germanischer Lloyd AG, nu@germanlloyd.org

Abstract

Rules on alternative designs and arrangements for High Speed Craft (HSC) and other vessels allow for innovative and cost effective new ship designs. From a statutory point of view, these designs may deviate from prescriptive rules in SOLAS as long as an adequate level of safety is maintained.
At Germanischer Lloyd, a systematic approach towards risk-based safety assessment is further developed, allowing the possibility to combine expert knowledge and competence with numerical simulation tools. The basis for this evaluation is to subdivide any possible structure incident scenarios into individual processes such as ignition of fire, generation and spread of smoke and evacuation procedures.
A short description of the general method is presented together with a review of the requirements of the new SOLAS2000 amendments

About SOLAS 2000

With the ratification of IMO's resolution MSC.99 (73) on 1st July 2002 , alternative fire safety concepts will come into force which deviate from the former regulations in the SOLAS convention. Ship design will thereby gain more freedom in selecting design solutions.

The new Regulation 17 supports the design of alternative safety standards, which at least matches that of a conventional model. The evidence for the equivalence shall be effected by means of a mechanical engineering procedure which allows for the replacement or partial supplement to the current usual application of the prescribed rules. In addition the procedure will control the resolution of formal issues concerning the test process and documentation.

"The engineering analysis shall be prepared and submitted to the administration, based on the guidelines developed by the Organisation and shall include, as a minimum, the following elements:
+ determination of ship type and spaces concerned;
+ identification of prescriptive requirements with which the ship or the spaces will not comply;
+ identification of the fire and explosion hazards of the ship or the spaces concerned;
+ identification of the possible ignition sources;
+ identification of the fire growth potential of each space concerned;
+ identification of the smoke and toxic effluent generation potential for each space concerned;
+ identification of the potential for the spread of fire, smoke or of toxic effluents from the spaces concerned to other spaces;
+ determination of the required fire safety performance criteria for the ships or the spaces concerned addressed by the prescriptive requirements;
+ performance criteria shall be based on the fire safety objectives and on the functional requirements of this chapter;
+ performance criteria shall provide a degree of safety not less than that achieved by using the prescriptive requirements; and
+ performance criteria shall be quantifiable and measurable;
+ detailed description of the alternative design and arrangements, including a list if the assumptions used in the design and any proposed operational restrictions or conditions; and
+ technical justification demonstrating that the alternative design and arrangements meet the required fire safety performance criteria.

(IMO Resolution MSC.99(73))"

Advantages for the Industry

The advantages of this development can be foreseen. By this means, individual solutions for single stages of construction or even complete ships can be agreed upon in the course of which, additional flexibility exists to realise competitive advantage. The attractiveness of passenger ships is dependant upon the spatial freedom of movement. In accordance with the current rules the architects were limited or restricted in the creativity and structuring of the spatial arrangements.

Other types of ships can also realise advantages, once cost saving potential has been utilised through selective adaptation of the fire protection measures to the respective local danger areas. In some instances an optimum agreement can result in direct cost savings, in other cases through organised planning one can also minimise the extent of the damage in a serious outbreak of fire.

Historically with the SOLAS Convention various groups of fire protection measures had separate requirements; for passive fire protection, the active fire control and the organisational emergency planning. All measures serve the overall ship safety, nevertheless to date it has not been possible to arrive at a comparable evaluation and a suitable determination of the key factors. This was first attempted through the resolution MSC.99 (73) for fire protection on board, whereby the comparison would be obtained through means of a mechanical engineering procedure. Since the aim is too maintain the current levels of safety, it should be possible through a specific improvement of one particular measure to generate an equivalent reduction of another. Figure 1 shows how the above mentioned three basic measures have to be linked (by a logical "OR") to establish the overall safety functionality.

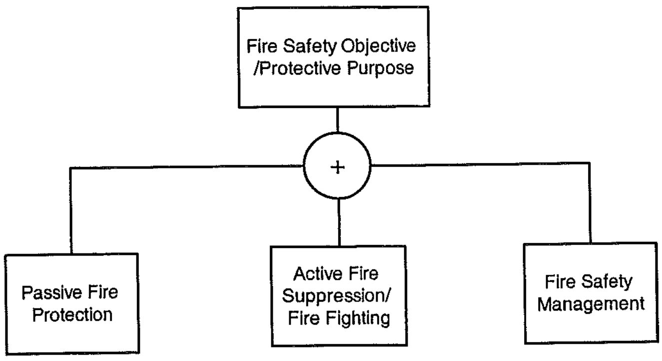

Figure1: Fire Safety Diagram(acc. NFPA 550) of measures for achieving the safety purpose

Here, through dependency upon ship type, specific combinations are conceivable which result from area of voyage, as well as economic and technical constraints. Because of the great variety of influences it is only possible to give examples of single cases whose realisation must be examined :

- For cruise and ferry ships fire protection walls can be moved or formed such that larger connected areas are created.
- In large ships with minimal crew strength, traditional philosophies of manual fire fighting can be given up in favour of a higher passive resistance combined with a fixed installed fire suppression measure.
- In all ship types, combinations of passive and active measures are conceivable in terms of protection (Water Cooled Fire Protection Walls).
- In all ship types it is possible to use fire fighting tactics as part of an all embracing safety concept, whereby traditional fire fighting installations and equipment can be relieved or superseded.

- In all ship types the expected extent of damage can be reduced through improved fire fighting tactical measures ; theoretically passive fire protection can be reduced.
- In high speed vessels light weight protection walls manufactured from alternative materials are already being used (in accordance with SOLAS/HSC code as equivalent design solution) .

The Alternative Assessment Method

The method of "performance based assessment" is clearly formulated in international fire protection and has been prepared in detail for structural engineering and heavy engineering. All noteworthy standards institutes (NFPA, ISO, BS, DIN) have already published corresponding regulations in which the theoretical framework along with the evidence from the practical undertakings are explained. Over the last twenty years great advances have been achieved in training methods resulting in improved safety.

For shipping it is possible to adapt the process. The implementation of the process within the frame of SOLAS is more exactly explained in the IMO publication "Guidelines on Alternative Design and Arrangements for Fire Safety, MSC/Circ 1002". The basis is the idea of a "comparable safety analysis" in which those implementing the same would be granted the choice in the range and the procedure. An investigation of the total ship is equally as possible as an evaluation of partial coverage of the vessel. In addition it is possible to use a deterministic as well as probabilistic judgement scales.

The IMO regulations speak of

- hazard identification in the presence of the fire;
- quantitative analysis on the basis of fire scenarios and measurable parameters;
- a comparative analysis of the prescribed SOLAS design and the alternative design.

The hazard identification considers the existing fire potential or load, the possibility of ignition, the probability of the occurrence of a sequence of events leading to the spreading of fire and the ways and means of fire control.
In addition a selection will be made from which design fire scenarios will be chosen from fire situations. These shall test and target specific protection measures within your design parameters.

Important in assisting are the reports concerning previous accidents and events. Luckily incidents of fie onboard seagoing ships are relatively rare and manageable such that in the shaping of the model they can be taken into consideration in their entirety. As such there is no need to incorporate generalised statistics, which are problematic to generate, especially when considering that the technology on ships is developing quicker than any safety that can be won via statistics.

SOLAS2000 also does not require any absolute evidence for risks to persons or material damage, although this evidence would be suitable for use in comparing long term development of safety technology in shipping. However the aim is to establish and prove conformity of the safety standards for a ship or construction stage. This is the first time that the possibility of this type of appraisal or assessment has opened itself to the shipping industry.

The mechanical engineering methods need to be accepted by the national flag administration supervisory bodies and can thereby deviate or differ from land to land. In principle two groups of methods can be distinguished:

1) Using the "deterministic" assessment one thinks of a pre-determined fire course, which can be calculated on a time based model. Through scaling of the input parameters with the design details causal results will be produced.
2) With the "probability assessment" one sees the fire as a random occurrence whereby the probability of such an event is covered by a secure statistic.

In the following representation emphasis is placed upon the design verification process. In principle however the design calculations are equally relevant since in both cases the same engineering methods are called upon, in such instances as the ability of walls and decks to resist fire or the simulation of the cooling effects of sprinkler systems.

The following flow diagram (*Figure 2*) illustrates the approach to the means of compliance between the alternative and prescriptive design. It begins with the provision of an initial prescriptive design. Under ideal circumstances it would be desirable to present the model of a completed sister ship which already fulfils the SOLAS Convention before introducing the alternative rules. In other cases, a prescriptive design has to be prepared.

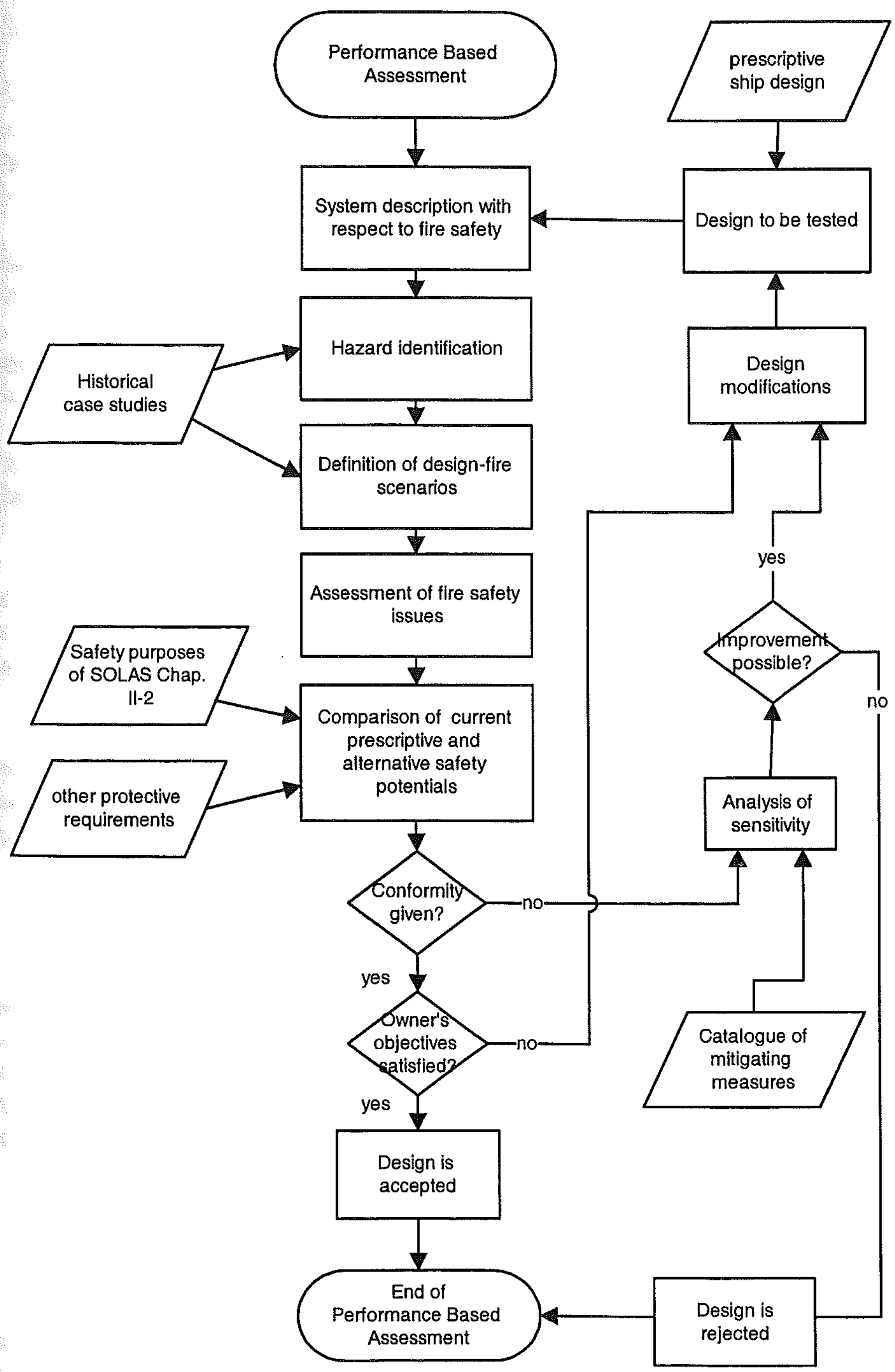

Figure 2: The verification process of alternative designs and arrangements

On the basis of this prescriptive design, a hazard analysis is used to determine a number of design fire scenarios. Each scenario shall serve as a measure for a specific safety precaution in the fire area under investigation. Thus, individual scenarios are defined for the design limits of fire detection, for the smoke layer development with respect to evacuation, for the smoke extraction system, for the sprinkler suppression efficiency, for the passive fire protection of the ceiling and the walls, and others. When under study or investigation it is usual to prepare between 30 and 100 scenarios.

The technical assessment of the fire protection includes a detailed calculation of design fire scenarios with regard to time required for the fire to spread and the possible control and fire fighting measures. The dynamics of the fire will be considered with respect to the numerical modelling. Other principle considerations include fire extinguishing measures and tactical models for the use of fire fighting personnel.

In addition to the foregoing an evacuation simulation should be carried out in which the aggravated conditions of smoke development under which passengers and crew must perform will be taken into consideration.

The level of safety achieved will be described in quantitative terms with the help of "Performance Criteria" the individual protection measures are subordinate to SOLAS 2000. A typical performance criteria is the temperature at the rear side of a fire rated bulkhead, or the toxic concentration of combustion gases. Apart from the Convention, the national flag administration supervisory bodies may stipulate higher standards.

The compliance comparison of the "prescriptive" design is fulfilled by virtue of its own definition. The objectives of the client however may not be fulfilled. The alternative design solution is therefore carried out and thereby becomes the deciding design.

Should the assessment comparison reveal different "Performance Criteria" the same should be corrected through suitable measures. Suitable technical and organisational measures should be formulated in a catalogue whereby it is possible for a sensitivity analysis to evaluate the influence the individual measure. Such an analysis can easily be carried out by means of a system analyst.

Once the improvement measures have been determined, the next design to be tested can be subjected to the compliance procedure. The compliance process can be proceeded until a satisfying solution has been found. In rare cases, the innovative design may be not improvable and a decision has to be taken to end the compliance procedure after some iterations.

The iterative character of the verification process can be recognised in the flow diagram (Figure 2).

The fact that an initial prescriptive ship design is necessary as a basis for comparison should be treated pragmatically. The design process should be accompanied by alternative, provisionally assessed, approximate methods. In this way it is possible to avoid mistakes and necessary work. However the final examination is extensive since the legal aspects of safety must be achieved and complied with. Furthermore a broad range of factors concerning technical, organisational and personnel must be defined and analysed.

Conclusions

With the new approach of alternative design verification, IMO's Marine Safety Committee initiated an important development in which owners and shipyards will be given more freedom in the implementation of new ideas. Above all, the flexibility in the selection of technical solutions shall be supported, by which a basic fire protection is guaranteed in accordance with the individual vessel construction, the kinds of cargo and other constraints of the operation. It can be foreseen that the design of cruise vessels and Ro-Ro ferries will be the first to benefit from this development.

Within the framework of the new SOLAS Regulation 17, the use of comparative performance criteria will be preferred instead of using absolute quantitative risk measures such as probability of loss of life (PLL) or probability of property loss (PPL). The need for a further development towards a full quantitative risk analysis (QRA) approach, as already established in aviation, off-shore or nuclear industries, is not currently foreseen.

References

IMO Resolution MSC 99(73). IMO Publication IMO-170E, London, 2001. ISBN 92-801-5110-X

Kuo, C. Managing Ship Safety, LLP, London, 1998

NFPA 550, Guide for the Fire Safety Concept Tree, National Fire Protection Association, Quincy, MA, 1995

ISO/TR13387, Part 1 to 8. Fire Safety Engineering, 1st Edition. International Standards, Association, 1999

IMO MSC/Circ. 2001, Guidelines on Alternative Design and Arrangements for Fire Safety. International Maritime Organisation, 26th June 2001.

SFPE Engineering Guide to Performance-based Fire Protection Analysis and Design of Buildings. National Fire Protection Association, Quincy, MA/USA, 2000. ISBN 0-87765-422-0

The Effect of Length in a Fast Boat

Francisco Pérez
Naval Architecture School, Madrid Towing Tank of the University
Avda Arco de la Victoria s/n, E 28015 Madrid (fperez@etsin.upm.es)

In conventional ships, the increase of ship length is sometimes used to reduce ship resistance. In the case of a fast ship, this is not so clear due to the effect of dynamic forces that are of minor importance for conventional vessels. Some fibreglass fast boats have a cylindrical aft-body (with constant shape) and the variation of the extension of this body can be easily changed in the shipyard.

CFD analysis is not accurate for such high Froude numbers where the viscous phenomena are important, so to obtain quantitative results of the resistance, dynamic lift and trim, experiments have to be done.

In this paper, based on tests carried out in the towing tank of the Naval Architecture School of Madrid, the effect of ship length is studied for two fast patrol boats with the same fore-body and different extension of the aft –body. Different dynamic variables such us lift and trim are compared and conclusions about the optimum range of application of every ship are obtained.

1 Introduction

Most naval architects regard length on the waterline as the most crucial factor of all. And the longer the length for the same mission, the easier the task of the naval architect. This applies in most the ship and boat designs, but not always. Other people involved in the project, operators or builders, see extra length as extra cost or other inconveniences. The idea of lengthening a design to gain important advantages in for example speed and seakeeping, is a difficult matter for some people.

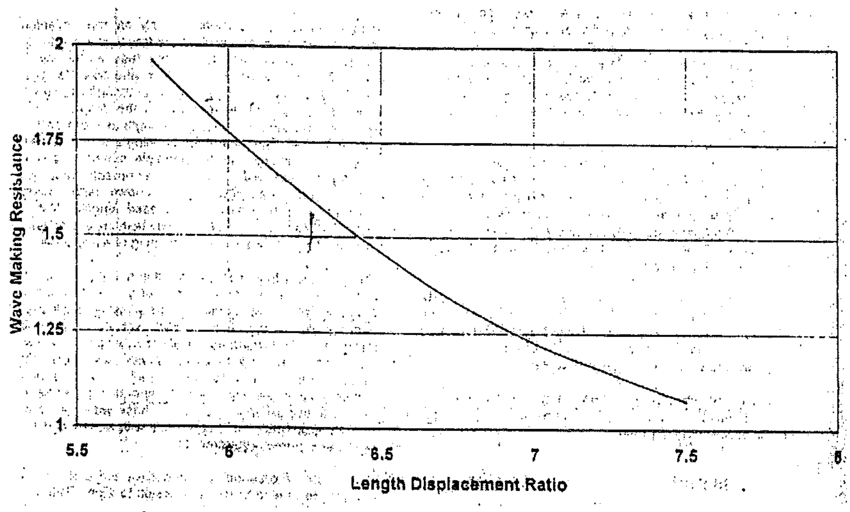

Fig. 1 Effect of L/Disp on wavemaking resistance

In the case of displacement ships, Fig. 1 from Warren (1999) is a good indicator of the influence of ship length in resistance. An appropriate length, not only improve resistance, but also other factors such us washing, noise levels and general arrangement can be improved. In this paper, we will see some examples on how ship length can affect a ship that is designed to work in the planing mode. Only ship resistance will be considered, although seakeeping and manoeuvrability aspects have to be studied.

2 Resistance vs. Speed

Remembering a ship theory class about ship resistance, Gonzalez (1989), at low values of ship Froude number based on ship length (Fnl), the origin of ship resistance is mainly frictional, and there are not appreciable dynamic effects.

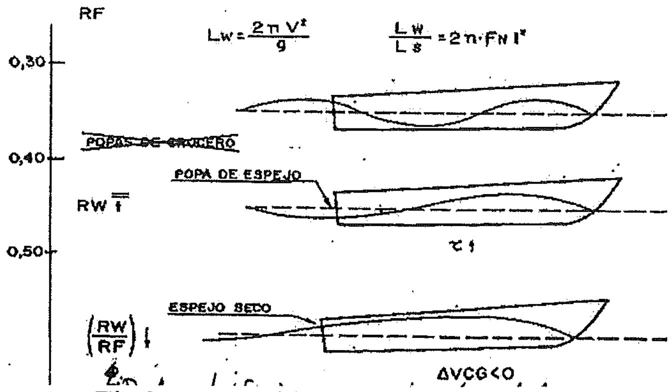

Fig 2 wave position as a function on Fnl

If speed is increased to Fnl about 0.35, the ship will sail over one wave length (Fig. 2), and the second wave crest will be under the stern, according to classical theory of the wave generated by a pressure point.

When Fnl is between 0.40 and 0.45, the second wave crest is beyond the stern and only the wave crest at the bow “supports” the ship. Now, the increase of wave resistance is very large and the ship is near the well known hump of the wave resistance curve. If the volume or beam at stern are small, the ship will trim by the stern and the bow wave will increase the wave making resistance. At that speeds, local velocities caused by round hull forms at the stern will rise, producing negative pressures which means that the ship will settle deeply and trim down by the stern. We can say that the ship is climbing the back of its own bow wave, and this is the limit of displacement vessels.

That is the reason of the wide transom stern, which produces some lift and reduces the bow trim. As lift increases with speed, the sinkage begins to reduce at these speeds in broad transom ships. At Fnl numbers above 0.50, the second wave crest will be far beyond the ship stern and therefore, no interference or amplification between bow and stern waves will be expected. The transom stern should remain dry if the ship design is good and wavemaking resistance will begin to be less important.

When Fnl is greater than 0.70, the ship centre of gravity is above its rest position and the trim will decrease slightly. Dynamic lift will be getting importance versus the hydrostatic forces and the thin divergent bow wave will grow spectacularly producing the spray phenomena. At Fnl above 1.0, the spray must be avoided (spray rails, knuckles,...) and for these speeds, a significant portion of total resistance will change from wavemaking to frictional resistance. The ship is fully planing now.

2 Lengthening a ship

From section two, if a displacement vessel in lengthened, Fnl is reduced, and for the same speed wavemaking resistance is reduced. As far as residuary resistance curve has humps and valleys, due to interference of ship generated waves, some Fnl numbers should be avoided and other are desired, Bertram (2000).

But if you are working with a planing boat with Fnl near 0.7, wavemaking resistance is less important than frictional resistance and an increase in ship length will produce and increment in wetted surface increasing the frictional effects. You have also to consider that your ship has to pass the hump of the resistance curve to start planing. If not, an increase in power means a slight increase in speed.

If you can not go over the hump speed, and the ship owner decides to install more power inside the ship, the longitudinal centre of gravity (LCG) goes back toward the transom. Ship trim is bigger than in the initial solution and so, generated waves and the wavemaking resistance will be bigger than the initial ship. And you cannot guarantee that your ship design will start planing.

For a shipyard that produces GRP fast boats, especially those forms designed for waterjet propellers with a prismatic aft form of constant deadrise angle, a change in length maintaining beam is easy to obtain, just enlarging or reducing the plastic mould. A variation in ship length produces changes in three magnitudes really important for the dynamic behaviour of a fast boat and that should be considered before enlarging:

- Displacement
- LCG
- Wetted surface

3 The Almeter and Clement method

J.M. Almeter, Almeter (1993) and E. Clement, Clement (1963) worked for years in the resistance study of planing hull forms. They use two interesting non-dimensional numbers to see the effect of different ship variables on the planing behaviour. These numbers are called the Almeter number, An, and the Clement number, Cn.

$$An = Disp / (\tfrac{1}{2} \cdot \rho \cdot LCG \cdot Bx \cdot V^2) \quad [1]$$
$$Cn = Vol / (LCG^2 \cdot Bx) \quad [2]$$

The principal effect of An is on the resistance, and an example can be seen on Fig. 3 applied to series 62, whilst Cn can be considered as a bottom loading coefficient (other authors use Vol/Bx^3). This Cn can be used to avoid high hump drags maintaining this coefficient low (< 0.2), but no information about the maximum hump speed can be obtained.

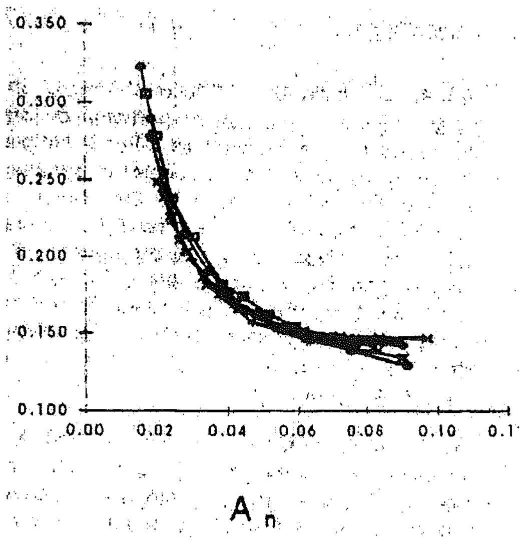

Fig. 3 Effect of An on the Resistance/Disp

Combining both factors, Almeter (1999), the effect of the different parameters on the hump appears. Log10(An) is plotted versus Resistance/Disp, for different values of Cn (Fig. 4). From Log10(An) > 0.0, the ship is working at displacement regime. Hump lays between –1.0 < Log10(An) < 0.0 and for Log10(An) < -1.0, the ship is fully planing. For Log10(An) values < -1.5, resistance starts to increase significantly. At these speeds, resistance is predominantly skin friction.

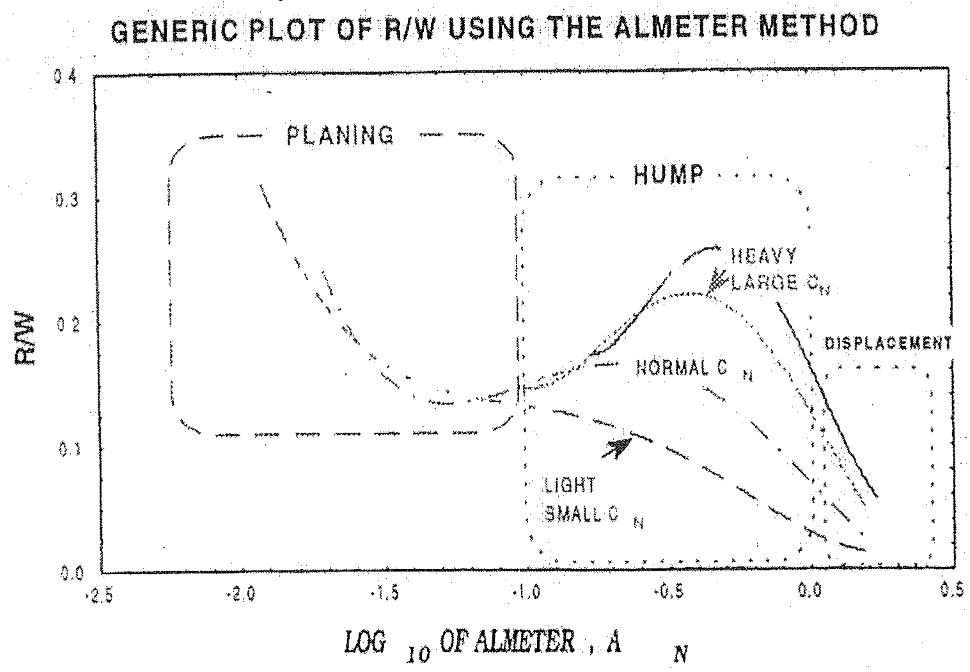

Fig. 4 Almeter – Clement Method

With this kind of graphs, the effects of the modification can be studied for the whole range of speeds because a change in length affects displacement, longitudinal centre of gravity and wetted surface.

4 An actual tested case

Two models (Fig. 5) of different length were tested in the Towing tank of the Naval Architecture School, in Madrid. The object of the investigation was to see if it was worth for a shipyard to enlarge one of its patrol boats designs. So, two models that were different only in the length of the prismatic aftbody were tested.

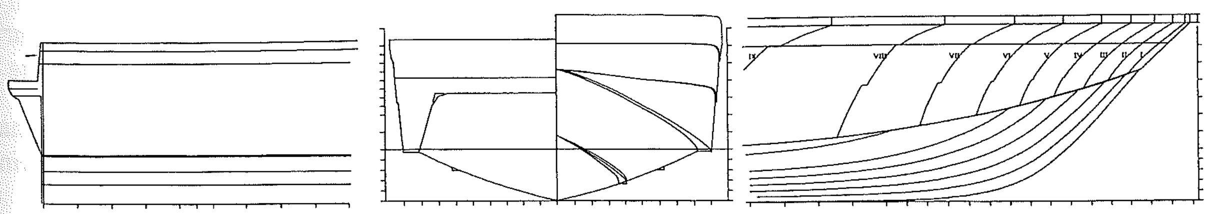

Fig. 5 Tested models

Model 1	Model 2
Lpp = 14 m	Lpp = 16 m
B = 4.8 m	B = 4.8 m
T = 0.75 m	T = 0.75 m
LCB = 5.98 m	LCB = 6.94 m
Disp = 21.9 ton	Disp = 25.5 ton

Draft was the same for the two models in order to maintain the planing behaviour of the hull and initial condition for both models was with zero trim angle. Drafts at fore and aft perpendicular were measured for every speed and used to obtain through hydrostatic calculations, displacement, LCB and wetted surface as a function of the speed. Results at model scale are shown in the following pictures.

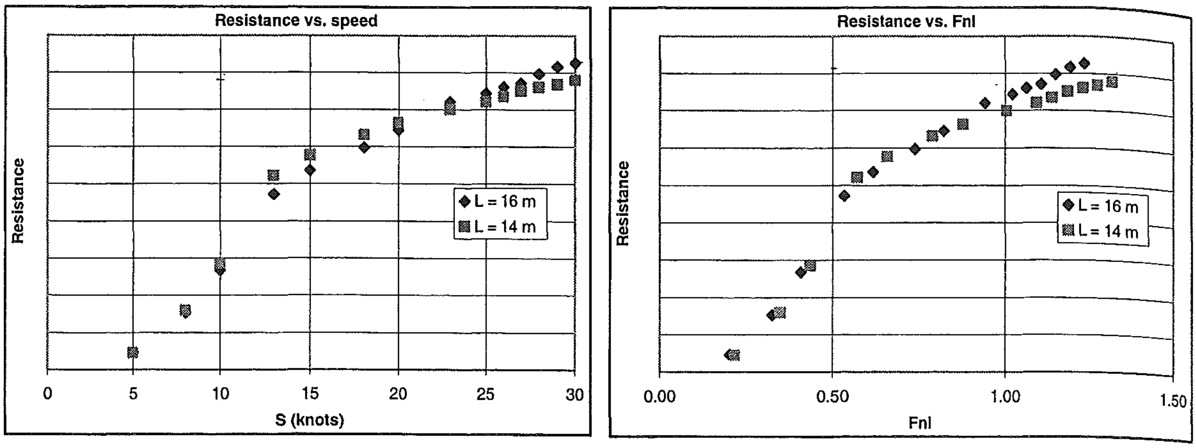

Fig. 6 Resistance comparison vs. speed and Fnl

As explained on the theory of section 3, the shorter ship is slightly better than the longer one for high speeds, or for Fnl > 0.9. The increase of the wetted surface for the longer ship increase skin friction which is no good for high speeds, whilst is slightly better for the speeds between 10 and 20 knots. In the presented case, for the medium speed of 15 knots, the bigger ship has 7.5% less resistance that the shorter one, but for maximum speed of 30 knots, the bigger one has 6% more resistance than the shorter one.

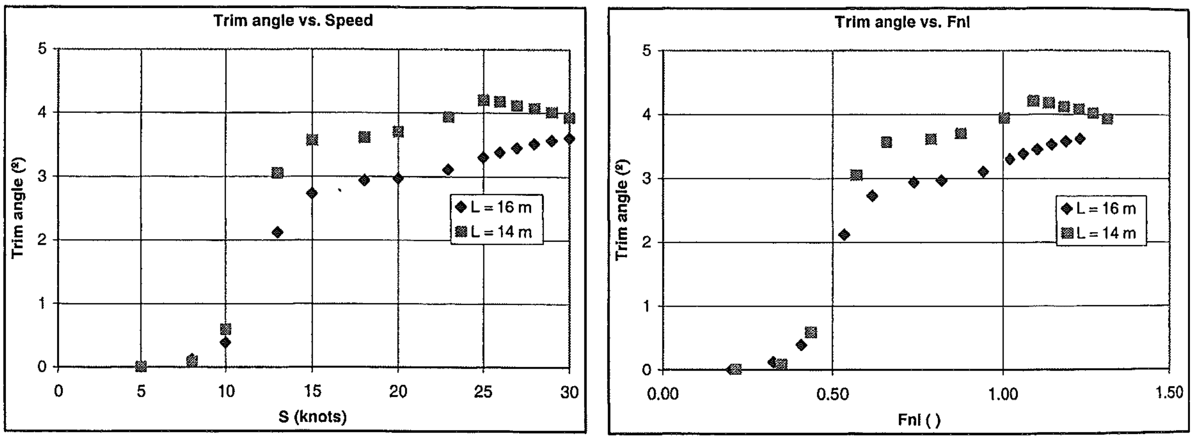

Fig. 7 Trim angle comparison vs. speed and Fnl

Due to the nearer position of the LCG to transom, the short ship is more sensible to dynamic trim than the long one. It is clearly shown on Fig. 7. A big trim angle affects seakeeping and visibility during navigation. Anyway, differences for the same speed are lower than 0.8 degrees.

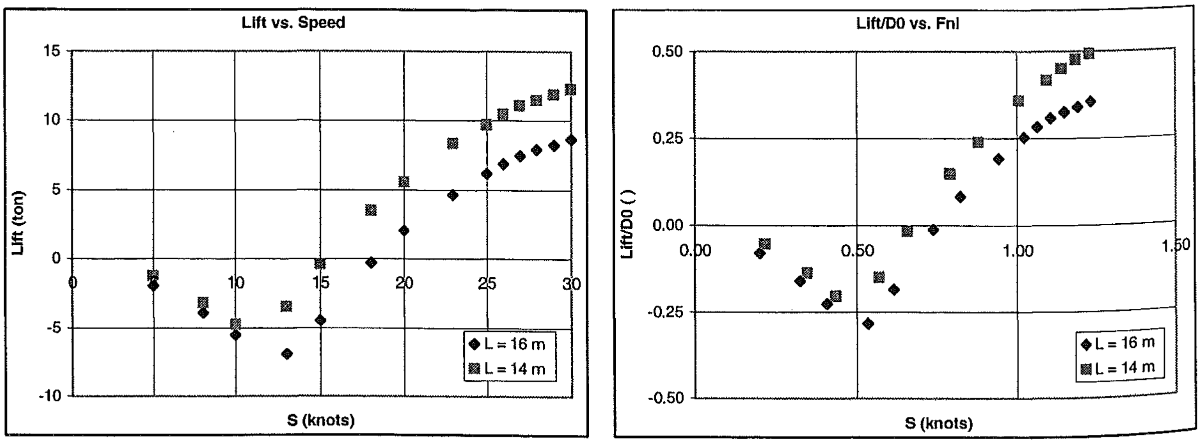

Fig. 8 Lift comparison vs. speed and Fnl

Measuring drafts in the fore perpendicular and in the aft perpendicular and using hydrostatic calculations, the dynamic displacement can be obtained. Subtracting this value to the ship weight, the vertical component of lift can be approximated. Due to the bow wave, the waterline is not a straight line and so, this technique is an approximation. Wetted surface is also obtained using hydrostatic calculation. Spray surface has not been measured.

The results of the comparison are shown on Fig. 8. It can be seen that a positive vertical force begins to act for Fnl near 0.5 and that for Fnl near 0.75, ship displacement is lower than the one at zero speed. The shorter ship is more sensible to lift than the longer and begins to rise earlier. This can not be good for seakeeping characteristics but probably it has better acceleration than the longer one.

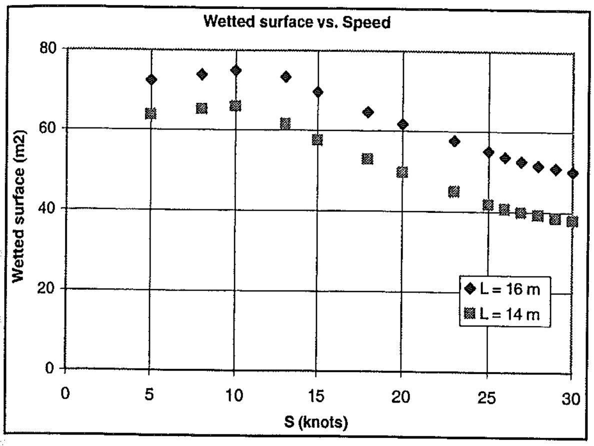

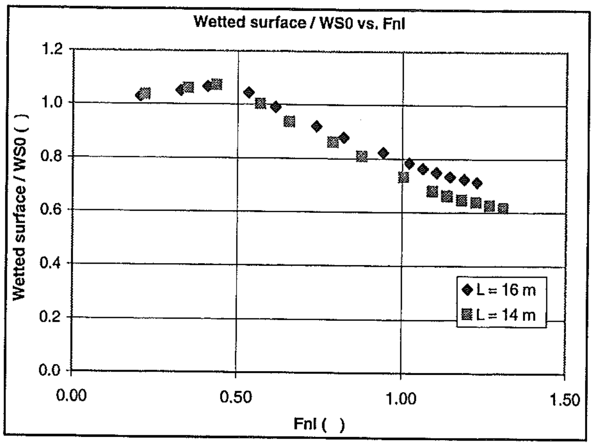

Fig. 9 Wetted surface comparison vs. speed and Fnl

Of course, the longer ship will have the longest wetted surface. Dividing the wetted surface by the value at zero speed and comparing with Fnl, it seems that this value is the same until Fnl > 0.5 where the shorter ship has a bigger trim angle than the longer one and it produces a comparative reduction in the wetted surface value.

4.1 Resistance at the hump

In order to see the effect of length before the planing regime, the Almeter and Clement method is applied. Loading coefficient for the longer boat is 0.11 and for the shorter one 0.15. These differences affects hump resistance as can be seen in Fig. 10.

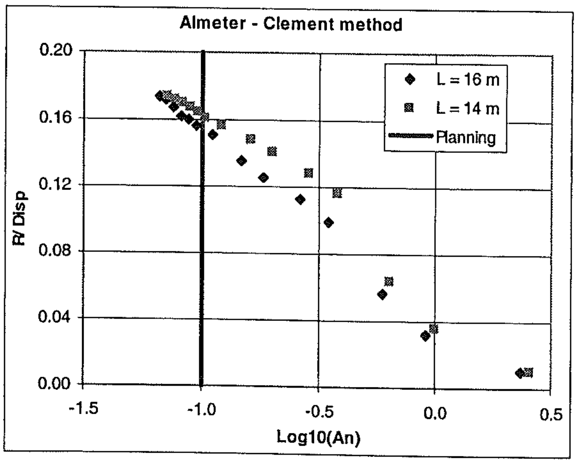

Fig. 10 Almeter Clement Method

The shorter ship is more charged on the bottom than the bigger one, so the hump is bigger and wavemaking resistance before the planing speeds. Anyway, differences between each other are little. In the planing speeds, the behaviour of both ships is practically the same.

6. Another example

In this case, a model without prismatic aftbody of constant area (Fig. 11) was tested and decisions about a change in length were suggested. Only the parent hull was tested at zero trim angle, and the resistance results were compared with the well known Savitsky method, Savitsky (1964).

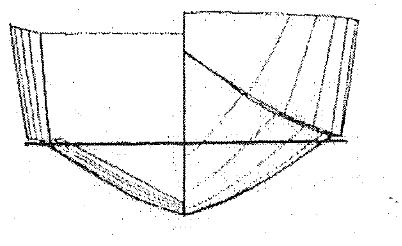

Fig 11 Tested model

The scaled variations studied were:

Tested model	Variation 1 (+L)	Variation 2 (-L)
Lpp = 11.2 m	Lpp = 12.2 m	Lpp = 10.2 m
B = 4.2 m	B = 4.2 m	B = 4.2 m
T = 0.8 m	T = 0.8 m	T = 0.8 m
LCB = 5.12 m	LCB = 5.58 m	LCB = 4.67 m
Disp = 12.5 t	Disp = 13.6 t	Disp = 11.4 t

As usual for planing forms, Savitsky method gives accurate enough values (Fig. 12, left) in the planing range. So the resistance of the two scaled variations in length was calculated using this method for high speeds. The results of the calculations are shown in Fig. 12. Like supposed, variation 2 has less resistance than the longer ones near Fnl = 1.

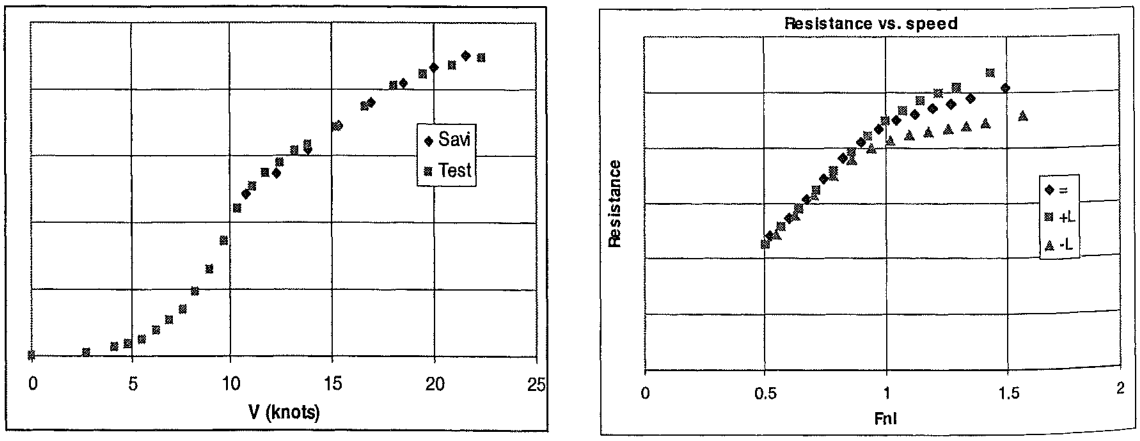

Fig. 12 Resistance and Savitsky results of the second example

Like in the example of section 5, the shortest ship improves resistance at high speeds due to the lower wetted surface. In contrast with the example of point 5, differences in the loading factor of the shortest ship in respect to the original ship are lower. So, the shortest ship is not so adversely affected in resistance near the hump (Fig. 13), as it was in section 5 where loading factors differed in 36%. In this case, differences are only of 9%.

Due to stern forms of this ship that has less volume at the stern than in the previous case, LCB position is more forward, diminishing load factor. This ship is not propelled using water-jets. From Fig. 12, the longest variation does not improve resistance at all, although trim angle is lower for this variation, like in section 5.

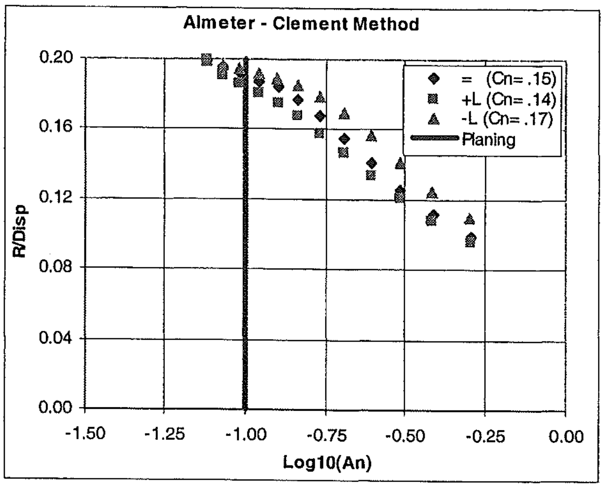

Fig. 13 Almeter Clement Method

But apart hydrodynamic aspects, practical reasons prevailed. Although the shorter boat needs less power than the original one, the ship owner opinion was that the modification was too short, and the boat was constructed with it original dimensions.

Conclusions

- Not only the effect on length should be studied when ship length is changed, but also the effect on LCG of the new ship and the loading factor on the bottom that this change produces should be considered.
- Shorter ships have the advantage on resistance over the hump, but the larger ships have a lower resistance value at the hump, and the installed power has to pass this point to start planing.
- Loading factor affects resistance value at the hump and the change in length should maintain this value near the original one in order to control resistance at the hump.
- LCG must be displaced forward if possible, when the ship is modified. This way, the loading factor on the bottom is lower and lower dynamic trims are obtained. Anyway, negative trim is not desirable, because the submerged bow will generate waves increasing the wave resistance at low Fnl.

Seakeeping remarks

Only resistance has been studied until that point, but some comments about the seakeeping comparison, González (1989), can be made.

- Low trim angle means reductions in pitch and heave motions, added resistance and impact acceleration in the pre-hump regime. And apart resistance, trim angle is the most difference between the bigger and the shorter one, which has bigger trim angles.
- Loading: in the post-hump region, motions and added resistance are slightly reduced if the loading coefficient is increased.

So, better seakeeping can be expected of the longer ship during operation due to its lower dynamic trim, but these differences will be reduced at planing speeds.

Acknowledgements

Juan Antonio Clemente from IZAR

References

ALMETER, J.M. (1993), *Resistance prediction of planing hulls – State of the art*, Marine Technology, vol. 30, Num. 4, October.

ALMETER, J.M. (1999), *Resistance prediction of planing craft from similar craft using the Almeter method*, Hydrodynamics of H.S.C., 24 – 25 November, London.

BERTRAM, V. (2000), *Practical Ships Hydrodynamics*. P. 67. Butterworth & Heinemann.

CLEMENT, E., and BLOUNT, D. (1963), *Resistance tests on a systematic series of planing hull forms*, SNAME Trans., Vol. 71.

GONZÁLEZ J.M. (1989), *Specific Hydrodynamic aspects of fast displacement ships and planing craft*, 13th WEGEMT School on design techniques for advanced marine vehicles and speed displacement ships, October, Delft.

SAVITSKY, D (1964), *Hydrodynamic design of planing hulls*, M.T. Vol. 1, October.

WARREN, N. and KECSMAR, J. (1999), *Practical aspects in the hydrodynamics of a fast craft*, Hydrodynamics of H.S.C., 24 – 25 November, London.

Paddle-Steamer DS „Gallia“ on the Lake Lucerne: High Tech of 1913 or 2002 ?

Werner Schäfer
Lake Lucerne Navigation Company, Werftstrasse 5, CH-6002 Luzern, w.schaefer@lakelucerne.ch

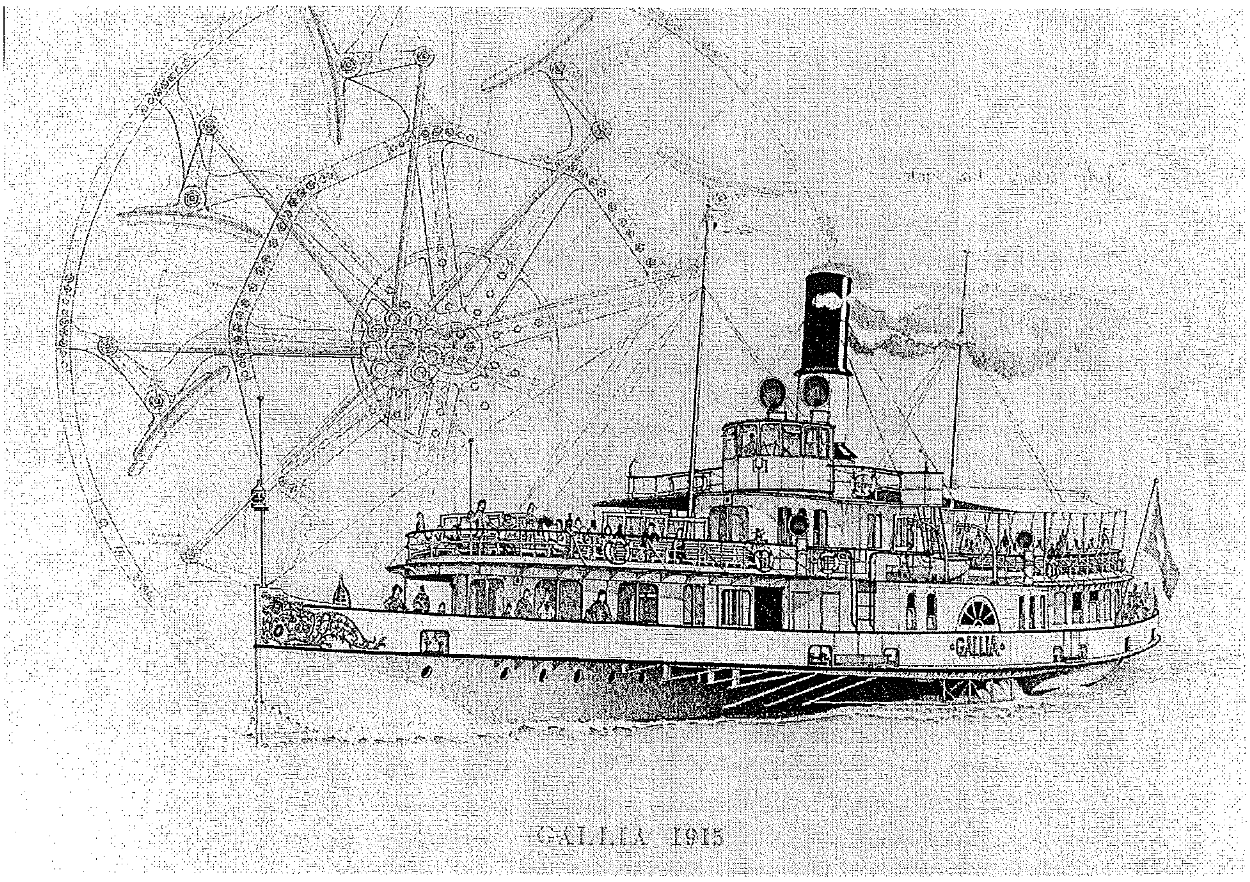

Abstract

High-Tech can be seen on its according year of design and construction. Therefore it is interesting to study a high-performance ship certain 100 years ago and to compare the results from then and today, within there then actual conditions and constraints. To build high performance ships, the operation area has to be known exactly. The passengers may have changed over hundred years but there expectations on a cruise with a ship / "Steamer" are surprisingly almost the same. What means high performance and skills for the Crew and the technical Staff yesterday and today in a wide lot of senses? A real Paddle-Steamer steamer is a fascinating masterpieces of technical science! It is, compared with today's power boats, is a very efficient platform with its hull form, lightweight construction, propulsion system and engine power. It is an environmentally friendly transport vehicle specially for sensitive areas and shallow waterways. The specific fuel consumption of old steam was a handicap, but with modern science, much better efficiency is achieved. Some figures about costs, manpower, maintenance, but also benefits are explained. With some examples of the restored steamer "Gallia" from Lake Lucerne, the problems and chances are presented. With their quality, reliability ambiance and emotional acceptance from the passengers, paddle-steamers are coming back to future as special high performance vehicles!

1. Passengers and guests

During the technical evolution, ship where is always seen as ultimate progress on its according year of design and construction. Therefore it is interesting to study a high-performance ship certain 100 years ago and to compare the results from then and today, within the past conditions and constraints.

In 1913 but also today in 2002 the increasing expectations in tourist- and public transportation demand for innovation and look-out into future. Past and today's travelers prefer and are used to fast, easy and comfortable moving in trains (Pullman or ICE), good level hotels, private-cars, yacht-cruise and today's airplanes. The Lake Lucerne Navigation Company's orientation and prosperity is based on the formula:

Q + S + A = GS > it means: **Q**uality + **S**ervice + **A**mbiance = **G**reat **S**uccess.

There are really all kind of passengers, luggage and equipment: 1913 as well 2002. Quality, service and ambiance? Within 100 years passengers the wishes and needs for a steamer cruise from the technical point of view has not really changed ! **> Annex 1**

The passengers and crews are still looking for :

- Absolute reliability in crew, ship and infrastructure within exceptional situations and weather
- smooth, correct and user determined functionality, lowest noise emission, no pollution
- well selected materials with excellent manufacturing, visible workmanship
- reserves in performance and speed, perfect landings, short maneuvering and stopping
- Individual taking-care of passengers, especially with no-experienced or elderly travelers
- integrated, optimized and harmonized full year timetable, punctuality, onboard-service
- seafaring romance with close nautical style, sound, bell, horn, commands, uniforms...
- Nautical adventure, action and show on boarding, cruising, landing, ship encountering
- observing and „being-seen" on gallery, on promenade decks, on the captains bridge etc.
- Naval equipment all over: ropes, riggings, anchors, rescue equipment, lights, fittings... etc.
- Youthful, stylish charm of interior furnishing, wooden decks-planks
- Discovering naval trait on exciting walks on board, visible equipment, powerful machinery
- but also calm, relaxed, tension free travelling, to enjoy the beautiful landscape

For the interior design only best stylist and finest materials were good enough! Fine and careful selected wooden outfit, textiles, ceilings, furnishing and decent lighting give, of course with a certain valuable difference for 2° and 1° class, a very charming and, for our fleet typical, travelling adventure. But the interior must withstand to the daily cruise of a broad, and different disciplined public on all weather conditions. Today's interiors with youthful techno-tropical style comes close to the desired feeling of the Belle Époque, hopefully without being „trashy"! The annual average of transported passengers is 2.3 Mio, 85 % of it from April to October. On a good summer weekend we transport 25000 to 35000 Passengers, approximately the same as in one complete month in winter. On berthing place, exchanges of up to 500 Passengers are not seldom. The ships have a capacity of 300 to 1200 passengers in day-service, but no cabins.

2. Operational area

The operational area itself has not much changed in the last 100 years, except the increase of traffic with private sport boats, more interlink to public transportation network, more laws and rules and in general less time for everything!

The Lake Lucerne with 8 interesting linked basins with a total of 114 m^2 offers a varied landscape ranging from the fertile shores of the lowland and the steep slopes of the alpine foothills to the vertical rock faces like fjords of the towering Alps surrounding the south part.

All year there is traffic of fishing boats, gravel cargo, sportive boats of all classes and with their more or less disciplined behavior. When strong winds occur, sailors and windsurfers line up like a wall of sails at the lake. The deep of the lake varies from 2.5 m up to 280m! The weather is typical mountain-like complex with turbulences and windfalls, it can change in short time from beautiful smooth to very hard and stormy. Especially the dangerous wind called "Föhn", known from the myth of „Wilhelm Tell", requires high nautical skill of our crews. The waves can vary from one basin to the other in direction and intensity, but mainly very short and to a maximum height of ca. 2 m. > **Annex 2**

The lake is a turntable-like transport network with the steamers routes, 4 cogwheel- and rope-railways, 7 area-cableways, 5 railway and numerous bus lines, all with lakeside stops. The main route has a length of 35 km, a day cruse with approx. 36 landings gives 100 km. A commuter cruse has up to 50 landings an about 120 km. Summer service takes up to 200 operation days. Ships with full year service make approx. 40'000 km in 350 days and up to a total of 14'000 landings/year! Daily commuter service is standard. Cargo had been important till ca. 1881 on the "Gotthard" route and till 1963 on the "Engelberg-Titlis" route > **Annex 3**

All 36 landing stations and are open berthing dockyards ore bridges on the shore. In general we have deep water conditions, there are only 3 small shallow water areas with a speed limit of 10 km/h. In Winter there exist almost never ice in the cruising lines. All scheduled links with the timetables provide excellent service to daily traveler and tourists. Therefore a minute like punctuality even with extreme high passenger quantity and all weather conditions is essential and requires fast ships with speed reserves but also perfect operational capabilities of the crews. Because of the average 15 min distances between berthing (terminals), a delay of 1 min at the (on)boarding procedures demands for example for 2 to 3 km/h higher speed till to the next terminal. The timetable bases on 23 km/h cruse speed but the steamer have to be able to speed up to 28- 30 km/h.

3. The company, crews, skilled workforce and the shipyard

The Lake Lucerne Navigation Steamer Company (SGV) is Switzerland largest operator of steamer and motor ships. Its fleet of 5 nostalgic original paddle steamers (built in the years 1901/02/06/13/28), and 15 elegant salon cruisers can accommodate a total of 13'000 passengers and on-board restaurant seat for 3'200 guests. > **Annex 4**

The steamers have been built from 1837 up to 1913 by Swiss company's like Sulzer and Escher-Wyss, transported in pieces over land, then assembled and completed in the company's own shipyard. When this companies stopped the shipbuilding in the twenties of last century, and due to the high number of personnel from the crews in winter (less steamers in operation), the SGV started to build their own motor ships. During the years a high qualified nautical crews same as skills in maintenance and shipbuilding was developed. About 130 of the 160 employees are in nautical service, 100 of them are skilled workers and involved in winter in maintenance and shipbuilding in the company. This gives a excellent synergy of motivated skilled employees, professional behavior and direct quality control, because of know-how and understanding of both sides of the problems!

In the last 100 years, the cost of manpower has increased tremendous, but the efficiency, flexibility and versatility of a skilled craft with all the modern machinery and equipment is much higher. In our company, each full year employee has at least two or tree jobs. Also cleaning, daily servicing, small repairs and preparing of the steamers for the cruse is done by the crew. Training is done with own management, captains and workshop masters as instructors, much more then in the older days! Result is a self-thinking, active and motivated employee, they have a really high performance and utility. Hundred years ago, our steamers have been operating with a nautical crew of 10 to 12 men for a capacity of 900 passengers, today we run same ships with a nautical crew of only 6 men an more jobs: 4 men on deck and 2 on the hand-operated original steam engine.

The operational base of the company with own shipyard, construction dock and full equipped workshops is within the shipyard, close to Lucerne. This gives a high flexibility with the personnel and a direct, fast, close acting servicing and maintenance.

The high performing catering service for our SGV fleet is operated by a leaseholder. The modern standardized equipment together on the catering base in the shipyard and on the steamers /motor-ships has a capacity for 3200 meals at same time. On a steamer, 300 guests must be attended „a la carte“ within extreme short time. The kitchens onboard contains hot-, cold-,and dessert section, about 5 tons of cargo at stores, cold storage, freezer/deep freezer, electric warming containers, combi-steamers, double, the dish-washing section. and of course, the onboard wine cellar.

4. Paddle-Steamer as a platform

Steamers from 100 years ago as a platform have been a *"well designed and optimized utility"*. There design where a combination of all physical, functional and geometric requirements together. The result was a majestic exterior and natural-born, physical-science related „ship“-!outlook. In a certain sense they were also the ultimate cry in high speed and interior furniture, but not like a floating fast-food container nor star-wars fantasy yachting outfit. > **Annex 5**

The ship of today as a technical platform has become more complex and with a great variety of equipment. Interesting is the steamers development in the last 100 years on Lake Lucerne in a comparison between 4 ships with similar task within 100 years with criteria's like: the weight of the ship, capacity of passengers, engine RPM, volume and weight of the propulsion power machinery.

The basic requirements for a steamer or a motor-ship on Lake Lucerne for 1913 or 2002, are surprisingly still similar like:

- "modern design", all year service, 1st and 2nd class for passengers,
- economic, reliable, good price, best manufacturing quality, experience taken in mind
- Swiss government regulations, Swiss ship insurance, max. environment protection
- reliable integration in the public transportation timetable within minutes
- guaranteed speed of 30 km/h, 27 km/h in normal service, stopping at max. 2 x ship length
- up to 50 Landings a day with fast maneuvers, no bow-rudder or thrusters
- numerous load-changes and partial load running, therefore good power reserve
- reliable, standard proved machinery, easy handling, easy maintainability
- capacity within 65 – 1200 passengers, length within 25 – 65 m, depth max. 1.5 m
- ship lines faired with deck-bay and sheer outside, but inside rooms floors flat, low weight
- heel over of max. 12°, moving passengers to one side, incl. wind load or centrifugal forces
- minimum air pollution, minimum noise, minimum waves

The difference for today in 2002 is mainly in :

- more toilets at today standards also for disabled persons
- the on-board-catering because of increased consummation on food & beverage
- hull and main structure in steel, upper deckhouse in aluminum
- 50 % passengers each on 2nd class on the main deck and 1st class on the upper deck
- Electric 400 V system with one AC-Generators driven by a steam turbine. 24 V DC basic and emergency system, > 1913 where all electricity in 110 V DC.

To see the development of hull design over a span over 100 years for the considerable speed of 30 km/h, tree ships of Lake Lucerne Navigation Company are compared:

Paddle-Steamer "Gallia"	1913, 330 ton, 32 km/h, 1100 HP, 60 m length x 7,2 m span
Motor ship "Schwyz"	1951, 265 ton, 30 km/h, 900 HP, 58 m length x 8,3 m span
Motor ship "Waldstätter,	1998, 260 ton, 31 km/h, 1200 HP, 58 m length x 8.3 m span

> **Annex 6**

The propulsion power needed for the paddle-steamer 1913 is less then for our most modern motor ships build 1998 and tested in a model basin! > **Annex 7**

1913, the structure in steel was all riveted in a fine network construction in tree dimensional forms. There were no pre-stress from welding so the forms could be kept exactly. The old rivets with a age of 100 years are still perfect! For repair purpose and for changes of steel plates on he hull, today we are welding, the welding rods outside are finally grinded. Today in restoring work and on new ships we apply for the superstructure's outside plating still rivets, because of a perfect faired alignment and a tension free structure (see airplanes!).

The 1-man wheelhouse is fully equipped for easy handling and surveying of the ship. The official navigation on this inland water bases on compass degrees, running time and speed (engine revolution). The GPS is introduced on the main steamers. Electric compass, x-axle deviation indicator (°/min) with autopilot, daylight radar, exact RPM instruments and all necessary display indication instruments, alarms, wireless radio, public radio, onboard communication, audio & sound equipment etc. are well and in good reach arranged. During cruise, pilot has so all helps for relaxed operation with our short distances between terminals and fast changing situations. More details about steamer design and construction are not task of this paper.

5. Steam power process

The paddle steamers high performing propulsion machinery is placed in the center of the narrow, low resistance hull, easy to access, to operate and to maintain. A 3D sketch helps to understand the installations and functions inside of a side-wheeler. > **Annex 8**

A steam power system with the external combustion has great advantages. For the often excessive load variations and overload demands on a inland lake passenger service, a steam boiler is a good power accumulator. The boilers from 100 years ago where coal fired. Because of grate cleaning, difficult firing, natural exhaust pull and other reasons with negative influence, the boiler seldom reached 100 % output. Fuel in great variation can be used. Information about power capacities in ton/h of inland lake ships don't exist. > **Annex 9**

The know-how of steam power about 10 years ago was low, therefore we had to do measurements on the whole power system, for example have been worked out: > **Annex 10**

- power requirement and load characteristic on typical cruises
- Energy flow measurements with the Universities of Hamburg and Lucerne
- Power flow with "Indicating" on the steam cylinders with special cooled measuring devises
- characteristic of the different systems of superheating the steam
- available reserve of steam power when a blackout occurs
- Demand on electrical power, produced with a steam turbine driven generator

The steam power process with superheated steam is divided 5 phases like: > **Annex 11**

- heating up the boiler water
- steaming of the boiler water
- superheating of the steam
- expansion on the engine (piston or turbine)
- condensation with a cooler or with direct water injection

1913 the steam power machinery where really high tech, some optimizations or improvements on the efficiency can be done today only due to modern material technology for example:

- maximizing the heat exchange on exhaust steam and boiler feed water
- increasing the process temperature and pressure by heat resistant steel

- improving and regulating the superheating process
- minimizing the exhaust gas temperature with a economizer
- maximizing the thermal insulation on all parts
- uninterrupted, constant operation of the steam boiler and combustion
- optimizations on the steam valves, piping and steam flow
- reducing the temperature in the condensation (pressure difference)

The all over balance of the energy process on a paddle steamer for original 1913 gives approx. 12 %, a modern steam engine could come up to 28 %. Because of the use of steam for propulsion, generator, pumps, hot water for the pantry and toilet's, heating, whistle, and with the steam burner of the old boilers, the energy flow is difficult to be worked out. A certain estimation is kept in the result. The all over energy and steam consumption can be measures with certain exactness but over a long period, i.e. approx. one day cruise. The so called "Sankey" – diagram explains in a easy way the steam system's energy flow of input, benefit, circulation and losses. **> Annex 12**

Interesting is the long disposability of a steamer when a full black-out occurs: > running for ½ hour or 8 km with still enough steam with 50 % boiler pressure available for a good landing procedure! This is also enough time to reset a breakdown of the burner. The lake Lucerne is max. 3 km broad, so that within 2 km a landing place can be reached. Would you try that with a diesel driven ship? **> Annex 13**

6. Steam boiler for ships

With our steamers, the original two steam boilers from 1913 after several pipe changes can not be kept anymore, so they have to be replaced. The following reasons and advantages leaded to a new tailor made the one only boiler, respecting the advantages of the old "scotch naval boiler": **> Annex 14**

- actual law, Swiss governmental constraints and rules
- modernizing the steaming process with today's know-how
- same stability and gravity centre, less weight, better use of available space
- investment, costs of adaptations in the hull structure
- economic running costs, fuel consumption, maintenance, lower inspection cost
- Availability, safety, redundancy, operation, less machinery

Energy production with a steam system have better combustion results especially a minimum of NOX because of "low" combustion temperatures. Various types of solid, liquid and gaseous fuel can be used. With controlled combustion a separate cleaning of exhaust gases is not necessary.
Heavy load or overload of the engine doesn't result in "black smoke. **> Annex 15**

7. Steam engine and paddle wheel

The two-cylinder diagonal compound engine was in its time a "absolutely high tech – high performance" machine, powerful, reliable, long living and very carefully manufactured.
The handling, operating and control of an original old steam engine system is still all by hand of the machinist. It needs a good trained and experienced person, who likes to work in a machine room all day. But on modern rebuilt engines with an automatic boiler, remote control is possible. Two men are necessary for the manoeuvres, during cursing one machinist can partly relax. To operate such a beauty, human sensors like ears, eyes, nose, fingers infrared, vibrations and memory are essential. More than that, this beautiful steam engines, a careful art of workmanship, visible for the passengers, are real jewels and together with the machinist on the handle great show-peaces ! **> Annex 16**

A steam engine with paddle wheels has a ideal torque characteristic on the driving shaft, operated by a good trained crew makes perfect landings with short, precise maneuvers! It stops at 1.5 length of the ship, a propeller/diesel driven needs 2.5 to 3.5 lengths of the ship.

No gearboxes, no transmissions, no trust bearings, no vibration- and shock absorbers, on exhaust dampers, no noise protection devices, just nothing then the excellent steam engine! In our area, bow or stern thrusters are not necessary and would only extend landing procedures. Today with good steering- and maneuvering techniques, there is no more need for assistance on landings from land site.

The paddle wheel is by far the best propulsion device for shallow water, has the greatest propulsion area, is protecting the river/canal soil and boundary, result in low waves. The propulsion efficiency with movable blades reaches 74 %, more than the best propellers. There is no electronics or automatism. They absorb easily normal-size floating wood and have no ground contact. Shaft seal is simple and above water level, control on the blades can be made easy and dry. For the Passengers, a paddle wheel is most attractive! >
Annex 17

In the year 2000 (!) was build a new high performance brand new two-cylinder diagonal exhaust steam engine with 16 bar and 400 °C superheated steam for an old paddle steamer on Lake Geneva, to replace with great exit the diesel-electric drive. The engine performs excellent, turns up under load in 4 seconds to max. revolutions of 60 RPM! Her fuel consumption is on 12 to 14 lt/km, comparing with similar old machines + Boiler with 18 to 22 lt/km. **> Annex 18**

8. Conclusions

The passengers may have changed over hundred years but there expectations on a cruise with a ship / "Steamer" are surprisingly almost the same. The personality of such steamers is great, they are so special with a touch of richness, confidante, adventure, reliability and freedom, same like passengers also want to be! A well and complete restored steamer has a comparable value then a new built ship.
Restoring of the old paddle-steamers of lake Lucerne with own personnel needs about 75'000 men-hours, approx. 6 Mio CHF and has a duration of 27 months. Live time circle with a good maintenance is excellent, 0ur fife steamers will reach easy 100 and another 100 years!

The new motor-ship "Waldstätter" 1998 was build with our own personnel with 72'000 men-hours and at 8 Mio CHF within 20 months, in our own shipyard. A similar new built paddle steamer with a modern steam power machinery could also cost approx. 8 to 9 Mio CHF. Because of remote control, the steamer could be operated like a motor ship with same crew members. The specific fuel consumption of old steam was a handicap, but with modern science, much better efficiency is achieved. Fuel for heating purposes like in a steam boiler is approx. 3 x less expensive like diesel fuel but the consumption with a steam engine is 3 – 4 times more. > Finally this are interesting but seldom known figures!

A real paddle steamer is a smooth running, environment-sparing transport vehicle specially for sensitive areas and shallow waterways. There is controlled combustion with re-generable fuels as local natural supplies offer.

In Switzerland, there are 12 paddle steamer in daily summer service, 3 projects for restoring or new building are in course. They are all full established and can not been anymore scrapped without serious problems with all public! The Lake Lucerne Navigation Company with its 5 paddle steamers and fifteen motor ships is still making benefit and is a healthy company.

With their fascinating masterpieces of technical science, quality, ambiance and emotional acceptance from the passengers, paddle-steamers have a come-back "back to future" as special high performance vehicles!
"Full steam ahead" ……is this only a captains dream, 1913 or 2002 ? **> Annex 18**

Annex 1: high performing rooms for passengers

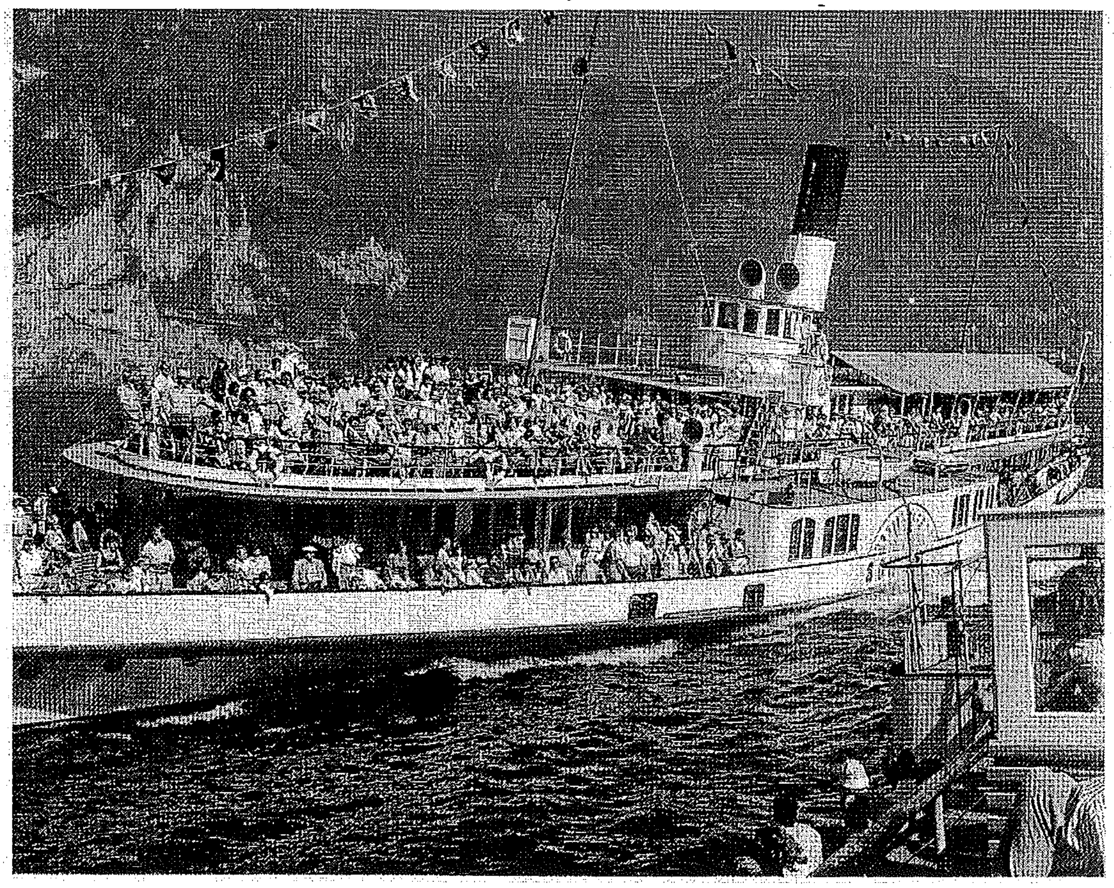

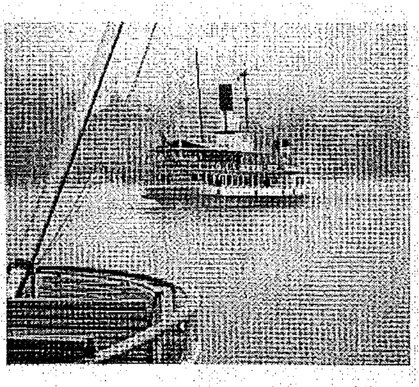

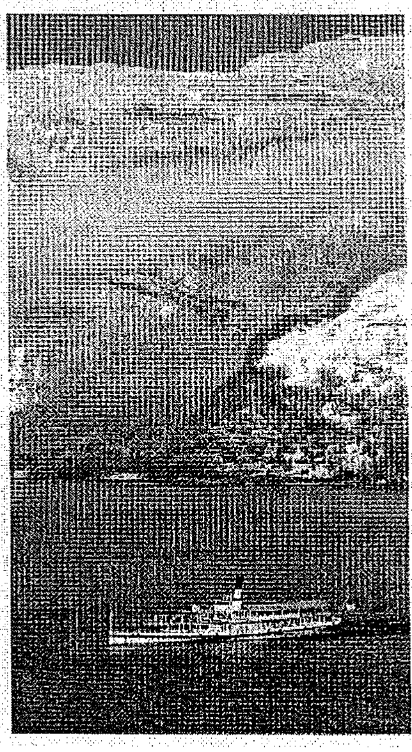

Annex 2: Panorama of Lake Lucerne, "Vierwaldstättersee"

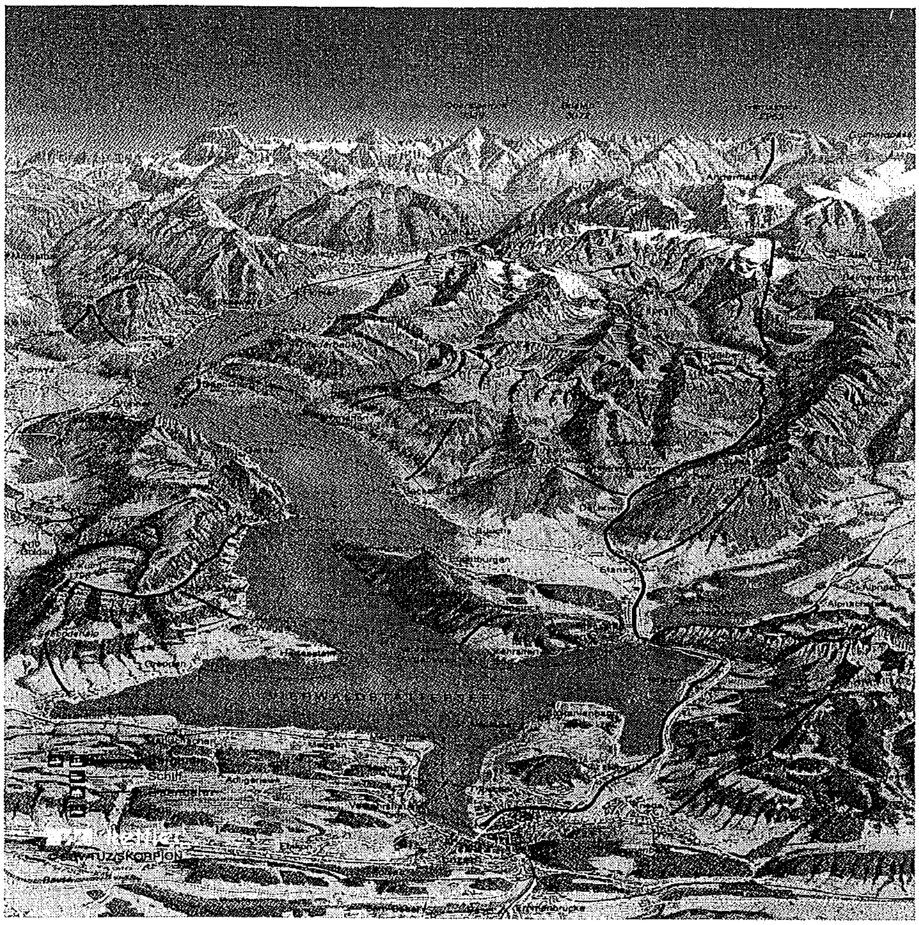

Annex 3: High performing Network of Swiss public transport system with Lake Lucerne

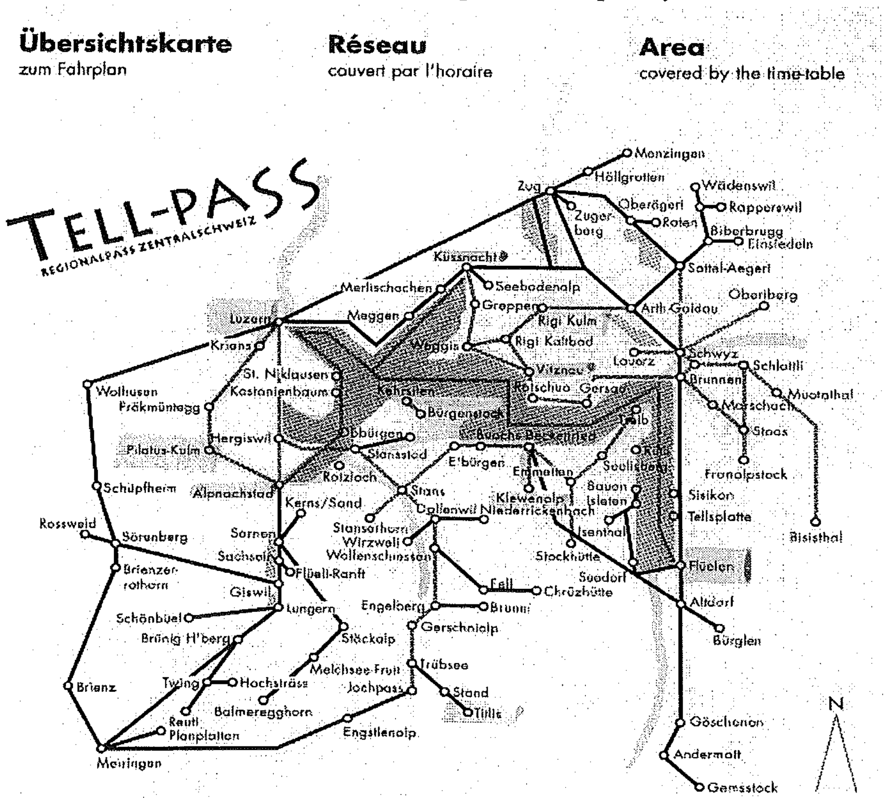

Annex 4: Technical data of the SGV-Fleet of Lake Lucerne Navigation, Switzerland

Lake Lucerne Navigation "Vierwald-stättersee"	Date of build or mayor overhaul, changes or restoring	Weight empty, ready to run	Engine Horse-Power	max. speed	Length over all	With over all	Load capacity		Sitting Places for passengers on:	
	Year	ton	HP	km/h	m	m	ton	Pass.	decks	rooms
Paddle - Steamer										
Stadt Luzern	1929/54/90	415	1300	26.5	63.5	15.2	90.0	1200	614	373
Gallia	1913/53/79/04	325	1080	30.0	62.9	14.5	67.5	900	605	245
Schiller	1906/52/77/00	302	700	27.9	63.0	14.3	67.5	900	570	270
Uri	1901/61/81/94	294	650	27.4	61.8	14.0	60.0	800	593	207
Unterwalden	1902/49/61/85	295	650	27.4	61.0	13.7	60.0	800	477	273
Motor-ships										
Europa	1976/95	230	1200	28.0	58.4	11.3	82.5	1100	521	314
Gotthard	1970/94	234	1200	28.5	58.4	11.3	90.0	1200	533	309
Winkelried	1963/92	241	1200	29.0	58.4	11.3	90.0	1200	585	276
Schwyz	1959	265	900	27.5	58.4	11.3	75.0	1000	560	296
Waldstätter	1998	260	1200	31.4	58.0	11.5	52.5	700	316	304
Rigi	1955/63/80/95	159	900	29.0	47.5	8.5	45.0	600	290	153
Pilatus	1966/94	111	450	26.0	40.3	8.2	30.0	400	211	131
Weggis	1990	195	710	27.3	48.2	9.7	30.0	400	129	171
Brunnen	1991	197	710	27.3	48.2	9.7	30.0	400	129	171
Flüelen	1991	201	710	27.3	48.2	9.7	30.0	400	129	171
Titlis	1951/62/75/01	113	440	29.0	43.2	8.3	22.5	300	142	104
Mythen	1931/56/89	35	480	21.5	31.6	5.0	15.0	200	20	110
Rütli	1929/89	31	240	21.0	22.4	4.9	10.5	140	16	71
Reuss	1926/92	29	240	21.0	22.5	4.9	10.1	135	16	40
Rütenen	1930/85	30	100	12.5	22.7	5.6	40.0	60	10	50

Annex 5: General Plan of a paddle steamer

SEITENANSICHT

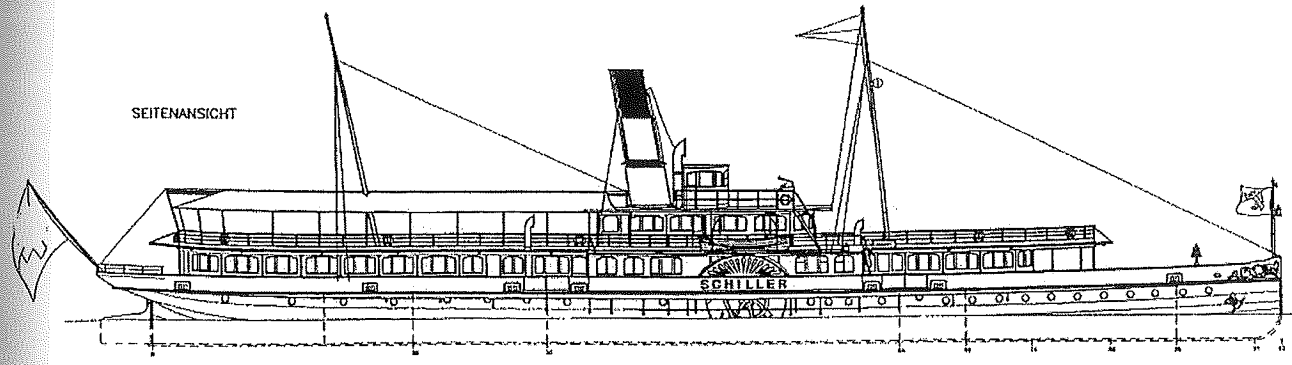

OBERDECK

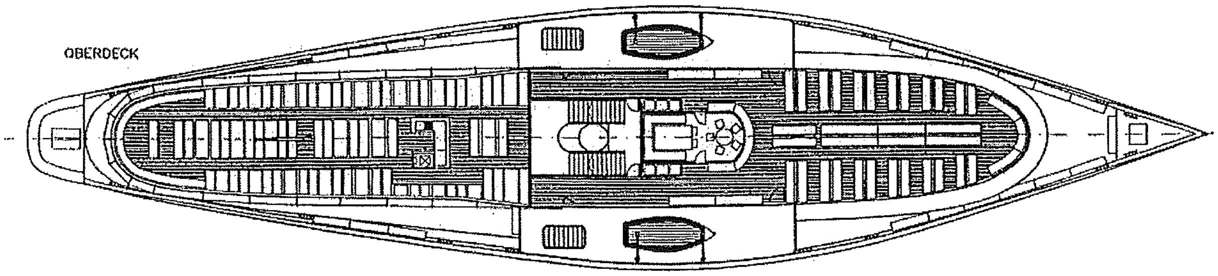

HAUPTDECK

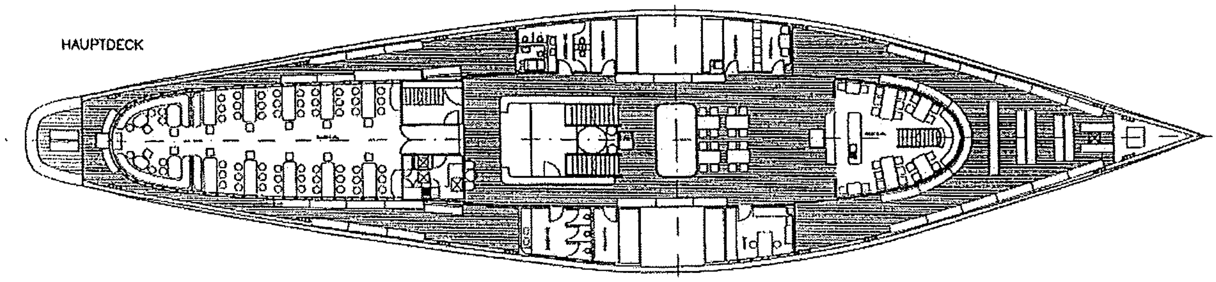

SCHALE

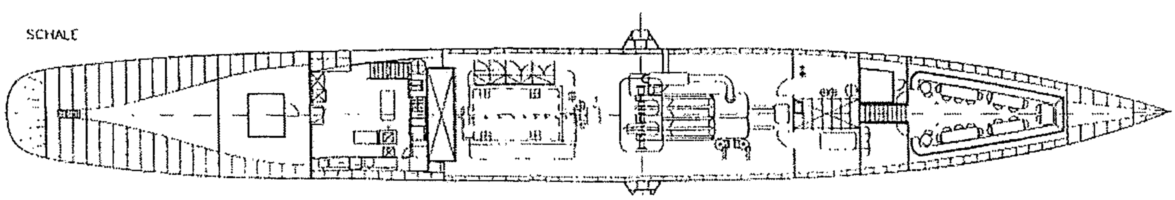

Annex 6: Comparison of 3 hull forms similar main data's from 1913, 1959, 1998

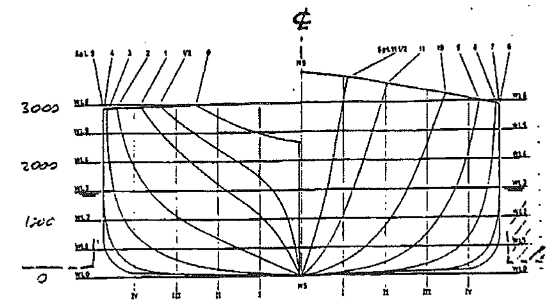

DS"Gallia", 1913, Steam-Sidewheeler, L_{cwl}=63m, W_{cwl} =7,2 m, 330 ton, 1100 HP, 32 km/h

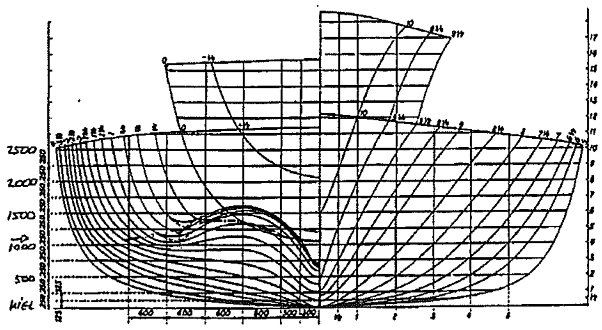

MS „Schwyz", 1959, 2-Prop.Motorship, L_{cwl}= 54m, W_{cwl}= 7,9m, 265 ton, 2x 450 HP, 30 km/h

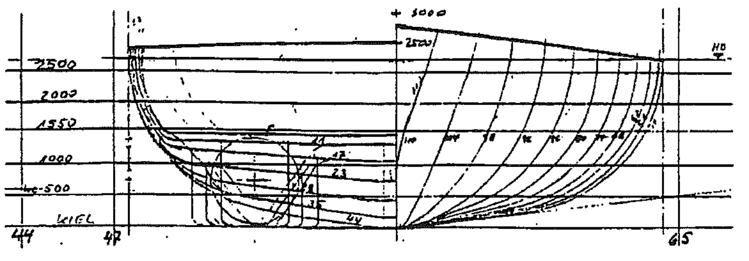

MS 700, 1997, 2-Prop.Motorship, L_{cwl} 57m, W_{cwl}= 8,0m, 280 ton, 2x 600 HP, 31 km/h

Annex 7: Ship-resistance, Propulsion requirements for two similar ships 1913 and 1998

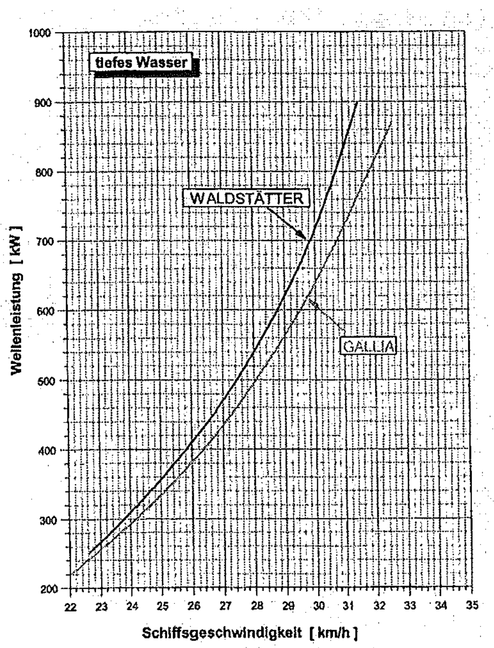

Annex 8: Paddle steamers high performing propulsion machinery, 3-D sketch

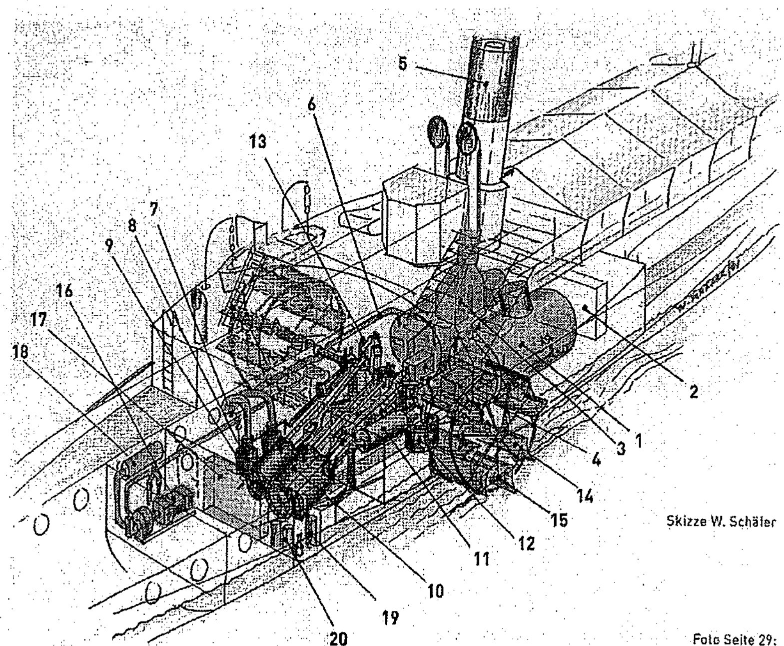

Foto Seite 29:
Maschinenanlage der «Gallia»

1	Dampfkessel	8	Ventilstöcke	15	Exzenterstangen
2	Treibstofftank	9	Hochdruckzylinder	16	Dampfturbogenerator
3	Überhitzer	10	Niederdruckzylinder	17	Elektro-Hauptverteilung
4	Brenner / Flammrohre	11	Kesselwasservorwärmer	18	Abdampfwärmetauscher
5	Kamin	12	Kondensationspumpe	19	Wasseraufbereitung
6	Heissdampfleitung	13	Kurbelwelle	20	Speisepumpen
7	Regulator	14	Schaufelräder		

Annex 9: **Load characteristic on a steam powered system**

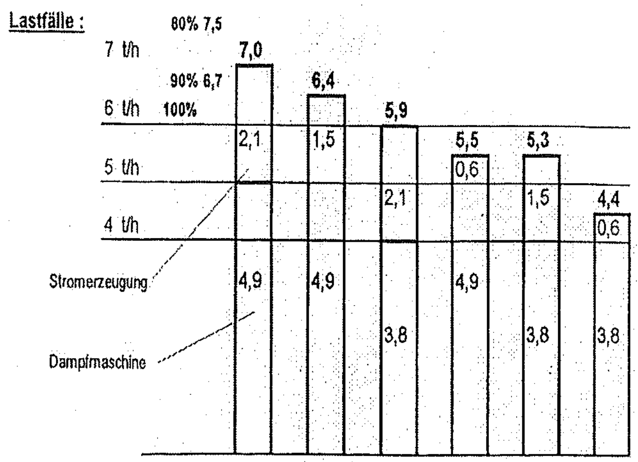

Reserve in Prozenten :							
	100%	-14	-7	2	9	13	36
	90%	-4	5	14	18	26	52
	80%	7	18	28	36	41	70

Annex 10: modern measurements on steam power system of a paddle-wheeler

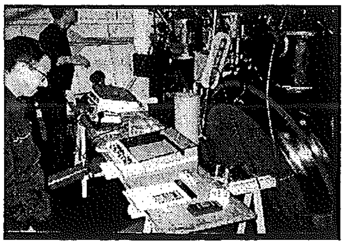

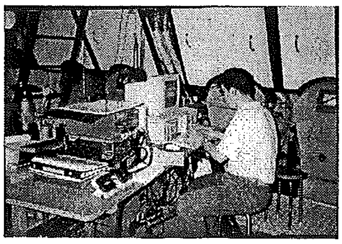

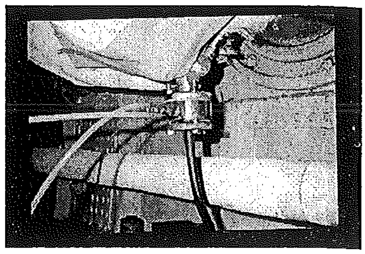

Annex 11: Diagram: t / s, (temperature / entrophy)

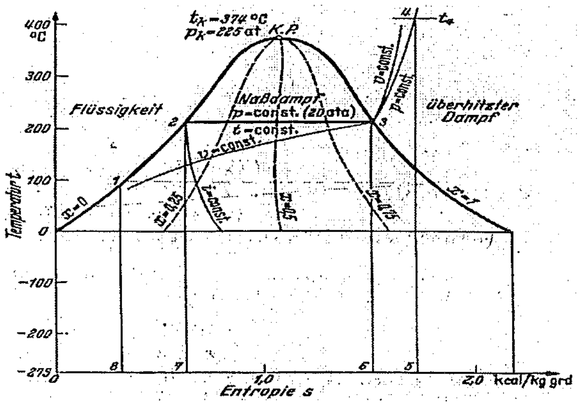

Annex 12: Paddle steamer's power system, Sankey diagram

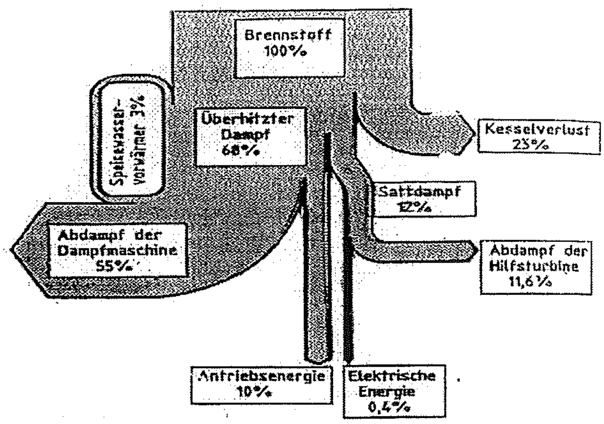

Annex 13: Available reserve of steam power when a blackout occurs

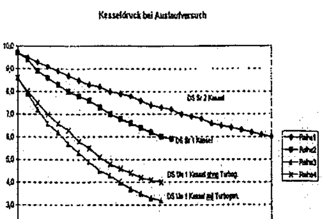

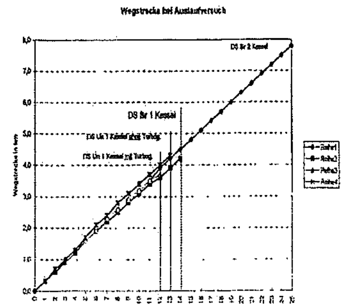

Auslaufversuche" mit Schaufelraddampfer, Messen der Wegstrecke bei Ausfall der Feuerung (Blackout)

Annex 14: Old and new boat-steam boiler

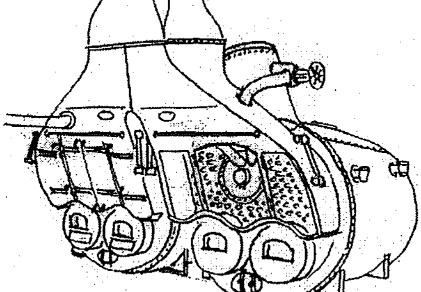

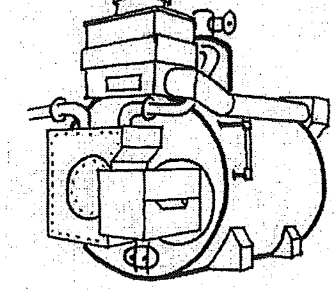

Annex 15: **Exhaust gases, comparing Diesel- or steam driven vehicles**

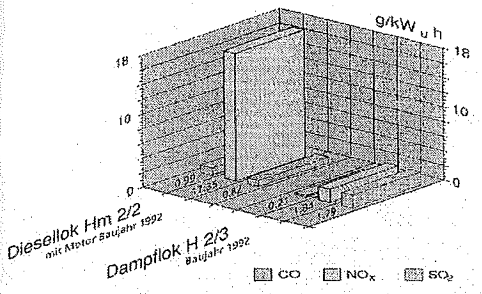

Vergleich der Abgaswerte der modernen SLM-Zahnraddampf-lokomotive mit einer vergleichbaren Diesellokomotive neuester Bauart.

Annex 16: **Two-cylinder diagonal compound engine for a side-wheeler, 1913**

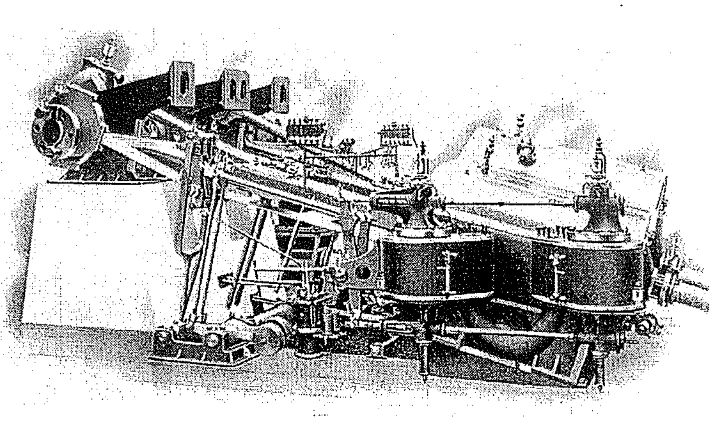

1.

Annex 17: **The paddle-wheel, a high performing propulsion**

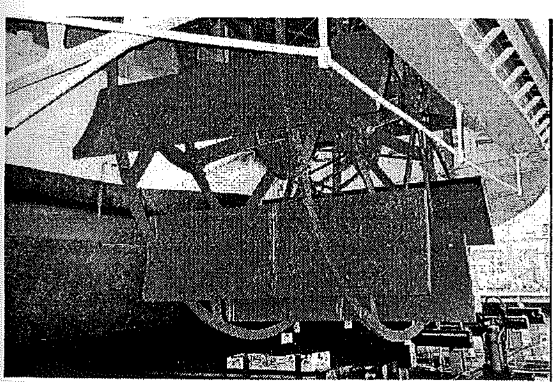

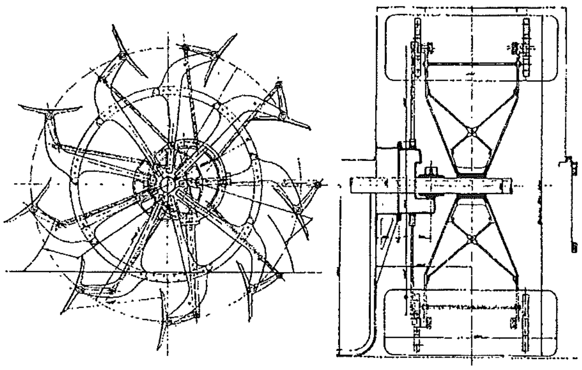

Annex 18: **a new High-tech steam engine, 2001**

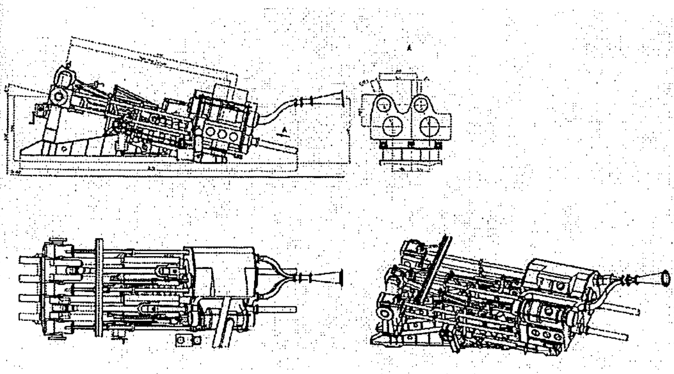

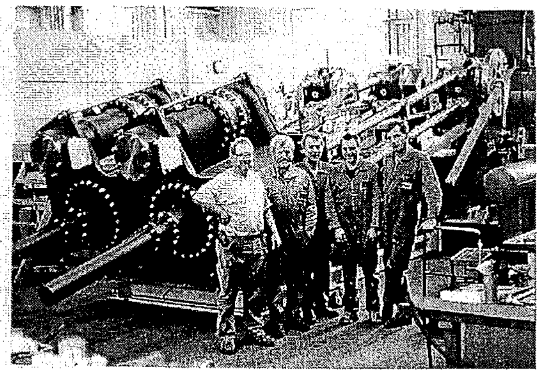

Annex 19: High performance on a captains dream, 1913 or 2002 ?

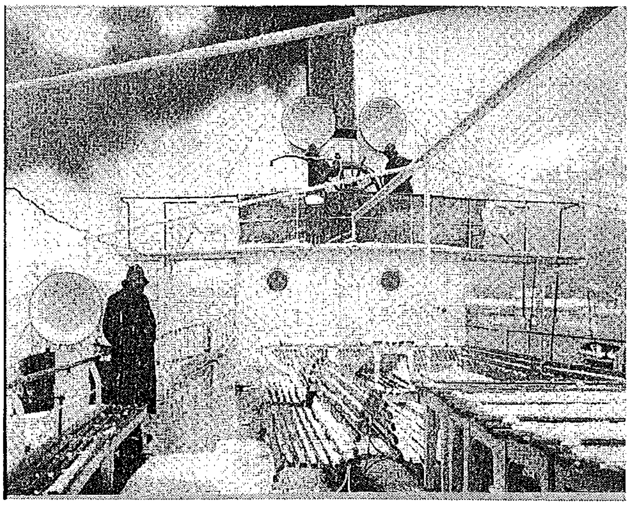

1928: Kapitän Josef Zimmermann mit der Filmdiva Liliane Harvey anlässlich der

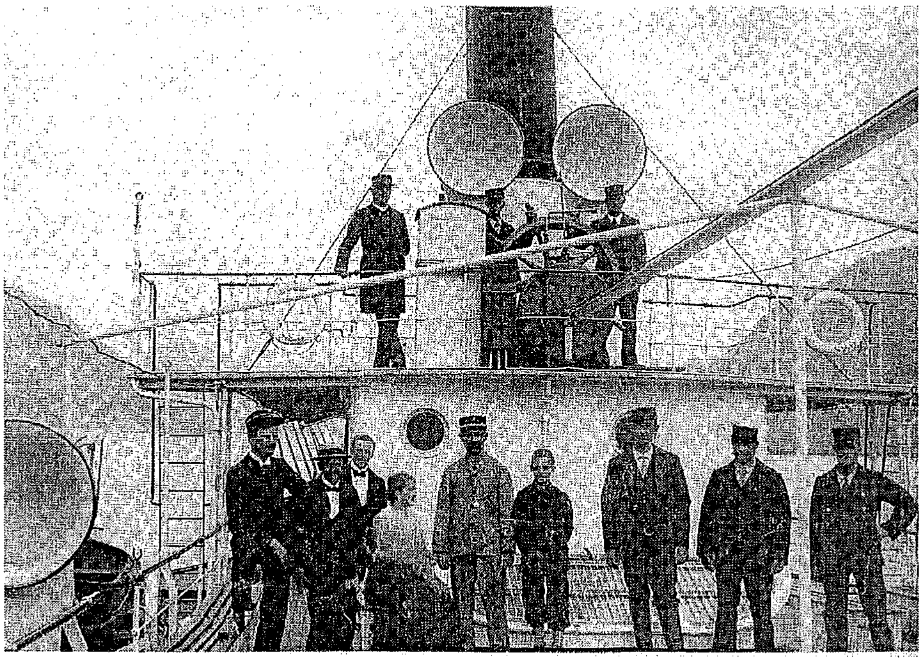

Aerodynamic Flow Computations for a Superfast Ferry

Daniel Schmode, TU Hamburg-Harburg, d.schmode@tu-harburg.de
Volker Bertram, ENSIETA, bertram@waves.insean.it

Abstract

The aerodynamic flow around the Superfast VI ferry built at HDW was computed using the finite-volume code Comet. The IGES description of the superstructure was simplified for the computational model, but still captures many details. For smoke tracing, multi-phase flow is simulated solving an additional transport equation for the smoke concentration. Similarly, thermic distributions at the funnel can be traced solving an energy equation. The ferry superstructure is complex and tetrahedral elements are used for largely automatic mesh generation. Results are compared to observations in wind tunnel tests. A main difficulty for practical applications is the creation of the CAD description of the ship superstructure. This point is exemplified in the present case study.

1. Introduction

While naval architects are usually concerned with <u>hydro</u>dynamics, <u>aero</u>dynamics play also a role in naval architecture and offshore engineering addressing issues like:

- Smoke propagation and related problems
- Operating conditions for helicopters
- Wind resistance and drift forces (particularly for ferries and car carriers)
- Ventilation of rooms

A typical application is smoke propagation. Problems occur frequently if recirculation zones behind the funnel attract smoke and particles. This problem is of particular importance for passenger ships and ferries. For these ships, also the passenger comfort on the upper deck is always a relevant aerodynamic problem.

The standard design tool for these issues today is the wind tunnel test. However, computational fluid dynamics (CFD) is increasingly applied in related industries for aerodynamic design problems, e.g. in civil engineering and automotive engineering. CFD offers in principle some advantages over wind tunnel tests:

- It is easy to store the whole flow field information. This allows *a posteriori* additional investigations and evaluations.
- There is better control over what is viewed or shown.
- CFD captures more details of the flow.
- In principle, also simulation of full-scale are possible. (We present here only simulations at model scale, because the focus was on validation with model tests.)
- The technique is non-intrusive.

Despite these advantages, CFD has been only recently applied to ship superstructures and then often in research projects due to the following difficulties:

- Complex geometry complicates grid generation
- Large computational domain in combination with required flow resolution lead to high cell counts and associated high computer resources.
- The flow physics are complex; the flows are turbulent and unsteady.

Several developments have contributed to overcome these difficulties:

- robust RANSE solvers (simulating turbulent flows) handling unstructured grids
- techniques to model filigree structures physically, but not geometrically
- improved software for largely automatic grid generation
- affordable parallel PC clusters supplying considerable computational power

The progress has supported an increasing number of CFD applications to maritime structures over the past decade. Førde et al. (1992) solved the inviscid Euler equations for a surface effect ship (SES). Wind resistance accounted for 25% of the total resistance for this 50-knot vessel. The CFD guided modification of the forward superstructure reduced in this case the wind resistance by 40%. Førde and Gjerde (1999) applied a RANSE solver to a 40 knot catamaran. Tai and Carico (1995), Tai (1996) simulated the aerodynamic flow around a destroyer using a RANSE solver to evaluate operational conditions for helicopters and airplanes. Tai (1995) presented similar applications to another ship. Drawing on the experience of initial studies of Leer-Andersen and Hughes (1996) at the Danish Technical University, Aage et al. (1997), Hvid et al. (1997) describe RANSE applications to a ferry and an offshore platform, Fig.1. The focus of the investigation was the prediction of wind forces and smoke propagation from funnels. Jensen et al. (1997) concluded that CFD was not yet competitive with wind tunnel tests due the high effort in grid generation, although the accuracy was already good.[1] SIREHNA (www.ec-nantes.fr/sirehna) conducted CFD simulations for smoke propagation for a combatant, but no details are published. Similarly the website of J.J.MacMullen & Associates features an advertisement for CFD simulations for ship structures, Fig.2.

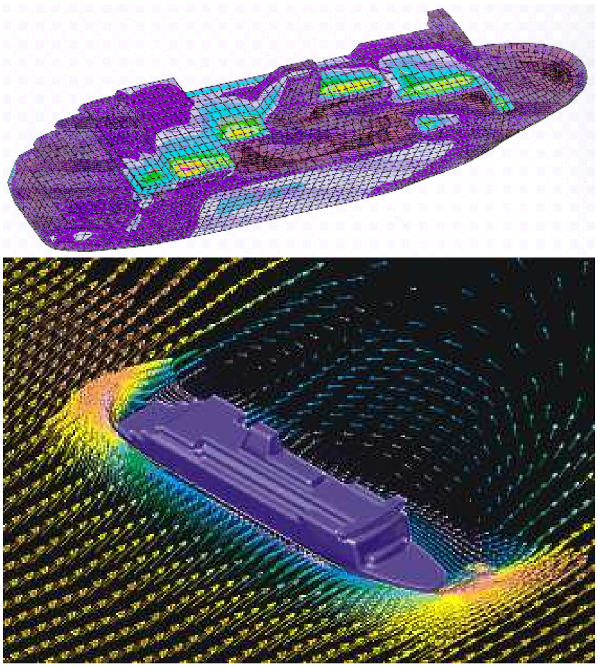

Fig.1: Wind loads and velocities at a cruise vessel, source: Danish Maritime Institute

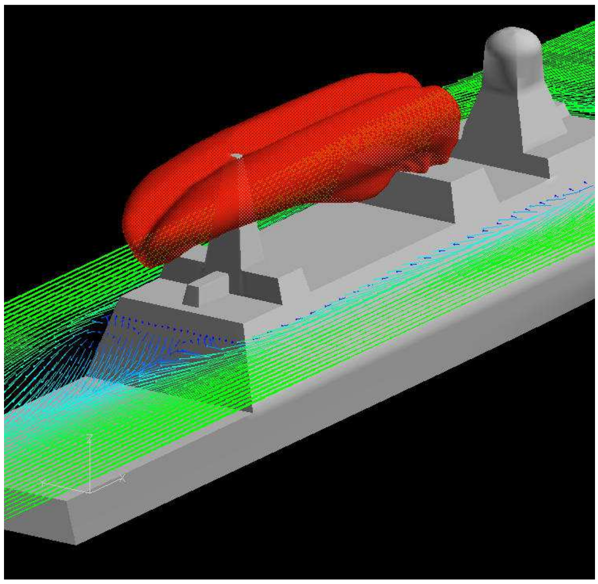

Fig.2: Aerodynamic simulations of JJMA for a naval combatant

The Naval Research Laboratory conducted in 1999 aerodynamic analyses for the destroyer DDG51 using the RANSE solver FAST3D, Fig.3. The focus of the studies was the design of the superstructures with respect to safe helicopter operation. The unsteady heat field was simulated for the original

[1] "The comparison of CFD, wind-tunnel tests, and full-scale measurements show an overall good agreement, even if large discrepancies are indeed seen at some wind directions. The differences between CFD and model-test results are not generally larger than between full-scale and model-scale results. Actually, the differences are not much larger than often found when the same vessel is tested in different wind tunnels. Therefore, it is concluded that determination of wind loads on ships and offshore structures by CFD is a realistic computational alternative to the experimental methods. However, due to the time involved in generating the computational mesh and in computing the solution, the CFD method is not at the moment economically competitive to routine wind-tunnel model testing."

version and a modified version. Researchers at Stanford University conducted aerodynamic studies for an assault vessel of the US Navy, cromagnon.stanford.edu/jship. Data for full-scale, wind tunnel model and CFD were compared to determine how to evaluate best the aerodynamic wake near the flight deck. The computations employed the RANSE solver Fluent using 650,000 cells. 130 CPU hours were needed for the simulation. In Korea, Jin et al. (2001) investigated the propagation of NO_2 from the funnel of a tanker varying various funnel geometry parameters. The simulations employed Fluent and tetrahedral grids with approximately 500,000 cells. The computations simplified the bow geometry and omitted some details like piping systems and radar mast. Yelland et al. (2001) computed the flow around several simplified generic cargoships to evaluate the influence of superstructures on wind measuring devices for meteorological research. El Moctar et al. (2001), El Moctar and Bertram (2002), Lindenau et al. (2002) present aerodynamic CFD applications of the Hamburg Ship Model Basin HSVA for a passenger ship and a fast SES.

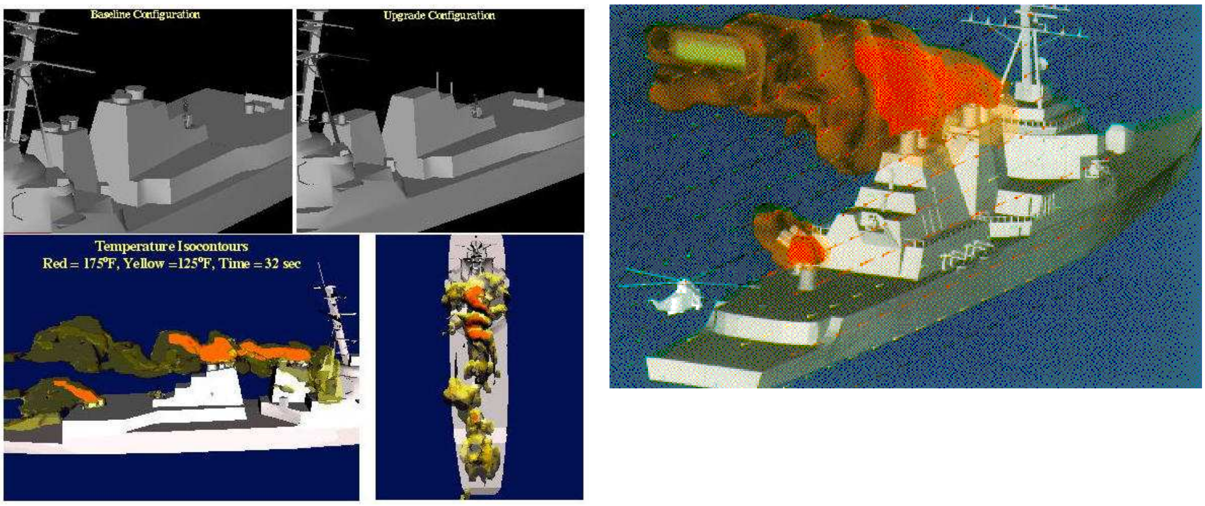

Fig.3: Smoke tracing for DDG51 destroyer, National Research Lab NRL

2. Grid generation

Here we describe yet another application from HSVA experience, namely to the “Superfast VI” ferry built by Howaldtswerke-Deutsche Werft AG (HDW), Fig.4, Mechsner (2001). The design features the trademark of all Superfast ferries: the funnel with two side wings. Main ship data are L_{oa}=203.90m, L_{pp}=185.60m, B=25.00m, T=6.40m, V=28.60m.

The grid generation started from an IGES description of the ship supplied by the shipyard. This is the usual procedure for grid generation for hydrodynamic CFD analyses of the underwater hull. However, in this case we were confronted with a considerable problem in data communication. The shipyard had a very detailed description for its own purposes containing every single rod of the railing, every little nook, etc, Fig.5. Our computers had to be reconfigured before we could even read the correspondingly large IGES file.

After reading the file, we found that we could not directly use it for grid generation, as the grid generator ICEM-CFD required simply connected areas without holes as boundary surfaces. Thus, the IGES description for the ship had to be stripped down and modified, Fig.6. This task took several weeks! In hindsight, it might have been faster and easier to create a new IGES description from paper plans. For future commercial applications, the lesson is that shipyards facilitate the work of CFD consultants (thus reducing cost) if they store IGES descriptions of intermediate level of detail before introducing all details needed for other purposes.

Fig.4: Superfast VI

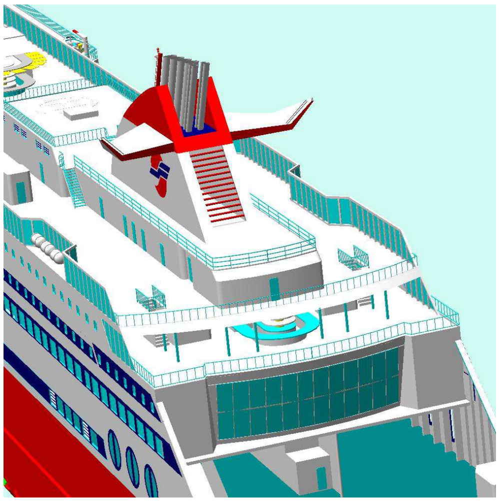

Fig.5: CAD description with great level of detail

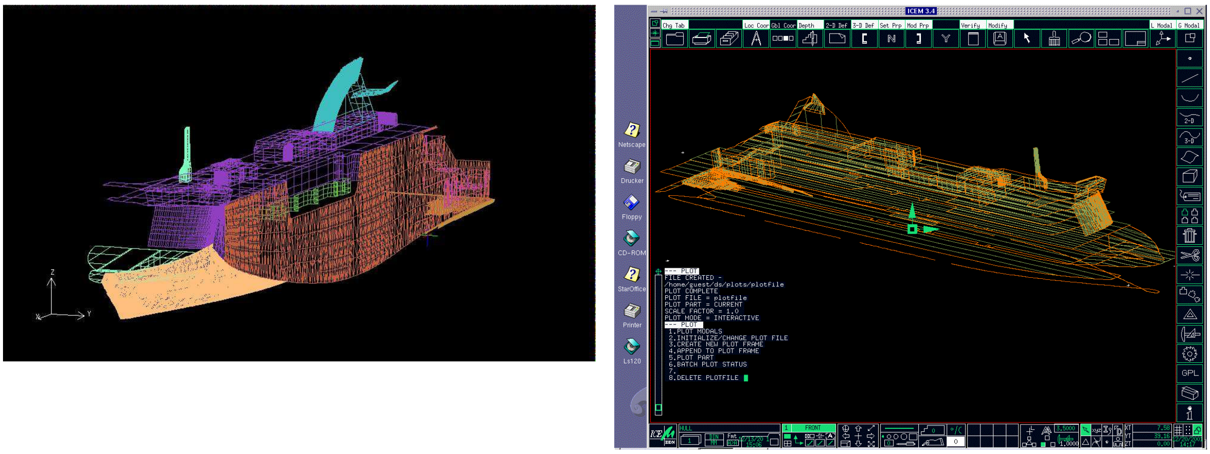

Fig.6: Intermediate stages during phase of preparing suitable IGES description

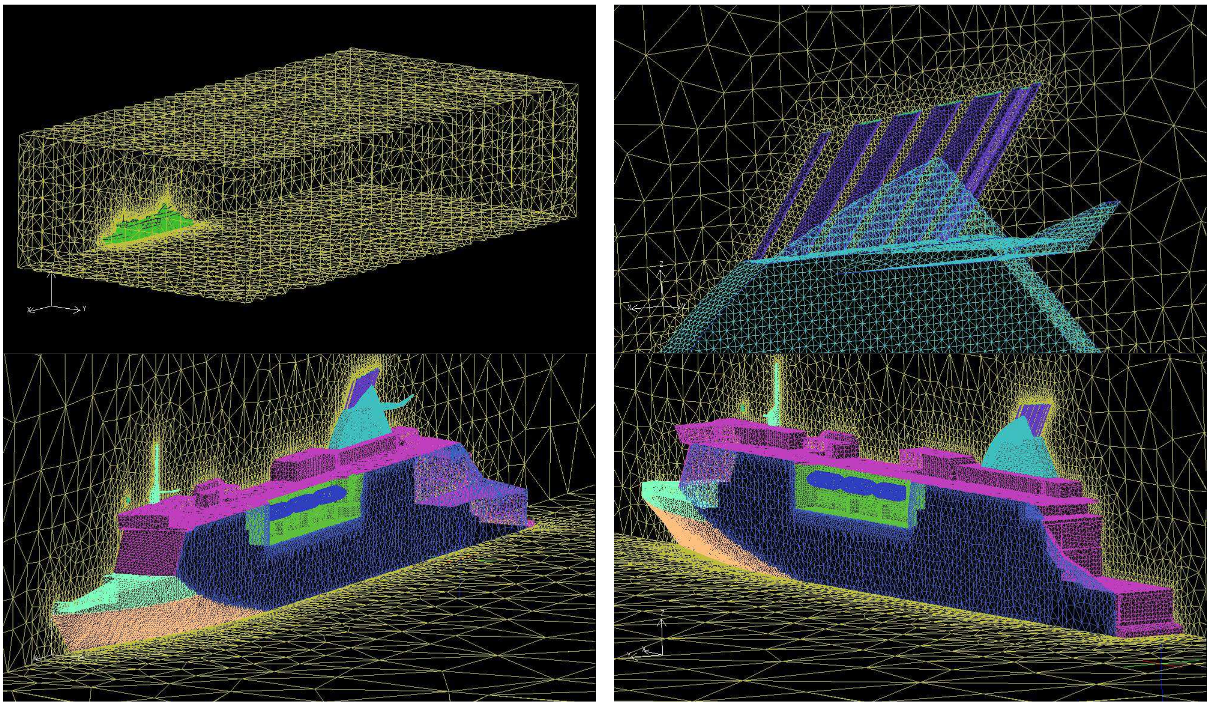

Fig.7: Grid for Superfast

After a suitable IGES description was created, the actual grid generation took less than a day employing tetrahedral elements. Several grids were created and tested with Comet showing again some unexpected problems (lack of convergence, singular pressure peaks at the domain edges). The causes for these were identified in the employed grid generator:

- ICEM generated cells with bad aspect ratio for grids that are too coarse (less than 500,000 cells in this case).
- For fine grids, ICEM generated sometimes erroneous grids with holes or overlaps at the edges of the computational domain. These grid errors were not automatically detected by ICEM, but destroy the whole solution in Comet.

An additional practical problem was that grid generation became very time-consuming from 2 million cells upward on the available computers. E.g. a simple saving of the grid took 30 minutes.

The standard grid mostly employed in the investigation had in the end 680.000 cells per symmetry half, extended from 1 L before the forward perpendicular to 2 L behind the aft perpendicular, 2 L to the side and 1 L in height (above the CWL plane), Fig.7.

3. Wind tunnel tests

Wind tunnel experiments were conducted with a wooden model scaled 1:150 in the wind tunnel of the former Institut für Schiffbau, now TU Hamburg-Harburg AB 3-13, Fig.8. The level of detail corresponded to that of the CFD model. The model was equipped with pipes to investigate also smoke propagation. The flow around the model was visualized using evaporated oil with background lighting, Figs.9-11. Wind forces were measured for apparent angles between 0° and 180° for a Reynolds number of $R_n=2.5 \cdot 10^6$.

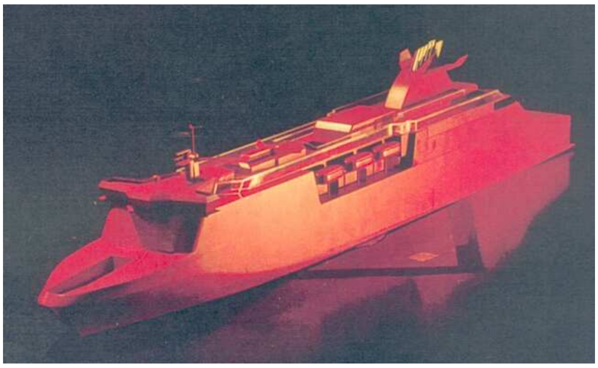

Fig.8: Wooden model in wind tunnel

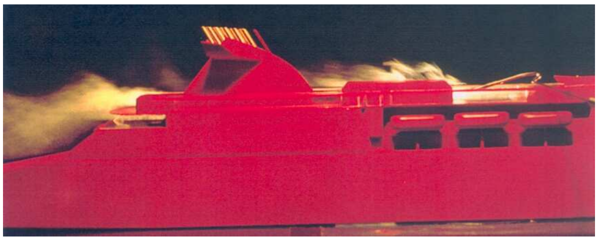

Fig.9: Wind tunnel 180° (head wind)

Fig.10: Wind tunnel 180° (head wind)

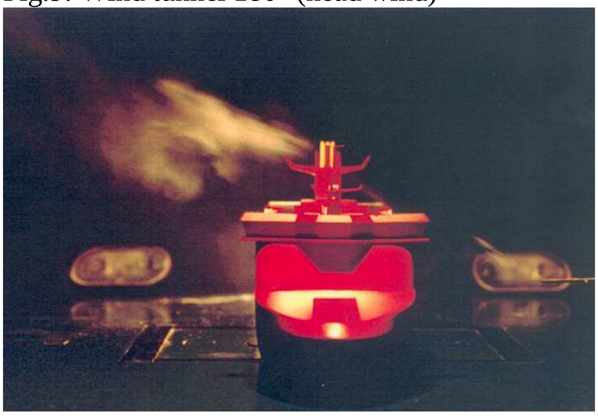

Fig.11: Wind tunnel 90° (beam wind)

The wind tunnel experiments were documented with photos which are most often difficult to interpret. Here, CFD is clearly better as details are easier and clearer to display, interpret communicate. Wind forces are given as non-dimensional force coefficients:

$C_x = F_x / (q \cdot A_L)$ $\quad C_y = F_y / (q \cdot A_L)$ $\quad C_z = F_z/(q \cdot A_L)$ (42)

$C_{mx} = M_x / (q \cdot A_L \cdot L_{oa})$ $\quad C_y = F_y / (q \cdot A_L \cdot L_{oa})$ $\quad C_z = F_z/(q \cdot A_L \cdot L_{oa})$ (43)

$q=½\cdot\rho_a\cdot U_a^2$ denotes stagnation pressure, ρ_a density of air, U_a relative wind velocity, A_L=4599m^2 lateral area.

4. CFD simulation

The aerodynamic flow around ships is turbulent and features massive separation. The appropriate numerical tool is thus a RANSE solver for turbulent flow. The flow is inherently fully turbulent and can be performed at the Reynolds numbers of the full-scale ship. Unlike in wind tunnel tests, there is no need for additional turbulence stimulators. The aerodynamic boundary layer is much thicker than the hydrodynamic boundary layer. This allows a coarser discretization of the fluid domain near the hull. Grids based on tetrahedral and prism elements become then feasible. These grids are much faster to generate than our usually employed grids based on hexahedral elements, as largely automatic grid generation procedures exist for tetrahedral elements.

We employed the commercial RANSE solver Comet for our analyses. The conservation equations for mass and momentum are solved in integral form using a finite volume method. The integrals are approximated using the midpoint rule. The variables respectively their gradients are determined using linear interpolation respectively central differences. The SIMPLE algorithm couples pressures and velocities. The Reynolds stress tensor (i.e. turbulence) is modeled using the RNG-k-ε turbulence model. Time is discretized using an implicit Euler scheme. For smoke propagation, we modeled the flow as two-phase flow in Comet. In addition to the usual transport equations we also solve an equation for the energy balance solving also the thermodynamic distribution in the air. We specify the exhaust temperature and velocity and then trace the development in an externally specified wind distribution. We use a uniform wind speed over height at the domain inlet. Fundamental theory and employed options of the code are described in detail in El Moctar and Bertram (2002).

Computations focused first on head wind (μ=180°) simulating smoke propagation. The exhaust velocity was specified as being the same as the relative wind speed. The exhaust temperature was set at 20° C (=293 K) as in the experiments. The exhaust density was set to that of air. Computed pressure distribution and smoke propagation were plausible, Fig.12. However, a comparison with wind tunnel results showed that the smoke dissipated too rapidly. The suspicion that the differences were due to insufficient grid resolution with associated numerical diffusion were verified by grid refinement. A new grid was generated with local grid refinement in the smoke region, Fig.13. The new grid had 950.000 cells per symmetry plane. Fig.14 shows that indeed the grid refinement makes the smoke cloud more focused now agreeing well with wind tunnel observations.

The exhaust gas is not heated in wind tunnel experiments to avoid problems with the plastic supply tubes. The influence of this modeling error was investigated numerically by computing also for a temperature of 327°C (=600 K). Also a change in turbulence level and the effect of Reynolds number (doubling and halving R_n) at the exhaust exit were investigated. All these variations hardly changed results. Fig.15 shows the turbulent energy k for head wind. One sees clearly how appendages like the antenna stimulate turbulence. Fig.16 shows the absolute value of the velocity. This display allows a quick understanding where stagnation areas of low velocity are formed. This information is useful for passenger comfort and helicopter operation.

Comparative computations with a coarse grid (315000 cells per symmetry half) showed that the chosen grid size was a suitable compromise between effort and flow resolution. Pressures coincided well with the finer grid, but only the finer grid captured smoke propagation correctly, Fig.17. All further computations for all angles of apparent wind, Fig.18, used the standard 1.360.000 cells (680.000 cells per symmetry plane). A local refinement as for the head wind case was not possible due to time limitations. Adaptive grids would be desirable for this problem.

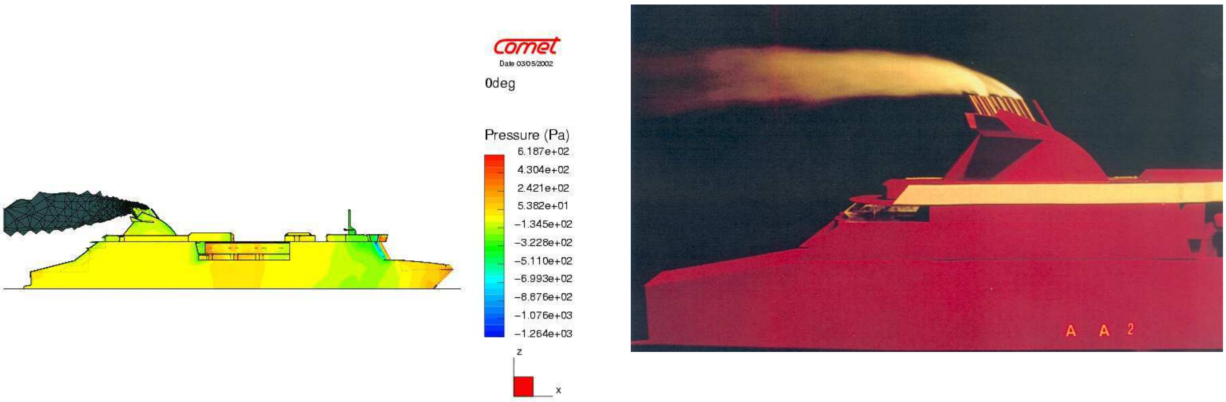

Fig.12: Smoke propagation for CFD (standard grid) and as observed in wind tunnel

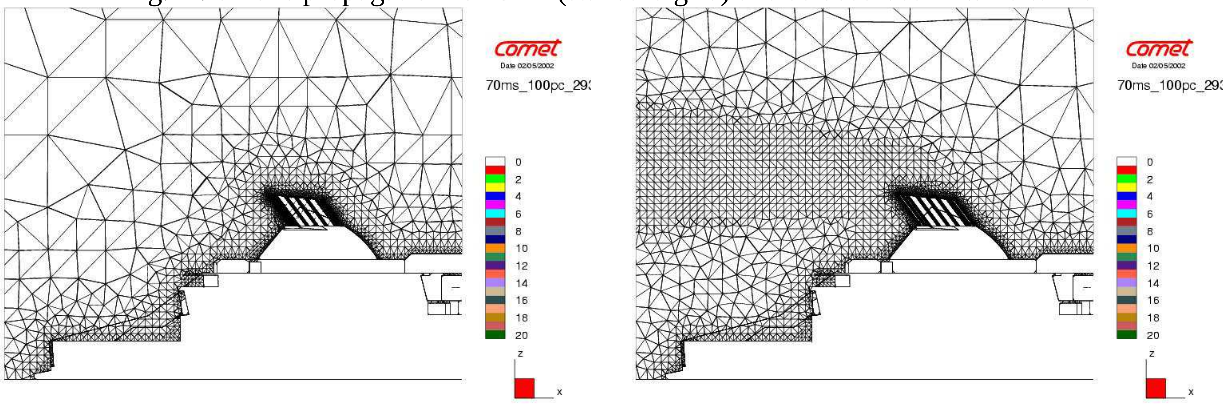

Fig.13: Original grid (left) and locally refined grid (right)

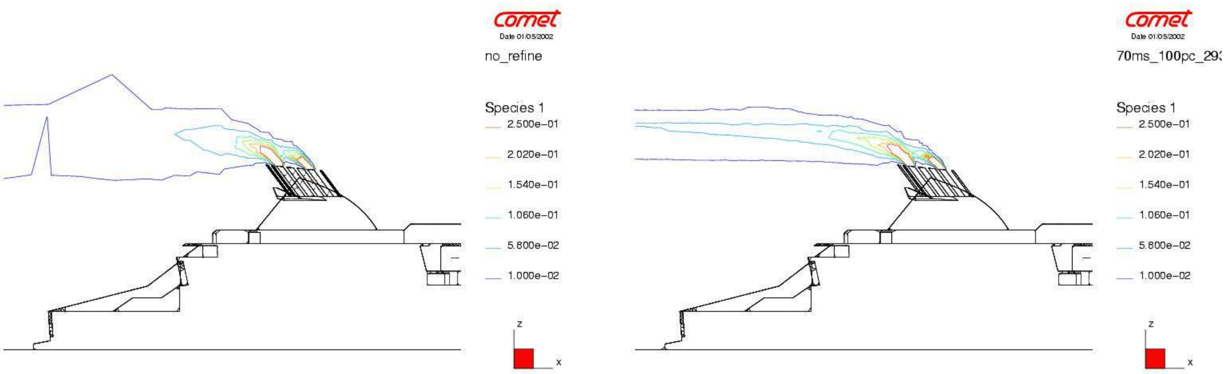

Fig.14: Smoke concentration for standard grid (left) and refined grid (right)

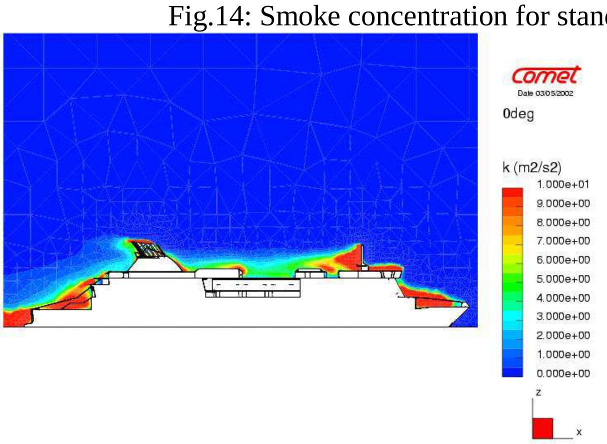

Fig.15: Turbulent energy k in head wind

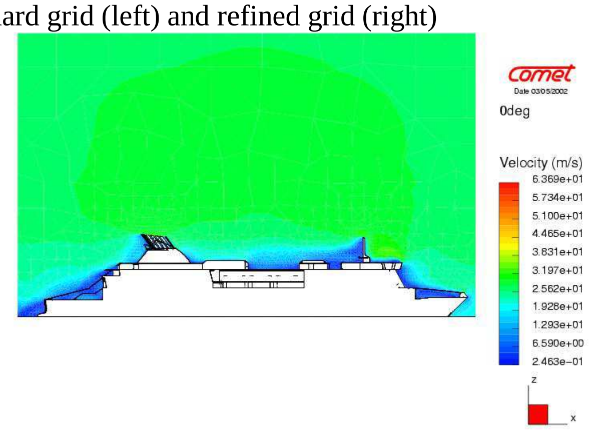

Fig.16: Absolute value of velocity for head wind

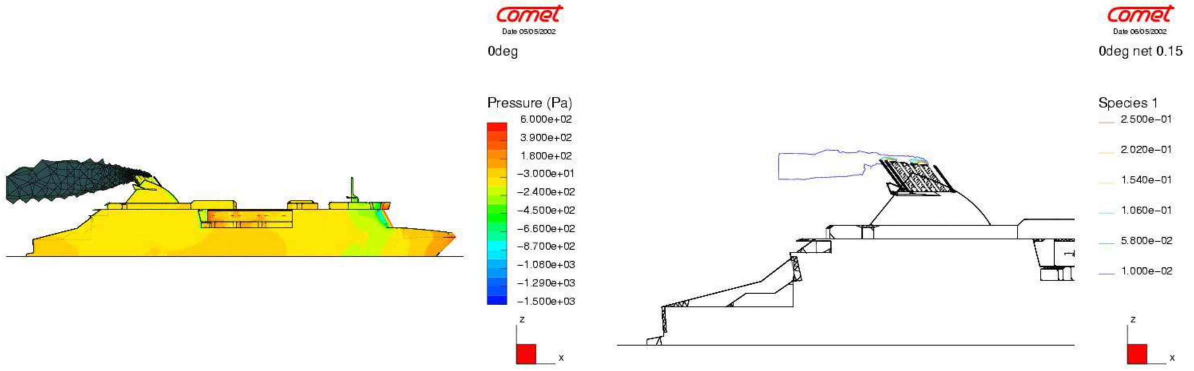

Fig.17: Pressure and smoke propagation in coarse grid for head wind

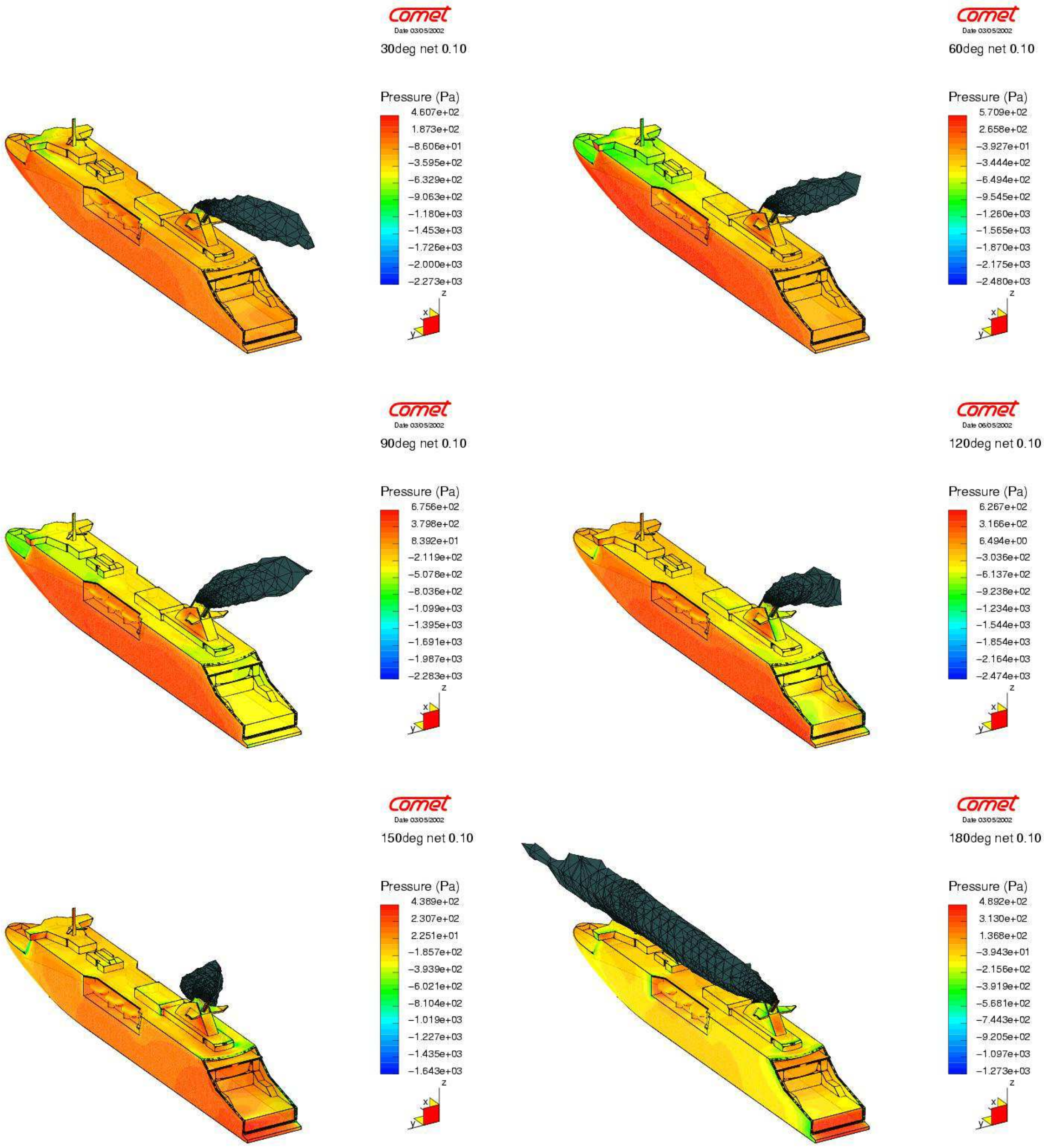

Fig.18: Pressure and smoke propagation for μ=150° to μ=0° in steps of 30°

The streamlines should already for moderate oblique flow massive recirculation on the lee side, while there is little vortex formation at the funnel, Fig.19. Table I and Fig.20 compare force coefficients for longitudinal force, transverse force and roll moment. The agreement is good for small to moderate oblique angles. The differences at larger oblique angles for transverse force and roll moment are probably due to the turbulence model which did not capture the separation properly.

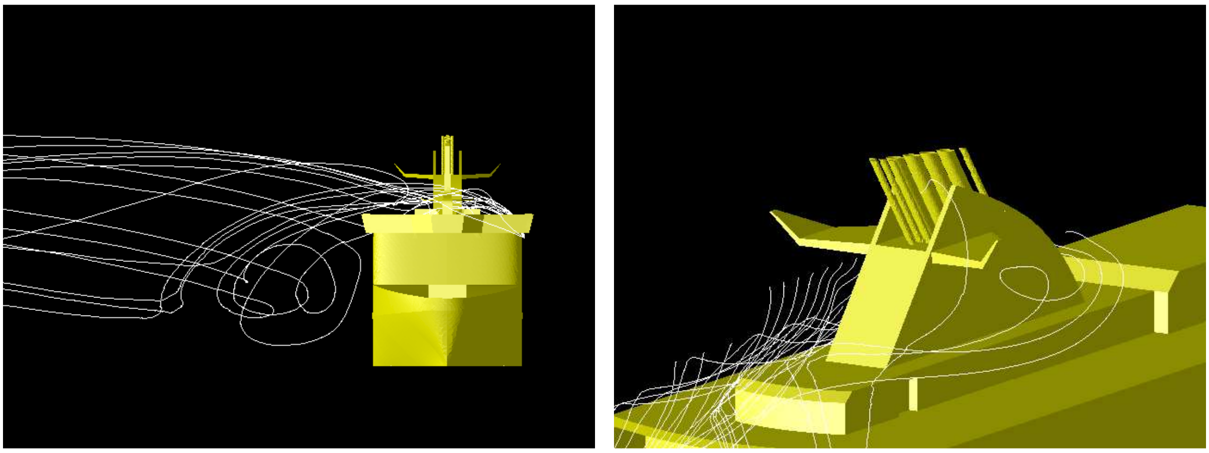

Fig.19: Streamlines for μ=150°

Table II: Force coefficients

	CFD			Experiment		
	C_x	C_y	C_{mx}	C_x	C_y	C_{mx}
180°	-0.0938	0.000	0.000	-0.078	-0.005	-0.003
150°	-0.0733	-0.559	-0.410	-0.070	-0.583	-0.356
120°	0.0508	-1.146	-0.796	-0.008	-0.780	-0.460
90°	-0.0094	-0.994	-0.668	0.007	-0.704	-0.415
60°	-0.0391	-1.076	-0.788	0.004	-0.822	-0.463
30°	0.0985	-0.563	-0.471	0.135	-0.571	-0.329
0°	0.1087	0.000	0.000	0.099	0.006	0.004

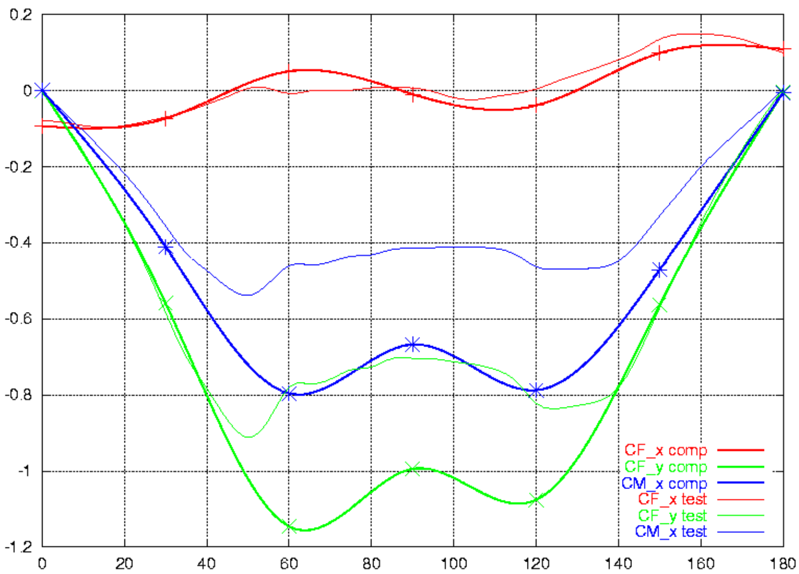

Fig.20: For coefficients for Superfast, experiment (thin lines) and CFD (thick lines)

References

AAGE, C.; HVID, S.L.; HUGHES, P.H.; LEER-ANDERSEN, M. (1997), *Wind loads on ships and offshore structures estimated by CFD*, 8th Int. Conf. Behaviour of Offshore Structures BOSS'97, Delft, pp.237-251

EL MOCTAR, O.M.; GATCHELL, S.; BERTRAM, V. (2001a), *RANSE simulations for aerodynamic flows around ship superstructures*, 4th Num. Towing Tank Symp., Hamburg

EL MOCTAR, O.M.; GATCHELL, S.; BERTRAM, V. (2001b), *Aerodynamische Strömungssimulation für Schiffe*, Hansa 138/9, 2001, pp.20-21

EL MOCTAR, O.M.; BERTRAM, V. (2002), *Computation of viscous flow around fast ship superstructures,* 24th Symp. Naval Hydrodyn., Fukuoka

FØRDE, M.; ØRBEKK, E.; KUBBERUD, N. (1992), *Reduction of aerodynamic drag of a high speed catamaran by using advanced CFD calculations*, 1. Int. Conf. Appl. CFD, Basel

FØRDE, M.; GJERDE, K. (1992), *High speed catamaran aerodynamics*, CFD'99, Ulsteinvik

HVID, S.L.; LEER-ANDERSEN, M.; HUGHES, P.H. (1997), *Wind load prediction on offshore structures using CFD*, Conf. Application of Fluid Dynamics in the Safe Design of Topsides and Superstructures, Inst. of Marine Eng., London

JENSEN, A.G.; SØNDERGAARD, T.; LIVESEY, F. (1997), *Wind comfort for cruise/passenger vessels*, Cruise&Ferry

JIN, E.; YOON, J.; KIM, Y. (2001), *A CFD-based parametric study on the smoke behaviour of a typical merchant ship*, PRADS'01, Shanghai, pp.459-465

LEER-ANDERSEN, M.; HUGHES, P.H. (1996), *Computations of wind loads on ships and offshore structures*, Dept. Naval Arch. & Offshore Eng., Danish Technical Univ.

LINDENAU, O.; BERTRAM, V.; EL MOCTAR, O.M.; GATCHELL, S. (2002), *Aerodynamic simulations for an SES employing virtual reality post-processing techniques*, 3rd High-Performance Marine Vehicles Conf. HIPER'02, Bergen

MECHSNER, A. (2001), *Zwei RoPax-Fähren der Superlative von HDW*, Schiff&Hafen 3, pp.31-33

TAI, T.C. (1996), *Effect of ship motion on DD-963 ship airwake simulated by multizone Navier-Stokes solution*, 21. Symp. Naval Hydrodynamics, Trondheim

TAI, T.C. (1995), *Simulation of LPD ship airwake by Navier-Stokes method*, 6th Asian Congr. Fluid Mechanics, Singapore

TAI, T.C.; CARICO, D. (1995), *Simulation of DD-963 ship airwake by Navier-Stokes method*, J. Aircraft 32/6, pp.1399-1401

YELLAND, M.J.; MOAT, B.I.; TAYLOR, P.K. (2001), *Air flow distortion over merchant ships*, Progress Report to Atmospheric Environment Service

Wave Resistance of Semi-Displacement High-Speed Catamarans through CFD and Regression Analysis

Adam Schwetz, Prasanta K. Sahoo,
Dept. of Maritime Engineering, Australian Maritime College, PO Box 986,
Launceston, TAS 7250, Australia.
botzee@bigpond.com, P.Sahoo@mte.amc.edu.au

Abstract

Predicting the resistance of catamarans has been of interest to naval architects for many years. Even though considerable amount of research has been carried out in this area, there remains a degree of uncertainty in the prediction of calm water resistance of catamaran hull forms. This research attempts to examine the calm water wave resistance characteristics of a series of transom stern, semi-displacement slender catamaran hull forms based on computational fluid dynamics (CFD) modeling.

While maintaining the same center of buoyancy and displacement, the influence of hull shape has been examined, specifically the effects of demihull spacing on round bilge, chine hull forms and various semi-swath configurations in the high-speed range corresponding to Froude numbers of 0.5 to 1.5. The results of CFD analysis *have been compared with experimental towing tank results* for *one of the models. The results obtained show considerable promise and development of an industry standard regression equation based on the data obtained from CFD analysis, model experiments and full scale ship trials can be seen as achievable.*

1. Introduction

Many studies have been conducted on the resistance prediction of high-speed semi-displacement catamarans, however to date a standard method for the calm water resistance prediction does not exist. There have been several studies into the calculation of the form factor (1+βk) including work by Armstrong (2000), Molland et al (1994) and Insel and Molland (1992). As research continues by academics into catamaran resistance, it is becoming generally accepted that the form of the total resistance coefficient should be given by equation (1) where the total resistance coefficient can be used in equation (2) to estimate the total resistance.

$$C_T = (1+\beta k)C_F + \tau C_{W\,\mathrm{DEMI}} \qquad (1)$$

$$R_T = \frac{1}{2} C_T \rho A V^2 \qquad (2)$$

The research conducted for this paper involves developing several regression equations to predict the hull interference factor τ and the demihull wave resistance coefficient $C_{W\,\mathrm{DEMI}}$, for a range of vessel parameter variations. Emphasis has been placed on ensuring the vessel parameters defined by the hull shapes are relevant to those vessels being currently produced by the high-speed ferry industry.

The catamaran wave resistance, C_W, was calculated using CFD analysis for 10 models, at Froude numbers of 0.4 to 1.5 at various hull separation ratios. The results from one model were compared with the C_R results from towing tank tests. In total 552 numerical towing tank runs were conducted, with the results used to generate several regression equations for the calculation of C_W for the demihull in isolation and C_W for catamaran configurations.

The research primarily concentrated on the following:

a) To examine the variation in C_W for a slender catamaran hull form, due to changes in the vessels lines plan, from hard chine to round bilge and semi-swath configurations, while maintaining the same displacement and centre of buoyancy over the range indicated in Table 1.
b) To examine the variation in C_W for a more general range of catamaran hull forms including chine, round bilge and semi-swath hull configurations over the range indicated in Table 2.

Table 1: Catamaran Geometric Parameters

Geometric Parameters	$L/\nabla^{1/3}$	LCB/LCF	S/L	C_B
Range of Application	9.2 to 9.6	0.97 to 1.2	0.15 to 5	0.49 to 0.66

Table 2: Catamaran Geometric Parameters (Range of Interest)

Geometric Parameters	$L/\nabla^{1/3}$	LCB/LCF	S/L	C_B
Range of Application	6.3 to 9.6	0.92 to 1.2	0.15 to 3	0.46 to 0.68

Effective power could now be calculated using equations (1) and (2), where the form factor (1+k) is calculated from the regression equation (9) given by Armstrong (2000) and the interference factor τ and the demihull coefficient of wave resistance $C_{W\ DEMI}$ are both calculated from regression equations developed during this investigation.

2. Background Work

The paper by Insel and Molland (1992) summarises a calm water resistance investigation into high-speed semi-displacement catamarans, with symmetrical hull forms based on experimental work carried out at the University of Southampton.

Two interference effects contributing to the total resistance effect were established, being viscous interference, caused by asymmetric flow around the demihulls which effects the boundary layer formation, and wave interference, due to the interaction of the wave systems produced by each demihull. Particulars of models tested by Insel and Molland (1992) are presented in Table 3. The particulars of the models used in the investigation are presented in Table 4.

Table 3: Catamaran geometric parameters [Insel and Molland (1992)]

Geometric Parameters	$L/\nabla^{1/3}$	L/B	B/T	C_B
Range of Application	6 to 9	6 to 12	1 to 3	0.33 to 0.45

Table 4: Model Particulars [Insel and Molland (1992)]

Models	$L/\nabla^{1/3}$	L/B	B/T	C_B	LCB/L from transom
C2	7.1	10	1.6	0.44	50%
C3	6.3	7	2	0.397	43.6%
C4	7.4	9	2	0.397	43.6%
C5	8.5	11	2	0.397	43.6%

Models C3, C4 and C5 were of round bilge hull form derived from the NPL series and model C2 was of the parabolic Wigley hull form. All models were tested over a range of Froude numbers of 0.1 to 1.0 in the demihull configuration and catamaran configuration with separation ratios, S/L, of 0.2, 0.3, 0.4 and 0.5. Calm water resistance, running trim, sinkage and wave pattern analysis experiments were carried out.

The authors proposed that the total resistance of a catamaran should be expressed by equation (3) :

$$C_{TCAT} = (1+\phi k)\sigma C_F + \tau C_w \qquad (3)$$

The authors state that for practical purposes, σ and ϕ can be combined into a viscous resistance interference factor β, where $(1+\phi k)\sigma = (1+\beta k)$ whence:

$$C_{TCAT} = (1+\beta k)C_F + \tau C_W \qquad (4)$$

noting that for demihull in isolation, $\beta = 1$ and $\tau = 1$, and for a catamaran, τ can be calculated from equation (5).

$$\tau = \frac{C_{W\,CAT}}{C_{W\,\mathrm{DEMI}}} = \frac{\left[C_T - (1+\beta k)C_F\right]_{CAT}}{\left[C_T - (1+k)C_F\right]_{DEMI}} \qquad (5)$$

The authors conclude that the form factor, for practical purposes, is independent of speed and should thus be kept constant over the speed range. This was a good practical solution to a complex engineering problem at that point in time. However this view is in sharp contradiction following research conducted by Armstrong (2000).

The derived form factors for the monohull configuration are as follows:

Table 5: Derived form factors [Insel and Molland (1992)]

	C2	C3	C4	C5
(1+k)	1.10	1.45	1.30	1.17

The authors also conclude that the viscous interference factor β is effectively independent of speed and should be kept constant across the speed range and it depends primarily on L/B ratio.

The authors further conclude that:

- The vessels tested have an appreciable viscous form effect, and are higher for catamarans where viscous interference takes place between the hulls.
- Viscous resistance interference was found to be independent of speed and hull separation, and rather is dependent on demihull length to beam ratio.
- Generally higher hull separation ratios result in smaller wave interference, with beneficial wave interference between Froude numbers of 0.35 to 0.42.
- Catamarans display higher trim angles than monohulls, and that the trim angle is reduced with increasing hull separation ratios.
- A ship to model correlation exercise is required for the extrapolation techniques presented to be validated.

The paper by Molland et al (1994), is an extension of the work conducted by Insel and Molland (1992). Additional models are tested with the particulars listed in Tables 6 and 7. The research and results are also detailed in the University of Southampton Ship Science Report 71, (1994).

Table 6: Particulars of Models [Molland et al (1994)]

	3b	4a	4b	4c	5a	5b	5c	6a	6b	6c
L/B	7.0	10.4	9.0	8.0	12.8	11.0	9.9	15.1	13.1	11.7
$L/\nabla^{1/3}$	6.27	7.4	7.41	7.39	8.51	8.50	8.49	9.50	9.50	9.50
B/T	2	1.5	2	2.5	1.5	2	2.5	1.5	2	2.5
C_B	0.397	0.397	0.397	0.397	0.397	0.397	0.397	0.397	0.397	0.397
LCB/L (%)	43.6	43.6	43.6	43.6	43.6	43.6	43.6	43.6	43.6	43.6

The work was extended to cover changes in breath/draught ratio (B/T) and a wider range of length to displacement ratios ($L/\nabla^{1/3}$). The models were of round bilge hull form with transom sterns and were generated from the NPL round bilge series.

Armstrong's thesis *entitled "A Thesis on the Viscous Resistance and Form Factor of High-speed Catamaran Ferry Hull Forms"*, [Armstrong (2000)], examines the current methods for predicting the resistance of recently designed high-speed catamarans. Current literature suggests large form factors are needed for correlation between model scale and full scale, which Armstrong claims, contradicts the expectation that long slender hull forms would have low values.

Armstrong's research was conducted using model tank testing, wind tunnel testing, CFD analysis and full-scale vessel sea trials. Armstrong reviews the work by Insel and Molland (1992) and Molland et al (1994) and notes that their values of the form factor (1+k) are considerably higher than those found during Armstrong's research. Armstrong attributes their higher form factor values to the resistance component associated with the transom drag, being incorrectly identified as being part of the viscous component of resistance.

Table 7: Model Form Factors [Molland et al (1994)]

Model	Monohull	S/L=0.2		S/L=0.3		S/L=0.4		S/L=0.5	
	(1+k)	1+βk	β	1+βk	β	1+βk	β	1+βk	β
3b	1.45	1.60	1.33	1.65	1.44	1.55	1.22	1.60	1.33
4a	1.30	1.43	1.43	1.43	1.43	1.46	1.53	1.44	1.47
4b	1.30	1.47	1.57	1.43	1.43	1.45	1.50	1.45	1.50
4c	1.30	1.41	1.37	1.39	1.30	1.48	1.60	1.44	1.47
5a	1.28	1.44	1.57	1.43	1.54	1.44	1.57	1.47	1.68
5b	1.26	1.41	1.58	1.45	1.73	1.40	1.54	1.38	1.46
5c	1.26	1.41	1.58	1.43	1.65	1.42	1.62	1.44	1.69
6a	1.22	1.48	2.18	1.44	2.00	1.46	2.09	1.48	2.18
6b	1.22	1.42	1.91	1.40	1.82	1.47	2.14	1.44	2.00
6c	1.23	1.40	1.74	1.40	1.74	1.45	1.96	1.44	1.91

The experimental techniques used by Insel and Molland (1992) measured C_w and not C_R. Equation (7) instead of equation (6) should have been used to calculate the form factor.

$$C_{TCAT} = (1+k)C_F + C_R \qquad (6)$$

$$C_{TCAT} = (1+k)C_F + C_W + C_{TR} \qquad (7)$$

C_{TR} applies to the transom drag force of (A_T•ρgh)

Armstrong also remarks that their assumption that the form factor would remain constant with trim is incorrect, and the technique used by Insel and Molland (1992), by testing the hull models with the transom stern emerged will only apply to the vessel in that operating condition. Armstrong found that equation (8) gave the best fit for calculating the form factor, based upon the regression analysis from full-scale vessels. Equation (8) was found to predict the form factor based upon CFD results within an accuracy of 2.2%, and is to be used in conjunction with the ITTC '57 ship model correlation line and the static wetted surface area.

$$(1+k)_{\text{model}} = 1.45 - 0.139\ \left(L/\nabla^{1/3}\right)^{0.6}(B/T)^{-0.1} \qquad (8)$$

Table 8: Range of parameters for equation 8 [Armstrong (2000)]

Geometric Parameters	$L/\nabla^{1/3}$	B/T	R_n	F_n
Range of Application	6.5 to 9.5	1.2 to 2.5	$3x10^6$ to $5x10^6$	0.6 to 1.0

Armstrong noted that at model scale the form factor appears to be independent of Froude number, and at full scale, the form factor is a function of F_n value and varies in accordance to equation (9).

$$(1+k)_{ship} = 1.72 - f\left(L/\nabla^{1/3}\right)^g (B/T)^{-0.1} \qquad (9)$$

Where: $1x10^9 < R_n < 2x10^9$

$f = 2.25.F_n^{\ 2} - 4.47F_n + 1.61$ valid for $0.6 < F_n < 1.0$

$f = 0.61$ for $F_n > 1.0$

$g = 0.76\text{-}1.09 f$

Armstrong (2000) concluded that the high values of form factor or correlation factor when comparing model and full-scale data were because the correlation factor cannot accurately be applied to viscous resistance when they contain both R_n and F_n terms. The separation of these terms allows a more accurate method of scaling from model scale to full scale.

Armstrong found that the ITTC '57 ship model correlation line over estimates the friction below $R_n = 7x10^6$ and underestimates the friction above $R_n=7x10^6$, in agreement with Grigson (1993). Armstrong (2000) also noted the difference in dynamic trim between model and ship scale, results in different underwater geometry between the two scales and therefore a difference in resistance.

3. Conclusions From Literature Review

The form factors published by Insel and Molland (1992) appear to be incorrect as the component of resistance produced by the transom stern was neglected in their calculations of C_W, and hence their calculated form factors are artificially larger to accommodate the smaller C_W values. While the location of the centre of buoyancy is in agreement with current production catamarans the block coefficients are smaller and the results may not be applicable to current high-speed aluminium catamarans.

While research continues into the field of catamaran resistance, it is clear that an industry standard technique for the calm water resistance prediction of high-speed semi displacement catamarans does not exist. The work by Armstrong (2000) allows the form factor to be predicted. A technique is required to predict the coefficient of wave resistance, which can then be used with the form factor to predict the total resistance coefficient.

4. Research Program

The present research program was devised to:

- Examine variations in C_W using CFD, while modifying basic hull parameters and maintaining the same displacement and LCB position.
- Examine variations in C_W using CFD, while modifying basic hull parameters, including the displacement and LCB.
- Compare C_W results of CFD with results from towing tank tests and develop regression model..

5. Systematic Series Development

The series of symmetrical hull shapes used in this study were generated by the author, and are believed to closely represent the hull forms being used in industry at the moment. The models are not mathematical in nature, and do not form part of any published systematic series. The body plans of models 1 to 10 are presented in Figure 1 and a summary of the particulars are presented in Table 11.

Table 11: Model Parameters

	M1-RB	M2-SS	M3-SS	M4-SS	M5-CH	M6-CH	M7-CH	M8-CH	M9-CH	M10-CH
$L/\nabla^{1/3}$	9.56	9.56	9.54	9.53	9.55	9.18	9.20	6.30	7.08	7.60
L/B	15.0	15.2	15.1	15.0	15.3	14.8	14.9	8.8	10.4	13.0
L/T	31.7	27.3	26.1	25.8	31.7	34.3	34.3	13.0	18.0	23.0
B/T	2.11	1.79	1.73	1.71	2.07	2.31	2.31	1.47	1.73	1.77
LCB/L in %	42	45	42	42	42	44	44	49	47	40
LCB/LCF	1.00	1.12	1.10	1.20	0.98	0.96	0.97	0.99	1.03	0.92
C_B	0.55	0.49	0.46	0.46	0.54	0.66	0.65	0.52	0.61	0.68
C_{WP}	0.79	0.74	0.71	0.65	0.84	0.89	0.88	0.86	0.87	0.85
i_E (deg)	8.68	8.66	3.15	2.10	9.16	16.60	13.60	38.00	15.00	15.00

Following a review of current vessel dimensions, hull model M1-RB was created which has a round bilge hull form and was designed to have an overall length of 50 meters, with a transom stern to accommodate two sets of Kamewa 71 series water jets on each demihull. The displacement was assumed to be 255 tonne, with the LCB located at around 42% and 44% of the waterline length, referenced from the transom. An amount of semi-swathness was added to model M1-RB to create models M2-SS, M3-SS and M4-SS, where the amount of semi-swathness increases from models M2 to M4. Model M5-CH was generated from model M1-RB by replacing the round bilge with a single chine, while maintaining the same displacement and LCB. Hull model M7-CH contains a hard chine and hull model M6-CH was generated from model M7-CH by rounding or filleting the hard chine, while maintaining the same displacement and LCB as models M1 to M5. Models M8-CH, M9-CH and M10-CH were included to examine the general effects of reducing $L/\nabla^{1/3}$. The displacements and LCB vary for models M8-CH to M10-CH.

6. Calculation Of Wave Resistance Coefficient

The wave resistance coefficients were calculated for each hull model using SHIPFLOW, a computational fluid dynamics (CFD) program developed by FLOWTECH International of Sweden.

The theoretical wave resistance coefficient, C_W, is calculated by splitting the flow into three regions where an efficient approximation of the flow equations may be made and a complete flow calculation may be accomplished in a few hours using the potential flow, as described by Larsson (1993). Figure 2 represents the zonal approach or regions used by SHIPFLOW to maximise computational efficiency.

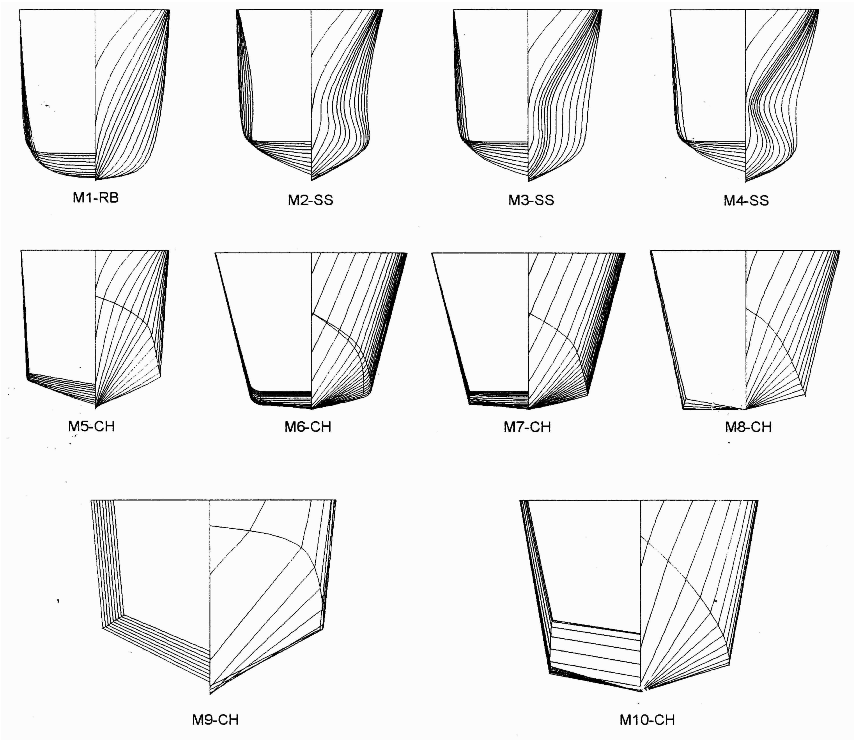

Figure 1. Body plans of models

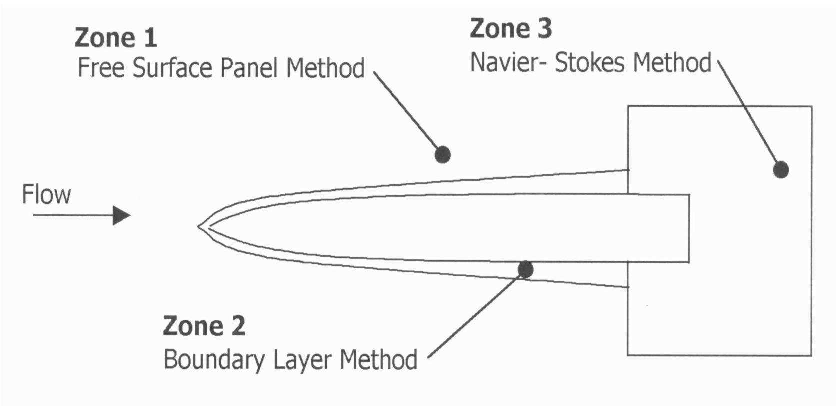

Figure 2: Calculation Zones in SHIPFLOW

- Flow in Zone 1 is calculated using a higher order panel method with linear or non-linear free surface boundary conditions.

- Flow in Zone 2 is calculated using momentum integral methods for laminar and turbulent boundary layers.
- Flow in zone 3 is calculated using the Reynolds-Average Navier-Stokes method with a k-epsilon turbulence model and a numerically generated body fitted coordinate system.

7. Comparison Of Shipflow Results With Experimental Results

The calculated C_W from SHIPFLOW for model M8-CH was compared with C_R measured from towing tank tests. The results are presented graphically in Figure 3 with values suppressed to protect confidentiality. A good correlation is seen to exist between the measured C_R from the towing tank and C_W calculated from SHIPFLOW.

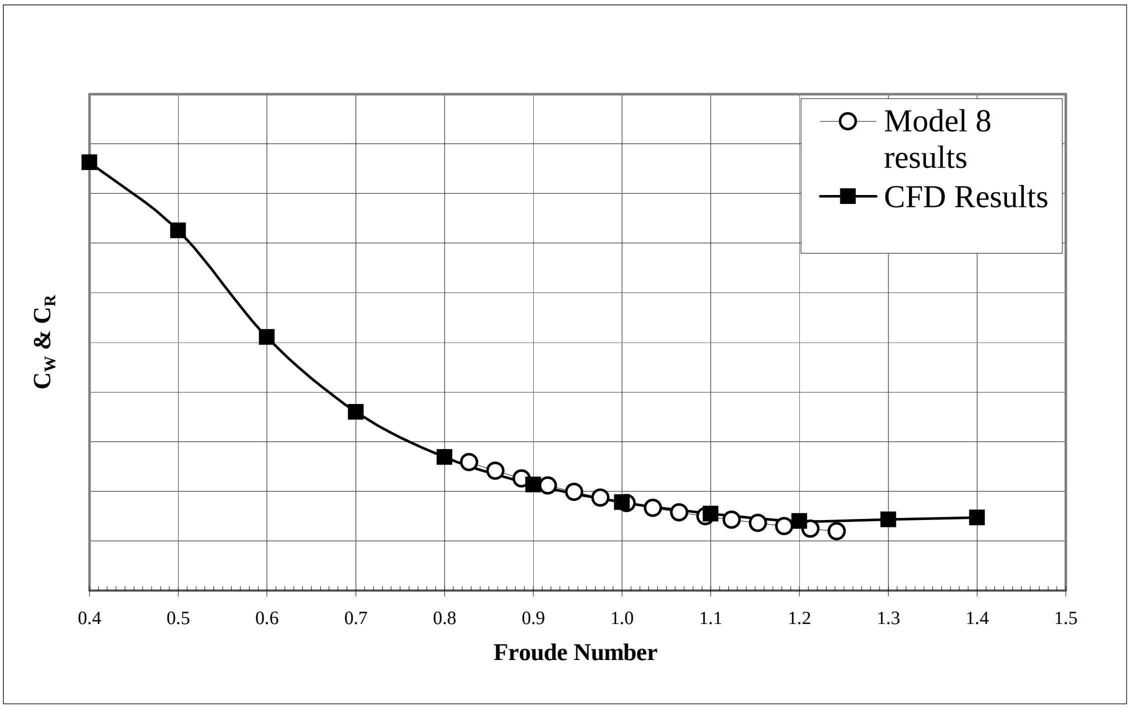

Figure 3: C_W comparison between CFD and Towing Tank Results

8. Regression Analysis

The wave resistance coefficient is assumed to be a function of the fundamental vessel parameters listed in equation (13).

$$C_W = f\left(L, B, T, C_B, C_P, C_M, \nabla, LCB, LCF, i_E, F_n, S, hullform\right) \qquad (13)$$

An indication of the amount of semi-swathness in the hull form is the location of LCF. The LCF moves aft of midships with an increasing amount of semi-swathness forward of midships. The ratio LCB/LCF led to define the non-dimensionalised hull form parameter to indicate the amount of semi-swathness the vessel might have. The variables in equation (13) following non-dimensionalising are presented in equation (14).

$$C_W = f\left(L/B, B/T, L/\nabla^{1/3}, LCB/LCF, S/L, C_B, C_{P,} C_{M,} i_E, F_n\right) \qquad (14)$$

A review of Table 11 indicates the significant variables, allowing equation (14) to be simplified into equation (15).

$$C_W = f\left(L/B, B/T, L/\nabla^{1/3}, LCB/LCF, S/L, C_B, i_E, F_n\right) \qquad (15)$$

Ideally it would be preferred to have the regression equation dependant on speed, so that one equation could be used to calculate C_W. Several attempts were made to include F_n in a speed dependent regression equation, however R^2 values in the order of 0.9 were being obtained. The loss of accuracy was deemed too high, so speed independent equations to predict C_W were developed for explicit F_n

values of 0.5 to 1.5 in steps of 0.1. The final speed independent regression equation is shown by equation (16).

$$C_w = f\left(L/B, B/T, L/\nabla^{1/3}, LCB/LCF, S/L, C_B, i_E\right) \qquad (16)$$

Although it can be argued, that C_B would cover variations in $L/\nabla^{1/3}$ it was decided not to remove any more independent variables, and rather rely on the regression analysis to remove the statistical insignificant variables. Following a review of the C_W results it was decided not to include the results at F_n value of 0.4. The inflection of the C_W curve at F_n of 0.4 for the demihull results, would increase the complexity of the regression equation and possibly reduce the accuracy of the regression equation, and as the role of the equation is to predict C_W for high-speed semi displacement catamarans, the exclusion of F_n of 0.4 from the regression equation will be of little consequence.

Equation (17) is the generalised equation chosen for the prediction of C_W. It is noted that predicting C_W for demihulls, the (S/L) term becomes 1.

$$C_W = C_1 \bullet (L/B)^{C_2} \bullet (B/T)^{C_3} \bullet \left(L/\nabla^{1/3}\right)^{C_4} \bullet (LCB/LCF)^{C_5} \bullet C_B^{C_6} \bullet i_E^{\,C_7} \bullet (S/L)^{C_8} \qquad (17)$$

9. Results

The wave resistance coefficient for a demihull can be predicted from equation (18), whose validity range is shown in Table 13, using the constants C_1 to C_4 from Table 14.

$$C_W = C_1\left(L/\nabla^{1/3}\right)^{C_2}(LCB/LCF)^{C_3} C_B^{\;C_4} \qquad (18)$$

Table 13: Range of Parameters for Equation 18

Geometric Parameters	$L/\nabla^{1/3}$	LCB/LCF	C_B	F_n
Range of Application	9.2 to 9.6	0.97 to 1.2	0.46 to 0.66	0.4 to 1.4

Table 14: Coefficients for Equation 18

F_n	C_1	C_2	C_3	C_4	R^2
0.4	1.539E+02	-5.058	-0.305		0.96
0.5	2.999E+02	-5.519	-0.466	-0.1339	0.98
0.6	3.606E+02	-5.715	-0.488	-0.1154	0.99
0.7	6.870E+02	-6.113	-0.591	-0.1080	0.99
0.8	1.813E+03	-6.637	-0.648	-0.0981	0.99
0.9	4.830E+03	-7.155	-0.775	-0.0933	0.99
1.0	2.988E+04	-8.064	-0.982	-0.1907	0.99
1.1	1.969E+05	-8.995	-1.191	-0.2920	0.99
1.2	1.394E+06	-9.932	-1.309	-0.3178	0.99
1.3	5.031E+06	-10.551	-1.392	-0.2913	0.99
1.4	5.498E+07	-11.690	-1.543	-0.3903	0.98

Table 15: Coefficients For Equation 19

F_n	C_1	C_2	C_3	C_4	C_5	C_6	C_7	R^2
0.5	2.151E+07	-12.180	-0.195	-0.042	0.018	2.818	-3.398	0.95
0.6	8.509E+03	-8.207	-0.235	0.000	0.000	1.942	-2.035	0.97
0.7	2.194E+04	-8.840	-0.180	-0.073	0.027	1.992	-2.215	0.92
0.8	5.508E+04	-9.388	-0.106	-0.182	0.042	2.012	-2.327	0.92
0.9	1.488E+05	-9.938	-0.046	-0.285	0.050	2.029	-2.399	0.96
1.0	1.303E+04	-8.590	-0.016	-0.422	0.026	1.583	-1.757	0.98
1.1	5.438E+03	-8.002	0.023	-0.403	-0.012	1.303	-1.264	0.96
1.2	8.261E+06	-12.005	0.015	-0.164	0.020	2.302	-2.473	0.97
1.3	1.440E+10	-16.090	0.004	0.072	0.102	3.230	-3.690	0.99
1.4	1.965E+12	-18.571	0.003	0.348	0.116	3.649	-4.052	0.99

The wave resistance coefficient for a catamaran can be predicted from equation (19), using the constants C_1 to C_7 from Table 15.

$$C_w = C_1 \left(L/\nabla^{1/3}\right)^{C_2} \left(S/L\right)^{C_3} \left(LCB/LCF\right)^{C_4} i_E^{\;C_5} \left(B/T\right)^{C_6} C_B^{C_7} \qquad (19)$$

The generalised wave resistance coefficient for a demihull can be predicted from equation (20), whose validity range is shown in Table 16, using the constants C_1 to C_5 from Table 17.

$$C_w = C_1 \left(L/\nabla^{1/3}\right)^{C_2} \left(LCB/LCF\right)^{C_3} \left(B/T\right)^{C_4} C_B^{C_5} \qquad (20)$$

Table 16: Range of Parameters for Equations 20

Geometric Parameters	$L/\nabla^{1/3}$	LCB/LCF	B/T	C_B	F_n
Range of Application	6.3 to 9.6	0.92 to 1.2	1.47 to 2.3	0.46 to 0.68	0.4 to 1.4

Table 17: Coefficients for Equation 20

F_n	C_1	C_2	C_3	C_4	C_5	R^2
0.5	0.30	-1.2168	-2.2795	-2.5075	1.4337	0.96
0.6	0.41	-1.4599	-1.9655	-2.4304	1.5754	0.98
0.7	0.68	-2.1421	-1.6111	-1.6934	1.1637	0.99
0.8	0.78	-2.4272	-1.5211	-1.4089	1.0263	0.99
0.9	0.87	-2.6947	-1.5148	-1.1202	0.8731	0.98
1.0	0.93	-2.9213	-1.5536	-0.8650	0.7080	0.98
1.1	1.00	-3.1409	-1.5821	-0.6142	0.5526	0.98
1.2	1.16	-3.3948	-1.5593	-0.3228	0.4110	0.97
1.3	1.38	-3.6728	-1.5278	0	0.2509	0.97
1.4	1.65	-3.9787	-1.5547	0.35234	0	0.97

The generalised wave resistance coefficient for a catamaran can be predicted from equation (21), using the constants C_1 to C_7 from Table 18.

$$C_w = C_1 \left(L/\nabla^{1/3}\right)^{C_2} \left(S/L\right)^{C_3} \left(LCB/LCF\right)^{C_4} i_E^{C_5} . C_B^{C_6} \left(B/T\right)^{C_7} \qquad (21)$$

Table 18: Coefficients for Equation 21

F_n	C_1	C_2	C_3	C_4	C_5	C_6	C_7	R^2
0.5	1.501	-2.632	-0.201	-1.554	-0.132	1.070	-1.460	0.99
0.6	1.122	-2.817	-0.305	-1.265	-0.090	0.971	-1.259	0.99
0.7	0.613	-2.734	-0.278	-1.290	-0.064	0.988	-1.317	0.99
0.8	0.282	-2.652	-0.195	-1.472	-0.052	0.996	-1.395	0.99
0.9	0.209	-2.668	-0.111	-1.645	-0.048	1.002	-1.422	0.99
1.0	0.356	-2.820	-0.056	-1.756	-0.052	0.964	-1.339	0.99
1.1	0.878	-3.129	0.000	-1.640	-0.068	0.974	-1.171	0.99
1.2	1.455	-3.476	0.000	-1.365	-0.092	1.051	-0.962	0.99
1.3	1.594	-3.615	0.000	-1.105	-0.069	1.179	-0.873	0.99
1.4	2.337	-4.056	-0.032	-0.658	-0.072	1.338	-0.614	0.99

The number of cases or equations used to calculate each regression equation is presented in Table 19.

Table 19: Data Points used in Regression Equations for each Cw

	C_{WDEMI} Eqn. 18	C_{WCAT} Eqn. 19	C_{WDEMI} Eqn. 20	C_{WCAT} Eqn. 21
Data Points or "Cases"	84	385	102	250

10. Comparative Analysis Of Results

The effective power of two catamarans were compared with full-scale speed trial data. The vessel particulars are presented in Table 20 and results are presented in Table 21.

Table 20: Vessel Particulars for Validation

	Vessel 1	Vessel 2
$L/\nabla^{1/3}$	7.993	7.990
B/T	1.901	1.490
LCB/LCF	1.00	0.92
S/L	0.224	0.207
WSA_{DEMI} (m^2)	167.9	98.85
C_B	0.659	0.599
i_E (deg)	7	16

Table 21: Comparison of Effective Power Prediction

Froude number	0.74	0.83
Speed (knots)	27.7	27.1
Effective power from full scale speed trials (kW)	2029	972
Estimated effective power from equations (kW)	2260	1153
Difference between estimated and actual power (kW)	+11.4 %	+18.6 %

The average error in percentage difference between the predicted values of C_W using regression equations (18) to (21) and C_W calculated using CFD is presented in Table 22. Although the average error appears reasonable, errors for some models were in the region of 15 %. The regression analysis was repeated to ensure human error was not the cause.

Table 22: Percentage Error In Predicted C_W vs CFD C_W

	Cw (Eqn. 18)	Cw (Eqn. 19)	Cw (Eqn. 20)	Cw (Eqn. 21)
Average error	1.50%	3.00%	6.30%	3.40%

11. Discussion

The wave resistance coefficient C_W calculated by SHIPFLOW for model M8-CH correlates well with the residuary resistance coefficient C_R measured experimentally from towing tank tests. While this is encouraging more comparison is required between SHIPFLOW and experimental work to ensure the accuracy of the SHIPFLOW results. A review of Figure 3 suggests that SHIPFLOW slightly over predicts C_W at higher Froude numbers. This may be attributed to the hydrodynamic lift generated by the bottom hull surfaces of the towing tank model. The results from SHIPFLOW for Froude numbers in excess of 1 must be viewed with caution, as the hydrodynamic lift was not modelled in the CFD analysis.

It was not possible to present all the figures developed during the analysis. However a few selected figures have been presented here for the sake of clarity. A review of Figures 4 and 5 show a general reducing trend in C_W with increased demihull spacing as expected. The amount of reduction decreases with increasing speed. At Froude numbers of 0.5 to 0.8, the separation distance between the demihulls significantly influences the coefficient of wave resistance. Catamarans with low demihull separation ratios will experience an increase in the calm water resistance. At Froude numbers of 0.8 to 1.0 the coefficient of wave resistance is increased at S/L ratios less than 0.2. At S/L ratios greater than 0.2 the coefficient of wave resistance remains more or less constant. At Froude numbers greater than 1, contribution of S/L ratio to the coefficient of wave resistance is insignificant.

Analysis indicated that model M2-SS at all speeds and separation ratios had the lowest coefficient of wave resistance. This cannot be attributed to any single hull parameter, rather a combination of hull parameters such as LCB/LCF ratio, L/B ratio and B/T ratio. In all cases models M6-CH and M7-CH were more efficient. A review of Table 11 suggest that minimising the wetted surface area is more important than minimising the coefficient of wave resistance for high-speed semi-displacement catamarans.

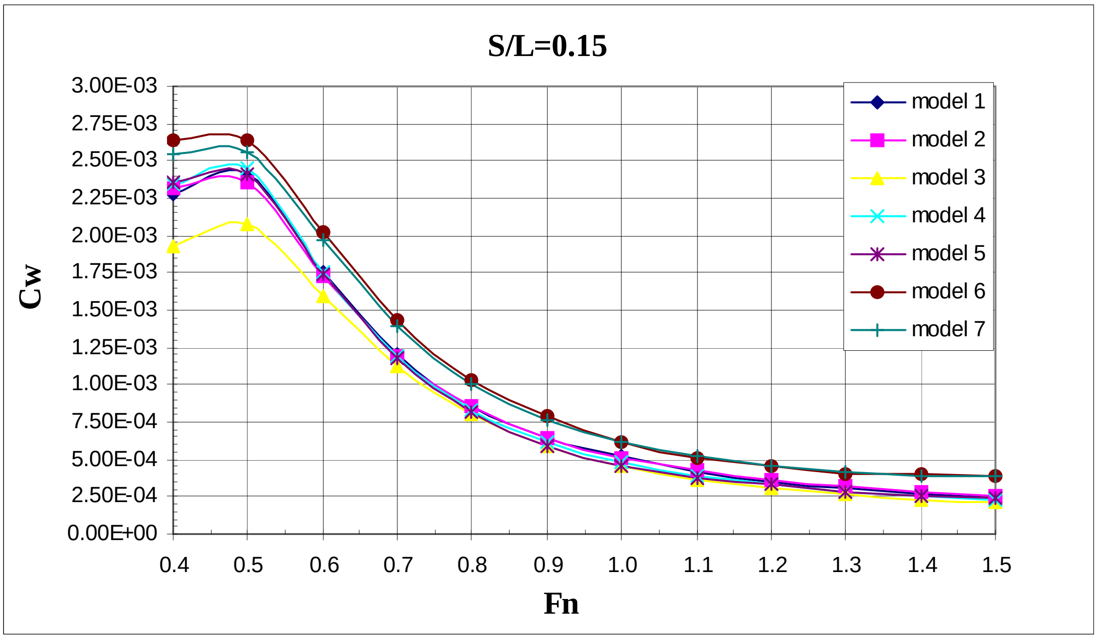

Figure 4: Cw at S/L ratio of 0.15

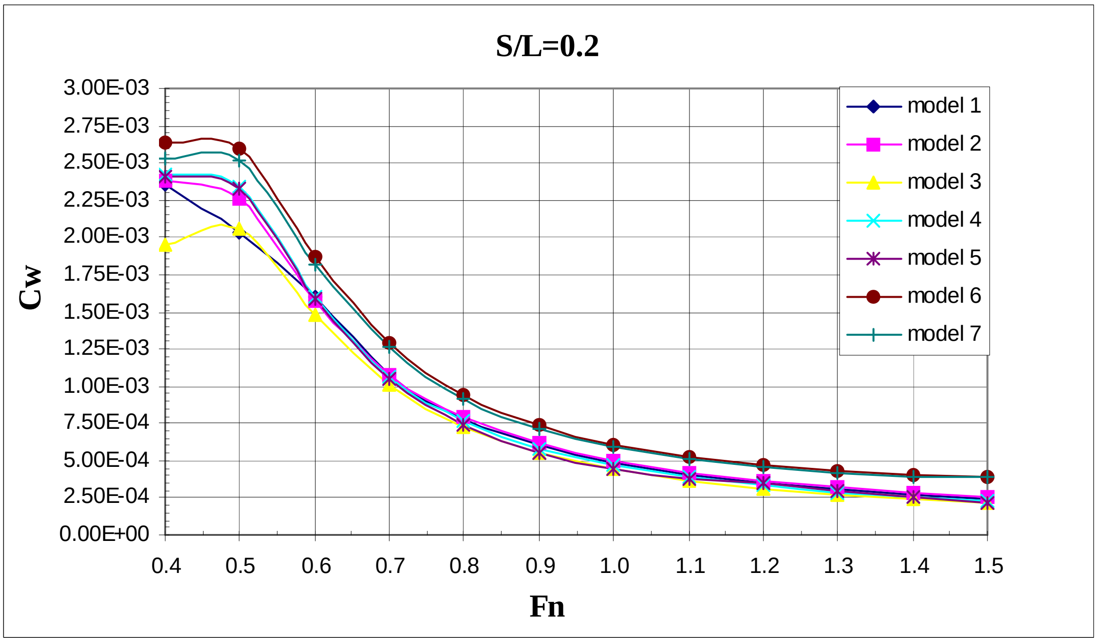

Figure 5: Cw at S/L ratio of 0.20

The analysis of wave resistance interference factor (τ) shows the additional wave resistance component due solely to the separation of the demihulls. In most cases the interference factor approaches 1.1 at Froude number in excess of 1.0. Models M6-CH and M7-CH show a minimum interference factor at a Froude number around 1.2 before increasing again at higher Froude numbers. Model M6-CH shows beneficial wave interference at Froude numbers of 1.2 to 1.3 at a separation ratio of 0.15.

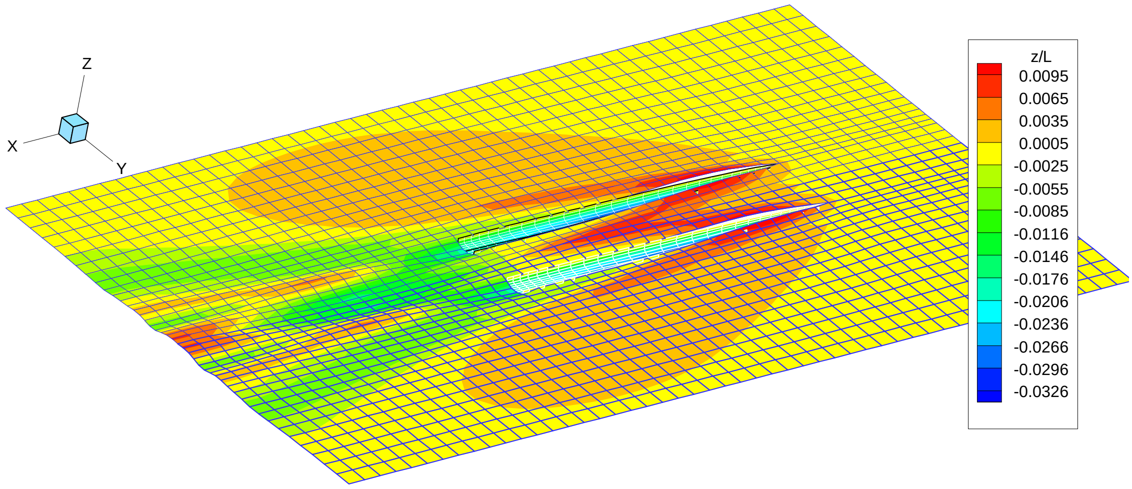

Figure 6: Wave Pattern for Model 4 at Fn=1.0 and S/L=0.2

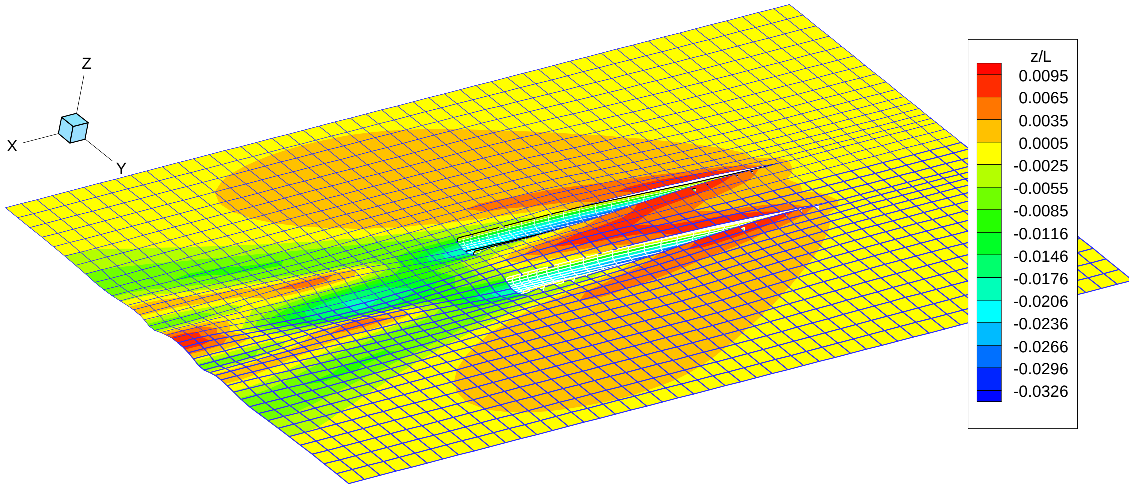

Figure 7: Wave Pattern for Model 5 at Fn=1.0 and S/L=0.2

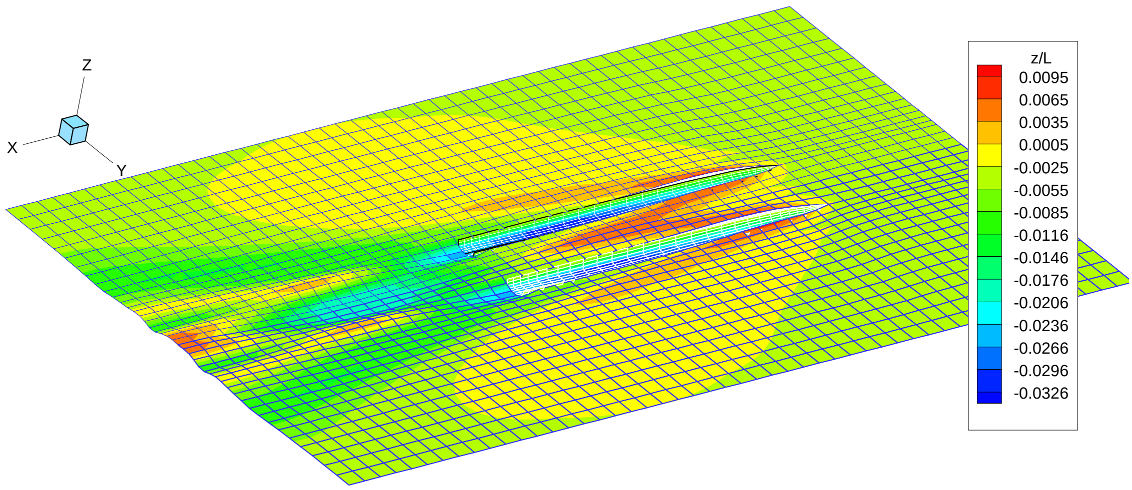

Figure 8: Wave Pattern for Model 6 at Fn=1.0 and S/L=0.2

Equations (18) to (21) can be used to calculate the absolute values of C_W with an accuracy of fifteen percent. The inaccuracy is attributed to the fact that seven of the ten models had similar length to displacement ratios, thus biasing the regression analysis towards the common length to displacement ratio. By varying the length to displacement ratios evenly in future work the accuracy of equations (18) to (21) will improve.

12. Conclusions

Regression equations have been developed to predict the wave resistance coefficient for high-speed semi displacement catamarans and for their demihulls acting in isolation. The wave resistance interference factor can be calculated by dividing the wave resistance coefficient of the catamaran by the wave resistance coefficient of the demihull. The calculated wave resistance coefficient from SHIPFLOW for one model was compared to the experimentally measured residuary coefficient from towing tank tests. A good correlation between the two exists. The analysis was used to predict the effective power and compared with full-scale speed trial data and a good correlation was also found to exist.

The regression equations and effective power prediction show promising results, however more model analysis and comparison with towing tank and full scale trial data is required to improve the accuracy of the regression equations. Comparisons however can be made at an early stage of design between fundamental hull form parameters and their influence on the calm water resistance of high-speed semi-displacement catamarans.

The following general comments can be made:

- Minimising the wetted surface area, rather than the wave resistance coefficient will lead to the optimum semi displacement calm water resistance hull form.
- Demihull spacing does not contribute significantly to the overall calm water resistance at high speeds (Froude numbers greater than 1).

13. Nomenclature

A	Wetted surface area (m^2)
B	Demihull beam at the waterline (m)
C_B	Block coefficient
C_F	ITTC (1957) ship model correlation line: $C_F = 0.075(\log R_n - 2)^{-2}$
C_R	Residuary resistance coefficient
C_T	Total resistance coefficient
C_W	Wave resistance coefficient
$C_{W\,CAT}$	Wave resistance coefficient for a catamaran
$C_{W\,DEMI}$	Wave resistance coefficient for a demihull in isolation.
C_{WP}	Waterplane area coefficient
C_∇	$C_\nabla = L/\nabla^{1/3}$
F_n	Froude number based upon waterline length.
i_E	Half waterline entry angle
L	Waterline length (m)
P_E	Effective Power (kW)
R	Vessel Resistance (N)
R_n	Reynolds number
S	Catamaran demihull spacing (m)
T	Draught (m)
(1+k)	Form factor
(1+βk)	Form factor including the viscous interference resistance factor β.
V	Velocity (m/s)
β	Viscous interference resistance factor
ρ	Fluid density (kg/m^3)
τ	Wave resistance interference factor
ν	Kinematic viscosity of fluid (m^2/s)
∇	Volumetric Displacement (m^3)
Δ	Displacement (tonne)

14. Abbreviations

CFD	Computational Fluid Dynamics
LCB	Longitudinal centre of buoyancy, reference from the transom
LCF	Longitudinal centre of floatation, reference from the transom
DWL	Design waterline
ITTC	International Towing Tank Conference
WSA	Wetted Surface Area

References

1. Armstrong, N.A. 2000, On the Viscous Resistance and Form Factor of High-Speed Catamaran-Ferry Hull Forms, PHD thesis, The School of Mechanical and Manufacturing Engineering, The University of New South Wales.

2. Insel, M. 1995, Resistance and Powering of High-Speed Marine Vehicles – Catamarans, *Australian Maritime Engineering Corporate Research Centre (AMECRC) Workshop*, June 1995 : Sydney, Australia, vol 3.

3. Insel, M. & Molland, A.F. 1992, An Investigation into Resistance Components of High-Speed Displacement Catamarans, *Transactions of Royal Institute of Naval Architects*, 1992, vol .134,pp 1-20.

4. Larsson, L. (1993), *Resistance and Flow Predictions Using SHIPFLOW Code* 19th WEGEMNT School, Nantes, France.

5. Molland, A.F., Wellicome, J.F. & Couser, P.R. 1994, Resistance Experiments on a Systematic Series of High Speed Displacement Catamaran Forms: Variation of Length-Displacement Ratio and Breath-Draught Ratio, *Ship Science Report No. 71*, March 1994, University of Southampton, United Kingdom.

6. Xuan, X. P., Kantimahanthi, K., Sahoo, P.K., 2001, Wave Resistance Prediction for Hard-Chine Catamarans by Regression Analysis, *Proceedings of 2nd International EuroConference on High-Performance Marine Vehicles, HIPER '01*, Hamburg, 2-5 May 2001, pp 382.

Parametric Analysis on Planing Hull

Mohammad Saeed Seif

Sharif University of Technology, seif@sharif.ac.ir

Abstract

High speed crafts are much different from conventional ships and their performance depends on many parameters. Thus researches and studies on these types of vessels are one of the most important issues in the marine industries. Planing craft is a very popular type of high speed crafts and is considered in this study for hydrodynamic evaluation. Empirical formulas and procedures in hydrodynamic analysis of planing crafts are very important and are reviewed first, then a compact software is developed for parametric study and the effects of different factors such as deadrise angle, length to beam ratio, longitudinal position of center of gravity, etc. are evaluated and some conclusions are derived.

The results will be highly valuable for predicting the craft characteristics in early step of design. They also can be used in an optimization procedure to improve the efficiency of the craft.

Nomenclature:

D_f	Frictional Drag	C_v	Speed coefficient
D_p	Pressure	V	Speed of the vessel
D	Total drag	b	breadth
EHP	Effective horsepower	C_{L_β}	Lift coefficient
Δ	Displacement	C_{F_0}	Frictional coefficient without roughness
C_p	Pressure coefficient	c	As defined in Fig.3
ρ	Water density	LCG	Longitudinal position of CG
β	Deadrise angle	VCG	Vertical position of CG
C_{L_0}	Lift coefficient	a	As defined in Fig.3
τ	Trim angle	λ	Length to beam ratio
ε	As defined in Fig.3	V_m	Speed of the water relative to the hull
f	As defined in Fig.3	Re	Reynolds number
ν	Systematic viscosity	C_F	Total frictional coefficient
ΔC_F	Roughness frictional coefficient allowance	a	As defined in Fig.3

Introduction

Planing crafts are very important among high speed crafts and this type of vessel plays an important role in different maritime activities. Proper design of such vessels requires very careful investigation of hull shape parameters. In addition, because of different application, such a study may help on discussing the vessel performance and operability quality. Planing craft have different modes of operations. In low speeds, the vessel behaves like a conventional displacement hull. But, by increasing the speed, hydrodynamic lift will be developed and the vessel start to rise up from the water. At top speed the vessels will be in planing mode and most of its weight is supported by hydrodynamic lift. Thus the vessel has a very small contact with water and very small frictional resistance as well. Savitsky [1] has presented an empirical procedure and formulas for evaluating frictional drag, total drag (D), effective power (EHP) and trim angle (τ). The method is based on many experimental works. In this paper, first the formulas and the definitions are explained. Then the effects of different parameters of hull shape have been studied and some conclusion are derived.

Preliminary analysis

As explained, Savitsky's method is an experimental based method and nowadays is used very widely. Of course, finalizing the design of a vessel body shape may require model test or full hydrodynamic analysis on the CFD basis. But in preliminary design stages, such methods are not efficient. So, in this section principles of Savitsky's method is explained. Then a parametric study is performed based on developed computer software.

The method was based on results of many wedge type model tests. Then some formulas were introduced for representing results in different values of shape parameters such as deadrise angle, length beam ratio, etc. These formulas are based on few coefficients. The first coefficient is defined as speed coefficient. It has the following definition:

$$C_v = \frac{V}{\sqrt{gb}} \qquad (1)$$

Next coefficient is lift force coefficient. It is defined as:

$$C_{L_\beta} = \frac{\Delta}{\frac{1}{2}\rho V^2 b^2} \qquad (2)$$

The above definition is for a vessel with constant deadrise angle. Thus for calculating lift coefficient in zero deadrise angle, following relationship is proposed:

$$C_{L_\beta} = C_{L_0} - 0.0065\beta C_{L_0}^{0.60} \qquad (3)$$

λ is defined as length to beam ratio of wetted surface (Fig.1) and It is calculated from the following relationship.

$$C_{L_0} = \tau^{1.1}\left(0.012\lambda^{1/2} + 0.0055\frac{\lambda^{5/2}}{C_v^2}\right) \qquad (4)$$

Since λ is not known in the above formula, it should be calculated for a range of trim angles, and the exact value will be specified after determination of equilibrium condition.

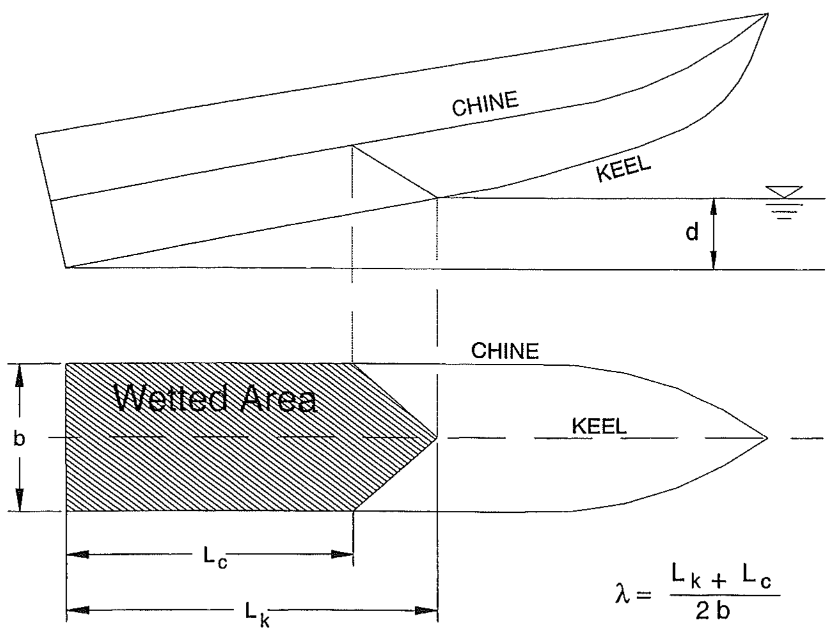

Fig.1: Definition for λ

The relative speed of water to the hull is an important quantity. It will affect frictional resistance. This speed is usually less than vessel speeds and can be evaluated by following formula for zero value of β.

$$V_m = V\sqrt{1 - \frac{0.012\tau^{1.1}}{\sqrt{\lambda}\cos\tau}} \qquad (5)$$

For arbitrary deadrise angles, there is no simple formula and some graphs given in Ref.1 may be used. The Reynolds number is necessary for calculation of frictional resistance and is defined as follows:

$$\mathrm{Re} = \frac{V_m \lambda b}{\nu} \tag{6}$$

Using this definition in connection with ITTC-57 method, frictional resistance is calculated as follows:

$$C_F = \Delta C_F + C_{F_0} = 0.0004 + \frac{0.075}{(\log_{10}\mathrm{Re} - 2)^2} \tag{7}$$

Thus, frictional resistance (D_f) is calculated through eq.8.

$$D_f = \frac{\rho V_m^2 b^2 C_F}{2\cos\beta\cos\tau} \tag{8}$$

In the other hand, based on Fig.3, There is a drag component from pressure force, which will produce additional drag as follows:

$$D_P = \Delta.\tan\tau \tag{9}$$

So, the total drag is summation of both components, or:

$$D = D_f + D_P \tag{10}$$

To find out equilibrium condition, it is necessary to specify the center of hydrodynamic pressure. The following formula is proposed:

$$C_P = 0.75 - \frac{1}{2.39 + 5.21\dfrac{C_v^2}{\lambda^2}} \tag{11}$$

The values of c, a and ε are also calculated by following formulas:

$$c = LCG - C_P \lambda b \tag{12}$$

$$a = VCG - \left(\frac{b}{4}\right)\tan\beta \tag{13}$$

$$\Delta\left\{\frac{[1 - \sin\tau\sin(\tau+\varepsilon)]c}{\cos\tau} - f\sin\tau\right\} + D_f(a - f) = 0 \tag{14}$$

The value of c is determined in such a way that eq.14 is fulfilled. Then other quantities are evaluated using abovementioned formulas. Finally, effective horsepower for the vessel can be evaluated as follows:

$$EHP = D.V \qquad (15)$$

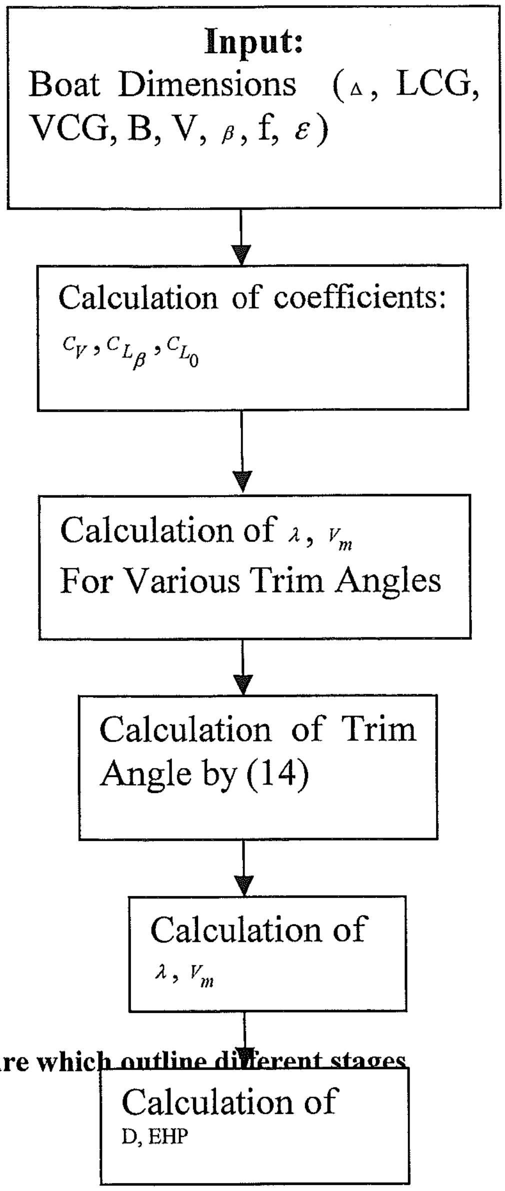

Fig.2: A brief procedure which outline different stages

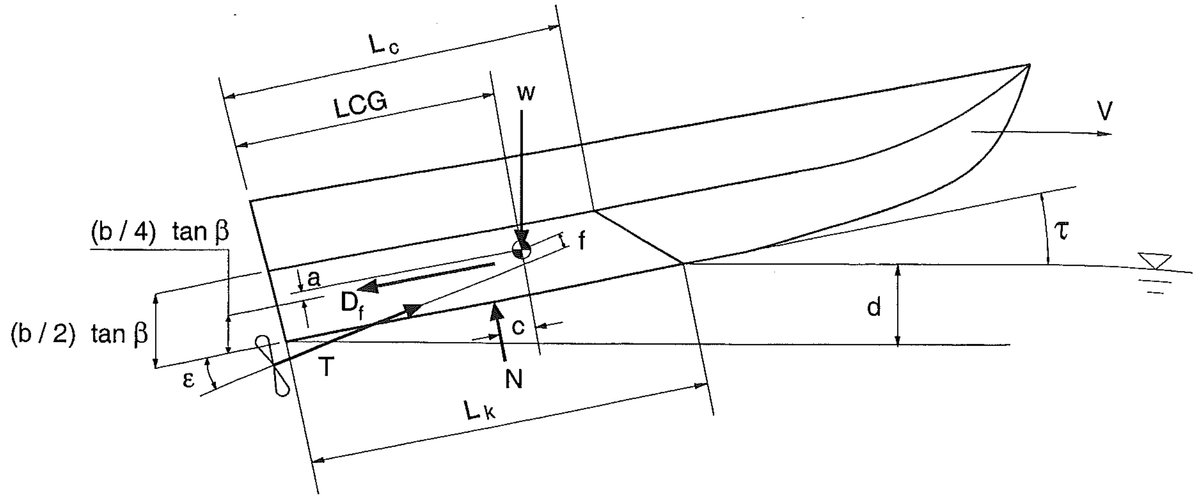

Fig.3: General definitions

Computer Software

According to the procedure, which was explained in previous section, a computer program has been developed. The program is based on general case (which means different longitudinal positions of center of gravity and center of pressure). But it can be also used for simple case (which means equal positions of center of gravity and center of pressure). So, it is possible to investigate errors due to the simple case assumption. For evaluating the accuracy of computer code, a comparison study is made by a body form of Series 62 [4]. The body from is shown in Fig.4. It is a hard chine type and its main particalars are as following:

$\Delta = 18.7$ ton
LCG = 6.695 m
VCG = 0.8 m
$\bar{b} = 3.807$ m
$\beta = 13^\circ$
f = 0.038 m
$\varepsilon = 10^\circ$

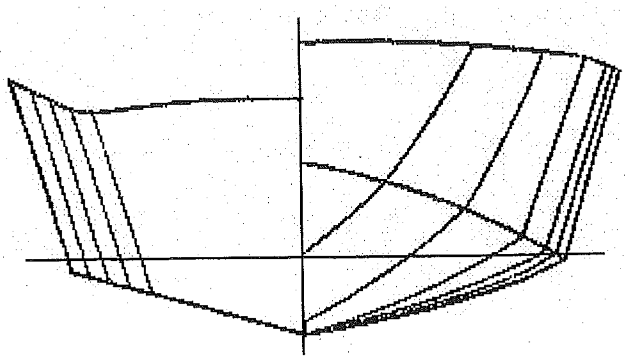

Fig.4: A typical body form of series 62

The selected body from has been tested by Clement and Blount [3]. The results is presented in Ref.3 and the ratio of length to beam is 4.09 for the model. Fig.5 shows resistance and trim of the model versus the speed. In this analysis other specifications are constant and speed is increased only. The figure shows four different results that are from the developed software (Acc. Savitsky method in simple and general case), results of Series 62 [3] and results of software recommended by Arenson Company [4]. Since savitsky method is valid in planing mode, its results are presented for high Found numbers. As it is seen from the figure, trim and resistance increases very much for lower speeds, which means the starting point of planing mode and its behavior can not be perdicted by Savitsky method.

In Fig.5 accuracy of the software can be evaluated as well. Series 62 results are for exact body plan, but Savitsky method consider simplified body plan and its results can not match very well with Series 62 results. As it is shown in Fig .5, results of simple case are not very different. In other word, considering the assumption for simple case does not affect the results very much. (Fig.6 shows differences).

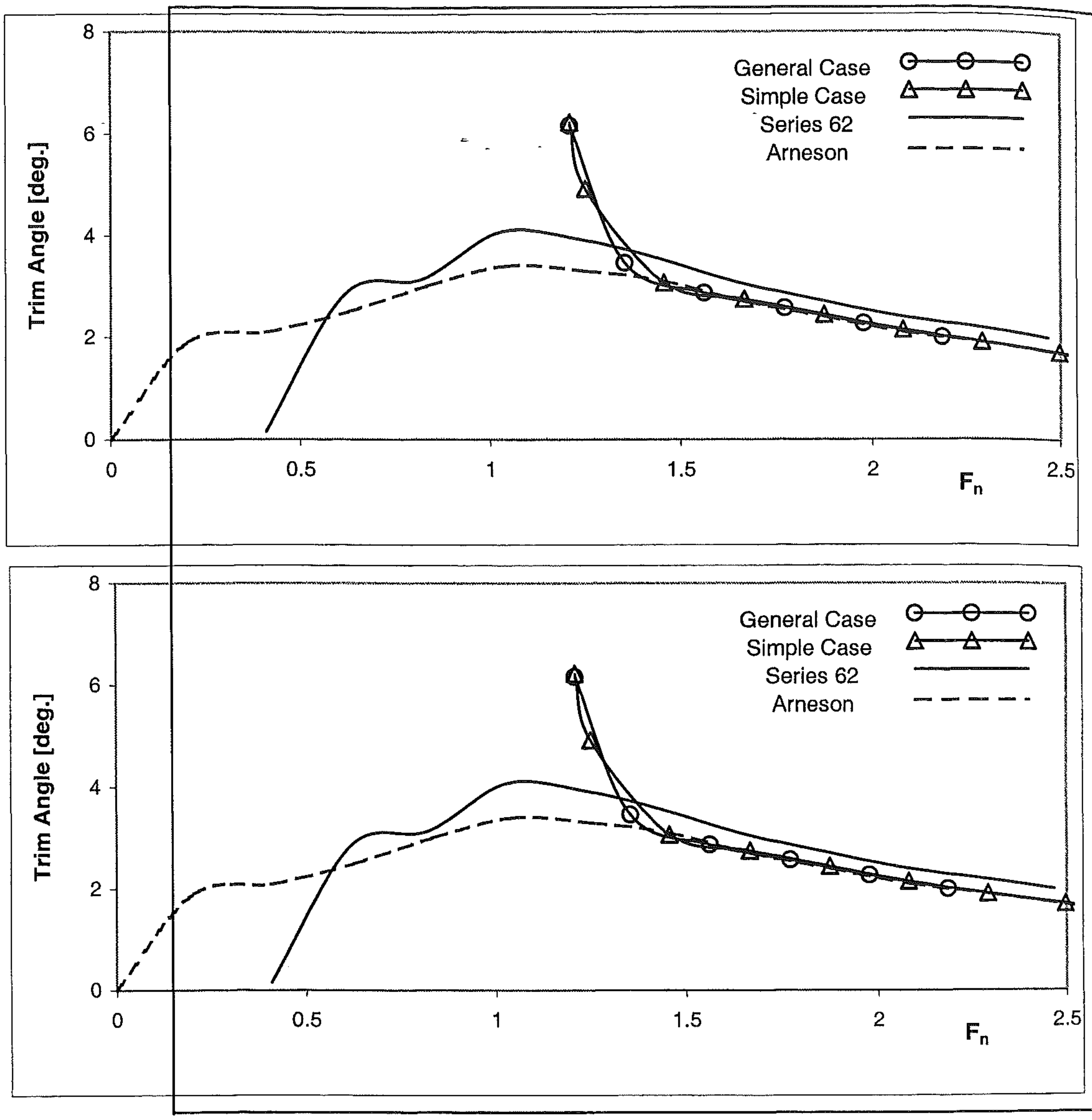

Fig.5: Atypical Serise 62 results

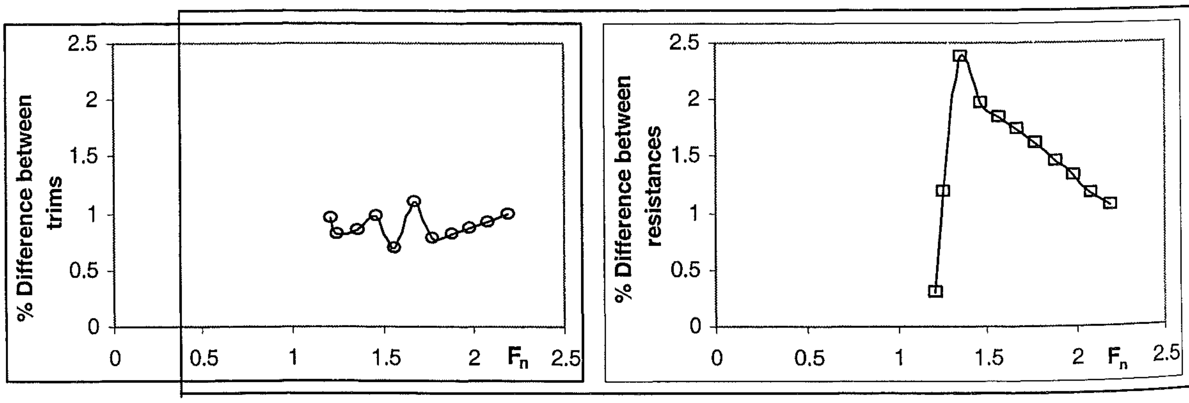

Fig.6: Differences between general case and simple case

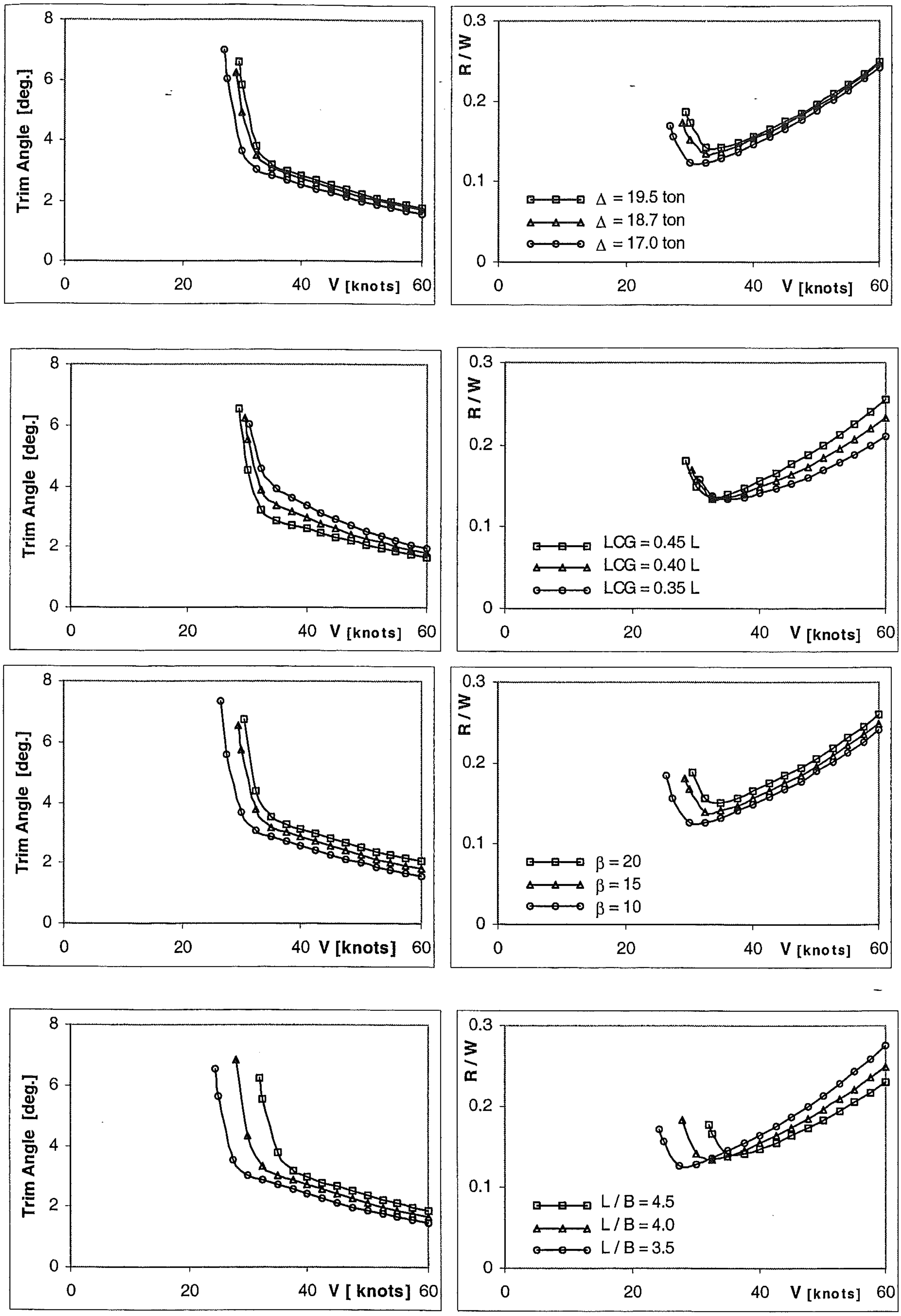

Fig.7: Parametic Study results

Parametric Study

As it was explained, the goal of present paper is to study the effects of different form parameters on performance of a planing hull. Fig.7 shows results of resistance and trim for different cases. The curves in this figure are evaluated for variation of displacement, LCG, deadrise angle, and length to beam ratio. In each case other parameters remain constant. So, each of them presents effects of specified parameters on the behavior of resistance and trim. According to the results, the following points are concluded:

1) Increase in displacement of the vessel causes more drag. The increment is considerable in lower speeds where planing is started. So, It may be concluded that displacement is very important in the ability of the vessel to start working in planing mode. Another point is that trim angle should be higher for providing more lift in the case of heavier vessel.
2) Longitudinal position of center of gravity is very important in the behavior of vessel. Resistance of vessel will be reduced for smaller values of LCG. But trim angle will be increased for higher values of LCG.
3) Higher values of deadrise angle will cause more resistance. It will also cause more trim angle.
4) Length to beam ratio can also have some effects. Trim will be increased for higher values of this ratio. But resistance in planing mode (higher speeds) will be decreased for higher values. As it is stated by Savitsky [5], suitable values are between 3 to 5 and longer values have better performance in a seaway.

Conclusions

Savitsky method is reviewed and differences between its results and a usual Series 62 hull is investigated. According to the numerical results, useful conclusions for preliminary design of planing hulls are made. These results show clearly the effects of some parameters such as displacement, LCG, deadrise angle and length to beam ratio. Another point is that Savitsky method has been developed for planing mode of operation. So studying behavior of vessel at displacement or at starting region of planing mode needs more research. These works can be based on CFD methods or experimental researches.

Reference

1- Daniel Savitsky, "Hydrodynamic Design of Planing Hulls", J. Marine Technology, vol. 1, No. 1, Oct. 1964, PP. 71-95.
2- SV.AA.HARVALD,"Resistance and Propulsion of Ships", john Wiley, 1983.
3- Eugene P. Clement and Donald L. Blount, "Resistance tests of a Systematic Series of Planing Hull Forms", Presented in Annual Meeting, New York, N. Y. Novamber 14 - 15, 1963.
4- "Planing Hull Resistance and Propulsion with Surface Propellers ", 1988 – 1989 , web Addresses: http://www.well.co/user/pk/SPApower.html.
5- Danial Savitsky and Jerry Gore, "Re – Evaluation of the planing Hull From" Journal of Hydronautics, Vol. 14, No .2, April 1980, pp. 34 – 47.

Application Of A Monte Carlo Simulation For Damage Stability Calculations

Jan Tellkamp, Flensburger Schiffbau–Gesellschaft, tellkamp@fsg-ship.de

Abstract

The stability analysis of ships is mainly determined by empirical stability criteria that are based on the experience from operated ships. As the existing stability rules focus on the methodology of the stability approval, no absolute safety–levels are known that have to be achieved.

Therefore it is not yet possible to evaluate an unconvential or conventional design with respect to intact and damage stability using first principle methods only. Opposed to this, applying such methods in the early design stage leads to a better understanding of the physical phenomena and helps to design safer ships.

There is a need for a new methodology, that takes into account risk performance based criteria that could be quantified and judged in line with traditional performance criteria like resistance, noise level, or pressure pulses.

In the present paper a methodology for determining the probability of the consequence *capsize after a collision* will be presented and applied to the design of a RoPAX–ferry. This methodology has been developed within the EU–funded research project NEREUS.

1 Introduction

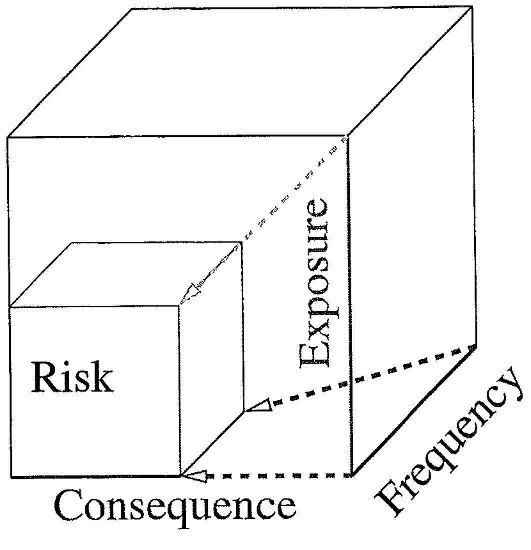

Figure 1: Elements of Risk

Today in the shipbuilding industry, two approaches towards safety have been settled. They are based on

- **prescribing design specificae**, e.g. the main engine room has to have A60 walls, or the exact position of the collision bulkhead.
- **prescribing physical properties**, e.g. the leverarm curve of an intact vessel has to meet certain criteria, or some stresses shall not be exceeded.

Missing is an approach explicitly quantifying risks:

- **prescribing acceptable risk levels**, e.g. the frequency of a certain hazard shall be lower than a certain rate λ.

All the approaches mentioned above represent different stages of knowledge, available methodologies, and different levels of risk perception in the society. As already discussed in [6], safety of technical systems like ships is achieved using one of the above mentioned strategies or a combination of them.

The common aim of these strategies is to ensure a minimum safety standard. But what is safety? Safety can be defined as the abscence of risk, which itself has three major elements:

1. consequence,
2. frequency, and
3. exposure,

as shown in figure 1. Examples for the elements of risk are intact–capsize in waves exceeding a certain waveheight as a consequence, the average time or rate λ between waves exceeding a certain waveheight as a frequency, and the time t sailing in an operational area with this frequency for that waveheight as exposure, respectively.

2 Risk Based Design Methodology

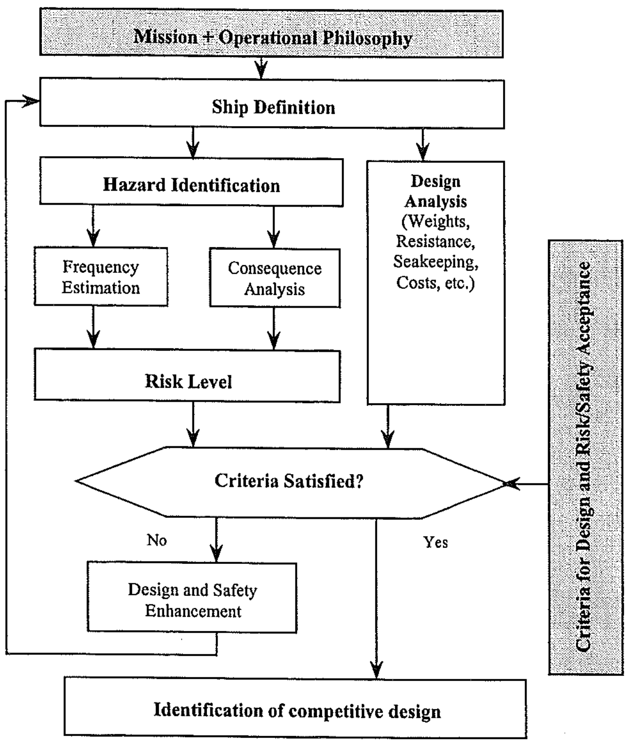

Figure 2: Risk–Based Design Procedure

A risk based design methodology has to meet several criteria:

- the methodology should be inline with or similar to current practise,
- it should be based on the use of first principle tools,
- it should be generic and comprehensive,
- the results should be quantities,
- the quality of the results should be quantifiable,

The methodology which is presented here and which fulfills these requirements was developed in the NEREUS–project, see [2]. Within this RBD–procedure a Monte–Carlo–Simulation will be used to calculate the probability of remaining afloat after a collision has occured to a vessel (encircled area in figure 3). The probability of remaining afloat under the condition a collision occured is:

$$P(collision \cap remain\ afloat) = P(remain\ afloat|collision) \cdot P(collision) \tag{1}$$

and, as these events are stochastically independent, equation (1) simplifies to

$$P(collision \cap remain\ afloat) = P(collision) \cdot P(remain\ afloat) \tag{2}$$

In this document an applicable Monte–Carlo–Simulation will be developed to be a useful tool within the RBD–procedure. The Monte–Carlo–Simulation will be used within the procedure for the estimation of the probability of capsizing following a collision.

To apply this methodology on the calculation of the probability of survival after a collision, which is encircled in figure 3, a set of tools was identified. These tools have been named F1–tool, C1–tool, C2–tool, and R1–tool, respectively. They are shown in figure 4. The F1–tool has the output 'collision impact and environmental conditions' in terms of damage extend and significant waveheight. From this the C1–tool determines the set of damaged compartments which together with the significant waveheight is input for the C2–tool. Here the ships' response is calculated, in terms of surviving these conditions or not. Finally, the R1–tool quantifies the risk of not surviving damaged conditions by means of giving the probability of survival.

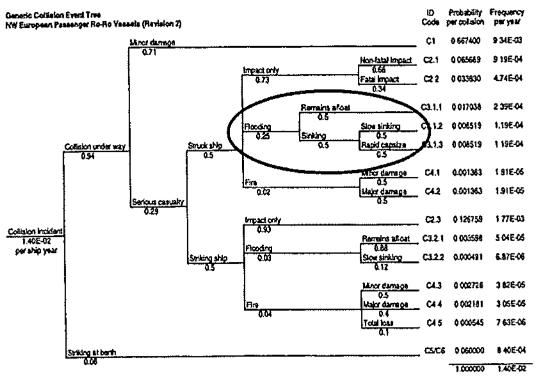

	Incidents (per ship year)	Minor Damage (per ship year)	Major Damage (per ship year)	Fatal Incidents (per ship year)	Total Loss (per ship year)
Frequency	1.40E-02	1.02E-02	3.82E-03	7.76E-04	2.53E-04
Percentage		72.74%	27.26%	5.54%	1.81%
Return Period	71	98	262	1,288	3,952

Figure 3: Event–Tree for collision incidents and their consequences

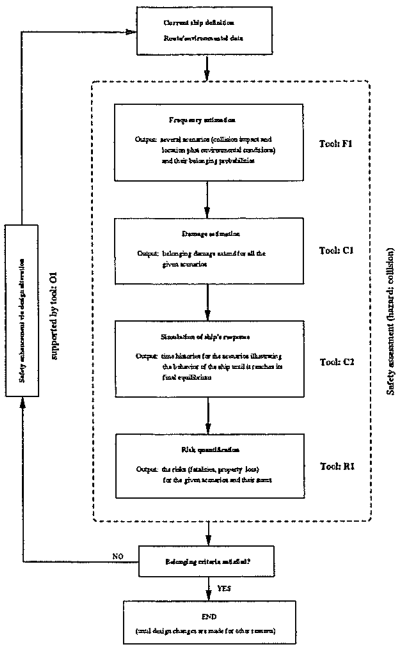

Figure 4: Flow diagram for the safety evaluation for collision incidents

3 Use of a Monte–Carlo–Simulation in Damage Stability Calculations

As damage stability calculations use several deterministic and random data and a functional correlation between input data and result is not known, the Monte–Carlo–Simulation is well suited for application to determine the contribution$P(remain\ afloat)$ to the survivability of ships as specified in equation (2).

The basic idea is to generate a random sample for the outcome of a random experiment, see figurre 5. From this sample statements on the random problem can be made. Details on Monte–Carlo–Simulations are given in [4] and [1].

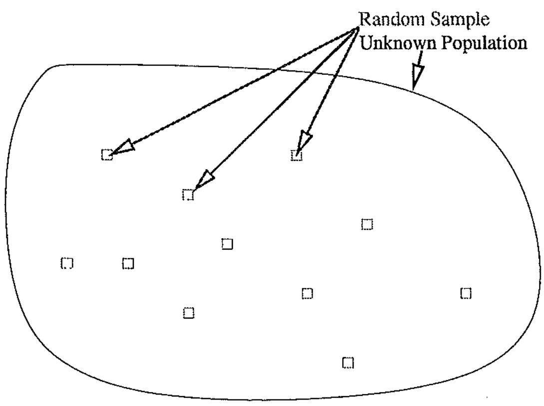

Figure 5: Random Sample as result of a Monte–Carlo–Simulation

3.1 Input data

The data used for damage stability calculations can be subdivided into deterministic data and random data:

1. deterministic data
   (a) Hullform
   (b) Compartmentation
   (c) loading condition and intact floating condition
      - mass and draught
      - vertical center of gravity
      - longitudinal center of gravity
      - transversal center of gravity
      - tank filling, permeability of the car–deck
2. random data
   (a) damage center on the hull, X_1
   (b) longitudinal damage extend, X_2
   (c) transversal damage extend, X_3
   (d) vertical damage extend, X_4
   (e) sea state, X_5

Item 1c can easily be treated deterministic, as in the building contract several loading conditions are specified and well known with all their properties, and typically a vessel is restricted to sail at this loading conditions. If they are not known, statistics could be applied.

3.2 Probability distributions

As the damage location and extend are taken as probabilistic data, appropriate distributions must be used. The distributions for damage center in longitudinal direction, damage length in longitudinal direction, and penetration depth in transversal direction are taken from [3].

The distributions of significant wave–heights shall be occording to the route Kiel–Oslo, defined in the specification, see [5]. This distribution might be given analytical or by means of a scatter–diagram. It will be beneficial if they include wave–lengths as well, as these are required for further investigations using time–domain codes.

3.3 Calculation of survivability using Monte–Carlo–Simulation

The output of a damage stability calculation using a Monte–Carlo–Simulation should be a figure, that allows to assess the survivability of this specific vessel on a scientific base. To do so, the probability of survival under the condition a damage, specified as a penetration of the outer shell, has occured should be calculated. This is the probability as specified in equation (2).

The application of Monte–Carlo–Simulation to damage stability problems could easily be outlined using pseudocode:

- set $c = 0$ and do n times...

1. generate $H_{\frac{1}{3}}$ and damage cuboid ...
2. generate list of damaged compartments from damage cuboid
3. generate buoyancy body taking into account loading condition
4. using SEM, calculate if $H_{\frac{1}{3}}$ will be survived
5. if yes, increase c by 1

- take
$$\frac{c}{n} = \hat{p} \tag{3}$$
as estimation for the probability p of surviving a damage on this loading condition

In the context of figure (4), the F1–tool – generation of damage cuboid and significant waveheight – can be identified as step 1. The C1–tool – consequence from damage cuboid – is equivalent to steps 2 and 3, and 4 forms the C2–tool – consequence from buoayancy body in waveheight. Equation (3) as an estimation for the survivability, whith the quality of the estimation quantified by equation (7), then is the R1–tool.

The Static Equivalent Method, SEM, is described in [7].

3.4 Level of confidence and magnitude of n

The type of the distribution of c is the binomial distribution. As the (random) outcome of the C2–Tool 0 or 1, it is not spatio-temporal, nor (random) number of occurences in an interval, nor distribution of distances between (random) events.

A binomial distribution is characterized by one parameter p. p gives the probability that the result of an experiment is *successful*, in our example *the ship survives a damage*, and $B(p, c, n)$ gives the probability that in n damage cases the ship survives c times:

$$P(C = c) = B(p, c, n) = \binom{n}{c} p^c (1 - p)^{(n-c)} \tag{4}$$

$$\mu_C = np \tag{5}$$

$$\sigma_C^2 = np(1 - p) \tag{6}$$

gives the probability that in n experiments c are successful.

In section 3.3 above for each loading condition a fraction $\frac{c}{n}$ is calculated. This fraction is taken as an estimation $\hat{p}$ for the probability p of surviving a damage, which is the unknown parameter of the binomial distribution. As this figure is the result of the generation of a random sample, it is a random value itself. Now the accuracy of this estimation must be determined.

A common way for this is giving an interval around $\hat{p}$, which contains p with a given probability:

$$P\Big(p \in [\hat{p} \pm \frac{\Delta_p}{2}]\Big) = 1 - \alpha \tag{7}$$

$1 - \alpha$ is called *level of confidence.* On this level of confidence the length of Δ_p is calculated for a binomial distribution to

$$\Delta_p \leq \frac{2}{\sqrt{n}} \sqrt{\hat{p}(1 - \hat{p})} z_{1-\frac{\alpha}{2}} \tag{8}$$

with $z_{1-\frac{\alpha}{2}}$ as the $(1 - \frac{\alpha}{2})$–quantile of the standard normal distribution. So n becomes

$$n \geq 4\hat{p}(1 - \hat{p}) \Big(\frac{z_{1-\frac{\alpha}{2}}}{\Delta_p}\Big)^2. \tag{9}$$

For a $B(p, c, n)$–distributed population

$$\hat{\sigma}^2 = \hat{p}(1 - \hat{p}) \leq \frac{1}{4} \tag{10}$$

surely is true and without a–priori information about p the size of the random sample has to be determined to

$$n \geq \left(\frac{z_{1-\frac{\alpha}{2}}}{\Delta_p} \right)^2 \tag{11}$$

4 Design Exercise

4.1 Input specification according to owners requirements

The following table summarizes the main topics of the input specification as agreed upon within the project. Note that for our design, only stability standard 1 (including SEM investigations) needs to be regarded according to the existing status of the stability rules.

PRELIMINARY OUTLINE OF SHIPOWNER'S REQUIREMENTS FOR INITIAL DESIGN1			
TYPE	CAR/PASS FERRY		
RANGE	12 days x 24 hrs full speed	288 hrs	Specifies fuel capacity *Max. fuel capacity: abt. 1,000 tons*
STABILITY STANDARD 1	SOLAS 90+ STOCKHOLM AGREEMENT -2 compartment - w/o transverse BHDs on car deck		For Stockholm Agreement application: take 4.0 m sign. wave height
STABILITY STANDARD 2	Harmonized Probabilistic Approach		To determine A./R values acc. to A265 and the proposed new harmonized rules (IMO-SLF-SDS)
SPEED service	25 knots		
Indicative Main Dimensions			Main dimensions to be optimized with respect to economy (building and operational cost) for given capacity and operational requirements, including the requested stability standards

LOA	200 m		*indicative*
LPP	185.5 m		*indicative*
B	27.5 m		*indicative*
T (draft max.)	6.7 m		*Not to be exceeded*
Capacities - Payload			
Deadweight	5000 mtons		*indicative*
Trailer lane meters			
Main Hold	1130 m		*indicative*
Lower Hold	270 m		*Indicative. Lower hold not a formal requirement! Total 1400 m trailer lane requested*
Private Car capacity			
Upper deck	210 cars		*Indicative*, upper deck to provide area for the indicated number of private cars and a maximum number of outside cabins
Hoistable decks	114 cars		*Indicative. Hoistable decks not a a formal requirement! Total 324 cars requested*
Passenger capacity	1800		*fixed*
Pass cabins	550		*Fixed, max. possible outside cabins*
Crew number	180		*fixed*
Crew cabins	150		*fixed*
Public spaces, incl. catering	$8000m^2$		

4.2 Reference Design

According to the specification, a reference design has been developed using SOLAS Reg. 8 and the Stockholm Agreement as regulations with respect to damage stability, see picture 6. The vessel is complying with the IMO intact stability code and has been subject to detailed investigations with respect to hydrodynamic efficiency, namely cavitation, seakeeping, passenger comfort, and hull resistance.

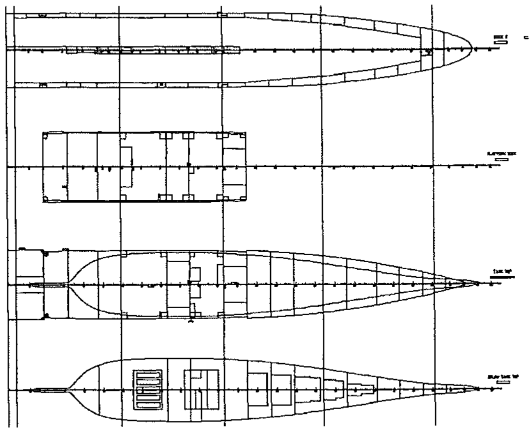

Figure 6: Reference Design, watertight compartmentation

4.3 Design Alternatives

RoRo-Deck Arrangement A set of design alternatives were defined and evaluated with respect to costs, lane meters, and survivability:

a reference Design, short center casing and long side casings

b just short center casing

c just long side casings

d short center casing and two short side casings each side

e long center casing

The survivability was calculated using the Monte–Carlo–Simulation on a level of significance of 95% with a confidence interval of ±2%. Given are the overall probabilities of survival and the survivabilities under the condition that the RoRo–Compartment is damaged. The changes in survivability are significant if they exceed 2%. From figure 7 it can be seen, that it was not possible to improve the survivability of the reference design on the given level of significance and confidence interval.

Hullform Modifications After the first design iteration was completed, the vessels lines were improved with respect to seakeeping performance as shown in figure 8 and figure 9.

The influence of these modifications on the damage stability performance of the vessel are shown in figure 10. The modifications do not change the ranking of the arrangements on the cardeck, and the changes in survivability taking into account all damage cases are not significant, as they are lower than 2%. But the changes for the survivability under the condition the RoRo–deck is damaged is improved significant for the arrangements A, C, and D.

	overall cost comparison	compartment cost comparison	bulkhead area cost comparison	lane meter variation (m)	survivability	
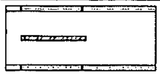 A	100%	100%	100%	0	91,8% 84,5%	of all damages of damages w/ RoRo-Comp
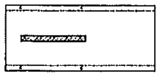 B	27%	14%	30%	0	89,0% 79,2%	
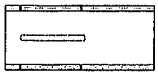 C	73%	86%	70%	79	92,2% 85,1%	
 D	73%	71%	73%	0	90,4% 81,9%	
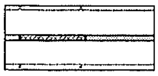 E	69%	43%	75%	- 89	86,1% 73,7%	

Figure 7: Comparison of Arrangements

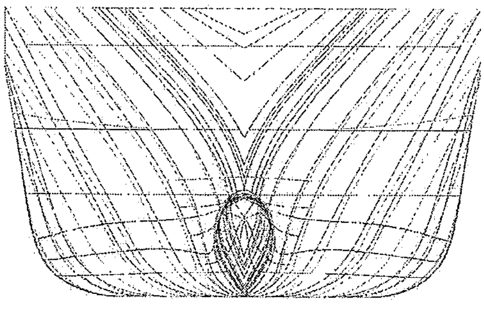

Figure 8: Hullform modification, Forebody

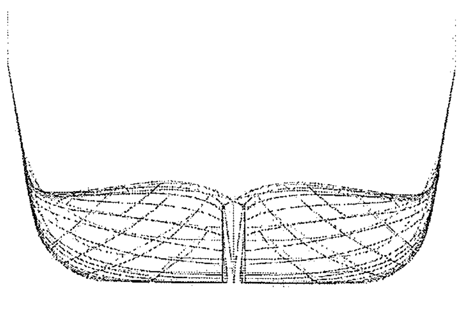

Figure 9: Hullform modification, Aftbody

	survivability	survivability modfd. Hull
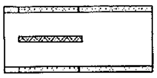 A	91,8% 84,5%	93.1% 87.2%
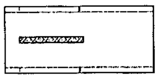 B	89,0% 79,2%	88,9% 79,4%
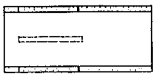 C	92,2% 85,1%	93,8% 88,4%
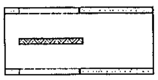 D	90,4% 81,9%	91,2% 84,3%
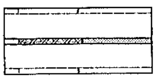 E	86,1% 73,7%	85,6% 73,2%

Figure 10: Comparison of Arrangements after Hullform Modification

5 Conclusions

A risk based design methodology was developed utilizing first principle tools for assessing the resistance against capsize for damaged RoPAX vessels. The requirements given on page 2 are kept. This methodology was successfully applied within a design exercise and is promising to be a valuable tool for the assessment of risks of arbitrary ships.

A Nomenclature

Symbol	Description
C	random number of survives in damaged condition
c	realization for C
$B(p, c, n)$	binomial–distribution
$f(X)$	probability density function
$F(X)$	probability function
λ	frequency of an event
$\overline{X}$	mean for X
μ_X	expected value for X
n	size of random sample
$N(\mu, \sigma^2)$	normal–distribution
p	probability of surviving a damage
$\hat{p}$	estimation for p as result of a Monte–Carlo–Simulation
Δ_p	confidence interval for p
$P(C = c)$	probability that the realisation for C equals c
π	uniform distributed random number
RNG	random number generator
S_X^2	standard deviation for X from random sample
σ_X^2	variance for X
t	period of an RNG
t	time of exposure
X	random Variable
x	realization for X
$1 - \alpha$	level of confidence

References

[1] Brian P. Flannery et al. *Numerical Recipes in C.* Press Syndicate of the University of Cambridge, Cambridge, 2. edition, 1995.

[2] P. Hakulinen, H. Cramer, J. Tellkamp, and I. Oestvik. WP2: Task 2.2, application of QRA methodology to competitive design. In NEREUS–*Project.* FSG/LMG/Deltamarin, September 2001.

[3] IMO. Explanatory notes to the SOLAS regulations on SUBDIVISION AND DAMAGE STABILITY OF CARGO SHIPS of 100 metres in length and over. IMO–paper, IMO, London, 1993.

[4] Donald E. Knuth. *Seminumerical Algorithms*, volume 2 of *The Art of Computer Programming.* Addison Wesley, Reading, Massachussets, 3. edition, September 1997.

[5] L Letizia. First Year Report January 2000–January 2001. In NEREUS–*Project.* SSRC, January 2001.

[6] Jan Tellkamp, Heike Cramer, and Stefan Krüger. Numerical Approach for Safety in Ship Design. In Miroslaw Gerigk and Jan Szantyr, editors, *Summer School Safety at Sea*, volume 1, Gdansk, August 2001.

[7] D. Vassalos and O. Turan. WP1:SEM – Static Equivalent Method: Background and Application. In NEREUS–*Project.* SSRC, June 2001.

3rd International EuroConference on High-Performance Marine Vehicles HIPER'02, Bergen, 14-17 September 2002, pp 392 - 406

Manoeuvring Aspects of Fast Ships with Pods

Serge Toxopeus, Maritime Research Institute Netherlands, S.L.Toxopeus@Marin.nl
Giedo Loeff, Maritime Research Institute Netherlands, G.Loeff@Marin.nl

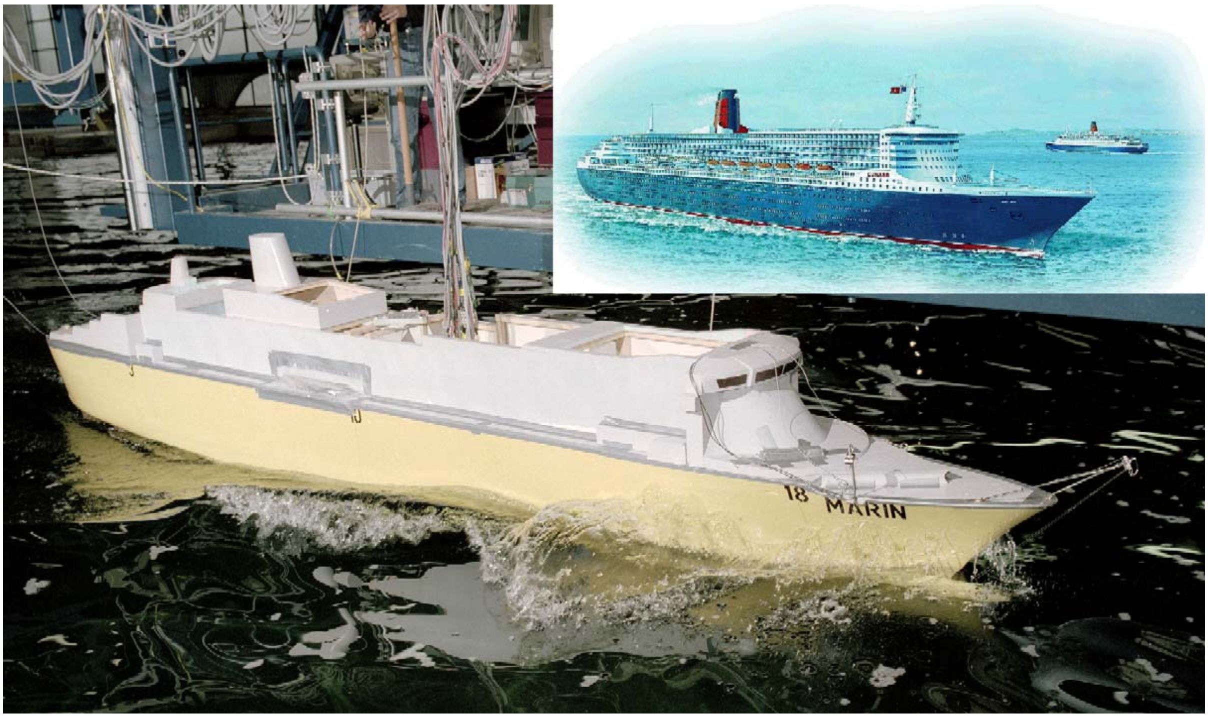

Figure 1. State of the art cruise liner with podded propulsion

Abstract

Currently an increasing number of modern ships is equipped with podded propulsors. Advantages are the possibility to use a diesel-electric propulsion plant and to increase the propulsive efficiency and the manoeuvrability of the ship. Besides application to cruise ships the pod concept is nowadays also applied to other ship types and to vessels of a higher speed range. Major benefits are normally obtained, but still areas of special attention exist. Due to the possibly large steering forces, large steering-induced heeling angles can occur. Additionally, the directional stability of ships with pods tends to be less than comparable ships with conventional propulsion. This paper describes the aspects of application of pods from a manoeuvring viewpoint, compares the manoeuvrability between ship designs with conventional propulsion and pod propulsion and highlights the benefits and points of attention. Design guidelines to improve the manoeuvring performance are given and operational issues are discussed.

1 Introduction

For the past ten years, an increase of the use of pod propulsion is discerned. The reason for this is claimed to be the increase in propulsive efficiency, comfort and increased manoeuvrability. Especially ships with diesel-electric propulsion appear to gain from this concept. Other advantages are the increased flexibility in engine room layout and the location of the engine room along the ship.

Currently, investigations on the design of pods are made from both a structural point of view as well as a hydrodynamics point of view. In the market several designs are spotted varying in number of propellers and general outline. Main suppliers are ABB Azipod, Rolls-Royce, Siemens-Schottel and

Wärtsilä Propulsion. From a structural point of view the accommodation of the electric motor, the mounting of the pod and the overall strength of the pod body are decisive for the design.
Information gathered from the Co-operative Research Ships (NSMB-CRS) studies and in-house measurements conducted at MARIN, points out that significant improvements are still to be made in the hydrodynamic design regarding the propulsion and steering efficiency of pods. General design aspects that are under investigation are:

- Torpedo and strut design
- Design and placement of fins attached to the pod housing
- Steerable flaps for course keeping
- Optimisation of orientation of the pod unit in all directions (lateral - transverse -horizontal plane)

Classically, the first cruise ships equipped with pods had two units installed. The largest ships delivered currently however have one fixed unit and two azimuthing units due to the current limitation of the power of the pods. The largest ship on order will be equipped with two fixed pods and two azimuthing pods. Using fixed pods poses a special challenge from a manoeuvring viewpoint: it means that only part of the total installed power will be available for steering and therefore a relatively insufficient steering ability might exist, in contrast to the ships with all units movable.

Several publications regarding the general optimisation of ships equipped with pods have been released, by for example Kurimo (1998), Lepeix (2001) and Hämäläinen (2001). However, these publications deal mostly with general issues or concentrate on the powering optimisation of the ship. Only marginal information regarding the manoeuvring specifics is found in public literature.

Obviously, considerable advantages exist from a manoeuvring viewpoint when pods are implemented in the design of the ship. However, without taking the appropriate measures, the directional stability of the ship or even the safety of the ship might be compromised due to the hull form design or the large steering forces of the pods. These measures, which are most of the time easily implemented, must be taken in the earliest stages of the design.

When judging the manoeuvring characteristics of ships, not only the basics as proposed by regulatory institutions should be verified, but also characteristics associated with the mission of the ship. For example, passenger ships should not obtain large heeling angles during manoeuvres and they should be able to manoeuvre without assistance in harbours. Therefore, these aspects should be studied during the design of the ship in order to guarantee the success of the ship.

This paper presents the characteristic features regarding the manoeuvrability of ships with pods and provides guidelines for the designer in order to avoid the disadvantages associated with pods.

2 Differences between conventional ships and pod ships

The hull lines of ships with pods are slightly different from comparable ships with conventional propulsion. To allow the pods to rotate 360°, the pods must be mounted at a flat surface of the hull. Additionally, because of strength considerations, the pods are presently only positioned with the strut vertically down when looking from behind. This means that the hull lines are very flat in the aft ship and that not much lateral area exists in the aft ship, compared to conventional ships. For sufficient directional stability and for docking a suitable centre line skeg is required. In Figure 2 and Figure 3, typical aft ship designs of respectively a conventional ship and a ship with pods are given. In these photographs, the difference in the aft ship hull lines is clearly seen: the V-shaped lines for the conventional ship against the pram shaped lines for the ship with pods. The necessity of pram shaped lines for vessels equipped with podded propulsion is questionable. If desired, more V-shaped sections could also be implemented in the ship design if compromises are made to the design of the pod. Currently new pod designs are entering the market which not necessarily require pram shaped lines.

It is however expected that the most optimum hull form to accommodate a podded propulsion arrangement has not been found yet. When the horse-drawn cart was replaced by the self-propelled vehicle, the first design still resembled a cart. The evolution towards the modern day vehicles endured numerous design changes, but it took a long time before all opportunities were explored. This analogy represents a typical trajectory of a technical evolution. The design of pods and the way of implementation in the ship-design are still in the course of evolution.

Figure 2. Typical optimised aft ship design of a conventional cruise vessel with twin propeller/twin rudder arrangement

Furthermore, the use of pods in the aft ship cancels the need for stern thrusters, but still increases the forces that can be generated while manoeuvring at low speeds. This is a major advantage of the application of pods. Additionally, because of the relatively large installed power of the pods compared to stern thrusters, it means that in almost all cases sufficiently large forces can be generated in the aft ship during crabbing operations. This leaves only the bow thrusters as the limiting factors in the crabbing ability of the ship.

When course keeping during transit, application of steering angles is required to keep the ship on the required course. For a ship with pods, this is done by rotating one or all of the pods. Because of the weight of the complete pod unit, this is considered to be more strainful for the equipment than when steering with rudders. Therefore pod manufacturers are currently contemplating using steerable flaps connected to the pod which may be used for course keeping. Alternatively, additional rudders for course keeping purposes have been studied in the past. However, the success of these additional rudders were limited.

3 Manoeuvring at speed

Research conducted on vessels outfitted with podded propulsion has gained valuable information about the merits and drawbacks related to the manoeuvring characteristics at speed. From free sailing experiments the general behaviour has been extensively evaluated. Several systematic research projects have been conducted on vessels equipped with either a conventional propeller-rudder propulsion arrangement or a podded propulsion arrangement in order to identify the best concept suitable to the vessel under consideration. For example, models used during such a study are

presented in Figure 2 and Figure 3. Some experiments consisted of captive measurements monitoring the forces and moments in all 6 degrees of freedom acting on the pod unit and on the hull.
Insight is obtained by conducting these experiments regarding the general behaviour of a vessel propelled by pods and detailed information of the forces working on the pods. Based on this knowledge an assessment of the manoeuvring characteristics at speed for high-speed vessels equipped with podded propulsion can be made. Other possible fruitful evolutions, such as hybrid propulsion arrangements and unconventional hull forms, will be interesting when disputing the application of podded propulsion in the design of high performance vessels.

Figure 3. Typical optimised aft ship design of a cruise vessel with podded propulsion and steering arrangement

3.1 Areas of interest

In order to identify the merits and drawbacks of the manoeuvring characteristics related to the implementation of podded propulsion in the design of high performance vessels, a few areas of interest will be discussed:

- Course keeping
- Turning and turn initiated roll
- Course keeping in waves

3.2 Course keeping

In order to sail in a safe and efficient way a vessel needs to have good course keeping capabilities. A gain in propulsion efficiency when applying podded propulsion could be of less importance when the course keeping behaviour reduces significantly. More effort (fuel) could be needed to sail a certain trajectory. Therefore it is very important to look at the course keeping capabilities of ships equipped with pods and especially in relation to conventional propeller-rudder configurations.

A vessel's course keeping ability in calm water is commonly benchmarked using standard manoeuvres, see for example reference IMO (1994). These standard manoeuvres are regularly conducted on model scale and full scale and can therefore be used to correlate a vessel with similar or other types of vessels. The International Maritime Organisation (IMO) proposed criteria for parameters derived from the standard manoeuvres. These criteria, described in IMO Resolution A.751(18) (1993), are commonly used to judge the manoeuvring characteristics of a vessel. Although comparing the manoeuvring performance with that of other podded vessels might be more sensible.

The parameters derived from standard zigzag manoeuvres identify the course changing and course checking ability of a vessel. Statistical data have been derived from a selection of ships of which data is available at MARIN and is presented in Figure 4. It should be remarked that the presented vessels are optimised concepts through extensive research.

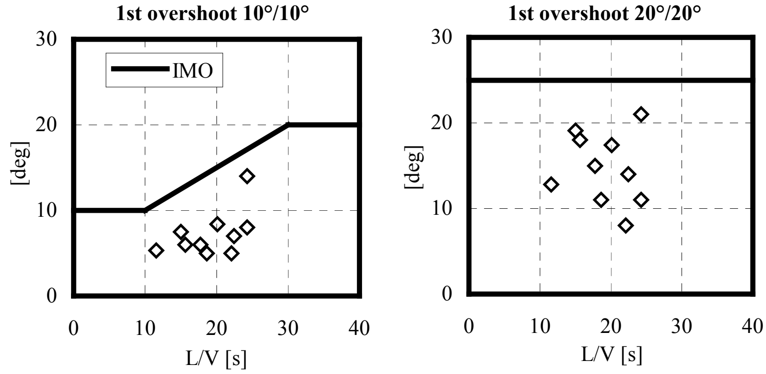

Figure 4. Overshoot angle statistics of ships with podded propulsion

The overshoot angles presented in Figure 4 are well within the criteria proposed by the IMO and are comparable to the average overshoot angles for all types of vessel in the MARIN database. From this it can be concluded that the tested vessels with podded propulsion perform well regarding the yaw checking and course keeping ability.
Data derived from systematic research on vessels with either conventional or podded propulsion enable a qualitative as well as quantitative comparison between both propulsion configurations. Figure 5 presents the overshoot angles for several comparable vessels, different approach speeds and steering angle / yaw check angle combinations. The meanline represents the situation where the overshoot angles for both steering units are equal.

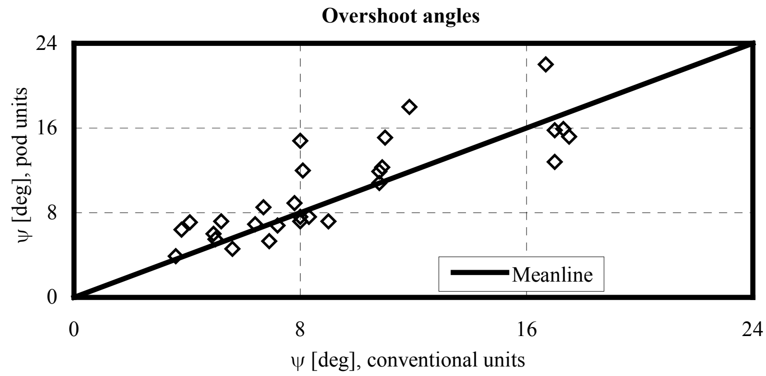

Figure 5. Overshoot angles of ships equipped with podded or conventional propulsion units

The vessels with the pod units tend to have slightly larger overshoot angles than those with the conventional propeller-rudder units. This tendency cannot be ascribed to a difference in propulsion units alone, other possible causes have to be questioned as well:

- Difference in rate of application of rudders or pods
- Difference in GM value
- Difference in the aft hull shape

Without questioning these aspects and judging their influence, no direct comparison between the steering units can be made.

According to the classification society and SOLAS requirements, the rate of application of pods has to fulfill the requirements for azimuthing thrusters to be at least 9 degrees per second whereas the rate of application of a rudder must be at least 2.32 degrees per second. In principle this requirement can be seen as a significant difference between both propulsion units. Increasing the rate of application of the rudders or pods influences the steering behaviour by speeding up the course changing and course checking ability. A kind of 'equilibrium' of both phenomena will result in different overshoot angles. A difference in rate of application of the rudders or pods can also influence the roll behaviour of the vessel, relating to the natural period of roll. This steering rate will be further discussed in section 3.3, as well as the influence of the GM value.

The influence of the afthull shape on the course keeping ability can be best discussed based on the measurement conducted with the pair of comparable vessels, shown in Figure 2 and Figure 3. The figures show a typical V-shaped aft ship for the conventional propeller rudder configuration and typical pram shaped aft ship for the podded propulsion configuration. From research it is known that these typical afthull shapes differ in their dynamical coursestable behaviour. It was derived from measurements that a V-shaped aft ship tends to have a better dynamical course stability than the extreme pram shaped aft ship. Knowing this the application of pram shaped lines in the design of a vessel with podded propulsion should be disputed. The compromise between optimum resistance, manoeuvring and seakeeping qualities will be dependent on the type, mission and application of vessel.

Another critical aspect of the application of pods is the supposed cavitation behaviour of a pod and propeller in an oblique flow. This cavitation issue will be very much of interest when evaluating the applicability of pods in the design of high performance craft. Pustoshny and Karprantsev (2001) presented and commented on cavitation observations on the *Elation* passenger cruiser. Their findings relevant to the manoeuvring characteristics of high performance craft can be best summarised in the following statements:

1. Pulling propellers on pods are normally exposed to an uniform wakefield, favouring good cavitation characteristics and reduce propeller-induced pressure fluctuations and vibrations while the vessel is sailing in a straight line without helm.
2. Angles of incidence larger than 5°-7° while course keeping become critical concerning cavitation.
3. The cavitation risk in a constant turn, for example a turning circle, is extensive. The speed in a constant turn will drop significantly due to large drift angles and yaw rate which are excited by large steering forces. Speed reduction yields an overloaded propulsion condition contributing to the risk of cavitation. The influence of the overloaded condition tends to be more significant than the influence of moderate inflow angles on the cavitation characteristics.

The application of pods in the design of vessels sailing very fast, say over 30 knots, is virtually unexplored. Cavitation on the propellers and on the pod houses due to strong propeller induced tangential and radial velocities is supposed to be critical and requires thorough research and development. Since cavitation inception speed is of utmost importance for high performance ships, application of pods must be studied thoroughly because of the more extreme working regimes to which the pods will be exposed and the subsequent larger reduction of cavitation inception speed during manoeuvres compared to conventional propelled high performance ships.
Alternatively the application of other control surfaces or units should be further explored. Steerable flaps at the trailing edge on the strut and additional rudders have been investigated concerning their applicability. The purpose of these additional control surfaces during course keeping at high speeds is preventing the oblique inflow angles on the pods and propellers and excessive use of the pod's steering gear. Experiments and calculations have been conducted with these alternative steering methods. However, both concepts, the steerable flap and also the additional rudders, were up to now not very fruitful.

Based on the discussion of the cavitation issue it is judged that this topic should be evaluated with absolute care. Further research and development will be required to address all observations and solutions should be studied further.

3.3 Turning and turn initiated roll

The standard IMO turning circle manoeuvre identifies the turning ability of a vessel. Statistical data have been derived from a selection of ships with podded propulsion of which information is available at MARIN and is presented in Figure 6. It should be remarked that the presented vessels are optimised concepts through extensive research.

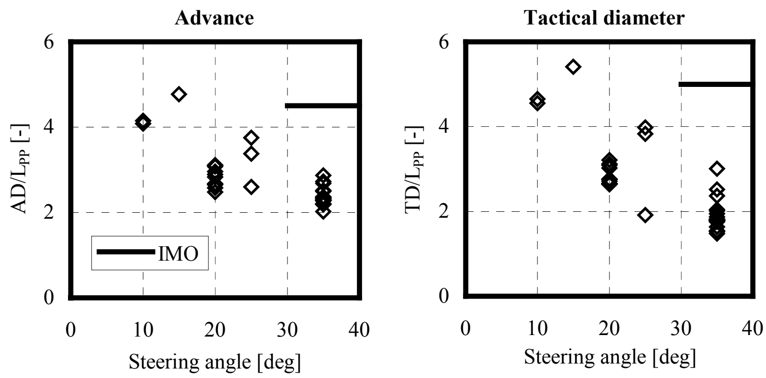

Figure 6. Turning circle statistics of ships with podded propulsion

The turning circle data presented in Figure 6 shows that the advance and tactical diameter are well within the criteria proposed by the IMO. Steering angles were limited to 35 degrees during the presented tests, however the criteria as proposed by the IMO apply to the largest possible steering angles. The turning ability of a podded propelled vessel will therefore be even better than shown in Figure 6.
Based on the experiments conducted with models equipped with either a conventional propulsion unit or a podded propulsion unit, a comparison can be made concerning their inherent turning ability. Figure 7 presents a comparison between the turning circle data of the two propulsion configurations. The meanline represents the situation when the values for both steering units are equal.

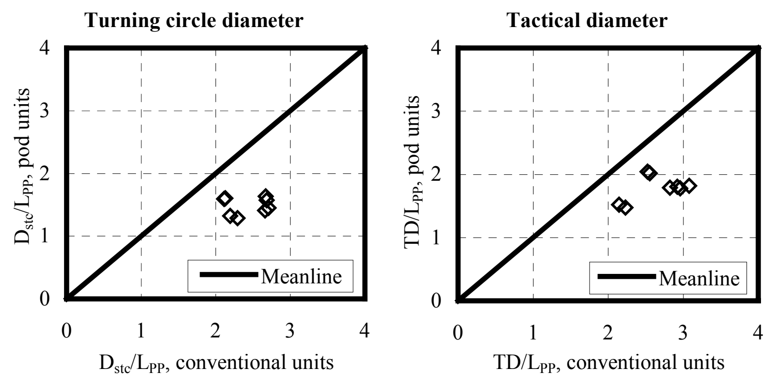

Figure 7. Turning circle data of ships equipped with podded or conventional propulsion units

It clearly shows that the turning ability of the vessels with the podded propulsion is better than the vessels with the conventional propeller-rudder arrangement. Clarifications for this superior turning ability can be ascribed to larger steering forces generated by the pod units, see Figure 11, and the larger speed loss. As a result of these large steering forces, larger drift angles and high speed loss were measured in the steady turning circle.

Turning ability itself is clearly not a problem when judging the applicability of podded propulsion. In current research, the roll behaviour while manoeuvring is the centre of attention. Especially for high speed vessels and vessels with a low GM value, heel is of importance. The effect works in two ways:

- High turning rate can cause large gyration forces and thus large roll motions
- Heel angles effect the turning rate and the course stability

The effect of roll motions on the manoeuvrability of a vessel has been studied and presented by for example Son and Nomoto (1981), Oltmann (1993) and Kijima and Furukawa (1998).

The importance of this issue related to the application of podded propulsion can be presented best using the statistics of heel angles, available at MARIN, that are endured by podded propelled vessels while manoeuvring, see Figure 8.

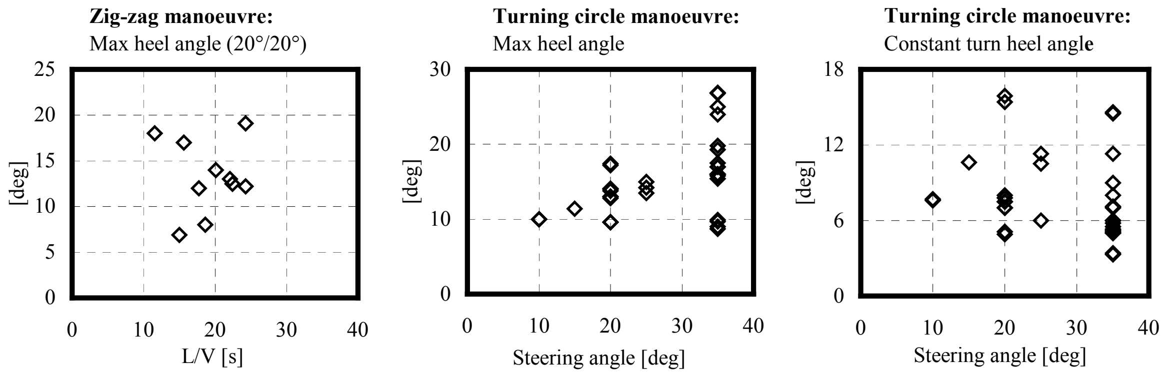

Figure 8. Roll angles during zig-zag and turning circle manoeuvres

At high speeds and large steering angles the maximum roll angles can go up to 28 degrees and the constant turn heel angles up to 17 degrees. The IMO does not provide recommendations regarding roll angles, but maximum roll angles while manoeuvring above 13 degrees and constant roll angles while turning above 8 degrees are thought to be very large. From the comparison studies, the relations presented in Figure 9 show how the roll angles during manoeuvres for both concepts correlate.

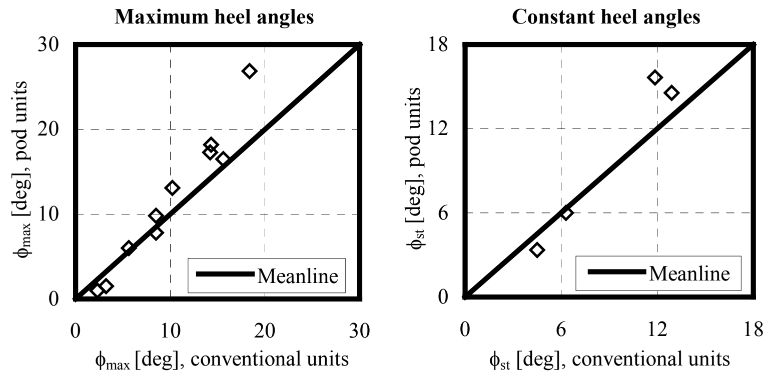

Figure 9. Roll angles while manoeuvring of ships equipped with podded or conventional propulsion units

Figure 9 shows that in general higher roll angles were measured for the vessels equipped with the podded propulsion. After thorough analysis of the results the differences in roll angles are judged to be best attributed to the following non-similarities between the comparable models:

- GM value
- Difference in hull shape, for example V shaped and extreme pram shape sections in the aft ship
- Steering rate of application of rudders or pods

- Force initiated by the steering unit

The heel angle ϕ obtained during turning is related to the instantaneous speed of the vessel U, the metacentric height $\overline{GM}$ and the turning diameter D_{stc}. Using basic transverse stability considerations this relation can be presented as follows:

$$\frac{\sin\phi \cdot g \cdot \overline{GM} \cdot D_{stc}}{U^2} = k$$

in which g is the gravity acceleration and k an almost constant factor. The applicability of the described relation was evaluated and it has been found out that the k-factors could not be derived as purely constant, disputing the liability of the relation. The relation however presents the trend sufficiently in order to study the relevant phenomena.
In theory, the GM value can be modified for any design without adapting the hull lines by modifying the KG value, being the vertical position of the centre of gravity. The influence of the hullshape on the roll behaviour is related to the following aspects:

- The metacentric height can be influenced by the hull shape. Within the same block ($L_{PP}{\cdot}B{\cdot}T$) the metacentric height can be modified by changing waterline area and the displacement volume.
- The drifting and yawing characteristics of the hull form will influence the speedloss and yaw rate while turning. In the above equation, it can be seen that the instantaneous speed U and the yaw rate, inversely related to the turning diameter D_{stc}, will influence the roll behaviour significantly.
- It is known that a pram shaped vessel has an inherent strong roll-yaw coupling. In comparison to a more V-shaped aft ship a sort of cambered waterline line is observed already at small heel angles for extreme pram shaped hull forms. Due to this cambered underwater body a hydrodynamic side force and yawing moment are introduced. This coupling will yield a built up of yaw rate and heel angle while turning. The trend is very pronounced for ships with a significant fore and aft asymmetry. Most high-speed ships have a bulbous bow for resistance optimisation and a pram type aft body. When this is combined with a low GM value, a significant roll and steer coupling will exist. This issue is applicable to the statistics presented in this paper.

The rate of steering application influences the roll behaviour significantly at each execute. In Figure 8 and Figure 9 very large heel angles can be observed occurring at the moment of a rudder or pod execute. The maximum roll angles during a turning circle and a zigzag manoeuvre are very related to this steering rate. It has also been observed during measurement that a vessel was excited in its natural period of roll due to a higher steering rate, introducing very large roll angles. Especially at high speeds it is advisable to avoid large heel angles due to a large steering rate. The problem is that the steering rate should match the classifications required for any azimuthing propulsion gear. A criterion applicable to tugs as well as high speed vessels should be disputed based on the different sailing characteristics and application of both vessel types.

3.4 Course keeping in waves

The course keeping behaviour of vessels equipped with podded propulsion sailing at high speeds in calm water, has been discussed in a previous paragraph. Evaluating the coursekeeping ability under environmental loads such as wind but especially waves will add interesting issues to the discussion.

A comparison study has been conducted with a vessel equipped with either a conventional propeller-rudder arrangement or a podded propulsion arrangement. In stern quartering waves it was observed that the concept with pods had better course keeping capabilities than the conventional propulsion concept. The steering band that will be used in 95% of the cases was approximately 30% smaller for the podded propulsion concept. Also smaller course deviations were measured. The absolute differences were however judged to be small. It should be noted that the steering rate of the podded propulsion concept was higher. The steering unit was therefore more active and able to respond quicker on dynamical wave loads.

4 Manoeuvring in confined waters

4.1 Steering forces at zero speed

Several model tests have been conducted in which the forces generated by pods were compared to forces generated by comparable rudders. In these cases, the ship model has been kept the same and the pods were replaced by rudders or specific aft ship designs were made for the pod configuration as well as for the propeller-rudder configuration, such that a more realistic comparison was possible.

In the figure below, Figure 10, an example is given of the longitudinal and lateral forces generated on the ship by the pods or rudders as a function of the steering angle for the bollard pull condition. Because during the bollard pull condition all steering force is generated by the propeller thrust, the longitudinal force F_x and lateral force F_y have been made non-dimensional by the propeller thrust T_p.

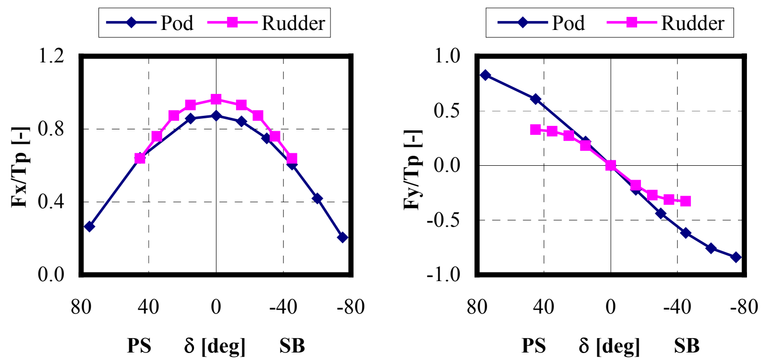

Figure 10. Longitudinal (left) and lateral (right) forces on the ship

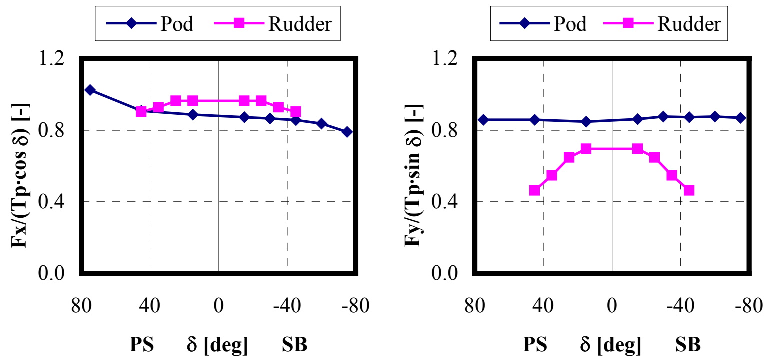

Figure 11. Longitudinal (left) and lateral (right) force coefficients

Based on these graphs the following conclusions can be drawn:

- In both cases, the thrust of the propeller is the same. However, it is seen that the longitudinal forces generated when using a rudder are found to be larger, indicating less thrust deduction for the ship with rudders. The reason for this is the set-up of the pod and rudder configurations.
- The slope of the curve for the longitudinal force is steeper for the rudder than for the pod configuration. This indicates a larger drag coefficient for the rudder than for the pod, even though the thrust of the pod propeller is not directed longitudinally anymore. When dividing the non-dimensionalised longitudinal force by the cosine of the steering angle δ, Figure 11 presented below is found. In these graphs, it is seen that the forces generated by the pod are almost horizontal and therefore are directed conform the direction of the propeller thrust.
- The lateral forces generated by the pod are larger than those generated by the rudder. Additionally, stall appears on the rudder at about 35°, while stall on the pod does not occur, due to

the fact that the force is directed in the direction of the propeller thrust. It is seen that at 45° of steering angle, the force generated by the pod is about twice the force of the rudder.
- The slope of the curve for the lateral force is steeper for the pod than for the rudder configuration. This indicates a higher "lift coefficient" for the pod than for the rudder.

4.2 Crabbing

For ships such as cruise ships or ferries, the crabbing ability is of major importance for the operability and effectiveness of the ship. When the ship is able to berth without any outside assistance, not only time is saved but also money in terms of tug fees. Therefore, for these types of ships, the crabbing ability should be investigated in the early stages of the design, to verify the bow and stern thruster capabilities and possibly the design of the superstructure.
Quadvlieg and Toxopeus (1998) have given examples of criteria that may be used to judge the crabbing ability of a ship in the early design stage. Additionally, the standard crabbing experiments as they are conducted at MARIN are described.

The standard set-ups for crabbing experiments with ships with pods and ships with conventional propellers and rudders are visualised in Figure 12. For experiments close to the quay, the side of the basin is used to model the quay structure. The experiments are in general conducted in three phases:
- Captive tests to obtain the forces and moments that can be generated by the devices.
- Wind tunnel tests to obtain the forces and moments for each wind direction.
- Combining the results of the previous two phases in order to obtain the crabbing ability of the ship.

During the experiments, two modes of operation can be distinguished: berthing or unberthing operation. In general, it is found that the unberthing mode is the most critical situation.

For conventional ships, one propeller is set to the so-called backing mode, while the other propeller is set to the balancing mode, cancelling the longitudinal force. The rudder behind the balancing propeller is set to several angles to obtain the relation between the steering angle and the generated forces and moments on the ship. During several projects, it was found that when operating close to the quay during unberthing operations, the best procedure was to set the quayside propeller to the backing mode and the other propeller to the balancing mode. When using the bow thruster in this case, the propeller slipstream coming from the backing propeller is blocked between the quay wall and the side of the ship, generating a pressure field, helping the ship to leave the quay.

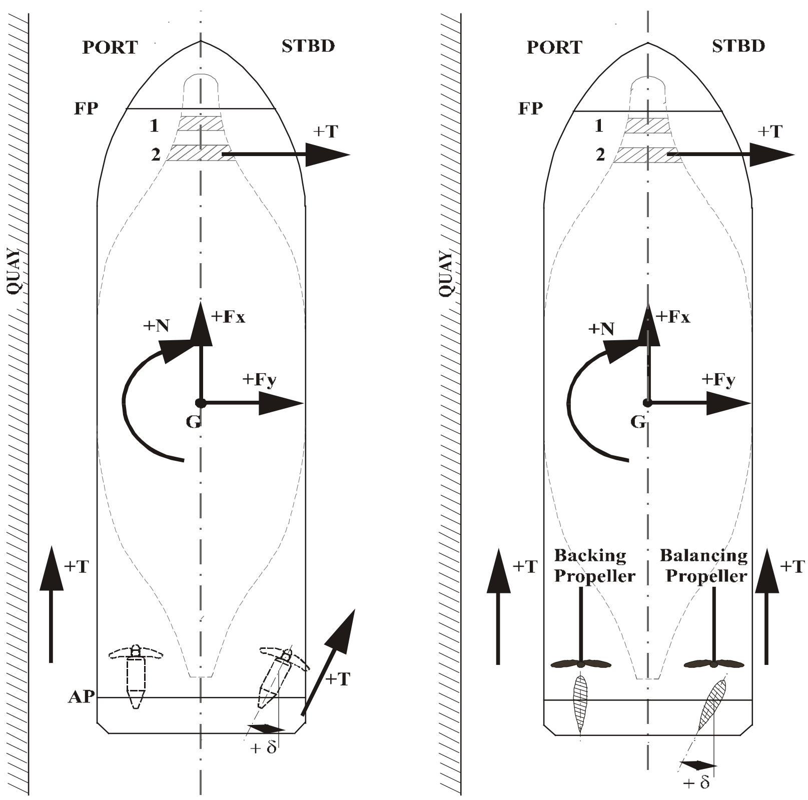

Figure 12. Set-up and sign definition for crabbing tests

For ships with pods, more flexibility is available in positioning the angle of both pods. In general, the angle of the quay side pod is varied, while the other pod, running at the same RPM, is used to cancel the longitudinal speed. In general, it is found that the optimum results for unberthing are found when the quay-side pod is directed with the trailing edge slightly aft of perpendicular to the quay (between 75° and 90° of steering angle) and the other pod directed with the trailing edge slightly forward (at about 90° to 120°).

When comparing the results of crabbing experiments with conventional steering arrangement and experiments with pods, in general it is found that the results for ships with pods are much more consistent than for conventional ships. This is mainly caused by the strong interaction between the conventional propulsion working in backing-balancing mode, creating a strong current between the quay and the ship. For ships with pods, this interaction is not introduced, which simplifies the operation of the ship during crabbing manoeuvres considerably.

Additionally, it became clear that for the conventional ship, the best crabbing results are found when using almost the complete amount of installed power. When using pods, only a limited amount of power is required. For example, some results show that to obtain about the same transverse force in combination with a pure sideways motion (zero yawing moment) about 75% of the installed power is required for the conventional ship against about 30% for the ship with pods. This not only means fuel savings, but also reduces the impact of the ship on the environment, such as quay erosion.

Because of the consistent and straight-forward results of the ship with pods, it is possible to combine the results of the captive experiments with wind tunnel results and obtain the so-called crabbing ability footprint, indicating the limiting wind speeds for each direction in which pure sideways crabbing is possible. In Figure 13, an example is given of such a crabbing ability footprint.

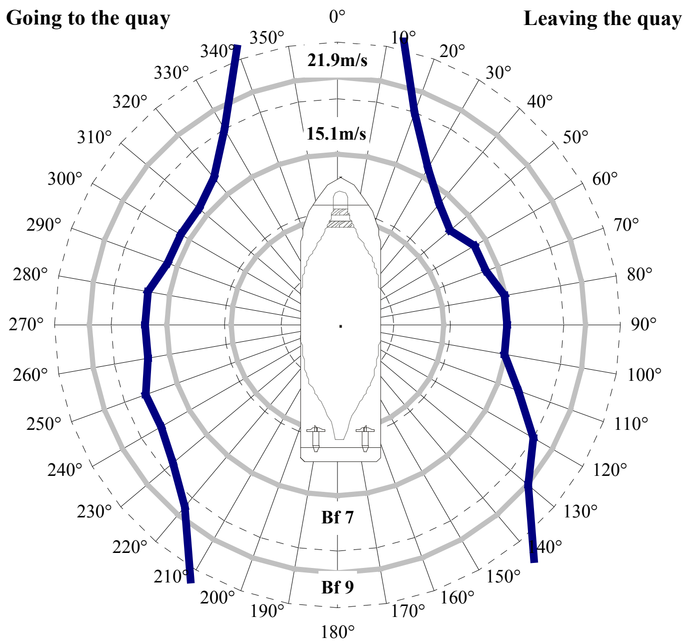

Figure13. Crabbing ability plot for a ship with pods

From the example crabbing ability plot, the following observations can be made:

- Crabbing in bow or stern winds poses no problems.
- Going to the quay can be done in stronger winds than when leaving the quay.
- Going to the quay is possible in winds up to Bf 7, irrespective of the direction of the wind.
- Leaving the quay is possible in winds up to Bf 7, except for bow quartering winds.

4.3 Low speed manoeuvring

The use of pods during slow speed manoeuvring differs significantly from the use of conventional steering arrangements. The helmsman has the possibility to rotate the pods in all directions and may use positive as well as negative propeller revolutions. For twin-podded ships, the steering angles of the pods are uncoupled, such that a large number of degrees of freedom is available, possibly confusing inexperienced helmsmen. When steering a ship, basically two state variables should be controlled: the speed of the ship and the heading of the ship.

Therefore, guidelines for operation of podded ships during slow speed manoeuvring were developed in the past using simulator studies. During these studies, the most comprehensive mode of operation of the pods was examined. One possible solution was to control speed and heading independent of

each other. In general, the ship was sailed with the pods running at the same RPM and positioned at an angle of about 45° with respect to the ship's centreline, with the trailing edges of the pods turned inward. It was proposed to control the speed of the ship by maintaining pod revolutions, but by reducing the angle of the pods. To control the heading of the ship, the RPM of one pod was increased while the RPM of the other pod was decreased with a corresponding amount. With this approach, the heading of the ship remained constant when controlling the speed and vice versa.
During the simulator studies and the subsequent full-scale operation of the ship, it was concluded that this approach provided a comprehensive, efficient and safe procedure of sailing the ship at low speeds in confined water.

5 Design guidelines

Based on the assessment of the applicability of podded propulsion in the design of high performance craft, as described in this paper, design guidelines can be composed. Relevant and significant guidelines are presented in the following paragraphs.

5.1 Hull form design.

As discussed it is observed that currently vessels outfitted with podded propulsion have extreme pram shaped frames in the aft ship. The necessity of these frame shapes is dependent on structural considerations. From a hydrodynamics point-of-view it needs to be further investigated which aft ship shape has the best all-round hydrodynamic characteristics that satisfies the ship design compromise. Manoeuvring, seakeeping and powering assessments should be made in such an evaluation. For instance, research indicates that the course keeping ability of V shaped sections in the aft ship tends to be better than for extreme pram shapes. Compromises to the pod design and innovative ways of installation of the pods could be required.
Another aspect of the hulldesign related with the subject is the centre-line skeg design, if applicable. A large skeg is recommended from a course keeping point of view. Turning ability is judged to be no problem due to the large steering forces. Larger skegs will also reduce large drift angles and yaw rates diminishing the heel angles. Disadvantages of the application of large centre-line skegs could be the interference with the pods at high steering angles. Especially in the crabbing situation the pods can be fully shielded by a large skeg. Another steering procedure could be used to avoid this problem. For each separate application a compromise should be made to the design of a centre-line skeg between course keeping abilities and crabbing abilities. In general, extending the centre skeg aft to about 2.5% of the length of the ship forward of the aft perpendicular provides sufficient lateral area, without compromising the crabbing ability.

5.2 Implementation of pod units in the hull design.

The way of orientating the pods under the vessel could be further optimised. In Figure 14 an example is presented of orientating pods under a vessel with V-shape sections. In this configuration the pods will loose some steering efficiency but will introduce a heeling moment while steering that counteracts the heeling moment initiated by the gyration and drift forces. The feasibility of such a configuration should be further examined through structural and hydrodynamic research. Significant improvements could be made by exploring this topic.

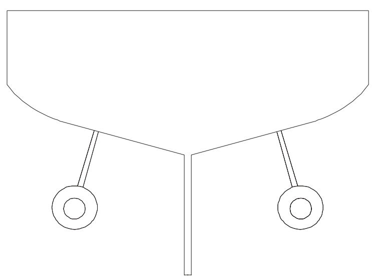

Figure 14:Orientation of pods

5.3 Pod design.

Several pod designs are nowadays spotted on the market according to different concepts unique for each manufacture. The concepts differ among other aspects, in strut design, number of propellers and presence of nozzles. It is judged that the steering efficiency could be further optimised by adapting the following parts of the unit:

- changing the torpedo and strut design
- adding fins
- adding steerable flaps for course keeping

Complications could be met regarding installation and constructive issues by changing the geometry of the pods. Suitable solutions should be found through constructive as well as hydrodynamical research.

The cavitation behaviour of the podded propulsion system is judged to be critical if pods are applied at higher speed ranges. Alternative control surfaces could be implemented in the design to avoid large angles of attack while course keeping and turning at high speed. However, previous research into additional rudders or steerable flaps has not proved to be successful up to now. Furthermore, optimisations of the propeller design as well as the strut design could prevent or reduce the occurrence of cavitation.

When using pods that can not rotate, as is done in some of the current designs of very large cruise vessels, the naval architect should beware of the fact that only part of the available power in the ship will be used for steering. This may reduce the manoeuvrability considerably compared to ships with all units movable. In these cases further manoeuvring assessments in the early design stages are required in order to ensure sufficient manoeuvring capacity of the ship.

5.4 Preventive measures against large roll motions.

In order to prevent large heel angles when steering at high speeds with a vessel equipped with podded propulsion unit(s), the following measures should be taken care of:

- Provide sufficient intact stability.
- Restrict large steering angles and steering rates when sailing at high speeds. Install a steering control system that only allows large steering angles and steering rates during slow speed or emergency manoeuvres.
- Increase the resistance to drift and yaw by adding course stabilising surface such as a (enlarged) centre-line skeg.
- Explore the possibility of an unconventional orientation of the pods as described in paragraph 5.2.

Furthermore, it is proposed that IMO should provide criteria regarding acceptable heel angles during manoeuvring and should require model tests and/or trials to demonstrate compliance with these criteria.

5.5 Ensuring sufficient crabbing ability

In order to ensure sufficient crabbing ability, it should be noted that due to the large forces that can be generated and available power of the pod units, the bow thrusters will be the limiting factor during crabbing operations. To reduce the forces in the bow of the ship, the centre of the lateral wind area of the ship can be shifted aft.

6 Conclusions

Implementing pods into the ship design potentially increases the performance of the ship in several areas comprising among others powering and manoeuvring. However, when not taking the appropriate measures, the success of the design with pods is not guaranteed. Already in the early design stage, the naval architect should recognise the areas of concern. From a manoeuvring point of view, it is found that large heeling angles can occur due to the large steering forces of the pods compared to conventional rudders. Additionally, due to the up to now rather conventional hull forms, the podded ship might suffer from course instabilities.

Extensive research during the past 10 years has shown that all difficulties can be overcome when recognised and dealt with in the early design stages. In this paper, the differences between conventional steering arrangements and pods are presented. Design guidelines are given to aid the naval architect to avoid the problems that are related to the application of podded propulsors. However, although these guidelines will help in avoiding problems during the operation of the ship, hydrodynamic evaluation using detailed calculations or model tests will still be required to avoid unforeseen situations.

References

Hämäläinen, R. and Heerd, J. van (2001). Triple Pod Propulsion in the World's Largest Ever Cruise Liner. *Practical Design of Ships and Other Floating Structures*, Shanghai, China.

IMO Resolution A.751 (18) (1993), *Interim Standards for Ship Manoeuvrability*.

IMO Draft MSC Circular 644 (1994), *Explanatory Notes to the Interim Standards for Ship Manoeuvrability*.

Kijima, K. and Furukawa, Y. (1998). Effect of Roll Motion on Manoeuvrability of Ship. *International Symposium and Workshop on Force Acting on a Manoeuvring Vessel*, Val de Reuil, France.

Kurimo, R. (1998). Sea Trial Experience of the First Passenger Cruiser with Podded Propulsion. *Practical Design of Ships and Mobile Units*, The Hague, The Netherlands.

Lepeix, R. (2001). Hydrodynamic Trends in Hull Lines of Podded Driven Large Cruise Vessels. *Practical Design of Ships and Other Floating Structures*, Shanghai, China.

Oltmann, P. (1993). Roll - An Often Neglected Element of Manoeuvring. *International Conference on Marine Simulation and Ship Manoeuvrability*, St. John's, Canada.

Pustoshny, A.V. and Kaprantsev, S.V. (2001). Azipod Propeller Blade Cavitation Observations During Ship Manoeuvring. *CAV2001 Fourth International Symposium on Cavitation*, Pasadena, USA.

Quadvlieg, F.H.H.A. and Toxopeus, S.L. (1998). Prediction of Crabbing in the Early Design Stage. *Practical Design of Ships and Mobile Units*, The Hague, The Netherlands.

Son, K. and Nomoto, K. (1981). On the Coupled Motion of Steering and Rolling of a High Speed Container Ship. *Journal of the Society of Naval Architects of Japan*, Vol. 150, 232-244.

Energy Dissipation in Sandwich Structures during Axial Crushing

Jesper Urban
Section for Maritime Engineering, Department of Mechanical Engineering,
Technical University of Denmark, DK-2800 Kgs. Lyngby, Denmark
E-mail: ju@mek.dtu.dk

Abstract

The purpose of this paper is to investigate the energy dissipation in sandwich structures during axial crushing. Axial crushing tests on six sandwich elements are described. The sandwich elements consist of a polyurethane core and E-glass/Polyester skin. The elements compare to full-scale structural elements in fast sandwich vessels. A nonlinear laminate analysis is presented. It includes the nonlinear shear behavior of the matrix material, coupled with a failure criteria by Tsai-Wu or Chang-Chang and progressive failure. The analysis is compared to experiments on $[\pm 45]_s$ *laminates. The skins from the sandwich elements are analyzed and key results are used in the following FE-crushing simulation. Two of the crushing tests are simulated with the explicit finite element software LS-DYNA. The key results are load-end shortening relationship and the energy dissipation. Good agreement between the numerical predictions and the experiments are obtained.*

1 Introduction

The development of passenger transportation at sea has grown fast over the past ten years and a new class of high speed crafts (HSC) sailing plus forty knots has emerged. These structures are highly optimized with respect to weight. New light weight materials such as Aluminum and Composites have been used instead of common ship building steel, to obtain sufficient weight reductions.

Luckily we have only experienced a small number of accidents so far, but the accidents show a devastating impact on the structure during grounding or collision incidents. Grounding accidents show structural damage extending the entire length of the vessel and it is widely accepted by the industry, that damage in a HSC is expected to be much more severe than in conventional vessels.

Knowledge about the ultimate strength and the energy absorbtion in a sandwich structure during axial crushing or tearing, is crucial in the design for safety during collision or grounding. Many of the existing models for energy absorbtion have been developed for ductile steel or aluminum and so far very little is known about energy absorbtion in sandwich structures. It is therefore obvious that more research is needed in this area, in order to be able to establish mathematical models for the crushing behavior of sandwich structures, that can lead into new design guidelines.

This paper is mainly concerned with axial crushing of sandwich structures. In order to investigate the crushing behavior of a sandwich structure, six full-scale sandwich elements have been tested

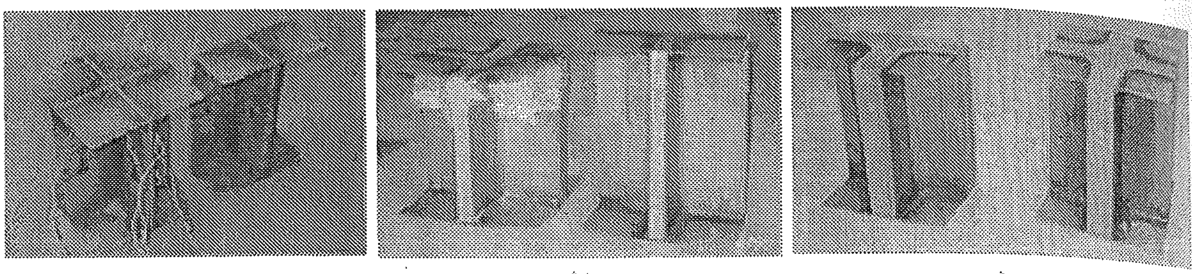

a) b) c)

Figure 1: *a) Small sandwich elements, GRX1 and GRT1. b) Medium-sized sandwich elements, GRX2 and GRT2. c) Large sandwich elements, GRT3 and GRX3.*

at DTU in Denmark. The elements compare to the structural elements from three high speed sandwich vessels. The elements have been compressed far beyond the ultimate load capacity, into the post buckling response and the load and end-shortening relationship has been measured. The observed crushing behavior has been described in details and pictures of characteristic failure modes are shown.

An analytical part is presented, containing a nonlinear laminate analysis of the skin. This includes the nonlinear shear behavior of the matrix, coupled with failure criteria by Chang-Chang and Tsai-Wu and progressive failure until ultimate failure. Comprehensive tests to determine the properties of the laminates have been made. The analysis is compared to experiments and key results are selected and used in the finite element simulation. Furthermore the critical wrinkling load and the global buckling stability are analyzed.

The crushing response of the sandwich elements are simulated with the nonlinear explicit finite element program LS-DYNA. Crushing forces from the numerical simulations are compared with the experimental results.

2 Experiments

Full-scale crushing experiments were performed on structural sandwich elements. The tests were made at DTU in Denmark. The test facility includes several hydraulic presses, tensile testing machines as well as data logging equipment.

2.1 Sandwich Specimens

Three different sizes of specimens were tested. These sizes correspond to three types of sandwich vessels. A cruciform element and a T-element for each size were tested, giving a total of six specimens. The T-element corresponds to the deck-panel and side-panel connection of the vessel, while the cruciform corresponds to the deck-panel and longitudinal bulk-head connection. The specimens are shown in Figure 1. The medium- and large elements, as opposed to the small elements, have an extra enforcement of laminate layer near the flange connection. The dimensions of the elements are given in Table 1.

The specimens were manufactured at the Danish shipyard *Danyard*, using hand lay-up. The sandwich structures were assembled of an E-glass/polyester laminate and a Polyurethane core. The core is manufactured by *Diab* and is an open cell foam core. The laminate was manufactured with a $[0, -45, +45, 90]_s$ lay-up configuration.

	GRX1	GRT1	GRX2	GRT2	GRX3	GRT3
Height (mm)	165	165	365	365	550	550
Width (mm)	125	125	300	300	500	500
Material thickness and area						
Core (mm)	5	5	30	30	90	90
Skin (mm)	3	3	3	3	3	3
Thick skin (Extra reinforced skin) (mm)	-	-	6	6	6	6
Skin area (mm^2)	830	1410	3074	4956	4830	6978
Core area (mm^2)	900	1175	12900	16860	55714	71645
Total area (mm^2)	1730	2585	15974	21816	60544	78623

Table 1: *Dimensions of sandwich elements.*

2.2 Crushing behavior during test

The crushing behavior of the small sandwich cruciform is shown in Figure 2.

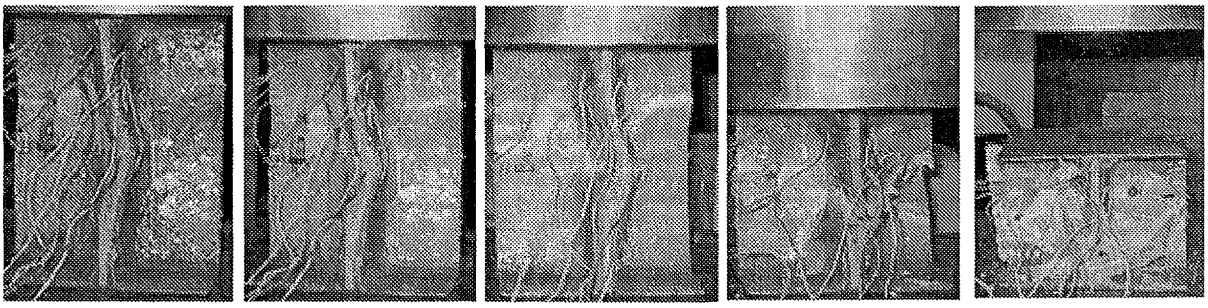

a) b) c) d) e)

Figure 2: Crushing behavior of small sandwich cruciform element, GRX1. (a) Forming of white bands of damaged laminate after exceeding the ultimate load carrying capacity. (b) Extensive buckling of the flange and de-bonding of core and skin. (c) Skin damage is spreading and core fracture begins. (d) Laminate is disintegrating and a complex contact mode of fractured parts of laminate and core appears. Pieces of matrix is breaking off. (e) Finally a very complex mixture of disintegrated laminate and core fracture appears.

The crushing behavior of the small sandwich elements can be divided into four parts.
a) In the initial part of the crushing scenario, the element is compressed axially without any out-of-plane deformations of the flanges. The structure is globally stable. When the ultimate load carrying capacity of the element is reached, the laminate fails and white bands of damaged laminate is formed across the flange. No indication, in terms of buckling or cracking noise, is given prior to reaching the ultimate load.
b) In the second part of the scenario, out-of-plane buckling of the flange appears and the white bands of damaged laminate are spreading out.
c) The extensive buckling and bending of the flanges induces shear failure in the core and delamination of the laminate. The laminate damage is still fairly located in the initial formed white bands.
d) Further compression leads to a complete breakage of the laminate and a complex contact mode of disintegrated laminate and fractures appears.

Sub-figure 2(e) shows the specimen after 100mm compression and many different damage modes appear. The final structure is best described as a complex mixture of fractured pieces of laminate and fractured core material. Figure 3 shows the crushing behavior of the medium cruciform.

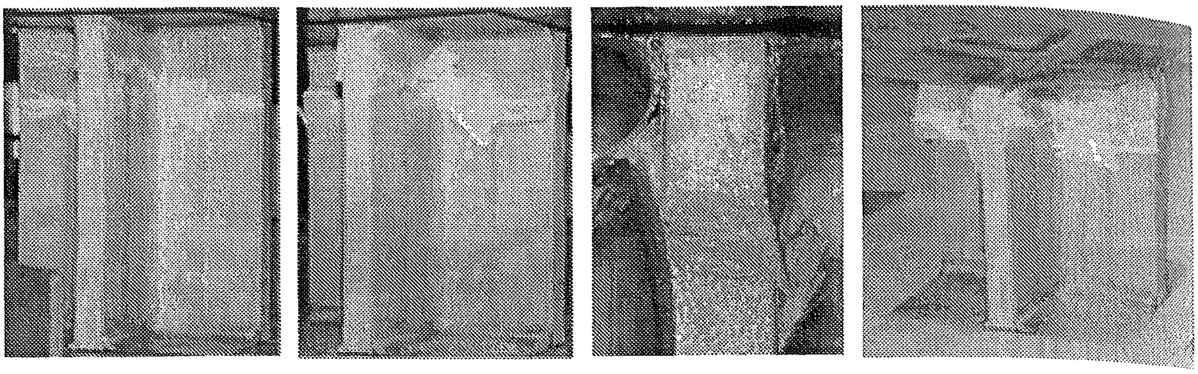

a) b) c) d)

Figure 3: Crushing behavior of medium sandwich cruciform element, GRX2. (a) Forming of white bands of damaged laminate after exceeding the ultimate load carrying capacity. (c) The damaged zone in the laminate is spreading out. The skin is delaminating and fracturing. The skin and core is de-bonding. (d) The core is compressed locally where the skin has failed. (e) Finally a very complex mixture of disintegrated laminate and core compression appears.

The crushing behavior of the mid-sized elements is different from the small elements, in the sense, that the flanges has less tendency to buckling. However, the crushing scenario has many similarities with the small elements. The crushing response can be divided into three steps.
a) Initially the element is compressed axially without any out-of-plane motions of the flanges. No indication of damage is given prior to reaching the ultimate load carrying capacity and failure of the laminate is seen as white bands of damaged laminate.
b) Further compression leads to delamination followed by de-bonding and finally breakage of the laminate. Sub-figure 3(c) shows the deformation of the core material. The core is crushed very locally, where the skin has failed and note that the core is crushed without expanding horizontally, i.e. a typical zero poison ratio behavior in the plastic region. The core is more or less un-deformed in the areas where the core is still supported by intact skin.
c) The behavior of the cruciform becomes very chaotic at deep crushing, with a complex mixture of laminate failure, fracture, delamination, de-bonding and crushed core material. The crushing behavior of the large elements is similar to the medium sized elements.

It is general for the six tested elements that no indication of failure is given prior to reaching the ultimate load. When reaching the ultimate load, white bands of damaged laminate is formed across the flanges with a width of the bands varying from $1cm$ to $5cm$. It is also general that the tested elements show a large degree of global stability and none of the elements fail in a global buckling mode. However, the cruciform elements experience more global stability than the T-elements due the symmetry of the cruciform.

2.3 Measured crushing force

Figure 4 show the crushing forces for the small sandwich elements.

The sandwich elements behave linearly until the ultimate load carrying capacity. No indication of failure before reaching the ultimate load is seen in the initial part of the load curve. Exceeding the ultimate capacity, the load decreases to a load level of 20% to 30% of the ultimate load. After further compression the load increases again. The energy absorbed in the small T-element is considerably lower than in the small cruciform element. Figure 5 show the crushing forces for the medium sized sandwich elements.

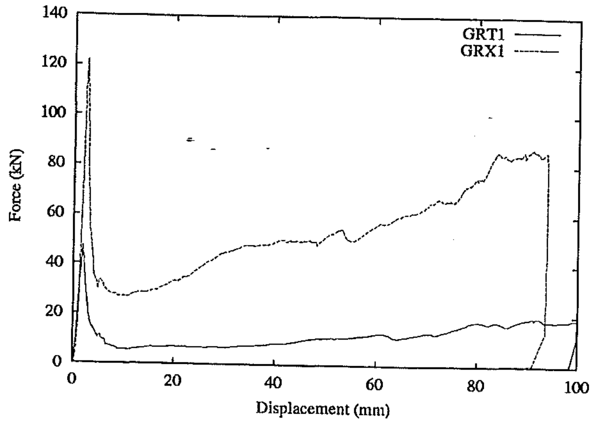

Figure 4: Crushing forces of small sandwich elements, GRT1 and GRX1.

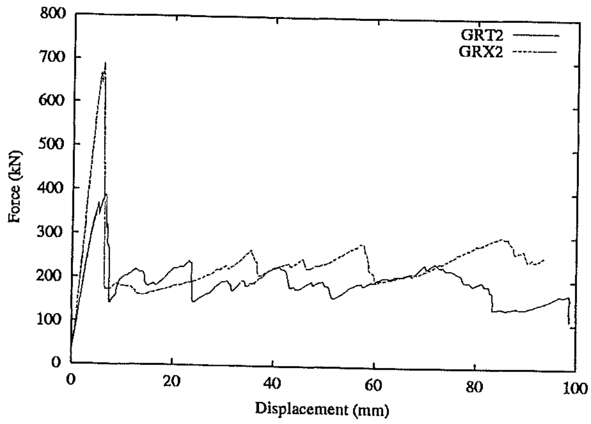

Figure 5: *Crushing force of medium sized sandwich elements, GRT2 and GRX2.*

The elements show a linear behavior until a load level of approximately 80% of the ultimate load. A small decrease in the load just before reaching the maximum capacity may indicate a first-ply failure. The force drops significantly after exceeding the maximum load and continues at a more or less constant level. The ultimate force of the T-element is significantly lower than the cruciform, while the force level at further compression is comparable for the two. Figure 6 show the crushing forces for the large sandwich elements.

The behavior of the large cruciform element is linear until a load level of 80% of the ultimate load, when some nonlinearity is seen in the load curve. The nonlinear behavior indicates elastic buckling, either global Euler buckling or skin wrinkling, failure in the skins or a combination of buckling and failure. A similar behavior is seen for the T-element. The force level drops with 25 to 50% after reaching the ultimate load and continues to decrease at further compression.

3 Analytical crushing calculation

Methods for predicting the ultimate strength of a sandwich element are presented in the following. This includes a nonlinear laminate analysis based on classical laminate theory with a nonlinear shear behavior, and progressive failure. The progressive failure is based on the Tsai-Wu [6] and Chang-Chang [2] failure criteria. Methods for predicting local and global buckling stability are also presented.

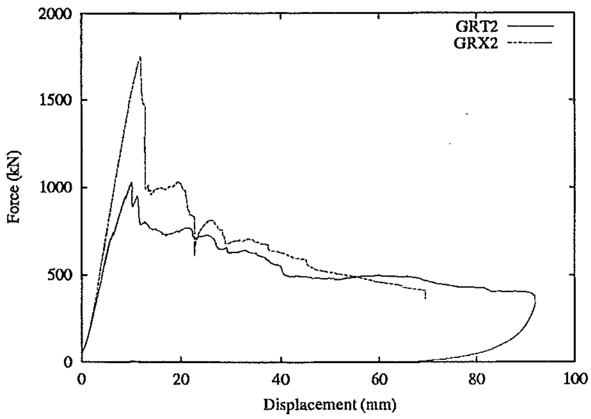

Figure 6: *Crushing force of large sandwich elements, GRT3 and GRX3.*

3.1 Nonlinear shear behavior

Composites normally show a linear elastic behavior until fracture in the fiber direction and in the transverse direction. It has been found that material nonlinearities in fiber-reinforced laminated composites can mostly be related to the nonlinearity in the shear-stress and shear-strain relation in each ply. As a result, a $[\pm 45]_s$, laminate exhibit strongly nonlinear behavior, while a $[0/\pm 45/90]_s$ laminate behaves almost linearly. A description of the nonlinear shear-stress/shear-strain relation is given by Hahn and Tsai [3] as

$$\gamma_{12} = \frac{1}{G_{12}}\sigma_{12} + \alpha\sigma_{12}^3 \tag{1}$$

An analysis of a composite laminate consisting of k unidirectional plies is shown in the following. Because of the nonlinearity in the shear equation, an incremental method must be applied in the laminate analysis. This means that the load has to be applied in a number of steps. The method is used to analyze the experiments performed on $[\pm 45]_s$ laminates. Assuming plain stress condition, the elastic properties of a unidirectional composite are given as

$$E_{11}, E_{22}, \nu_{12}, \nu_{21}, G_{12}, \alpha$$

where α is a parameter describing the nonlinearity in shear. The constitutive relation for the unidirectional ply in the n'th load step is

$$\left\{ \begin{array}{c} d\sigma_{11} \\ d\sigma_{11} \\ d\sigma_{12} \end{array} \right\}_{n+1}^{k} = \left[\begin{array}{ccc} Q_{11} & Q_{12} & 0 \\ Q_{12} & Q_{22} & 0 \\ 0 & 0 & Q_{66,n+1} \end{array} \right]^{k} \left\{ \begin{array}{c} d\varepsilon_{11} \\ d\varepsilon_{22} \\ d\gamma_{12} \end{array} \right\}_{n+1}^{k} \tag{3}$$

where

$$\begin{aligned} Q_{11} &= E_{11}/(1-\nu_{12}\nu_{21}) \\ Q_{22} &= E_{22}/(1-\nu_{12}\nu_{21}) \\ Q_{12} &= \nu_{12}E_{11}/(1-\nu_{12}\nu_{21}) \\ Q_{66,n+1} &= G_{12}^{*} \end{aligned} \tag{4}$$

Note that Q_{11}, Q_{22} and Q_{12} remains unchanged throughout the analysis while $Q_{66,n+1}$ is a reduced shear modulus. Transformation of the above constitutive relation into a rotated coordinate system is given as

$$
\begin{aligned}
\overline{Q}_{11,n+1} &= U_{1,n+1} + U_{2,n+1}cos(2\theta) + U_{3,n+1}cos(4\theta) \\
\overline{Q}_{22,n+1} &= U_{1,n+1} + U_{2,n+1}cos(2\theta) + U_{3,n+1}cos(4\theta) \\
\overline{Q}_{12,n+1} &= U_{4,n+1} - U_{3,n+1}cos(4\theta) \\
\overline{Q}_{66,n+1} &= U_{5,n+1} - U_{3,n+1}cos(4\theta) \\
\overline{Q}_{16,n+1} &= \tfrac{1}{2}U_{2,n+1}sin(2\theta) + U_{3,n+1}sin(4\theta) \\
\overline{Q}_{26,n+1} &= \tfrac{1}{2}U_{2,n+1}sin(2\theta) - U_{3,n+1}sin(4\theta)
\end{aligned} \tag{5}
$$

where

$$
\begin{aligned}
U_{1,n+1} &= \tfrac{1}{8}(3Q_{11} + 3Q_{22} + 2Q_{12} + 4Q_{66,n+1}) \\
U_{2,n+1} &= \tfrac{1}{2}(Q_{11} - Q_{22}) \\
U_{3,n+1} &= \tfrac{1}{8}(Q_{11} + Q_{22} - 2Q_{12} - 4Q_{66,n+1}) \\
U_{4,n+1} &= \tfrac{1}{8}(Q_{11} + Q_{22} + 6Q_{12} - 4Q_{66,n+1}) \\
U_{5,n+1} &= \tfrac{1}{8}(Q_{11} + Q_{22} - 2Q_{12} + 4Q_{66,n+1})
\end{aligned} \tag{6}
$$

The membrane stiffness of the laminate is now given as

$$A_{ij,n+1} = \sum_{k=1}^{N} \overline{Q}^{k}_{ij,n+1} t_k, \quad i,j = 1,2,6 \tag{7}$$

where t_k is the thickness of the k'te ply. The relation between membrane forces and the global strains of the laminate is given as

$$dN_{ij,n+1} = A_{ij,n+1} d\epsilon_{ij,n+1} \tag{8}$$

The laminate strain increments are calculated in each load step by

$$d\epsilon_{ij,n+1} = A^{-1}_{ij,n+1} dN_{ij,n+1} \tag{9}$$

where $dN_{ij,n+1}$ is the applied load increment and $A^{-1}_{ij,n+1}$ is the inverse of the in-plane membrane stiffness. Note that the above equation is only valid for a symmetric laminate ($B = 0$). The laminate strain increments are then transformed into the local coordinate system for each ply and the total strains in each ply are calculated as

$$\epsilon^{k}_{ij,n+1} = d\epsilon^{k}_{ij,n+1} + \epsilon^{k}_{ij,n}, \quad i,j = 1,2,6 \tag{10}$$

The normal stress increments, σ_{11} and σ_{22} are obtained directly from Eq.(3), while the shear stress σ_{12} has to be calculated from the nonlinear shear equation Eq.(1). The reduced shear modulus is then given as

$$G^{*}_{12} = \frac{\sigma_{12,n+1}}{\gamma_{12,n+1}} \tag{11}$$

This value is inserted into Eq.(4) until convergence of the reduced modulus is obtained and the next load increment can be applied.

The nonlinear laminate analysis can know be coupled with either a Tsai-Wu or a Chang-Chang failure criterion. The failure criterion has to be applied in each load step for each ply and progressive failure can be determined. The following section shows how the failure criteria and the nonlinear laminate analysis can be coupled with progressive damage.

3.2 Progressive failure in laminates

The strength of a uni-directional composite ply is characterized by five constants

X_t - Longitudinal tensile strength
Y_t - Transverse tensile strength
X_c - Longitudinal compressive strength
Y_c - Transverse compressive strength
S_c - Shear strength

The strength properties are obtained from uni-axial tensile and compressive tests of composite specimens. At least five specimens are needed to obtain the strength parameters. X_t, Y_t, X_c and Y_c are obtained by tensile and compressive tests on uni-directional composites in respectively the fibre-direction and 90 degrees to the fibre-direction, while the shear strength S_c, is obtained by tensile test on a symmetric $[\pm 45]_s$ composite. It must be emphasized that the failure criteria are only valid for uni-directional composites.

In a nonlinear progressive analysis of a laminate, the load is applied in increments. After applying a load increment, failure is checked in each of the plies. According to Chang-Chang [2], four different failure modes are considered. These are

- Tensile fiber mode failure
- Compressive fiber mode failure
- Tensile matrix mode failure
- Compressive matrix mode failure

If one of the four failure modes is detected, the corresponding stiffness is reduced or simply deleted. The four failure modes are given below.

Tensile fiber failure:

$$\sigma_{11} > 0 \qquad \text{then} \qquad \left(\frac{\sigma_{11}}{X_t}\right)^2 + \beta\left(\frac{\sigma_{12}}{S_c}\right) - 1 \begin{cases} \geq 0 & \text{failed} \\ < 0 & \text{elastic} \end{cases} \tag{12}$$

At failure the following modulus and poisons ratios are set to zero.

$$E_{11} = E_{22} = G_{12} = \nu_{21} = \nu_{12} = 0, \quad \text{at failure}$$

With β=1 we get the original criterion of Hashin [4] in the tensile fiber mode. For β=0 we get the maximum stress criterion, which is found to compare better to experiments.

Compressive fiber failure:

$$\begin{aligned} \sigma_{11} < 0 \qquad & \text{then} \qquad \left(\frac{\sigma_{11}}{X_c}\right)^2 - 1 \begin{cases} \geq 0 & \text{failed} \\ < 0 & \text{elastic} \end{cases} \\ & \text{with} \qquad E_{11} = \nu_{21} = \nu_{12} = 0, \quad \text{at failure} \end{aligned} \tag{13}$$

Tensile matrix failure:

$$\begin{aligned} \sigma_{22} > 0 \qquad & \text{then} \qquad \left(\frac{\sigma_{22}}{Y_t}\right)^2 + \left(\frac{\sigma_{12}}{S_c}\right)^2 - 1 \begin{cases} \geq 0 & \text{failed} \\ < 0 & \text{elastic} \end{cases} \\ & \text{with} \qquad E_{22} = \nu_{21} = G_{12} = 0, \quad \text{at failure} \end{aligned} \tag{14}$$

Compressive matrix failure:

$$\sigma_{22} < 0 \qquad \text{then} \qquad \left(\frac{\sigma_{22}}{2S_c}\right)^2 + \left[\left(\frac{Y_c}{2S_c}\right)^2 - 1\right]\left(\frac{\sigma_{22}}{Y_c}\right) + \left(\frac{\sigma_{12}}{S_c}\right)^2 - 1 \begin{cases} \geq 0 & \text{failed} \\ < 0 & \text{elastic} \end{cases}$$

$$\text{with} \qquad E_{22} = \nu_{21} = \nu_{12} = G_{12} = 0, \quad \text{at failure} \tag{15}$$

The failure in the compressive and tensile fiber mode can also be based on the Tsai-Wu [6] criterion given as

$$\frac{\sigma_{22}^2}{Y_c Y_t} + \left(\frac{\sigma_{12}}{S_c}\right)^2 + \frac{(Y_c - Y_t)\sigma_{22}}{Y_c Y_t} - 1 \begin{cases} \geq 0 & \text{failed} \\ < 0 & \text{elastic} \end{cases} \tag{16}$$

The failure modes for the compressive and tensile matrix failure are however, still based on the Chang-Chang failure criterion. In the following this coupled criterion is refereed to as an Tsai-Wu criterion.

The two failure criteria by Tsai-Wu and Chang-Chang, the nonlinear laminate analysis and the progressive failure were implemented in a computer program.

3.3 Laminate analysis

In order to test the program, comprehensive tensile and compressive tests were performed on 30 pieces uni-directional (UD) plies and 30 $[\pm 45]_s$ laminates. From the tests on the UD-plies, the following key results of ply stiffnesses and strengths were found. $E_{11} = 21.4$ GPa, $E_{22} = 6.4$ GPa, $\nu_{12} = 0.266$, $\nu_{21} = 0.079$, $\alpha = 3.0(Pa)^{-3}10^{-24}$ and $X_t = 388$ MPa, $X_c = 299$ MPa, $Y_t = 23$ MPa, $Y_c = 83$ MPa, $S_c = 76$ MPa.

A nonlinear laminate analysis with progressive failure is performed on a $[\pm 45]_s$ laminate. The laminate is loaded until total failure for 3 different loading angles in tension and compression. The results are compared with experiments in Figure 7.

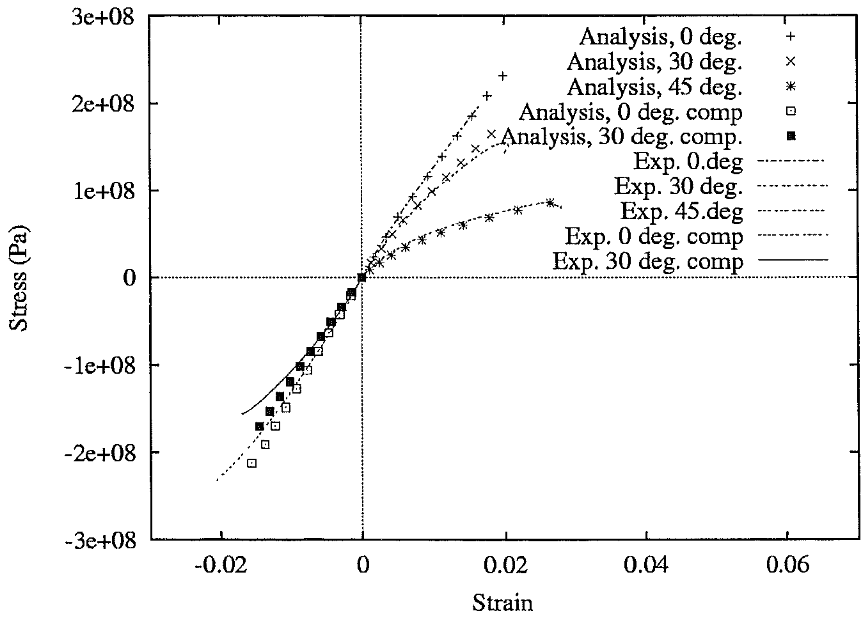

Figure 7: *Non linear laminate analysis with progressive damage vs. experiments.*

The laminate analysis compares well with the experiments in tension. The analysis correctly predicts the nonlinear behavior at 45 degrees as well as the progressive failure and the decrease in stiffness for 0 degrees loading angle. The initial behavior in compression is well predicted by the analysis, while the theory underestimates the nonlinear behavior in large compression. However, the maximum compressive stress capacities still compares well with the experiment. The nonlinear laminate analysis can now be used to calculate the ultimate in-plane capacity of the $[0, -45, 45, 90]_s$ skin, that is used in the sandwich elements. Note that the above mentioned analysis only consider in-plane loading and not a moment loading. The maximum compressive capacity is calculated to -206 MPa.

3.4 Wrinkling

In a sandwich structure, it is not sufficient only to check the global buckling stability of the structure. A local stability phenomena of the skin can be present and this is called "face wrinkling". Face wrinkling may be viewed as buckling of a thin column (the faces) supported by a continuous elastic medium (the core). Hoff [5] and Allen [1] has derived equations for the critical load. Both derivations assume the mid-plane of the core to remain flat and the models are based on an energy method and a differential equation method respectively.

The critical face stress for a symmetrical shape of the wrinkling is according to Hoff [5]

$$\sigma_{cr} = 0.91\sqrt[3]{E_f E_c G_c} \tag{17}$$

where E_f, E_c and G_c are the face modulus, the core modulus and the core shear modulus respectively. The above formula is only valid if the zone, h is smaller than half the core thickness, $t_c/2$. For the anti-symmetrical case the following result is obtained

$$\sigma_{cr} = 0.91\sqrt[3]{E_f E_c G_c} + 0.33 G_c \frac{t_c}{t_f} \tag{18}$$

Allen [1] found in his analysis the critical stress to be

$$\sigma_{cr} = 0.78\sqrt[3]{E_f E_c G_c} \tag{19}$$

which is close to the result obtained by Hoff. Hoff also showed that the equations can be used for a wide panel with predominantly plane strain, by substituting the corresponding E-modulus by

$$E^* = \frac{E}{1-\nu^2} \tag{20}$$

The critical wrinkling stresses calculated for the skins in the sandwich elements are shown in Table 2.

Sandwich element	GRT1	GRX1	GRT2	GRX3	GRT3	GRX3
σ_c (sym.) (MPa)	209	209	209	209	209	209
σ_c (anti-sym.) (MPa)	126	126	143	143	196	196

Table 2: *Critical wrinkling stresses.*

The anti-symmetrical case gives the lowest buckling stress.

3.5 Global stability

Before the laminate capacity and critical wrinkling stresses can be compared to the experiments, the global stability of the elements has to be determined. The stability limit for a panel with three simply supported edges and one free edge is given below.

$$\sigma_c = \frac{1}{a^2 h}\left(D_{11}\pi^2 + 12\left(\frac{a}{b}\right)^2 D_{66}\right) \tag{21}$$

where D_{11} and D_{66} is the bending stiffnesses of the plate, h is the thickness on which the load is acting, and a and b are the length and width of the panel.

Sandwich element	GRT1	GRX1	GRT2	GRX3	GRT3	GRX3
σ_c (MPa)	351	351	262	262	461	461

Table 3: *Global buckling stresses.*

4 Numerical simulation of axial crushing of sandwich elements

Numerical simulations of the crushing behavior of the two large sandwich elements, GRT3 and GRX3 are shown in the folowing. The nonlinear explicit finite element program, LS-DYNA has been used for this purpose. In the finite element models of the sandwich elements are included the core, modelled with solid elements and the skin, modelled with shell elements. The shell element used for the skin, is an under-integrated Belytschko-Tsai shell element, with one in-plane integration point and 4 nodes. In order to treat laminate theory, 8 through-the-thickness integration points are used. A constant-stress solid element with one integration point and 8 nodes is used for the core. The core material model includes the three stages of the compressive behavior, namely the initial elastic behavior until yield, the following yielding of the core, with a constant plateau-stress with zero Poison's ratio and finally the densification stage at which the core is fully compressed and acts like a solid material. The skin material model includes the $[0, -45, 45, 90]_s$ stacking sequence of the laminate. The material model of the skin is based on classical laminate theory, including the nonlinear shear behavior of the matrix. The progressive ply failure of the skin is included in the calculation by reducing the stiffness of failed plies. The stiffness is set to zero when failure is predicted by the Chang-Chang or the Tsai-Wu failure criteria.

The skin is completely removed, by an "element-kill"-routine, when all plies have failed. The interface of the core and the skin is modelled with a contact surface. De-bonding of the skin and core is controlled by a quadratic shear and normal stress failure criteria. Contact after de-bonding is controlled by contact surfaces. The boundary conditions acting on the finite element model are, a support plate on which the sandwich element rests and a ram plate that compresses the element at a given displacement rate. A contact surface between the ram plate and the top plate of the element and a contact surface between the lower plate of the element and the support plate, transfer forces into the structure.

Figure 8 shows a picture sequence of the numerical simulation of the axial crushing of the large sandwich cruciform.

The numerical simulation shows many similarities compared to the experiments. Prior to the ultimate load, the laminate buckles and forms short waves. After reaching the ultimate load, the laminate fails and elements are deleted across the flange. The core is compressed locally were the laminate has failed. Further compression leads to spreading of the damage zone in the laminate. De-bonding between the laminate and the core is seen. The sandwich element is still globally stable after 100mm of compression. The crushing force is compared with the experiment in Figure 9

The calculated crushing force for the cruciform element compares well with the experiment in the elastic range. The elastic stiffness of the element is calculated correct. The ultimate force

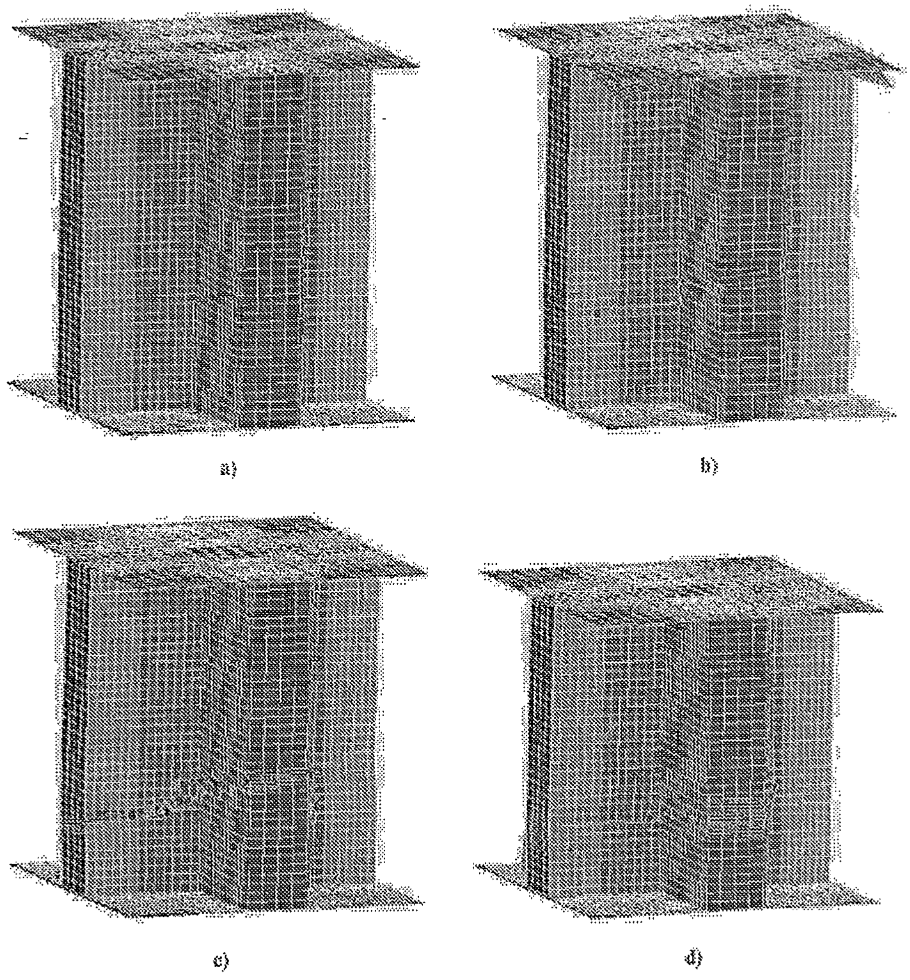

Figure 8: Numerical crushing simulation of large sandwich element, GRX3. (a) Short waves are formed just before laminate fails. (b) Laminate fails horizontally across the flange. The core is compressed locally where the laminate has failed. (c) Damage is spreading out in the laminate. Laminate is de-bonding from the core. (e) Final stage of the crushing.

is calculated to $1500kN$, while the ultimate force from the experiment is measured to $1750kN$. The crushing behavior after the ultimate load also compare well with the experiment. The mean crushing force after $70mm$ is $596kN$ and $699kN$ in the experiment. Figure 10 shows the crushing force from the numerical simulation of the large sandwich T-element, GRT3.

The ultimate load for the T-element determined by the numerical simulation compares well with the experiment. The ultimate load from the simulation is $1060kN$, while the measured ultimate load is $1028kN$. It is seen that the crushing force after reaching the ultimate load is significantly under-predicted in the numerical model. The mean crush force from the simulation is $352kN$. $539kN$ is measured in the experiment. The two simulations indicate that a damage mechanism contributing to the absorbed energy during crushing, is not being captured by the numerical model. However, the two simulations still show that the overall characteristic crushing behavior is reproduced by the numerical model.

5 Comparison

In the following are compared the results from experiments, laminate analysis and numerical simulations. The ultimate loads and the mean crushing forces from the experiments and numerical

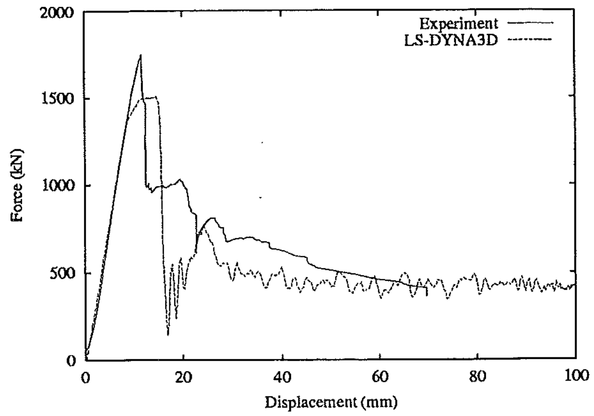

Figure 9: *Crushing force for large sandwich cruciform GRX3. Numerical simulation vs. experiment.*

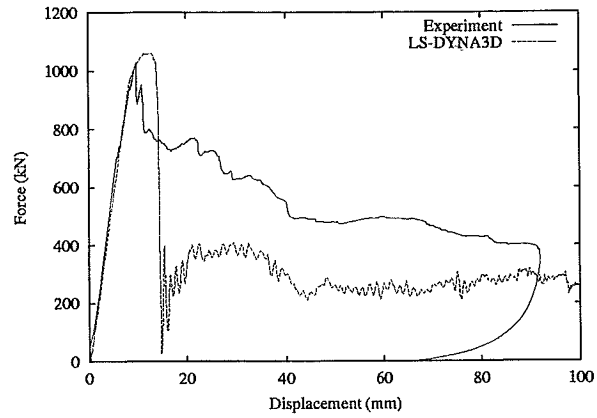

Figure 10: *Crushing force for large sandwich T-element, GRT3. Numerical simulation vs. experiment.*

analysis are given in Table 4 for the six specimens

	GRT1	GRX1	GRT2	GRX2	GRT3	GRX3
$F_{ult,exp}$ (kN)	47	122	388	688	1028	1749
$F_{ult,LS-DYNA}$ (kN)	-	-	-	-	1060	1500
$F_{mean,exp}$ (kN)	12	54	191	239	539	699
$F_{mean,LS-DYNA}$ (kN)	-	-	-	-	352	596

Table 4: *Ultimate load and mean crushing force.*

If subtracting the load carried by the core from the ultimate load, the maximum stress in the skin can be calculated as

$$\sigma_{u,skin} = \frac{F_{ult} - \sigma_{core} A_{core}}{A_{skin}} \tag{22}$$

where σ_{core} is the plateau-stress of the core material after exceeding the yield stress, A_{skin} is the cross-sectional skin area and A_{core} is the cross-sectional area of the core. In Table 5 are shown the mean crushing forces and the ultimate loads, normalized with the cross-sectional area of the skin and total cross-sectional area, respectively.

The difference between F_{ult}/A_{skin} and $\sigma_{u,skin}$ is small and therefore only a minor part of the ultimate load is taken by the core. The variation in maximum stress in the skin is significant, it

	GRT1	GRX1	GRT2	GRX2	GRT3	GRX3
F_{ult}/A_{skin} (MPa)	54	85	116	130	183	251
$\sigma_{u,skin}$ (MPa), (σ_{core}=2.6 MPa)	54	85	115	130	183	224
F_{mean}/A_{total} (MPa)	7	21	12	11	9	9

Table 5: *Normalized forces.*

varies from 54 MPa in GRT1 to 224 MPa in GRX3. It is seen that the mean crush force for the medium sized and large elements is in the range of 9 to 12 MPa, while the mean crushing force for the small T-element is significantly below this level and the small cruciform is significantly above this level.

Now the local laminte strength, the critical wrinkling stress and the global critical stress can be compared. The critical wrinkling stress is lowest of three cases and this will be the cause for initial failure of the sandwich elements.

Failure stress	GRT1	GRX1	GRT2	GRX3	GRT3	GRX3
Experiment (MPa)	**54**	**85**	**115**	**130**	**183**	**224**
Analysis						
Laminate analysis (MPa)	206	206	206	206	206	206
Wrinkling (MPa)	126	126	143	143	196	196
Global stability (MPa)	351	351	262	262	461	461
Min. of analysis (MPa)	**126**	**126**	**143**	**143**	**196**	**196**
Difference	133%	48%	24%	10%	7%	13%

Table 6: *Experiment, laminate analysis, wrinkling, global stability.*

The analytical prediction of the ultimate load is inaccurate for the small sandwich elements, while the prediction for the medium sized and large elements is within 24% of the experimental values.

6 Conclusion

Six tests have been performed on sandwich elements. Load and end-shortening relations and strains have been measured. Characteristic failure modes and a typical crushing behavior have been described. Four failure modes have been identified for the small sandwich elements and three characteristic modes for the medium and large elements. The first part of the crushing response is linear elastic until the ultimate load is reached. No indication of failure is seen prior to reaching the ultimate load. Damage is seen in the laminate skins as white bands across the flange. The load decreases dramatically after reaching the ultimate load. In the second part, the damage is spreading out, delamination and de-bonding is seen. The core is compressed axially where the laminate has failed to support the core. The final stage of compression is complex, with a mixture of laminate failure, fracture, delamination, de-bonding and compressed core material. A characteristic mean crushing stress varying between 9 and 12 MPa is found for the medium and large elements. No characteristic value was found for the small elements. The ultimate stress level in the skin varied between 54 and 251 MPa and no characteristic values for the ultimate load was found from experiments.

A nonlinear laminate analysis was presented. The analysis is based on an incremental laminate theory. The analysis includes the nonlinear shear behavior of the matrix coupled with either a Tsai-Wu or a Chang-Chang failure criteria. Progressive failure is included in analysis by evaluating the damage in each ply in each load step. Selected stiffness properties are deleted in case of a ply failure. The analysis was compared with experiments performed on $[\pm 45]_s$ laminates. The analysis compare well with the response in tension, while in compression the nonlinear behavior is under predicted. The ultimate stresses compare well with experiments in tension and compression. The laminate analysis is used to predict the strength of the sandwich skins. The wrinkling stress and the global buckling stress have been calculated for the six elements. The ultimate strength of the elements is predicted within 24% of the experimental values for the medium and large elements, while for the small elements the prediction is inaccurate.

A numerical analysis of the crushing behavior of the two large sandwich elements was performed with LS-DYNA. The simulation includes the material behavior of the core and the laminate. Progressive failure is included in numerical model, as well as de-bonding between the skin and core. Correct boundary conditions are applied to the model by using contact surfaces. The numerical simulation of the crushing behavior of the two large sandwich elements, revealed that the main characteristic crushing behavior can be reproduced by the finite element model. These include, progressive laminate failure, core compression, de-bonding between the core and skin, contact between core and skin after laminate failure and friction.

The initial elastic response compared very well with the experiments, which means that the correct stiffness of the plies was used. Note that these were based on experiments on single UD-plies. It was shown that the ultimate strength is predicted within 15% while the mean crushing force is underestimated with up to 35%. This indicates that an important damage mechanics is not taken into account in the simulation.

Acknowledgement

Diab has delivered core and fiber material for the specimens. *Danyard* has manufactured the specimens. The support is gratefully acknowledged. This work is a part of the *Nordsandwich* project.

References

[1] H.G. Allen. *Analysis and Design of Structural Sandwich Panels.* Pergamon Press, Oxford, 1969.

[2] F.K. Chang and K.Y. Chang. A progressive damage model for laminated composites contaning stress concentrations. *J. of Composite Materials*, 21:834–855, 1987.

[3] H.T. Hahn and S.W. Tsai. Nonlinear elastic behavior of unidirectional composite laminate. *J. of Composite Materials*, 7:102–110, 1973.

[4] Z. Hashin. Failure criteria for unidirectional fiber compsites. *J. of Applied Mechanics*, 47:329–334, 1980.

[5] N.J. Hoff and S.E. Mautner. Buckling of sandwich type panels. *J. of Aeronautical Sciences*, 12:285–297, 1945.

[6] S.W. Tsai and E.M. Wu. A general theory of strength for anisotropic materials. *J. of Composite Materials*, 5:58–80, 1971.

Experimental Investigation on Propeller Wash Using Laser Doppler Anemometry

D. Wang dazheng.wang@ncl.ac.uk,
M. Atlar mehmet.atlar@ncl.ac.uk
E. Mesbahi ehsan.mesbahi@ncl.ac.uk

Department of Marine Technology,
University of Newcastle upon Tyne

An experimental investigation into propeller wash in cavitation tunnel has been carried out using Laser Doppler Anemometry (LDA). The velocity field around and inside the slipstream of a model propeller operating behind a catamaran demi-hul, was measured using LDA to assess potential impact of the propeller's slipstream on beds of waterways, quay walls or banks of waterways. A simple mathematical model was also presented to evaluate additional wash waves to be caused by the propeller in the free surface. Within the limitation of the restricted tunnel measurement space, some preliminary conclusions on the propeller wash have been reached.

Key Words: Wash, Propeller slipstream, LDA

1. Introduction

With the increased volume of high-speed transport in waterways, more and more attention has been paid to various destructive effects caused on marine environment. The effect of wash caused by fast ships is one of such environmental problems and has been recently attracting greater concern.

Part of the wash effect is associated with the "surface waves" generated by the vessel's hull and its propulsor, which could have significant destructive effects on shoreline, river banks and marine life as well as endangering or causing problems to the small pleasure boat industry, anglers, fishermen and holidaymakers [1], [2], [3]. Other part of the wash effect is associated with "flow field induced by the propeller's slipstream and hull bottom flow". As fast vessels navigate in rivers, channels or shallow waters, the velocities induced by the propeller slipstream and hull bottom will attack on the bed and banks of rivers, harbour basins and channels, and could create significant erosive force on them [4], [5].

The main objective of the present study is to investigate the role of the propeller in wash effect by measuring velocity field around a model propeller operating behind a representative hull model using and LDA system in a cavitation tunnel. Therefore series of flow measurements have been taken with the model of a medium speed catamaran ferry in the Emerson Cavitation Tunnel of Newcastle University [6]. Based upon the analyses of the measurements certain conclusions have been reached, which may be limited to the case studied here as well as subjected to the limitation introduced by the physical dimensions of the cavitation tunnel facility.

The investigation presented in this paper is part of the activities of the Newcastle University within the project FLOWMART (**F**ast **LO**w **W**ash **MA**ritime **T**ransportation). This project is being sponsored by the European Community under the Framework-5 (Growth) Programme during 1999-2002 [7]. The research carried out in FLOWMART primarily focuses on the development of practical design tools for quantifying the wash effects by utilising the state of the art knowledge and combination of numerical modelling, model experiments and full-scale measurements using latest technologies.

2. Experimental Set-up

In the following, a brief description of the experimental set-up used for the wash measurements is presented. This includes the scaling of the ship and its propeller, in fitting to the cavitation tunnel which has a predefined measuring section, as well as the arrangement of the LDA system to be able to measure a reasonable part of the propeller wake region within the limited measuring space of the tunnel.

2.1 Dummy hull

The flow measurement is taken around the model of a 35m medium speed catamaran used in the FLOWMART project. In order to simulate the flow around the hull, especially the aft section of the ship, a dummy hull had to be manufactured. Dummy hull is a close representative of a proportionally scaled hull model used in medium size cavitation tunnels. Due to constraints of the tunnel measuring section (L x B x H = 3.0m x 1.21m x 0.80m, resp.), only part of the aft body of the ship, which approximates to about 33% Lpp, was correctly scaled with a scale ratio of 7.39. The fore body of the model was re-designed to match the aft. Furthermore, only the port demi-hull of the catamaran was modelled with the assumption that the flow around each demi-hull of the catamaran is symmetric. It is also assumed that interaction between the demi-hulls can be ignored from the point view of propeller hydrodynamics, though this interaction will effect the demi-hull wake distribution. This assumption is reasonable when the free surface is not taken into consideration, which is the case in most of small to medium size cavitation tunnel tests. Finally, although the use of dummy hull would necessitate the simulation of the nominal wake flow, this exercise was not carried out due to unavailability of this data when the measurements were taken.

2.2 Propeller model

The main parameters of the full-scale propeller and the model propeller are as follows [8]:

	Full scale	**Model**
Diameter	1.7(m)	230(mm)
Hub diameter	0.34(m)	46(mm)
Pitch ratio at 07R	0.762	0.7616
Blade area ratio	0.85	0.85
Number of blades	5	5
Scale ratio	7.39	1

2.3 LDA system, arrangement and measurement mesh

- *LDA system*

The LDA used in the Emerson Cavitation Tunnel is a two-dimensional system and utilises back-scattering mode for flow measurements. It is a two-component fibre-optic DANTEC system combined with PDA (Phase Doppler Anemometry) facility that can measure particle size characteristics of the flow as well as velocities. Only the LDA facility has been used in this investigation and technical data of the system are given in Tables 1 and 2.

- *Arrangement and setting*

Two components of the flow in a plane can be measured approaching with four-beam laser from one direction at a time. In order to measure the third component of the flow it is necessary to approach from another direction. In the present test set-up, the measurements were taken from the underneath and side windows of the tunnel measuring section. This kind of set-up requires an accurate method to align the traverse set-up corresponding to the two different measurement directions in order to make sure that the measurement volume is coincident for both directions. The set up of the optics and traverse system for both sets of measurements is shown in Figure 1.

In order to make sure that the laser beams focus on the same measuring volume from both directions, it is important to align the traverse of the LDA with the tunnel flow direction by setting a reference point for both directions. This reference point was marked at the tip of the propeller boss cap. The alignment of the LDA with the flow direction was achieved by aligning the traverse of LDA with the side-wall of the measuring section. Within the length of the traverse (950mm), the error of the alignment was in the order of ±0.5 m. Following the alignment of the traverse the origin of the traverse can be easily set by moving the measurement volume to the reference point through computer drive. This procedure was used for setting the origin of the traverse at both locations. The error for setting the origin of the traverse was in the order of ±0.25mm.

- ***The measurement mesh and coordinate system***

The main measurement mesh was in the wake of the propeller, as shown in Figure 2. In the Y - Z plane, a 26 × 26 mesh was set with the origin at the tip of propeller cap. The interval between two nodes is 10 mm in both Y and Z directions. In the X direction, a 26 × 26 mesh in the Y – Z plane was set at 10 mm intervals until a total of 150 mm distance was covered. In addition, three 26 × 26 meshes were set at intervals of 50 mm.

The directions of the coordinate system are also shown in Figure 2. The directions of measured velocities in the three axes are positive when velocities have the same directions with the axes.

3. Propeller velocity field measurements

As the propeller wash is to be determined by the induced velocity field, it is necessary to evaluate the flow field around the propeller. However, this flow field is unsteady and the difficulty in measuring an unsteady flow is that the flow is time dependent. Therefore the time history samples of measurement should be large enough to reach the required accuracy. Generally speaking it is impossible to measure the unsteady flow filed using the LDA technology alone. Although the propeller's velocity field is unsteady, fortunately, it is periodical and can be measured by using the encoder technique. As many velocity samples as required can be collected provided that these samples are collected at the same time in a given period using an encoder. Basically, the function of the encoder is to trigger the measurement process at a specific time in a cycle and this will guarantee each sample is acquired at the same point in time. In the present measurements, the encoder was triggered, at 12'clock position of the first blade, by a Transistor Transistor Logic (TTL) pulse equating to one pulse per propeller revolution.

3.1 Test cases

In order to investigate the propeller wash phenomena in detail, three sets of flow measurements tests were carried out in FLOWMART project as in the following:
A. 3-D nominal wake flow measurement behind dummy hull at propeller disk position;
B. 3-D velocity field measurements behind the propeller in open water and
C. 3-D velocity field measurements behind the propeller with the dummy hull.

As the results from case ***C*** are very similar to those from case ***B*** from the viewpoint of propeller wash, this paper only presents and discusses the test results from case ***C***. The results from case ***A*** will be used to calculate the propeller induced velocity filed from the measured total velocity values. The full report of the above test results can be found in [9], [10]

3.2 Operating condition

The operating condition of the catamaran was 15.2 knots at 1620 RPM of engine through 3.06:1 reduction gearbox or 529 RPM of propeller. The advance coefficient $J = \frac{Vs}{nD}$ is 0.521. As the wake effect was neglected the exact advance coefficient was not critical from the viewpoint of propeller wash in general and therefore, $J = \frac{Vs(1-w)}{nD}$ = 0.50 was chosen for the operating condition.

Prior to the tests carried out behind the hull, open water tests were carried out to obtain hydrodynamic data of the propeller that would allow the accurate setting of the test conditions for behind the hull tests. As the hull changes the flow characteristics of the measuring section, the only reliable method of setting the test conditions is by setting the RPM of the propeller for the required J value and adjusting tunnel speed until the thrust matches the value of the open water test at required J value. In the behind hull condition, the rotation rate at J=0.50 of open water test was chosen and tunnel speed was adjusted to obtain the thrust corresponding to the value at J=0.50 of open water results.

3.3 Cavitation and free surface simulations

In the present tests, the cavitation number was not simulated due to the deformation possibility of plexiglas windows of the tunnel under vacuum. This deformation would result the windows acting like a lens, and as a consequence bending the laser beams, thus reducing the quality and accuracy of the test data. It was also assumed that cavitation would have minor effect on the velocity field of the propeller.

Also no free surface was simulated in these tests because of the limited size of the tunnel measuring section. The free surface was assumed to be replaced by the tunnel ceiling that was similar to the double hull effect. Thus the contribution to wave wash from the propeller could not be included in the present experiments. However a simple mathematical model has been established to evaluate this effect on the free surface later in the paper.

3.4 Relevant parameters setting

The LDA system used in the investigation is an integrated system. Laser, optics and traverse are integrated into one system. The measurement process, data acquisition and data processing are controlled by a software package called "PDA Flow and Particle Software" developed by DANTEC. Optimising of some parameters of the package is essential to obtain the accurate and reliable measurement results described as in the following.

- ***Correction for calibration factor for traverse axis***

3-D traverse of the laser system is driven by computer to position the laser beam to the measurement point. The accuracy of positioning depends on the calibration factor for traverse axis. These calibration factors are set to 80 or 160 by default and they are only valid for the case where laser beam travels in a single medium. For the case of cavitation tunnel, where laser travels from one medium (air) to another (water), one of these factors, whose axis is parallel with laser travel direction, must be corrected by the ratio of refractive indexes of the two mediums, which is 1.344 (water):1 (air).

- ***Optimisation of PDA processor property setting***

The main parameters to optimise are normally the velocity validation and the valid data rate. There are several properties of the PDA that will affect the velocity validation and valid data rate. Among these properties the most significant one is the "High Voltage Property" of the system. This can be set to any value from 0 to 2000 volt individually for every photomultiplier depending on the measured velocity and seeding condition. In the present tests, the typical high voltage range was set to 700 to 1000 volts for channel U1, which was set for X-axis, and 900-1300 volts for channel U2 to achieve more than 70% velocity validation with valid data rate changing from 0.05 to 2.0.

4. Analysis of results

As stated in the Introduction section of the paper, the propeller wash referred here is the wash effect caused by the propeller-induced velocities and this can be further categorised in two types based on how they are generated.

The first type of wash effect is felt under the free surface and directly caused by the propeller induced velocities. When the propeller operates, depending upon the loading condition, it can induce velocities, which could be as large as ship speed, in its surroundings, particularly in its racing column. These velocities can produce considerable erosive forces on the sea/river bed/bank as well as quay wall when ship navigates in the river, channel or harbour.

The second type of wash effect is felt on the free surface as an indirect result of the propeller induced velocities. When the propeller operates in the proximity of free surface, it acts as translating and rotating sources and sinks which will disturb the free surface and produce additional waves. These waves will be superimposed with waves produced by the hull alone to cause wash on coastline or bank of river when ship navigates in the river and channels.

The first type of wash can be evaluated through the measurement of velocities induced by the propeller behind the hull. The velocities measured by this way, however, will be the total velocities including the effect of the hull flow (i.e. nominal wake flow) as well as the propeller induced velocities. Within this framework, the measured nominal wake flow velocities of the dummy hull are presented in the following section (Section 4.1). The propeller wash effect caused directly by the propeller induced velocities is evaluated and discussed in Section 4.2, 4.3 and 4.4 in terms of their effects in the axial, radial and tangential direction, respectively.

The second type of wash effect felt at the free surface is evaluated qualitatively through the amplitude of the axial component of the propeller induced velocities and results are presented in Section 4.5

4.1 The nominal velocities behind dummy hull

Prior to the total velocity field measurements, which would include the propeller's effect, the 3-D nominal wake velocities behind the dummy hull were measured and results are shown in Figures 3 to 5 at the propeller plane. As stated earlier, since no target wake data were available when these tests started, the actual wake flow of the ship was not simulated and it was assumed that this wake difference would not, generally speaking, affect the propeller wash.

4.2 Propeller induced velocity varying in the axial direction

Because of the limited accessibility of the tunnel windows, only 350 mm (about 1.5 propeller diameters) distance at the downstream of the propeller could be measured in the axial direction. The variation of the propeller induced velocities (V_i), which were calculated from the total (U_t) and nominal (U_{wn}) velocities measured (i.e. $V_i = U_t - U_{wn}$), are shown in Figures 6 to 8 and 15. The total velocities were measured at eight points (y, z = -55, -65, -75, -85, -95, -105, -115 and –125 mm) on each of 7 planes located at (x = -29, 7, 47, 87, 117, 167, 217 and 267 mm), while the nominal velocities were also measured at the same points, but only on the propeller disk plane located at x = -57 mm.

Figure 6 shows the variations of average (in time) axial component (Vx) of induced velocities along the axial direction. It seems that, within radii r/R less than 0.7, Vx gradually increases along the axial direction and the maximum value could be as high as the tunnel flow speed (ship speed). Near the tip region, r/R=0.7 to 0.9, Vx fluctuates considerably while outside the racing volume, Vx is very small and close to zero.

Figure 7 presents the variation of average (in time) radial component (Vr) of induced velocities along the axial direction. It shows that Vr will reduce rapidly to zero from negative value at r/R = 0.5 to 0.9, then slightly increases to a certain positive value along the axial direction within the measured distance from the propeller disk.

The variation of the average tangential component (Vt) of the induced velocities are shown in Figure 8, from which, it appears that, within radii r/R less than 0.70, Vt will slightly reduce along the axial direction. Near the tip r/R=0.7 to 0.9, Vt gradually reduces to those outside the racing volume, which is kept nearly unchanged within measured distance along the axial direction.

Figure 15 shows the resultant induced velocity, UR, ($=\sqrt{V_x^2+V_r^2+V_t^2}$), varying along the axial direction. It appears that the UR has the similar trend in variation as the Vx component. From the mid propeller radius to the hub, the magnitude of UR slightly increases and could be the same or higher than the ship speed, depending on propeller loading. When r/R is greater than 0.9, UR will rapidly reduce to about 7% of ship speed at one propeller radius distance at the downstream of the propeller disk, and its magnitude is kept nearly unchanged along the axial direction within the measured distance.

The trend described in the above paragraph suggests that the significant propeller induced velocities remain in the racing volume and their magnitude slightly increase along the axial direction.

The resultant induced velocities could be same as or higher than ship speed depending on the propeller loading. These large velocities in the racing volume along the axial direction might produce large erosive forces on the wall of quay or curved river bank. Outside the racing volume, the resultant velocities will reduce rapidly to about 7% of ship speed (depending on the propeller loading) at one propeller radius downstream of the propeller. It appears that the main contribution to the resultant induced velocities comes from the axial and tangential components.

4.3 Propeller induced velocities varying in the radial direction

Figures 9 to 11 and Figure 16 show trends of the average induced velocities along the radial direction while the trends in time domain along the radial direction are shown in Figures 12 through 14.

Figure 9 presents the variation of Vx along the radial direction. It seems that, on all measured planes, this component rapidly reduces to very small value near the propeller tip.

The variation of Vr along the radial direction is shown in Figure 10. It can be seen that, on plane x=-29 (propeller trailing edge), Vr reaches to a peak value at r/R=0.92 and then gradually reduce to a small value. The variation trends of Vr are similar to the planes at x=7 and 47 though their amplitudes much smaller, and Vr changes its direction near plane at x = 47. On all other planes measured, the average radial induced velocities are much smaller and change very little along the radial direction.

The variation trends of Vt are much similar to those of the axial induced velocities along the radial direction as shown in Figure 11.

Figure 16 shows the resultant velocity (UR) variation along the radial direction. It appears that UR will rapidly reduce to a small value, which is about 7% of ship speed, at r/R = 0.95, and then becomes nearly constant along the radial direction for all planes away from the propeller disk. UR reaches its largest value on the plane at the trailing edge (x= -29), and smallest value near plane x = 47 (about one propeller radius distance from propeller disk) along the radial direction when r/R > 1.0.

From the above observations it appears that, although resultant induced velocities will rapidly reduce to a small value at r/R =0.95 to 1.0 and will remain to be small along the radial direction, UR can still reach to 18% of ship speed at r/R =1.1 to 1.2. This situation will create some concern when ship navigates in very shallow harbour basins or waterways where depth of water may be just above draught of ship. In these cases, shallow water will have significant effect on the propeller induced velocities, which can be estimated as high as the twice the values of those experienced in deep water based on the mirror-image principle.

4.4 Total propeller velocity varying along the circumferential direction

In order to show the propeller disturbance in the circumferential direction, it is thought to be better to present the measured total velocities (i.e. nominal wake velocity + propeller induced velocity) to be able to distinguish the trends in variations.

Figures 12 to 14 show the variation of the total velocities measured at x=-29, which is the plane tangent to the propeller's trailing edges.

Figure 12 shows the variation of the axial velocity component along the circumferential direction for one propeller revolution. This figure clearly shows the variation of this component including the effect of the propeller's five-blade in one revolution. It seems that, near tip region r/R= 0.7 to 0.9, velocities fluctuate considerably, while the variation of the axial velocities gradually turns to be flat from r/R = 0.9 to 1.54. The variation of the radial and tangential components of the total velocities appears to have very similar trends with those of the axial total velocities as shown in Figures 13 and 14.

4.5 Evaluation of wash caused by propeller generated waves

As stated earlier, no free surface was simulated in the present tests. Therefore the wash caused by propeller generated waves can not be evaluated quantitatively from the current investigation. However from Bernoulli's equation and free surface boundary condition, the elevation of free surface can be evaluated as in the following [11]:

$$\eta = -\frac{1}{g}\left(\frac{\partial \phi}{\partial t} + \frac{1}{2}\nabla\phi \cdot \nabla\phi\right) \quad (1)$$

Where η is the elevation of free surface; ϕ is the velocity potential of due to propeller's disturbance; g is gravitational acceleration.

Based on linearized free surface assumption, equation (1) can be simplified as:

$$\eta = -\frac{1}{g}\frac{\partial \phi}{\partial t} = -\frac{1}{g}\frac{\partial \phi}{\partial x}\frac{\partial x}{\partial t} = -\frac{U}{g}\frac{\partial \phi}{\partial x}. \quad (2)$$

Where $\frac{\partial x}{\partial t}$ is ship speed U; $\frac{\partial \phi}{\partial x}$ is the axial component of velocity induced by propeller on the free surface. From equation (2), the amplitude of waves generated by the propeller can be determined by

$$A_w = \eta_{\max} - \eta_{\min} = \frac{U}{g}\left(\frac{\partial \phi}{\partial x}_{\max} - \frac{\partial \phi}{\partial x}_{\min}\right) = \frac{U}{g}A_v \quad (3)$$

Where A_w is the amplitude of wave generated by propeller; $A_v = \left(\frac{\partial \phi}{\partial x}_{\max} - \frac{\partial \phi}{\partial x}_{\min}\right)$ is the amplitude of axial component of induced velocities.

From equation (3), it appears that amplitude of wave will be proportional to the production of ship speed and the amplitude of axial component of the induced velocities. By substituting the propeller induced velocities measured in equation (3), approximate values of the wash velocities induced at the free surface can be obtained.

Figure 17 shows the variation of the axial component of the induced velocities along the axial direction. It seems that A_v will slightly increase along the axial direction.

The variation of A_v along the radial direction is shown in Figure 18. It appears that A_v will rapidly reduce to a small value (4% to 14% of ship speed) at r/R = 1.1. From r/R =1.1 to 1.54 (measured), A_v on all planes will slightly reduce to about 4% of ship speed.

From the above, it seems that A_v would be less than 4% of ship speed (depending on propeller loading) at a distance of one propeller diameter above the propeller shaft axis.

5 Conclusions

Upon the analysis of the results obtained from this study and bearing in mind the physical limitation of the cavitation tunnel, the following conclusions on the effect of propeller wash can be reached:

- Propeller has two potential ways to contribute to wash phenomena that could be destructive for marine environment: In one way, velocities induced by the propeller could directly produce erosive forces on beds of waterways and harbour basins, walls of quay or banks of curved waterways; In other way, the propeller will induce additional disturbances on the free surface that will be combined with the hull generated waves producing destructive effect on the coastlines or banks of waterways.
- The most significant erosive effect from the propeller is expected to occur in the propeller's racing volume where the resultant flow velocities could be as high as the ship speed depending on the propeller loading. The magnitude of these velocities will slightly increase downstream along the shaft axis.
- Along the radial direction, the propeller induced wash velocity will rapidly reduce to a small value near to the propeller tip.

- Although not measured directly, the simple numerical approach applied in this study indicates that the propeller induced waves in the free surface is expected to be quite small (A_v is 4% of ship speed) compared to the wash velocities created in the racing volume.

References

1. Camfield, F. E., Ray, R. E. L., and Eckert, J. W., (1980), " The Possible Impact of Vessel Waves on Bank Erosion", U.S. Department of Transportation, Unites State Coast Guard, Office of Research and Development, Washington, Report No. CG-W-1-80.
2. Kofoed-Hansen, H., and Mikkelsen, A. C., (1997), "Wake Wash from Fasr Ferries in Denmark", FAST97, $th International Conference on Fast Sea Transportation, Sidney, Australia, Vol. 1, pp. 471-478.
3. Hannon M. A., Varyani K. S., (1999), "The Wash Effect of High-Speed Ferries in Coastal and Inland Waterways", International conference on coastal and inland waterways, RINA, London UK.
4. Thom, R.M., A.B. Borde, P.J. Farley, M.C. Horn and A. Ogston. Batelle (1996) "Passenger-only ferry propeller wash study: threshold velocity determinations and field study, Vashon Terminal". Batelle Marine Sciences Laboratory, Report to WSDOT. PNWD-2376/UC- 000.
5. Hamill, G.A., Stewart, D.P.J., Johnston, H.T (1999) "Propeller wash scour near to quay structures". Journal of Waterway, Port, Coastal and Ocean Engineering. American Society of Civil Engineers, Vol. 125 No. 4. pp 170-175
6. Atlar, M., (2000) "A History of the Emerson Cavitation Tunnel and its Role in Propeller Cavitation Research", NCT'50 International Conference on Propeller Cavitation, Newcastle upon Tyne, UK.
7. European Commission, Community Research (2002) "The Competitive and Sustainable Growth Programme 199-2002 Project Synopses: Land Transport and Marine Technologies", RTD activities supported under the Growth Programme, Luxembourg, ISBN 92-894-2077-4
8. Alpha Marine Ltd, (March 1997) ''SIMICAT' Analytical Propeller Design and Powering Performance Calculations', Athens.
9. Wang, D., Atlar, M., Paterson, I., Danisman, D.B. and Mesbahi, E. (2001) "Slipstream (WASH) Measurements with Model Propeller of a Catamaran behind a Dummy Hull Using an LDA System", FLOWMART Technical report: FM-WP2-T22-ST222-UNEW-TEC01
10. Wang, D., Atlar, M., Paterson, I., Danisman, D.B. and Mesbahi, E, (2001) "Slipstream (WASH) Measurements with Model Propeller of a Catamaran in Isolation Using an LDA System", FLOWMART Technical report: FM-WP2-T22-ST221-UNEW-TEC01
11. J. N. Newman, (1977) "Marine Hydrodynamics", The MIT Press.

Table 1 Main technical data of 2-D Laser and Phase Doppler Anemometry system

Laser Type	Argon-Ion
Class & power	Class IV 3W
Transmitting optics	60 mm FiberFlow probe
Receiving optics	The 57×40 FiberPDA
Detector unit	The 58N70 FiberPDA
Signal processor	The 58N80 MultiPDA
Computer	The Pentium II PC with an interface board, for controlling, processing and storing the data.
Traversing system	3-D lightweight

Table 2 Optical specifications for 60 mm FiberFlow probe

Wave length	λ	nm	500
Beam separation	ED	mm	38
Beam waist	Ed	mm	1.35
Receiver aperture	Da	mm	47
Focal length	f	mm	600
Beam intersection angle	θ	rad	0.0798
Diameter of focused laser beam	df	μm	283
Measured volume diameter	dx	μm	283
Measured volume length	dz	mm	8.89
Fringe separation	δ	μm	7.90
Fringe number			35

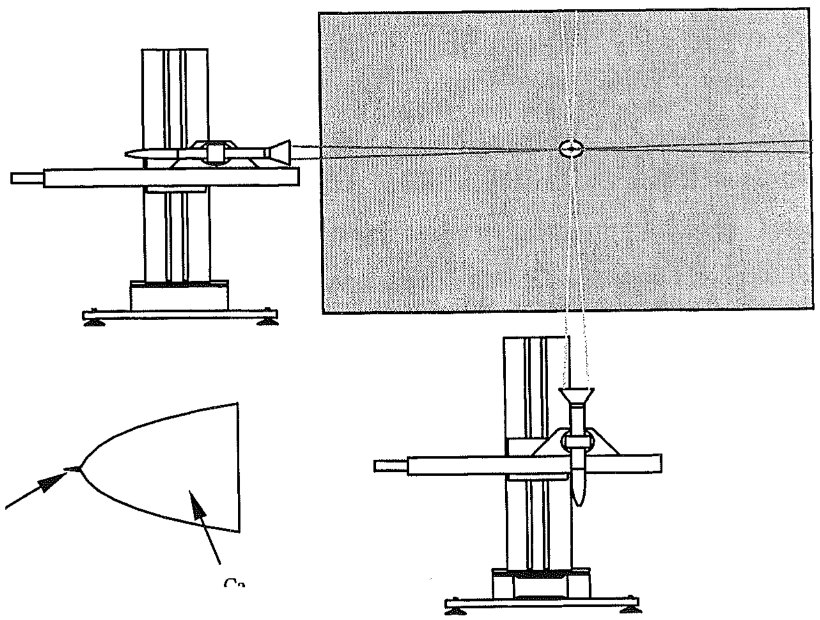

Figure 1 LDA alignment in cavitation tunnel

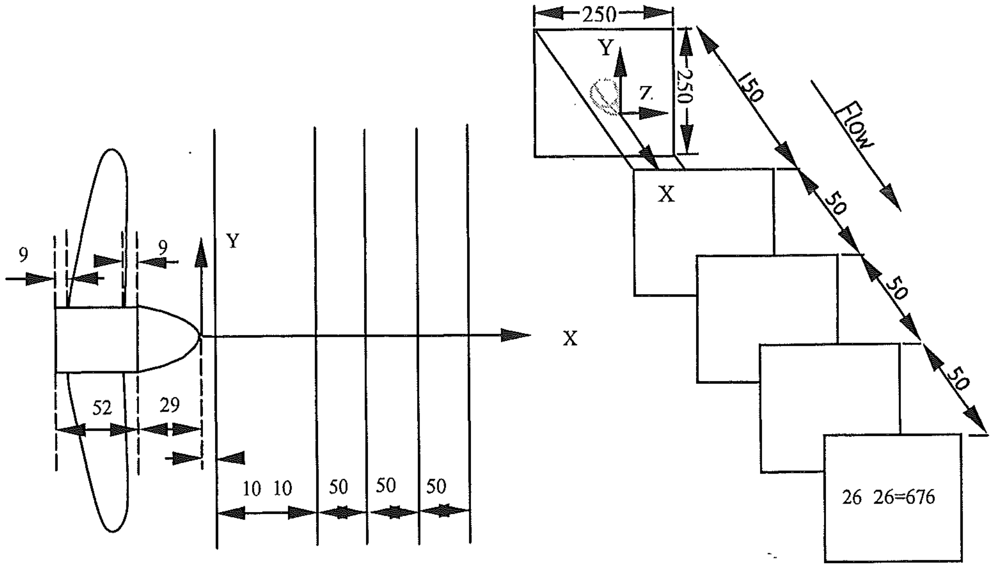

Figure 2 Measuring mesh and coordinate system

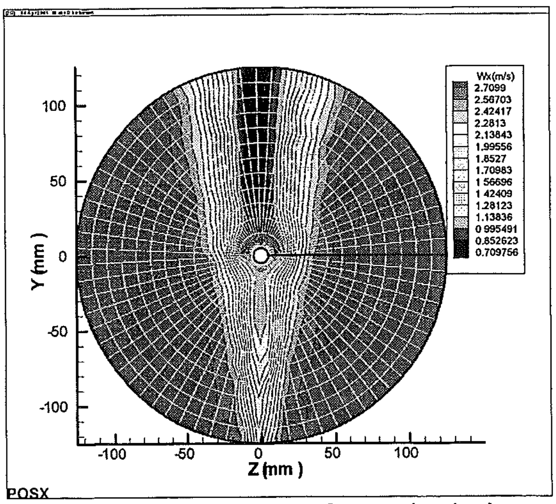

Figure 3 Axial component of normal velocity distribution Wx (m/s)

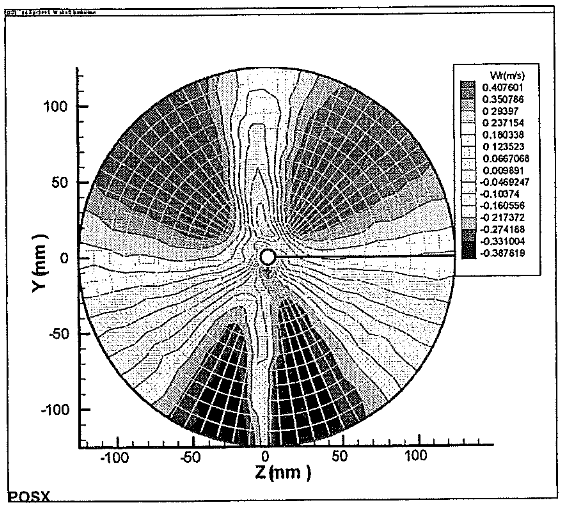

Figure 4 Radial component of normal velocity distribution Wr(m/s)

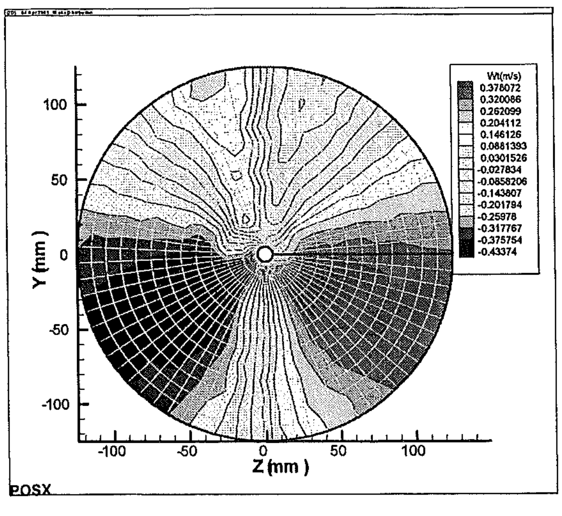

Figure 5 Tangential component of normal velocity distribution Wt (m/s)

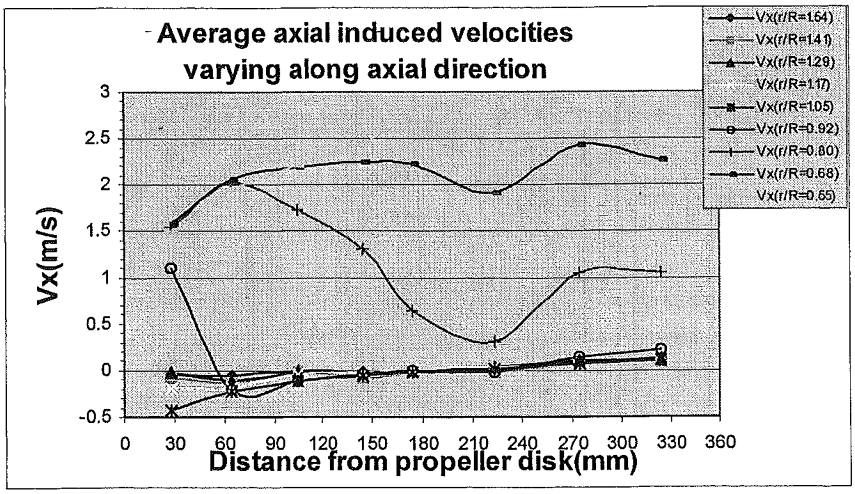

Figure 6 Average axial induced velocities varying along axial direction

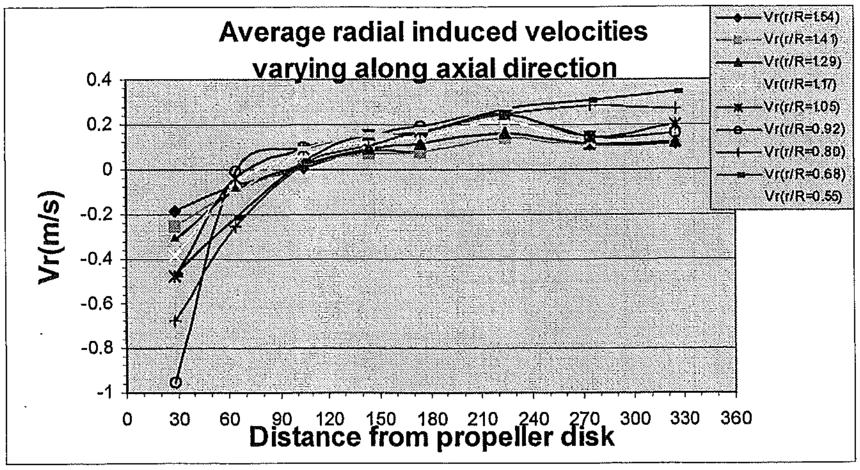

Figure 7 Average radial induced velocities variation along axial direction

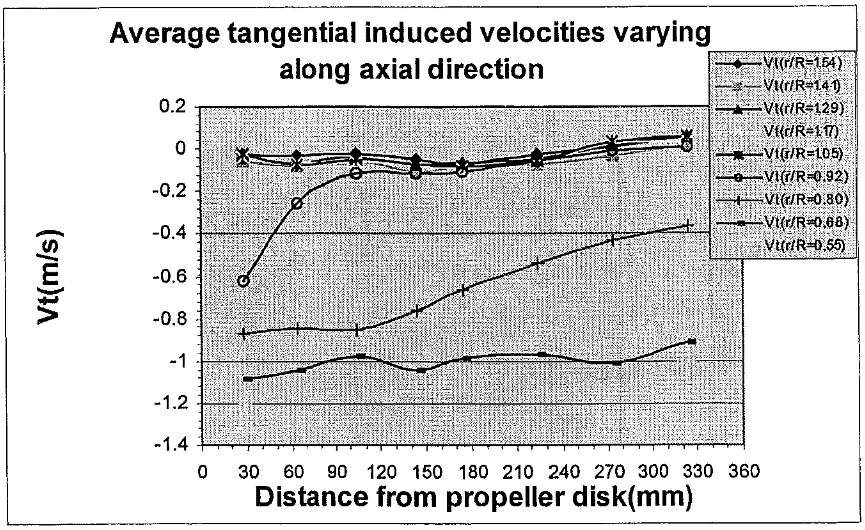

Figure 8 Average tangential induced velocities varying along axial direction

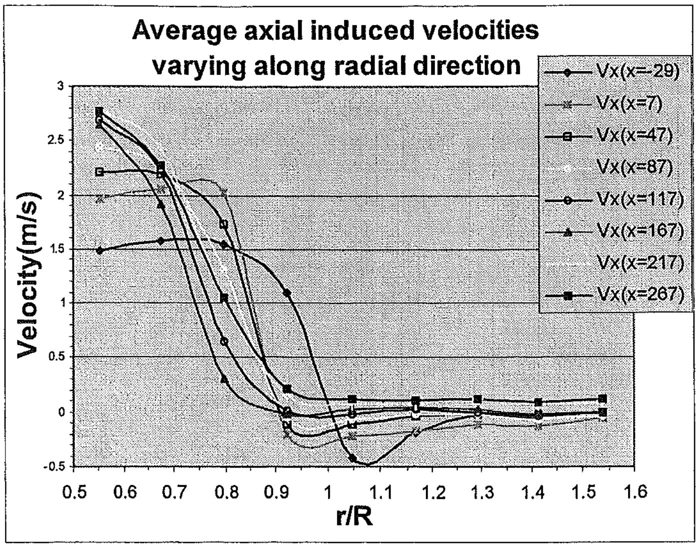

Figure 9 Average axial induced velocities varying along radial direction

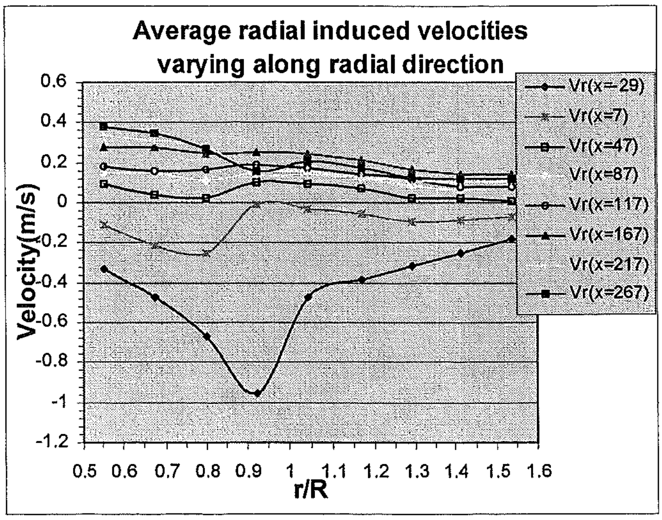

Figure 10 Average radial induced velocities varying along radial direction

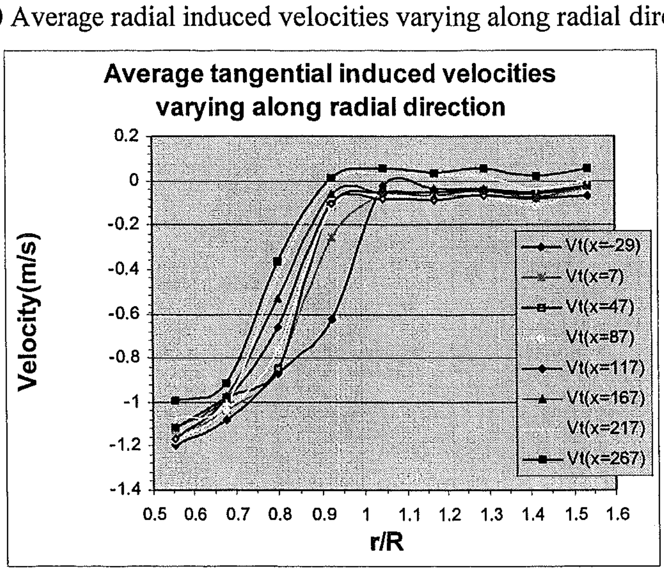

Figure 11 Average tangential induced velocities varying along radial direction

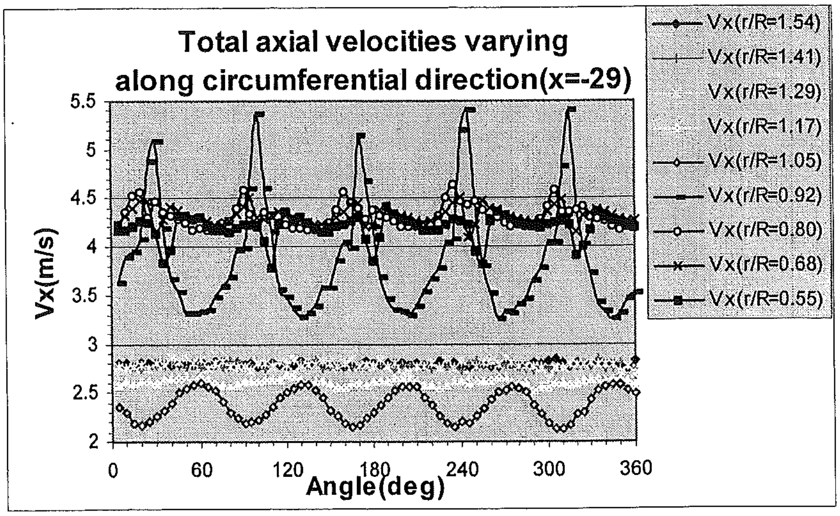

Figure 12 Total axial velocities varying along circumferential direction

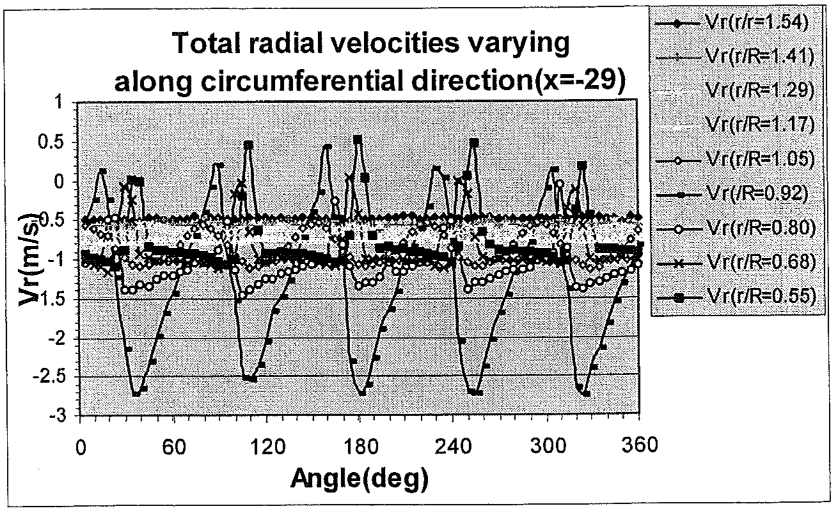

Figure 13 Total radial velocities varying along circumferential direction

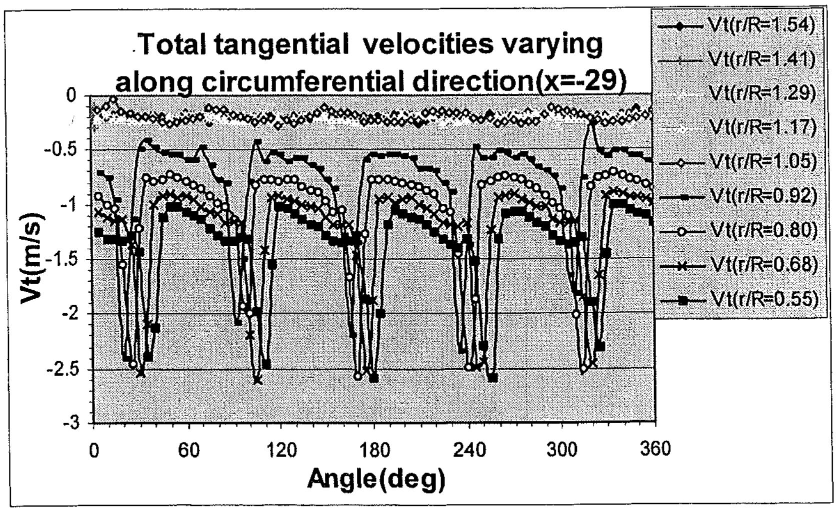

Figure 14 Total tangential velocities varying along circumferential direction

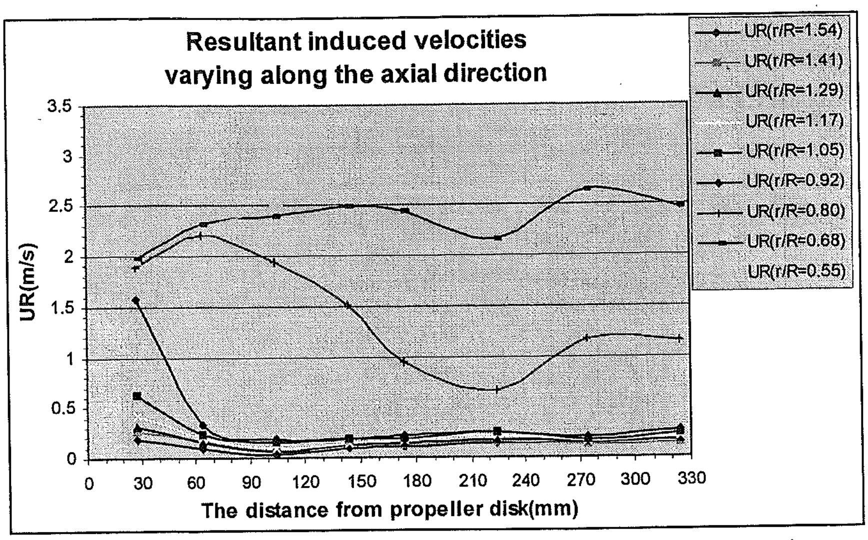

Figure 15 Resultant induced velocities varying along the axial direction

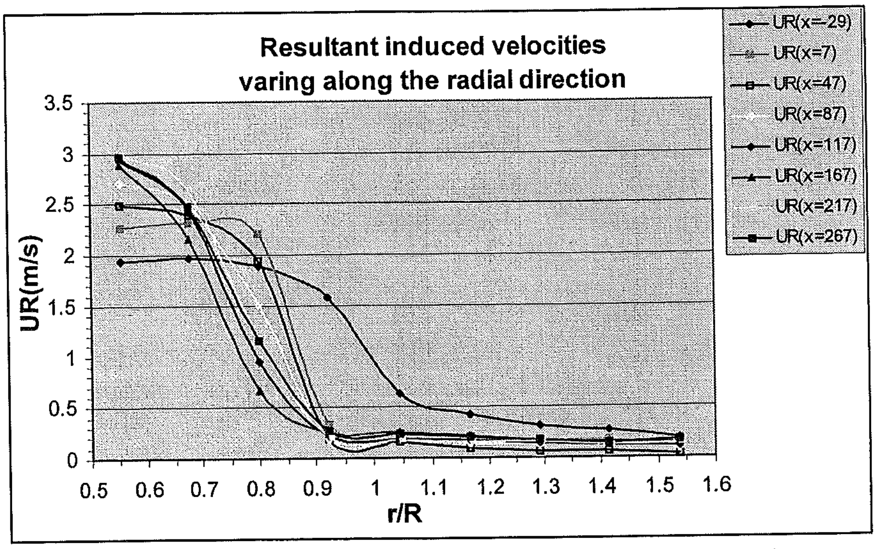

Figure 16 Resultant induced velocities along the radial direction

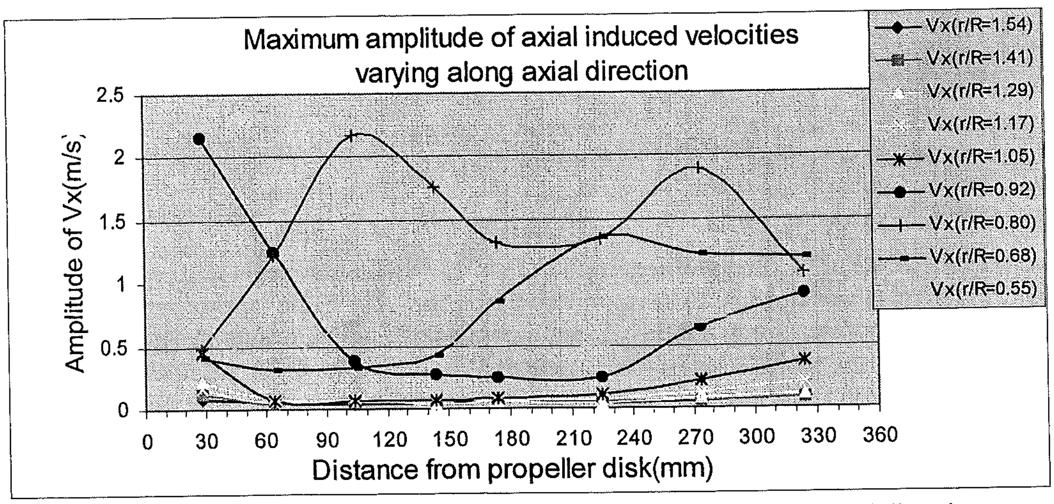

Figure 17 Amplitude of axial induced velocities varying along axial direction

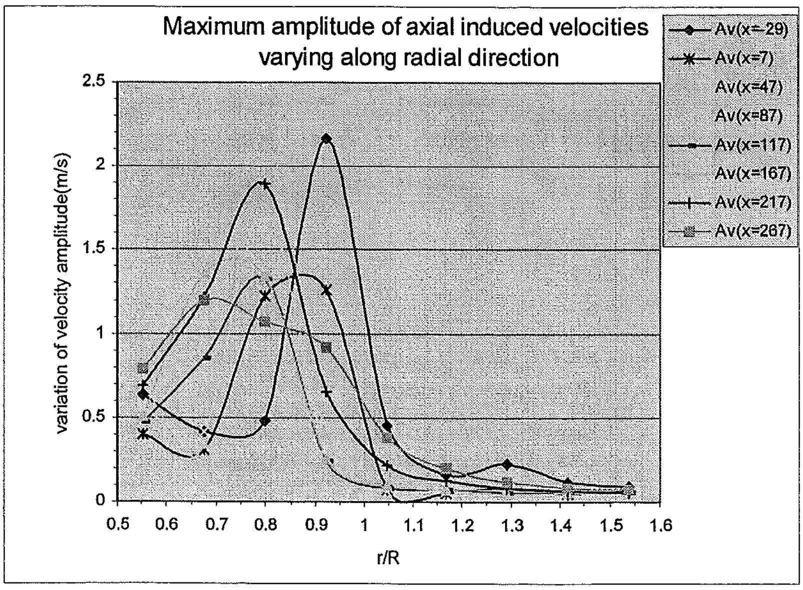

Figure 18 Amplitude of axial induced velocities varying along the radial direction

An investigation into the course stability and control of a fast, pod driven Ropax

Michael D Woodward – Newcastle University – m.d.woodward@ncl.ac.uk

David Clarke – Newcastle University – david.clarke@ncl.ac.uk

Mehmet Atlar – Newcastle University – mehmet.atlar@ncl.ac.uk

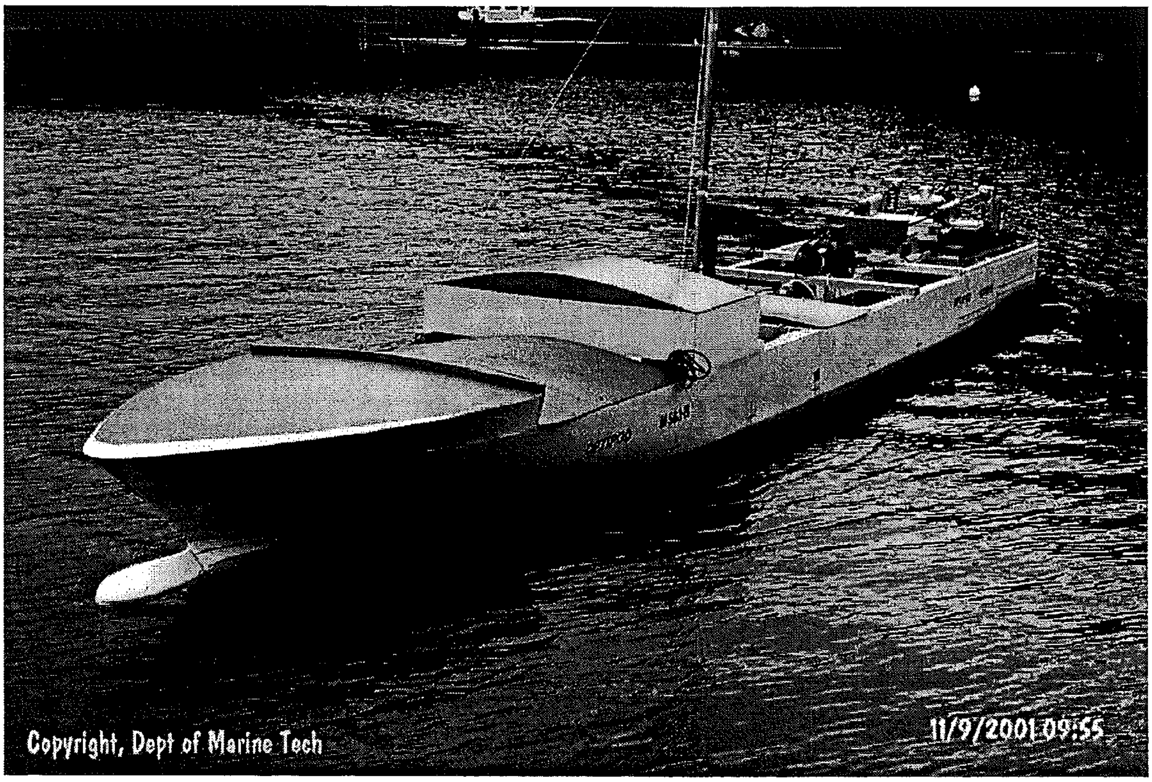

The last decade has seen growing interest in the use of azimuthing pods. The OPTIPOD Ropax has a length between perpendiculars of 172.2 metres, a design speed of 28 knots and is driven by two puller type pods. An understanding of the manoeuvring characteristics of this and other podded ships has been sought through the development of semi-empirical design tools. These design tools together with captive model tests and free-running model tests are used to evaluate the manoeuvring behaviour of the OPTIPOD Ropax.

Background

The International Maritime Organisation (IMO) requires that all ships over 100 metres in length and all Chemical tankers and Gas carriers are to comply with certain manoeuvring criteria, IMO (1993). Through these criteria, the specific tests and their application have evolved to evaluate ships with conventional propulsion and control arrangements, namely rudders and fixed or controllable pitch propellers. Then, the question must be raised as to the applicability of these criteria for podded ships. The way in which a pod unit applies its control force and the hydrodynamic interactions for both control and course stability are undoubtedly different from that of a conventional rudder arrangement. Clearly, an understanding of the physical phenomena must be sought if the criteria are to be applied with any level of confidence. The manoeuvring characteristics of ships fitted with podded propulsion units can be considered to have two significant differences from conventional arrangements. Firstly, and more obviously, the removal of the rudder and propeller and replacement with pod propulsors will result in a considerable alteration in the thrust and lift characteristics. Considering first the classical arrangement, the propeller accelerates the flow over the rudder, increasing its lift characteristics and helping to stabilise the ship. Also, when in the dead ahead position, a similar argument can be made for puller type pods. When the rudder is put across it still benefits from this accelerated flow, however, as the pod rotates so does the propeller race. This results in the pod body remaining at a zero angle of attack to the accelerated flow and can thus only produce a lift proportional to the square of the ship forward speed. Conversely, the accelerated flow now acts as a control force in its own right and will continue to do so at low or even zero forward speed. Secondly, the presence of pods will necessitate a modification of the hull form. To make room for the azimuthing capabilities of the pods the hull aft body must become more pram like and consequently broader at the stern to maintain buoyancy. The aft body water-plane-area can increase moving LCF aft and LCB and the CoG both move forward; all affecting the hydrodynamic characteristics of the bare hull.

OPTIPOD project

Within the above framework, the ongoing EU 5th Framework project OPTIPOD (2000) addresses the design of podded ships including safety and risk. Manoeuvrability is considered to be one of the most prominent safety issues relating to this type of design. One part of the project includes the model testing of the subject Ropax with both conventional and podded propulsion arrangements. Changes to the hull form have been minimised to make the results comparative; the general propulsion and control arrangements are shown in Fig.1. Kanar and Glodowski (2001a, Kanar and Glodowski (2001b) report on a series of free-sailing model tests that have been conducted by CTO at the Lake Wdzydze test centre including the IMO criteria and other informative experiments. Semi-empirical equations for the prediction of the manoeuvring derivatives have been derived and the obtained predicted values are validated by comparison with captive test results reported by Misiag (2002) and the free-sailing tests. This paper reports on the progress achieved so far, concerning the prediction of manoeuvring derivatives and validation as described above.

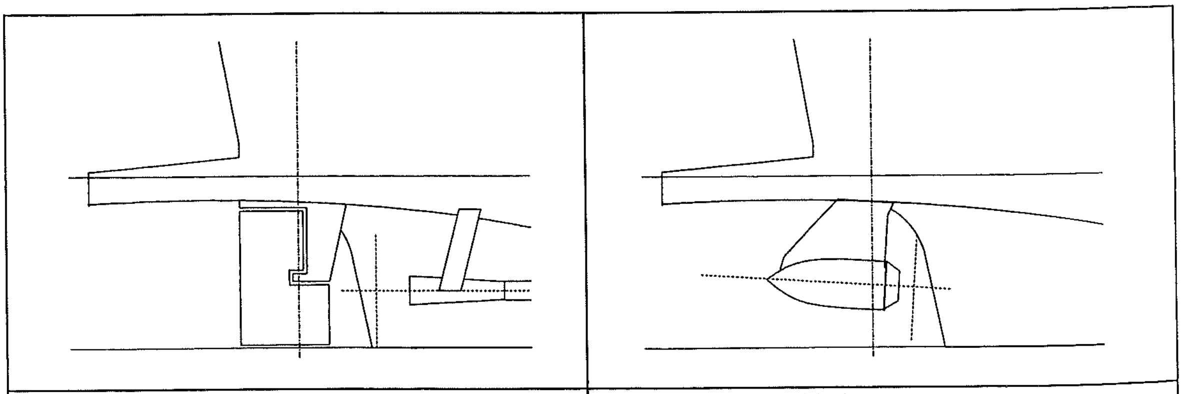

Conventional Arrangement	Podded Arrangement

Fig. 1 - Propulsion and Control arrangements

Table 1 - Ship Particulars

Parameter	Units	Classical		Podded	
Hull form details		Ship	Model	Ship	Model
Length bp	m	172.200	7.487	172.200	7.487
Length wl	m	193.970	8.433	193.970	8.433
Breadth	m	28.400	1.235	28.400	1.235
Draught fwd	m	6.600	0.289	6.600	0.289
Draught aft	m	6.600	0.289	6.600	0.289
Displacement	m^3	19744.400	1.623	19460.000	1.599
Wetted surface	m^2	5803.000	10.970	5673.000	10.720
Block coefficient	-	0.613		0.601	
Amidships coefficient	-	0.987		0.969	
Prismatic coefficient	-	0.621		0.620	
Water plane coefficient	-	0.905		0.878	
Longitudinal radius of gyration	-	0.260		0.260	
Propeller diameter	m	5.361	0.233	5.300	0.230
Pitch	m	5.897	0.256	7.362	0.320
BAR	-	0.600		0.758	
Number of blades	-	4		4	
Rotation	-	inward		inward	
Lateral area of Pod/Rudder	m^2	29.75	0.0562		

Semi-empirical derivative estimation tools

The objective is to formulate semi-empirical tools for the prediction of the manoeuvring derivatives based only on a knowledge of the ships primary dimensions, ratios and coefficients. Using the low aspect ratio wing theory put forward by Jones (1956), Clarke *et al.* (1982) describes how the ships hull can be assumed to be a low aspect ration wing turned on its side. This assumes that the respective derivative terms are functions of the square of the draught length ration multiplied by an appropriate constant as shown in Eqs.(1). Clarke et al. (1982) goes on to show how the constant terms shown in Eqs.(1) can be replaced with functions of the horizontal added mass; extending the slender body strip theory method to yield expressions for the derivatives which are dependant on hull shape.

$$Y'_v = -\pi\left(\frac{T}{L}\right)^2[1]; \qquad Y'_r = -\pi\left(\frac{T}{L}\right)^2\left[-\tfrac{1}{2}\right]; \qquad N'_v = -\left(\frac{T}{L}\right)^2\left[\tfrac{1}{2}\right]; \qquad N'_r = -\left(\frac{T}{L}\right)^2\left[\tfrac{1}{2}\right] \tag{1}$$

To reduce computational time at the preliminary design stage, a regression method has been employed to replace the added mass functions and yield hull ratio and coefficient dependant expressions for the derivatives. A data base has been compiled containing the manoeuvring derivatives, principal dimensions, ratios and coefficients of some 64 ships. These coefficients have been further supplemented by the inclusion of the 'aft body shape parameter, $_a$, as defined in Eq.(2) where the prismatic (C_{Pa}) and water-plane coefficients (C_{Wa}) are for the aft body only. Finally, a multi-variant linear analysis was performed to examine the variation between the descriptive parameters and the manoeuvring derivatives.

$$\sigma_a = \frac{(1-C_{Wa}}{(1-C_{Pa})} \quad) \tag{2}$$

Multi-variant analysis

Only predictor variables that tend to zero for a flat plate were selected, then the correlation between these variables was examined. Any variables with a Pearson's r partial correlation coefficient in excess of 0.8 were excluded from further analysis in an attempt to reduce interaction. The terms on the right hand side of the above Eqs.(1) were then multiplied back through both the constant term and the proposed variables. The multi-variant regression analysis was then performed using the predictor variables given in Table 2.

Table 2 – Predictor variables

$\left(\frac{T}{L}\right)^2$	$\frac{TB}{L^2}$	$\frac{T^2B}{L^3}$
$C_B\frac{T^2B}{L^3}$	$\sigma_a\frac{T^2B}{L^3}$	$\frac{T^3B}{L^4}$
$\frac{D_PT}{L^2}$	$C_B\frac{TB}{L^2}$	$C_B\frac{TBx_G}{L^3}$

Where L, B and T are the length at the water line, breadth and draught respectively. C_B is the block coefficient; σ_a is the aft body shape parameter as defined in Eq.(2); x_G is the distance from amidships to the CoG positive forward; finally, D_P is the distance between hull and keel line at the propeller plane.

Control derivative

The stabilising effect of the rudders has been estimated using the method suggested by Crane *et al.* (1989) who goes on to show that the control force is equal in magnitude as in Eq.(3).

$$Y'_{\delta_R} = -(Y'_v)_f \qquad \text{(3)}$$

For the prediction of the pod stabilising effect the relationship given in Eq.(4) was assumed. Where L and U are the model length and velocity respectively and where appropriate prediction equations have been derived for effective area of strut A_S, flow velocity over pod body u_P and for the effective aspect ratio leading to the lift curve slope estimate.

$$(Y'_v)_P = -\left|\frac{A_S}{L^2}\left(\frac{u_P}{U}\right)^2\frac{\partial C_L}{\partial \delta}\right| \qquad \text{(4)}$$

As noted in the introduction the control force does not however benefit from the accelerated flow but does gain a thrust component as shown in Eq.(5).

$$Y'_{\delta_P} = \frac{A_S}{L^2}\frac{\partial C_L}{\partial \delta} + \frac{Thrust}{\frac{1}{2}\rho U^2 L^2}$$

$$\therefore Y'_{\delta_P} = \frac{A_S}{L^2}\frac{\partial C_L}{\partial \delta} + X'_{UU} \qquad \text{(5)}$$

Derivative prediction

Figure 2 shows the regression analysis for the linear velocity derivative of sway force due to sway velocity. The plot also shows four predicted and measured values for the OPTIPOD Ropax pertaining to four different Froude numbers. Clearly, Froude number influences the attained derivative value however all prediction are considered to lay within acceptable error margins for this regression analysis.

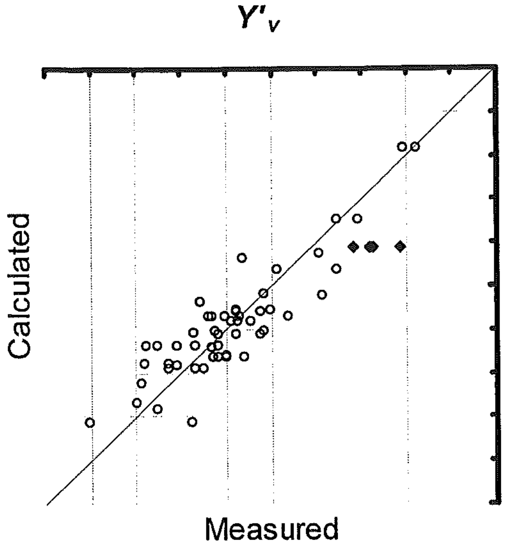

Fig. 2 – Sway force derivative due to sway velocity

Figure 3 shows the regression analysis for the linear velocity derivative of sway force due to yaw rate. The plot also shows the predicted and measured value for the OPTIPOD Ropax.

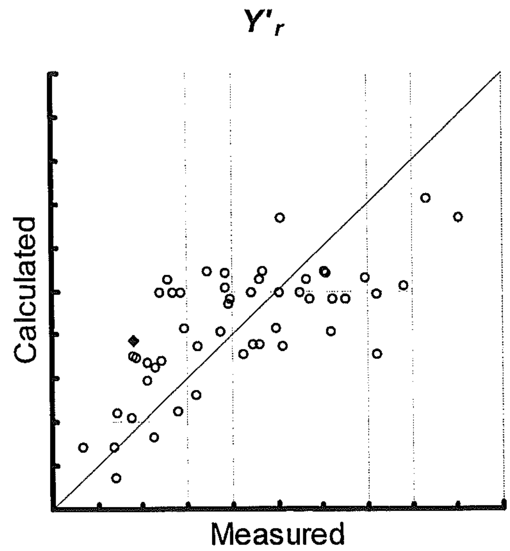

Fig. 3 – Sway force derivative due to yaw rate

Database member ◆ OPTIPOD Ropax

Figure 4 shows the regression analysis for the linear velocity derivative of yaw moment due to sway velocity. The plot also shows four predicted and measured values for the OPTIPOD Ropax pertaining to four different Froude numbers. Again, the effect of Froude number on the attained derivative is clear.

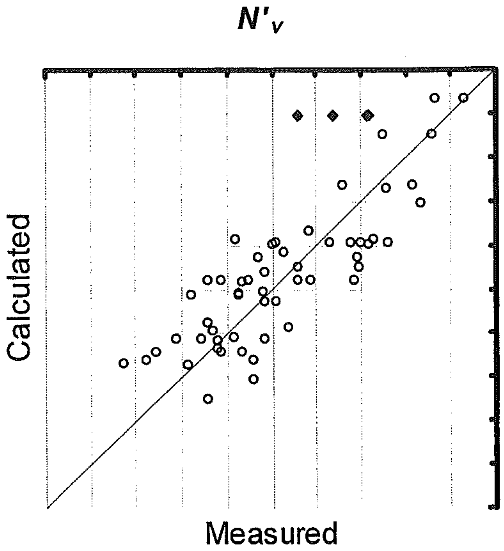

Fig. 4 – Yaw moment derivative due to sway velocity

Figure 5 shows the regression analysis for the linear velocity derivative of yaw moment due to yaw rate. The plot also shows the predicted and measured value for the OPTIPOD Ropax

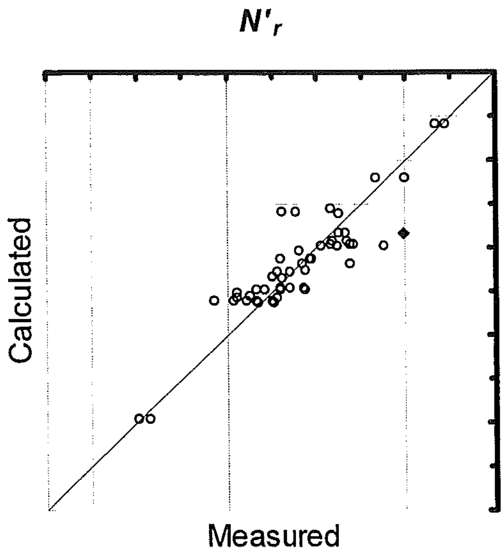

Fig. 5 – Yaw moment derivative due to yaw rate

Database member ◆ OPTIPOD Ropax

Dynamic course stability
Assuming the time constant form, Eq.(6), as original suggested by Nomoto *et al.* (1957); where T_i' are the time constants of the yaw rate equation and K' is the gain. The stability boundary is reached when one of the characteristic roots of Eq.(6) become zero which is true when T_1' or T_2' become infinite. Then, for T_1' or T_2' to be infinite Nomoto shows that Eq.(7) must be equal to zero (e.g. $C = 0$).

$$T_1'+T_2'\ \dddot{r}'+\left(T_1'+T_2'\right)\ \ddot{r}'+\dot{r}'\big) = K'\delta + K'\,T_3'\,\dot{\delta} \tag{6}$$

$$Y_v'\left(N_r' - m'x_g'\right) - N_v'\left(Y_r' - m'\right) = C \quad) \tag{7}$$

From the analysis the results given in Table 3 are obtained. It should be noted that the criteria represents the stability boundary and the magnitude should not be taken as a measure of stability. The results clearly indicate directional stability. Also, direct spiral tests performed show positive gradient for both the classical and podded models indicating that both models are in fact dynamically stable.

Table 3 – Stability criteria

	Classical Ropax	Podded Ropax
Predicted Stability Criteria	0.000033	0.000014

Turning circle tests
The turning circle manoeuvre as required by IMO(1993) was performed for both the classical and podded free-sailing models. Figure 6 shows the advance in ship lengths plotted against helm angle. Clearly, both arrangements more than comply with the IMO requirement of 4.5 ship lengths for a 35 deg. applied helm angle. It is also evident that the podded ship shows some improvement over the classical arrangement.

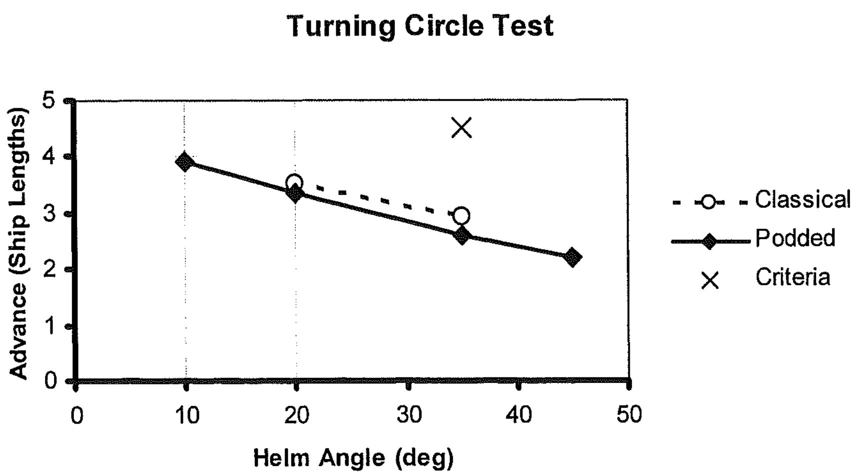

35^0 Turning test	Classical	Podded	Criteria
Advance (Ship lengths)	2.94	2.59	4.50

Fig. 6 – Advance in turning circle test

Figure 7 shows the transfer in ship lengths plotted against helm angle. Although not an IMO requirement this again demonstrates the superior manoeuvring performance of the podded ship.

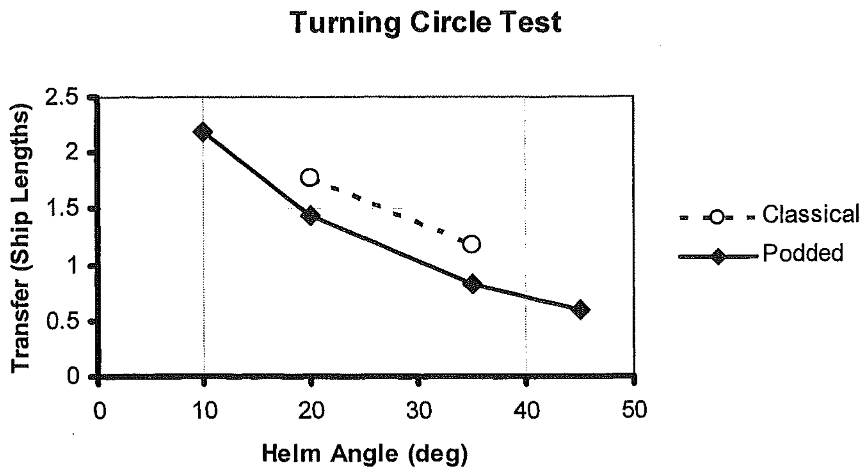

35^0 Turning test	Classical	Podded	Criteria
Transfer (Ship lengths)	1.17	0.82	–

Fig. 7 – Transfer in turning test

Figure 8 shows the tactical diameter in ship lengths plotted against helm angle. Again, both arrangements more than comply with the IMO requirement; being 5 ship lengths for a 35 deg. applied helm angle. And again, it is also evident that the podded ship shows some improvement over the classical arrangement.

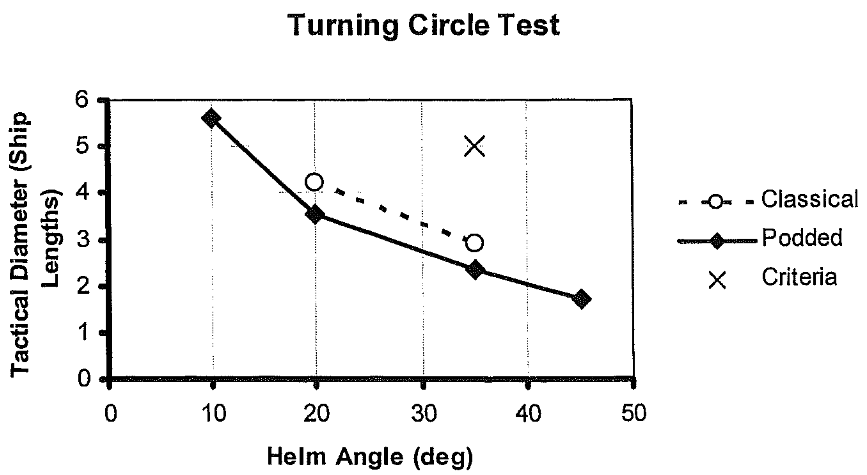

35^0 Turning test	Classical	Podded	Criteria
TD (Ship lengths)	2.89	2.33	5.00

Fig. 8 – Tactical diameter in turning circle test

Zig-Zag manoeuvre

The Zig-Zag manoeuvre was conducted for both classical and podded models as required by IMO (1993). Figure 9 shows the first and second overshoot angles for the podded model; clearly demonstrating compliance with the IMO criteria throughout the speed range. Further, Table 4 gives the first and second overshoot angles for both the classical and podded models at test speed. Again the podded model shows improvement over the classical arrangement.

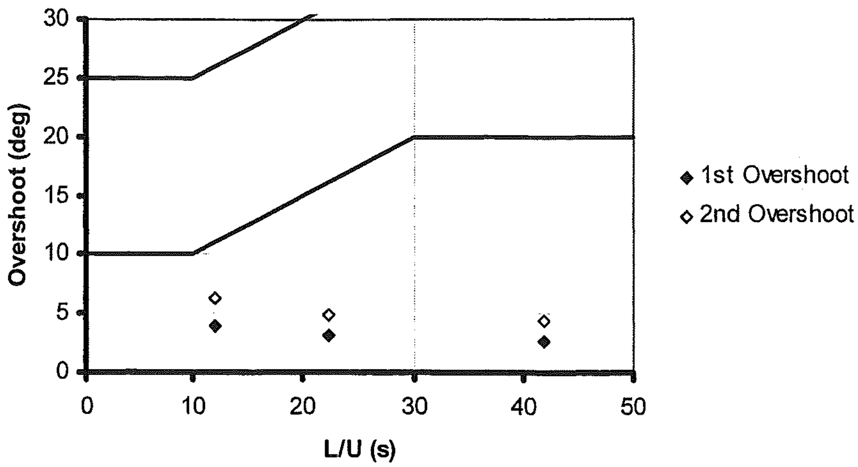

Fig. 9 – Podded Ropax overshoot angles

Table 4 – Zig-zag comparison

10/10 Zig-zag test	**Classical**	**Podded**	**Criteria**
First overshoot (deg)	8.95	3.85	11.00
Second overshoot (deg)	8.25	6.30	26.00

Discussion

All tests indicate improvement in the manoeuvring characteristics for the podded model while also maintaining directional stability. The turning circle tests show improvement in all criteria over a range of applied helm angles. The Zig-Zag tests show compliance with the criteria over the speed range and improvement of the over shoot angles when compared to the classical model. Direct spiral tests performed on both models showed positive initial gradient of the same magnitude.

For a classical rudder arrangement, it is not possible to increase the control force magnitude without modifying the stabilising effect, see Eq.(3). However, Eqs.(4) and (5) indicate that it is possible, with careful design, to increase the control force generated by a pod without increasing the stabilising effect. As shown by Clarke and Yap (2001), an ability to change Y'_δ without effecting Y'_v is advantageous when designing for improved manoeuvrability.

Conclusion

Although the IMO criteria may not indicate the full potential of the podded design it does however provide satisfactory comparison with the classical design. These initial investigations indicate that the IMO criteria manoeuvres can be applied with like for like helm angles and with comparable results.

Nomenclature

L	Length wl (m)
B	Breadth (m)
T	Draught (m)
ζ'_a	Aft body shape parameter (-)
C_B	Block coefficient (-)
C_{Wa}	Aft body water-plane area coefficient (-)
C_{Pa}	Aft body prismatic coefficient (-)
D_P	Distance between hull and keel line at the propeller plane.
A_S	Effective area of strut (m^2)
u_P	Flow velocity over pod body (m/s)
U	Ship forward speed (m/s)
$\frac{\partial C_L}{\partial \delta}$	Lift curve slope for pod (-)
Y'_v	Non-dimensional partial derivative of sway force w.r.t. sway velocity (-)
$(Y'_v)_f$	Fin stabilising contribution of Y'_v (-)
$(Y'_v)_P$	Pod stabilising contribution of Y'_v (-)
$Y'_{\delta R}$	Rudder control force derivative (-)
$Y'_{\delta P}$	Pod control force derivative (-)
Y'_r	Non-dimensional partial derivative of sway force w.r.t. yaw rate (-)
N'_v	Non-dimensional partial derivative of yaw moment w.r.t. sway velocity (-)
N'_r	Non-dimensional partial derivative of yaw moment w.r.t. yaw rate (-)
X'_{UU}	Non-dimensional partial derivative of surge force w.r.t. surge velocity (-)
T'_i	Nomoto equation time constants (-)
K'	Nomoto equation gain term (-)
m'	Non-dimensional mass (-)
x'_g	Non-dimensional CoG (-)
r'	Non-dimensional radius of turn (-)
$\dot{r}'$	First derivative of r (-)
$\ddot{r}'$	Second derivative of r (-)
δ	Helm angle (deg)
$\dot{\delta}$	Rate of change of helm angle (deg/s)
C	Stability criteria (-)

References

Clarke, D., Gedling, P. and Gedling, G. (1982) "*The Application of Manoeuvring Criteria in Hull Design Using Linear Theory*" *The Royal Institution of Naval Architects.*

Clarke, D. and Yap, M. L. R. (2001) "*A multi-criteria view of the IMO manoeuvring requirements*" *Trans RINA,* **143,** 98 110.

Crane, C. L., Eda, H. and Landsburg, A. (1989) "*Principals of Navel Architecture, Chapter IX - Controllability*" **3 - Motion in waves and controlibillity,** 191 422.

IMO (1993) "*Resolution A.751(18) - Interim standards for ship manoeuvrability*".

Jones, R. T. (1956) "*Properties of low-aspect-ratio wings at speeds below and above the speed of sound*" *NACA, Report No.835.*

Kanar, J. and Glodowski, R. (2001a) "*Classical ropax results of free model manoeuvring tests model M-565 - No.RH 2000/T-231E*" *CTO Ship design and research centre.*

Kanar, J. and Glodowski, R. (2001b) "*Podded ropax results of free model manoeuvring tests model M563-B - No.RH2001/T-112E*" *CTO Ship design and research centre.*

Misiag, W. A. (2002) "*Identification of mathematical model parameters of ship manoeuvring for podded ropax vessel, analysis and results of bare hull captive model tests model M-563A - No.RH2002/T-000E*" *CTO Ship design and research centre.*

Nomoto, K., Taguchi, T., Honda, K. and Hirano, S. (1957) "*On the steering qualities of ships*" *Int. Shipbuilding Prog(4),* 354.

OPTIPOD (2000) "*Annex 1 - Optimal design and implementation of azimuthing pods for the safe and efficient propulsion of ships*" *European Commission RTD FP5 project,* **GRD1-1999-10294.**

A Scale Effect Check about Resistance Estimation of Planing Boats

Yasushi Yoshida, Wessex Institute of Technology, Southampton/UK, wit@wessex.ac.uk

Abstract

This paper is concerned with a scale effect check about resistance estimation of planing boats. As an example, 14 in scale ratio of ship to model is taken for the case of the PT boat having 35 m in overall length, 9 m in width, 1304.3 kN (133.0 tonf) in displacement and three propellers. Sottorf say that up to 10 in scale ratio is effective to estimate resistance on the basis of a series of towing tank test data by using plate models having flat shape bottom. Author's model having 14 in scale ratio seems to be smaller one than the one having 10 in scale ratio (limit value), which causes us to discuss the scale effect problem.

The total resistance is presumed by empirical equations based on a series of towing tank test data using 13 kinds of 2.5 m length models. The equations have been made by author up to 3.5 in Froude number on the basis of displacement volume at intervals of 0.5. The PT's top speed 41.19 kt equals to 3.0 in Froude number.

Propulsive coefficient (EHP / SHP) equals to 0.50 in high speed range, which shows reasonable resistance estimation.

Reasonable balance of resistance and thrust at the top speed was obtained by synthetic discussion between the two. Up to the top speed the difference between thrust and resistance shows also reasonable value.

Trim angle change values presumed by the equations show reasonable tendency against the ones of trial tests.

1. Introduction

Sottorf's experiment says: " The model on the scale of one to ten, which is defined as $\lambda_F = 10$, should be the least effective model." (see Fig. 1), *SOTTORF (1938).*

His experimental data were obtained by a set of towing tank tests using rectangular plates at 3.74 in Froude number F_∇ ($= V / (\nabla^{1/3} g)^{1/2}$) under 0.109 in load coefficient C_B ($= \mathbf{A} / (b^2 \, 0.5 \, \rho V^2)$). **A** means the lift that takes the value of total weight. b, V and ρ are a plate's width, velocity and density, respectively. Up to about 10° in attack angle α, slide numbers ε ($= \mathbf{W} / \mathbf{A}$) are calculated by the theoritical equation against the scale ratios from $\lambda_F = 32$ to 1, which draw the $\varepsilon - \alpha$ curves as shown in Fig. 1. **W** means resistance. $\lambda_F = 1$ means the full-scale plate having 2.4 m in width and 9216 kgf in displacement. Marks "⊖" and "⊗" are the experimental data at $\lambda_F = 1$ and 2, respectively. $\lambda_F = 2$ means its half scale model. All data at scale ratios are plotted on the figure, using several kinds of marks "○".

2. Discussion about Sottorf's experiment

Three items will be discussed on the basis of Fig. 1.

2.1. The least glide number

The least ratio of resistance to lift **W** / **A** ($= \varepsilon$) will be discussed.

According to the curve for $\lambda_F = 1$, $\varepsilon = 0.12$ at $\alpha = 3° \; 30'$ is obtained. While the experimental data show that $\varepsilon = 0.14$ at $\alpha = 5$. The difference of values between theoritical and experimental one equals to 0.02 against ε and 1° 30' against α, respectively. The error percentage of ε is 14.3 % for selecting measured value as to be denominator. When we successively join the points of the least ε for each λ_F by dotted line, α_{opt} lone is obtained.

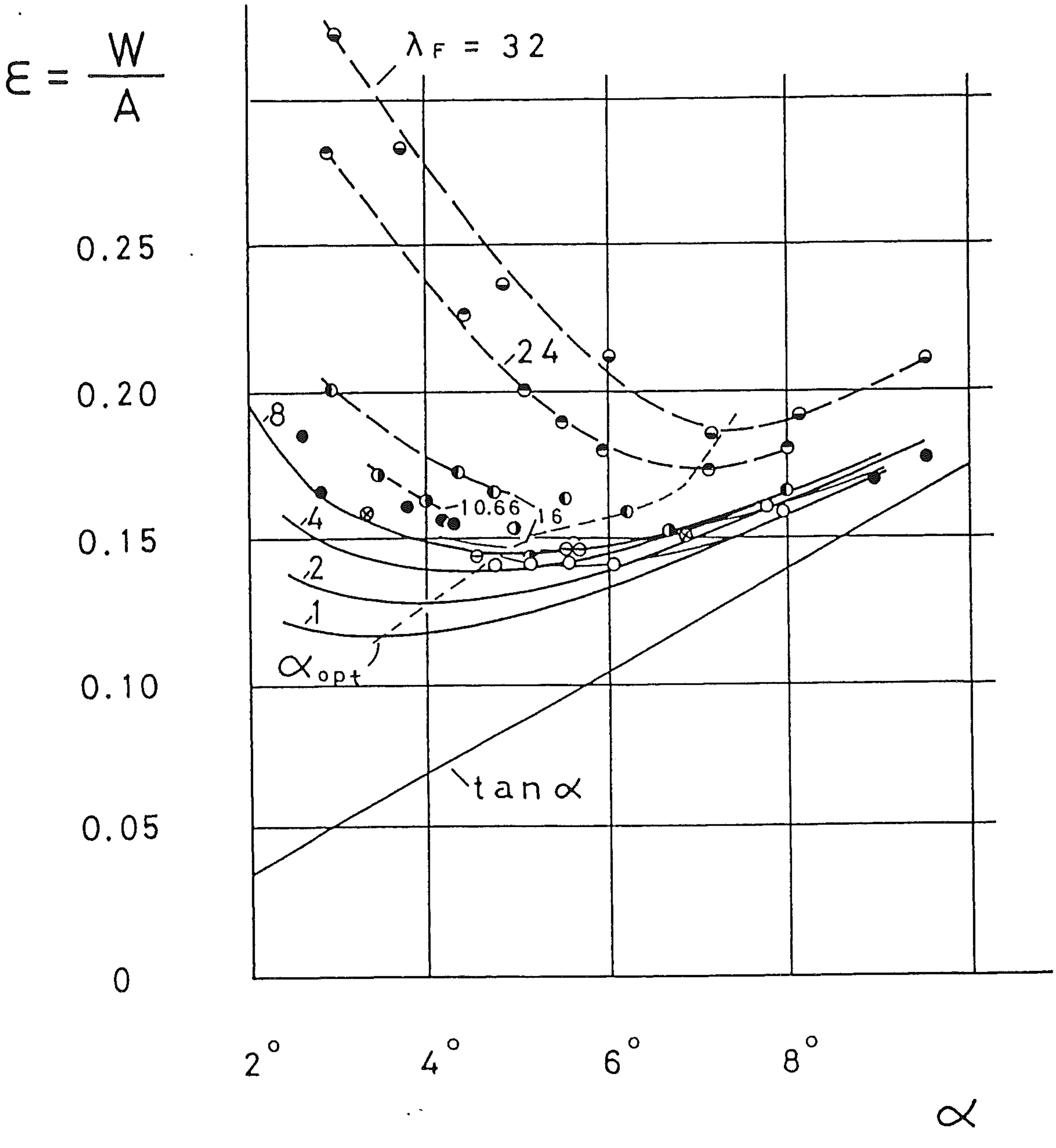

Fig. 1: Sottorf´s experimental data

2.2. Surface tension

The less dimension a model has, the more surface tension effect the model get.

Experimental data under strong influence of surface tension cannot be used to presume resistance etc.. Under 5 gf / cm^2 in mean bottom pressur, the effect has been found remarkably. λ_F= 8 or 10 may be the value for the least effective model. The point at the change of slope on α_{opt} line is seen at λ_F = 10.66. In order to find the least ratio of resistance to lift **W / A** (= ε) about full-scale plate, larger models than the one having λ_F = 8 or 10 in scale ratio are desireble.

2.3. Asymptotic line

Tan α is common asymptotic line for every λ_F.

3. Scale ratio

As an example the resistance performance of the P T having 35 m in overall length, 9 m in width and 1303.4 kN (133.0 tonf) in displacement, *RAYMOND (1975),* will be discussed in this paper. 41.19 kt at the top speed was obtained, which is 3.0 in Froude number F_∇ (= V / ($\nabla^{1/3}$ g)$^{1/2}$).

Author uses data of a series of towing tank tests to presume P T's resistance performance. The tests were done up to 3.5 in Froude number by using thirteen kinds of 2.5 m length models in Japan Defense Agency's towing tank (Meguro Towing Tank Tokyo), *YOSHIDA (1999).*
As one of the examples the model having 588.40N (60.00 kgf) in displacement is towed, which has been shown on pp. 183-185 in the reference *YOSHIDA (2001).* On this example the data having 3-5 g f / cm^2 in bottom pressure were measured by manometer near chine line at ord. 6.

The P T's floating positions at F_∇ = 0.5, 1.0 and 3.0 are shown on p. 192 in the reference *YOSHIDA (1997).* The difference of floating positions between the one at 0 and 1.0 in Froude number cannot be seen. The maximum wave making resistance is got at 1.0 in the number. At 3.0 in the number P T has already got into planing condition. In this case the scale ratio is given as λ_F= 14. The P T's and model's frictional resistance coefficient C_{f0} are plotted on Schoenherr's frictional resistance coefficient curve, showing the difference of Reynolds numbers as the parts written " ship " and " model " on Fig. 2.

4. Presuming Resistance Performance

4.1. Difficulty of Presuming Resistance

Though planing boat's hull is traditional, reasonable design bases are so few that engineers manage to design and make boats by the method of trial and error through their experience and sence.

In high speed range planing boats change their floating position, which enable us to estimate their resistance performance with difficulty. Dynamic lift together with making a tub on transom, which may be considered as the increment of a boat's overall tength, should be taken into consideration in addition to resistance. These phenomena make us analyze with much difficulty, by which we will take long time until the contribution to design a hull form.

Also experimental analyses require (1) the tank in which large models can be towed with high speed and (2) a long time against damping of wave after a towing test. Few towing tank produce the experimental data.

4.2. Towing Tank Test

Up to 3.5 in Froude number a set of total resistance coefficient C_t(= R / 0.5 ρ V^2 $\nabla^{2/3}$), trim angle change $\Delta\theta$ and non-dimensional draft change at transom ΔD (= ΔD' / b_t or ΔD' / $\nabla^{1/3}$) is obtained by measuring total resistance R, trim angle change $\Delta\theta$ and dip of keel at transom ΔD' at intervals of 0.5 in Froude number. V, g, ∇ and ρ mean speed, gravity acceleration, displacement

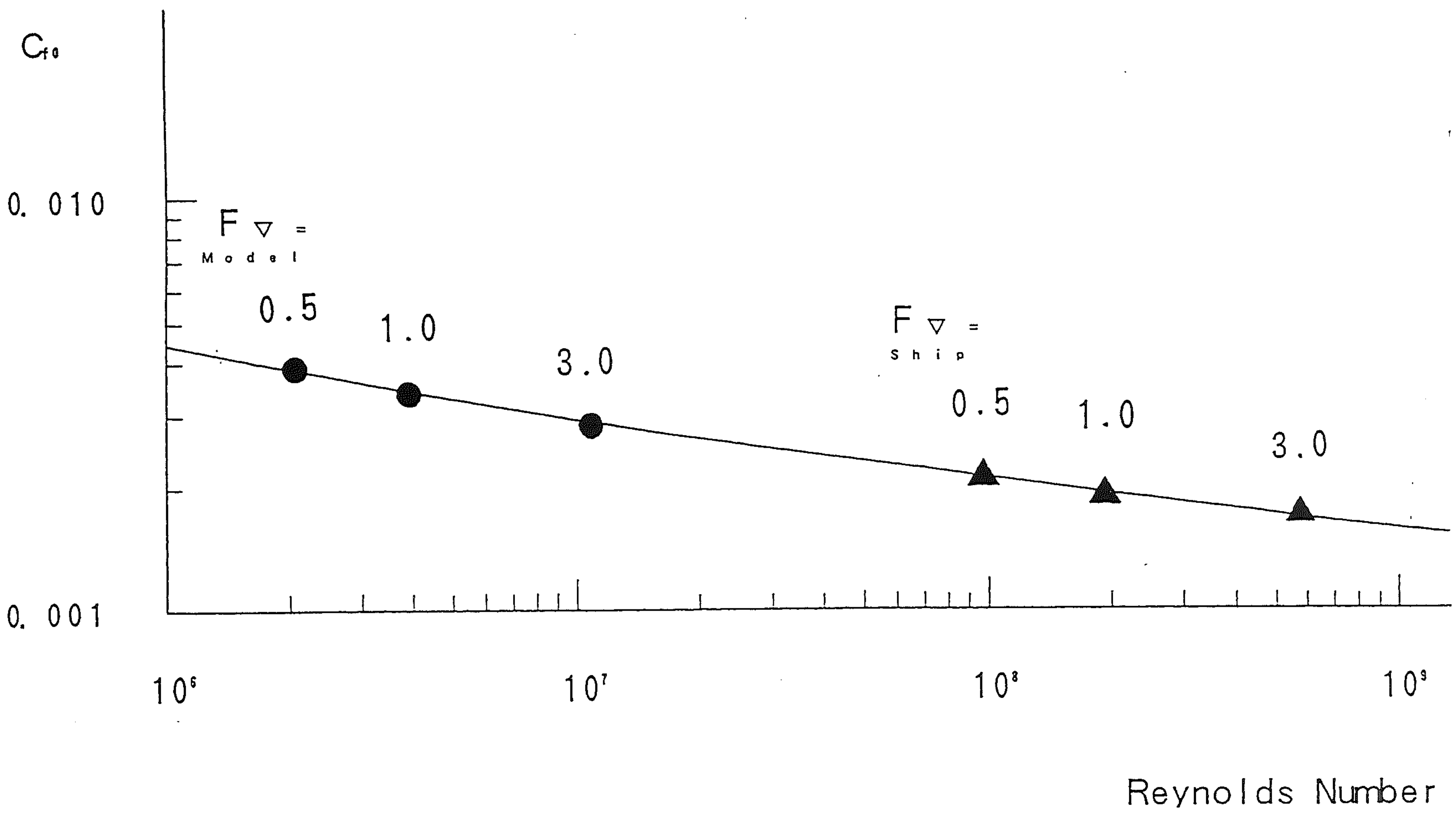

Fig. 2: Frictional resistance coefficient

volume and density, respectively. θ means initial trim angle, which is the angle between water line at rest and the straight line between the points on keel line at ord. 10 (stern) and 5 (midship). $\Delta\theta$ takes positive when bow up. ΔD takes positive for decreasing draft. b_1 is half width at stern.

A boat having 100 tonf in displacement runs at a velocity of 46 kt, which means about 3.5 in Froude number.

4.3. Resistance Performance

A planing boat's resistance performance differs from a displacement type ship's one. In high speed range planing boats change their floating position. Keel end point together with rotation of hull form by $\Delta\theta$ around this point determines a floating position. Keel end point is obtained by sum of initial draft and $\Delta D'$ whose sign should be considered. C_t , $\Delta\theta$ and ΔD are expressed by non-dimensional form for the law of similarity, showing a pattern as increasing speed, *DEGTYAREV (1998), YOSHIDA (1999)*. Frictional resistance is obtained by wetted surface area and frictional resistance coefficient. Wetted surface area can be calculated by the area under water line which is based on floating position.

4.4. Boat's Resistance

As an example, the resistance of the P T having 35 m in overall length, 6 m in width 1303.4 kN (133.0 tonf) in didplacement, *RAYMOND (1975)*, was obtained. A set of C_t, $\Delta\theta$ and ΔD at a Froude number is presumed by the empirical equations based on the data of the above-mentioned towing tank test, using four hull form parameters $L / \nabla^{1/3}$, $h_2 / \nabla^{1/3}$, $b_2 / \nabla^{1/3}$ and θ . L is the length from ord.10 (stern) to 0 (bow). h_2 and b_2 are chine height from base line (or keel line) and half width) at ord. 5 (midship). θ is trim angle at rest. Two kinds of empirical equations are made by the method of least squares, *DEGTYAREV (1998), NAGAI (1993)*. The one is the linear equation which consists of these four hull form parameters. $(L / \nabla^{1/3})^2$ and θ^2 are added to the linear equation, which makes the other equation i. e. the quadratic equation.

The P T's total resistance R_s is obtained by these equations. The dotted line in Fig. 3 shows the R_s obtained by the linear equation and the solid line the quadratic equation.

The balance of resistance and thrust of the boat should be discussed.

5. Trial Test

The P T has a propeller at center driven by gas turbine together with two side propellers driven by each Diesel engine. Viewed from bow, propeller at center rotates clockwise and two side ones rotate counter-clockwise.

A series of trial tests of the P T was done in Setonaikai sea Japan (E 131° 15′ 14″ , N 33° 57′ 9″). At each engine rate, speed V_s (k t), trim angle change $\Delta\theta$ (deg.) and each propeller shaft revolution N (rpm) together with propeller shaft horsepower S H P (ps) were measured during the test.

41.19 kt at the top speed was obtained.

6. Thrust

All propellers have cavitation at the top speed, *YOSHIDA (2000)*. It is difficult to presume thrust of a propeller having cavitation.

A little changing propeller items will cause propeller to get no cavitation. No cavitation will be got under the condition $V_a \leqq V_{ac'}$. V_a and $V_{ac'}$ mean inflow velocity into propeller and critical inflow velocity into propeller against origination of cavitation, respectively. The condition of $V_a = V_{ac'}$ is taken to get a propeller having high efficiency. An approximate value of the P T's thrust will be obtained under such a condition. During analysis wake fraction ω is taken as zero because of high speed. Propeller efficiency η will be obtained by the overlay system, *YOSHIDA (2000), TANAKA*

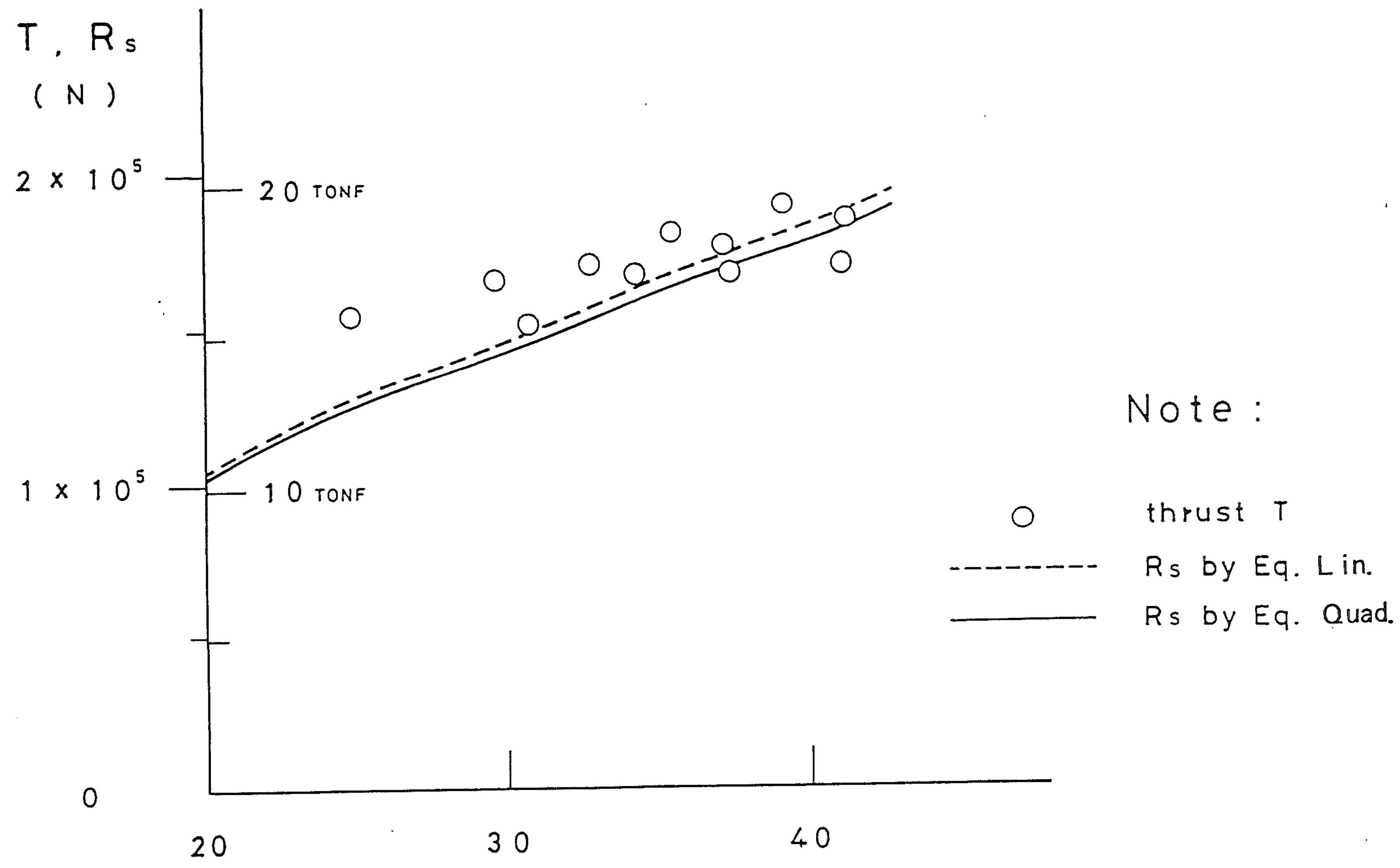

Fig. 3: PT boat´s thrust and resistance

(1981). The system is based on the experimental data which have been shown in the references *GAWN (1957), GAWN (1952) and EGGERT (1930)*.

Then thrust horsepower T H P is got by S H P $\times \eta$ under the condition that delivered horsepower D H P equals to propeller shaft horsepower S H P.

T H P's horizontal component give us thrust, which is compared with resistance.

6.1. Thrust of New Center Propeller at the top speed

Center propeller's diameter D, ratio of pitch to diameter p / D and blade area ratio B A R are as follows: D = 1.040 m, p / D = 1.196 and B A R = 0.60. Shaft horsepower S H P and propeller shaft revolution N at the top speed were measured as follows: S H P = 4680 ps and N = 1704 rpm. The analysis by the overlay system were done.

A little changing propeller items will cause propeller to get no cavitation. Although enlarging area of propeller is one of the methods for no cavitation, there are few propeller which exceed 1.10 in B A R. Keeping B A R 1.10 level, a trial will be done by increasing D to 1.100 m level. p / D = 0.75 and η = 0.49 are obtained under the condition $V_a = V_{ac'} = 41$ kt.

Center propeller's thrust T_c is obtained as $T_c = 7821$ kgf.

6.2. Thrust of New Propellers of sides at the top speed

About one of these propellers the discussion will be done. Side-propeller's diameter D, ratio of pitch to diameter p / D and blade area ratio B A R are as follows: D = 0.830 m, p / D = 1.000 and B A R = 1.10. Shaft horsepower S H P and propeller shaft revolution N at the top speed were measured: S H P = 2780 ps and N = 1706 rpm. The analysis by the overlay system were done.

A little changing propeller items will cause propeller to get no cavitation. A trial will be done by increasing D to 1.000 m level and decreasing B A R to 0.95 level.

p / D = 0.80 and η = 0.57 are obtained under the condition $V_a \leqq V_{ac'}$, which has no cavitation. $V_a = 41$ kt, $V_{ac'} = 42$ kt are obtained.

Side-propeller's thrust T_s is obtained as $T_s = 5471$ kgf

6.3. Total Thrust at the top speed

Total Thrust is obtained as follows:

$$T = T_c + 2 \times T_s$$

$$= 7821 + 2 \times 5471 = 18763 \text{ kgf}$$

$$= 184002 \text{ N.}$$

7. Trim angle change

Trim angle change $\triangle\theta$ at a speed was measured. As shown in Fig.4, $\triangle\theta$ was under estimated here, but the dependence on speed is quite similar. The difference of $\triangle\theta$ values between prediction and trial test one is due to scale effect.

8. Conclusions

Calculation shows that about 97 % of each propeller's T H P contribute to horizontal component, which gives the P T thrust. Total thrust T should be compared with total resistance R_s.

Total thrust T at V_s was obtained against not only at the top speed but also other speed as shown in Fig. 3 by applying the present method to trial test data under constant D and p / D. The results are plotted by "○" marks, which have enough thrust against R_s except at the top speed. Seeing curves

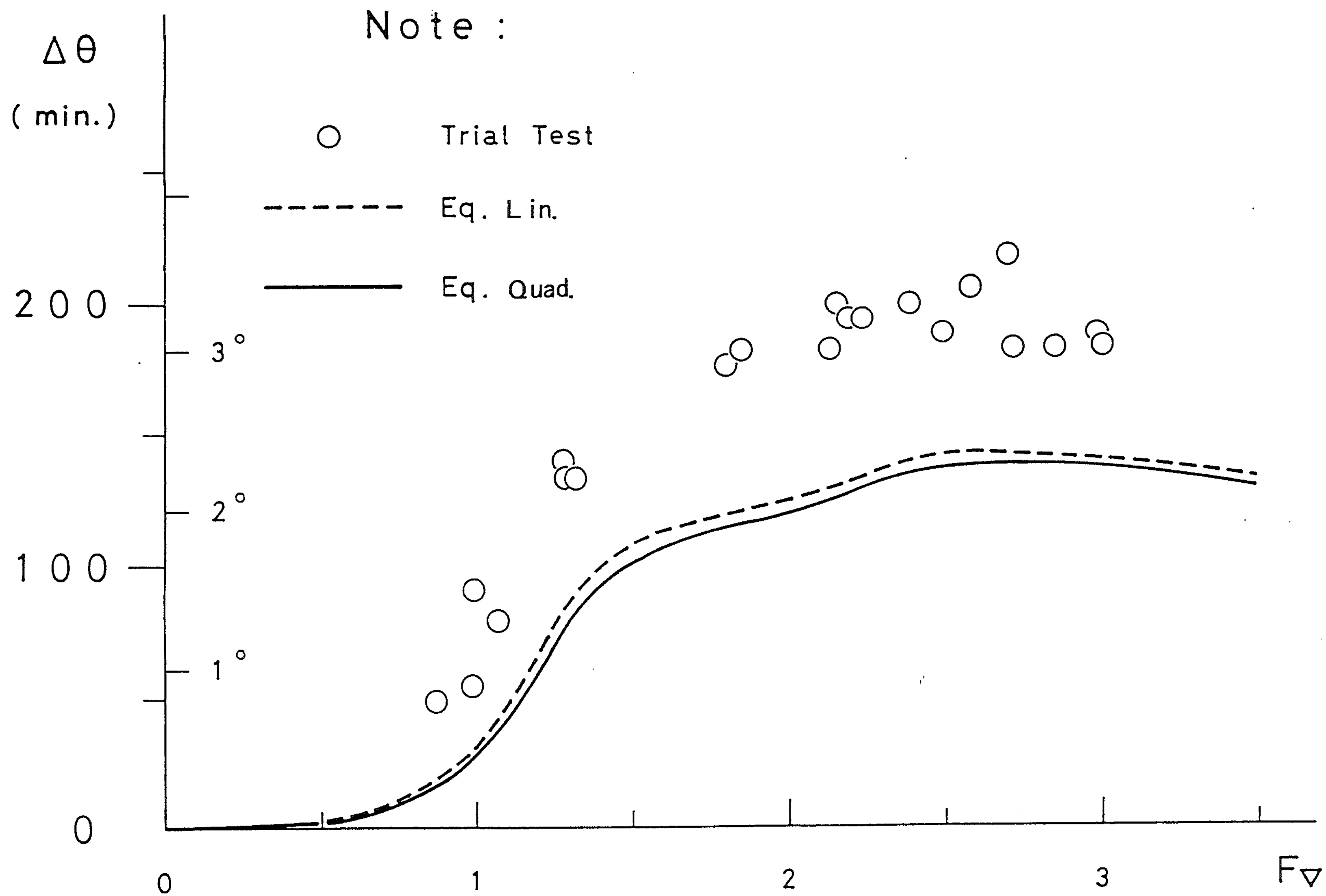

Fig. 4: Trim angle change

and trial test data in Fig. 3, we can admit Attwood's proposition. Attwood has proposed that overestimation of thrust by 10 % at a design speed is recommendable in case of not having reliable information, *ATTWOOD (1922)*.

Propulsive coefficient η_T (= E H P / S H P) shows 0.50 in high speed range, which is reasonable value. E H P is effective horsepower.

The difference of $\triangle\theta$ values between prediction and trial test one is due to scale effect.

References

ATTWOOD, E. L. (1922), *Text-Book of Theoretical Naval Architecture.*

DEGTYAREV, A. B.; KROLENKO, S. I. & YOSHIDA, Y. (1998), *A Mathematics for Design and Development of Optimum Hull Form Applying to Obtain a Planing Boat's Hull Form Parameter Set the Minimum Resistance,* I S C' 98 Proceedings, St.Petersburg, Section A, Vol.1, pp. 202-214.

EGGERT, E. F. (1930), Propeller Cavitation, Trans. S N A M E, p. 58.

GAWN, R. W. L. (Sep. 1952), *The Effect of Pitch and Blade Width on Propeller Performance,* I N A Vol. 94. pp. 716-817.

GAWN, R. W. L. & BURRILL, L. C. (1957), *The Effect of Cavitation on the Performance of a Series of 16-Inch Model Propellers,* Trans. I N A, Vol. 99.

NAGAI, T. & YOSHIDA, Y. (Aug. 1993), *Estimation of Resistance, Trim and Draft of Planing Craft,* Ship Technology Research Vol. 40 / Schiffstechnik Vol.40 · Heft 3, pp. 133-137.

RAYMOND, V. & BLACKMAN, B. (eds.) (1975-1976), *Jane's Fighting Ships,* London, p. 213.

SOTTORF, W. (15 Mar. 1938), *Versuch mit Gleitflächen, IV, Teil. Analyse, Werft Reedere Hafen, 19 Jahrgang,* Heft 6, pp. 66-67.

TANAKA, H.; ARAKI, K. & YOSHIDA, Y. (Mar. 1981), *Study of Nomogram for Reseach and Design in High-Speed-Craft's Propeller Hull Form and of it's Application,* Transactions of the West-Japan Society of Naval Architects, No. 61 pp. 113-124.

YOSHIDA, Y. (22-27 Sep. 1 1997), *Lowering a planing Boat's Maximum Trim Angle Change,* Proceedings of the 6-th International Conference on Stability of ships and Ocean Varna, Bulgaria, Vol Ⅱ, Bogdanov, P. A. (ed.), pp. 191-198.

YOSHIDA, Y. (1999), *Optimum Design of a Planing Boat's Hull Form,* Marine Technology Ⅲ, (eds.) Graczyk, T.; Jastrzebski, T. & Brebbia, WIT Press, pp. 3-13.

YOSHIDA, Y. (Oct.23-27 2000), *An Approximate Value of Planing Boat Thrust,* Proceedings of Sixth International Symposium on marine Engineering Tokyo 2000, Vol. Ⅰ, The Marine Engineering Society in Japan, pp 135-142.

YOSHIDA, Y. (2001), *A Planing Boat's Thrust and Resistance,* Marine Technology IV, (eds.) Brebbia, C. A.; Graczyk, T. & Jastrzebski, T., WIT Press, Southampton, Boston, pp. 181-192.

A Procedure for Design of Low-Wash High-Speed Monohull Ferries

Ivan Oestvik, LMG Marin, ivan.oestvik@lmgmarin.no
George Zaraphonitis, National Technical University of Athens, zar@deslab.ntua.gr
Jean-Jacques Maisonneuve, Sirehna, jean-jacques.maisonneuve@sirehna.ec-nantes.fr

Abstract

The paper describes the development and application of a procedure for the design of low-wash high-speed monohull ferries. The paper derives from work in the FLOWMART project, which is an on-going EU FP5 RTD project, which focuses on both monohulls and catamarans.

One of the main aims of the work reported upon in this paper has been to integrate wash assessment in the ship design process pertaining to monohull design. A short background is initially provided on the FLOWMART project and on high-speed monohulls.

The FLOWMART Project

February 2000 was the official starting date for the € 3.1 million project 'FAST LOW-WASH MARITIME TRANSPORTATION (FLOWMART)' [1] partly funded by the European Commission under the 4th Framework Programme and which will last until January 2003. The project is undertaken by a consortium of 11 partners having complimentary skills/expertise coming from 5 European countries. The partners are: FBM Marine Ltd., ALSTOM Leroux Naval, University of Strathclyde - Ship Stability Research Centre, National Technical University of Athens - Ship Design Laboratory, Alpha Marine Ltd., Sirehna, SSPA Maritime Consulting AB, Marintek, Tjärnö Marine Biological Laboratory, Department of Marine Technology - University of Newcastle upon Tyne and LMG Marin AS.

The main goal of the project is to develop guidelines and criteria to minimise the wash effects from High Speed Marine Vehicles (HSMV) and propose measures to limit its environmental impact. Through this process tools will be identified, modified and developed and will subsequently be used during the development of guidelines and criteria. The project comprises five technical work packages (WPs):

WP 1 – Numerical Modelling and Simulation
The objective is to develop/validate state-of-the-art tools by co-ordinating the efforts of the partners. All partners are involved with specific tasks within the WP to investigate, develop/validate different tools to and identify the most suitable tools. The development of each tool is screened thoroughly by other WP partners in order to obtain the maximum benefit from the findings.

WP 2 – Model Experiments
The objective is to provide sufficient and complementary experimental data to WP1 for tool development/validation by taking account various parameters, which are believed to be important for wash/design assessment. The experimental results are vital for the successful progress/completion of other WPs.

WP 3 – Full Scale Trials
The objective is to measure wash and motions from a number of high-speed crafts (HSC) in their operational environment at full scale under trials conditions. The wash database will be used to evaluate the performance of the CFD calculations (WP1) and model testing programme (WP2), whereas the motion data will be studied for any existing relationships between ride quality and wash-making characteristics.

WP 4 – Development and verification of Demonstrators
The objective is to validate the numerical tools (WP1) and apply these with the aim of developing low-wash monohull and catamaran design. Tool developers from WP1 will be involved with the validation by using the experimental input from WP 2 and WP 3. This WP will develop a monohull and a catamaran design as design examples utilising the available software tools from WP1. A low-wash design methodology will be the main deliverable from this WP extracting the experience from the design work.

WP 5 – Proposal of Criteria and Guidelines
The objective is to develop a set of proposals and guidelines for design and operations of high-speed craft (HSC) to reduce the wake wash generation and its impacts on environment and operation of other marine vehicles. This WP also aims to develop a wash impact assessment methodology based on the data/experience produced in the project.

The work reported upon in this paper derives from the WP4 work regarding monohull design.

High-speed monohull ferries[1]

There are numerous types of monohulls; displacement, semi-displacement or semi-planing and planing. This paper focuses on the utilisation of a monohull, described later in this paper, which falls into the latter two categories. The technology associated with planing and semi-planing monohulls is today mature. Recent efforts in the development of semi-planing monohulls, however, have led to larger length-to beam ratios, pushing high-speed designs toward long slender ships. These monohulls can be considered advanced in that they are pushing the limit of the state-of-the-art.

A planing hull has the majority of its weight supported by dynamic lift with the small remaining part of the weight supported by buoyancy or hydrostatic lift. These hullforms are typically of the hard-chine type with a Froude Number over 0.9 or a Volumetric Froude Number over 3.0. Another characteristic of planing hulls is the occurrence of complete flow separation at the transom and the sides. There are many variations of planing and semi-planing monohulls, which include round-bilge, hard-chine, double-chine, and stepped hulls. Cross sections of some of these hullforms are shown in Figure 1.

Small combat ships and high-speed patrol craft of light displacement and round-bilge have been used since the early 20th century. These designs have to a large extent been replaced by (double) hard-chine hullforms. Note the successful implementation of the deep-V hullform, considered a double-chine hybrid, for improved seakeeping performance.

[1] The material in this section derives mainly from the EFFISES [2] WP1 Report "Review of State of the Art on Fast Maritime Transportation & Set-up of Techno-Economic Database for Fast Marine Vehicles" by A D Papanikolaou, N Georgantzi and G Papatzanakis from NTUA-SDL of 30 June 2001.

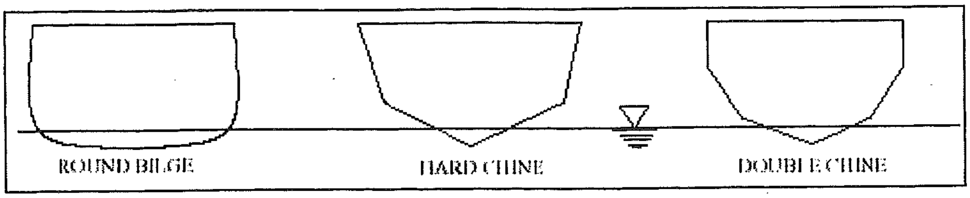

Figure 1: Types of planing monohulls

The trend towards larger capacity has pushed the length of fast-ferry monohulls beyond 100 meters. Principal characteristics of a number of operating vessels are shown in Table 1. Figure 2 and 3 show some typical planing monohulls.

Table 1: Characteristics of some planing monohulls

Characteristics	Guizzo Aquastrada	Albayzin Mestral	NVG Asco Corsaire	MDV 1200 Pegasus
Length, m	101.8	96.2	102	100
Beam, m	14.5	14.6	15.4	17.1
Draft, m	2.12	2.1	2.4	2.75
Hull Depth, m	9.5	8.9	5.2	10.7
Power, MW	27.93	21.6	24	27.5
Displacement, t	1034	946	1100	1200 est.
Speed, kts	41	35	37	38
Passengers	450	450	500	800
Cars (or Buses + Cars)	126	84	148 (4 + 108)	175 (6 + 106)

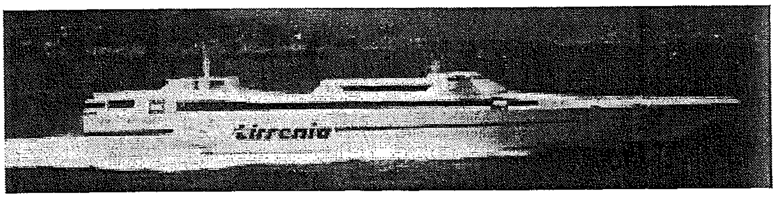

Figure 2: Aquastrada

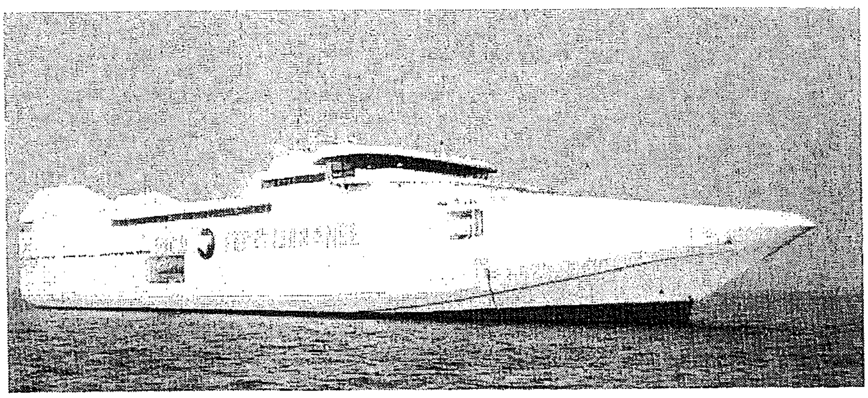

Figure 3: NVG Asco Corsaire

Several designers and shipyards have experience with planing and semi-planing/semi-displacement monohulls, for military, passenger and passenger/car ferry applications. The large number of vessels in service provides a wealth of operational statistics. Construction of these hullforms is relatively simple. They have large usable volume aft for machinery plant and the fitting of water jet propulsion. They combine large deadweight capacity with relatively high speeds. Typically, power plants and propulsion systems of high output are necessary to achieve high speeds. Growth in vessel size might be limited by the power needed to reach and sustain operation in the planing and semi-planing speed regime. Roll stability is often an issue for displacement monohulls, but not for typical planing to semi-planing monohulls, which tend toward a wider beam. However, the recent trend toward higher length-to-beam ratios even for planing monohulls may raise concerns about static and dynamic roll stability in turns. Note also that transverse and longitudinal stability is an issue for the small planing craft (*"porpoising"* phenomenon). Heave and pitch motions and vertical accelerations of planing and semi-planing vessels may be severe at high speed in rough water. Thus, hull size may be inflated to limit these motions, lowering the deadweight-to-displacement ratio. However, active ride control has been shown to help in this regard. Hull-bottom slamming is also an issue for planing monohulls, because of passenger comfort and structural design.

A background on the FLOWMART project and on high-speed monohulls has been provided and the paper descends into the development and application of a low-wash design procedure for high-speed monohulls. The work focuses on utilizing he Corsaire 11000 design by Chantiers de l'Atlantique, as a test platform in order to optimise its already good wash characteristics.

Design procedure

The goal of any design process is to meet the objectives of the ship owner in the best possible way. The objectives pertain to: economy (maximise income, minimise costs), operation (ability to perform a number of travels in given areas, harbours and sea conditions), safety (stability, fire prevention, manoeuvrability, etc.), passenger comfort and environment. Wash effects are part of the latter category in line with emission, noise, etc.

Currently the designer have no readily available means within the ship design process in order to assess the wash effects resulting from the ship hull. One of the aims of the FLOWMART project is to integrate wash assessment in the ship design procedure. This is achieved through the extension of the well-known sequential ship design spiral with a new module, termed wash assessment, as a supplement to already existing modules, such as stability, structures, resistance, etc... An alternative or complementary approach is also investigated in the Flowmart project, which tends to integrate those aspects in a parallel way through optimal design techniques. The work presented in this paper should be seen as extending the well-known ship design spiral with a new module, termed wash assessment, as a supplement to already existing modules, such as stability, structures, resistance, etc. illustrates these approaches.

A recent approach, which is feasible when all design criteria can be numerically assessed, is to perform multi-disciplinary optimisation with the help of design search tools. In this paper, this approach has been undertaken, oriented towards wash assessment/optimisation. In order to enable numerical assessment of wash, WP1 software tools developed/refined (in the FLOWMART project) have been utilised, as described later in this paper.

The wash criterion depends on the kind of wash effects to be assessed. However, for the demonstration purpose, a simple criterion related with the height of the generated wave is selected as follows:

$$W = \sqrt{\frac{1}{x_2 - x_1} \int_{x_1}^{x_2} \zeta(x)^2 \, dx}$$

ζ	wave elevation
x	abscissa on the chosen longitudinal cut
x_1	starting point for the integration
x_2	ending point for the integration, chosen at a zero crossing point
x_2-x_1	= L which is constant

There are two ways for decreasing this criterion. The first one consists in changing operational parameters (speed, route…) so that wash effect at given location is kept low. The second one consists, for given operational conditions, in changing the hull shape. In this paper, the second approach is undertaken. The procedure itself is however able to deal with both approaches, provided that numerical models exist to relate operational and shape parameters to the ship operational and performance criteria.

Thus the problem at hand, for one given ship type, is to minimise wash along the ship route, through the combined adjustment of ship shape, with constant displacement and satisfactory performances in other aspects like stability, seakeeping, manoeuvring, etc. The problem is simplified by looking at only one location along the ship's route for wash assessment. To ensure compliance with intact stability requirements and at the same time aiming at acceptable roll motion, certain limits are posed on the vessel's GM. The other design constraints are considered only through the range limitation of the design parameters variations. The problem finally dealt with is:

- Minimize W in deep water at a distance of Lpp/2, for a speed of 37 knots.
- Ship displacement in the range [1000 t - 1200 t].
- GM in the range [0.25 - 6.00 m].
- Transom stern surface area (TSA) greater than 4.16 m^2 for propulsion purpose.

The FLOWMART partners have selected the original hull form of the HSC Corsaire 11000 designed by Chantiers de l'Atlantique as a test platform for the wash optimisation procedure. The Lpp is 87.5 m, its displacement is 1040 t, GM value is 5.53 m and its transom stern area is 13.73 m^2. The ship propulsion is guaranteed by four water-jets installed on the transom stern providing for a maximum speed of 40 knots.

The optimisation problem is addressed by two teams, on the basis of specifications provided by Chantiers de l'Atlantique. Both teams used the same tools, but were free to choose ship shape parameterisation and design space search approaches. The team 1 consists of Sirehna and Chantiers de l'Atlantique in collaboration with SSPA and Team 2 of NTUA and LMG Marin. The results from the two teams were compared in the end of the design work and the best design was selected and put forward to model testing in order to verify wash calculations done by the WP1 software tools.

Software description

The design process is based on the use of one CAD parametric modelling tool (here the Napa software), associated with a potential flow calculation code (Shipflow from Flowtech [3]), that constitutes a calculation chain able to calculate design criteria (wave wash, ship resistance, stability criteria) for given sets of design variables (shape parameters).

This calculation chain is embedded into a design search framework (modeFrontier, [4]), which enables any type of investigation, among which:

- parametric studies, design of experiments,
- approximation or interpolation of the involved function with help of response surface of different types, from linear or quadratic approximation to neural nets approximation,
- mono-objective optimisation with deterministic and/or stochastic algorithms,
- true multi-objective optimisation with genetic algorithms, which enable to outline the set of solution that best fit both objectives (Pareto set),
- multiple criteria decision making tools that enable the designer to select the most relevant solutions within a set of solutions, on the basis of his own choices or preferences,
- statistical and graphical analysis of the results, able to outline design trends,
- robust design approaches which enable to objectively define trade-off between performance (best solutions in term of objectives) and stability (best independence of the solution vs. variations in design variables).

The purpose of the present application utilising one calculation chain is demonstrative; the same procedure can be applied to more complex, multiple calculation chains in order to take into account other ship design aspects, such as resistance, structures, stability, etc.

The Napa, Shipflow and Frontier tools were used by both teams, in two ways: one local implementation, in which all components were locally available on one computer, and one distant implementation, in which the CAD tool was located at Chantiers de l'Atlantique, St Nazaire, the flow analysis tools at SSPA, Gothenburg, and the modeFrontier framework at Sirehna, Nantes. This last approach was carried out in combination with some work regarding distributed computing performed through other EC funded projects. This has illustrated the flexibility of the design procedure.

Application

The *process flow* used in the study is shown in Figure 4. The calculation chain consists of two components:

- Napa reads the parameters file and produces geometric outputs to be used for the design assessment within the optimisation or to check compliance with the imposed constraints, and the offset files for the hydrodynamic calculation.
- Shipflow uses this offset file to perform the hydrodynamic calculation and outputs hydrodynamic results (resistance, wash and trim) that are used in the optimisation problem.

The first step consists in adjusting the set of *design variables* and their range of variations so that:

- Sufficient freedom can be ensured in shape variations.
- The combination of the design variables lead to sufficiently acceptable and calculable shapes.
- The main design objective (ship main characteristics and expected performances) are satisfied.
- The design space is as connected consistent and simple as possible.

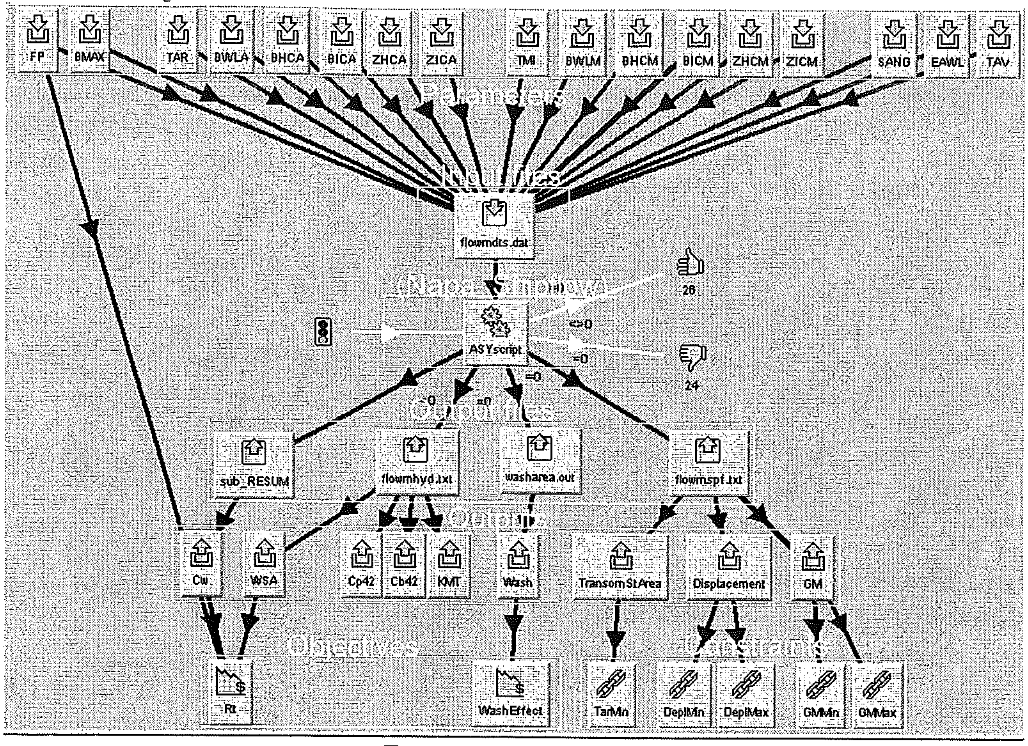

Figure 4: Process flow

The parameterisation chosen by *Team 1* is based on a set of 19 parameters managing the shape as illustrated in Figure 5.

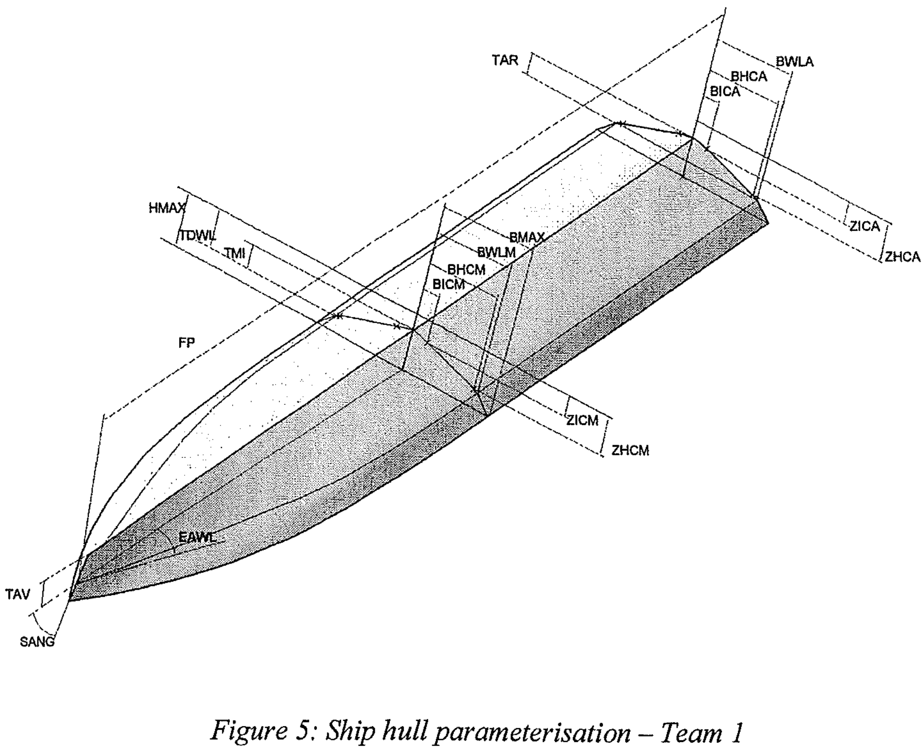

Figure 5: Ship hull parameterisation – Team 1

The optimisation process used by Team 1 uses involves Genetic Algorithm (MOGA) coupled with Gaussian Process response surface available in modeFrontier. Initially a first group of designs is computed. This initial set, named first generation, is generated using a random method in order to cover all directions of design space. When the calculation of the first generation is completed, the genetic algorithm evaluates the design space shape and generates new points employing a method of selection-reproduction and selection-mutation.

Progressively the performances of new generations improve and a global solution is reached. The problem is set as a multi-objective optimisation problem, consisting in minimising the total resistance and the wave wash. So the solution consists in finding the Pareto frontier, i.e. a set of points with dominant performances.

Every generation requires 40 points (approximately 2 points per parameter) and every flow evaluation takes 35 minutes. In order to reduce the calculation effort, only 60% of new generation points are really calculated (real points), the remaining 40% being extrapolated using response surface technique (virtual points). In addition, a preliminary test is performed on the geometric constraints in order to avoid useless hydrodynamic calculations, which are only approximated in these areas. Such an approach is possible thanks to the robustness and flexibility of the algorithms.

After 112 real evaluation and 48 extrapolated points, two interesting solutions are found (shapes 143 and 151) on a Pareto frontier, which is rather narrow as both objectives are not so conflicting: wave wash tends to vary like the wave resistance (see Figure 6).

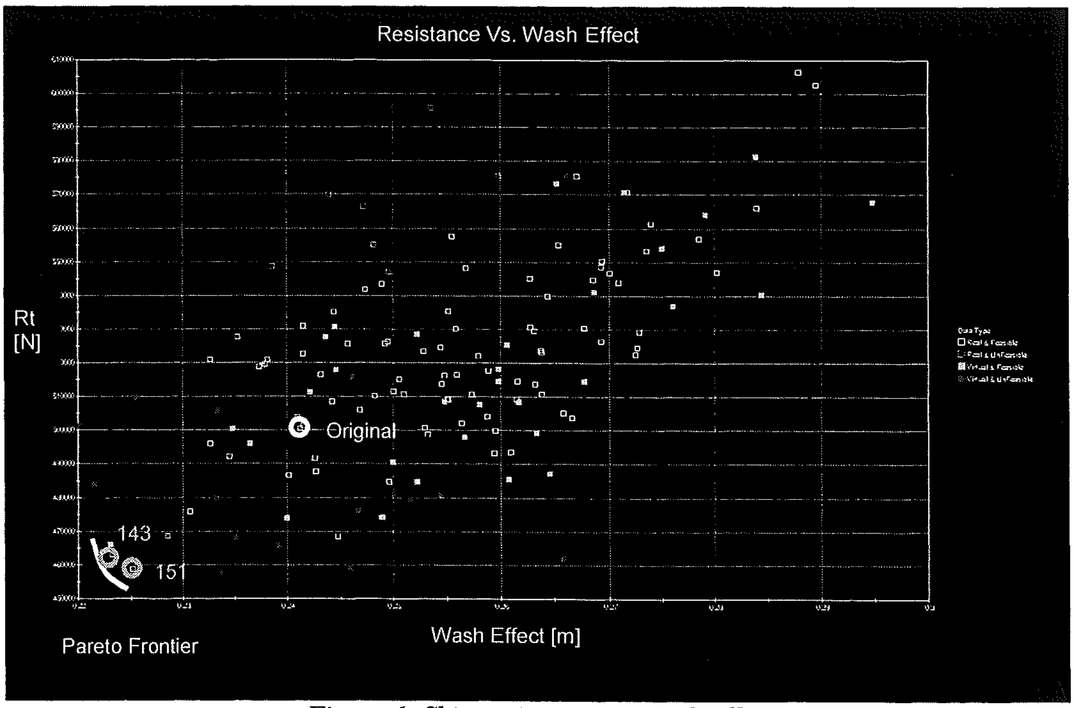

Figure 6: Ship resistance vs. wash effect

Nevertheless some parameters influence both objectives in opposite way. An analysis shows that some parameters, like the parameters regarding the ship front part, have different and inverse proportionality with the resistance R_t and wash W. This conflict however is not dramatic, especially near the optimal zone (see Figure 7).

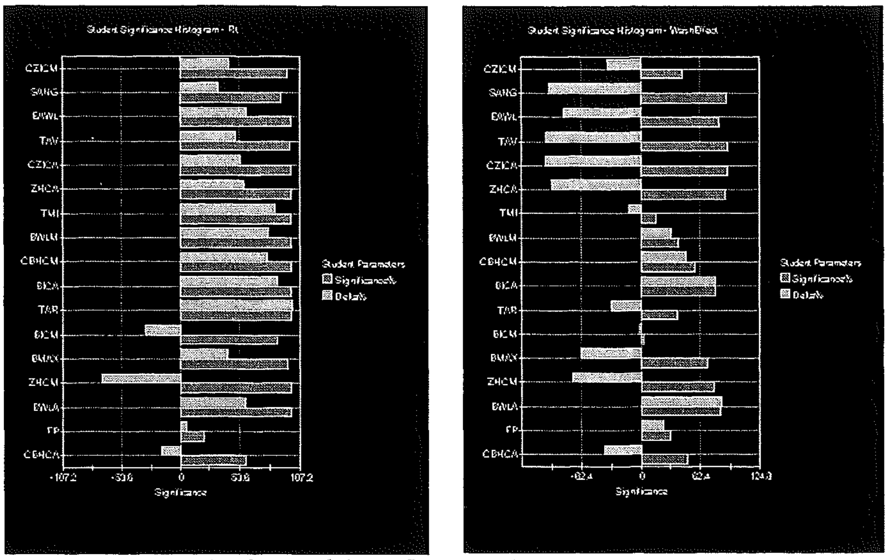

Figure 7: Analysis of the influence of variables on two outputs: total resistance and wave wash

Figure 8 shows the original shape some of the most interesting solutions obtained after the optimisation process.

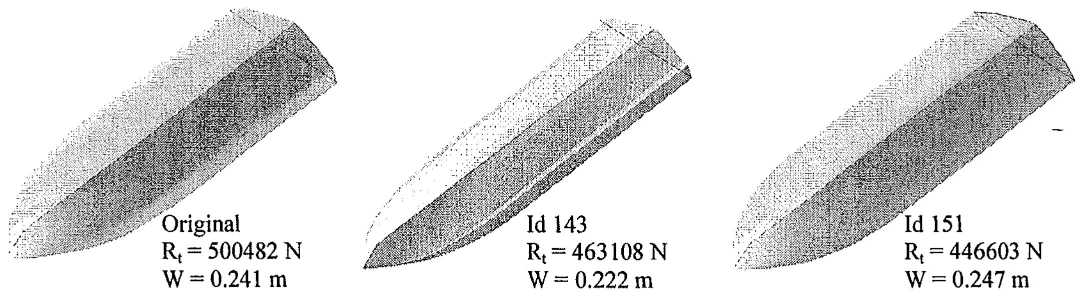

Figure 8: Comparison of original and two alternative shapes

The parameterisation chosen by the *Team 2* is again based on 19 design parameters, as shown in Figure 9.

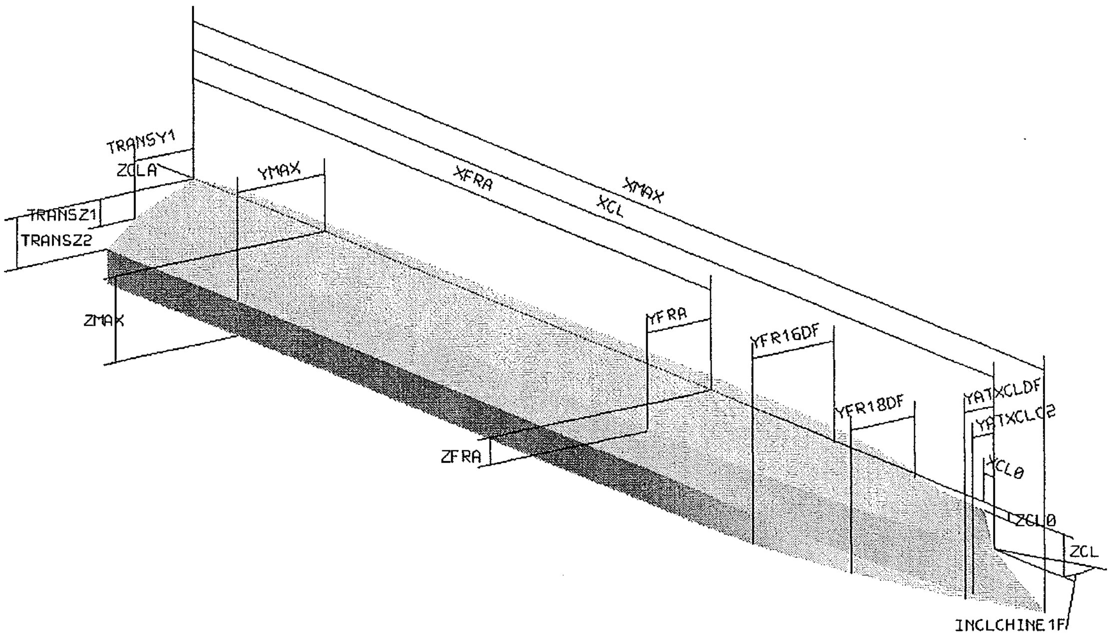

Figure 9: Ship hull parameterisation – Team 2

The optimisation process used by Team 2 is based again on the application of Genetic Algorithm (MOGA) method, using the same software tools. The basic difference between the two approaches consists in the selection of the design variables and consequently on the derivation of the hullforms. For example, in the second approach, the vessel's displacement has been considered fixed, equal to 1035t for all the hullforms generated during the optimisation.

The hullform parameterisation as applied by Team 2 is based on a set of 19 parameters (see Figure 10). Among them, some parameters are necessary for the body definition, but they are considered to have minor effect on the vessel's hydrodynamic performance, while others are used to define the external dimensions or the upper part of the vessel. During the optimisation these parameters were considered fixed and only the remaining 7 parameters were varied.

The results obtained by Team 2 are presented in Figure 11. The horizontal and vertical axes correspond to the total resistance (in kN) and the predicted wash measure (in m). A number of 284 cases have been evaluated. Among them, some interesting designs are observed at the lower left part of the graph, denoted by their numbers (hull no 47, 118, 282). The corresponding hullforms are presented in Figure 11.

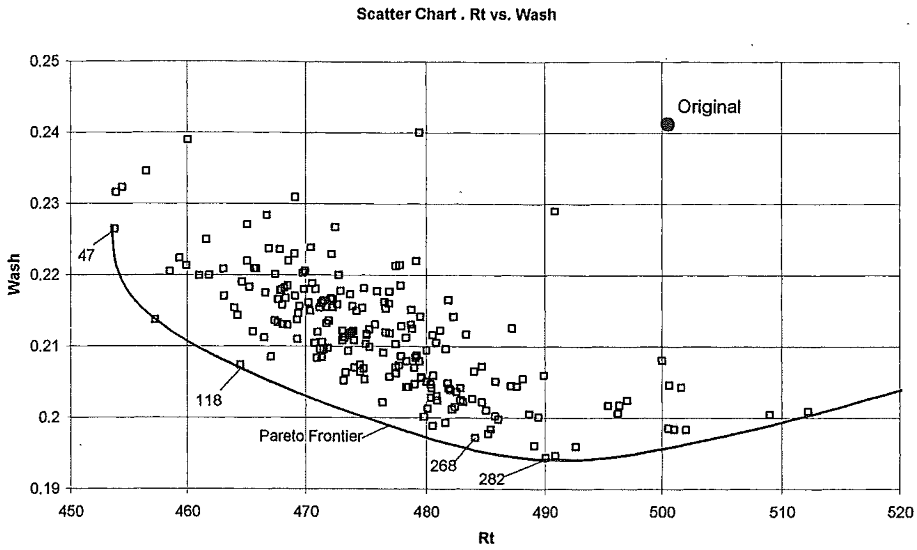

Figure 10: Total vs. wave resistance

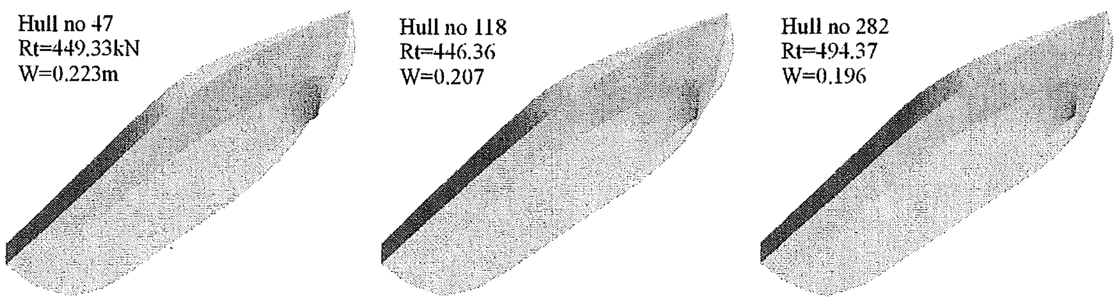

Figure 11: Comparison of alternative hullforms

In Figure 12, the original hullform and the selected designs are *compared* with respect to their total resistance and wash waves. As can be seen from the graph, the design no 151 by Sirehna team 1 exhibits the lowest total resistance per tone of displacement (10.2% reduction with respect to the original hull) and a 6.2% reduction of wash waves per tone. Minimum wash waves are predicted for the design no. 282 by NTUA team 2 (18.5% reduction compared to the original vessel), while the total resistance is almost constant (0.5% reduction). A compromise between wash and resistance reduction is obtained for hull no 118 by NTUA team 2. Calculations with this hull revealed a 13.9% wash reduction and 6.7% reduction in total resistance.

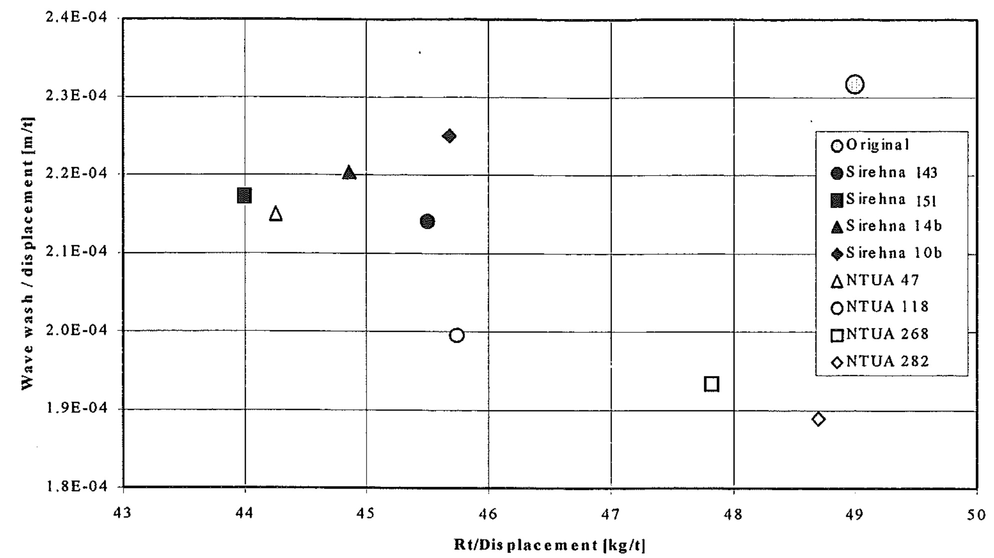

Figure 12: Comparison between Team 1 and Team 2 hull shapes

Conclusions

The work presented in this paper has aimed at illustrating for the first time the integration of wash assessment in the ship design process. This has been achieved through the development and application of a design procedure, which has been outlined in the above section. The procedure has been utilised to improve an existing design pertinent to wash and resistance. The procedure results are currently being assessed through model experiments for the developed design (hull no. 118) in order to validate the numerical calculations for wash and resistance. The procedure must also be further validated against other designs prior to drawing conclusions upon the applicability of the described procedure.

Acknowledgement

Acknowledgements are due to the European Commission for funding the FLOWMART project, as well as to Michael Leer-Anderson at SSPA, who provided support for calculation, although SSPA were not directly involved in the work on the monohull HSC. The staff at NTUA, Sirehna and Chantiers de l'Atlantique, St Nazaire (and especially Loïc Morand) should also be mentioned.

References

1. FLOWMART - FAST LOW-WASH MARITIME TRANSPORTATION, European Commission Contract No. GRD1-1999-10959, Coordinated by SSRC-University of Strathclyde, February 2000-January 2003.
2. EFFISES - Energy Efficient Safe Innovative Ships and Vehicles, European Commission Contract No. GRD1-2000-25847, Coordinated by SES Europe AS, March 2001-February 2004.
3. SHIPFLOW, http://www.flowtech.se/Shipflow/
4. ModeFRONTIER, http://www.esteco.it/

Direct Nonlinear Hydrodynamic Analyses For High Speed Craft

Wouter Pastoor, DNV, Hydrodynamics and Structures, Wouter.Pastoor@dnv.com
Trym Tveitnes, DNV, Hydrodynamics and Structures, Trym.Tveitnes@dnv.com
Øyvind Pettersen, DNV, Hydrodynamics and Structures, Oyvind.Pettersen@dnv.com
Olav Nakken, DNV, HSLC & Passenger Ships, Olav.Nakken@dnv.com

Abstract

Direct calculations for High Speed Craft is an important issue due to their specific design, e.g. lightweight structures and advanced hullforms, and due to their operation, namely high service speeds. The DNV classification rules give requirements and guidance for direct analyses. An overview is given of the rule requirements for direct analysis of High Speed Light Craft (HSLC), with emphasis on the hydrodynamic calculations. The practical application of nonlinear analyses according to these rules is described. For classification of other ships than HSLC the classification notation CSA-2 (Computational Ship Analysis) is applicable when direct analyses are applied. A summary of this class notation is given and a general strategy for nonlinear hydrodynamic assessments is presented. This strategy is a guidance to determine nonlinear design hydrodynamic loads based on a 20 years return period and a scatter diagram approach. It is a rational assessment procedure with different levels of complexity but without endless nonlinear calculations. Special features in the assessment scheme are the possibility to include slamming in the hydrodynamic analyses, apply direct load transfer of hydrodynamic pressures and accelerations to a FE model and conduct whipping analyses by using the slamming events as excitation sources. Special attention is paid to reduce the amount of nonlinear simulations by rational determination of critical sea states and by using advanced response conditioning techniques to replace random irregular simulations. A summary is given of the WASIM nonlinear hydrodynamic program and the integration of slamming in the simulations.

1. Introduction

Structural weight is a very critical aspect when designing high speed craft. These type of vessels are characterised by strong 3 dimensionally shaped hullforms that can lead to severe (nonlinear) hydrodynamic loading, like impact loads due to slamming. Rational design of such structures based on sound hydrodynamic and structural analyses is thus important and is a process, which is still under development. DNV has supported safe structural design using direct analyses, both by classification services, classification notes as well as the consultancy services DNV is providing.

Concerning the classification of ships it is the HSLC rules that provide the industry with clear requirements for direct hydrodynamic and structural analyses, see Pt.3 Ch.9 *Direct Calculation Methods* of the HSLC rules. For classification of other types of ships, above 100 metres, it is the classification notation CSA-2, *Computational Ship Analysis*, see Pt.3 Ch1. Sec.16 of the ship classification rules DNV (2002), that provides requirements when carrying out direct hydrodynamic and structural analyses. Within the consultancy services analysis tools have been and are developed and applied for many years. A clear example is the nonlinear hydrodynamic WASIM program.

This paper gives and overview of direct analyses requirements and the practical application of direct calculations, with emphasis on the hydrodynamics. First a summary of the HSLC direct analysis requirements is given with information on the practical application of nonlinear hydrodynamic assessments according to these rule requirements. Subsequently a summary is given of the classification notation CSA-2, which gives requirements for direct analyses of ships above 100 metres not classed according to the HSLC rules. The last part of this paper presents a general strategy for nonlinear hydrodynamic analyses with special attention paid to the characteristics of high speed craft. The purpose of the scheme is to determine nonlinear design loads based on a 20 years return period and a scatter diagram for the longterm wave description. As nonlinear computations are time consuming design sea states have to be identified in order to reduce the amount of nonlinear

calculations to a practically feasible amount. This requires special attention as the resulting design loads should be defined such to represent a 20 years return period.
A key element in the general assessment scheme is the DNV WASIM program. A summary is given of the program with emphasis on the integration of slamming in the program. The paper ends with conclusions and gives a discussion on the present status of hydrodynamic capabilities as well as future developments and research requirements.

2 Hydrodynamic analysis of High Speed Light Craft

The DNV rules for HSLC give explicit requirements for direct analysis, see DNV HSLC rules (2002). A summary of the chapter is given below, with main emphasis on the hydrodynamic analyses. This wave load analysis part is slightly different described as in the present rules as it contains some proposed revisions. How to apply the direct analysis rule requirements practically for nonlinear analyses is described in the second paragraph.

2.1 DNV Rules for HSLC for direct calculation of design wave loads

Pt.3 Ch.9 of the HSLC rules describe requirements for direct calculation methods. This chapter includes requirements for hydrodynamic analyses, global as well as local finite element models, ultimate strength and fatigue strength analyses. Of particular interest in this paper are the hydrodynamic analyses. The rapid development of numerical prediction tools and increasing computer capabilities give the possibility of advanced hydrodynamic assessments in the early design phases of ships. As the weight of high speed vessels is of great importance the need for accurate wave load predictions is inevitable in order to design safe lightweight structures. A great advantage of these HSLC rules for direct calculations is that it allows replacement of numeric rule formulas by direct analyses providing thus more flexibility to the designer/builder/owner.

HSLC represent a large variety of ship types, dimensions, shapes, speeds and operations. This implies that the rules should be flexible, which means that direct calculation requirements are provided for different levels of direct analyses depending on the complexity of the vessel. The more complex a design the more rule formulas may be replaced by direct calculations. However, as more rule formulas are replaced, the requirements for direct analyses have to increase. Three levels are therefore provided and shortly discussed hereafter with special attention to the hydrodynamic analyses involved.

Level 1: Local analysis

For all types of craft, independent of size and type it may be necessary to conduct local structural analyses. For this level the rule minimum loads are to be used unless they are inappropriate and a hydrodynamic analysis may be required for verification of the rule minimum loads. Types of local analyses are:

- Compartment model, main framing and girder system
- Frame and girder model
- Local structure model
- Stress concentration model

Level 2: Rule verification analysis

This level is applicable for monohulls and twinhulls over 50 meter length. Although rule formulas are available for global loads it is realised that these may not be fully appropriate due to e.g. speed, size, form and operation. In such cases a hydrodynamic analysis is needed for verification of global design loads. In many cases a linear analysis will be sufficient, but craft, which can exhibit significant nonlinear behaviour, such as wavepiercers with a centred bow, a nonlinear analysis may have to be performed. This is especially important if rule design loads are to be deviated from.

Level 3: Alternative rule analysis

This highest level is primarily applicable to craft for which there are no rule formulas for the global loads available, e.g. trimarans, pentamarans etc. Additionally this level is also applicable in the following cases:

- The hull form is such that the rule formulas are not expected to give reliable design loads.
- The operational profile is such that the rule loads and acceptance criteria are not considered adequate.
- The designer or yard wants to deviate from the rule requirements for global strength in order to optimise the hull structure.

At this level the global design loads are to be analysed by nonlinear hydrodynamic analyses. Secondly, the global design load cases are to be analysed using direct transfer of these design loads to the structural finite element model.

Wave loads and motion analyses

Classification of a ship implies that it is fit for purpose. Thus the HSLC rules for wave loads and motion analyses specify that design loads are to be based on a 20 year return period or equivalent and on the operational restrictions of the craft. Here we see a principal difference between conventional ships and HSLC. Namely a design speed/sea state curve is to be specified for a HSLC describing the maximum operational limits of the vessel. Operating above it's limits might endanger the structural integrity. An example of a speed/ sea state curve is given in Figure 1.

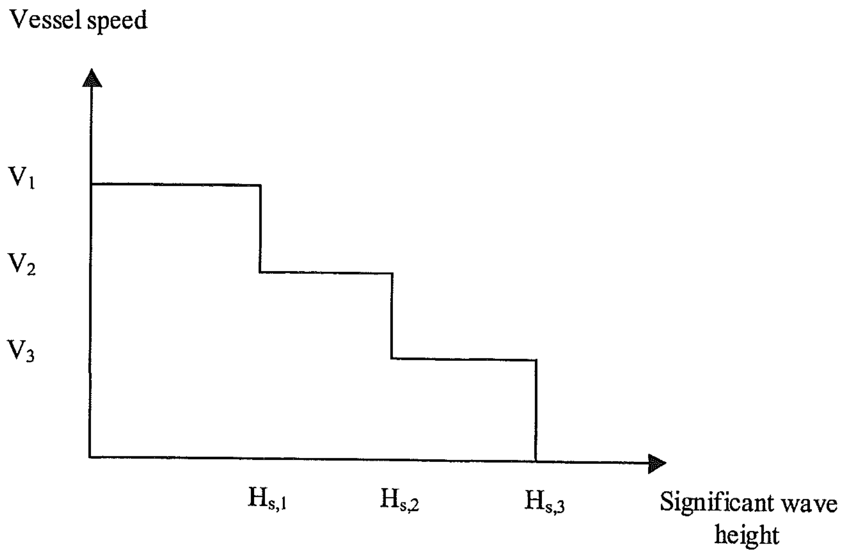

Figure 1 Speed/Sea state curve for a HSLC

As seen the significant wave height defines the upper speed limits. If the upper significant wave height is exceeded the craft shall seek a place of refuge at slow speed. Secondly, it may not leave port if the maximum significant wave height might be encountered during the voyage. The speed/ sea state curve can be derived from rule formulas, which determines the relationship between maximum allowed speed and significant wave height for a given design vertical acceleration. Important aspects determining the curve are the craft size, hull form and operation. Obviously the speed/ sea state curve is of importance when determining design motions and loads. Any direct calculation should therefore be based on this curve. A more specific description of the calculation of design wave loads as described in the HSLC rules using the speed/sea state curve will be given.

Design loads for conventional ships are based on longterm analyses using a scatter diagram. The consequence of applying a speed/sea state curve is however that the determination of an extreme becomes quite different. For HSLC short term extreme response statistics are used to define design values. This is to be done for the worst combination of speed and sea state (H_s, T_z) within the allowed operational profile. To define design values based on a short term approach one needs to specify a sufficiently low probability level to account for two factors:

- The HSLC may encounter the worst sea state relatively often during it's operational lifetime.
- The significant wave height is estimated by the crew through visual observation, which is uncertain and thus introduces the risk that the actual waves are underestimated and the vessel is operated above it's limits.

DNV has thus defined the design level to 1% of the extreme probability distribution.

In case of a linear analysis assuming Rayleigh distributed amplitudes the extreme value corresponding to an exceedance level of 1% is defined by,

$$R_{\text{linear}} = \sigma\sqrt{2\ln\frac{N}{0.01}} = 1.25\cdot\sigma\sqrt{2\ln N} \tag{1}$$

where

N = number of amplitudes in a short term period of 3 hours

σ = response standard deviation

Thus we see that the design value is 25% larger than the expected extreme in 3 hours, which is to account for both uncertainty factors mentioned above. Assuming a 1000 response cycles per hour, the linear design value is then formulated as,

$$R_{\text{linear}} = \left[5\cdot\sigma(Tz,\mu)\cdot H_s(V)\right]_{\text{worst}} \tag{2}$$

Here the standard deviation is calculated for a sea state with a wave height of 1 meter and the extreme is to be taken from the worst combination of heading, speed and sea state.

In case of a nonlinear analysis is the shape of the amplitude probability distribution not known and therefore the design value is to be determined differently. The expected extreme in 3 hours is to be determined using a time domain simulation. Subsequently the design value is formulated by,

$$R_{\text{nonlinear}} = 1.25\cdot R_{\text{most prob, 3 hrs}}\left(H_s, T_z, \mu, V\right)_{\text{worst}} \tag{3}$$

Thus the factor of 1.25 is taken equal as for a linear analysis to account for the two uncertain factors as discussed previously.

How to apply this nonlinear direct calculation approach in a practical way is discussed in the following paragraph.

2.2 Practical application of nonlinear calculations according to HSLC rules

The rule requirements are quite detailed and clear but practical application does raise some questions, mainly concerning nonlinear hydrodynamic analyses. An important step in the procedure is to define the worst condition, which is used as design sea state. How to identify this is dealt with hereafter. A second question is how to conduct a time domain simulation and determine the expected extreme from that simulation; especially the simulation length and the statistical post-processing of nonlinear responses are discussed.

Identification of the worst condition

Two different approaches are presented to identify the worst condition, which serves as design case. Generally nonlinear programs are time consuming; not only the simulation itself but the pre and post-processing can be cumbersome. Consequently the amount of nonlinear simulations is to be kept to a minimum, which calls for an intelligent procedure to identify the worst condition.

The first approach is based on the assumption that the response behaviour is mildly nonlinear, which implies that nonlinear severe behaviour corresponds with linear severe behaviour. Consequently we can use the linear response model to identify the worst condition, which is a fast and straight forward procedure. Thus for the speed and significant wave heights from the speed/sea state curve a sufficient number of combinations with wave periods and headings are to be composed and assessed linearly to reveal the worst combination. In that procedure the wave periods are selected such that it gives a good coverage of the possible combinations. Secondly, the significant wave height is reduced according to the wave steepness criterion from Classification Note 30.5, see DNV (2000), if appropriate.

Having established the worst condition a nonlinear simulation is conducted for that specific sea state, heading and speed. Due to the nonlinear behaviour it might well be that the worst condition is shifted a bit from the linear worst condition. In order to check this it is advised to conduct nonlinear simulations as well for “adjacent“ conditions to the identified condition, which means:

- Wave periods are varied +0.5 and –0.5 seconds from the identified worst period
- Heading is varied +15 and –15 degrees from the identified worst heading
- Worst significant wave height and period for one larger and one smaller vessel speed are selected from the speed/sea state curve. This means that if the worst condition was found for speed V_2, see Figure 1, the worst sea state conditions for speed V_1 and V_3 are to be evaluated as well.

If one of these extra simulations gives more severe response behaviour that condition is then to be considered as design condition.

The second approach to identify the worst condition is utilised if the linear model is not a good identifier for extreme events. We are then forced to use a nonlinear identification procedure. Short nonlinear simulations are conducted for a set of sea states, speeds and headings from which the worst is selected. Typically these short simulations lasts 30 minutes. The set of sea states, speeds and headings is composed by selecting possible wave periods for the significant wave height/speed combinations from the speed/sea state curve. Again the significant wave heights are reduced according to the wave steepness criterion from CN 30.5, DNV (2000), if appropriate. For most responses it is quite straight forward to select the most critical wave heading or at least to narrow the possible ones. Typically a set of sea states and speeds to be simulated for worst condition identification is plotted in the Figure 2

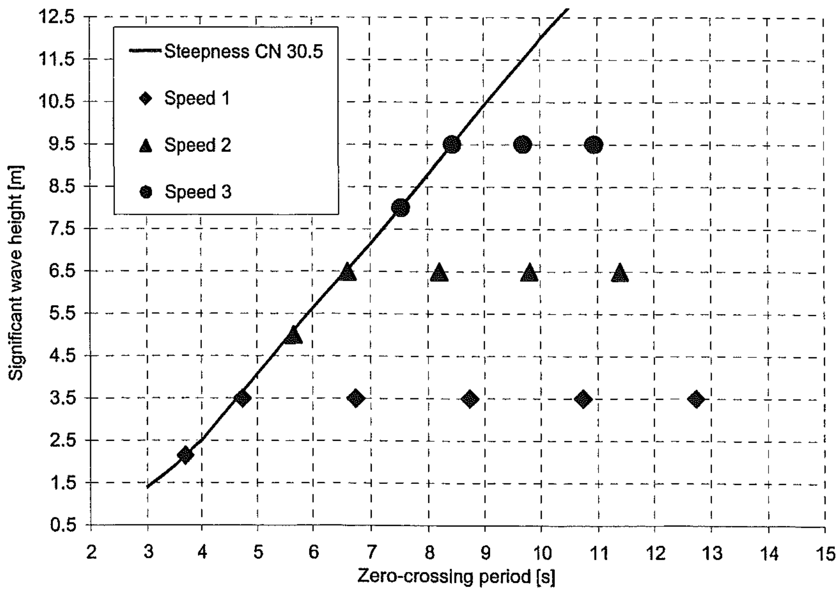

Figure 2 Selected sea states for worst condition identification

In order to select the worst condition from the set of short term simulations it is advised to study the response probability function derived by statistical post processing of the simulations and to estimate the expected extreme in half an hour from those curves. By comparing these values on the basis of wave period one obtains a trend for all three speeds. By doing so one can compensate for inaccuracy due to the short simulation length. If one point falls out of the trend it is most likely due to the short simulation. Although it is more easy to determine the response RMS values and compare these to identify the worst condition it can be misleading. For example hogging bending moment amplitudes decrease and the sagging amplitudes increase with respect to linear amplitudes but the response RMS value remains equal to the linear response RMS value!

Simulation length and expected extreme determination

In order to determine the expected nonlinear extreme in 3 hours from a short term simulation it is advised to conduct a simulation, which is at least longer than those 3 hours. Statistical post-processing of the response time history gives the amplitude exceedance probability distribution as well as the response period. Next the expected extreme can be determined from this curve by interpolation. <u>Extrapolation of the probability curve is to be avoided</u>. If slamming occurs rarely and one does not encounter a slam in a 20 minutes simulation the extreme at a 3 hours exceedance probability level might be underestimated by an extrapolation. Often a mathematical fit is applied to the data and used in subsequent calculations. This fitting can be done in many ways and no preference can be given as to which mathematical probability function to use, as these functions do not reflect the nonlinear physics at hand. Discrete probability curves might show pronounced bends, because of wetdeck slamming for example. It is therefore equally defendable to sketch a line by hand through the data points instead of using a complex mathematical function with a sophisticated fit procedure! The only precondition is that the curve should fit the data well for the purpose it will be used for. If extremes are the subject to study, the tail of the distribution is of key importance, but not when fatigue is the issue. One should therefore always be careful using fitting procedures and visually check if a mathematical distribution is accurate enough. An example of this is shown in Figure 3, taken from Pastoor (2002). The exceedance probability distribution is shown for the midship sagging bending moment amplitudes of a navy frigate. Random irregular model experiments and conditioned irregular experiments were conducted. The latter is described later in the paper. In addition to the experiments the linear result is shown, composed by using the experimentally determined transfer function with the measured wave spectrum of the random irregular tests. Two, often applied, fit function have been used, i.e a Hermite moment fit, see Winterstein (1994) and a Weibull fit. As seen the experimental data show that the sagging bending moments do not increase so much for the lower exceedances. This is mainly because the amount of green water on deck becomes a “reducing factor”, while the bow flare is mild, slamming is very mild as well. When considering the expected extreme in 3 hours the error from the two fitted functions is not large but when we consider the tail of the distribution large errors will be introduced.

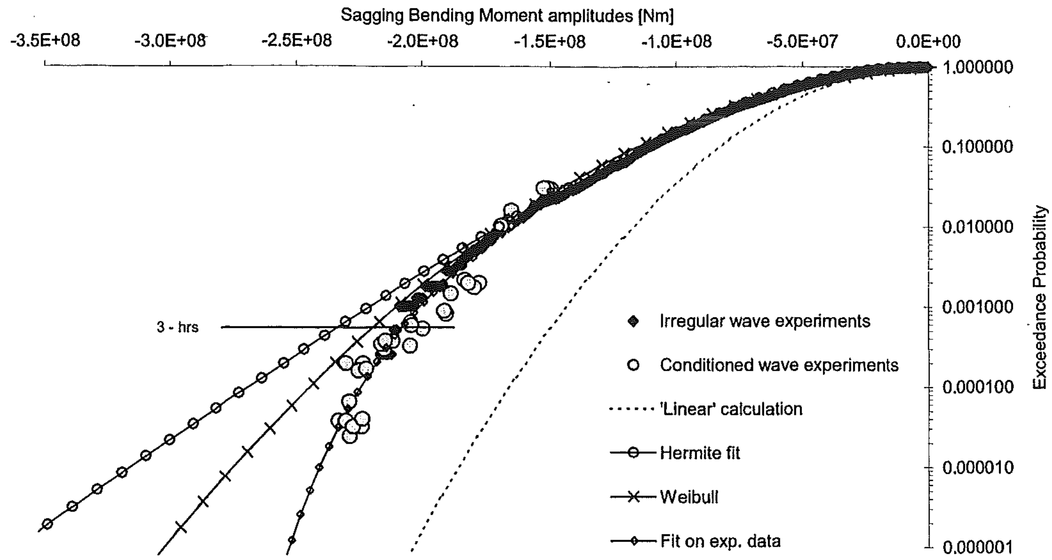

Figure 3 Midship sagging bending moment in a frigate, head waves, Hs=4.3m, Tz=7.4s, 12 knots

3. General nonlinear hydrodynamic analysis

The previous part of the paper was dedicated to direct hydrodynamic analyses of High Speed Light Craft with special attention to the rule requirements for direct analyses. But what are current practices when the vessel is a high speed craft but will not be classed according to the HSLC rules? The DNV classification rules give the possibility of a class notation when direct calculations are conducted. This class notation is called CSA-2 and stands for *Computational Ship Analysis*. The first paragraph gives a short summary of this notation. The rules for this Class notation provide guidance and preconditions how to conduct a direct analysis. Depending on ship type, operation and client's interest the direct analysis can be done in different ways and at different levels of complexity. Concerning nonlinear assessments no straight forward commonly adopted procedure is available. It is therefore that the second paragraph presents a general strategy in order to provide some guidance how a nonlinear hydrodynamic analysis can be conducted. The scheme and it's different levels of complexity reflect the present capabilities at DNV to provide direct nonlinear analyses as consultancy services for the marine industry. A summary is given of the nonlinear ship motion and load program DNV-WASIM, with special emphasis on the integrated slamming procedure. An example of this finalises this part.

3.1 DNV class notation CSA-2 – Computational Ship Analysis

The procedure for CSA-2 is using a selected set of loading conditions defined in the vessels loading manual as basis for direct hydrodynamic analysis and finite element response analysis. The strength analysis is then to be carried out for the most extreme loading situation checking local structural areas as well as the complete hull girder capacity. Fatigue analyses of both longitudinal and transverse structural elements are to be carried out. The extreme loads are to be calculated for a 20-year return period using wave scatter diagrams for the North Atlantic. This will serve as basis for the wave load analysis with respect to the calculation of hull girder and main girder system stress response as well as hull girder capacity analysis. Fatigue loads are to be based on 10^{-4} probability of exceedance. However, other probability levels may be accepted provided a consistent direct analysis procedure has been used. Wave scatter diagrams for a world-wide trading pattern, will serve as basis for the fatigue analysis, unless a more severe fatigue environment has been specified. The hull structural scantlings are however not to be less than determined by the main class requirements.

3.2 A general strategy for nonlinear hydrodynamic analyses

In the following a general strategy is presented to perform nonlinear hydrodynamic analyses. Note that this scheme is a general strategy and is not specified in the rules or classification notes but can serve as basis for a CSA-2 analysis. The approach presented here describes hydrodynamic analyses conducted in order to establish nonlinear design loads based on a 20 year return period and a scatter diagram approach. Thus no speed/sea state restriction is specified. Figure 4 shows this general strategy for direct nonlinear hydrodynamic analyses, which is discussed subsequently in more detail.

The first step in the assessment procedure is to analyse the vessel type, it's operational conditions and environmental conditions. Based on this and past experience critical responses are to be identified. Or they are simply specified; e.g. hull girder bending moment, shear force and torsional moment at prescribed hull girder cuts.

Advanced nonlinear hydrodynamic programs are time consuming thus full scatterdiagram assessments are not possible, especially not when it has to be done for different headings and loading conditions. Of key importance is thus to reduce the amount of calculations by identifying the most critical sea states with respect to the responses under investigation. Two paths are outlined and are very much in line with the procedure for design sea state identification for HSLC. Either a linear response model is used or a series of short nonlinear simulations are used. The latter is rather easy to use as we can utilise the 20 years contour of significant wave height and period. Selecting for example 8 combinations of Hs and Tz on the contour and perform 30 minutes simulations is enough to identify the worst combination which can serve as design sea state. Again it is advised to estimate the expected extreme in 30 minutes and use that value for worst condition identification. When using the linear model to identify critical sea states the *Coefficient-of-Contribution* method is applied, see Larsen and Passano (1990). A short explanation is given. First a longterm analysis is carried out to establish the long term response distribution. From this distribution the expected lifetime extreme is obtained. Next, every sea state within the scatter diagram is analysed to determine it's contribution to the exceedance probability of that lifetime expected extreme. This contribution is defined in terms of the following coefficient.

$$CoC(H_s,T_z,\mu)=\frac{Q_{ST}\left(R_{lifetime}\middle|H_s,T_z,\mu\right)\cdot p(H_s,T_z)\cdot p(\mu)\cdot w_{H_s,T_z,\mu}}{Q_{LT}\left(R_{lifetime}\right)} \tag{4}$$

where

$Q(\ )$ is exceedance probability function

$p(H_s,T_z)$ is the sea state probability

$p(\mu)$ is the heading probability

$w_{H_s,T_z,\mu}$ is weighfactor : relative number of amplitudes within each sea state

In other words this coefficient indicates the likelihood that the lifetime expected extreme occurs in that sea state. With this approach the response behaviour in a sea state and the nominal duration of that sea state for the lifetime of the ship are accounted for.

Having identified critical sea state(s) two possibilities are used presently. One is straight forward, namely random irregular simulations, which is equal to the HSLC direct analysis approach. The other method uses conditioned irregular simulations, which is named MLER (Most Likely Extreme Response).

Random irregular simulation

A random irregular simulation is conducted by generating discrete wave components from the wave spectrum of the identified design sea state and simulate that with a nonlinear program. This approach is very similar to the simulations according to the HSLC rules. According to the HSLC rules short term analyses are carried out to determine the expected extreme in 3 hours. Because the vessel might encounter this sea state much more often during the lifetime of the vessel than the 3 hours of the simulation a correction is applied to the expected extreme. Likewise we have to correct the determined nonlinear extreme values here as well in order to be representative for a 20 years lifetime. The CSA-2 classification note does not provide requirements or guidance as the HSLC rules do. Different options are possible to define the 20 years value.

- When using the CoC method one can simulate a series of sea states with decreasing criticality. By estimating the nonlinear extreme cumulatively one can estimate the longterm value by extrapolation.
- Estimate the duration for the identified design sea state in order to encounter the lifetime linear extreme as expected extreme. By simulating the design sea state with the nonlinear program with that determined duration the nonlinear extreme representing the 20 years lifetime is obtained. The problem might be that the duration is long and thus impractical. In that case one has to reply on extrapolation.
- Most easy is the case when a design sea state on the 20 years contour is used. The short term nonlinear extreme can then serve as design value.

Different levels of complexity are possible when post-processing random irregular simulations.

1. Statistical post-processing of the responses gives probability distributions from which expected extremes are to be determined.
2. Applying load transfer of the hydrodynamic pressures to a FE model. An important aspect is to select appropriate extreme cases from the irregular simulation.

Additionally a FEM whipping analysis can be conducted if slamming has been incorporated in the irregular simulation. By selecting slamming incidences from the irregular simulation design impact loading for the whipping analysis can be composed. The results from the time domain analysis can be superposed to the results of the two options described above to establish total extreme responses. The slamming induced load can increase significantly. Of importance is to take care of the time incidence the slam occurs. Considering vertical bending moment the slamming typically occurs somewhat earlier than the maximum wave induced bending moment. If slamming is accounted for in the nonlinear simulations the probability distribution of the load can usually not be used directly as the program calculates for a rigid body and thus slamming loads induces large sectional loads, whereas the hull reacts in an elastic way to those high frequency excitations. Filtering of the time series is an appropriate way to correct for this. It is important that only the slamming induced load effects are filtered out and not the nonlinear wave induced contributions. Typically nonlinear wave induced loads can be of second and third order. Thus filtering out high frequency components should be done for frequencies above three times the highest encounter frequency.

Conditioned irregular simulation – MLER (Most Likely Extreme Response)

This method conditions an irregular incident wave such that at a prescribed timestep the expected linear extreme occurs. Simulating this short incident wave with a nonlinear program gives at the same timestep the corresponding nonlinear extreme. The basic assumption is thus that the nonlinear extremes more-or-less coincide with the linear extremes. In other words the linear model should be a good identifier of extreme events. But how is the incident wave conditioned? Of course many wave profiles are possible, which induce the same linear extreme at the same timestep. But if this linear extreme is encountered a large number of times we can determine the average profile around that extreme. A good model for this most likely response profile is the response autocorrelation function. Using the response time sequence together with the linear transfer function the incident wave causing that response profile can be determined. This wave is then used in the short nonlinear simulation. Advantages of this method are,

- It is fast, typically 30 to 80 seconds nonlinear simulation is enough
- The whole wave spectrum and transfer function are used
- Inswing dynamics are accounted for

In case of a conditioned irregular simulation one explicitly calculates a nonlinear extreme corresponding to the lifetime expected linear extreme. Accordingly one does not have to apply a correction and can use the resulting nonlinear extreme directly.
The conditioned irregular simulation is considered an improvement over the regular design wave approach, which is used often. For that method the linear extreme is divided by the peak of the transfer function to obtain a wave amplitude. This wave amplitude is then simulated with the transfer function peak period as a regular wave to determine a nonlinear correction factor for the linear extreme. In case of transfer functions with a sharp clear peak the regular design wave gives satisfactory results but in case of wide response functions or double peaked transfer functions the regular design wave can be unreliable, see for instance Adegeest *et al* (1998) and Pastoor (2002).
Different levels of post-processing of the conditioned simulations are possible, equally when conducting random irregular simulations. Direct use of the MLER calculation gives the desired expected nonlinear extreme. Load transfer of the hydrodynamic pressures to a FE model gives a more detailed response behaviour and these two options can be extended by incorporating a whipping analysis using the slamming induced excitation from the MLER simulation.
When applying the conditioned irregular simulation option an extra possibility is available, namely to conduct a series of conditioned irregular simulations for different linear extremes all with known exceedance probabilities. This procedure is called EMLER, Extended Most Likely Extreme Response. Performing thus a series of MLER calculations a series of nonlinear extremes are obtained, which correspond to the set of linear extremes and their exceedance probabilities. This means that the full nonlinear extreme probability distribution is obtained by only simulating a small number of short nonlinear irregular simulations, which is an important achievement with respect to the computational time.

Extreme response evaluation

Having established extreme response values they should be evaluated by comparison with the acceptance criteria applicable. In case the EMLER approach is followed a reliability assessment is possible, if the capacity is available in terms of a probability distribution.

For both paths in the scheme it is emphasised that one is not confined to basic response types. Any transfer function can be used. For example if the stress in a bottom longitudinal at the connection with a transverse web is of interest a simple transfer function can be established using basic response parameters, like the vertical bending, horizontal bending and local hydrodynamic pressure,

$$H_{\sigma}(\omega)=H_{hwbm}(\omega)\left[\frac{y}{I_{zz}}\right]-H_{vwbm}(\omega)\left[\frac{z-e_z}{I_{yy}}\right]-H_p(\omega)\left[\frac{r_p s l_e^2}{12Z}\right] \tag{5}$$

After the nonlinear calculation a FEM analysis can be applied in order to get more accurate estimates of the stress instead of such a simplified formula.

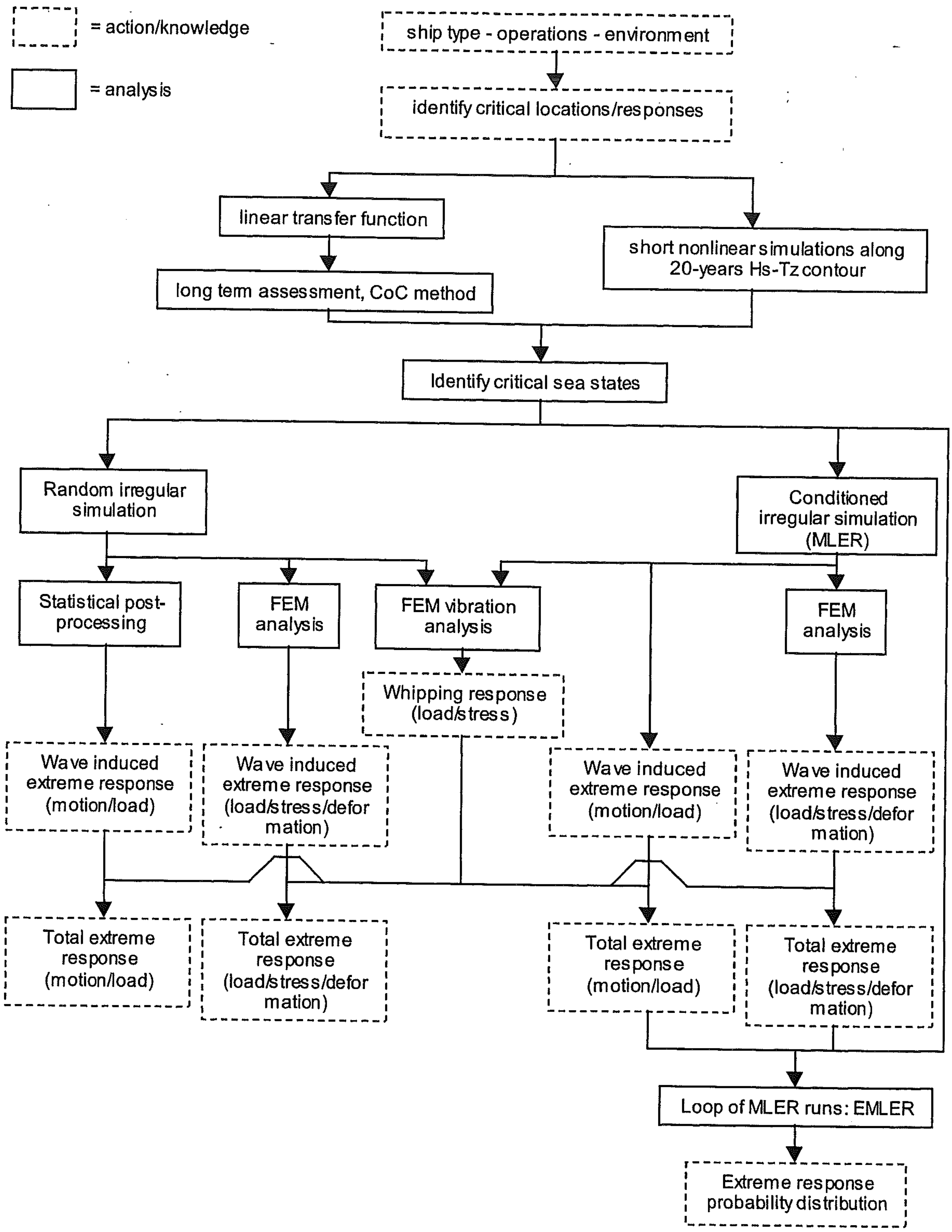

Figure 4 General procedure for nonlinear hydrodynamic analyses

3.3 WASIM – DNV's nonlinear hydrodynamic program

In the past decade nonlinear ship hydrodynamic programs have developed rapidly, supported by increasing computer capabilities. From the mid-eighties to the mid-nineties DNV was involved in the development of the SWAN program at MIT. Since 1996 DNV is further developing the program internally and is now named WASIM. It is one of the most advanced nonlinear hydrodynamic programs and is made robust and applicable for many different ship types and types of analyses like,

- Extreme response analyses,
- Fatigue analyses,
- Operability studies,
- Bow and stern impact studies

Because the program accounts properly for 3 dimensionality, forward speed, transom stern flow, and bow flare it is well suited for the analysis of high performance vessels. Of particular interest is the integrated slamming module, which gives the possibility to account for slamming induced pressures in long irregular simulations without significant increased computational costs. Below some details of the WASIM program are given with special attention to the integration of slamming.

WASIM – nonlinear hydrodynamic program

The WASIM program is a 3-D potential flow program solving the motion equations in 6 degrees of freedom in the time domain with an autopilot model keeping the vessel on course.
The program solves the flow problem based on a boundary element approach. Panels are distributed over the hull and the still water surface. The fluid flow problem is split in a steady and unsteady part. The steady part solves first the double body flow, which is used as base flow around the hull. Next the steady wave potential is solved for with a linearisation around the base flow and a linearised free surface boundary condition. This steady analysis gives a prediction of the trim and sinkage of the vessel and secondly calculates the interaction of the base flow with the unsteady flow, in terms of the so-called *m*-terms.
For the unsteady problem the hydrodynamic forces are split into the common division of radiation, diffraction, Froude-Krylov and restoring forces. The first two components are still treated linear in WASIM but the last two are calculated nonlinearly by integrating the incident wave pressure over the instantaneous wetted surface of the hull defined by the instantaneous position and orientation of the vessel. In addition (passive) fin forces and viscous roll damping forces can be added. The incident waves are modelled according to linear wave theory.
For transom stern ships at forward speed a wake sheet is applied to force the flow such that it detaches at the transom stern edge.

Slamming integration in the WASIM program

Slamming is an important effect for high speed ships, especially if they have significant bow flare. Besides high local pressures at the bow (or flat stern configuration), large vertical accelerations occur and global hull girder loads can increase significantly. Consequently it is important to take this phenomenon into account. The procedure utilised in the WASIM program is based on a pre-process slamming analysis with a 2 dimensional boundary element program based on the CRSLAM program, Skeie *et al* (1996). This program solves the impact problem by a boundary value problem. It is not capable to handle knuckle or flow detachment. The results of this pre-process calculation are used in WASIM to calculate impact pressures during slamming events.

The boundary value problem for a slamming event is formulated such that the potential is splitted as,

$$\phi(\bar{x},t)=V_R(t)\cdot\Psi(\bar{x},h) \qquad (6)$$
$$V_R=\text{relative velocity}$$

This is possible as the control boundary is solely described by the penetration depth, h, and with $\phi = 0$ on the free surface. By doing so it is possible to describe the impact pressure as a function of a time-invariant potential solution and a pressure coefficient, where both are only functions of the position on the hull and the immersion depth.

$$p(\bar{x},t) = -\rho \dot{V}_R \cdot \Psi(\bar{x},h) + \frac{1}{2}\rho C_s(\bar{x},h) \cdot V_R^2 \qquad (7)$$

In addition the pre-process calculation determines the rate of change of the immersion depth, which is linearly dependent on the relative velocity. This information is used in the WASIM simulation to update the immersion depth. The relevant part of the ship is divided into strips. For every strip a slamming analysis is conducted for unit relative velocity at different immersions. By storing the results in a database these can be utilised in the WASIM simulation to calculate impact pressures on the hull by transferring the 2 dimensional pressure results to the panels of the 3 dimensional hull. As the time steps and length scales as used in the slamming analysis are much smaller than in the WASIM simulation we have to take account for this by time averaging.

As said previously WASIM solves the rigid body problem. A slamming event results thus in large sectional loads. Therefore these cannot be used directly. An example is shown in the figure below, where the result is filtered. The resulting differences in the probability functions are large as seen in Figure 6. The great benefit of the integrated slamming is to get more realistic motion behaviour. Secondly the results can be used to define realistic load cases for whipping analysis and use that to correct the amplitude distribution of the filtered data in Figure 6.

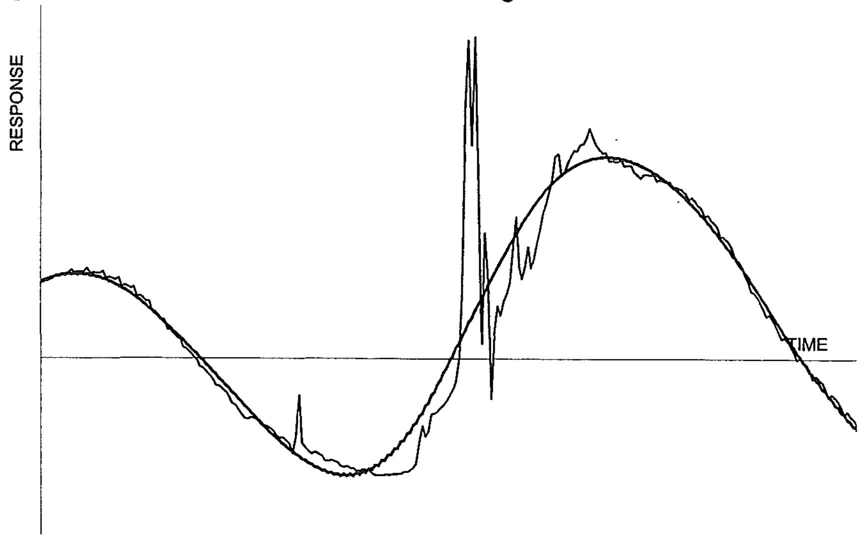

Figure 5 Raw and filtered bending moment response with a slamming load

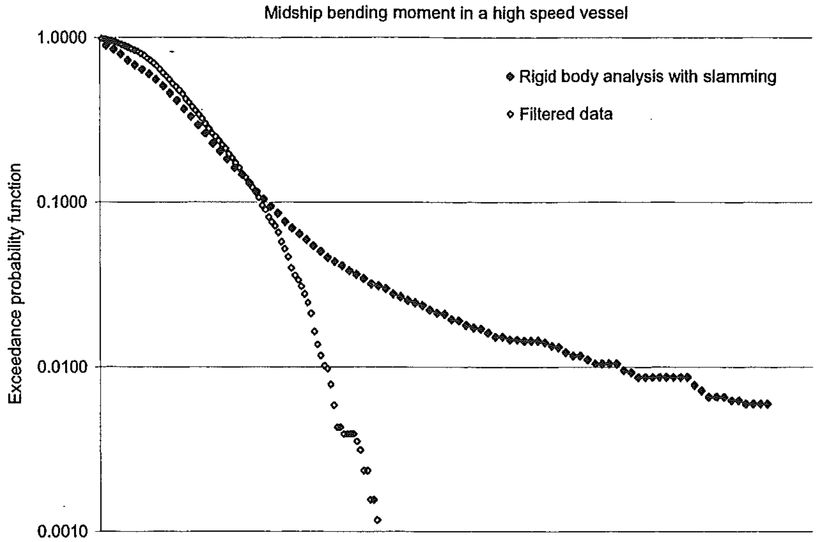

Figure 6 Midship sagging bending moment with raw rigid body slamming and filtered response

4. Conclusions and discussion

A general overview is given of nonlinear hydrodynamic analyses to determine design loads for HSC, within the context of DNV classification and consultancy services at DNV. The classification requirements for direct analysis of HSLC have been summarised with emphasis on the hydrodynamics. The practical application or nonlinear hydrodynamic simulations is discussed based on these rule requirements. How to identify design conditions, how long to conduct the simulations and how to derive expected extremes is described. A summary has been given of the requirements for the CSA-2 class notation. In addition to that a general strategy is presented to perform nonlinear hydrodynamic assessments to determine lifetime design values based on a scatter diagram approach. The DNV WASIM program is described, which is used to conduct nonlinear hydrodynamic analyses, with special attention to the integration of slamming in the simulations.

Discussion

An alternative analysis procedure to determine design loads, would be the combined application of speed restrictions depending on sea state and a scatter diagram. Such an approach is somewhat more complicated than the two procedures outlined in this paper, i.e.

- Short term analysis based on speed/sea state curve with a safety factor to correct for longterm and wave observation errors by the crew.
- Long term analysis based on a scatter diagram approach without speed restrictions

But such an alternative approach might be more accurate as it combines the realistic aspects of the two approaches presented here, i.e. speed restrictions and a scatter diagram. An important difficulty will be the identification of critical sea states especially if the linear model is not appropriate for that purposes. As we can't restrict a nonlinear identification analysis with short simulations to the 20 years contour only. We need to assess more sea states in that case.

The conditioned irregular simulations, the MLER method, have clear advantages over the random irregular simulations and regular wave simulations but the application should be verified for more cases in order to get more experience as to the applicability range concerning the accuracy. Presently these conditioned simulations are defined such that it conditions a single response, but it is possible to condition on two responses as well. For example if design slamming pressures on the bow are required we might have to condition slamming, where the conditioning is to be done based on the relative motion and velocity. It is in this case not possible to condition directly on the pressure, as we do not have a linear transfer function available. In that case the most likely response profile can be determined by prescribing the relative wave elevation equal to the draft and prescribing a relative velocity. Using the statistical properties of relative motion and velocity a conditioned simulation can be defined resulting in an expected impact pressure.

Accurate predictions of motion and loads depend very much on the accuracy of the applied tool. The WASIM tool has developed consistently over the years and will be in the future. Better capturing the effects of green water on the loads is an important aspect. Secondly the integration of the slamming is presently done by using a 2D method and cannot account for water entry cases when the vessel has a heel angle.

The EMLER approach, whereby the nonlinear extreme probability function is obtained, can be used in a reliability assessment when combining it with the capacity probability distribution. It is this approach which is most tempting to perform but is also the most complicated. Application to gain experience, variational studies and improved numerical tools will in the future support this type of analysis together with an increasing need as risk and safety become more and more integrated parts within design and engineering projects. Accordingly the ship hydrodynamic and structural disciplines are to develop further in order to feed this need together with the development of rational strategies integrating the various disciplines in order to improve the safe design of ships. To illustrate the importance of a risk based approach the results from Figure 3 are discussed a bit further. As shown in that figure the tail of the amplitude distributions are quite different between the experiments, linear calculations and fitted functions. It is this tail that is used when calculating the extreme probability density function, see Figure 7. The overlap of this function with the density function of the hull girder capacity will define the reliability, which will be quite different as seen from this figure. To illustrate this the expected maximum sagging bending moment in 1 out of 10.000 ships is determined as to model the limiting structural capacity. These values are compared with the expected 3-hour extremes. Both results for the different methods are shown in Figure 8. The linear value for both the 3 hours extreme and the 10.000 ships maximum value are normalised. For the conditioned irregular experiments the increase is smaller for the maximum in 10.000 ships than for the 1-hour extreme. The Weibull fit presents a larger increase and the Hermite model shows a much larger increase.

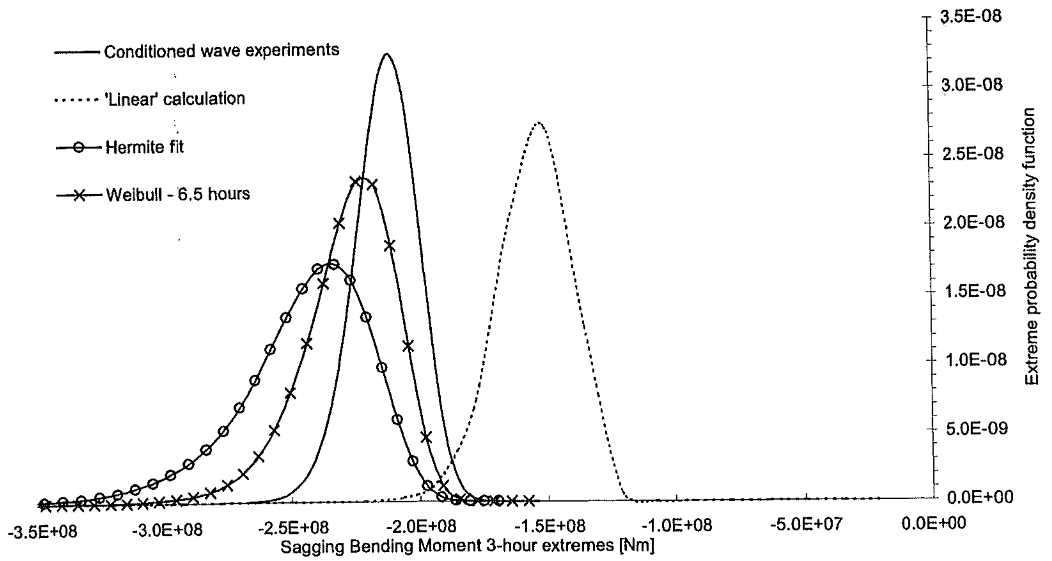

Figure 7 3 hours sagging extreme probability function

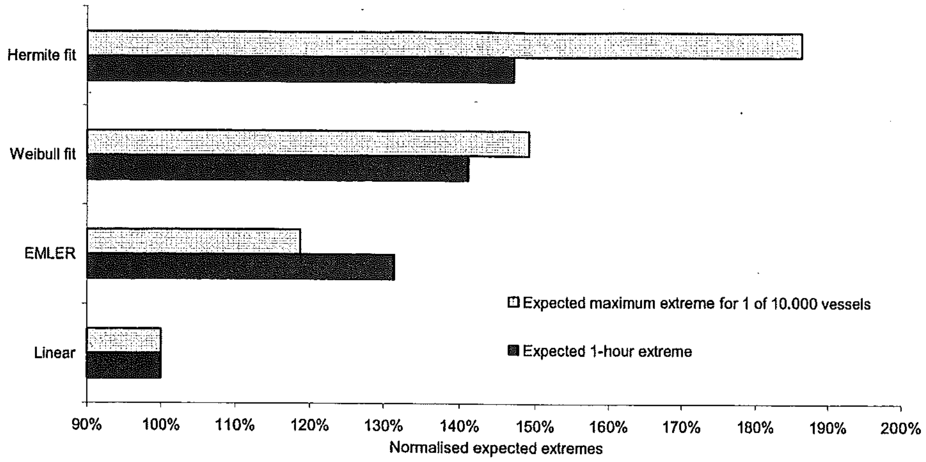

Figure 8 Expected 3 hour extreme and maximum expected extreme for 10.000 ships

5. References

Adegeest, L.J.M., Braathen, A., Vada, T. (1998) 'Evaluation of methods for estimation of extreme non-linear ship responses based on numerical simulations and model tests', 21st Symposium on Naval Hydrodynamics, Office of Naval Research.

DNV (2001) 'Rules for Classification of High Speed, Light Craft and Naval Surface Craft', Det Norske Veritas, Norway.

DNV(2002) 'Rules for Classification of Ships', Det Norske Veritas, Norway.

DNV (2000) 'Environmental Conditions and Environmental Loads', Classification Notes 30.5, Det Norske Veritas, Norway.

Larsen, C.M., Passano, E. (1990)' Extreme response estimation for marine risers', 14th WEGEMT School, Trondheim.

Pastoor, L.W. (2002) 'On the assessment of nonlinear ship motions and loads', Ph.D. thesis, Delft University of Technology, Delft, the Netherlands.

Skeie, G, Kvålsvold, J., Nestegård, A. (1996) 'Computer program CRSLAM for prediction of slamming pressures', DNV report no. 96-2039.

Winterstein, S.R., Lange, C.H., Kumar, S. (1994) 'FITTING: A subroutine to fit four moment probability distributions to data', Report RMS-14, Reliability of Marine Structures Program, Civil Eng. Dep., Stanford University.